COPPER(II), NICKEL(II), COBALT(II), AND IRON(II) COMPLEXES OF CONJUGATED ORGANIC LIGANDS AS POTENTIAL DYE-SENSITISED SOLAR CELL MATERIALS

ANITA MARLINA

FACULTY OF SCIENCE
UNIVERSITY OF MALAYA
KUALA LUMPUR

2015

COPPER(II), NICKEL(II), COBALT(II), AND IRON(II) COMPLEXES OF CONJUGATED ORGANIC LIGANDS AS POTENTIAL DYE-SENSITISED SOLAR CELL MATERIALS

ANITA MARLINA

DISSERTATION SUBMITTED IN FULFILMENT OF THE REQUIREMENT FOR THE DEGREE OF DOCTOR OF PHILOSOPHY

FACULTY OF SCIENCE
UNIVERSITY OF MALAYA
KUALA LUMPUR

2015

UNIVERSITI MALAYA

ORIGINAL LITERARY WORK DECLARATION

Name of Candidate: ANITA MARLINA

Registration/Matric No: SHC110072

Name of Degree: DOCTOR OF PHILOSOPHY

Title of Project Paper/Research Report/Dissertation/Thesis ("this Work"):

COPPER(II), NICKEL(II), COBALT(II), AND IRON(II) COMPLEXES OF CONJUGATED ORGANIC LIGANDS AS POTENTIAL DYE-SENSITISED SOLAR CELL MATERIALS

Field of Study:

I do solemnly and sincerely declare that:

(1) I am the sole author/writer of this Work;
(2) This Work is original;
(3) Any use of any work in which copyright exists was done by way of fair dealing and for permitted purposes and any excerpt or extract from, or reference to or reproduction of any copyright work has been disclosed expressly and sufficiently and the title of the Work and its authorship have been acknowledged in this Work;
(4) I do not have any actual knowledge nor do I ought reasonably to know that the making of this work constitutes an infringement of any copyright work;
(5) I hereby assign all and every rights in the copyright to this Work to the University of Malaya ("UM"), who henceforth shall be owner of the copyright in this Work and that any reproduction or use in any form or by any means whatsoever is prohibited without the written consent of UM having been first had and obtained;
(6) I am fully aware that if in the course of making this Work I have infringed any copyright whether intentionally or otherwise, I may be subject to legal action or any other action as may be determined by UM.

Candidate's Signature Date: 11 June 2015

Subscribed and solemnly declared before,

Witness's Signature Date: 11 June 2015

Name: ASSOC. PROF. DR. NORBANI ABDULLAH

Designation:

ACKNOWLEDGEMENT

Foremost, Alhamdulillah and thanks Allah S.W.T. with all gracious and merciful for giving me the strength and ability to complete this research successfully. I would like to express my sincere gratitude to my supervisor, Assoc. Prof. Dr. Norbani Abdullah, for continuous support, patience, motivation, enthusiasm, and immense knowledge.

I also wish to record my thanks to my colleagues at the Inorganic Chemistry Research Laboratory for their friendship and kindness through the years it take for me to complete this research, and to all staff in the Chemistry Department as well as in Faculty of Science, University of Malaya.

This project was financially supported by the scholarship from the Department of Higher Education Malaysia (Malaysia International Scholarship 2012), the High Impact Research Grant (UM.C/625/1/HIR/MOHE/05) from the Fundamental Science of Self Assembly (FS2A) research group headed by Prof. Dr Rauzah Hashim, and Postgraduate Research Grant (PV056/2012A).

A special word of thanks also goes to my family, particularly my mother, my husband and my children (Jason and Kevin) for their love, continuous support and encouragement throughout my life.

ABSTRACT

The primary aim of this research was to synthesize and characterize metals(II) complexes of conjugated organic ligands as potential dye-sensitised solar cell materials. The ligands were synthesized from the reactions of 2,6-diamino-4-phenyl-1,3,5-triazine with pyrrole-2-carboxaldehyde (*H_2L1*), 2,5-thiophenedicarboxaldehyde (*H_2L2*), 2,5-thiophenedicarboxylic acid (*H_2L3*), and acetylenedicarboxylic acid (*H_2L4*). These complexes were formed from the reactions of the ligands with metal(II) ethanoates ($[M_2(CH_3COO)_4]$ and metal(II) hexadecanoates ($[M(CH_3(CH_2)_{14}COO)_4]$), where M = Cu(II), Ni(II), Co(II), and Fe(II).

A total of 32 complexes were successfully synthesized and fully characterised. The structures of these complexes were deduced from CHN microanalyses, FTIR spectroscopy and UV-vis spectroscopy. Their magnetic properties were determined at room temperature by the Gouy method, their optical bandgaps were deduced by electronic spectroscopy (UV- visible and fluorescence spectroscopy), the lifetimes of their excited complexes were determined by fluorescence spectroscopy, and finally their thermal and mesomorphic properties by thermogravimetry (TG), differential scanning calorimetry (DSC), and polarising optical microscopy (POM).

$\{[Ni_2(CH_3(CH_2)_{14}COO)_4(L4)]\}_n$ was diamagnetic, while all other complexes were paramagnetic. The geometries for all complexes depend on the metal(II) ion, namely octahedral, square pyramidal and square planar. The decomposition temperatures of all complexes were in the range 142 °C – 255 °C. The optical bandgaps of these complexes obtained from the absorption spectroscopy were in the range of 3.4 eV – 3.8 eV, while the values obtained from the emission spectroscopy were in the range of 1.7 eV – 2.1 eV. The lifetimes of the excited complexes were in the range of 2.4 ns – 3.4 ns. Complexes with ligands *L3* and *L4* exhibited mesomorphisms.

ABSTRAK

Tujuan utama penyelidikan ini adalah untuk mensintesis dan mencirikan kompleks logam(II) dengan ligan organik terkonjugat sebagai bahan berpotensi sel suria terpekakan pewarna. Ligan-ligan disintesiskan daripada tindak balas 2,6-diamino-4-fenil-1,3,5-triazina dengan pirol-2-karboksaldehid (*H_2L1*), 2,5-tiofenadikarboksaldehid (*L2*), asid 2,5-tiofenadikarboksilik (*L3*), dan asid asetilenadikarboksilik (*L4*). Kompleks terbentuk daripada tindak balas ligan-ligan ini dengan logam(II) etanoat ($M_2(CH_3COO)_4$] dan logam(II) heksadekanoat ([$M_2(CH_3(CH_2)_{14}COO)_4$]), dengan M = Cu(II), Ni(II), Co(II), dan Fe(II). Sejumlah 32 kompleks berjaya disintesiskan dan dicirikan sepenuhnya.

Struktur kompleks dideduksikan daripada mikroanalisis CHN, spektrometri FTIR, dan spektroskopi UV-vis. Sifat magnet ditentukan pada suhu bilik melalui kaedah Gouy, jalur optik dideduksikan daripada spektroskopi elektron (spektroskopi UV-vis dan pendarfluor), tempoh hayat kompleks teruja ditentukan daripada spektroskopi pendarfluor, dan akhir sekali sifat terma dan mesomorfik melalui termogravimetri (TG), kalorimeter pembeza imbasan (DSC), dan mikroskopi pengutuban optik (POM).

{[$Ni_2(CH_3(CH_2)_{14}COO)_4$(*L4*)]}$_n$ adalah diamagnetik, manakala semua kompleks lain adalah paramagnetik. Geometri untuk semua kompleks bergantung pada ion logam(II), iaitu sama ada oktahedral, piramid segiempat, dan sesatah segiempat. Suhu penguraian kompleks ini adalah dalam julat 142 °C – 255 °C. Jalur optik kompleks ini, yang ditentukan daripada spektroskopi penyerapan, adalah dalam julat 3.4 eV – 3.8 eV, manakala nilai daripada spektroskopi penyerapan adalah dalam julat 1.7 eV – 2.1 eV. Tempoh hayat kompleks teruja adalah dalam julat 2.4 ns – 3.4 ns. Kompleks dengan ligan *L3* dan *L4* menunjukkan mesomorfisme.

TABLE OF CONTENTS

LIST OF FIGURES

LIST OF TABLES

LIST OF SCHEMES

CHAPTER 1 INTRODUCTION

Scientists have been interested for a long time in harvesting of sunlight energy either to drive useful chemical transformations or to convert the light directly into electrical energy. Two publications in Nature by Grätzel and coworkers have a dramatic impact on the focus of research for scientists interested in photochemical conversion and storage of solar energy [1, 2]. Dye-sensitized solar cells (DSSC) are an option for a low-cost production of solar cells [3]. Additionally, DSSC is the outcome of the cross fertilization concept used in photovoltaic solar cells (PV) and nanoscience, nanotechnology, and light-induced electron transfer reactions.

Transition metal complexes with low lying excited states are finding increasing use as photosensitizers. Most work focussed on polypyridine complexes and metalloporphyrins. The low-lying metal-to-ligand charge transfer (MLCT) and ligand-centered (π–π*) excited states of these complexes are fairly long-lived to participate in electron transfer processes. The emissive nature and high quantum yields allow development of devices [4]. Current DSSC materials were polypyridyl ruthenium(II) complexes. However, these materials have limitations in terms of cost and toxicity. As alternatives, Suzanne Ferrere *et al*., focussed on cheaper and less toxic Fe(II) complexes [5-7].

The photovoltaic effect have been demonstrated with liquid crystal solar cells by Hirotake *et al.* [8, 9]. They reported that in a nematic liquid crystal cell, this effect was induced by the difference of mobility between the positive and negative ions. Nematic liquid crystal represent an attractive new approach to organic photovoltaic cells. Their self-assembling properties allow a new way to generate a vertically separated distributed interface between electron donating and accepting materials for improved

device efficiency. The materials are also solution processable, and compatible with roll-to-roll processing for large-scale manufacture [10].

Hence, this research project was focussed on the bandgap (optical and electrochemical) and mesomorphisms of copper(II), nickel(II), cobalt(II), and iron(II) complexes with π-conjugated ligands derived from the reactions between 2,4-diamino-6-phenyl-1,3,5-triazine with pyrrole-2-carboxaldehyde, 2,5-thiophenedicarboxaldehyde, 2,5-thiophenedicarboxylic acid and acetylenedicarboxylic acid. These complexes are expected to have better photosensitization (especially absorption of lower photonic energy) and redox properties compared to non-conjugated complexes.

A total of thirty-two (32) complexes were prepared by step-wise syntheses. These materials were characterised by elemental analyses, Fourier transform infrared spectroscopy, UV-visible spectroscopy, fluorescence spectroscopy, cyclic voltammetry, room-temperature magnetic susceptibility by the Gouy method, thermogravimetry, differential scanning calorimetry and optical polarization microscopy. The findings of this research were accepted for publication in two ISI journals, and were presented at national and international conferences (**Appendix**), as listed below:

1. Norbani Abdullah, Mohamed Hamid Elsheikh, Nik Muhd Jazli Nik Ibrahim, Suhana Mohd Said, Mohd Faizul Mohd Sabri, H.H. Masjuki and Anita Marlina, *Magnetic, Thermal, Mesomorphic and Thermoelectric Properties of Mononuclear, Dimeric and Polymeric Iron(II) Complexes with Conjugated Ligands*, RSC advances, 2015, 5, p.50999-51007. DOI: 10.1039/C5RA07100C.
2. Norbani Abdullah, Anita Marlina, Abdul Rahman Nordin, Suhana Mohd Said, Muhamad Faris Roslan and Afiq Azil, *Photophysical and Electrochemical Studies of Multinuclear Complexes of Iron(II) with Acetate and Extended Conjugated N-Donor Ligands*, The Scientific World Journal, 2015, Article ID 860537. http://dx.doi.org/10.1155/2015/860537

3. Norbani Abdullah, Afiq Azil, Anita Marlina and Nur Linahafizza M. Noor, *Magnetic, Photophysical and Thermal Properties of Complexes of Iron(II) with Structurally Different Schiff Bases*, Asian Journal of Chemistry, 2015, Vol. 27 (7), p.2359-2364. DOI:10.14233/ajchem.2015.17829.
4. Anita Marlina, Norbani Abdullah, *Synthesis And Characterisation Of Copper(II) Complexes Of Conjugated Schiff Bases As Artificial Photosynthetic Materials*, International Conference Ionic Liquid 2013, 11-13 December 2013, Langkawi, Kedah. (Oral)
5. Anita Marlina, Norbani Abdullah, Nur Linahafizza Mohd Noor, and Afiq Azil (2013) *Thermal studies of iron(II) Schiff base complexes*, Joint Malaysia-UK Symposium on Inorganic Chemistry 2013, 5 Dec 2013, Universiti Malaya, Kuala Lumpur. (Poster)
6. Anita Marlina and Norbani Abdullah, *Synthesis And Characterisation of Nickel(II) Complex of A Conjugated Schiff Base as Artificial Photosynthetic Material: $[Ni_2(C_{19}H_{13}N_7)_2(CH_3COO)_2].2CH_3COOH$),* 4th Penang International Conference for Young Chemists 2013 (ICYC 2013), 30 Jan 2013– 1 Feb 2013, Penang. (Oral)
7. Anita Marlina, Mumtazah Maridi, Lailatun Nazirah Ozair, and Norbani Abdullah, *Low Band-Gap Photovoltaic Materials*, Fundamental Sciences of Self-Assembly Seminar 2012 (FSSA 2012) 28 February 2012, University Malaya, Kuala Lumpur. (Poster)
8. Anita Marlina, Mumtazah Maridi, Lailatun Nazirah Ozair, Norbani Abdullah, *Low Band-Gap Photovoltaic Materials*, NUS-UM-CU Trilateral Mini Symposium, 15 December 2011, NUS, Singapore. (Poster)
9. Anita Marlina, Norbani Abdullah, *Synthesis And Characterisation Of Copper(II) Complex As Low Band-Gap Photovoltaic Material*, 24th Regional Symposium of

Malaysian Analytical Sciences (SKAM-24), 21-23 November 2011, Langkawi, Kedah. (oral)

This thesis contains five chapters. **Chapter 1** introduces the objective of the research, the complexes prepared, the instrumental techniques involved, and lists the publications of the research findings. **Chapter 2** presents the theories and literature reviews relevant to the research, namely photovoltaic technologies, dye-sensitized solar cell, coordination polymer, and liquid crystal. **Chapter 3** presents the syntheses of the complexes and the instrumental techniques used to characterise them. **Chapter 4** presents the results and discussions, and finally **Chapter 5** presents the conclusions and suggestions for future works. A list of references is included at the end of each chapter, and appendices at the end of the thesis.

References

[1] Fujishima, A., Honda, K., *Nature*, 238 (**1972**) 37-38.

[2] O'Regan, B., Grätzel, M., *Nature*, 353 (**1991**) 737-740.

[3] Grätzel, M., *Nature*, 403 (**2000**), 363-363.

[4] Kalyanasundaram, K., Grätzel, M., *Coordination Chemistry Reviews*, 177 (**1998**) 347-414.

[5] Ferrere, S., Gregg, B. A., *Journal of the American Chemical Society*, 120 (**1998**) 843-844.

[6] Ferrere, S., *Chemistry of Materials*, 12 (**2000**) 1083-1089.

[7] Ferrere, S., *Inorganica Chimica Acta*, 329 (**2002**) 79-92.

[8] Hirotake, K., Yoshiro, K., Takeo, O., *Japanese Journal of Applied Physics*, 11 (**1972**) 1385.

[9] Susumu, S., *Japanese Journal of Applied Physics*, 20 (**1981**) 1989.

[10] Carrasco-Orozco, M., Tsoi, W. C., O'Neill, M., Aldred, M. P., Vlachos, P., Kelly, S. M., *Advanced Materials*, 18 (**2006**) 1754-1758.

CHAPTER 2 LITERATURE REVIEW

2.1 Introduction

The Sun conveys solar energy to Earth consistently, freely and for unlimited time. The benefit of solar energy includes sustainability, renewability and environmental friendly. In addition, solar energy can be converted into other forms of energy. As examples, it is used to provide electrical energy for small items such as calculators and watches, and heat energy for homes and industries [1]. However, solar energy is an intermittent source as it is unavailable on a cloudy or rainy day. Therefore, many systems are designed with either some kind of energy storage feature, or a backup source of energy, such as the electric grid.

2.2 Photovoltaic Technologies

Basically, there are four technologies involved in solar energy: passive solar, solar heating, solar thermal electric, and solar photovoltaic (PV). Passive solar uses solar energy in the form of heat and light, especially for buildings. Solar heating uses a solar collector that concentrates heat in either water pipes or an air handling system, which then distributes the hot air or water through the building. These two technologies are used in small-scale applications.

On the other hand, solar thermal electric is used in large-scale applications, such as to heat a fluid for the production of high pressure and high temperature steam. The steam is then converted into mechanical energy in a turbine and into electricity from a conventional generator coupled to the turbine. In general, this technology has the same concept as solar heating [2].

PV is an environmental-friendly technology currently available because it uses chemicals to convert light to electricity. This process is called the PV effect. The term photovoltaic was a combination of the Greek word *phos* means light, and *volt* in honour of the inventor of the electric battery, Alessandro Volta (1745-1827). In 1839, a French

physicist, Alexandre-Edmond Becquerel discovered the photovoltaic process. Then, in 1883 the American inventor, Charles Fritts built the first solar cell, using selenium with a thin film of gold as the semiconductor [3-6].

The PV effect was discovered in 1954 when scientists at Bell Telephone discovered that silicon created an electric charge when exposed to sunlight [6]. Previously, solar cells were used to power space satellites and smaller items. Nowadays, solar PV technology is used to power homes, businesses, and large power stations.

PV technology continued to advance over recent decades. It leads to the development of photovoltaic systems connected to networks. This has prompted an industry whose main objective is to supply modules for large photovoltaic farms to generate electricity. The increased conversion performance, such as proportion of sunlight that the cell transforms into electric energy, is fundamental in making this energy source more cost-efficient and competitive.

2.2.1 PV system

Advanced research on materials for PV has led to a better understanding on effective capture of photons at reactive site and transfer of the excitation energy. Basically, light harvesting is very important in photosynthesis. Understanding the concept(s) involved in this natural process provides an excellent platform for understanding how photo-excitation can be directed and improved using assemblies of light-absorbing molecules. The light energy is captured by complexes or molecules that subsequently funnel it to reaction centres on 10-100 ps timescale [7-11]. More specifically, light harvesting relies on the process of electronic energy transfer, which is stored momentarily (nanoseconds) by molecules in excited state-within networks of light-absorbing molecules (chromophore) to a target chromophore or trap. This timescale constrains the size of the chromophore arrays attached to the reactive site, or how far excitation energy can travel (excitation diffusion length) [12].

Many researchers have developed a dye-based molecule that mimics the light harvesting complex found in plants. The system is designed to absorb all wavelengths of light, which could allow for small powerful solar cells that work well in low light and indoors. The major limitation of materials in current use is the need for high light intensity levels. The photochemical reactions caused by high energy photons degrade the device [13]. This phenomenon is called photon annihilation, whereby all excess photons being harvested is lost as heat.

Plants avoid this problem by having light harvesting or antenna complexes (**Figure 2.1**). The complexes contain an array of proteins and pigment molecules, including chlorophyll. These absorb photons and then direct their energy towards a reaction centre to produce chemical energy. In addition, these allow plants to make nutrient in dim light conditions, and also protecting themselves from photon annihilation by storing the energy in their pigments. Many researchers have been attempting to mimic this natural antenna system in PV cells by applying photosensitive dyes. However, the necessary molecules were difficult to produce and stabilise due to their complexity.

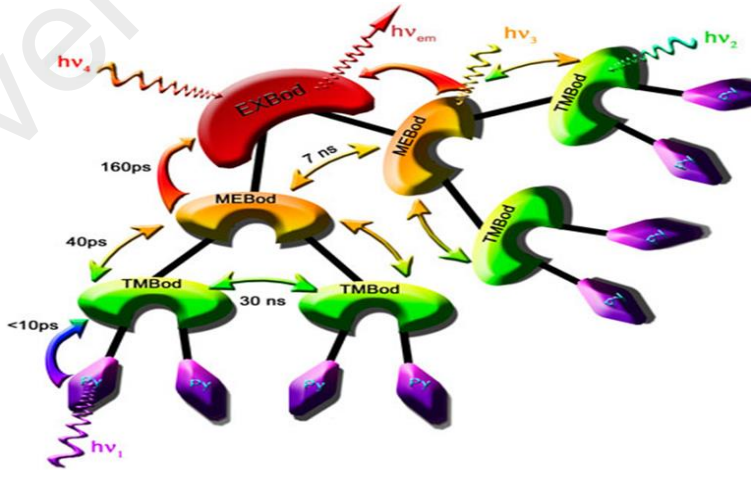

Figure 2.1 Synthetic antenna allows energy from photons to be shuttled to the reaction centre without any destructive annihilation [13].

A beam of sunlight contains photons of different energy (which is related to the different wavelengths of the solar spectrum). When these photons strike a PV cell, they

may be reflected, passed through, or absorbed into the cell. However, only the absorbed photons with energy greater than the bandgap energy can generate electricity. When photons are absorbed, their energy is transferred to the electrons of the PV material. These energetic electrons are able to 'free' themselves and become part of a current in an electrical circuit (**Figure 2.2**) [5] .

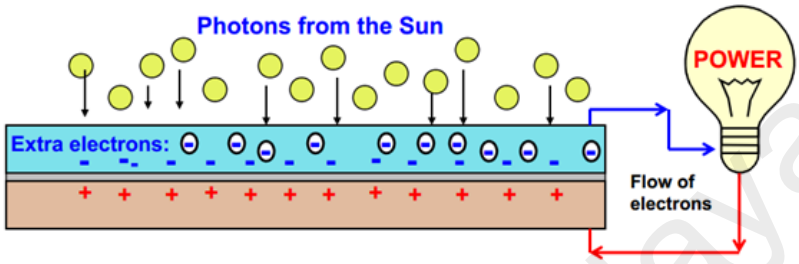

Figure 2.2 Electron mobility in a PV cell

However, the electrical properties of an insulated cell will not allow it to produce sufficient energy to make a standard voltage electric device work (12, 24 or 48 volts). Hence, PV cells are connected electrically in series and/or parallel circuits to produce higher voltages, currents and power levels. In order to increase power output, many PV cells are connected to form modules, which are further assembled into larger units called arrays (**Figure 2.3**). Photovoltaic modules consist of PV cell circuits sealed in an environmentally protective laminate, and are the fundamental building blocks of PV systems. Photovoltaic panels include one or more PV modules assembled as a pre-wired, field-installable unit. A photovoltaic array is the complete power-generating unit, consisting of any number of PV modules and panels.

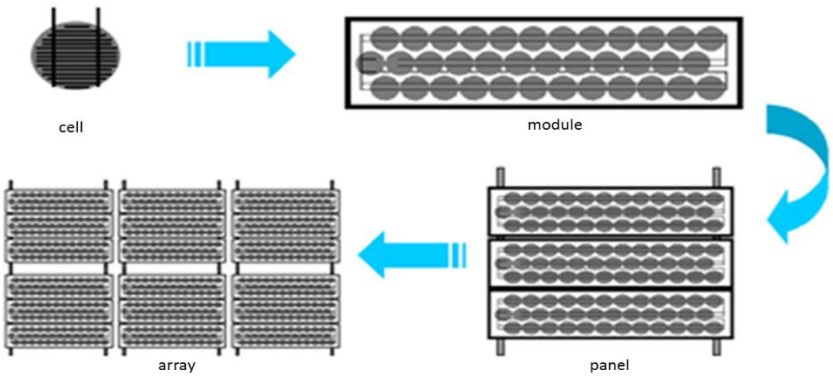

Figure 2.3 Photovoltaic cells, modules, panels and arrays

2.2.2 Development of PV cell

The requirements for an ideal PV materials are: (1) band gap between 1.1 and 1.7 eV; (2) direct band structure; (3) readily available and non-toxics; (4) easy and reproducible deposition technique, suitable for large area production; (5) good photovoltaic conversion efficiency; and (6) long-term stability [14].

At present, over 90% of PV cells are made of silicon. Silicon is best suited to enhancing the efficiency of the modules as it is a semiconductor metaloid (combined properties of metals and insulators). High purity silicon is the raw material from which PV cells are produced (and the price of cells is affected by high purity silicon feedstock availability and prices and reclaimable silicon availability and prices). There are different types of cells, such as monocrystalline silicon (Mono c-Si), polycrystalline silicon (Multi c-Si), and thin film (non-crystalline) (**Figure 2.4**) [15].

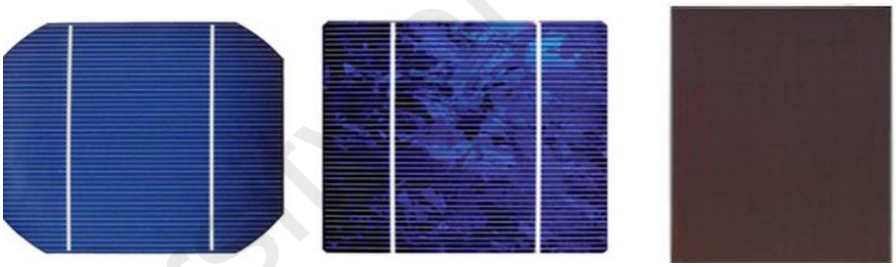

(a) (b) (c)

Figure 2.4 Type of silicon cells: (a) monocrystalline, (b) polycrystalline, (c) thin film

A thin-film solar cell (TFSC), also called a thin-film photovoltaic cell (TFPV), is a second generation solar cell. It is made by depositing one or more thin layers, or thin film (TF) of photovoltaic material on a substrate, such as glass, plastic or metal. This type of solar cells are commercially used in a number of technologies, including cadmium telluride (CdTe), copper indium gallium diselenide (CIGS), and amorphous and other thin-film silicon (a-Si, TF-Si) [16]. Thin film cells are approximately half the manufactured cost of crystalline silicon cells, but are less

efficient than crystalline silicon cells. Thin film panels are also very flexible and can be incorporated into/onto building materials [17-22].

A typical silicon PV cell is composed of a thin wafer consisting of an ultra-thin layer of phosphorus-doped (*n*-type) silicon on top of a thicker layer of boron-doped (*p*-type) silicon. These *n*-type and *p*-type semiconducting materials act as insulators at low temperatures and as conductors when exposed to heat or light energy. An electrical field is created near the top surface of the cell where these two materials are in contact, called the *p*-*n* junction. When sunlight strikes the surface of a PV cell, this electrical field provides the momentum and direction to light-stimulated electrons, resulting in a flow of current when the PV cell is connected to an electrical load (**Figure 2.5**) [23].

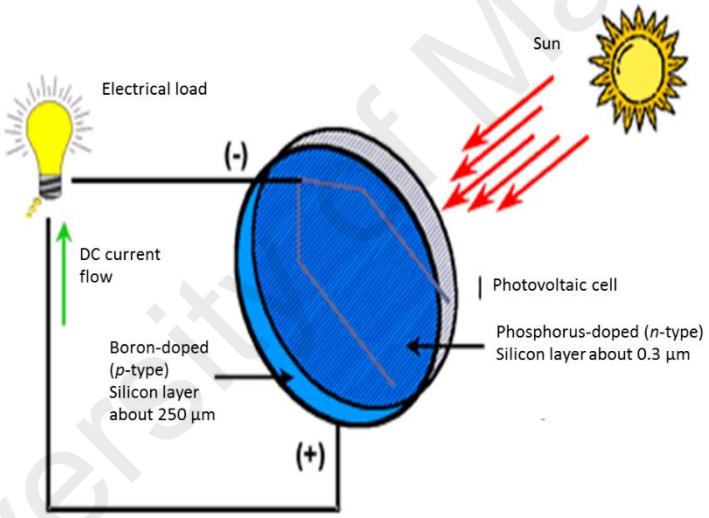

Figure 2.5 Diagram of a *p*-type and *n*-type of PV cell

Under an open circuit, a typical silicon PV cell produces about 0.5 - 0.6 V DC, where there is no load. The current and power end product of a PV cell depends on its efficiency and size (surface area). It is also proportional to the intensity of sunshine striking the surface of the cell. For instance, a typical commercial PV cell with a surface area of 160 cm^2 will produce about 2 watts peak power under peak sunlight conditions. Nevertheless, if the sunlight intensity were 40% of the peak value, this cell would produce about 0.8 watts [23].

The significant part to design a better PV cell is a steady supply of photons at an appropriate wavelength. For example, Anthony Harriman and Raymond Ziessel [24] have developed a new synthetic light-harvesting array using difluoro-boradiazaindacenes (*F-Bodipy*), better known by the commercial name of BODIPY (**Figure 2.6**). A new molecule of *Bodipy* dye has been prepared by replacing the fluorine substituent present in the more conventional chromophore with aryl substituents, such as pyrene. These molecules were expected to prevent photon loss and avoid the formation of highly energetic states that would degrade a device. In addition, these molecules are intended to collect all wavelengths, quickly convert UV light into far-red light, avoiding reactive intermediates and channel the photons to the solar cell [13].

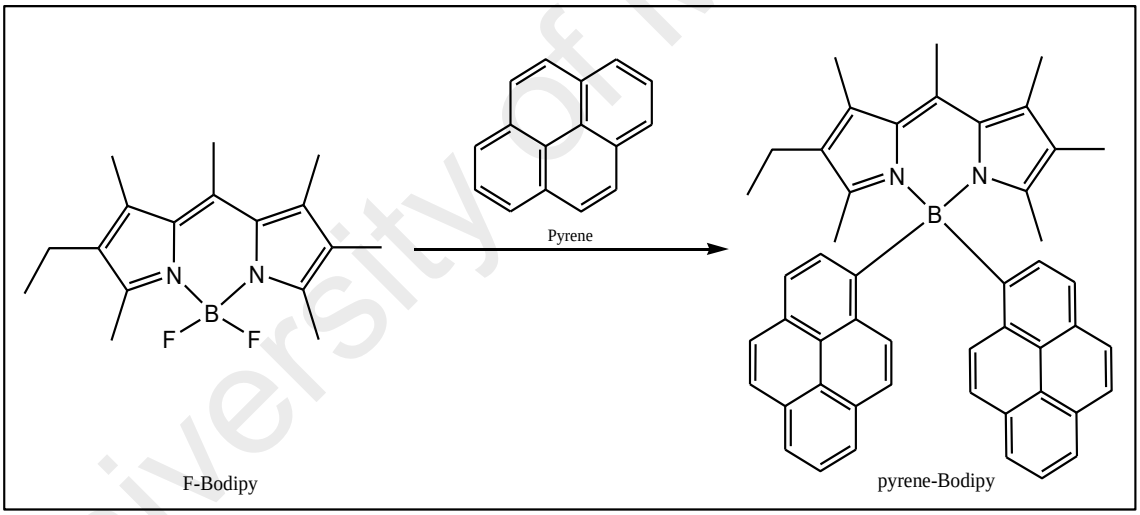

Figure 2.6 Synthetic light-harvesting compound

Furthermore, Anthony *et al*. reported that the absorption spectrum exhibited a band at 517 nm (ε_{max}, 64500 L mol^{-1} cm^{-1}) for *F-Bodipy*, while for *pyrene-Bodipy* at 526 nm (ε_{max}, 46000 L mol^{-1} cm^{-1}). These were assigned to $\pi \rightarrow \pi^*$ transition. The fluorescence measurement of *F-Bodipy* showed an emission peak at 538 nm and its lifetime was 6.2 ns. On the other hand, the emission peak of *pyrene-Bodipy* was 562 nm and its lifetime was 2.0 ns. For *F-Bodipy*, its optical bandgap was 2.40 eV, which is in

excellent agreement with electrochemical band gap, 2.38 eV. For *pyrene-Bodipy*, its optical bandgap was 2.35 eV, while its electrochemical bandgap was 2.55 eV.

2.2.3 Bandgap Energy

The bandgap of a semiconductor is the minimum energy required to excite an electron in its bound state into a free state where it can participate in conduction. The band structure of a semiconductor gives the energy of the electrons on the *y*-axis, and is called a "band diagram" (**Figure 2.7**). The lower energy level of a semiconductor is called the "valence band" (E_v), while the energy level at which an electron can be considered free is called the "conduction band" (E_c). The band gap (E_g) is the gap in energy between the valence band and conduction band. [6, 25].

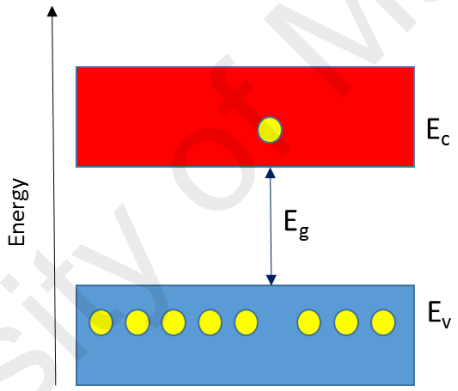

Figure 2.7 Semiconductor band

Once the electron becomes excited into the conduction band, it is free to move about the semiconductor and participate in conduction. However, the excitation of an electron to the conduction band will also allow an additional conduction process to take place. As it leaves behind an empty space for an electron. An electron from a neighbouring atom can move into this empty space. When this electron moves, it leaves behind another space. The continual movement of the space for an electron, called a "hole", can be illustrated as the movement of a positively charged particle through the crystal structure. Consequently, the excitation of an electron into the conduction band results in not only an electron in the conduction band but also a hole in the valence

band. Thus, both the electron and hole can participate in conduction and are called "carriers".

In general, a material with a bandgap of less than about 3 eV is regarded as a semiconductor. A material with a bandgap of greater than 3 eV will commonly be regarded as an insulator. A number of ceramics such as silicon carbide (SiC), titanium dioxide (TiO_2), barium titanate ($BaTiO_3$) and zinc oxide (ZnO) have bandgaps around 3 eV. Such ceramics are often referred to as wide-band-gap semiconductors [26].

There are two bandgap semiconductors, such as direct bandgap and indirect bandgap. In a direct band gap semiconductor, the top of the valence band and the bottom of the conduction band occur at the same value of momentum (**Figure 2.8**). In contrast, for an indirect band gap semiconductor, the maximum energy of the valence band occurs at a different value of momentum to the minimum in the conduction band energy. The difference between the two is important in optical devices.

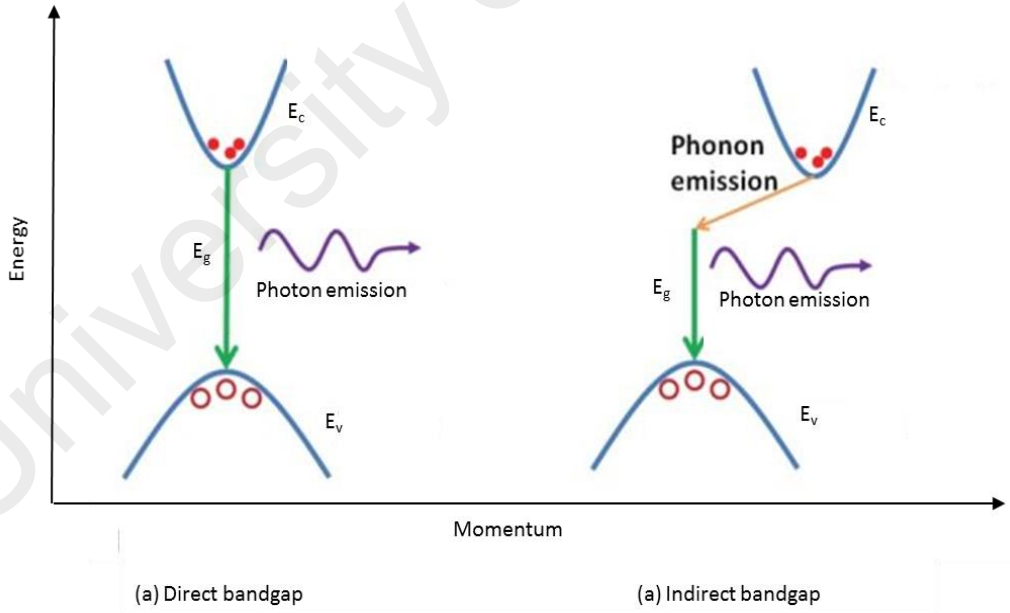

Figure 2.8 Direct and indirect bandgap

A photon of energy E_g, where E_g is the band gap energy, can produce an electron-hole pair in a direct band gap semiconductor quite easily because the electron does not need to be given very much momentum. However, an electron must also undergo a

significant change in its momentum for a photon of energy E_g to produce an electron-hole pair in an indirect band gap semiconductor. This is possible, but it requires such an electron to interact not only with the photon to gain energy, but also with a lattice vibration called a phonon in order to either gain or lose momentum [5, 6].

The same principle applies to recombination of electrons and holes to produce photons. The recombination process is much more efficient for a direct band gap semiconductor than for an indirect band gap semiconductor, where the process must be mediated by a phonon. As a result of such considerations, many researchers have been working on gallium arsenide and other direct band gap semiconductors to make optical devices such as LEDs and semiconductor lasers.

A molecule has the highest occupied molecular orbital (HOMO) and the lowest unoccupied molecular orbital (LUMO). HOMO and LUMO are sometimes referred to as frontier orbitals. The energy difference between the HOMO and LUMO, or HOMO-LUMO gap, is generally the lowest energy electronic excitation that is possible in a molecule. The wavelengths absorbed by a compound can be used as a measure of the HOMO-LUMO gap.

A typical ground-state molecule has electrons in the lowest possible energy levels under the molecular orbital formalism. According to the Pauli principle, at most two electrons can occupy a given orbital, and if an orbital contains two electrons, they must be in opposite spin state. If the molecule absorbs light whose energy is larger than this gap, an electron in the HOMO may be excited to the LUMO. This is called the molecule's excited state (**Figure 2.9**) [27].

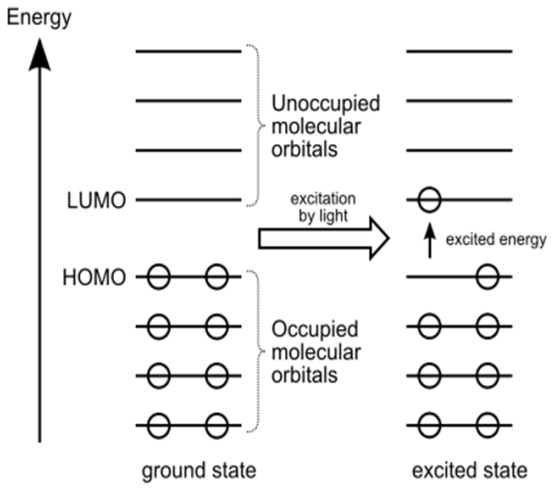

Figure 2.9 HOMO and LUMO gap

There are two ways in which the band gap of a material may be determined: (1) optical spectroscopy (absorption and emission); and (2) electrochemistry (cyclic voltammetry).

Absorption spectroscopy is used to evaluate the optical absorption band gap of materials. In this spectroscopy, the absorbance process measures the energy difference between the ground state and the excited state. Since there are a number of vibrational states associated with both the ground state and the excited state, the absorbance spectrum appears as a broad band instead of a line. The "true" band gap, (E_{00}), the energy difference between the lowest vibrational states of the ground and excited states, is difficult to measure. However, the most commonly accepted approximation is the onset of absorption from the low energy side. The onset value is the intersection of the extrapolations of the linear parts of the spectrum (**Figure 2.10**).

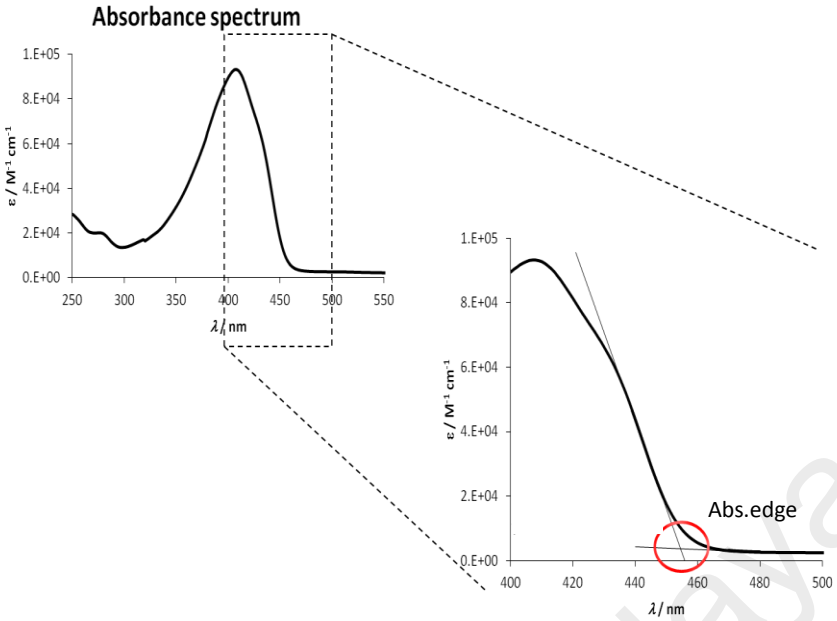

Figure 2.10 Method of bandgap calculation from absorption spectrum

The formula used to calculate the bandgap energy of a compound using an absorption spectrum is:

$$E_g = \frac{hc}{\lambda}$$

where E_g is bandgap (in eV); h is Planck constant (6.62 x 10^{-34} J s); c is speed of light (3 x 10^8 m s^{-1}); and λ is absorption edge (m). The conversion factor is: 1 J = 6.24 x 10^{18} eV. For example, the value calculated for TiO_2 by Jayant Dharma and Aniruddha Pisal [28] by this method (**Figure 2.11**) was 3.02 eV.

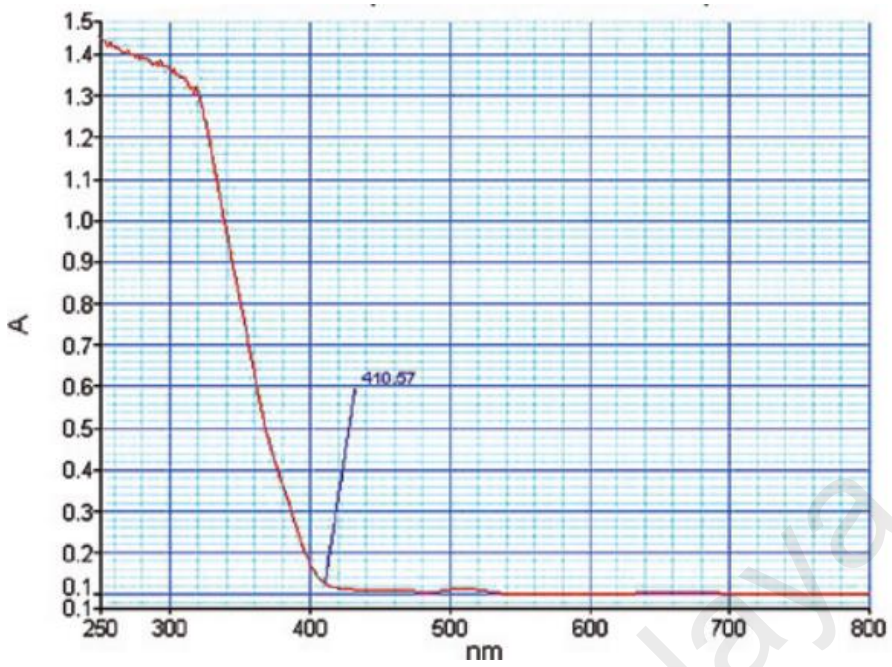

Figure 2.11 UV-vis spectrum of TiO_2

The absorption property, especially the absorption in visible region, are very important for PV materials [29]. Low bandgap materials (Eg < 1.8 eV) are of interest because their absorption spectra cover from the visible to the near-infrared region [30, 31].

Emission spectroscopy measures the emission of radiation by a material that has been excited. Fluorescence spectroscopy is one type of emission spectroscopy which records the intensity of light radiated from the material as a function of wavelength. It is a non-destructive characterization technique.

Fluorescence is a fast decay process, where the emission rate is around 10^8 s^{-1} and the lifetime is around 10^{-9} - 10^{-7} s [32]. It occurs when the electron in the excited state has an opposite spin compared to the ground state. From the laws of quantum mechanics, this is an allowed transition, and occurs rapidly by emission of a photon. Fluorescence disappears as soon as the exciting light source is removed.

After an electron is excited from the ground state, it needs to relax back to the ground state. This relaxation or loss of energy, can be achieved by a combination of non-radiative decay (loss of energy through heat) and radiative decay (loss of energy

through light). Non-radiative decay by vibrational modes typically occurs between energy levels that are close to each other. Radiative decay by the emission of light occurs when the energy levels are far apart. This is because loss of energy through vibrational modes across the band gap can result in the breaking of bonds. This phenomenon is shown in Jablonski diagram (**Figure 2.12**).

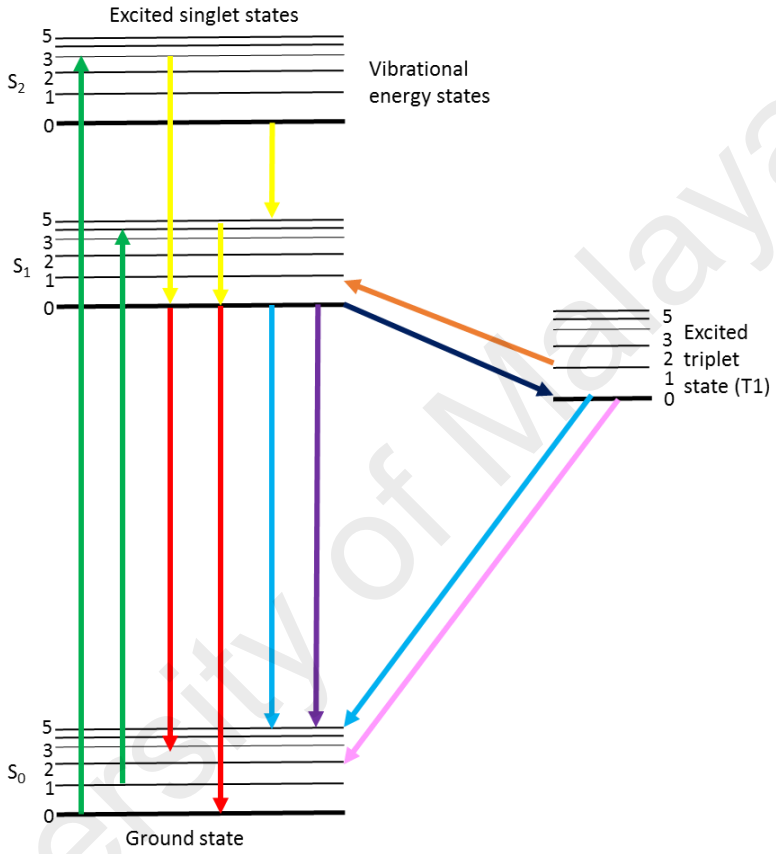

Figure 2.12 Jablonski energy diagram [33] (green: excitation/absorption; yellow: internal conversion and vibrational conversion; red: fluorescence; dark blue: intersystem crossing; purple: quenching; blue: non-radiative relaxation; orange: delayed fluorescence; pink: phosphorescence)

The fluorescence process is governed by three important events, all of which occur on timescales that are separated by several orders of magnitude. Excitation of a molecule by an incoming photon happens in femtoseconds (10^{-15} s), while vibrational relaxation of excited state electrons to the lowest energy level is much slower and can be measured in picoseconds (10^{-12} s). The final process, emission of a longer

wavelength photon and return of the molecule to the ground state, occurs in nanoseconds (10^{-9} s) [33].

The peak of fluorescence spectra may be used to calculate the optical bandgap as well. Jameson *et al.* [32] reported that: for a pure substance in solution, the fluorescence spectrum is (1) invariant (independent of the excitation wavelength); (2) lies at longer wavelengths than the absorption; and (3) to a good approximation, a mirror image of the absorption band of the lowest frequency. Also, in their report, the presence of appreciable Stokes shift is principally important for practical applications of fluorescence because it allows to separate (strong) excitation light from (weak) emitted fluorescence using appropriate optics. For example, Thirugnanasambandan and Marimuthu [34] investigated Pb nanopowder as a new semiconductor. Its photoluminescence spectrum (**Figure 2.13**) showed the Stokes shift of 4 nm (excitation: 376 nm, fluorescence: 380 nm) and 5 nm (excitation: 754 nm, fluorescence: 759 nm). The E_g values were 3.28 eV (λ_{em} = 380 nm) and 1.64 eV (λ_{em} = 759 nm), respectively.

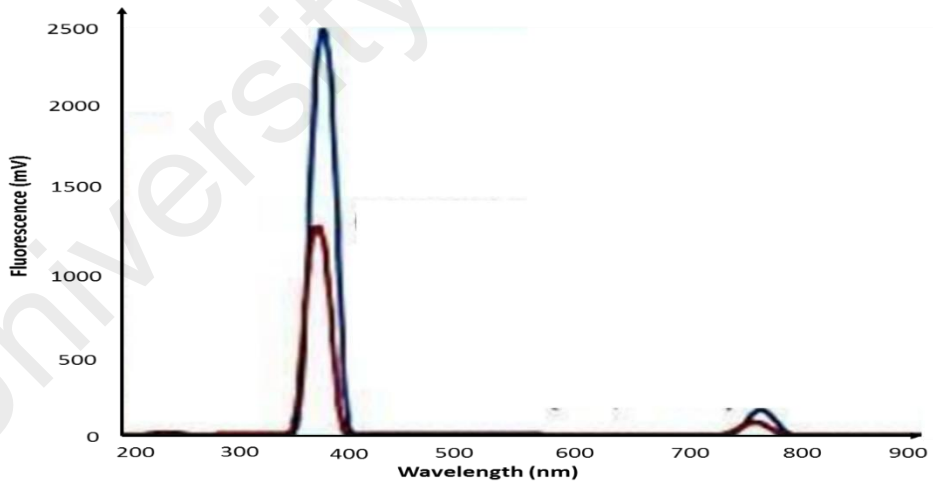

Figure 2.13 Photoluminescence spectrum of Pb nanopowder (red: excitation, blue: fluorescence) [34]

Cyclic voltammetry (CV) is a very versatile potentiodynamic electrochemical technique which allows to be probed the mechanics of redox and transport properties of a system in solution [40]. This is accomplished with a three electrode arrangement

whereby the potential relative to some reference electrode is scanned at a working electrode while the resulting current flowing through a counter (or auxiliary) electrode is monitored in a quiescent solution. In a CV experiment, the working electrode potential is ramped linearly versus time. After the set potential is reached, the working electrode potential is ramped in the opposite direction to return to the initial potential. These cycles of ramps in potential may be repeated as many times as desired. The current at the working electrode is plotted versus the applied voltage (i.e., the working electrode potential) to give a CV trace, called voltammogram (**Figure 2.14**) [35].

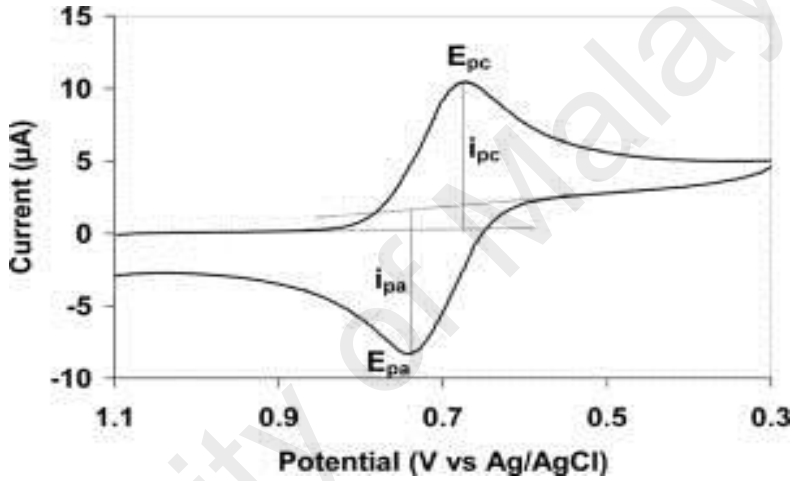

Figure 2.14 Cyclic voltammogram (E_{pc}: cathodic peak potential, E_{pa}: anodic peak potential; i_{pc}: cathodic current; i_{pa}: anodic current)

When the potential of the working electrode is more positive than that of a redox couple present in the solution, the corresponding species may be oxidized and produce an *anodic* current (i_a). Similarly, on the return scan, as the working electrode potential becomes more negative than the reduction potential of a redox couple, reduction may occur to cause a *cathodic* current (i_c). By IUPAC convention, anodic currents are positive and cathodic currents negative [36].

Three types of electron transfer may occur, depending on their electrochemical behaviour, namely reversible, irreversible and quasi-reversible electrochemical reaction. Reversible electron transfer occurs when there is an equilibrium mixture of products and reactants. Reversibility is associated with a fast electron transfer and slow mass

transport. The criteria of a reversible process is shown in **Figure 2.14**, where the values of the peak separation, $\Delta E_p = E_{pa} - E_{pc} = 59$ mV (assuming one-electron process) and $i_{pc}/i_{pa} = 1$ [37].

Quasireversible electron transfer arises from a slow electron transfer from the product back to the initial state. The ΔE_p value for this process is greater than 59 mV. For example, Farhana Haque *et al*. [38] studied the cyclic voltammetry of the redox reaction of Cu(II) in the presence of ascorbic acid, They reported that at the scan rate of 100 mV, a cathodic peak (-301.4 mV) and an anodic peak (+291.52 mV) appeared as Cu(II) underwent a two-step one electron transfer electrochemical redox reaction (**Figure 2.15**). Its ΔE_p value was 592.92 mV.

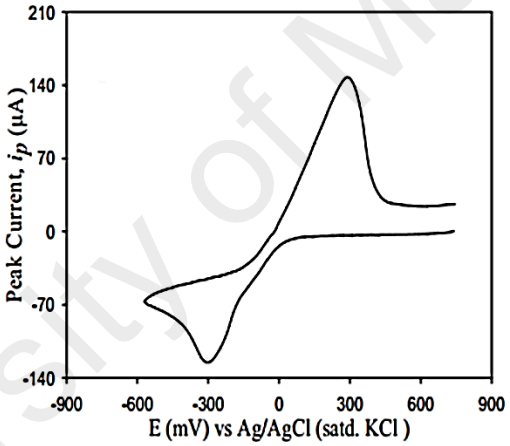

Figure 2.15 CV of Cu(II) in the presence of ascorbic acid [38]

For an irreversible redox process, the change in thermodynamic state from the product to the reactant cannot be precisely restored. For an irreversible process, the voltammogram show only one peak (whether oxidation or reduction). Sometimes the irreversibility behaviour occurs when there is a destructive process of a species, which then lead to the formation of a more stable geometry. As an example, the CV of copper(II) acetate, (a binuclear complex) in acetic acid-methanol mixture as solvent reported by Toledo *et al*. [39], showed in, there are two cathodic peaks (about +0.02 V and -0.4 V) and three anodic peaks (-0.16 V, +0.02 V, and +0.36 V) (**Figure 2.15).**

Hence, the oxidation and reduction potentials are (E_a = +0.02 V, E_c = +0.02 V) and (E_a = -0.16 V, E_c = -0.4 V). However, E_a = +0.36 V was considered as irreversible reaction.

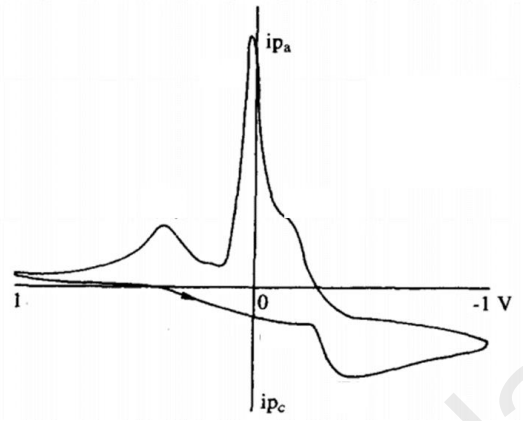

Figure 2.16 CV of copper(II) acetate [39]

This technique is also a dynamic electrochemical method to estimate the HOMO and LUMO energy levels of a compound [40]. It gives direct information of the oxidation and reduction potentials of materials. The oxidation process corresponds to removal of electron(s) from the HOMO energy level, while the reduction process corresponds to addition of electron(s) to the LUMO energy level. The current arises from transfer of electrons between the energy level of the working electrode and the molecular energy levels of the material under study. The onset potentials of oxidation and reduction of a material can be correlated to the ionization potential and electron affinity according to the empirical relationship proposed by Bredas *et al.* [41-43]. These are on the basis of a detailed comparison between valence effective Hamiltonian calculations and experimental electrochemical measurements. This correlation can be expressed as [44]:

$$HOMO = -(E_{onset\ ox} + 4.4)$$
$$LUMO = -(E_{onset\ red} + 4.4)$$

where $E_{\text{onset ox}}$ and $E_{\text{onset red}}$ are the onset potentials of oxidation and reduction, respectively, and E_g is the band gap. Thus, $E_g = |HOMO - LUMO|$. The onset

potentials are determined from the intersection of two tangents drawn at the rising current and baseline charging current of the CV traces.

As an example, Jessica Lohrman *et al.* [45] studied the electrochemical behaviour of semiconducting carbon nanotube and covalent organic polyhedron–C60 nanohybrids for light harvesting. They reported that the onset oxidation potential and onset potential reduction of cage or fullerene binding complex (C_{60}) were +0.86 V and -1.03 V, respectively (**Figure 2.17**). From these values, HOMO and LUMO, calculated using above formula, were -5.26 eV and -3.37 eV. Accordingly, its E_g value was 1.89 eV.

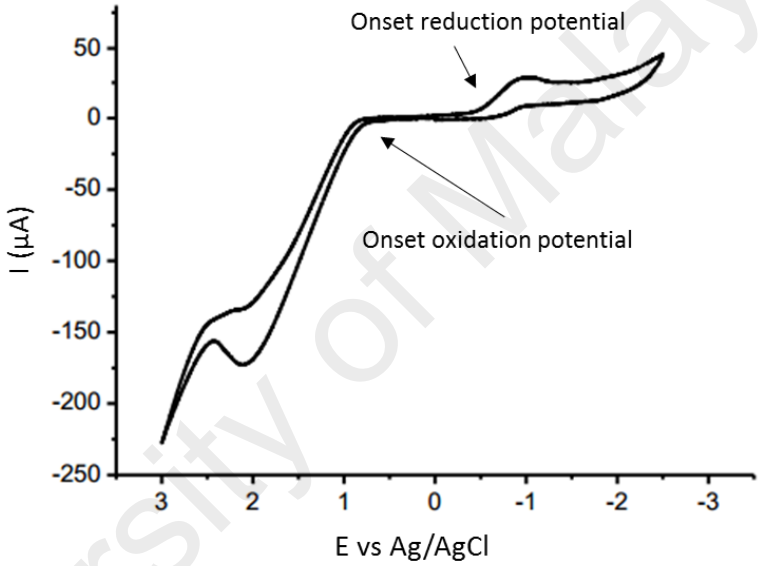

Figure 2.17 Cyclic voltammogram of cage C_{60} [45]

2.2.4 Carrier lifetime

There are two primary categories of carrier lifetime (τ): recombination and generation. Recombination lifetime is the decay of excess minority carriers because of recombination, while generation lifetime is the average time taken to generate an electron-hole pair. However, the term 'lifetime' normally refers to the recombination lifetime of excess minority carriers [4, 5].

When solar radiation falls on a solar cell, generation of electrons and holes occurs, and the equilibrium conditions in material is disturbed. The process of recombination of carriers is opposite to that of the generation of carriers. In this process, excited electrons

fall back from the conduction band to the valence band, reoccupying an empty energy state (a hole) in the valence band, thus electron-hole pairs get destroyed. In this way, recombination process is an equilibrium restoring mechanism. The recombination of generated carriers is not desirable in PV cell operation, and should be avoided as much as possible. The rate of recombination is one of the important PV cell efficiency limiting parameters [6].

The lifetime of minority carriers is of particular interest in solar cells due to its effect on potential cell efficiency. The carrier lifetime should be high. A material having low structural defects and low undesirable impurity concentration can have high carrier lifetime. The value of τ can be as low as nanoseconds to as high as milliseconds. For example, silicon is considered a good PV material because its carrier lifetime is more than a few microseconds.

The minority carrier lifetime is considered the most critical and variable parameter in PV materials. Well-established photoconductivity techniques (e.g. quasi-steady state photoconductivity) are often used to determine the minority carrier lifetimes for indirect bandgap materials, such as silicon, that have longer minority carrier lifetimes (20 μs – 1 ms) [46]. However, these techniques are not effective at measuring the minority carrier lifetimes of direct bandgap materials, which typically range from 500 ps to 100 ns, or materials that have many traps and low doping levels [47]. For direct bandgap materials, optical techniques such as one-photon time-resolved photoluminescence (TRPL) are often used to estimate the minority carrier lifetime [48].

The fluorescence lifetime is a measure of the time a fluorophore spends in the excited state before returning to the ground state by emitting a photon [33]. This is an indicator of the time available to be gathered from the emission spectrum. During the excited state lifetime, a fluorophore can undergo conformational changes as well as interact with other molecules and diffuse through the local environment. The decay of

fluorescence intensity as a function of time in a uniform population of molecules excited with a brief pulse of light is described by an exponential function:

$$I(t) = I_0 \, .e^{-t/\tau}$$

where $I(t)$ is the fluorescence intensity measured at time t, I_0 is the initial intensity observed immediately after excitation, and τ is the fluorescence lifetime. Formally, the fluorescence lifetime is defined as the time in which the initial fluorescence intensity of a fluorophore decays to 1/e (approximately 37%) of the initial intensity (**Figure 2.18**). This quantity is the reciprocal of the rate constant for fluorescence decay from the excited state to the ground state. The lifetimes of fluorophores can range from picoseconds to hundreds of nanoseconds.

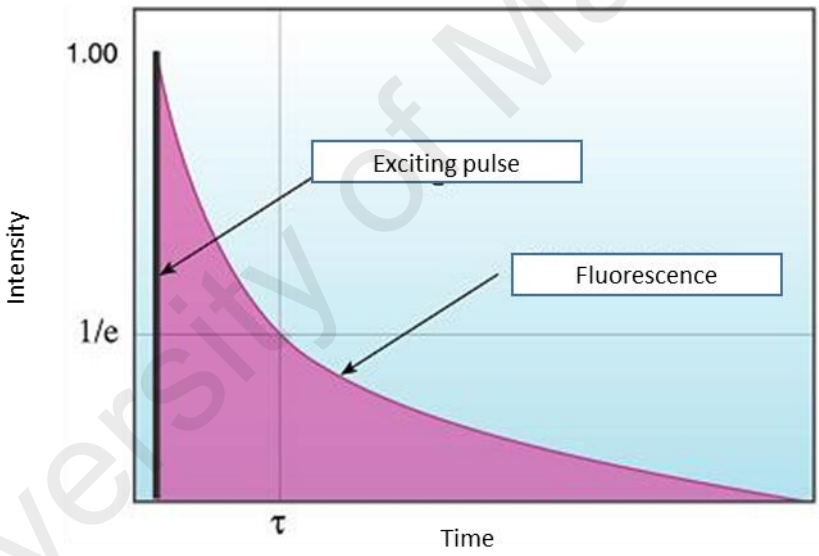

Figure 2.18 Fluorescence lifetime decay profile

Lifetime can be measured using time-resolved fluorescence spectroscopy. There are three common techniques used in this spectroscopy: the stroboscopic technique (strobe), the time-correlated single photon counting technique (TCSPC) and the frequency modulation or phase shift technique (phase). The first two are time-domain techniques while the last one is a frequency-domain technique.

The time-domain techniques are very similar in what they measure and in the way data are analysed. The differences are mainly in the hardware, they use different

detection electronics and different pulsed light sources, although the same light sources can be used with both techniques.

The time-domain techniques are direct techniques. They measure fluorescence decay curves (fluorescence intensity as a function of time) directly and the experimenter has full advantage of seeing the physical mechanism in the course of the experiment. Frequently, a qualitative judgement about a particular mechanism can be made by examining raw decay data and a proper fitting function can be thus selected.

In order to obtain the fluorescence lifetime, the profile of instrument response function (excitation pulse) has to be measured in addition to the fluorescence decay. This is because the lamp (laser) pulse has a finite temporal width, which distorts the intrinsic fluorescence response from the sample. This effect is called convolution.

In a typical experiment, two curves are measured: the instrument response function (IRF) using a scatterer solution and the decay curve. Analysis is then performed by convoluting the IRF with a model function (e.g. a single exponential decay or a double exponential decay or some other function) and then comparing the result with the experimental decay. This is done by an iterative numerical procedure until the best agreement with the experimental decay curve is achieved.

For example, Marco Bonnizoni studied the fluorescence lifetime of fluorescein, a common organic dye [49]. The decay is known to follow a single-exponential law in the selected experimental conditions, but the actual signal measured is convoluted with a complex instrument response function. The decay curve (**Figure 2.19**) was fit to a single exponential model by deconvolution of the IRF as described above. The τ value was 3.81 ns.

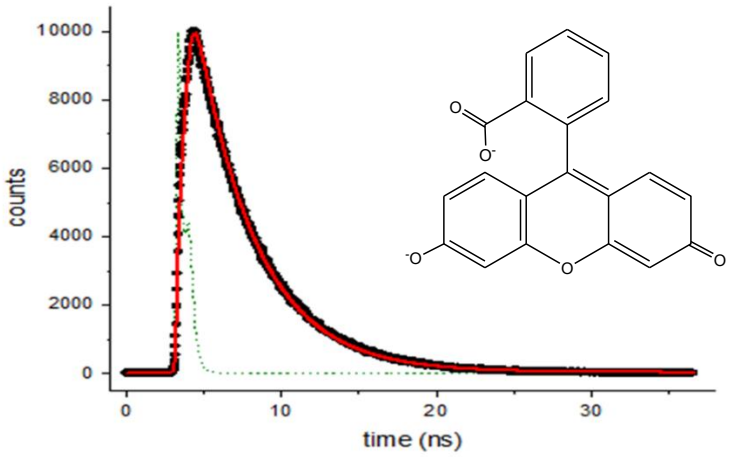

Figure 2.19 Fluorescence decay profile of fluorescein dye in H_2O (black: experimental decay; green: IRF; red: single exponential fit)

The stroboscopic technique (Strobe) is the most recent and electronically the simplest. It utilizes a pulsed light source (a nanosecond flash lamp or a laser) and measures fluorescence intensity at different time delays after the pulse. As a result, a fluorescence decay curve is collected. The diagram (**Figure 2.20**) shows the basic elements of a strobe instrument that utilizes a nanosecond flashlamp. One of the advantages of the stroboscopic technique is the ability to utilize low frequency lasers (e.g. nitrogen laser), which are relatively inexpensive and at same time provide very high-energy pulses and can pump dye lasers thus resulting in excellent excitation wavelength coverage [33].

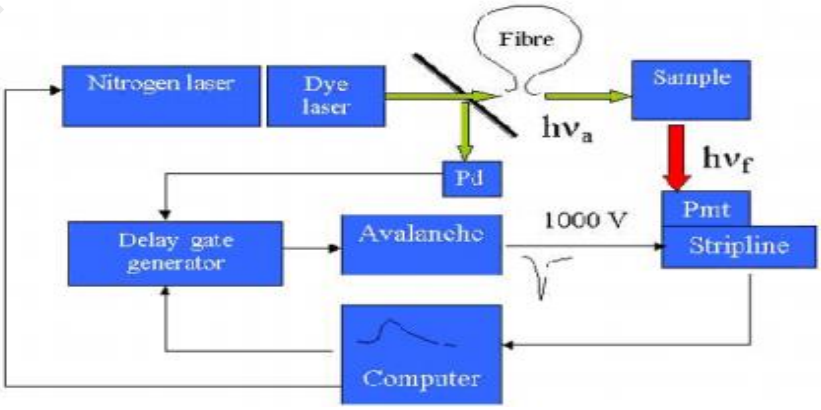

Figure 2.20 Block diagram of an N_2/Dye Laser-based stroboscopic system [33]

For example, the lifetime of $[Ru(bipy)_3]^{2+}$, a photosensitizer, studied by the stroboscopic method by Arunachalam *et al*. was 890 ns [50]. The value was in good agreement with that obtained by other methods [51].

2.3 Dye-Sensitized Solar Cell

A dye-sensitized solar cell (DSSC) is a third generation PV cell that shows great promise because of its low-cost and simplicity. DSSC converts visible light into electrical energy. This class of advanced PV cell is similar to artificial photosynthesis by the way it mimics nature in absorbing light energy.

DSSC is based on a semiconductor formed between a photo-sensitized anode and an electrolyte, a photoelectrochemical system. The modern version of a dye solar cell, also known as the Grätzel cell, was originally co-invented in 1988 by Brian O'Regan and Michael Grätzel. This work led to the development of the first high efficiency DSSC in 1991 [52, 53]. Michael Grätzel was awarded the 2010 Millennium Technology Prize for this invention [54].

DSSC is a disruptive technology that can be used to produce electricity in a wide range of light conditions, enabling the user to convert both artificial and natural light into energy to power a broad range of electronic devices. The advantages of DSSC are low-light performance, optimised performance, higher temperature performance, low energy manufacturing process, ecological friendly, variety of substrates and versatile product integration (highly flexible, durable and lightweight). The efficiency of DSSC has continued to increase in the last 20 years, with a confirmed record of 14.1% [54].

2.3.1 The concept of sensitisation

A DSSC functions because of the interactions between the anode and cathode of the cell, and TiO_2 nanoparticles, which are coated with a light-sensitive dye and surrounded by an electrolyte. The anode is transparent, like glass, so that sunlight can be absorbed by the inner parts of the solar cell. Between the anode and the cathode is a mesh TiO_2

nanoparticles that act like a roadway for the electrons (electricity) coursing through the cell. The TiO_2 nanoparticles are coated with a light-absorbing dye that convert photons (light) into electricity [53, 55, 56].

In a DSSC, the electrons need to be flowing from one end of the cell to the other (from the cathode to the anode). The electrons (electricity) travel through the electrolyte (I^-) and the TiO_2 nanoparticles to create an electric current. TiO_2 nanoparticles are transparent and normally used as conductors because of their unique ability to be 'welded' together and form one huge network for the electrons to travel through (**Figure 2.21**) [50].

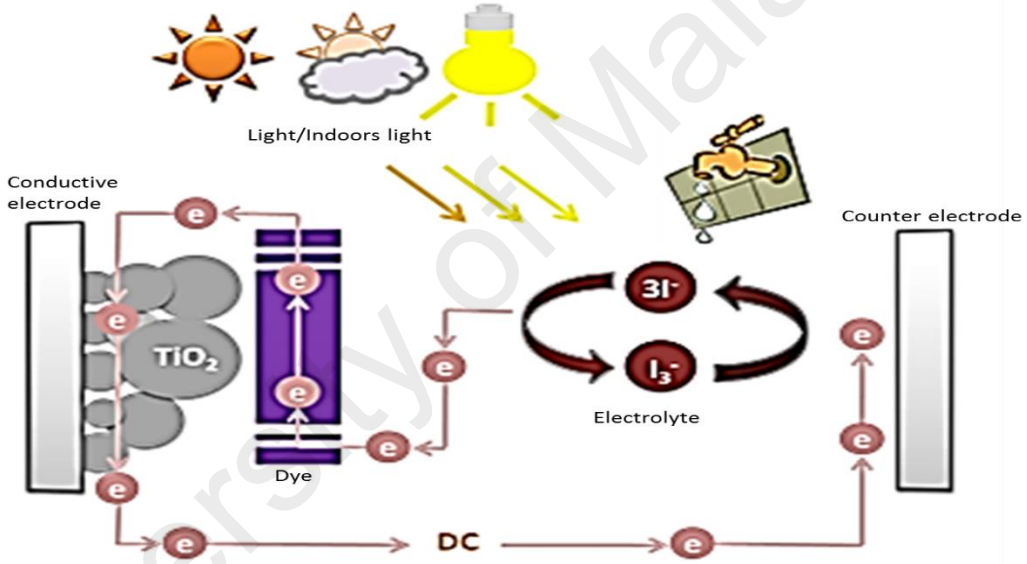

Figure 2.21 DSSC system [57]

The electrons originate from the dye molecules coating the TiO_2 nanoparticles when they are hit by light (photons). Different colour dyes can absorb different wavelengths of light, which in turn carry different amounts of energy. The dye molecule enters an excited state, and emits an electron. The emitted electron travels through the TiO_2 nanoparticles until it reaches the anode, or is lost to I^- because of defects in the TiO_2 nanoparticles.

After emitting one of its electrons, a dye molecule will start to decompose unless it receives another electron to replace the one it lost. In this state, the dye molecule

cannot emit any more electrons. This is the reason the dye-coated TiO_2 molecules are immersed in I^- solution (I^- ion is able to replace the electrons lost by the dye molecules). When this occurs, I^- ion is oxidized to I_3^-, which will float around until it comes in contact with the cathode. Each I_3^- ion received two electrons from the cathode, which reduces it back to three I^- ions [58].

The dyes used in early experimental cells (circa 1995) were sensitive only in the high-frequency end of the solar spectrum (UV and blue). The most efficient DSSC demonstrated to date were all based on ruthenium dyes developed by the Grätzel group, such as N3, N719 and 'black dyes' (**Figure 2.22**) [59]. Suyoung Hwang *et al*. [60] reported that the electrochemical bandgap of N3 and N719 were 2.4 eV and 2.6 eV, respectively.

The "black dye", notably "triscarboxy-ruthenium terpyridine" [Ru(4,4',4"-$(COOH)_3$-terpy)$(NCS)_3$], was a newer versions introduced (circa 1999) [61-63]. It had a much wider frequency response and was efficient right into the low-frequency range of red and IR light. The wide spectral response results in the dye having a deep brown-black colour. The dyes have an excellent chance of converting a photon into an electron, originally around 80% but improving to almost perfect conversion in more recent dyes, the overall efficiency was about 90%, with the "lost" 10% being largely accounted for by the optical losses from the top electrode [61].

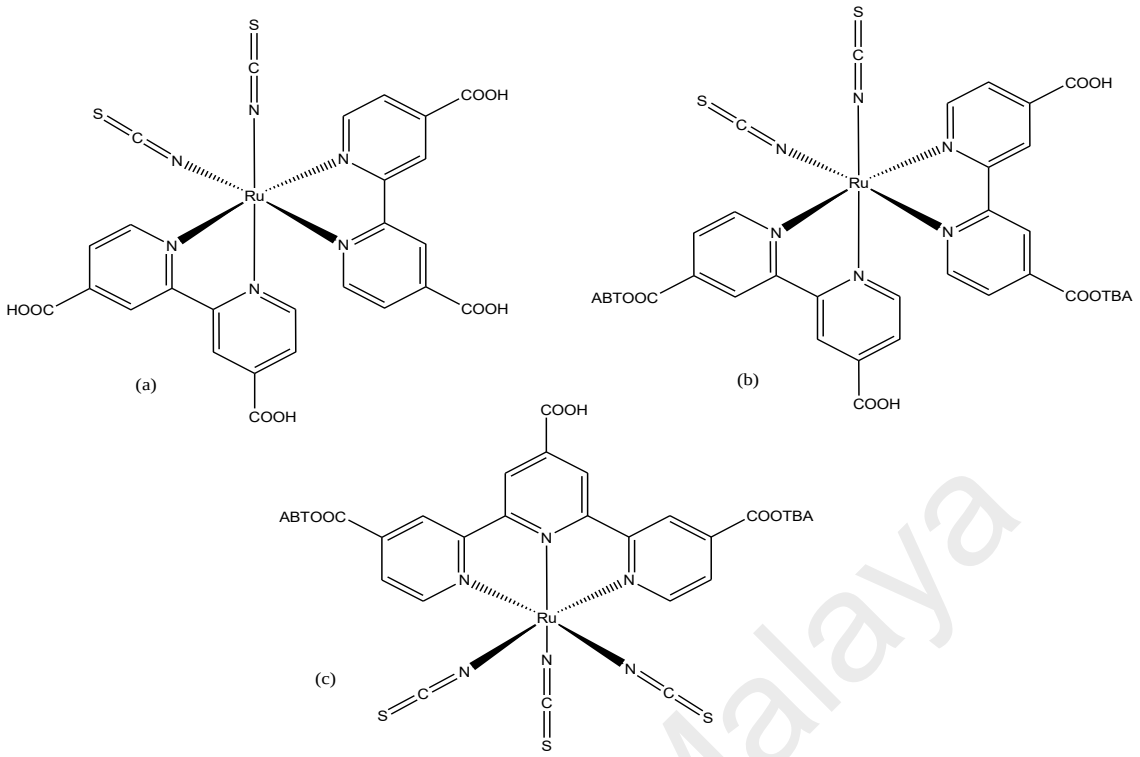

Figure 2.22 Dyes: (a) N3; (b) N719; and (c) black dye. TBA = tetrabutylammonium cation

Another example of a dye molecule is ruthenium amphiphilic dye, Z-907 (*cis*-$Ru(H_2dcbpy)(dnbpy)(NCS)_2$, where H_2dcbpy is 4,4′-dicarboxylic acid-2,2′-bipyridine and dnbpy is 4,4′-dinonyl-2,2′-bipyridine (**Figure 2.23**). This dye was investigated by Peng Wang *et al.* [64], who reported that it has an increased tolerance to water in the electrolytes and its lifetime was 30 μs.

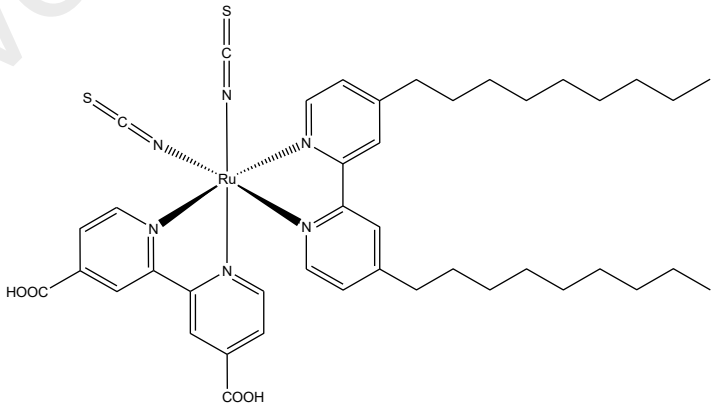

Figure 2.23 Dye Z-907 [64]

In 2007, Wayne Campbell experimented with a wide variety of organic dyes based on porphyrin [65]. In nature, porphyrin is the basic building block of

hemoproteins, which include chlorophyll in plants and hemoglobin in animals. He reports an efficiency on the order of 5.6% using these low-cost dyes [66].

2.3.2 Coordination metal complexes

Stringent requirements that need to be fulfilled by potential PV materials are: (1) intensity and spectral range of coverage of light absorption in the visible, near-IR and IR regions; (2) tenability of the absorption band(s); (3) photophysical properties (types and number of excited states, their lifetimes and quantum yields for radiative and non-radiative processes); and (4) redox properties in the ground and excited states. For redox-sensitizers or redox-mediators, additional requirements are reversibility and stability of the oxidized or reduced forms. In all of these cases, transition metal complexes with polypyridines (such as 1,10-phenanthroline and 2,2';6',2''-terpyridine), porphine or phthalocyanine (**Figure 2.24**) as ligands, which are examples of conjugated organic molecules, come out clearly as sensitizers of preferred choice [62]. The low-lying metal-to-ligand charge transfer (MLCT) and ligand-centered (π - π*) excited states of these complexes are fairly long-lived to participate in electron transfer processes.

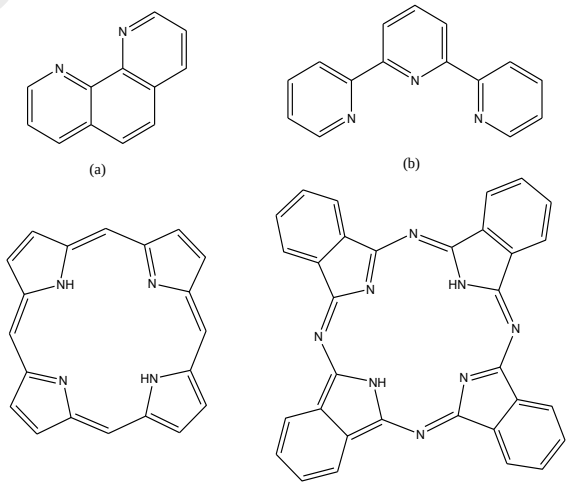

Figure 2.24 Structural formula of (a) 1,10-phenanthroline, (b) 2,2';6',2''-terpyridine, (c) porphine, and (d) phthalocyanine

Transition metal complexes are constructed from one or more central metal atom(s) or cation(s) surrounded by several inorganic or organic molecules or anions in fixed geometrical arrangement (mainly octahedral, square pyramidal, square planar or tetrahedral) dictated by the metal. Many of the properties of transition metal complexes are adequately described by the crystal field theory.

In crystal field theory, a ligand lone pair is modelled as a point negative charge (or as partial negative charge of an electric dipole) that repels electrons in the *d* orbitals of the central metal ion. The theory concentrates on the resulting splitting of the *d* orbitals of the groups with different energies, and uses that splitting to rationalize and correlate the optical spectra, thermodynamic stability, and magnetic properties of complexes [67]. This theory is widely used to explain the electronic structure, coordination modes, color, and magnetic properties.

For example, an octahedral complex, $[Cu(H_2O)_6]^{2+}$, has six H_2O ligands coordinated to the central metal ion. In this case, the five *d* orbitals split into two sets of different energy (**Figure 2.25**). The d_{xy}, d_{xz} and d_{yz} orbitals (known as t_{2g} orbitals) are lower in energy, while d_z^2 and $d_{x^2-y^2}$ (known as e_g orbitals) are higher in energy. The energy difference between the two levels is known as octahedral crystal field splitting (Δ_o).

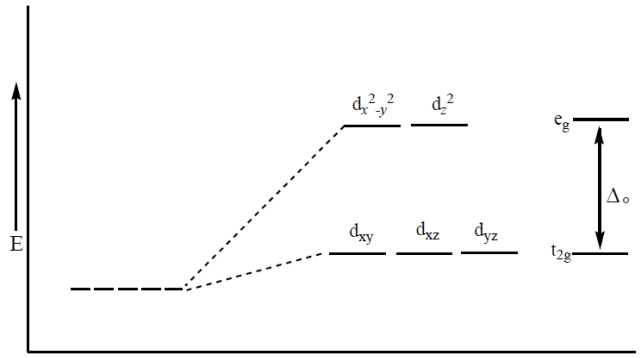

Figure 2.25 Crystal field splitting of *d* orbital in octahedral complexes [67]

When light passes through a solution of $[Cu(H_2O)_6]^{2+}$, one of its electrons in t_{2g} orbital is excited to e_g orbital. This process is known as electronic transition. A photon of light is absorbed and the light of the complementary colour is transmitted. The intensity of light passing through an absorbing material is reduced according to Beer's law: $I = I_0 e^{-\alpha l}$, where I is the measured intensity after passing through the material, I_0 is the initial intensity, α is the absorption coefficient (cm^{-1}), and l is the path length (cm). The Beer-Lambert law introduces the concentration of an absorbing species into the above relationship, and is used in work with solutions [68]. The absorbance of a sample A can be expressed as:

$$A = log_{10}\left(\frac{I_0}{I}\right) = \varepsilon cl$$

where A is the absorbance of the sample (dimensionless), ε is the molar absorption coefficient (L mol^{-1} cm^{-1}), and c is the molar concentration of the solution (mol L^{-1} or M).

The ε value ranges from 0-100 (pale colours) to >100,000 (intense colours) due to selection rules (**Table 2.1**) [69]. The selection rules governing transitions between electronic energy levels of transition metal complexes are: spin rule and Laporte rule. There are two spin rule, namely spin allowed and spin forbidden. For spin allowed, a transition must involve no change in spin state ($\Delta S = 0$), while any transition in which $\Delta S \neq 0$ is strongly forbidden (**Figure 2.26**).

Table 2.1 Intensities of the different transitions

Type of electronic transition	ε_{max} (L mol^{-1} cm^{-1})
Spin forbidden, Laporte forbidden	< 1
Spin allowed, Laporte forbidden	1-10
Spin allowed, Laporte forbidden (with *d-p* mixing, i.e. tetrahedral)	10-100
Spin allowed, Laporte forbidden (with intensity stealing)	100-1000
Spin allowed and Laporte allowed (e.g. CT)	1000-50000

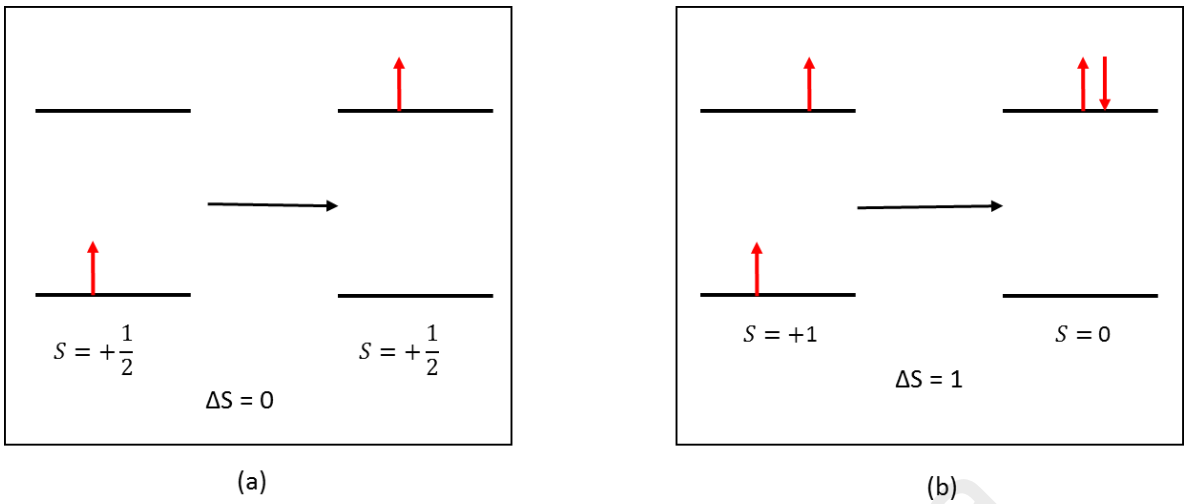

Figure 2.26 Spin rule: (a) spin allowed, (b) spin forbidden

Laporte rule is named after Otto Laporte [70]. In a molecule or ion possessing a centre of symmetry, transitions are not allowed between orbitals of the same parity, for example *d* to *d*. In other words, there must be change in parity ($\Delta L = \pm 1$), where L is the total resultant of orbital angular momentum. Examples of forbidden transitions are $s \rightarrow s$, $d \rightarrow d$, and $p \rightarrow f$. Complexes affected by this rule have octahedral and square-planar (centrosymmetric) geometries (**Figure 2.27**). The rule is not applicable to tetrahedral complexes as it does not contain a centre of symmetry (non-centrosymmetric).

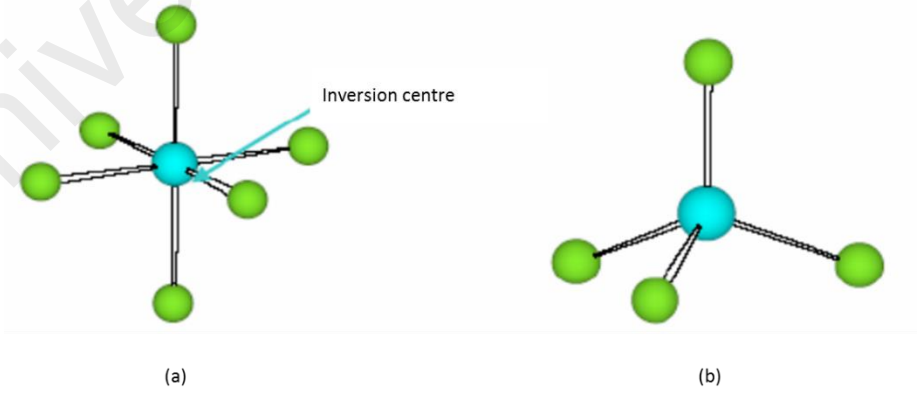

Figure 2.27 Geometries of complexes: (a) octahedral; (b) tetrahedral.

In coordination metal complexes, there are two types of electronic transition: *d-d* and charge transfer (CT) transitions. According to Laporte rule above, *d-d* electronic transitions are forbidden. However, it can only in the visible region as a result of a

breakdown in centrosymmetric system of an octahedral complexes, resulting in weak peaks.

The CT transitions occur in the UV and/or visible region(s), and are intense and selection rule allowed. The direction of the electron transfer is determined by the relative energy levels of these orbitals: (1) ligand-to-metal charge transfer (LMCT), and (2) metal-to-ligand charge transfer (MLCT). For LMCT, the transition may occur from the filled ligand molecular orbitals (σ, σ^*, π, π^*, n) to the empty or partially filled metal *d*-orbitals (**Figure 2.28(a)**) [71]. This process results in the reduction of the metal. On the other hand, MLCT may occur if the metal is in a low oxidation state (electron rich) and the ligand possesses low-lying empty orbitals (e.g., CO or CN^-) (**Figure 2.28(b)**) [72]. Hence, this process results in the oxidation of the metal.

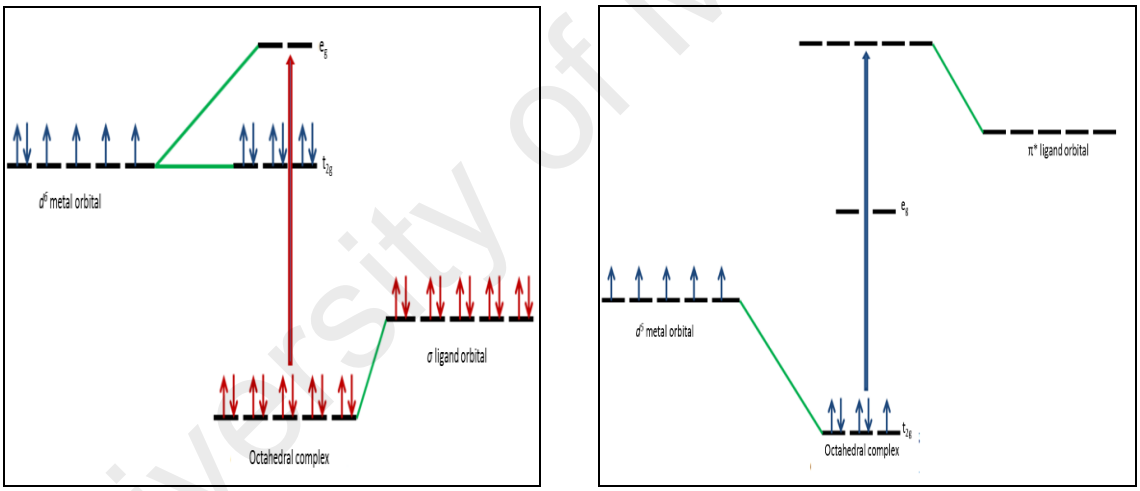

(a) (b)

Figure 2.28 CT transitions: (a) LMCT, (b) MLCT

Spectroscopic studies of Fe(II) and Ru(II) complexes with tris-2,2'-bipyridine (**Figure 2.29**) has been done by Johanna [73]. It was found that Fe(II) complexes has two peaks at 295 nm (ε_{max}, 12100 L mol^{-1} cm^{-1}) and 520 nm (ε_{max}, 1010 L mol^{-1} cm^{-1}), which were assigned to ligand-to-ligand transition ($\pi \rightarrow \pi^*$), and MLCT ($t_{2g} \rightarrow \pi^*$), respectively. In addition, Ru(II) complex has similar peaks at 285 nm (ε_{max}, 56500 L mol^{-1} cm^{-1}), and 453 nm (ε_{max}, 6430 L mol^{-1} cm^{-1}). This MLCT wavelength was in good agreement with that reported by Duchovnay [74].

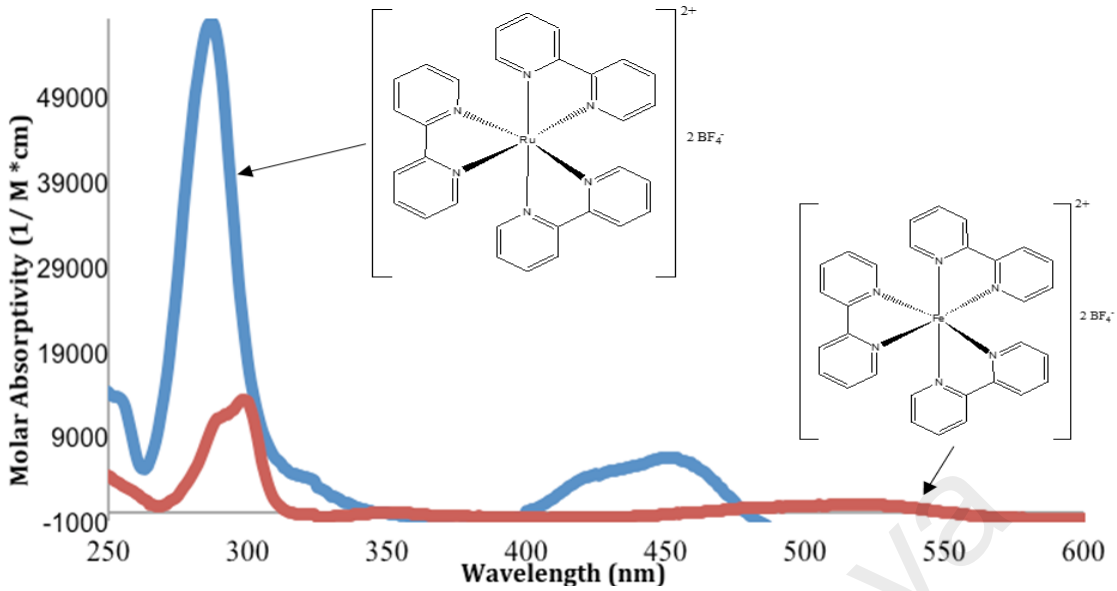

Figure 2.29 Absorption spectra of $[Fe(bipy)_3](BF_4)_2$ and $[Ru(bipy)_3](BF_4)_2$ complexes [73]

Tanabe and Sugano calculated the splitting of the energy levels arising from the electronic configuration d^2 to d^8 under the action of the ligand field of octahedral symmetry, and the results are presented graphically, called as Tanabe-Sugano diagram [75, 76]. In this diagram, states of other spin multiplicities are also included making it possible to assign spin forbidden transitions. In these diagrams, the term energies, E, are expressed as E/B (y axis) and plotted against Δ_o/B (x axis), where B is the Racah parameter. This parameter describe various aspects of inter-electronic repulsion.

Tanabe–Sugano diagrams can be used for both high-spin (HS) and low-spin (LS) complexes and to predict the size of the ligand field necessary to cause HS-to-LS transition. The zero of energy in a Tanabe Sugano diagram is always taken as the lowest term. Hence, the lines in the diagrams have abrupt changes of slope when there is a change in the identity of the ground term brought about by the change from HS to LS with increasing field strength.

In a centrosymmetric ligand field, such as in octahedral complexes of transition metals, the arrangement of electrons in the *d*-orbitals is not only limited by electron repulsion energy, but it is also related to the splitting of the orbitals due to the ligand field. This leads to many more electron configuration states than is the case for the free

ion. The relative energy of the repulsion energy and splitting energy defines the high-spin and low-spin states (**Figure 2.30**). High spin complex corresponds to weak ligand field, while low spin complex correspond to strong ligand field. The splitting energy, Δ_o, of high spin is lower than the splitting energy of low spin.

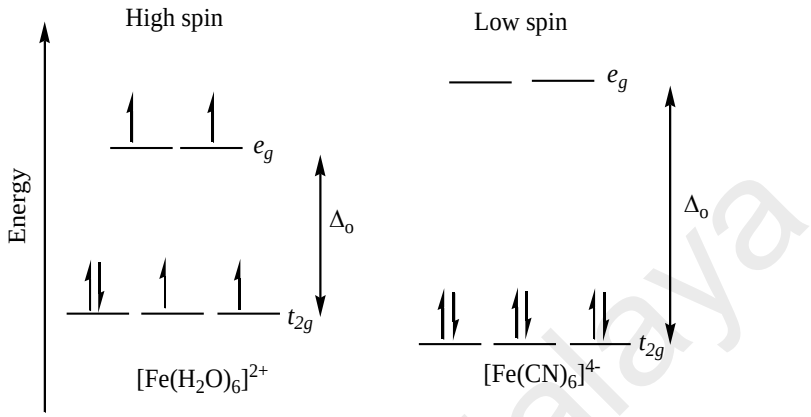

Figure 2.30 High spin and low spin electronic configuration for iron(II) complexes

For example, a weak field $[Fe(H_2O)_6]^{2+}$ complex can be assigned to the spin allowed *d-d* transition $^5T_{2g} \rightarrow {}^5E_g$, which is characteristic of high-spin ground state. It directly gives the value of 10,000 cm^{-1} in the absorption spectrum (**Figure 2.31**). On the other hand, the strong field $[Fe(CN)_6]^{4-}$ complex, corresponds to the spin-allowed *d-d* transition $^1A_{1g} \rightarrow {}^1T_{1g}$, which is characteristic for a low-spin ground state. A second band at still higher energy has been attributed to the $^1A_{1g} \rightarrow {}^1T_{2g}$ transition [77].

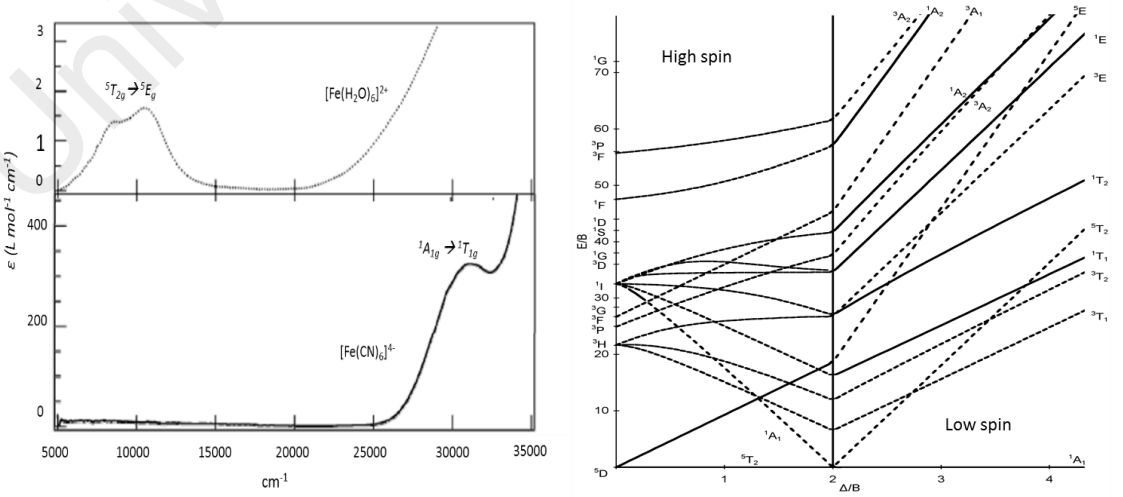

(a) (b)

Figure 2.31 (a) Absorption spectra of high spin and low spin, (b) Tanabe Sugano diagram of d^6

In coordination metal complexes, the electron configuration can deduce their magnetic properties. The number of unpaired electrons in a specific compound indicates how magnetic the compound is. The electron configuration of a transition metals (*d*-block) changes in a coordination complex due to the repulsive forces between electrons in the ligands and electrons in the compound. Depending on the strength of the ligand, the compound may be diamagnetic or paramagnetic. A compound is diamagnetic when it contains no unpaired electrons. In contrast, a compound that contains one or more unpaired electrons is paramagnetic [69].

On the other hand, many compounds, in which the neighbouring magnetic centres can interact (or couple) with each other, lead to magnetic ordering of the bulk material. This can take two main forms, ferromagnetism and antiferromagnetism (**Figure 2.32**). Ferromagnetism occurs if the magnetic moments all line up in parallel. The μ_{eff} value is generally much greater than $\mu_{\text{spin-only}}$ due to the cooperative effect of the spins coupling in parallel which reinforces the bulk magnetic moment. If the magnetic moments line up antiparallel with respect to one another, the compound becomes antiferromagnetic. In antiferromagnetic compounds, μ_{eff} value tends to be somewhat less than $\mu_{\text{spin-only}}$ since the coupling of the spins into an anti-parallel arrangement results in the individual magnetic moments cancelling one another out.

(a) (b)

Figure 2.32 Magnetism: (a) ferromagnetic, (b) antiferromagnetic

The magnetic susceptibility can be experimentally determined by Gouy method. The method involves weighing a sample of the complex in the presence and absence of a magnetic field and observing the difference in weight. From this measurement, the mass magnetic susceptibility, χ_g (cm^3 g^{-1}), is obtained. Then, the molar magnetic susceptibility, χ_M (cm^3 mol^{-1}), can be obtained using following equations:

$$\chi_M = \chi_g \text{ x FW}$$

where, FW is formula weight of complexes (g mol^{-1}). The χ_M value is positive for paramagnetic compounds, and for diamagnetic compounds negative [78].

In general, the magnetic susceptibility data are given in the form of the temperature dependence of the so-called effective magnetic moment, μ_{eff} (Bohr Magneton = B.M.) defined as [79, 80]:

$$\mu_{eff} = \sqrt{\frac{3k\chi_M T}{N\beta^2}} = \sqrt{8\chi_M T}$$

where, k = Boltzmann's constant, T = absolute temperature, β = Bohr Magneton, N is Avogardo's number.

Robert *et al*. [81] studied the electronic spectral and magnetic susceptibility of mononuclear Ni(II) and Co(II) carboxypeptidase complexes. They reported that the absorption spectrum of Ni(II) complex exhibited weak bands at 1060 nm, 685 nm, and 408 nm. These were assigned to the three spin-allowed *d-d* transitions $^3A_{2g}$ *(F)* → $^3T_{2g}$ *(F)*, $^3A_{2g}$ *(F)* → $^3T_{1g}$ *(F)*, and $^3A_{2g}$ *(F)* → $^3T_{1g}$ *(P)*, respectively. Its μ_{eff} was 2.84 B.M, which indicates a paramagnetic complex. For Co(II) complex, the absorption spectrum showed two bands at 1115 nm and 572 nm, which were assigned to $^4T_{1g}$ *(F)* → $^4T_{2g}$ *(F)*, and $^4T_{1g}$ *(F)* → $^4A_{2g}$ *(F)*, respectively. This indicates a high-spin octahedral complex. Its μ_{eff} was 4.40 B.M. This value is higher than the μ_{eff} spin-only, 3.87 B.M., thus, the complex was ferromagnetic.

Most of the coordinated ligands used as a photosensitizer (dye) are nitrogen heterocycles. This is due to a delocalized π or aromatic ring system, which are capable of complexing with a variety of metal ions. The metal complexes formed have reasonably good solubility in many solvents, and exhibit low-lying electronically excited states ($\pi - \pi^*$, *d* - *d**, and *d* - π^* (MLCT)).

For example, Suzanne Ferrere [82, 83] has extensively investigate new photosensitizers based on $[Fe^{II}(L)_2(CN)_2]$, where L = substituted 2,2′-bipyridine, such as $[Fe^{II}$(4,4′-dicarboxylic acid-2,2′-bipyridine$)_2(CN)_2]$ (**Figure 2.33**). The absorption spectrum of $[Fe^{II}$(4,4′-dicarboxylic acid-2,2′-bipyridine$)_2(CN)_2]$ showed three absorption bands at 610 nm (ε_{max}, 8400 M^{-1} cm^{-1}), 426 nm (ε_{max}, 8300 M^{-1} cm^{-1}), and 318 nm (ε_{max}, 27000 M^{-1} cm^{-1}). These indicate that the complex exhibit an intense metal-to-ligand charge transfer (MLCT) transitions in the visible region of the spectrum. For this complex, the low lying ligand field (LF) states of iron(II) deactivate the initially populated MLCT states, resulting in very short (ps–ns) MLCT lifetimes [84] (**Figure 2.34**). However, it was argued that although the MLCT lifetime of the complex was prohibitively short for sensitizing intermolecular or solution reactions [85, 86], electron injection from adsorbed dyes into nanocrystalline TiO_2 occurs within several hundred fs, and thus competes with depopulation of initially populated excited states [87-89]. Further evidence for a 'hot' electron injection mechanism was the wavelength-dependent sensitization exhibited by the iron complex, found to be much more efficient from the higher energy MLCT absorbance band than the lower energy MLCT band [82, 90].

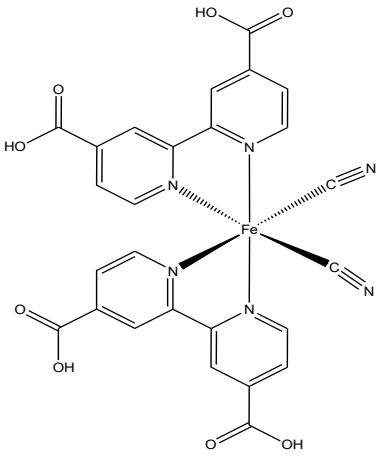

Figure 2.33 Structural formula of $[Fe^{II}$(4,4′-dicarboxylic acid-2,2′-bipyridine$)_2(CN)_2]$ [82]

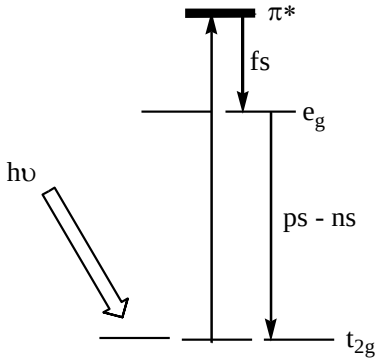

Figure 2.34 Qualitative depiction of the relative differences in t_{2g} and π* orbitals for [FeII(4,4′-dicarboxylic acid-2,2′-bipyridine)$_2$(CN)$_2$]

Complexes using Schiff base ligands have important role in development of inorganic chemistry, biochemistry and environment chemistry. Schiff bases (or imines) have the general formula RN=CR' where the R and R' are alkyl, aryl, cycloalkyl or heterocyclic groups. They are formed by condensation reaction that occurs when aldehydes and some ketones react with primary amines. The general preparation of Schiff bases and reports of metal complexes of these types of ligands were firstly published in the 1860s (**Figure 2.35**) [91, 92].

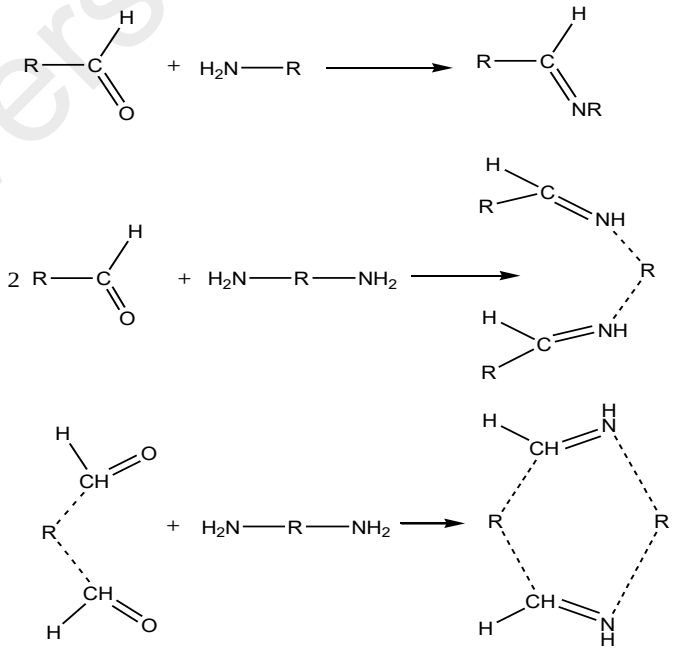

Figure 2.35 Schiff base reaction

Schiff bases have a chelating structure and are in demand due to the ease of formation and remarkable versatility. In addition, Schiff bases have been extensively studied because of their high potential permutations. Magnetic susceptibility, absorption spectra, elemental analysis, molecular weight determination, conductivity and thermal analysis of many Schiff bases and their complexes have been reported [93-95].

For instance, a new copper(II) complex with Schiff base containing pyrrole ring (**Figure 2.36**) was investigated by Ali Ourari *et al*. [96]. The Schiff base ligand was synthesized by reaction of 6-(3'-N-pyrrolpropoxy)-2-hydroxyacetophenone and ethylenediamine. The objective of their study was to elaborate a new coordination compound bearing pyrrole units which have been found to be very useful for catalytic applications in various fields of organic, inorganic and bioorganic synthesis. The FTIR spectrum of the complex showed a strong absorption band at 1602 cm^{-1}, assigned to the azomethine (C=N) stretching vibration. Its electronic spectra, recorded in DMF solution, exhibited three absorption bands at 288 nm, assigned to π-π^* transition, 351 nm, assigned to *n*- π^* transition, and 550 nm assigned to *d-d* transition.

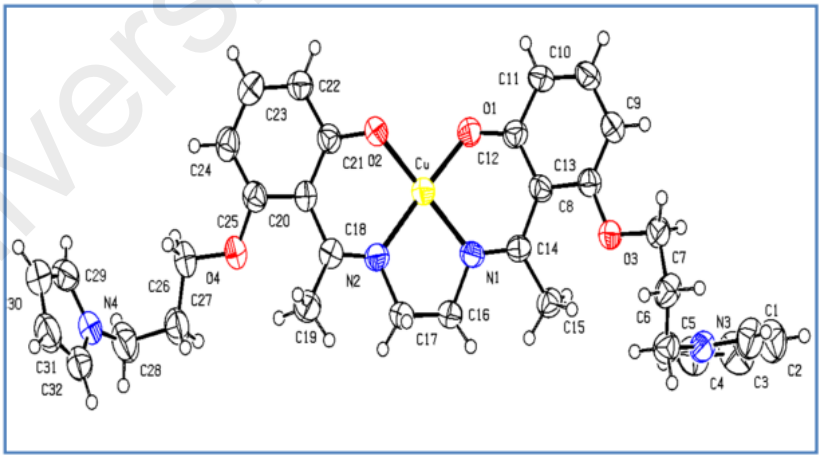

Figure 2.36 Copper(II) complex with Schiff base containing pyrrole ring

Its CV (**Figure 2.37**) was performed in acetonitrile solutions at the scan rate of 100 mV s^{-1} within the potentials window -1.8 V to +1.6 V. It showed two reduction waves at -0.904 V, assigned to the reduction of Cu(II) to Cu(I), and at -1.143 V,

assigned to the reduction of Cu(I) to Cu(0). In addition, there were five oxidation waves at -0.975 V, assigned to the reoxidation of Cu(0) to Cu(I), -0.697 V, assigned to the reoxidation of Cu(I) to Cu(II), +0.323 V, tentatively attributed to the oxidation Cu(II) to Cu(III), +0.841 V, corresponded to the anodic oxidation pyrrole moieties leading to the formation of poly(pyrrole) film, and +1.525 V, assigned to the oxidation of the Schiff base ligand.

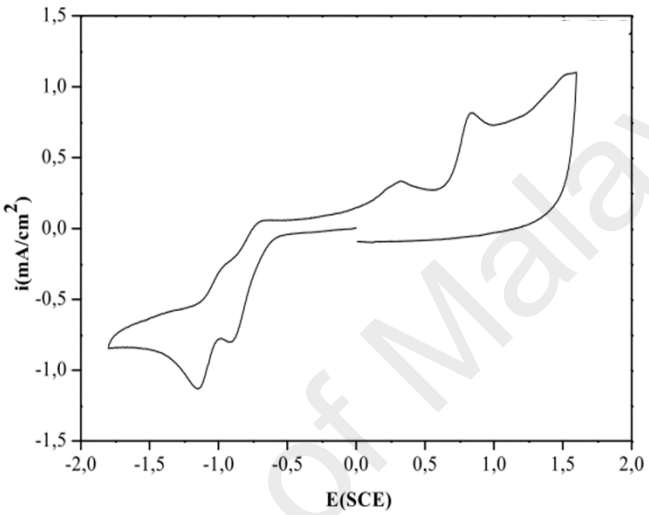

Figure 2.37 CV of copper(II) complex with Schiff base containing pyrrole ring [91]

Another work has been reported by E. Tas *et al*. [97] for a new novel Schiff base ligand [*N*,*N*-(3,4-benzophenon)-3,5-Bu$^t_2$-salicylaldimine] (**Figure 2.38**). Their objective were to establish a comparative electro-spectrochemical study on the new Schiff-base mononuclear metal complexes based on the different molecular structures with NONO donor sites. It was found that all complexes of Cu(II), Ni(II), Co(II), and Fe(II) were mononuclear and tetradentate coordination. Their FTIR spectra showed very strong and sharp bands located in the range 1598 - 1615 cm^{-1}, assigned to the C=N stretching vibrations. These bands are shifted by 17-5 cm^{-1} to lower wavenumber due to participation of the C=N group of this ligand in binding to the Cu(II), Co(II), Ni(II), and Fe(II) ions.

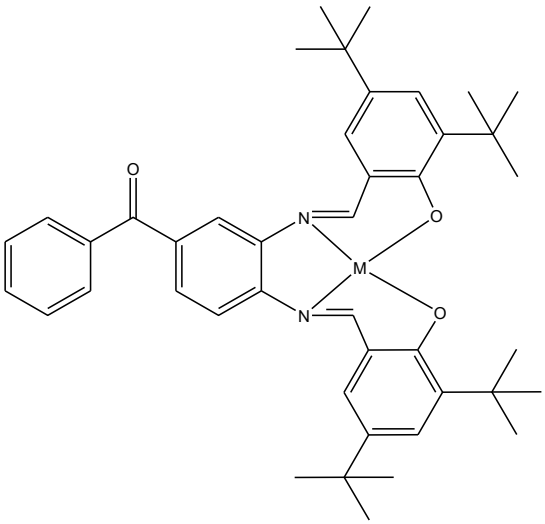

Figure 2.38 [*N*,*N*-(3,4-benzophenon)-3,5-Bu$^t_2$-salicylaldimine]

The electronic spectra of the free ligands in $CHCl_3$ and DMSO showed strong absorption bands in the ultraviolet region (263 – 408 nm), that could be attributed respectively to the $\pi \rightarrow \pi^*$ and $n \rightarrow \pi^*$ transitions in the benzene ring. Furthermore, for Cu(II), Co(II), Ni(II), and Fe(II) complexes, weak absorption bands were observed at 460 nm and 634 nm for Cu(II) complex, at 452 nm and 510 nm for Co(II) complex, at 503 nm and 559 nm for Ni(II) complex, and at 434 and 619 nm for Fe(II) complex (in $CHCl_3$, DMSO and EtOH). These bands are considered to arise from the forbidden *d*-*d* transition. Except for Ni(II) complex, which was diamagnetic, Co(II) (3.55 B.M.) and Fe(II) (3.9 B.M) were high spin. In addition, Cu(II) (1.74 B.M) was paramagnetic with no interaction between the Cu(II) atoms.

From the TGA and DTA scan, these mononuclear metal complexes have different thermal stabilities. The decomposition temperature of all complexes were in the range 182 – 287 °C. The most thermally stable compound was Cu(II) complex, while the least thermally stable compound was Fe(II) complex.

The electrochemical properties were studied only for Cu(II) and Ni(II) using cyclic voltammetry (**Figure 2.39**) in dichloromethane (CH_2Cl_2) containing 0.1 M TBAP as the supporting electrolyte. The CV of the ligand showed one anodic peak at 1.20 V

(E_{pa}) and one cathodic peak at −1.45 V (E_{pc}) versus Ag/AgCl (scan rate of 0.010 V s^{-1}). For Cu(II) complex, two quasireversible redox processes were observed when the potential was increased from 0 V to +1.5 V. The first wave redox process (E_{pa1} = +1.11 V; E_{pc1} = +1.18 V) was assigned to the redox process of Cu(II)/Cu(III), and the second wave redox process (E_{pa2} = +1.30 V; E_{pc2} = +1.20 V) was assigned to the redox process of the ligand. However, there was one cathodic peak at -1.39 V, when the potential was reduced from 0 V to -1.5 V. This was assigned to the irreversible reduction process of the ligand. The electrochemical behaviour for Ni(II) complex was similar to that of the [Cu(II)] complex under the same experimental conditions (E_{pa1} = +1.10 V, E_{pc1} = +1.12 V; E_{pa2} = +1.32 V; E_{pc2} = +1.18 V; E_{pc3} = -1.41 V).

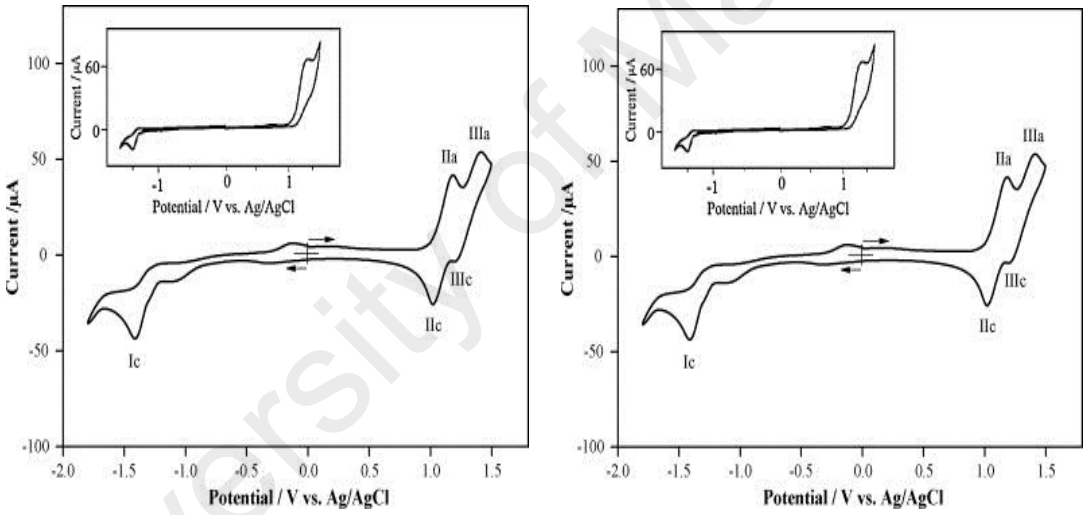

(a) [Cu(II)] (b) [Ni(II)]

Figure 2.39 CV of Cu(II) and Ni(II) complexes [97]

2.3.3 Coordination polymers

A coordination polymer is an inorganic or organometallic polymer structure containing metal cation centres linked by organic ligands. More formally a coordination polymer is a coordination compound with repeating coordination entities extending in 1, 2, or 3 dimensions [98, 99]. A polymeric ligand is considered as a polymeric substance that contains coordinating groups or atoms (mainly N, O, and S). A polymeric ligand can be obtained by the polymerization of monomers containing coordinating sites or by the

reaction between a polymer and a low-molecular weight compound having coordinating ability. In a polymer-metal complex, it has a specific structure as the metal ion is surrounded by a structured polymer chain. Moreover, it shows unique properties which are distinctly different from their low-molecular weight analogues. These unique properties originate from the properties of the polymer backbone.

In many scientific and technological fields, coordination polymers recently showed potential applications in material science as luminescence, magnetism, conductivity, porous, chiral or non-linear optical, molecular storage, and catalytic [100-103]. Furthermore, coordination polymers are commercialized as dyes.

Polymer complexes may be classified into three different groups according to the position occupied by the metal.

(1) *Complexation of polymeric ligand with metal ions*. These may be further divided into two categories: (a) pendant metal polymer complexes, and (b) inter/intra-molecular bridged polymer complexes.

In a pendant metal complex, the metal ion is attached to the polymer ligand function, which is appended on the polymer chain. Based on the chelating abilities of the ligands, pendant complexes are classified as monodentate or polydentate polymer metal complexes. An example of a monodentate polymer studied by Kurimura *et al.* [104] was obtained from the reaction between poly(4-vinylpyridine) (PVP) with metal chelates *cis*-$[Co(en)_2Cl_2]Cl.H_2O$ (en = ethylenediamine) (**Figure 2.40**). They reported that the coordination was very clear, the effect of the polymer chain was clearly exhibited, and the polymer complex was very often soluble in water or in organic solvents. On the other hand, polydentate pendant polymer complexes can be formed when the polymer pendant coordination group has a polydentate structure.

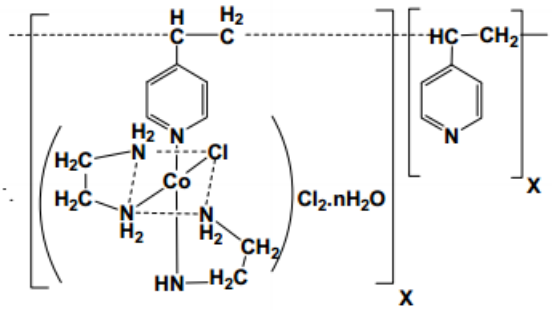

Figure 2.40 *cis*-[Co(en)$_2$PVPCl] $Cl_2.nH_2O$

Inter- or intra- molecular bridged polymer complexes are formed from the reaction of polymer ligands with metal ions. The coordination structure of the resulting polymer metal complex is not clear. In addition, the polymer complex is sometimes insoluble in water or in organic solvents. It is usually difficult to distinguish between the inter and intra-molecular bridging. The simplest example of this type of polymer complex is the poly(vinyl alcohol)(PVA)-Cu(II) complex (**Figure 2.41**) [105].

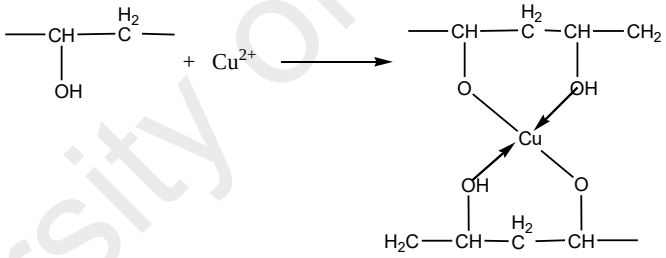

Figure 2.41 Poly(vinyl alcohol)(PVA)-Cu(II) complex

(2) *Complexation of multifunctional ligands with a metal*. When bifunctional ligands form a complex with metal ions having more than two labile ligands (easily replaceable), a polymer complex is formed through metal ion bridging. For example, Epstein and Wildi [106] investigated the electrical properties of a polymer of copper phthalocyanine (**Figure 2.42**). They concluded that this type of polymer-metal complex was a *p*-type semiconductor.

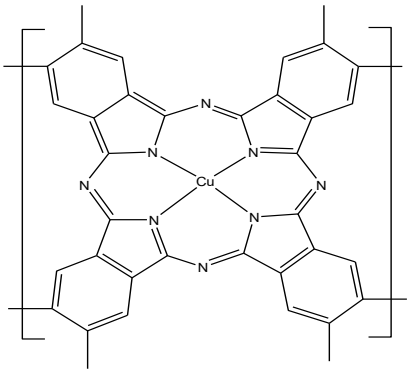

Figure 2.42 Poly(copper phthalocyanine)

(3) *Polymerization of metal containing monomers*. Polymer containing the metal as part of a pendant or substituent group may be formed when complex possessing functionalized ligands undergo polymerization. The most widely studied are vinyl complexes and their derivatives, formed through radical polymerization of vinyl monomer containing transition metal ions. Vinyl compounds of metal complex are polymerized giving polymer metal complexes. For instance, Diab *et al*. [107] prepared and characterized poly(2-acrylamidophenol) (PAP) homopolymer and polymer complexes of 2-acrylamidophenol (AP) with Cu(II), Ni(II), and Co(II) chlorides (**Figure 2.43**).

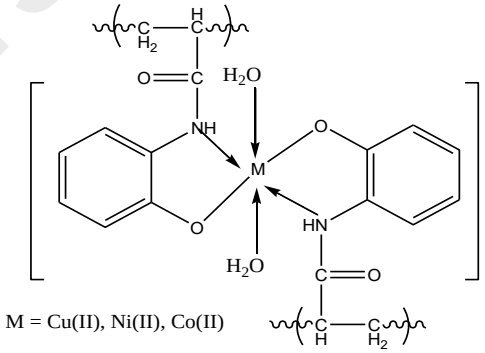

Figure 2.43 Polymer complexes of 2-acrylamidophenol (AP) with Cu(II), Ni(II), and Co(II)

Yu Ma *et al*. [108] synthesized Cu(II) coordination polymer with azide and bipyridine-based zwitterionic carboxylate ligands. They studied the structures and magnetism of Cu(II) complex, $[Cu_4O(L)_4(N_3)_2]_n(ClO_4)_{4n}\cdot 3nH_2O$, where L was 1-carboxylatomethyl-4,4'-bipyridinium (**Figure 2.44**). The IR spectrum of the complex

showed $v_{as}(N_3)$ vibration at 2110 cm^{-1}, $v_{sym}(N_3)$ vibration at 1315 cm^{-1}, and $v_{as}(COO)$ and $v_s(COO)$ vibrations at 1610 cm^{-1} and 1371 cm^{-1}. Its temperature dependent magnetic susceptibility ($\chi_M T$) at 2-300 K was about 1.23 emu K mol^{-1}, which was significantly lower than the spin-only value (1.50 emu K mol^{-1}) expected for four isolated Cu(II) ions. This suggested antiferromagnetic interactions in the complex.

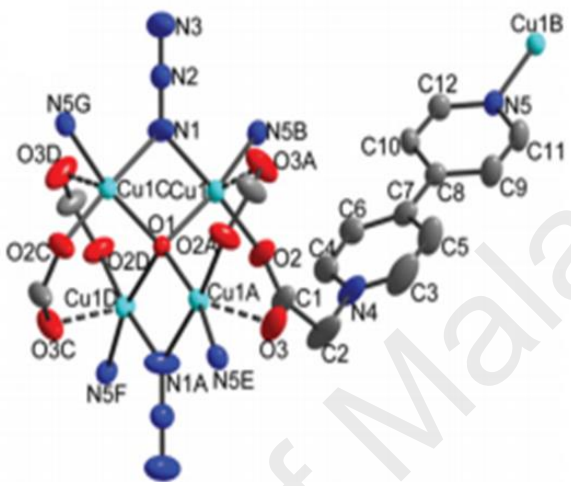

Figure 2.44 $[Cu_4O(L)_4(N_3)_2]_n(ClO_4)_{4n}\cdot 3nH_2O$ [103]

The most common ligands used in the coordination polymer, such as bipy, bpe, and bpethy (**Figure 2.45**), are quite rigid. Therefore, many researchers recently have synthesized more flexible ligands. For example, a new type of long conjugated Schiff-base ligand has been studied by Yu-bin Dong *et al*. [109], namely, 1,4-bis(3-pyridyl)-2,3-diaza-1,3-butadiene (**Figure 2.46(a)**). This ligand (a Schiff base) was reacted with Co(II) nitrate to form a coordination polymer complex (**Figure 2.46(b)**). The specific geometry of this ligand, including the different relative orientations of N-donors and the zig-zag conformation of the spacer moiety (-CR=N-N=CR-) between the two pyridyl groups, may result in coordination polymers with novel network patterns. The decomposition temperature of Co(II) complex was 200 °C.

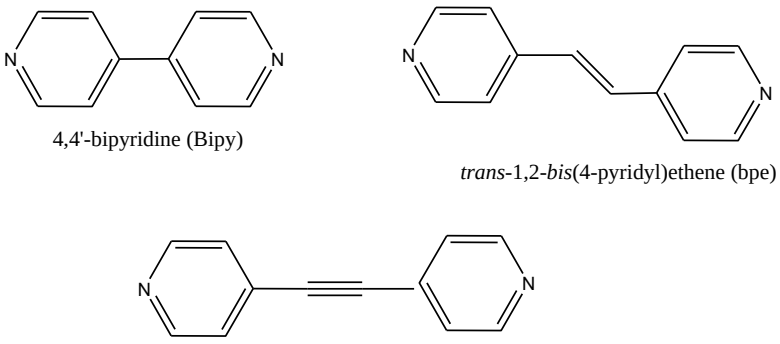

Figure 2.45 Rigid organic ligands used in the coordination polymer

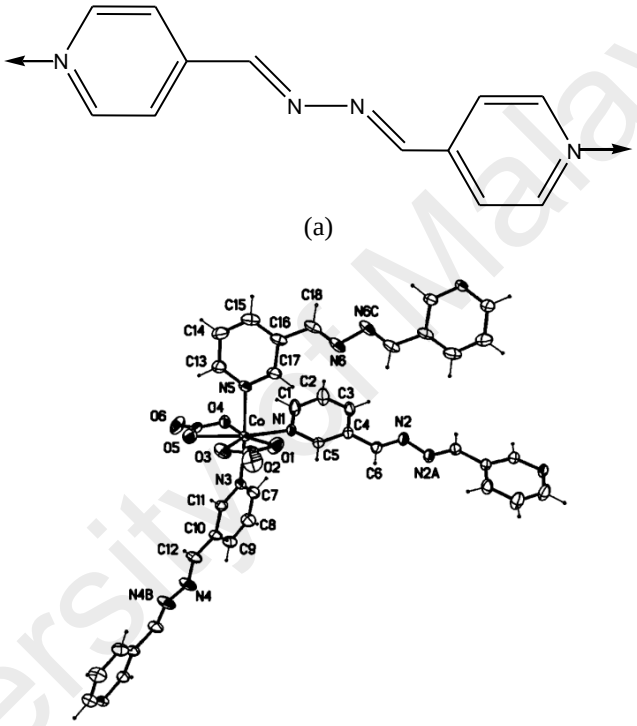

Figure 2.46 Coordination polymer with Schiff base ligand (a) ligand 1,4-bis(3-pyridyl)-2,3-diaza-1,3-butadiene, (b) Co(II) complex [104]

Pal *et al*. [110] investigated the polymeric square-pyramidal Cu(II) complexes containing acetate bridges, namely $[Cu_2(\mu\text{-}O_2CCH_3)_2(pabh)_2]$ and $[Cu_2(\mu\text{-}O_2CCH_3)_2(pamh)_2]$ (**Figure 2.47**). It was observed that the ligand binds the metal ion via the pyridine-N, the imine-N and the amide-O atoms. The electronic spectra of the complexes in methanol showed a *d-d* transition in the visible region (687‑694 nm). The complexes were redox active, and in each case, two reduction responses were

observed in the potential range −0.06 V to −0.29 V and −0.60 V to −0.70 V (vs. Ag/AgCl) in methanol.

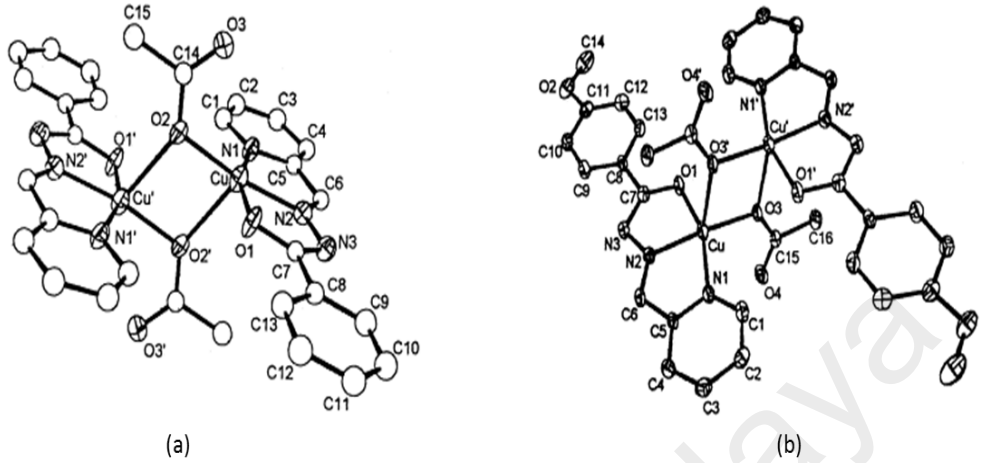

Figure 2.47 Polymeric square pyramidal Cu(II) complex; (a) $[Cu_2(\mu\text{-}O_2CCH_3)_2(pabh)_2]$, (b) $[Cu_2(\mu\text{-}O_2CCH_3)_2(pamh)_2]$. (pabh = 2-pyridine-carboxaldehyde aroylhydrazonespyridine; pamh = 2-pyridine-carboxaldehyde methyl-aroylhydrazones) [105]

The polymeric complexes of Co(II) with 5-chloro-2-hydroxyacetophenone oxime (CHAO) and 3,5-dichloro-2-hydroxyacetophenone oxime (DCHAO) were synthesized and characterized by Keemti Lai [111]. It was found that that the complex was octahedral and the magnetic moment were 1.93 B.M, indicating a low-spin Co(II) atom. Additionally, the geometry at Co(II) centre was octahedral, where coordinating with unsaturated oxygen atom of the oximino group (**Figure 2.48**).

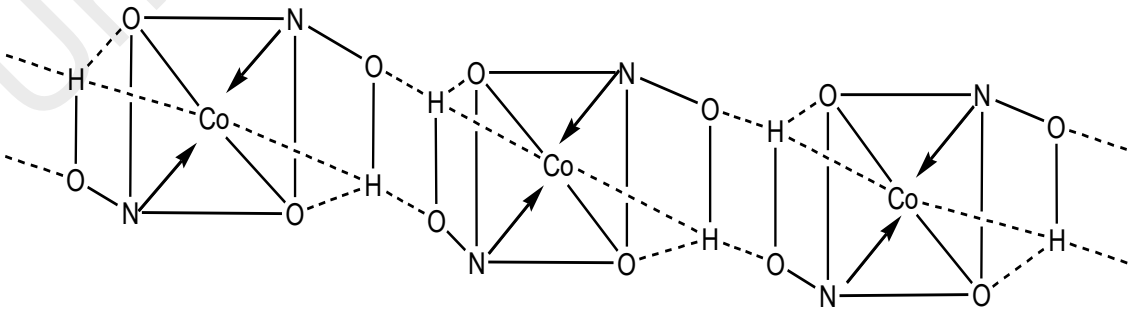

Figure 2.48 A polymeric cobalt(II) complex [106]

A novel series of conjugated coordination polymers of Cu(II), Ni(II), Co(II) and Fe(II) (**Figure 2.49**) were synthesized using Heck polycondenstaion or by metal

chelation after polymerization by Shengwen Yuan *et al*. [112]. The IR spectra showed C=O stretching vibration around 1625 - 1655 cm^{-1}; CH_2 and CH_3 stretching vibration around 2850 - 2930 cm^{-1}; deformation bending around 1460 - 1490 cm^{-1}. It was found that MLCT transition for Cu(II), Ni(II) and Co(II) were in the range 400 - 560 nm. These overlapped with the $\pi - \pi^*$ intraligand transition of bpy (around 423 nm). However, the MLCT band of the Fe(II) complex extended further to about 620 nm and the $\pi - \pi^*$ intraligand transition was at 310 nm. In all of the polymers, the metal ions were paramagnetic. The Ni(II) complex was ferromagnetic, Cu(II) complex was antiferromagnetically coupled, while both Co(II) and Fe(II) complexes were high spin.

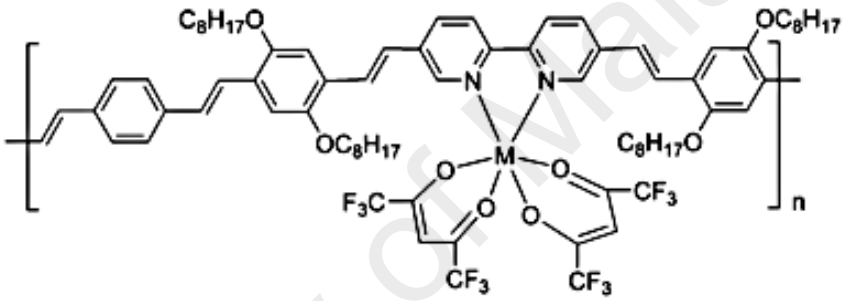

Figure 2.49 Conjugated polymers containing metal complexes (M = Cu(II), Ni(II), Co(II), and Fe(II) [112]

Coordination polymers also have high thermal stability. For example, the decomposition temperature (T_d) for all complexes presented above were in the range of 220 - 268 °C. They also have low glass transition temperatures (T_g around 55 °C) due to the presence of long alkyl side chains and bulky metal complexes. The polymers exhibited emission peaks around 590 nm upon excitation at MLCT wavelength. The cyclic voltammetry (CV) for the Co(II) complex showed an irreversible anodic peak at +0.754 V corresponding to oxidation of Co(II) to Co(III), while that for the Fe(II) complex showed a weak reversible reduction-oxidation couple with $E_{½}$ = 0.422 V corresponding to Fe(II/III).

2.4 Liquid Crystals

2.4.1 Introduction

The liquid crystal state is a distinct phase of matter observed between the crystalline (solid) and isotropic (liquid) states [113]. Crystalline materials demonstrate long range periodic order in three dimensions, while an isotropic liquid has no orientational order. Substances that are not as ordered as a solid, yet have some degree of alignment are properly called liquid crystals.

Liquid crystals generally have several common characteristics. The distinguishing characteristic of the liquid crystalline state is the tendency of the molecules (mesogens) to point along a common axis, called the director. This is in contrast to molecules in the liquid phase, which have no intrinsic order. In the solid state, molecules are highly ordered and have little translational freedom. The characteristic orientational order of the liquid crystal state is between the traditional solid and liquid phases and this is the origin of the term mesogenic state, used synonymously with liquid crystal state. The average alignment of the molecules for each phase is shown in **Figure 2.50**.

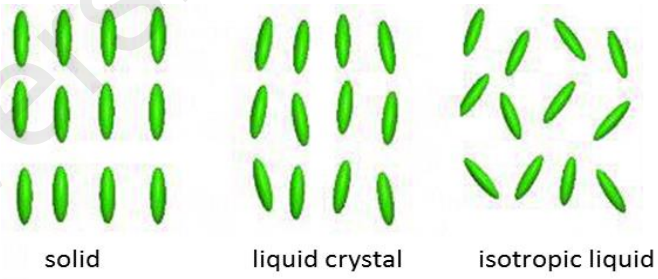

Figure 2.50 The characteristic orientational order of the liquid crystal state compared to a solid and a liquid

The study of liquid crystals began in 1888 when Friedrich Reinitzer, an Austrian botanist, observed that cholesteryl benzoate (**Figure 2.51**) had two distinct melting points. In his experiments, Reinitzer increased the temperature of the solid sample and watched the crystal change into a hazy liquid. As he increased the temperature further, the material changed again into a clear, transparent liquid [114].

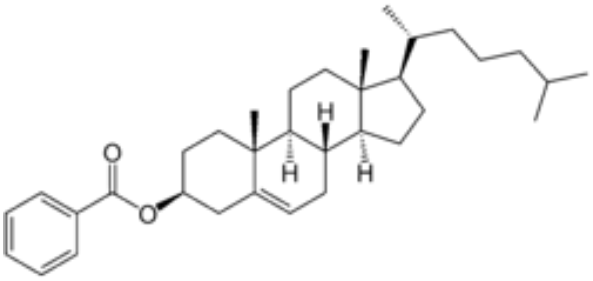

Figure 2.51 Cholesteryl benzoate molecule

An essential requirement for mesomorphism to occur is that the molecule must be highly geometrically anisotropic in shape, like a rod-like (calamitic) or a disc-like (discotic). Depending on the detailed molecular structure, the system may pass through one or more mesophases before it is transformed into the isotropic liquid. Transitions to these intermediate states may be brought about by purely thermal processes (thermotropic mesomorphism) or by the influence of solvents (lyotropic mesomorphism).

For example, the self-organization of anisotropic molecules in liquid crystalline phases is shown in **Figure 2.52**. Rod-like molecules form a nematic liquid, in which the longitudinal axes of the molecules are parallelly aligned to a common preferred direction ("director"). The structures are rigidness of the long axis, strong dipoles and/or easily polarizable substituents. On the other hand, disc-like molecules arrange to molecule-stacks (columns), in which the longitudinal axes are also aligned parallelly to the director. As a result of their orientational order, liquid crystals exhibit anisotropic physical properties, just like crystals [115].

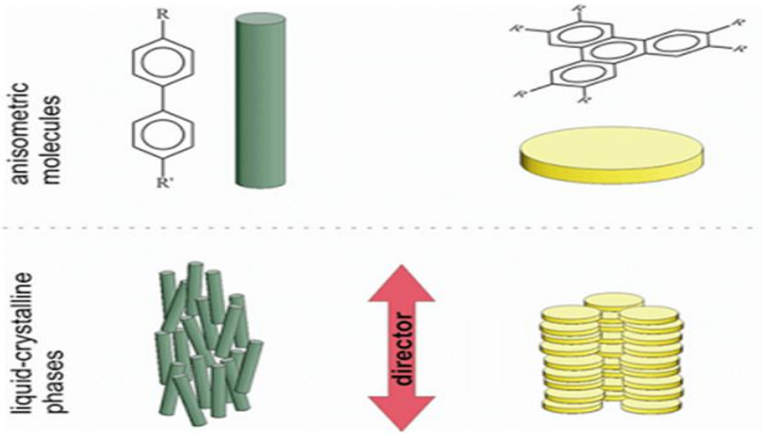

Figure 2.52 Self-organization of anisometric molecules in liquid-crystal phases: green: rod-like (calamitic), yellow: disc-like (discotic)

Vast majority of thermotropic liquid crystals are composed of rod-like molecules. They are classified into three types: smectic, nematic, and cholesteric (chiral nematic) (**Figure 2.53 (a-c)**). In contrast, the disc-like structures are divided into two distinct categories: columnar and nematic (**Figure 2.53 (d,e)**). Unlike the classical nematic of rod-like, the phase of nematic disc-like is optically negative.

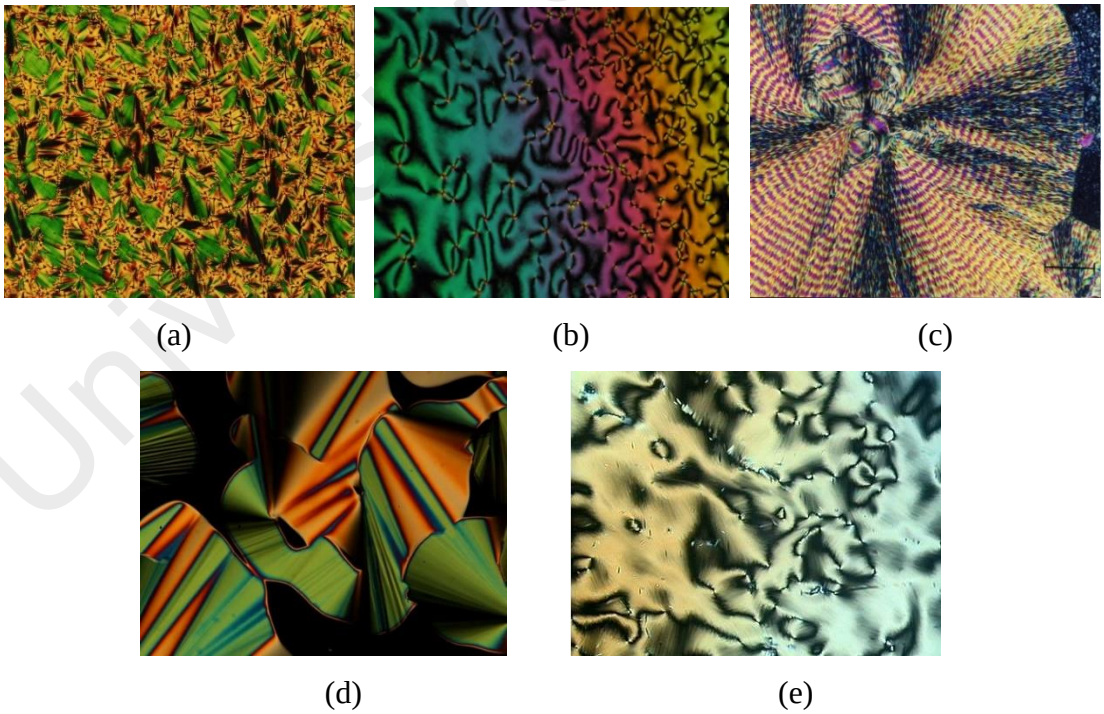

Figure 2.53 Types of liquid crystal: (a) smectic, (b) nematic rod-like, (c) cholesteric, (d) columnar, (e) nematic disc-like

Most liquid crystals exhibit polymorphism, or a condition where more than one phase is observed in the liquid crystalline state. For example, Daniel *et al*. [116]

investigated novel selenoesters fluorescent liquid crystalline exhibiting a rich phase polymorphism. They reported that the selenoester with a longer alkyl chain possesses a rich polymorphism, as shown below:

Cr → SmI → SmC → N → I (heating cycle)

I → N → SmC→ SmI → SmX → Cr (cooling cycle)

where, Cr is crystalline, SmI is smectic I, SmC is smectic C, SmX is smectic X and I is isotropic liquid.

Thermotropic mesophases are detected and characterized by two major methods, namely optical polarization microscopy (POM) and differential scanning calorimetry (DSC).

For POM, a small amount of the material was placed between two crossed polarizers. The sample was then heated and cooled. As the isotropic phase would not significantly affect the polarization of the light, it would appear very dark, whereas the crystal and liquid crystal phases will both polarize the light in a uniform way, leading to brightness and colour gradients. This method allows for the characterization of the particular phase, as the different phases are defined by their particular order, which must be observed.

DSC allows for a more precise determination of phase transitions and transition enthalpies. In DSC, a small sample is heated in a way that generates a very precise change in temperature with respect to time. During phase transitions, the heat flow required to maintain this heating or cooling rate will change. These changes can be observed and attributed to various phase transitions, such as key liquid crystal transitions.

2.4.2 Liquid crystals for PV cells

The research of liquid crystal for PV cells was done by Gwomei Wu *et al*. [117]. They designed and fabricated novel birefringent liquid crystal polymer-coated silicon solar

cells. The prepared liquid crystal polymer precursor solution was fluidic and could flow like liquid. It was distributed uniformly on a solar cell surface by the traditional spin-coating technique. They have demonstrated that the novel birefringent liquid crystal polymer coatings showed good enhancement in energy conversion efficiency at inclined incident angles for photovoltaic silicon solar cells. A higher degree of improvement was observed with a larger incident angle. The results showed that the 1%-precursor liquid crystal polymer-coated solar cell samples exhibited an enhancement of 1.97% at the incident angle of 15°. The enhancement was further increased to 3.05% at a larger incident angle of 30°.

Advanced research of developing this material could replace or eliminate the costly chemical etching or texturing. The expensive sunlight tracking system might not be needed any more. The objective in achieving higher solar cell energy conversion efficiency with a more environmentally friendly technology could thus be implemented by a proper design of the birefringent liquid crystal polymer film coating structures.

In general, crystalline molecular organic materials exhibit better transport properties than their polymeric counterparts. However, single crystals are difficult and costly to process, a disadvantage which can be overcome by utilizing discotic liquid crystals since their columnar structure resembles the aromatic stacking in single crystalline conductors. Schmidt-Mende *et al.* [118] recently used hexabenzocorone-based discotic liquid crystal (**Figure 2.54**) as hole transporting layer to construct an efficient organic photovoltaic solar cell.

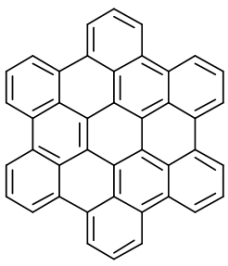

Figure 2.54 Hexabenzocorone

The supramolecular assemblies of disc-shaped molecules, such as hexaalkylthio-triphenylene (TP) and hexaalkylthio-tricycloquinazoline (TCQ) (**Figure 2.55**) have been synthesized by Sandeep Kumar [119]. The molecules exhibited columnar phase, in which the disc are stacked one on top of another to form columns. Discotic liquid crystal form columnar mesophases probably due to intense π-π interactions of polycyclic aromatic cores. The separation between the aromatic cores is of the order 3.5 Å so that there is considerable overlap of π orbitals.

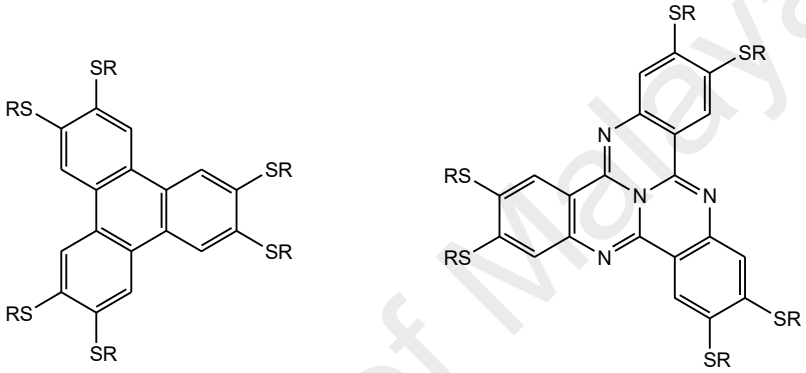

hexaalkylthio-TP hexaalkylthio-TCQ

Figure 2.55 Supramoleculars disc-shaped

According to their research, supramoleculars disc-shaped have very high charge carrier mobility, 0.1 cm^2 V^{-1} s^{-1}. Hence, they offer potential applications as organic charge transport materials in a variety of devices such as one-dimensional conductors, photoconductors, field-effect transistors, photovoltaic solar cells, etc.

Discotic liquid crystalline semiconductors are divided into two types: (a) *p*-type, in which the majority of charge carriers are holes, and (b) *n*-type, where the majority of charge carriers are electrons. Both *p*-type discotic liquid crystals, such as triphenylene, dibenzopyrene and hexabenzocoronene, and *n*-type discotic liquid crystals, such as tricycloquinazoline, anthraquinone and perylene, are shown in **Figure 2.56 (a-e)**.

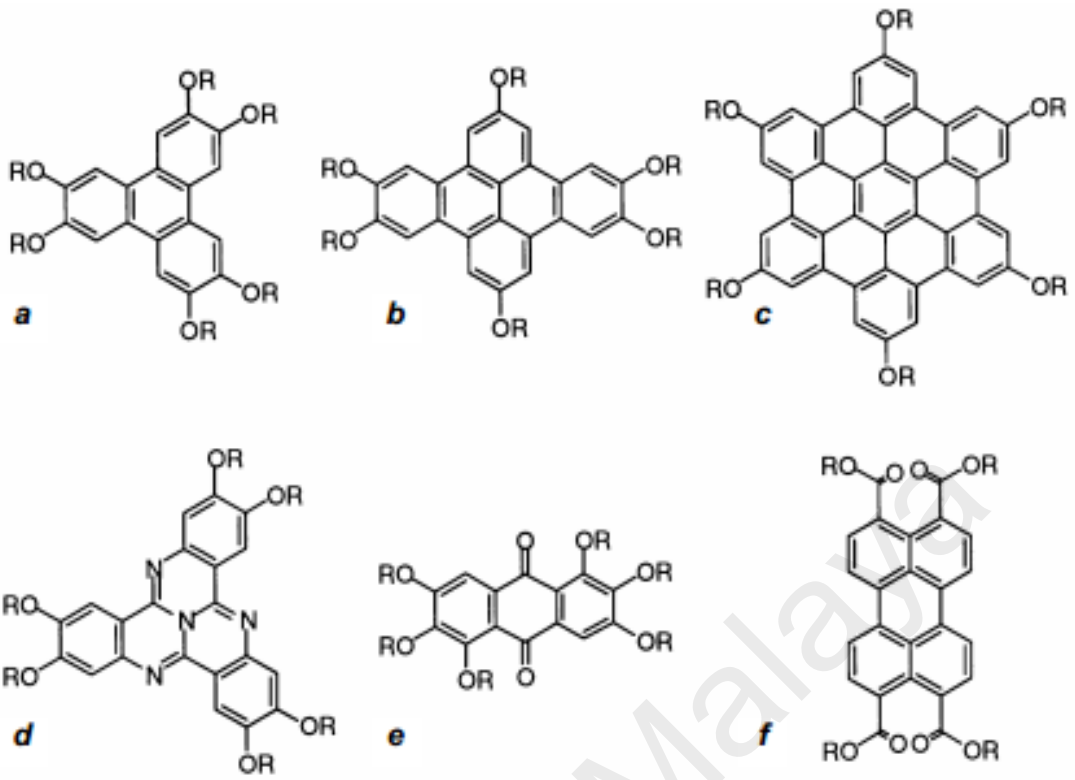

Figure 2.56 Chemical structure of *p*-type (a–c) and *n*-type (d–f) discotics

Schmidt-Mende *et al*. constructed a *p*/*n*-type PV cell using discotic liquid crystalline hexabenzocoronene as the hole-transporting layer and a perylen dye (N,N'-bis(1-ethylpropyl)-3,4,9,10-perylene-bis(dicarboximide)) (**Figure 2.57**) as electron transporting layer (**Figure 2.58**). This compound has the highest hole mobility ever reported for a discotic liquid crystal. The device made by Schmidt-Mende *et al*. exhibits external quantum efficiencies (EQEs) up to 34% and power efficiencies of up to ~2%.

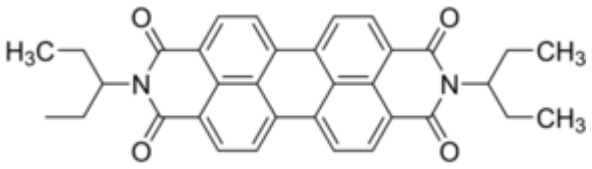

Figure 2.57 Perylene dye

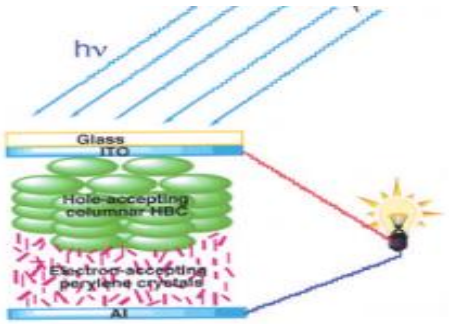

Figure 2.58 Schematic diagram of bilayer PV cell

A novel of perylene-based were studied by Chunghong Lei *et al*. [120]. It was found that their electron-acceptors have similar electron affinities. However, different thermotropic phases are blended with nematic liquid crystalline electron-donors with a fluorene-thiophene structure to form single layer photovoltaic devices. The best results were obtained when the nematic donor was mixed with an amorphous acceptor to give a supercooled nematic glass at room temperature. Atomic force microscopy operating in the phase contrast mode revealed phase separation on a nanometer scale with a broad distribution of domain sizes peaking at 26 nm. The morphology of the different blends was correlated with the performance of the photovoltaic devices. Power conversion efficiencies up to 0.9 % were obtained with excitation at 470 nm.

References

[1] Retrieved from http://greenliving.lovetoknow.com/ on 20 October 2014

[2] Jha, A. R., *Solar Cell Technology and Applications*, CRC Press, Technology Engineering, Florida, 2009.

[3] Gevorkian, P., *Sustainable Energy System Engineering: The Complete Green Building Design Resource*, McGraw Hill Professional, USA, 2007.

[4] Tiwari, G. N., Dubey, S., *Fundamentals of Photovoltaic Modules and Their Applications*, The Royal Society of Chemistry, Cambridge, UK, 2010.

[5] Cook, G., Billman, L., Adcock, R., *Photovoltaic Fundamentals, in, Solar Energy* Research Institute (SERI), Washington, US, 1991.

[6] Solanki, C. S., *Solar Photovoltaics: Fundamentals, Technologies and Applications*, 2nd ed., PHI Learning Private Limited, New Delhi, India, 2011.

[7] Sundström, V., Pullerits, T., van Grondelle, R., *The Journal of Physical Chemistry B*, 103 (**1999**) 2327-2346.

[8] van Grondelle, R., Dekker, J. P., Gillbro, T., Sundstrom, V., *Biochimica et Biophysica Acta (BBA) - Bioenergetics*, 1187 (**1994**) 1-65.

[9] Grossman, A. R., Bhaya, D., Apt, K. E., Kehoe, D. M., *Annual Review of Genetics*, 29 (**1995**) 231-288.

[10] Cheng, Y. C., Fleming, G. R., *Annual Review of Physical Chemistry*, 60 (**2009**) 241- 262.

[11] Cogdell, R. J., Gall, A., Köhler, J., *Quarterly Reviews of Biophysics*, 39 (**2006**) 227-324.

[12] Scholes, G. D., Fleming, G. R., Olaya-Castro, A., Grondelle, R. v., *Nature Chemistry*, 3 (**2011**) 763-774.

[13] Ziessel, R., Ulrich, G., Haefele, A., Harriman, A., *Journal of the American Chemical Society*, 135 (**2013**) 11330-11344.

[14] Mcevoy, A., Markvart, T., Castaner, L., *Solar Cells Materials, Manufacture and Operation*, 2nd ed., Elsevier, Ltd, Oxford, UK, 2013.

[15] Heywang, W., Zaininger, K. H., *Silicon: The Semiconductor Material*, Springer Verlag, Berlin, Germany, 2004.

[16] Pearce, J., Lau, A., *International Solar Energy Conference*, Nevada, USA, 15-20 June 2002, 181-186.

[17] Becker, C., Ruske, F., Sontheimer, T., Gorka, B., Bloeck, U., Gall, S., Rech, B., *Journal of Applied Physics*, 106 (**2009**) 084506.

[18] Gall, S., Becker, C., Conrad, E., Dogan, P., Fenske, F., Gorka, B., Lee, K.Y., Rau, B., Ruske, F., Rech, B., *Solar Energy Materials and Solar Cells*, 93 (**2009**) 1004-1008.

[19] Green, M. A., *Solar Energy*, 74 (**2003**) 181-192.

[20] Bergmann, R. B., Werner, J. H., *Thin Solid Films*, 403-404 (**2002**) 162-169.

[21] Green, M. A., *Solar cells: Operating principles, technology, and system applications*, Prentice Hall, Inc., US, 1982.

[22] Aberle, A. G., *Journal of Crystal Growth*, 287 (**2006**) 386-390.

[23] Retrieved from http://why-sci.com/solar-power/ on 20 October 2014.

[24] Goze, C., Ulrich, G., Mallon, L. J., Allen, B. D., Harriman, A., Ziessel, R., *Journal of the American Chemical Society*, 128 (**2006**) 10231-10239.

[25] Wurfel, P., *Physics of Solar Cells: From Basic Principles to Advanced Concepts*, 2nd ed., Wiley-VCH Verlag GmbH&Co, Weinheim, Germany, 2009.

[26] Walle, C. G. V. d., *Wide-band-gap Semiconductors*, 7th ed., Elsevier, New York, USA, 1992.

[27] Schmid, G., *Nanotechnology: Principles and fundamentals*, Wiley VCH, UK, 2008.

[28] Dharma, J., Pisal, A., *Simple Method of Measuring the Band Gap Energy Value of TiO_2 in the Powder Form using a UV/Vis/NIR Spectrometer*, retrieved from http://www.perkinelmer.com/content/applicationnotes/ on 3 July 2014.

[29] He, Y., Zhao, G., Peng, B., Li, Y., *Advanced Functional Materials*, 20 (**2010**) 3383- 3389.

[30] Abdullah, N., Mohamadin, M. I., *Advanced Materials Research*, 347-353 (**2011**) 738-741.

[31] Henkelman, G., Jóhannesson, G., Jónsson, H., *Progress on theoretical chemistry and physics*, Kluwer Academic Publishers, (**2000**) 269-300.

[32] Jameson, D. M., Croney, J. C., Moens, P. D. J., *Methods in Enzymology*, 360 (**2003**) 1-43.

[33] Lakowicz, J. R., *Principles of Fluorescence Spectroscopy*, 3rd ed., Springer, USA.

[34] Theivasanthi, T., Alagar, M., *Research and Application of Material*, 1 (**2013**) 36-43.

[35] Wang, J., *Analytical Electrochemistry*, 3rd ed., John Wiley & Sons, Inc., New Jersey, 2006.

[36] Scholz, F., *Electroanalytical Methods: Guide to Experiments and Applications*, Springer, Heidelberg, Germany, 2010.

[37] Bard, A. J., Faulkner, L. R., *Electrochemical Methods: Fundamentals and Applications*, 2nd ed., Wiley VCH, New Jersey, 2000.

[38] Haque, F., Rahman, M., Ahmed, E., Bakshi, P., Shaikh, A., *Dhaka University Journal of Science*, 61(2) (**2013**) 161-166.

[39] Toledo, I., Arancibia, M., Andrade, C., Crivelli, I., *Polyhedron*, 17 (**1998**) 173-178.

[40] Nicholson, R. S., Irving, S., *Analytical Chemistry*, 36 (**1964**), 706-723.

[41] Bredas, J. L., Silbey, R., Boudreaux, D. S., Chance, R. R., *Journal of the American Chemical Society*, 105 (**1983**) 6555-6559.

[42] Brownell, L.V., Robins, K. A., Jeong, Y., Lee, Y., Lee, D. C.,*The Journal of Physical Chemistry C*, 117 (**2013**) 25236-25247.

[43] de Leeuw, D. M., Simenon, M. M. J., Brown, A. R., Einerhand, R. E. F., *Synthetic Metals*, 87 (**1997**) 53-59.

[44] Misra, A., Kumar, P., Srivastava, R., Dhawan, S. K., Kamalasanan, M. N., Chandra, S., *Indian Journal of Pure and Applied Physics*, 43 (**2005**) 921-925.

[45] Lohrman, J., Zhang, C., Zhang, W., Ren, S., *Chemical Communications*, 48 (**2012**) 8377-8379.

[46] Sinton, R. A., Cuevas, A., Stuckings, M., In *Quasi-steady-state photoconductance, a new method for solar cell material and device characterization*, Proceedings of Photovoltaic Specialists Conference of the Twenty Fifth IEEE, 1996, pp. 457-460.

[47] Ahrenkiel, R. K., Call, N., Johnston, S. W., Metzger, W. K., *Solar Energy Materials and Solar Cells*, 94 (**2010**) 2197-2204.

[48] Metzger, W. K., Albin, D., Levi, D., Sheldon, P., Li, X., Keyes, B. M., Ahrenkiel, R. K., *Journal of Applied Physics*, 94 (**2003**) 3549-3555.

[49] Bonizzoni, M., In *Nonlinear Curve Fitting in Supramolecular Chemistry Analysis*, OriginLab Corporation, USA, 2010, retrieved from http://www.originlab.com/.on 20 October 2014

[50] Vijayaraj, A., Prabu, R., Suresh, R., Manoharan, S., Anandan, S., Narayanan, V., *Turkish Journal of Chemistry*, 37 (**2013**) 344-357.

[51] Montalti, M., Cedi, A., Prodi, L., Gandolfi, M. T., *Handbook of Photochemistry*, 3rd ed., CRC press Taylor & Francis Group, Florida, US, 2006.

[52] O'Regan, B., Grätzel, M., *Nature*, 353 (**1991**) 737-740.

[53] Wang, Q., Ito, S., Grätzel, M., Fabregat-Santiago, F., Mora-Seró, I., Bisquert, J., Bessho, T., Imai, H., *The Journal of Physical Chemistry B*, 110 (**2006**) 25210-25221.

[54] Wan, H., *Dye-Sensitized Solar Cells*, The University of Alabama, Department of Chemistry, 2004, retrieved from http://dyesensitizedsolarcell.weebly.com/ on 12 November 2014

[55] Dell'Orto, E., Raimondo, L., Sassella, A., Abbotto, A., *Journal of Materials Chemistry*, 22 (**2012**) 11364-11369.

[56] Clifford, J. N., Planells, M., Palomares, E., *Journal of Materials Chemistry*, 22 (**2012**) 24195-24201.

[57] Moudam, O., In *High efficiency for Dye-Sensitized Solar Cells with water-based electrolyte*, Proceedings of International Renewable and Sustainable Energy Conference, One'Cos, Ouarzazate, Maroco, 2013.

[58] Kalyanasundaram, K., *Dye-sensitized Solar Cells*, CRC Press, 2010.

[59] Ryan, M., *Platinum Metals Review*, (**2009**) pp. 216-218.

[60] Hwang, S., Lee, J.H., Park, C., Lee, H., Kim, C., Park, C., Lee, M. H., Lee, W., Park, J., Kim, K., Park, N.G., Kim, C., *Chemical Communications*, (**2007**) 4887-4889.

[61] Hagfeldt, A., Grätzel, M., *Chemical Reviews*, 95 (**1995**) 49-68.

[62] Kalyanasundaram, K., Grätzel, M., *Coordination Chemistry Reviews*, 177 (**1998**) 347-414.

[63] Gerfin, T., Grätzel, M., Walder, L., *Progress Inorganic Chemistry*, 44 (**1997**) 345-393.

[64] Wang, P., Zakeeruddin, S. M., Moser, J. E., Nazeeruddin, M. K., Sekiguchi, T., Grätzel, M., *Nature Materials*, 2 (**2003**) 402-408.

[65] Campbell, W. M., Jolley, K. W., Wagner, P., Wagner, K., Walsh, P. J., Gordon, K. C., Schmidt-Mende, L., Nazeeruddin, M. K., Wang, Q., Grätzel, M., Officer, D. L., *The Journal of Physical Chemistry C*, 111 (**2007**) 11760-11762.

[66] Wang, Q., Campbell, W. M., Bonfantani, E. E., Jolley, K. W., Officer, D. L., Walsh, P. J., Gordon, K., Humphry-Baker, R., Nazeeruddin, M. K., Grätzel, M., *The Journal of Physical Chemistry B*, 109 (**2005**) 15397-15409.

[67] Atkins, P., Overton, T., Rourke, J., Weller, M., Armstrong, F., in: Inorganic Chemistry, W. H. Freeman and Company, New York, 2010.

[68] Petty, M. C., *Molecular Electronics: From Principles to Practice*, John Wiley & Sons. Ltd, England, UK, 2007.

[69] Raj, G., *Advanced Inorganic Chemistry*, 12th ed., Stayendra Rastogi Mitra, India, 2010.

[70] Laporte, O., Meggers, W. F., *Journal of Optical Society America*, 11 (**1925**) 459-460.

[71] Wang, Y., *The Journal of Physical Chemistry*, 96 (**1992**) 764-767.

[72] Paris, J. P., Brandt, W. W., *Journal of the American Chemical Society*, 81 (**1959**) 5001-5002.

[73] Retrieved from http://www.odinity.com/comparing-tris-22-bipyridine-complexes-iron-ii-ruthenium-ii-spectroscopy-electrochemistry/ on 15 November 2014.

[74] Duchovnay. A., *Comparative Electrochemistry, Electronic Absorption Spectroscopy And Spectroelectrochemistry Of The Monometallic Ruthenium Polypyridyl Complexes [Ru(bpy)(dpb)$_2$](PF6)$_2$*. MSc. Thesis. Faculty of the Virginia Polytechnic Institute, State University, Blacksburg, Virginia, 2011.

[75] Sathyanarayana, D. N., *Electronic Absorption Spectroscopy and Related Techniques*, Universities Press Ltd., Hyderabad, India, 2001.

[76] Atkins, S., *Inorganic Chemistry*, 5th ed., Oxford University Press, UK, 2010.

[77] Hauser, A., Spin Crossover in Transition Metal Compounds I, In *Ligand Field Theoretical Considerations*; P. Gütlich, H. A. Goodwin (Eds.) Springer Berlin Heidelberg, 2004, pp. 49-58.

[78] Lewis, S. J., Wilkins, R. G., *Modern coordination chemistry: Principles and Methods*, Interscience Publishers Inc., New York, USA, 1960.

[79] Kahn, O., *Molecular Magnetism*, VCH Publisher, Inc., USA, 1993.

[80] Hoppe, J. I., *Journal of Chemical Education*, 49 (**1972**) 505.

[81] Rosenberg, R. C., Root, C. A., Gray, H. B., *Journal of the American Chemical Society*, 97 (**1975**) 21-26.

[82] Ferrere, S., *Chemistry of Materials*, 12 (**2000**) 1083-1089.

[83] Ferrere, S., *Inorganica Chimica Acta*, 329 (**2002**) 79-92.

[84] Winkler, J. R., Sutin, N., *Inorganic Chemistry*, 26 (**1987**) 220-221.

[85] McCusker, J. K., Walda, K. N., Dunn, R. C., Simon, J. D., Magde, D., Hendrickson, D. N., *Journal of the American Chemical Society*, 115 (**1993**) 298-307.

[86] Creutz, C., Chou, M., Netzel, T. L., Okumura, M., Sutin, N., *Journal of the American Chemical Society*, 102 (**1980**) 1309-1319.

[87] Tachibana, Y., Moser, J. E., Grätzel, M., Klug, D. R., Durrant, J. R., *Journal of Physical Chemistry*, 100 (**1996**) 20056.

[88] Ellingson, R. J., Asbury, J. B., Ferrere, S., Ghosh, H. N., Sprague, J. R., Lian, T., Nozik, A. J., *The Journal of Physical Chemistry B*, 102 (**1998**) 6455-6458.

[89] Hannappel, T., Burfeindt, B., Storck, W., Willig, F., *The Journal of Physical Chemistry B*, 101 (**1997**) 6799-6802.

[90] Ferrere, S., Gregg, B. A., *Journal of the American Chemical Society*, 120 (**1998**) 843-844.

[91] H, S., *Annual Chemical Pharmacies Suppl*, 3 (**1864**).

[92] Hobday, M. D., Smith, T. D., *Coordination Chemistry Reviews*, 9 (**1972**).

[93] Thomas,R., Thomas, J.,Parameswaran, G., *Indian Journal of Chemistry*, A21 (**1982**).

[94] Khalil, M. M., Attia, A.E., *Journal of Chemical & Engineering Data*, 44 (**1999**) 180-184.

[95] Mukherjee, A., Saha, M. K., Rudra, I., Ramasesha, S., Nethaji, M., Chakravarty, A. R., *Inorganica Chimica Acta*, 357 (**2004**) 1077-1082.

[96] Ourari, A., Aggoun, D., Ouahab, L., *Inorganic Chemistry Communications*, 33 (**2013**) 118-124.

[97] Tas, E., Kilic, A., Durgun, M., Küpecik, L., Yilmaz, I., Arslan, S., *Spectrochimica Acta Part A: Molecular and Biomolecular Spectroscopy*, 75 (**2010**) 811-818.

[98] Batten Stuart, R., Champness Neil, R., Chen, X. M., Garcia-Martinez, J., Kitagawa, S., Öhrström, L., O'Keeffe, M., Paik Suh, M., Reedijk, J., *Pure and Applied Chemistry*, (**2013**) pp. 1715.

[99] Batten, S. R., Neville, S. M., Turner, D. R., *Coordination Polymers: Design, Analysis and Application*, RSC, Cambridge, 2009.

[100] Janiak, C., *Dalton Transactions*, (**2003**) 2781-2804.

[101] James, S. L., *Chemical Society Reviews*, 32 (**2003**) 276-288.

[102] Batten, S.R., Murray, K.S., *Coordination Chemistry Reviews*, 246 (**2003**) 103-130.

[103] Maspoch, D., Ruiz-Molina D., Veciana, J., *Journal of Materials Chemistry*, 14 (**2004**) 2713-2723.

[104] Kurimura, Y., Tsuchida, E., Kaneko, M., *Journal of Polymer Science Part A-1: Polymer Chemistry*, 9 (**1971**) 3511-3519.

[105] Suzuki, T., Shirai, H., Hojo, N., *Journal of Inorganic Organometallic Polymer*, 4 (**1994**) 251-260.

[106] Epstein, A., Wildi, B. S., *The Journal of Chemical Physics*, 32 (**1960**) 324-329.

[107] Diab, M. A., El-Sonbati, A. Z., El-Sanabari, A. A., Taha, F. I., *Polymer Degradation and Stabilisation*, 23 (**1988**) 83-90.

[108] Ma, Y., Cheng, A. L., Tang, B., Gao, E. Q., *Dalton Transactions*, 43 (**2014**) 13957-13964.

[109] Dong, Y. B., Smith, M. D., zur Loye, H. C., *Inorganic Chemistry*, 39 (**2000**) 4927-4935.

[110] Sangeetha, N. R., Pal, S., *Polyhedron*, 19 (**2000**) 1593-1600.

[111] Lal, K., *Polymer Bulletin*, 3 (**1980**) 297-299.

[112] Yuan, S., Jaramillo, R., Rosenbaum, T. F., Yu, L., *Macromolecules*, 39 (**2006**) 8652-8658.

[113] Chandrasekhar, S., *Liquid Crystals*, 2nd ed., University Press, Cambridge, UK, 1992.

[114] Reinitzer, F., *Monatshefte für Chemie*, 9 (**1888**) 421-441.

[115] Stegemeyer, H., *Liquid Crystals Today*, 4 (**1994**) 1-2.

[116] Rampon, D. S., Rodembusch, F. S., Schneider, J. M. F. M., Bechtold, I. H., Goncalves, P. F. B., Merlo, A. A., Schneider, P. H., *Journal of Materials Chemistry*, 20 (**2010**) 715-722.

[117] Wu, Q., Esteghamatian, M., Hu, N. X., Popovic, Z., Enright, G., Tao, Y., D'Iorio, M., Wang, S., *Chemistry of Materials*, 12 (**1999**) 79-83.

[118] Schmidt-Mende, L., Fechtenkötter, A., Müllen, K., Moons, E., Friend, R. H., MacKenzie, J. D., *Science*, 293 (**2001**) 1119-1122.

[119] Kumar, S., *Supramolecular assemblies of disk-shaped molecules,* Proceedings of International Conference On Electronic and Photonic Materials, Devices and Systems, University of Culcutta, Kolkata, India, 2006.

[120] Lei, C., Al Khalifah, M. S., O'Neill, M., Aldred, M. P., Kitney, S. P., Vlachos, P., Kelly, S. M., *Calamatic liquid crystal blends for organic photovoltaics*, Proceedings of Organic Photovoltaics IX Conference, 2008, pp.705214-705219.

CHAPTER 3 EXPERIMENTAL

3.1 Introduction

This research is focused on the synthesis and characterization of complexes of Cu(II) (d^9), Ni(II) (d^8), Co(II) (d^7) and Fe(II) (d^6) ions with mixed ligands (ethanoate or hexadecanoate, and conjugated imine or amide). These complexes were designed to be low band-gap solar cell and/or spin crossover materials, and for the hexadecanoate complexes, mesogenic materials.

The imine and amide ligands were synthesized from the condensation reaction of 2,4-diamino-6-phenyl-1,3,5-triazine with: (a) pyrrole-2-carboxaldehyde to form *H_2L1*; (b) 2,5-thiophenedicarboxaldehyde to form *L2*; (c) 2,5-thiophenedicarboxylic acid to form *L3*; and (d) acetylenedicarboxylic acid to form *L4*. These ligands were then reacted with $[M(RCOO)_2]$ (M = Cu, Ni, Co, Fe; R = CH_3COO and $CH_3(CH_2)_{14}COO$). The general synthetic paths for these ligands and complexes are shown in **Scheme 3.1.**

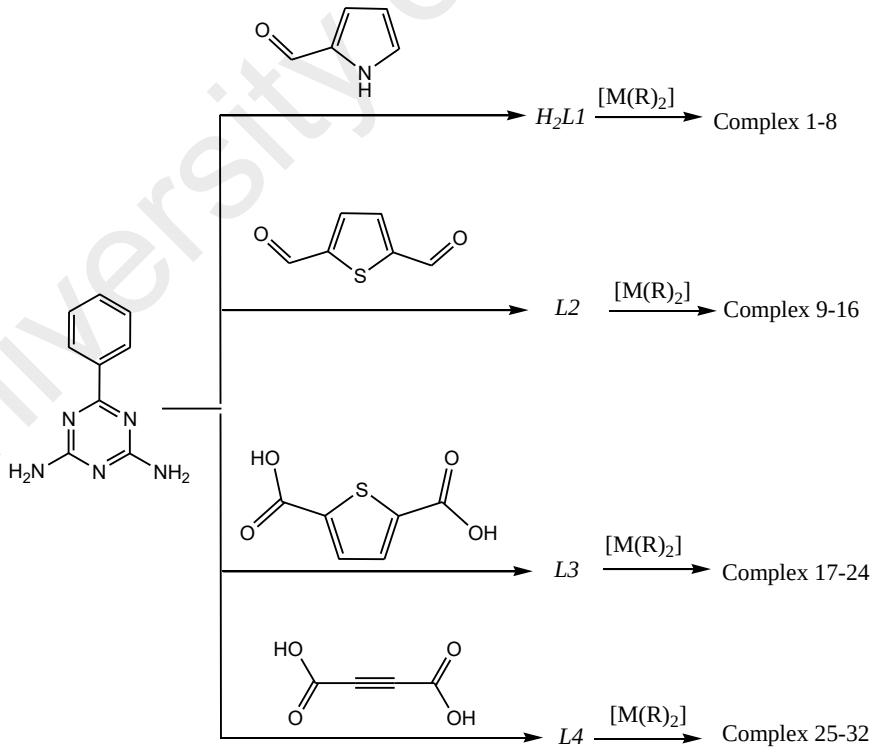

Scheme 3.1 General synthetic paths for **Complexes 1-32**

A total of four ligands, 8 precursor complexes and 32 designed complexes were synthesized and characterized. The ligands were characterized by ^{1}H-nuclear magnetic

resonance spectroscopy (^{1}H-NMR), CHN elemental analyses, and FTIR spectroscopy. The complexes were characterized by CHN elemental analyses, FTIR spectroscopy, UV-vis spectroscopy, fluorescence spectroscopy, magnetic susceptometry by the Guoy method, thermogravimetry (TGA), differential scanning calorimetry (DSC), polarised optical microscopy (POM), and cyclic voltammetry (CV).

3.2 Chemicals

All chemicals (**Table 3.1**) were commercially available and used as received.

Table 3.1 Chemicals used in the research, arranged in alphabetical order

Name	Chemical Formula	Formula Weight (g mol^{-1})	Supplier
Acetylenedicarboxylic acid	HOOC-C≡C-COOH	114.06	Aldrich
Cobalt(II) acetate tetrahydrate	$Co(CH_3COO)_2.4H_2O$	249.08	R&M
Cobalt(II) chloride hexahydrate	$CoCl_2.6H_2O$	237.93	R&M
Copper(II) acetate	$Cu(CH_3COO)_2$	181.63	Aldrich
Copper(II) chloride dihydrate	$CuCl_2.2H_2O$	170.48	R&M
2,4-Diamino-6-phenyl-1,3,5-triazine	$C_9H_9N_5$	187.20	Merck
Iron(II) acetate	$Fe(CH_3COO)_2$	173.93	Aldrich
Iron(II) chloride tetrahydrate	$FeCl_2.4H_2O$	198.81	R&M
Nickel(II) acetate tetrahydrate	$Ni(CH_3COO)_2.4H_2O$	248.84	Aldrich
Nickel(II) chloride hexahydrate	$NiCl_2.6H_2O$	237.69	R&M
hexadecanoic acid	$CH_3(CH_2)_{14}COOH$	256.42	Aldrich
Pyrrole-2-carboxaldehyde	C_5H_5NO	95.10	Merck
2,5-Thiophenedicarboxaldehyde	$C_6H_4O_2S$	241.46	Aldrich
2,5-Thiophenedicarboxylic acid	$C_6H_4O_4S$	172.16	Aldrich

3.3 Syntheses

3.3.1 Ligands

(a) H_2L1, $C_{19}H_{15}N_7$

An ethanolic solution of pyrrole-2-carboxaldehyde (11.69 g; 123 mmol) was added into an ethanolic suspension of 2,4-diamino-6-phenyl-1,3,5-triazine (11.52 g; 61.5 mmol), followed by a few drops of glacial acetic acid. The reaction mixture was heated under reflux for 2 hours. A brownish precipitate formed was filtered off from the hot reaction mixture, and washed with ethanol, and dried in an oven at 80°C. The yield was 15.84 g (68.3%).

(b) L2, $C_{19}H_{21}N_5O_2S$

The procedure was the same as for H_2L1 (**Section 3.3.1(a)**), using 2,4-diamino-6-phenyl-1,3,5-triazine (2.83 g; 15.1 mmol) and 2,5-thiophenedicarboxaldehyde (3.64 g; 15.1 mmol). The product was a brown powder, and the yield was 5.74 g (88.7%).

(c) L3, $C_{15}H_{11}N_5O_3S$

2,4-Diamino-6-phenyl-1,3,5-triazine (18.89 g; 100.9 mmol) was added portionwise to a solution of 2,5-thiophenedicarboxylic acid (12.93 g; 100.9 mmol) in absolute ethanol (100 mL). The mixture was refluxed for 2 hours and then left to cool to room temperature. A white powder formed was filtered off, washed with ethanol and dried in an oven at 80°C. The yield was 31.15 g (97.9%).

(d) L4, $C_{13}H_7N_5O_2$

The procedure was the same as for L3 (**Section 3.3.1(c**)), using 2,4-diamino-6-phenyl-1,3,5-triazine (6.38 g; 34.0 mmol) and acetylenedicarboxylic acid (3.88 g; 34.0 mmol). The product was a pale yellow powder, and the yield was 8.04 g (78.4%).

3.3.2 Metal(II) hexadecanoates

(a) Copper(II) hexadecanoate

A suspension of hexadecanoic acid (33.59 g; 130.9 mmol) in aqueous ethanol (v/v, 1:1; 200 mL) was magnetically stirred and heated on a hot plate until a clear solution formed (about 2 hours). A solution of sodium carbonate (6.94 g; 65.5 mmol) was then added portionwise, and the reaction mixture was magnetically stirred and heated for another hour. The solvents were removed on a rotary evaporator to give sodium hexadecanoate as a white powder. The yield was 36.51 g (90.1%).

Sodium hexadecanoate (7.03 g; 25.3 mmol) was dissolved in aqueous ethanol (v/v, 1:1; 200 mL). Copper(II) chloride dihydrate (2.15 g; 12.5 mmol) was added gradually to the solution, the mixture was stirred and heated for 30 minutes, and left to cool to room temperature. The greenish-blue precipitate formed was filtered off, washed with ethanol and dried in an oven at 80°C. The yield was 6.53 g (71.1%).

(b) Nickel(II) hexadecanoate

The procedure was the same as for copper(II) hexadecanoate (**Section 3.3.2(a)**), using sodium hexadecanoate (7.63 g; 27.0 mmol) and nickel(II) chloride hexahydrate (3.26 g; 13.5 mmol). The product was a greenish powder, and the yield was 7.77 g (71.3 %).

(c) Cobalt(II) hexadecanoate

The procedure was the same as for copper(II) hexadecanoate (**Section 3.3.2(a)**), using sodium hexadecanoate (7.05 g; 25.3 mmol) and cobalt(II) chloride hexahydrate (3.01 g; 12.5 mmol). The product was a purple powder, and the yield was 7.13 g (70.9%).

(d) Iron(II) hexadecanoate

The procedure was the same as for copper(II) hexadecanoate (**Section 3.3.2(a)**), using sodium hexadecanoate (7.70 g; 27.9 mmol) and iron(II) chloride tetrahydrate (2.75 g; 13.8 mmol). The product was a brown powder, and the yield was 7.57 g (72.4%).

3.3.3 Metal(II) carboxylate-L1 complexes

*(a) $[Cu_2(CH_3COO)_2(H_2O)_2(L1)]$ (**Complex 1**)*

Copper(II) ethanoate (0.91 g; 5.0 mmol) was added to an ethanolic suspension of $C_{19}H_{15}N_7$ (1.71 g; 5.0 mmol), and the mixture was heated under reflux for 3 hours. The green powder formed was filtered from the hot reaction mixture, washed with ethanol, was dried in an oven at 100°C. The yield was 2.29 g (87.4%).

*(b) $[Ni_2(CH_3COO)_2(H_2O)_2(L1)]$ (**Complex 2**)*

The procedure was the same as for copper(II) ethanoate-*L1* (**Section 3.3.3(a)**), using nickel(II) ethanoate tetrahydrate (2.38 g; 9.6 mmol) and $C_{19}H_{15}N_7$ (3.26 g; 9.6 mmol). The product was a grey powder, and the yield was 4.77 g (84.6%).

*(c) $[Co_2(CH_3COO)_2(H_2O)_2(L1)]$ (**Complex 3**)*

The procedure was the same as for copper(II) ethanoate-*L1* (**Section 3.3.3(a)**), using cobalt(II) ethanoate tetrahydrate (1.46 g; 5.9 mmol) and $C_{19}H_{15}N_7$ (2.0 g; 5.9 mmol). The product was a purple powder, and the yield was 4.13 g (92.6%).

*(d) $[Fe_3(CH_3COO)_4(H_2O)_3(L1)].H_2O$ (**Complex 4**)*

The procedure was the same as for copper(II) ethanoate-*L1* (**Section 3.3.3(a)**), using iron(II) ethanoate (0.96 g; 5.5 mmol), $C_{19}H_{15}N_7$ (1.89 g; 5.5 mmol), and about 0.1 g of ascorbic acid (as an antioxidant). The product was a black solid, and the yield was 2.77 g (97.2%).

*(e) $[Cu_2(CH_3(CH_2)_{14}COO)_2(L1)]$ (**Complex 5**)*

The procedure was the same as for copper(II) ethanoate-*L1* (**Section 3.3.3(a)**), using copper(II) hexadecanoate (2.29 g ; 2.0 mmol) and $C_{19}H_{15}N_7$ (0.68 g; 2.0 mmol). The product was a green powder, and the yield was 2.23 g (75.0%).

(f) $[Ni_2(CH_3(CH_2)_{14}COO)_2(H_2O)_2(L1)]$ ***(Complex 6)***

The procedure was the same as for copper(II) ethanoate-*L1* (**Section 3.3.3(a)**), using nickel(II) hexadecanoate (0.09 g; 0.2 mmol) and $C_{19}H_{15}N_7$ (0.05 g; 0.2 mmol). The product was a greenish powder, and the yield was 0.13 g (92.8%).

(g) $[Co_2(CH_3(CH_2)_{14}COO)_2(H_2O)_2(L1)]$ ***(Complex 7)***

The procedure was the same as for copper(II) ethanoate-*L1* (**Section 3.3.3(a)**), using cobalt(II) hexadecanoate (0.15 g ; 0.3 mmol) and $C_{19}H_{15}N_7$ (0.09 g; 0.3 mmol). The product was a blue powder, and the yield was 0.18 g (75.0%).

(h) $[Fe_2(CH_3(CH_2)_{14}COO)_2(H_2O)_2(L1)]$ ***(Complex 8)***

The procedure was the same as for copper(II) ethanoate-*L1* (**Section 3.3.3(a)**), using iron(II) hexadecanoate (0.15 g ; 0.3 mmol), $C_{19}H_{15}N_7$ (0.09 g; 0.3 mmol), and about 0.1 g of ascorbic acid. The product was a cream powder, and the yield was 0.21 g (87.5%).

3.3.4 Metal(II) carboxylate-L2 complexes

(a) $\{[Cu(CH_3COO)_2(L2)].H_2O\}_n$ ***(Complex 9)***

The procedure was the same as for copper(II) ethanoate-*L1* (**Section 3.3.3(a)**), using copper(II) ethanoate (0.13 g; 0.7 mmol) and $C_{19}H_{21}N_5O_2S$ (0.34 g; 0.7 mmol). The product was a green powder, and the yield was 0.33 g (70.2%).

(b) $\{[Ni(CH_3COO)(L2)].2H_2O\}_n$ ***(Complex 10)***

The procedure was the same as for copper(II) ethanoate-*L1* (**Section 3.3.3(a)**), using nickel(II) ethanoate tetrahydrate (0.35 g; 1.4 mmol) and $C_{19}H_{21}N_5O_2S$ (0.45 g; 1.4 mmol). The product was a pale green powder, and the yield was 0.63 g (78.8%).

*(c) {[Co(CH$_3$COO)$_2$(L2)].2H$_2$O}$_n$ (**Complex 11**)*

The procedure was the same as for copper(II) ethanoate-*L1* (**Section 3.3.3(a)**), using cobalt(II) ethanoate tetrahydrate (0.18 g; 0.7 mmol) and $C_{19}H_{21}N_5O_2S$ (0.25 g; 0.7 mmol). The product was a purple powder, and the yield was 0.35 g (81.4%).

*(d) {[Fe(CH$_3$COO)$_2$(L2)].2H$_2$O}$_n$ (**Complex 12**)*

The procedure was the same as for copper(II) ethanoate-*L1* (**Section 3.3.3(a)**), using iron(II) ethanoate (0.18 g; 1.0 mmol), $C_{19}H_{21}N_5O_2S$ (0.34 g; 1.0 mmol), and about 0.1 g ascorbic acid. The product was a brown powder, and the yield was 0.43 g (82.7%).

*(e) {[Cu(CH$_3$(CH$_2$)$_{14}$COO)$_2$(L2)].H$_2$O}$_n$ (**Complex 13**)*

The procedure was the same as for copper(II) ethanoate-*L1* (**Section 3.3.3(a)**), using copper(II) hexadecanoate (1.17 g; 1.0 mmol) and $C_{19}H_{21}N_5O_2S$ (0.49 g; 1.0 mmol). The product was a green powder, and the yield was 1.41 g (85.5%).

*(f) {[Ni(CH$_3$(CH$_2$)$_{14}$COO)$_2$(L2)].2H$_2$O}$_n$ (**Complex 14**)*

The procedure was the same as for copper(II) ethanoate-*L1* (**Section 3.3.3(a)**), using nickel(II) hexadecanoate (0.75 g; 1.3 mmol) and $C_{19}H_{21}N_5O_2S$ (0.63 g; 1.3 mmol). The product was a yellow-green powder, and the yield was 0.92 g (66.7%).

*(g) {[Co(CH$_3$(CH$_2$)$_{14}$COO)$_2$(L2)].2H$_2$O}$_n$ (**Complex 15**)*

The procedure was the same as for copper(II) ethanoate-*L1* (**Section 3.3.3(a)**), using cobalt(II) hexadecanoate (0.62 g; 1.1 mmol) and $C_{19}H_{21}N_5O_2S$ (0.53 g; 1.1 mmol). The product was a pale purple powder, and the yield was 0.95 g (82.6%).

*(h) {[Fe(CH$_3$(CH$_2$)$_{14}$COO)$_2$(L2)].2H$_2$O}$_n$ (**Complex 16**)*

The procedure was the same as for copper(II) ethanoate-*L1* (**Section 3.3.3(a)**), using iron(II) hexadecanoate (0.94 g; 1.7 mmol), $C_{19}H_{21}N_5O_2S$ (0.79 g; 1.7 mmol), and about

0.1 g ascorbic acid The product was an orange powder, and the yield was 1.08 g (62.6%).

3.3.5 Metal(II) carboxylate-L3 complexes

(a) {[Cu(CH$_3$COO)$_2$(L3)]}$_n$ ***(Complex 17)***

The procedure was the same as for copper(II) ethanoate-*L1* (**Section 3.3.3(a)**), using copper(II) ethanoate (1.42 g; 7.0 mmol) and $C_{15}H_{11}N_5O_3S$ (2.39 g; 7.0 mmol). The product was a green powder, and the yield was 2.57 g (67.5%).

(b) {[Ni$_2$(CH$_3$COO)$_4$(L3)].5H$_2$O}$_n$ ***(Complex 18)***

The procedure was the same as for copper(II) ethanoate-*L1* (**Section 3.3.3(a)**), using nickel(II) ethanoate tetrahydrate (1.95 g; 7.8 mmol) and $C_{15}H_{11}N_5O_3S$ (2.66 g; 7.8 mmol). The product was a green powder, and the yield was 3.58 g (77.7%).

(c) {[Co(CH$_3$COO)$_2$(L3)].2H$_2$O}$_n$ ***(Complex 19)***

The procedure was the same as for copper(II) ethanoate-*L1* (**Section 3.3.3(a)**), using cobalt(II) ethanoate tetrahydrate (1.97 g; 7.9 mmol) and $C_{15}H_{11}N_5O_3S$ (2.69 g; 7.9 mmol). The product was a purple powder, and the yield was 3.64 g (78.1%).

(d) {[Fe$_2$(CH$_3$COO)$_4$(L3)].2H$_2$O}$_n$ ***(Complex 20)***

The procedure was the same as for copper(II) ethanoate-*L1* (**Section 3.3.3(a)**), using iron(II) ethanoate (1.92 g; 11 mmol), $C_{15}H_{11}N_5O_3S$ (3.75 g; 11 mmol), and about 0.1 g ascorbic acid. The product was a brown powder, and the yield was 4.98 g (87.8%).

(e) {[Cu$_2$(CH$_3$(CH$_2$)$_{14}$COO)$_4$(L3)].2H$_2$O}$_n$ ***(Complex 21)***

The procedure was the same as for copper(II) ethanoate-*L1* (**Section 3.3.3(a)**), using copper(II) hexadecanoate (0.54 g; 0.5 mmol) and $C_{15}H_{11}N_5O_3S$ (0.16 g; 0.5 mmol). The product was a pale yellow powder, and the yield was 0.53 g (75.7%).

(f) {[$Ni_2(CH_3(CH_2)_{14}COO)_4(L3)$]}$_n$ ***(Complex 22)***

The procedure was the same as for copper(II) ethanoate-*L1* (**Section 3.3.3(a)**), using nickel(II) hexadecanoate (0.80 g; 1.4 mmol) and $C_{15}H_{11}N_5O_3S$ (0.48 g; 1.4 mmol). The product was a pale greenish powder, and the yield was 0.84 g (65.6%).

(g) {[$Co(CH_3(CH_2)_{14}COO)_2(L3)$]}$_n$ ***(Complex 23)***

The procedure was the same as for copper(II) ethanoate-*L1* (**Section 3.3.3(a)**), using cobalt(II) hexadecanoate (0.24 g; 0.4 mmol) and $C_{15}H_{11}N_5O_3S$ (0.14 g; 0.4 mmol). The product was a blue powder, and the yield was 0.24 g (64.9%).

(h) {[$Fe(CH_3(CH_2)_{14}COO)_2(L3)].3H_2O$}$_n$ ***(Complex 24)***

The procedure was the same as for copper(II) ethanoate-*L1* (**Section 3.3.3(a)**), using iron(II) hexadecanoate (0.33 g; 0.6 mmol), $C_{15}H_{11}N_5O_3S$ (0.19 g; 0.6 mmol), and about 0.1 g ascorbic acid. The product was a pink powder, and the yield was 0.38 g (73.0%).

3.3.6 Metal(II) carboxylates-L4 complexes

(a) {[$Cu(CH_3COO)_2(L4)$]}$_n$ ***(Complex 25)***

The procedure was the same as for copper(II) ethanoate-*L1* (**Section 3.3.3(a)**), using copper(II) ethanoate (0.51 g; 2.8 mmol) and $C_{13}H_7N_5O_2$ (0.74 g; 2.8 mmol). The product was a green powder, and the yield was 1.23 g (98.4%).

(b) {[$Ni_2(CH_3COO)_4(L4)$]}$_n$ ***(Complex 26)***

The procedure was the same as for copper(II) ethanoate-*L1* (**Section 3.3.3(a)**), using nickel(II) ethanoate tetrahydrate (0.58 g; 2.3 mmol) and $C_{13}H_7N_5O_2$ (0.66 g; 2.3 mmol). The product was a pale green powder, and the yield was 1.13 g (91.1%).

*(c) {[Co(CH$_3$COO)$_2$(L4).2H$_2$O]}$_n$ (**Complex 27**)*

The procedure was the same as for copper(II) ethanoate-*L1* (**Section 3.3.3(a)**), using cobalt(II) ethanoate tetrahydrate (0.66 g; 2.7 mmol) and $C_{13}H_7N_5O_2$ (0.71 g; 2.7 mmol). The product was a purple powder, and the yield was 1.17 g (85.4%).

*(d) {[Fe$_2$(CH$_3$COO)$_4$(L4)].2H$_2$O}$_n$ (**Complex 28**)*

The procedure was the same as for copper(II) ethanoate-*L1* (**Section 3.3.3(a)**), using iron(II) ethanoate (0.56 g; 3.2 mmol), $C_{13}H_7N_5O_2$ (0.85 g; 3.2 mmol), and about 0.1 g ascorbic acid. The product was a brown powder, and the yield was 1.12 g (79.4%).

*(e) {[Cu(CH$_3$(CH$_2$)$_{14}$COO)$_2$(L4)]}$_n$ (**Complex 29**)*

The procedure was the same as for copper(II) ethanoate-*L1* (**Section 3.3.3(a)**), using copper(II) hexadecanoate (0.34 g; 0.3 mmol) and $C_{13}H_7N_5O_2$ (0.08 g; 0.3 mmol). The product was a green powder, and the yield was 0.37 g (89.2%).

*(f) {[Ni$_2$(CH$_3$(CH$_2$)$_{14}$COO)$_4$(L4)]}$_n$ (**Complex 30**)*

The procedure was the same as for copper(II) ethanoate-*L1* (**Section 3.3.3(a)**), using nickel(II) hexadecanoate (0.47 g; 0.8 mmol) and $C_{13}H_7N_5O_2$ (0.24 g; 0.8 mmol). The product was a pale green powder, and the yield was 0.43 g (60.6%).

*(g) {[Co(CH$_3$(CH$_2$)$_{14}$COO)$_2$(L4)].2H$_2$O}$_n$ (**Complex 31**)*

The procedure was the same as for copper(II) ethanoate-*L1* (**Section 3.3.3(a)**), using cobalt(II) hexadecanoate (0.22 g; 0.4 mmol) and $C_{13}H_7N_5O_2$ (0.11 g; 0.4 mmol). The product was a bluish-green powder, and the yield was 0.20 g (60.7%).

*(h) {[Fe$_2$(CH$_3$(CH$_2$)$_{14}$COO)$_4$(L4)].2H$_2$O}$_n$ (**Complex 32**)*

The procedure was the same as for copper(II) ethanoate-*L1* (**Section 3.3.3(a)**), using iron(II) hexadecanoate (0.79 g; 1.4 mmol), $C_{13}H_7N_5O_2$ (0.39 g; 1.4 mmol), and about

0.1 g ascorbic acid. The final product was a grey powder, and the yield was 0.72 g (61.0%).

3.4 Instrumental Analyses

3.4.1 Elemental analyses

The elemental analyses were recorded on a Perkin-Elmer CHNO/S 2400 Series II elemental analyser. The sample (about 1-2 mg) was wrapped in a thin aluminium capsule (5 x 8 mm) and folded into a tiny piece. It was then placed into the analyzer and heated to a maximum temperature of 1000 ˚C.

3.4.2 Fourier transform infrared spectroscopy

Fourier transform infrared spectroscopy (FTIR) was performed on a Perkin Elmer Frontier FTIR spectrometer equipped with a diamond attenuated total reflectance (ATR) attachment. A small amount of the sample was placed in the diamond hole, and its spectrum recorded over the range of 400-4000 cm^{-1}.

3.4.3 ^{1}H-NMR spectroscopy

^{1}H-NMR spectra were recorded on a JEOL FT-NMR lambda 400 MHz spectrometer. The solvent was DMSO-d_6. The chemical shifts were reported in ppm using the residual protonated solvent as the reference.

3.4.4 UV-vis spectroscopy

The UV-vis spectra were recorded between 1000-200 nm on a Shimadzu UV-vis-NIR 3600 spectrophotometer. An exactly known mass of a sample was dissolved in a suitable organic solvent in a 10-ml volumetric flask. The solution was placed into a 1-cm quartz cuvette and inserted into the spectrometer holder. The data were collected with the solvent as the background. The molar absorptivity (ε) was calculated using the Beer–Lambert's law: $A = \varepsilon c \ell$, where A is the absorbance, c is the molarity of the solution (mol dm^{-3}), and ℓ is the path length (1 cm).

3.4.5 Photoluminescence spectroscopy

Excitation and emission photoluminescence spectra were recorded on a PTI QuantaMaster™ 40 spectrofluorometer. The sample was held in a quartz fluorescence cuvette (l = 1 cm x 1 cm) and fluorescence was detected at 90^{o} to the excitation beam with the corrected background. The solvent used was DMSO. The emission spectra was measured by exciting the sample at excitation wavelength for each complex and collecting the emitted fluorescence. Slit widths were adjusted for excitation emission.

Fluorescence lifetime measurement was performed on a TimeMaster (TM-200) LED-Based Strobe Lifetime spectrofluorometer obtained from Photon Technology International and using the stroboscopic technique. The observed fluorescence decay was analysed using Felix GX^{TM} data acquisition and analysis software. Data was recorded in 100 ps time intervals within 50 – 70 ns observation window. The instrument response function (IRF) was measured from the scattered light and estimated to be ~1.5 ns (full width at half maximum). The measured transients were fitted to multiexponential functions convoluted with the system response function. The fitting procedure is based on the Marquardt algorithm where the experimental data are compared to a model decay convoluted with the IRF. The fit was judged by the value of the reduced chi-squared (χ^2).

3.4.6 Room-temperature magnetic susceptibility

The mass magnetic susceptibility (χ_g) was recorded at room-temperature (298 K) on a Sherwood automagnetic susceptibility balance by the Gouy method, using distilled water (0.72 x 10^{-6} c.g.s) as the calibrant. The grinded sample was carefully packed into a narrow cylindrical tube to a length of about 1.5 cm, and its weight was recorded. The corrected molar magnetic susceptibility (χ_M^{corr}) and the effective magnetic moment (μ_{eff}) were calculated from the following relationships:

$$x_M = \chi_g \, x \, (\text{formula weight})$$

$$\chi_M^{corr} = \chi_M - \chi_{dia}$$

$$\mu_{eff} = 2.83\sqrt{\chi_M^{corr}T - N\alpha}$$

where T is the absolute temperature in Kelvin, χ_{dia} is the diamagnetic correction of the components of the ligands and associated ion, and $N\alpha$ is the temperature independent paramagnetism of each metal(II) (**Appendix**). The diamagnetic corrections for cations, anions, and individual atoms and are given in units of 10^{-5} /g atom.

3.4.7 Thermogravimetry

The thermogravimetric analysis (TGA) was recorded from 50 ^{o}C to 900 ^{o}C on a Perkin-Elmer 4000 TG/DTA thermal instrument with the scan rate of 20 ^{o}C min^{-1}. The sample was analysed under N_2 gas with a flow rate of 10 cm^3 min^{-1}. An empty alumina pan was placed in the holder and tared. Then the sample (3 - 5 mg) was loaded onto the pan and the weight recorded.

3.4.8 Differential scanning calorimetry

The differential scanning calorimetric scan (DSC) was performed on a Mettler Toledo DSC 822. The weight of sample (2-4 mg) in an aluminium pan was initially recorded on a Mettler Toledo microbalance. The sealed aluminum containing the sample was then loaded into the DSC instrument. The sample was heated from 25 ^{o}C to about 150 ^{o}C at the heating rate of 10 ^{o}C min^{-1}, and then cooled from 200°C to 25°C at the cooling rate of 10 ^{o}C min^{-1} under N_2. The onset temperatures were quoted for all peaks observed. The normalized area under each of the heat flow curve was determined using the system software of the instrument.

3.4.9 Cyclic voltammetry

The cyclic voltammograms (CV) were recorded on a Gamry Instrument Reference 600 potentiostat/galvanostat/ZRA. Tetra-*n*-butylammonium tetrafluoroborate (TBATFB) (0.1 M) was used as the electrolyte, a glassy carbon electrode was used as the working

electrode, a saturated calomel electrode (SCE) was used as the reference electrode, and a platinum wire was used as the counter electrode. The initial and final voltage was 0 V, and the potential range was +1.5 V to -1.5 V. The scan rate was 100 mV s^{-1}. The samples (0.005 M) were prepared in THF and were bubbled with N_2 gas for 1 min prior to the analysis.

3.4.10 Polarizing optical microscopy

The optical textures of selected samples were observed on an Olympus polarizing microscope equipped with a Mettler Toledo FP90 central processor and FN82HT hot stage. A minute amount of the sample was sandwiched between two microscope slides, and then heated at the rate of 5-10 °C min^{-1}, and cooled at the rate of 2-5 °C min^{-1}. The magnification was 50X, and the photomicrographs were captured by the computer connected to the microscope.

CHAPTER 4 RESULTS AND DISCUSSION

4.1 Introduction

The main objective of this research was to prepare low band gap complexes as potential artificial photosynthetic and/or molecular magnetic materials. The complexes were also designed to be thermally stable, and mesomorphic (for long alkyl chain carboxylates).

The complexes were formed from the reactions of metal(II) ethanoates ($[M_2(CH_3COO)_4]$ or metal(II) hexadecanoates ($[M_2(CH_3(CH_2)_{14}COO)_4]$), where M = Cu(II), Ni(II), Co(II), and Fe(II), with ligands synthesized from the reactions of 2,6-diamino-4-phenyl-1,3,5-triazine and pyrrole-2-carboxaldehyde (*H_2L1*), 2,5-thiophenedicarboxaldehyde (*L2*), 2,5-thiophenedicarboxylic acid (*L3*), or acetylenedicarboxylic acid (*L4*) (**Scheme 3.1**).

4.2 Metal(II) Complexes of *H_2L1*

4.2.1 Synthesis of H_2L1

The ligand *H_2L1* was obtained as a brownish powder from the reaction of 2,6-diamino-4-phenyl-1,3,5-triazine with pyrrole-2-carboxaldehyde. The yield was 68.3%. The reaction equation is shown in **Scheme 4.1.**

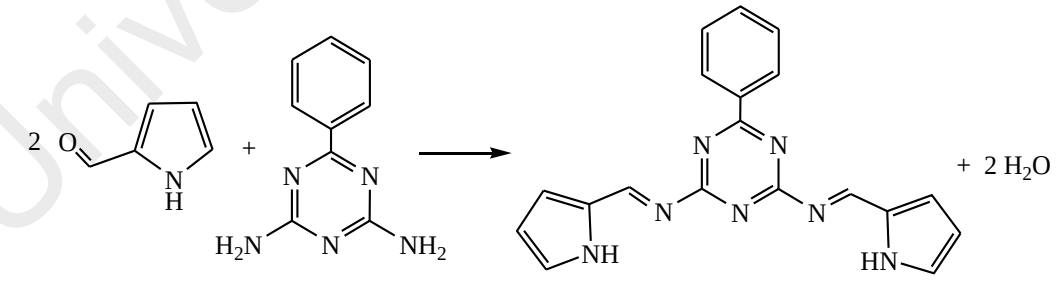

Scheme 4.1 Reaction equation for the preparation of *H_2L1*

The results of the **elemental analyses** (66.9% C, 4.9% H, 29.0% N) were in good agreement with the values calculated for the chemical formula $C_{19}H_{15}N_7$ (formula weight, 341.4 g mol^{-1}; 66.9% C, 4.4% H, 28.7% N).

Its ^{1}H-NMR spectrum (**Figure 4.1**) shows a broad peak at 6.75 ppm for the amine (H-8) and aromatic protons (H-5, H-6 and H7), a multiplet in the range 7.43- 7.52 ppm for the aromatic protons (H-1 and H-2), and peaks at 8.23 - 8.25 ppm for the azomethine (H-4, HC=N) and aromatic protons (H-3).

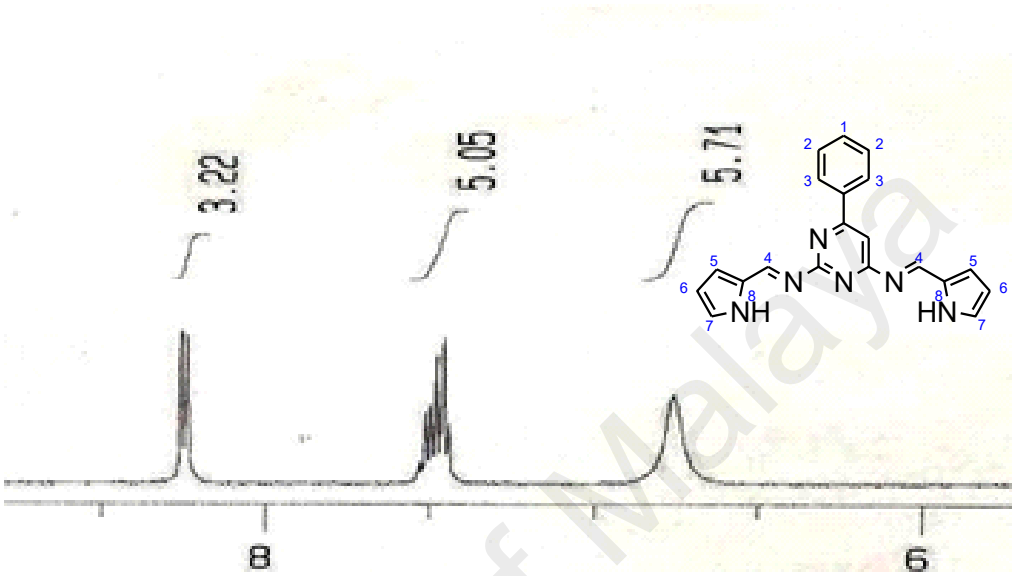

Figure 4.1 ^{1}H-NMR spectrum for *H_2L1*

Table 4.1 The ^{1}H-NMR peak assignment for *H_2L1*

Chemical Shift (ppm)	Integral	Multiplicity	Assignment
6.75	5.71	broad singlet	H-4, H-8
7.43 - 7.52	5.05	multiplet	H-1, H-2, H-6, H-7
8.23 - 8.25	3.22	doublet	H-3, H-5

The **FTIR** spectrum for *H_2L1* is shown in **Figure 4.2**, and the peak assignments are given in **Table 4.2** (which also include the data for the corresponding metal(II) complexes for later discussion). Hence, the spectrum shows the presence of functional groups expected for the ligand.

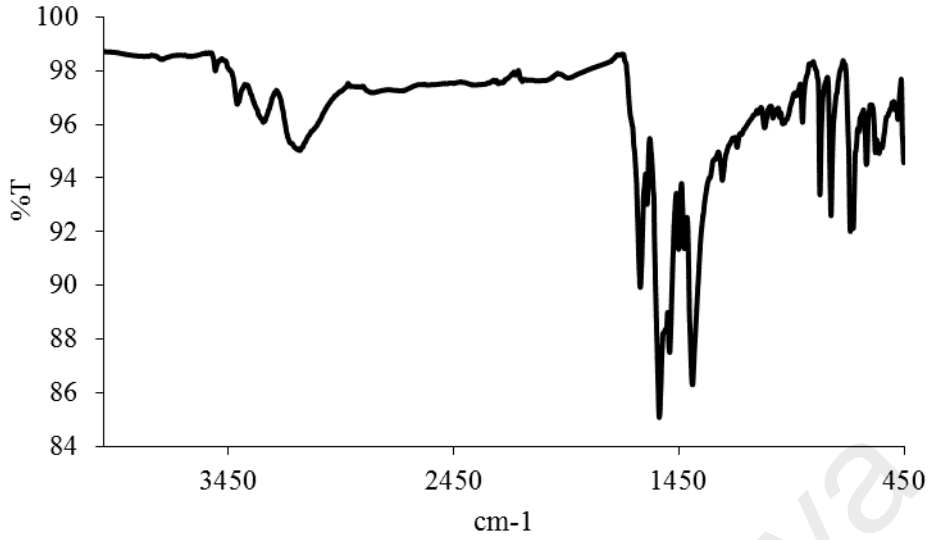

Figure 4.2 FTIR spectrum of *H_2L1*

Table 4.2 FTIR data (in cm^{-1}) and assignments for *H_2L1* and its complexes

Compound	N-H	O-H	CH_2 (asym)	CH_2 (sym)	C=N	COO (asym)	COO (sym)	M-N
H_2L1	3134br	-	-	-	1621s	-	-	-
1	-	3224br	-	-	1616m	1530s	1423s	547w
2	-	3304br	-	-	1592w	1531s	1399s	508m
3	-	3410br	-	-	1541w	1533s	1410s	510w
4	-	3304br	-	-	1611w	1534s	1396s	501m
5	-	-	2914s	2849 m	1617m	1584s	1441s	596m
6	-	3300m	2918s	2850s	1613m	1537m	1399m	573m
7	-	3306m	2917s	2848 m	1617m	1524s	1394m	549w
8	-	3333br	2918s	2850s	1618s	1530s	1393m	578m

s = strong; m = medium; w = weak; br = broad

4.2.2 Reaction of copper(II) ethanoate with H_2L1

Copper(II) ethanoate ($[Cu_2(CH_3COO)_4]$) reacted with *H_2L1* (mole ratio 1:1) to give a green powder (**Complex 1**), and the yield was 87.4%. It was soluble in DMSO, but insoluble in water and common organic solvents.

The **elemental analytical** data for the complex (44.9% C; 3.6% H; 15.4% N) were in excellent agreement with those calculated for the chemical formula $Cu_2C_{23}H_{23}N_7O_6$ (44.5% C; 3.7% H; 15.8% N; formula weight, 620.56 g mol^{-1}).

Combining these data with spectroscopic data discussed below, the proposed structural formula for the complex is $[Cu_2(CH_3COO)_2(H_2O)_2(L1)]$ (**Figure 4.3**).

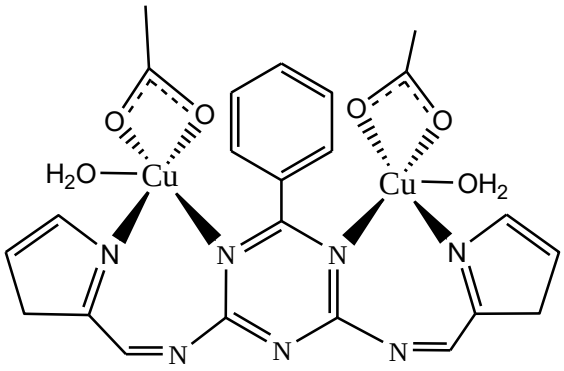

Figure 4.3 Proposed structure of **Complex 1**

Its **FTIR** spectrum (**Table 4.2**; **Figure 4.4**) shows a weak broad peak at 3398 cm^{-1} for O-H, a medium peak at 1616 cm^{-1} for C=N (imine), a strong peak at 1530 cm^{-1} for $\bar{\upsilon}_{asym}COO$, a strong peak at 1423 cm^{-1} for $\bar{\upsilon}_{sym}COO$, and a peak at 547 cm^{-1} for Cu-N stretch. The ΔCOO value ($\bar{\upsilon}_{asym}COO - \bar{\upsilon}_{sym}COO$) was 107 cm^{-1}, suggesting a chelating CH_3COO^- ligand [1].

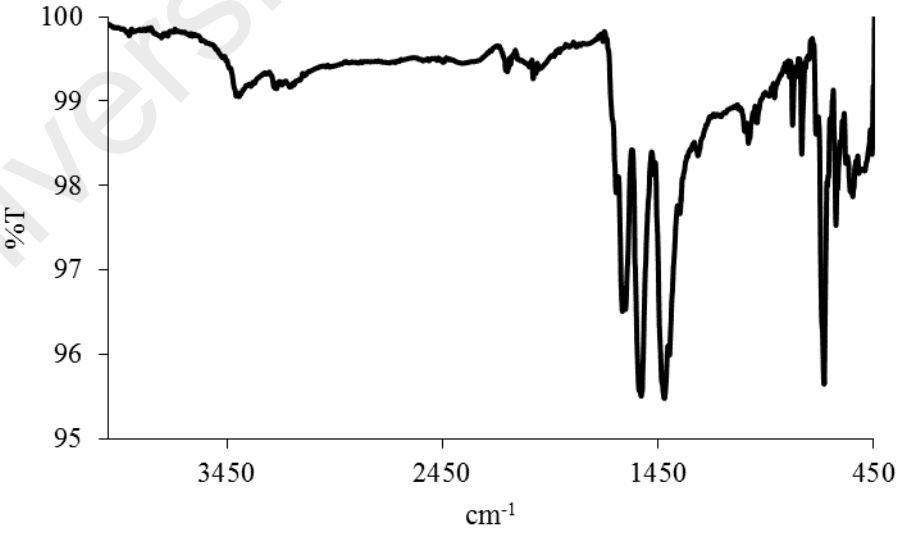

Figure 4.4 FTIR spectrum of **Complex 1**

Its **UV-vis** spectrum in DMSO (**Figure 4.5**) shows a broad *d-d* band at 713 nm (ε_{max}, 266 M^{-1} cm^{-1}), assigned as $^2B_2 \rightarrow {}^2B_1$ electronic transition, a shoulder band at 403 nm (ε_{max}, 617 M^{-1} cm^{-1}) assigned as $^2B_2 \rightarrow {}^2E$ electronic transitions, and an intense

band at 273 nm (ε_{max}, 9219 M^{-1} cm^{-1}) assigned as ligand-to-metal charge-transfer transition (LMCT). These suggest that both Cu(II) centres have a square pyramidal geometry [2-5].

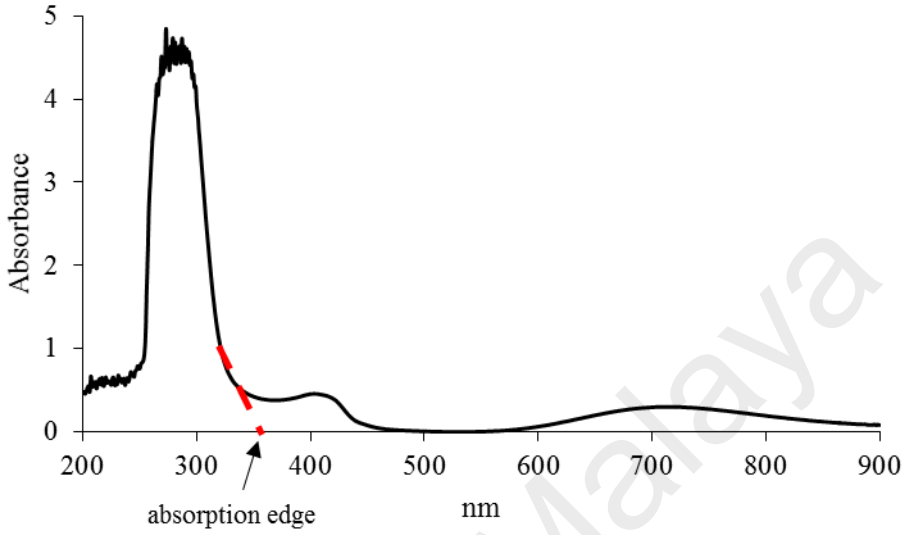

Figure 4.5 UV-vis spectrum of **Complex 1**

The **optical bandgap** (E_o) was calculated from electronic absorption and fluorescence spectra, using the equation: $E_o = hc/\lambda$, where h = Planck constant (6.626 x 10^{-34} J s^{-1}), c = velocity of light (3.0 x 10^8 m s^{-1}), and λ = absorption edge of charge-transfer (CT) band or emission edge. The calculated value in joule (J) was then converted to electron volt (eV) using the conversion factor: 1 J = 6.24 x 10^{18} eV. The most simple and direct method used to calculate the E_o value is by determining the wavelength at which the extrapolation of the absorption edge crosses the baseline [6-8], as shown in **Figure 4.5**. For **Complex 1**, the line crosses at 360 nm, hence the estimated E_o value was 3.4 eV.

Upon excitation at 273 nm (LMCT band), its **fluorescence** spectrum shows three overlapping peaks at 362 nm, 462 nm and 536 nm (**Figure 4.6)**. It may be inferred from this that there were three paths for the excited electron to lose its energy. The Stokes shift value, which is the difference between the band maxima of the absorption and emission spectra of the same electronic transition, are 189 nm. The larger Stokes shift is ideal for multicolour labelling and DSSC application as it can minimize overlap

between excitation and emission peaks. Thus, it may inhibit dye-dye quenching effects for photosensitizer.

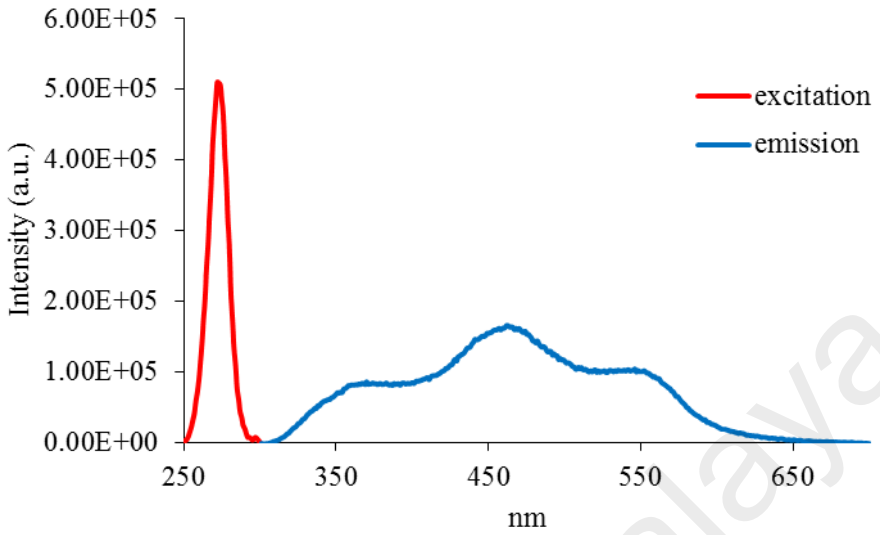

Figure 4.6 Fluorescence spectrum of **Complex 1** (λ_{ex} = 273 nm)

Its E_o value, calculated from λ_{edge} = 602 nm, was 2.1 eV. This is 1.3 eV narrower than the E_o value calculated from the absorption spectrum.

The fluorescence lifetime ($\boldsymbol{\tau}$) of an excited complex may be obtained from the best curve fitting analysis of its decay curve. The fitting procedure is based on the Marquardt algorithm, where the experimental data are compared to a model decay convoluted with the instrumental response function (IRF). IRF is typically measured as a response of the instrument to scattered excitation pulse. Deviations from the best fit are characterized by the reduced χ^2:

$$\chi^2 = \frac{1}{N-n-1}\sum_{1}^{N}\frac{(I(i)calc - I(i))^2}{s(i)^2}$$

where N is the number of data channels, n is the number of fitting parameters, and s is the standard deviation. The best fit is determined when χ^2 is close to 1.

The decay curve ($\lambda_{max,\ emission}$ 462 nm) for **Complex 1** is shown in **Figure 4.7**. From it, the value of $\boldsymbol{\tau}$ was 2.8 ns. Hence, the lifetime of its excited complex was much shorter than that of [Ru(2,2'-bipyridine-4-4'-dicarboxylic acid)$_2$(NCS)$_2$] (τ = 50 ns).

However, it is sufficient to allow for electronic injection into the conduction band of the semiconductor (TiO_2) in a dye-sensitised solar cell, reported to occur within femtoseconds.

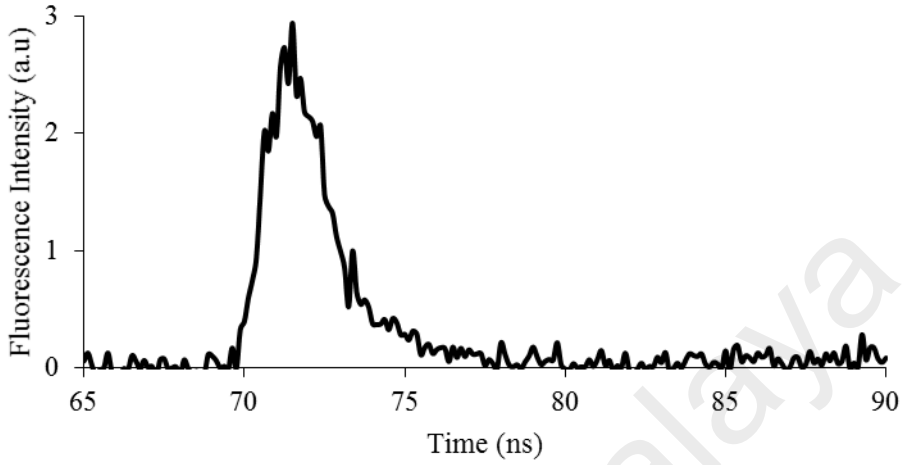

Figure 4.7 Fluorescence decay of **Complex 1**

Next, upon excitation at 403 nm (*d-d* transition), its **fluorescence** spectrum shows a peak at λ_{max} 477 nm (**Figure 4.8)**. Its E_o, calculated from λ_{edge} = 613 nm, was 2.0 eV and its $\boldsymbol{\tau}$ value, calculated as before from its decay curve, was 2.6 ns. Its Stokes shift was 74 nm.

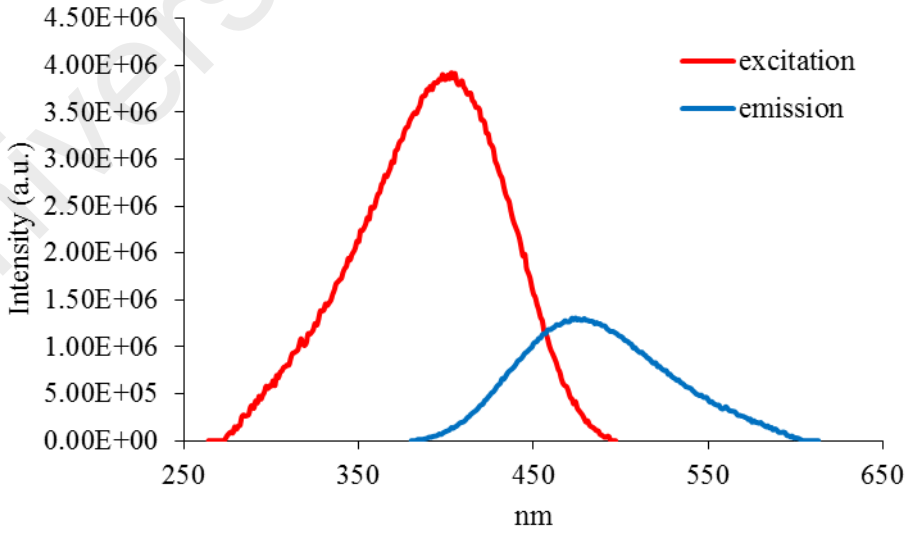

Figure 4.8 Fluorescence spectrum of **Complex 1** (λ_{ex} = 403 nm)

Its **CV** (**Figure 4.9**) was recorded cathodically from 0 V within the potential window of -1.5 V to +1.5 V and scan rate 100 mV s^{-1}. The voltammogram showed two

cathodic peaks at -0.64 V and -1.10 V, and three anodic peaks at +0.02 V, +0.35 V and +1.16 V. The copper-based redox processes are shown in **Scheme 4.2**. The anodic peak at +1.16 V is tentatively assigned to the oxidation of *L1*. This electrochemical behaviour is similar to complex $[Cu_2L(NO_2)_2(H_2O)_2]ClO_4.H_2O$, where L = 2,6-[(N-phenylpiperazin-1-yl)methyl]-4-substituted phenols, E_c = -0.67 V, -1.14 V; E_a = +0.06 V, +0.08 V) [9].

$$[Cu(II)Cu(II)] \underset{+0.35\ V}{\overset{-0.64\ V}{\rightleftharpoons}} [Cu(II)Cu(I)] \underset{+0.02\ V}{\overset{-1.10\ V}{\rightleftharpoons}} [Cu(I)Cu(I)]$$

Scheme 4.2 The redox processes of **Complex 1**

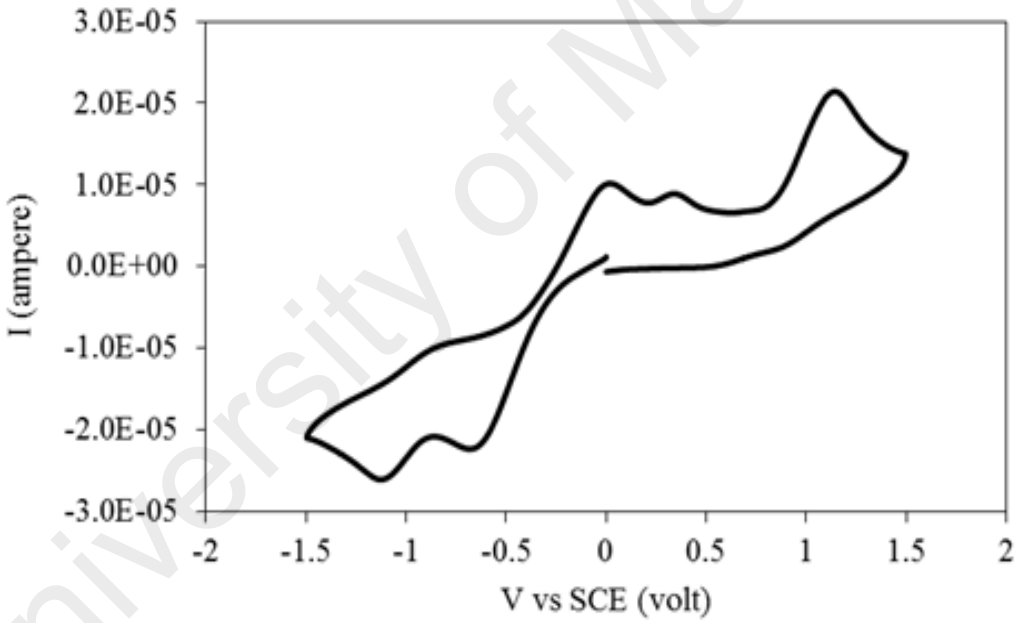

Figure 4.9 CV of **Complex 1**

The peak separations (ΔE_p) were 990 mV and 1120 mV. Both values are greater than the expected value for a reversible redox process (59 mV). Hence, both Cu-based redox processes were quasireversible, indicating extensive structural distortions upon reductions.

As comparison, the E_c and E_a values for $[Cu_2(C_6H_4COO)_4(CH_3CH_2OH)_2]$ were -0.35 V and = +0.39 V (ΔE_p = 740 mV), respectively [10]. Similar deduction was made for $[Cu_2(RCOO)_4(RCOOH)_2]$ (R = 2-hexyldecanoate) [11]

The electrochemical bandgap (E_e) may be calculated using the relationship: E_e = |HOMO – LUMO|, where HOMO was the highest occupied molecular orbital (HOMO = onset oxidation peak voltage + 4.4) eV, and LUMO was the lowest unoccupied molecular orbital (LUMO = onset reduction peak voltage + 4.4). The value of +4.4 is the standard electrode potential of saturated calomel electrode (SCE) as a reference electrode.

For **Complex 1**, the values for HOMO and LUMO were 3.90 eV (onset oxidation potential = -0.50 V) and 4.10 eV (onset reduction potential = -0.30 V), respectively. Hence, its E_e value was 0.2 eV. The significantly lower E_e value compared to E_o (absorption, 3.4 eV; emission, 2.1 eV) is expected as the electrochemical process involved an electron in the antibonding 3*d* orbital of Cu(II), while the optical process involved photonic excitation of an electron from the orbital(s) of the ligand to that of Cu(II) (LMCT).

The value of the effective **magnetic moment** (μ_{eff}) was calculated using the following equation:

$$\mu_{eff} = 2.83[T(\chi_M^{corr} - N\alpha)]^{½}$$

where χ_M^{corr} is the corrected molar magnetic susceptibility, T is the temperature in Kelvin, and Nα is the temperature-independent paramagnetism (TIP) for the metal ion (60 x 10^{-6} cm^3 mol^{-1} per Cu^{2+} ion). The value of χ_M^{corr} was in turn calculated from the following equations:

$$\chi_M = \chi_g \text{ x FM}$$

$$\chi_M^{corr} = \chi_M - \chi_{dia}$$

where χ_M = molar magnetic susceptibility, χ_g = gram magnetic susceptibility (obtained directly from the instrument), FM = formula mass of the complex, and χ_{dia} = magnetic susceptibility of all diamagnetic atoms obtained from Pascal's constants.

For **Complex 1**, the $\boldsymbol{\mu_{eff}}$ value, calculated from the values of FM = 620.56 g mol^{-1}, χ_g = 0.25 x 10^{-5} cm^3 g^{-1}, χ_M = 1.58 x 10^{-3} cm^3 mol^{-1}, and χ_{dia} = -3.05 x 10^{-4} cm^3 mol^{-1}, was 2.15 B.M. at 298 K. This value is lower than expected for a dimeric copper(II) complex (2.45 B.M.) [12]. Hence, there exists an antiferromagnetic interaction between the adjacent Cu(II) atoms in the complex [3, 13, 14].

The **TGA** trace (**Figure 4.10**) shows an initial weight loss of 5.8% in the temperature range of 160 – 231 °C, assigned to the evaporation of two coordinated H_2O molecules (expected, 5.8%). The next weight loss of 72.7% in the temperature range of 231 – 768 °C is assigned to the decomposition of two CH_3COO^- and *L1* ligands (expected, 73.7%). The amount of residue at temperatures above 768 ^oC was 21.5% (expected, 20.5 % assuming pure CuO) [15, 16]. The result support the formula proposed for **Complex 1**, and shows that it has a high decomposition temperature (T_{dec} = 231 ^oC).

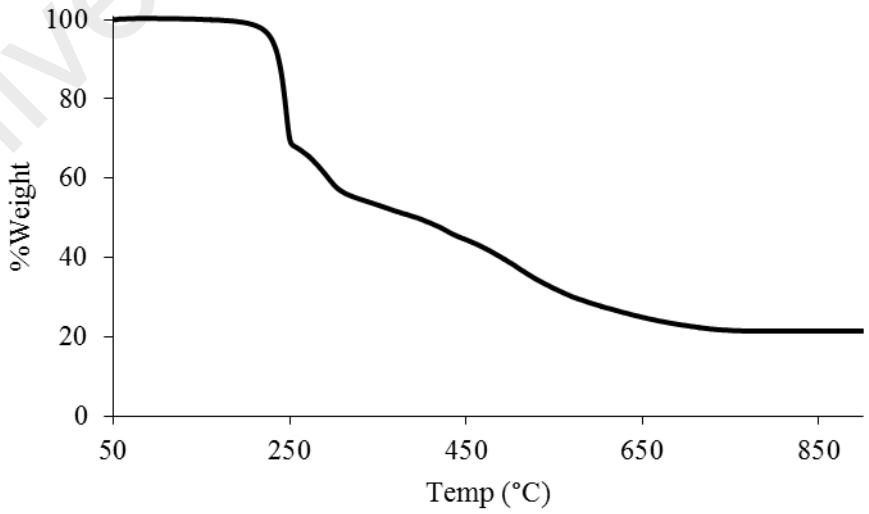

Figure 4.10 TGA of **Complex 1**

4.2.3 Reaction of nickel(II) ethanoate with H_2L1

Nickel(II) ethanoate tetrahydrate ($[Ni(CH_3COO)_2].4H_2O$) reacted with *H_2L1* (mole ratio 1:1) to give a green powder (**Complex 2**), and the yield was 79.4%. Its solubility was similar to **Complex 1**.

The **elemental analytical** data for the complex (45.0% C; 3.5% H; 15.8% N) are in excellent agreement with those calculated for the chemical formula $Ni_2C_{23}H_{27}N_7O_6$ (formula weight, 610.86 g mol^{-1}; 45.2% C; 3.8% H; 16.0% N). Combining these with the spectroscopic data discussed below, its proposed structural formula is $[Ni_2(CH_3COO)_2(H_2O)_2(L1)]$ (**Figure 4.11**), which is similar to **Complex 1** ($[Cu_2(CH_3COO)_2(H_2O)_2(L1)]$).

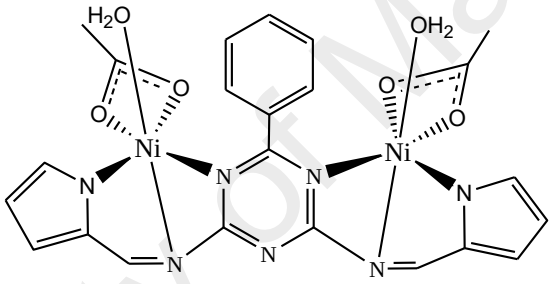

Figure 4.11 Proposed structure of **Complex 2**

Its **FTIR** spectrum (**Table 4.2**; **Figure 4.12**) shows the presence of the expected functional groups. The ΔCOO value was 132 cm^{-1}, suggesting a chelating CH_3COO^- ligand.

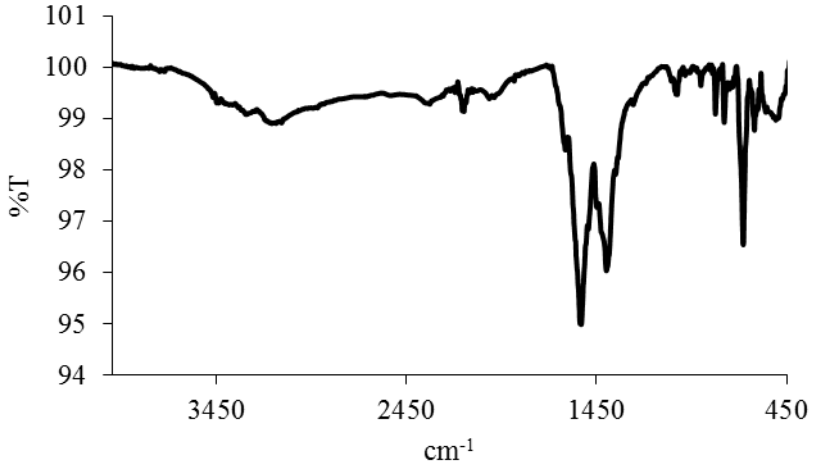

Figure 4.12 FTIR spectrum of **Complex 2**

Its **UV-vis** spectrum in DMSO (**Figure 4.13**) shows *d-d* bands at 769 nm (ε_{max}, 76 M^{-1} cm^{-1}), 500 nm (ε_{max}, 108 M^{-1} cm^{-1}), and 412 nm (ε_{max}, 216 M^{-1} cm^{-1}). These bands are assigned to $^3A_{2g}$ (F) → $^3T_{2g}$ (F), $^3A_{2g}$ (F) → $^3T_{1g}$ (F), and $^3A_{2g}$ (F) → $^3T_{1g}$ (P) electronic transitions, respectively [17, 18]. These data suggest octahedral geometry at Ni(II) centres. An intense band observed at 273 nm (ε_{max}, 2.0 x 10^4 M^{-1} cm^{-1}) is assigned to the MLCT transition.

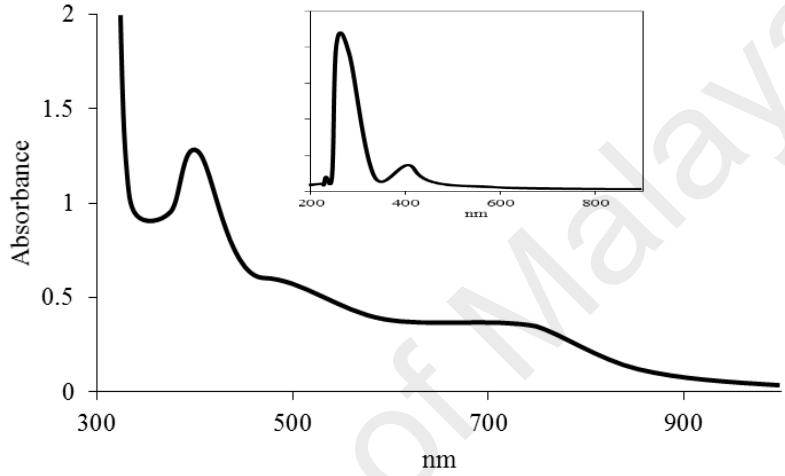

Figure 4.13 The UV-vis spectrum of **Complex 2**

Its E_o value, calculated from λ_{edge} = 361 nm, was 3.4 eV. The value was the same as **Complex 1** ($[Cu_2(CH_3COO)_2(H_2O)_2(L1)]$; 3.4 eV)

Upon excitation at 273 nm (MLCT transition), its **fluorescence** spectrum shows three peaks at λ_{max} 365 nm, 459 nm and 553 nm (**Figure 4.14**). These suggest three different paths for the excited complex to return to the ground state. Its E_o, calculated from λ_{edge} = 694 nm, was 1.8 eV. Its $\boldsymbol{\tau}$ value, calculated as before from its **decay curve** (**Figure 4.15**), was 2.7 ns. This value is also similar to **Complex 1** (2.8 ns). Additionally, its Stokes shift was 186 nm.

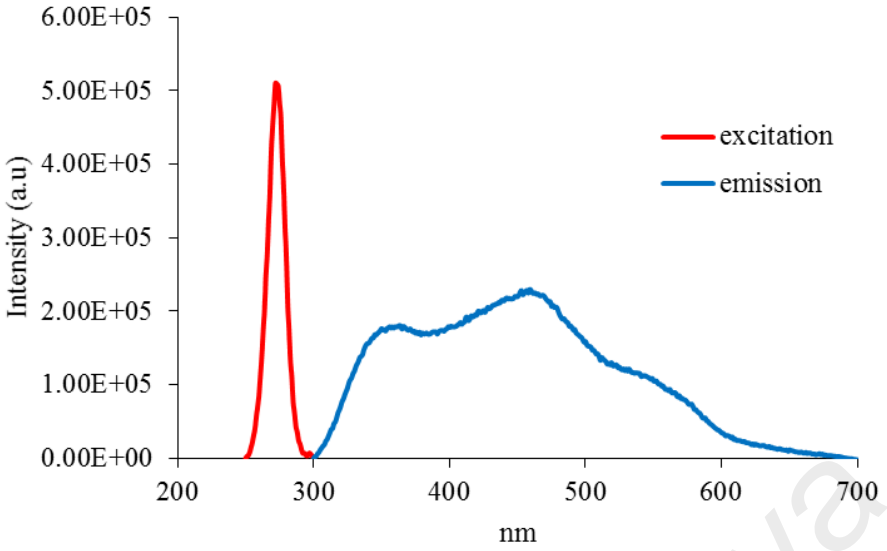

Figure 4.14 Fluorescence spectrum of **Complex 2** (λ_{ex} = 273 nm)

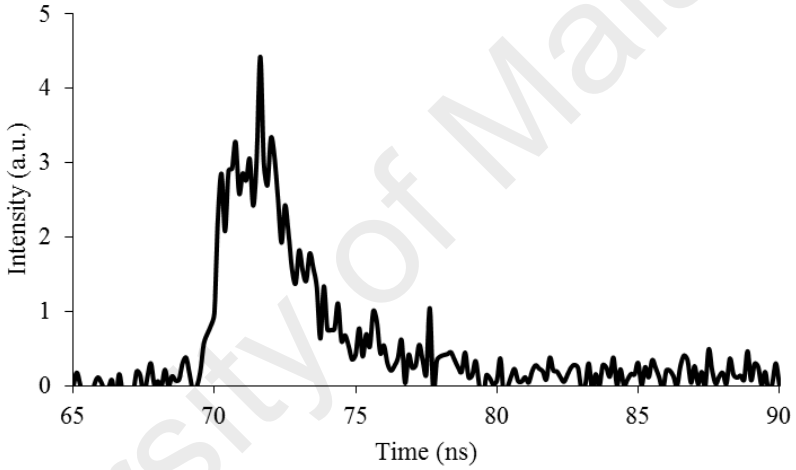

Figure 4.15 Fluorescence decay of **Complex 2** (λ_{ex} = 273 nm)

However, upon excitation at 412 nm (*d-d* transition), its **fluorescence** spectrum shows a peak at λ_{max} 425 nm (**Figure 4.16**). Its E_o, calculated from λ_{edge} = 456 nm, was 2.7 eV, and its $\boldsymbol{\tau}$ value, calculated as before from its decay curve, was 2.9 ns. Its Stokes shift was 13 nm.

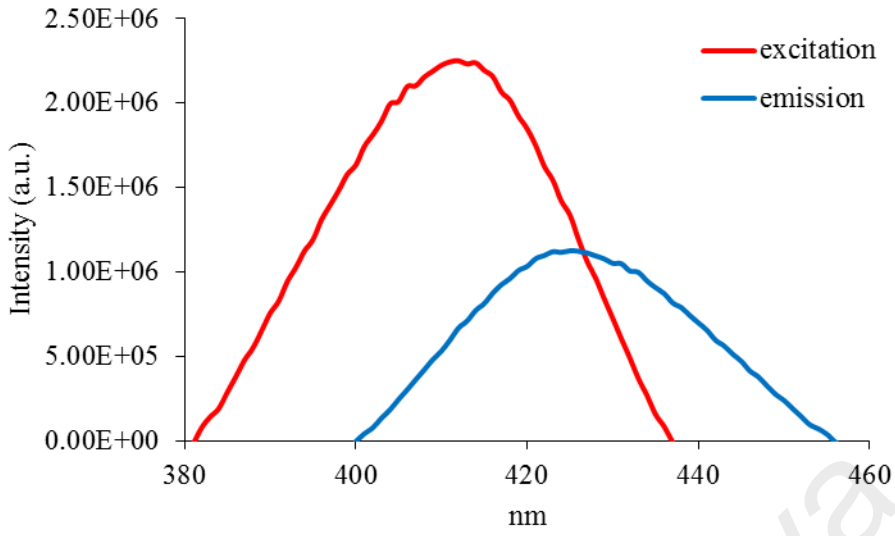

Figure 4.16 Fluorescence spectrum of **Complex 2** (λ_{ex} = 412 nm)

Its **CV** (**Figure 4.17**), recorded anodically from 0 V within the potential window of +1.5 V to -1.5 V, showed an anodic peak at +1.13 V, but no corresponding cathodic peak. The anodic peak is assigned to the oxidation of *L1* as suggested for **Complex 1**. This means that both Ni(II) atoms in **Complex 2** were redox inactive. Hence, the value of E_e for the complex cannot be calculated.

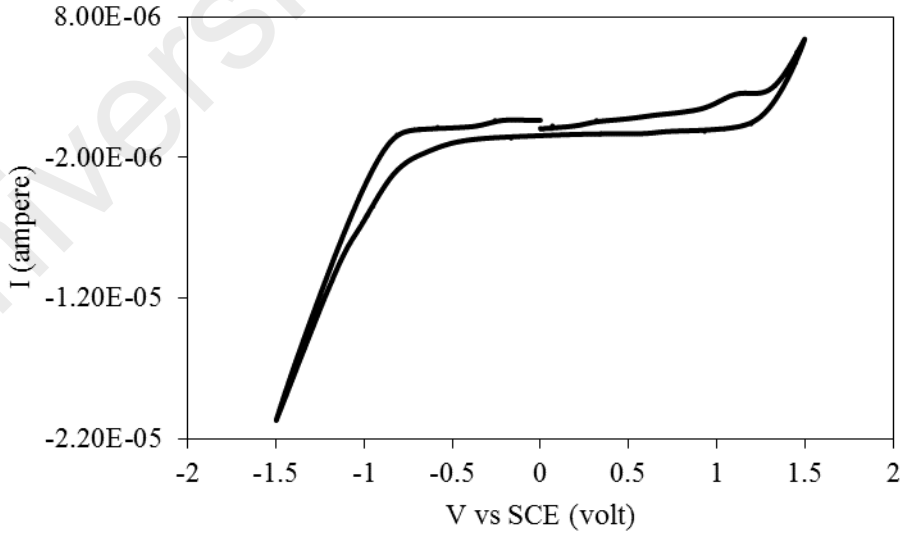

Figure 4.17 CV of **Complex 2**

Its μ_{eff} value, calculated as before from the values of FM = 610.86 g mol^{-1}, χ_g = 0.255 x 10^{-5} cm^3 g^{-1}, χ_M = 8.20 x 10^{-3} cm^3 mol^{-1}, and χ_{dia} = -3.05 x 10^{-4} cm^3 mol^{-1},

was 4.52 B.M. at 298 K. The value is in agreement with the expected value for a dinuclear Ni(II) complex (4.00 B.M.). Hence, it may be inferred that there was no electronic interaction between the Ni(II) centres in **Complex 2** [19].

Its **TGA** trace (**Figure 4.18**) shows an initial weight loss of 6.3% in the temperature range of 75 – 130 °C, assigned to the evaporation of two coordinated H_2O molecules (expected, 5.9%). This is followed by a weight loss of 71.1% in the temperature range of 238 – 900 °C, assigned to the decomposition of two CH_3COO^- and *L1* ligands (expected, 74.9%). However, the amount of residue at temperatures above 900 ^oC cannot be ascertained as there was no plateau at this temperature (due to incomplete combustion of the organic ligands). Hence, the complex (T_{dec} = 238 ^oC) was as thermally stable than **Complex 1** ($[Cu_2(CH_3COO)_2(H_2O)_2(L1)]$; T_{dec} = 231 ^oC).

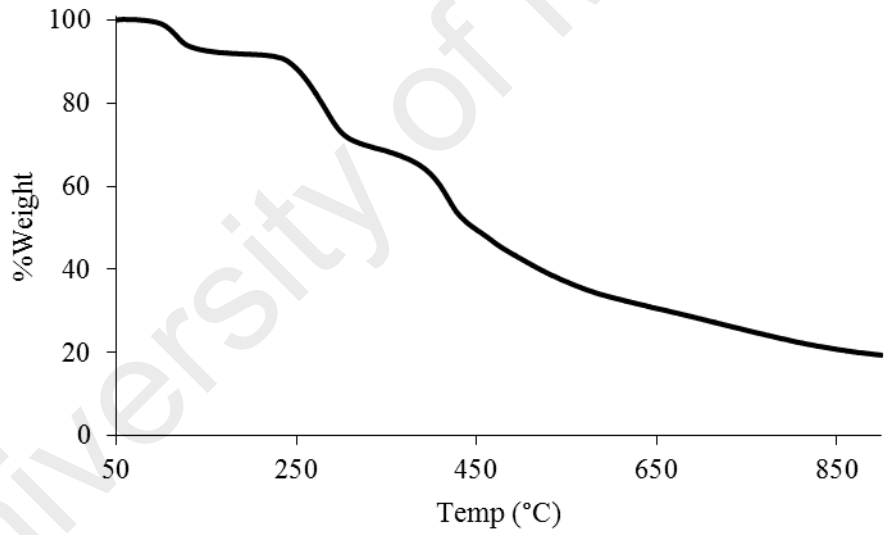

Figure 4.18 TGA of **Complex 2**

4.2.4 Reaction of cobalt(II) ethanoate with H_2L1

Cobalt(II) ethanoate tetrahydrate ($[Co(CH_3COO)_4].4H_2O$) reacted with *H_2L1* (mole ratio 1:1) to give a purple powder (**Complex 3**), and the yield was 93.6%. Its solubility was similar to the previously discussed complexes.

The **elemental analytical** data for the complex (44.8% C; 4.1% H; 15.8% N) are in excellent agreement with those calculated for the chemical formula $Co_2C_{23}H_{25}N_7O_6$ (45.0% C; 4.1% H; 15.9% N; formula weight, 613.35 g mol^{-1}). Combining these with the spectroscopic data discussed below, its proposed structural formula is $[Co_2(CH_3COO)_2(H_2O)_2(L1)]$ (**Figure 4.19**), which is similar to **Complex 2** $[Ni_2(CH_3COO)_2(H_2O)_2(L1)]$.

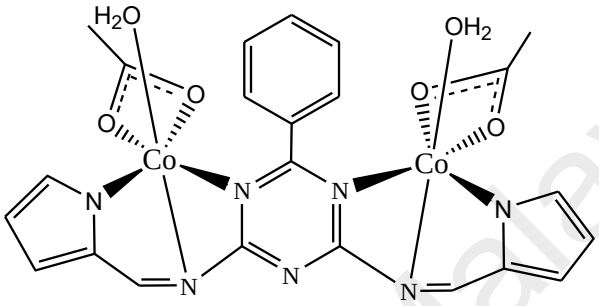

Figure 4.19 Proposed structure of **Complex 3**

Its **FTIR** spectrum (**Table 4.2**; **Figure 4.20**) shows the presence of the expected functional groups. The ΔCOO value was 123 cm^{-1}, suggesting a chelating CH_3COO^- ligand.

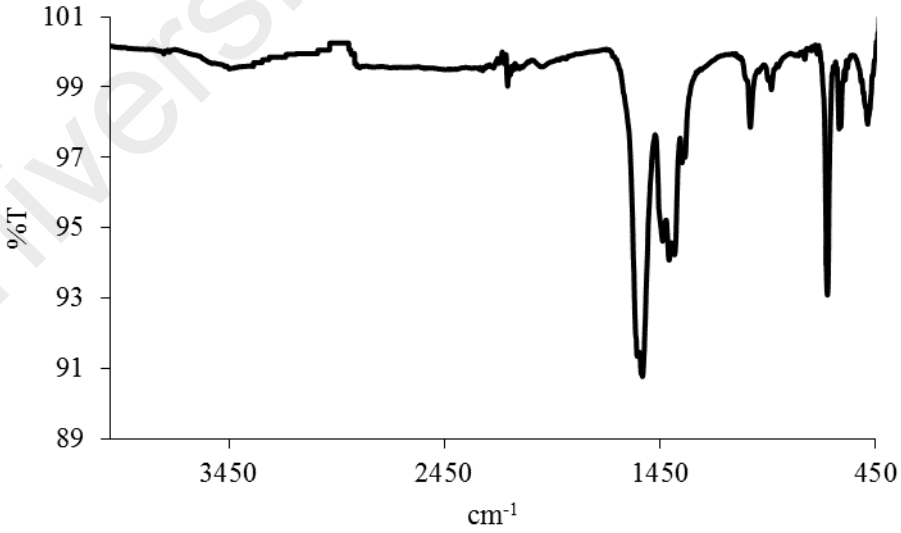

Figure 4.20 FTIR spectrum of **Complex 3**

Its **UV-vis** spectrum in DMSO (**Figure 4.21**) shows overlapping *d-d* bands at 640 nm (ε_{max}, 234 M^{-1} cm^{-1}) assigned to $^4T_{1g}(F) \rightarrow {}^4T_{2g}$ (F) transition, 541 nm

(ε_{max}, 296 M^{-1} cm^{-1}) assigned to $^4T_{1g}$ (F) → $^4T_{1g}$ (P) transition, and 410 nm (ε_{max}, 123 M^{-1} cm^{-1}) assigned to $^4T_{1g}$ (F) → $^4A_{2g}$ (F) electronic transition. Hence, the complex has two high spin Co(II) centres. From this, it may be inferred that the ligands were weak field. Additionally, there is an intense band at 282 nm (ε_{max}, 9159 M^{-1} cm^{-1}) assigned to the MLCT transition.

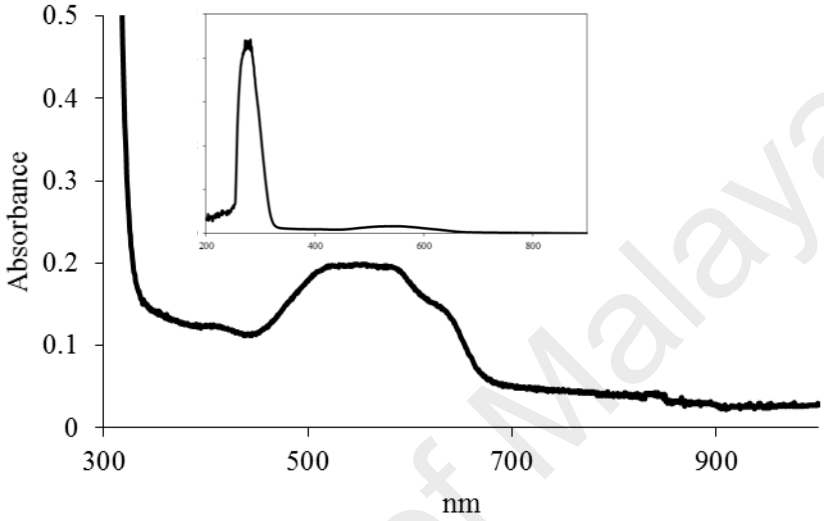

Figure 4.21 UV-vis spectrum of **Complex 3**

Its E_o value, calculated from λ_{edge} = 361 nm, was 3.4 eV. This is the same as **Complexes 1** ($[Cu_2(CH_3COO)_2(H_2O)_2(L1)]$; 3.4 eV) and **2** ($[Ni_2(CH_3COO)_2(H_2O)_2(L1)]$; 3.4 eV).

Upon excitation at 282 nm (MLCT transition), its **fluorescence** spectrum shows three overlapping peaks at 359 nm, 462 nm, and 546 nm (**Figure 4.22**). The results are similar to for **Complex 2** and may be similarly explained. Its E_o, calculated from λ_{edge} = 700 nm, was 1.8 eV. The value of its $\boldsymbol{\tau}$, calculated as before from its **decay** curve (**Figure 4.23**), was 2.7 ns. It Stokes shift value was 180 nm.

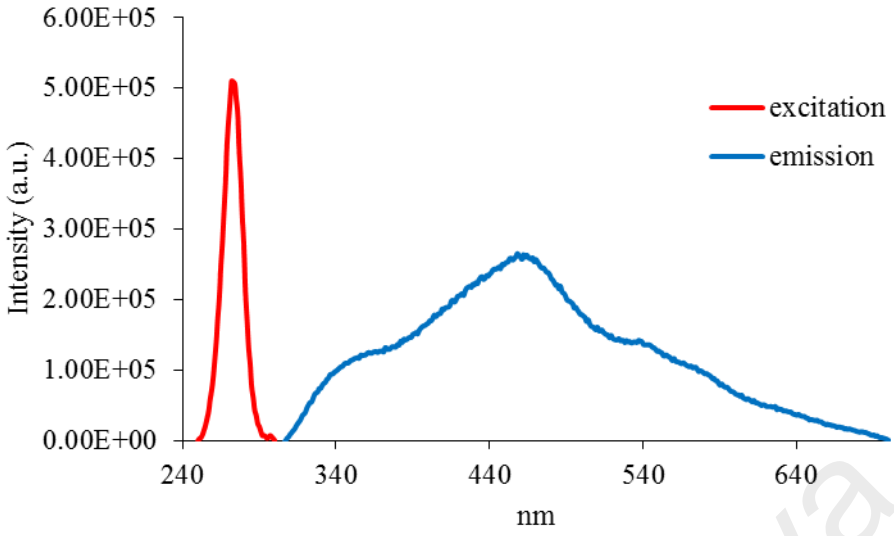

Figure 4.22 Fluorescence spectrum of **Complex 3** (λ_{ex} = 282 nm)

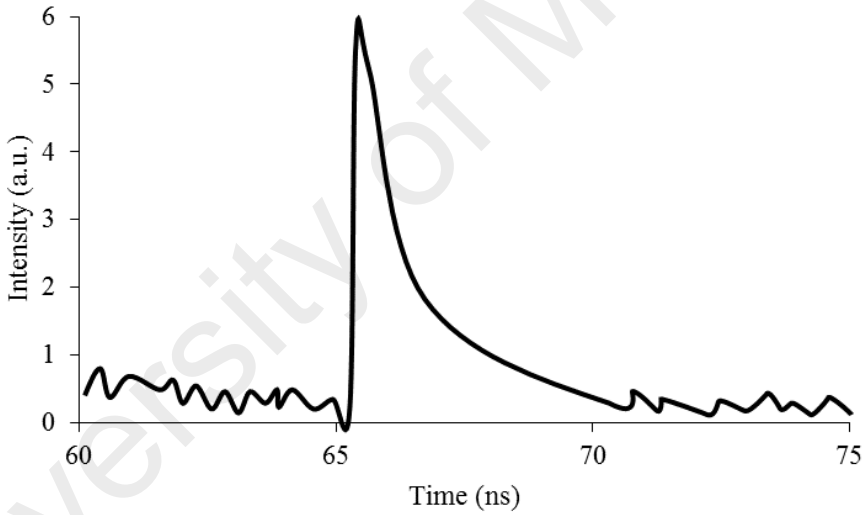

Figure 4.23 Fluorescence decay of **Complex 3**

Also, upon excitation at 410 nm (*d-d* transition), its **fluorescence** spectrum shows a peak at λ_{max} 419 nm (**Figure 4.24)**. Its E_o, calculated from λ_{edge} = 428 nm, was 2.8 eV, and its $\boldsymbol{\tau}$ value, calculated as before from its decay curve, was 2.9 ns. In addition, its Stokes shift was 9 nm.

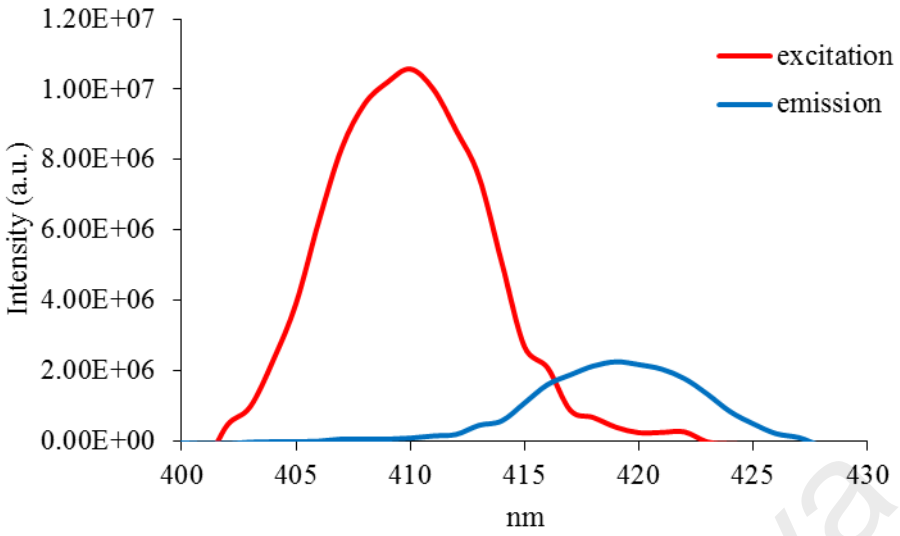

Figure 4.24 Fluorescence spectrum of **Complex 3** (λ_{ex} = 410 nm)

Its **CV** (**Figure 4.25**), recorded anodically from 0 V within the potential window of +1.5 V to -1.5 V, showed an anodic peak at +1.14 V and the corresponding cathodic peak at -1.04 V. These are assigned to the oxidation and reduction of *L1*, respectively. This means that Co(II) atom in **Complex 3** was redox inactive. Hence, its E_e value cannot be calculated.

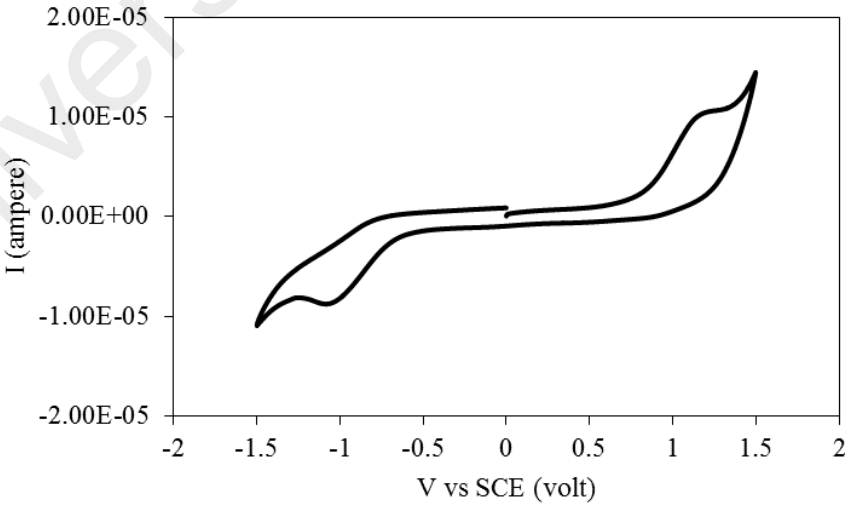

Figure 4.25 CV of **Complex 3**

Its $\boldsymbol{\mu_{eff}}$ value, calculated as before from the values of FM = 613.35 g mol^{-1}, χ_g = 2.45 x 10^{-5} cm^3 g^{-1}, χ_M = 1.50 x 10^{-2} cm^3 mol^{-1}, and χ_{dia} = -3.05 x 10^{-4} cm^3 mol^{-1},

was 6.06 B.M. at 298 K. This is higher than the expected value for a dinuclear high-spin Co(II) complex (d^7) (5.48 B.M.), suggesting a ferromagnetic interaction between the Co(II) centres [20].

Its **TGA** trace (**Figure 4.26**) shows an initial weight loss of 5.7% in the temperature range of 69 – 241 °C, assigned to the evaporation of two coordinated H_2O molecules (expected, 5.9%). The next weight loss of 66.8% in the temperature range of 241 - 618 °C is assigned to the decomposition of two CH_3COO^- and *L1* ligands (expected, 74.5%). The amount of residue at temperatures above 618 °C was 27.5% (expected 19.6%, assuming pure CoO) [14]. Hence, the complex (T_{dec} = 241 °C) was as thermally stable as **Complexes 1** ($[Cu_2(CH_3COO)_2(H_2O)_2(L1)]$; T_{dec} = 231 °C) and **2** ($[Ni_2(CH_3COO)_2(H_2O)_2(L1)]$; T_{dec} = 238 °C).

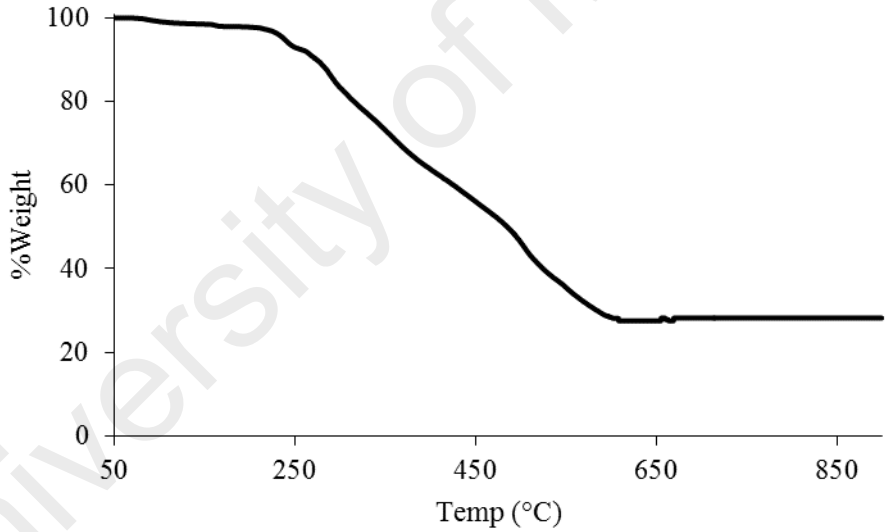

Figure 4.26 TGA of **Complex 3**

4.2.5 Reaction of iron(II) ethanoate with H_2L1

Iron(II) ethanoate ($[Fe_2(CH_3COO)_4]$) reacted with *H_2L1* (mole ratio 1:1) to give a black solid (**Complex 4**), and the yield was 97.2%. Its solubility was similar to the previously discussed complexes.

The results from the **elemental analyses** (39.6% C; 3.8% H; 12.1% N) are in excellent agreement with those calculated for the chemical formula $Fe_3C_{25}H_{30}N_7O_{10}$

(39.8% C; 4.1% H; 12.0% N; formula weight, 815.13 g mol^{-1}). Combining these with the spectroscopic data discussed below, its proposed structural formula is $[Fe_3(CH_3COO)_4(H_2O)_3(L1)].H_2O$ (**Figure 4.27**). Hence, unlike Cu(II), Ni(II) and Co(II), which formed dinuclear complexes, Fe(II) formed a trinuclear complex with the same ligand. It is further noted that Fe(II) acetate was also trinuclear [21, 22].

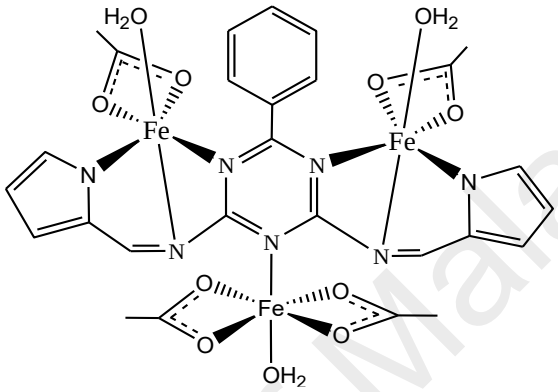

Figure 4.27 Proposed structure of **Complex 4** (lattice H_2O molecule is not shown)

Its **FTIR** spectrum (**Table 4.2**; **Figure 4.28**) shows the presence of the expected functional groups. The ΔCOO value is 138 cm^{-1}, suggesting chelating CH_3COO^- ligand [1]. For IR spectral simulation, the complex was modelled on Accelrys Material Studio (version 6.1), which employs the density functional theory (DFT) [23]. The results show a better fit for experimental and simulation data. The first principle code DMol3 calculates the vibrational intensities from the atomic polar tensors (A), usually called Bohr effective charges. A is a second derivative energy with respect to the Cartesian coordinates and dipole moments.

$$A_{i,j} = \frac{\partial E}{\partial q_i \partial \mu_i}$$

The intensity of a particular mode was calculated by squaring all transition moments of the mode and expressed in terms of the A matrix and eigenvectors of the mass-weighted Hessian. F:

$$I_i = \left(\sum_{j,k} F'_{i,j} A_{j,k}\right)^2$$

where *F'* refers to the eigenvectors of the normal mode, i.

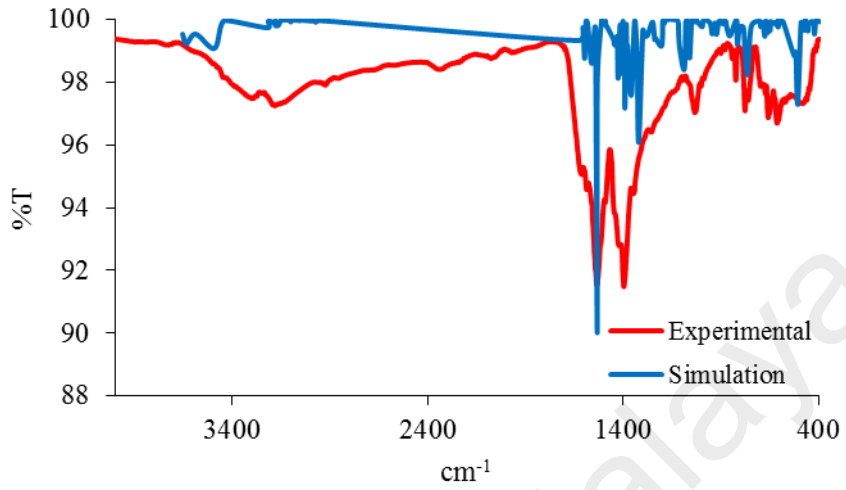

Figure 4.28 The experimental and simulated IR spectra of **Complex 4**

Accordingly, it is confirmed that the proposed structure is in agreement with molecular model (**Figure 4.29**).

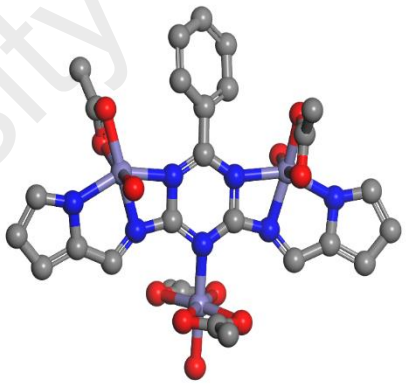

Figure 4.29 Molecule model of **Complex 4** (H atoms are removed for clarity)

Its **UV-vis** spectrum in DMSO (**Figure 4.30**) shows a broad band at 700 nm (ε_{max}, 137 $M^{-1}cm^{-1}$) assigned to ${}^5T_{2g} \rightarrow {}^5E_g$ electronic transition of HS Fe(II), a shoulder at 340 nm (ε_{max}, 420 $M^{-1}cm^{-1}$) assigned to ${}^1A_{1g} \rightarrow {}^1T_{1g}$ electronic transition of LS Fe(II) [24, 25] and an intense band at 267 nm, assigned to MLCT transition. These suggest that the complex has both HS and LS Fe(II) atoms and octahedral geometry at Fe(II) centres.

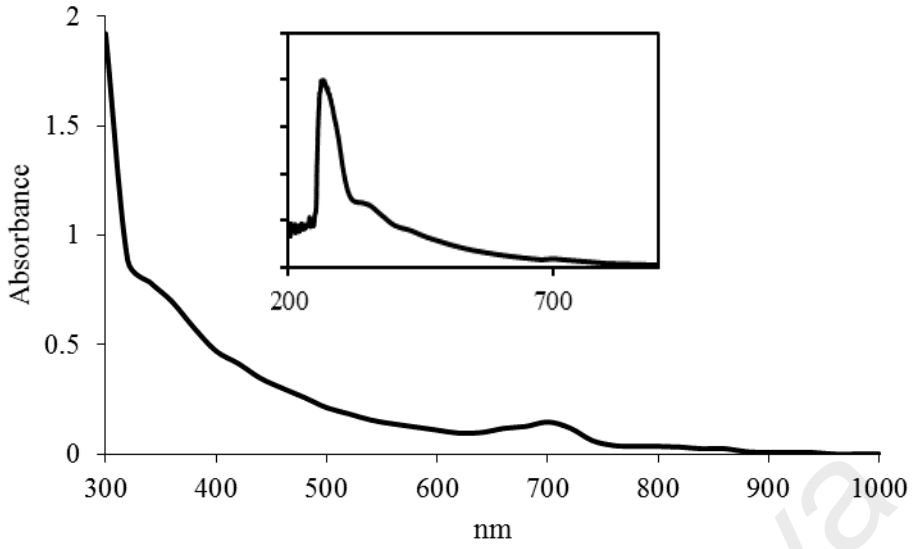

Figure 4.30 UV-vis spectrum of **Complex 4**

Its E_o, calculated as before from λ_{edge} (352 nm), was 3.5 eV. The value was similar to **Complexes 1** ([$Cu_2(CH_3COO)_2(H_2O)_2(L1)$]; 3.4 eV), **2** ([$Ni_2(CH_3COO)_2(H_2O)_2(L1)$]; 3.4 eV) and **3** ([$Co_2(CH_3COO)_2(H_2O)_2(L1)$]; 3.4 eV).

Upon excitation at 267 nm (MLCT band), its **fluorescence** spectrum shows a peak at λ_{max} 496 nm (**Figure 4.31)**. Its E_o, calculated from λ_{edge} = 700 nm, was 1.8 eV. Its τ, calculated as before from its **decay** curve (**Figure 4.32**), was 2.8 ns. Additionally, its Stokes shift was 229 nm.

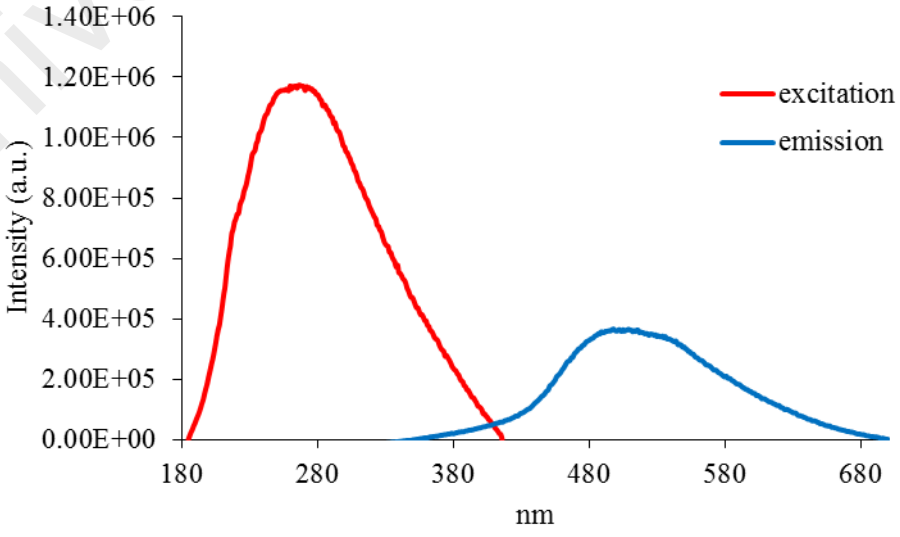

Figure 4.31 Fluorescence spectrum of **Complex 4** (λ_{ex} = 267 nm)

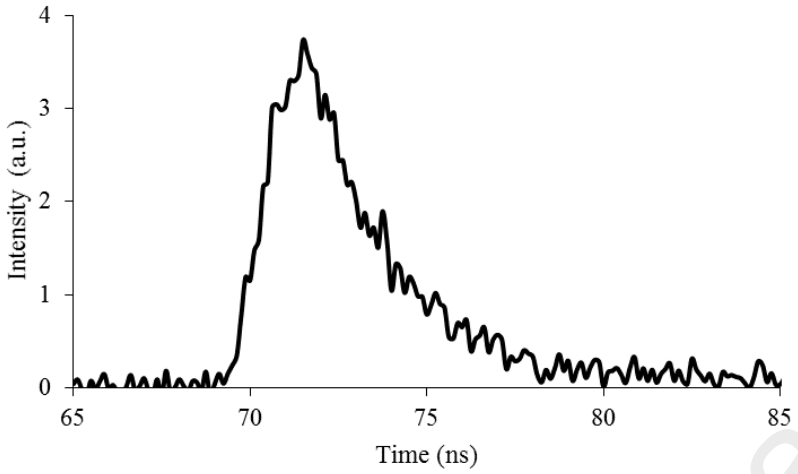

Figure 4.32 Fluorescence decay of **Complex 4**

Upon excitation at 700 nm (*d-d* transition), its **fluorescence** spectrum shows a peak at λ_{max} 730 nm (**Figure 4.33)**. Its $E_{o,}$ calculated from λ_{edge} = 880 nm, was 1.4 eV, and its $\boldsymbol{\tau}$ value, calculated as before from its decay curve, was 1.5 ns. Its Stokes shift was 30 nm.

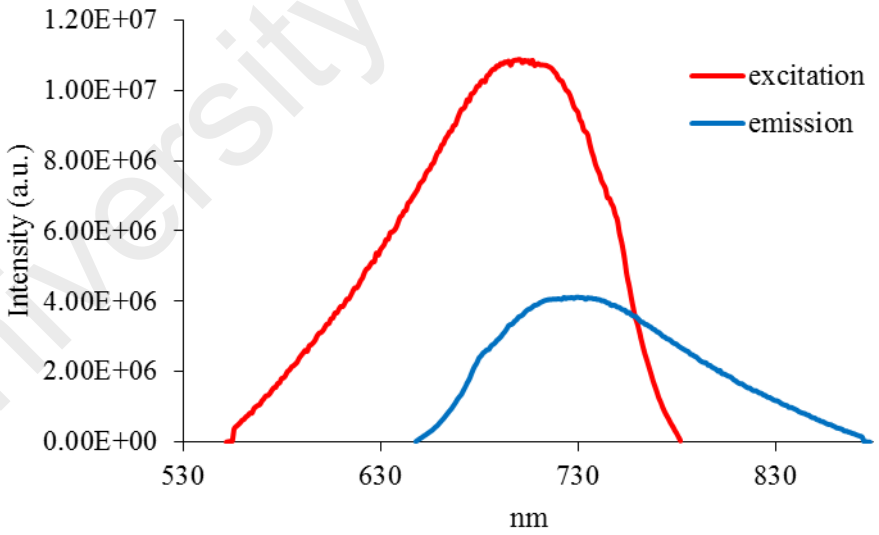

Figure 4.33 Fluorescence spectrum of **Complex 4** (λ_{ex} = 700 nm)

Its **CV** (**Figure 4.34**), recorded anodically from 0 V within the potential window of +1.5 V to -1.5 V, showed an anodic peak at +0.99 V when the electrode potential was increased from 0 V to +1.5 V, followed by a cathodic peak at -1.01 V when the electrode potential was reduced from +1.5 V to -1.5 V. This may be assigned to ligand-

based redox processes. The Fe-based redox process is not observed in the voltammogram, indicating that the three Fe(II) atoms in the complex were redox inactive. Hence, the value of E_e for the complex cannot be calculated.

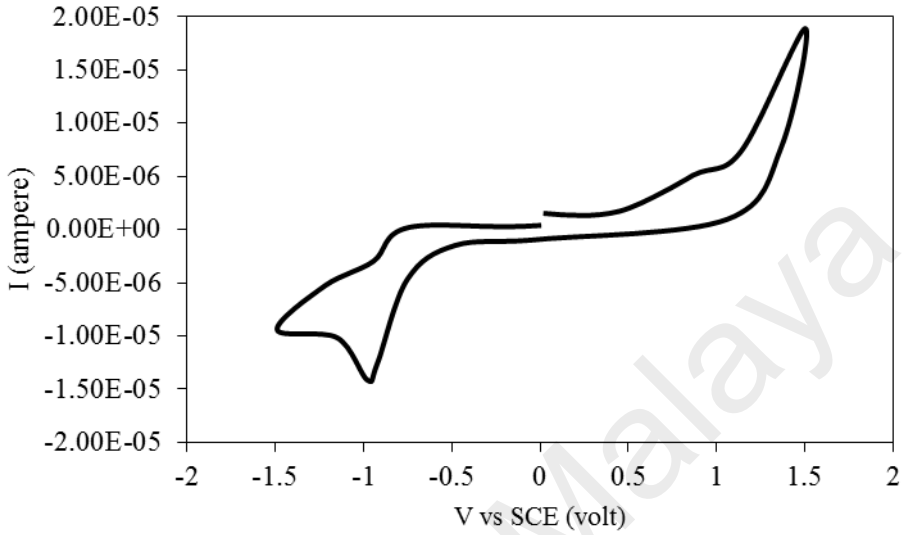

Figure 4.34 CV of **Complex 4**

Its μ_{eff} value, calculated as before from the values of FM = 815.13 g mol^{-1}, χ_g = 2.17 x 10^{-6} cm^3 g^{-1}, χ_M = 1.77 x 10^{-3} cm^3 mol^{-1}, and χ_{dia} = -2.53 x 10^{-4} cm^3 mol^{-1}, was 2.23 B.M. at 298 K. This is much lower than the expected value for a trinuclear high-spin Fe(II) complex (8.49 B.M.).

The variable-temperature magnetic susceptibilities for the complex were measured using a SQUID magnetometer in the temperature range of 300 K – 2 K. A plot of $\chi_M T$ *vs.* T (**Figure 4.35)** shows that its $\chi_M T$ values decreased gradually from 2.5 cm^3 K mol^{-1} at 300 K to about 0.9 cm^3 K mol^{-1} at 25 K, and then more abruptly to about 0.4 cm^3 K mol^{-1} at 2 K. From these observations, it may be inferred that: (a) the complex was made up of 27.7% HS and 72.3% LS Fe(II) atoms at 300 K (since the expected $\chi_M T$ value for a trinuclear octahedral HS Fe(II) complex at this temperature is 9.03 cm^3 K mol^{-1} [12]; and (b) on cooling, the HS Fe(II) atom(s) in the complex underwent a SCO transition to LS Fe(II).

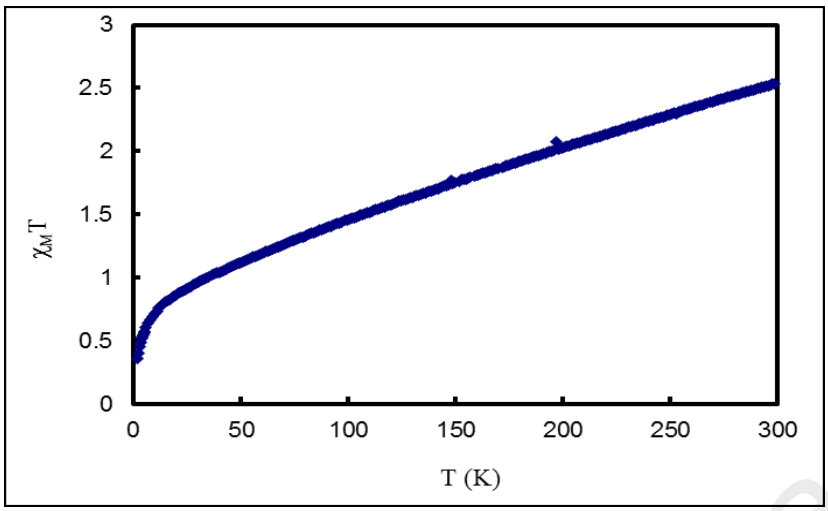

Figure 4.35 Plot of $\chi_M T$ versus T for **Complex 4** on cooling from 300 K to 2 K

Its **TGA** trace (**Figure 4.36**) shows the total weight loss of 79.0% in the temperature range of 59 – 700 °C, assigned to the evaporation of one lattice H_2O and three coordinated H_2O molecules, and the decomposition of four CH_3COO and *L1* ligands (expected, 79.3%). The amount of residue at 700 °C was 21.0% (expected, 20.7% assuming pure Fe). Hence, **Complex 8** (T_{dec} = 199 °C) was the least thermally stable compared to **Complexes 1** ($[Cu_2(CH_3COO)_2(H_2O)_2(L1)]$; T_{dec} = 231 °C), **2** ($[Ni_2(CH_3COO)_2(H_2O)_2(L1)]$; T_{dec} = 238 °C), and **3** ($[Co_2(CH_3COO)_2(H_2O)_2(L1)]$; T_{dec} = 241 °C).

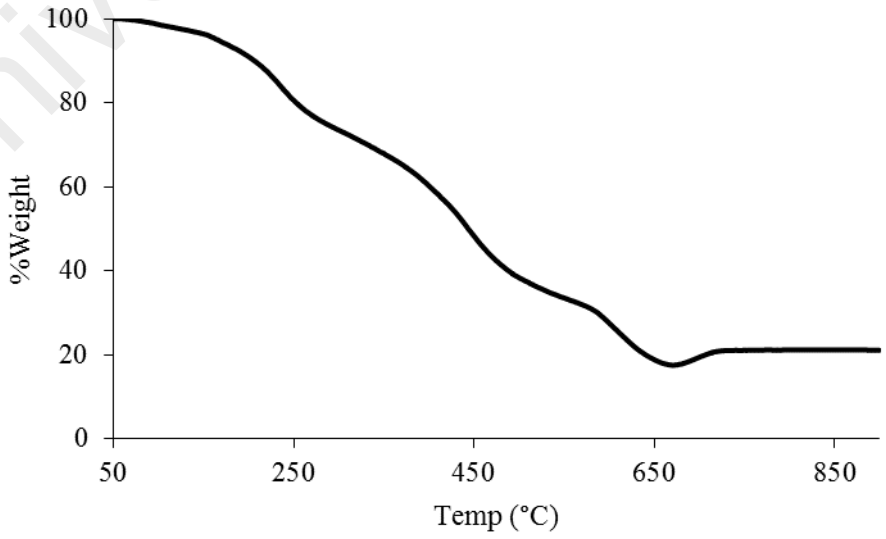

Figure 4.36 TGA of **Complex 4**

4.2.6 Reaction of copper(II) hexadecanoate with H_2L1

Copper(II) hexadecanoate ($[Cu_2(CH_3(CH_2)_{14}COO)_4]$) was obtained as a green powder from the reaction of sodium hexadecanoate with copper(II) chloride dihydrate. The equations for the reactions are shown in **Scheme 4.3**.

$$CH_3(CH_2)_{14}COOH \xrightarrow[\substack{\Delta \\ C_2H_5OH,\ H_2O}]{Na_2CO_3} CH_3(CH_2)_{14}COONa \xrightarrow[\substack{\Delta \\ C_2H_5OH,\ H_2O}]{CuCl_2.2H_2O} [Cu_2(CH_3(CH_2)_{14}COO)_4]$$

Scheme 4.3 Reaction equation for the preparation of $[Cu_2(CH_3(CH_2)_{14}COO)_4]$

The **elemental analytical** results (66.9% C; 10.3% H) were in excellent agreement with those calculated for the chemical formula $Cu_2C_{64}H_{124}O_8$ (66.9% C; 10.9% H; formula weight, 1148.76 g mol^{-1}). Its structural formula (**Figure 4.37**) is proposed based on a combination of spectroscopic data discussed below. Hence, the complex has the paddle-wheel structure, similar to that of $[Cu_2(CH_3COO)_4(H_2O)_2]$ [26].

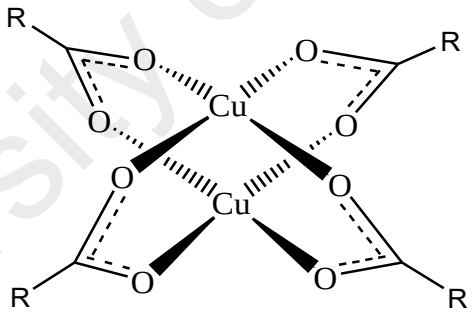

R = $CH_3(CH_2)_{14}$

Figure 4.37 Proposed structural formula for $[Cu_2(CH_3(CH_2)_{14}COO)_4]$

Its **FTIR** spectrum is shown in **Figure 4.38**, and the peak assignments are given in **Table 4.3** (which also include the data for other metal(II) hexadecanoates for later discussion). The value of ΔCOO (138 cm^{-1}) suggests a bidentate bridging $CH_3(CH_2)_{14}COO^-$ ligand [1], and hence a binuclear complex.

Table 4.3 FTIR data (in cm^{-1}) and assignments for $[M_2(CH_3(CH_2)_{14}COO)_4]$

Metal(II)	O-H	CH_2 (asym)	CH_2 (sym)	COO (asym)	COO (sym)	M-O
Cu(II)	-	2914s	2849m	1584s	1446m	464w
Ni(II)	3363br	2917s	2850m	1549s	1428s	476m
Co(II)	3363br	2917s	2850m	1543s	1432s	473m
Fe(II)	3378br	2917s	2849m	1575s	1441s	464m

s = strong; m = medium; w = weak; br = broad

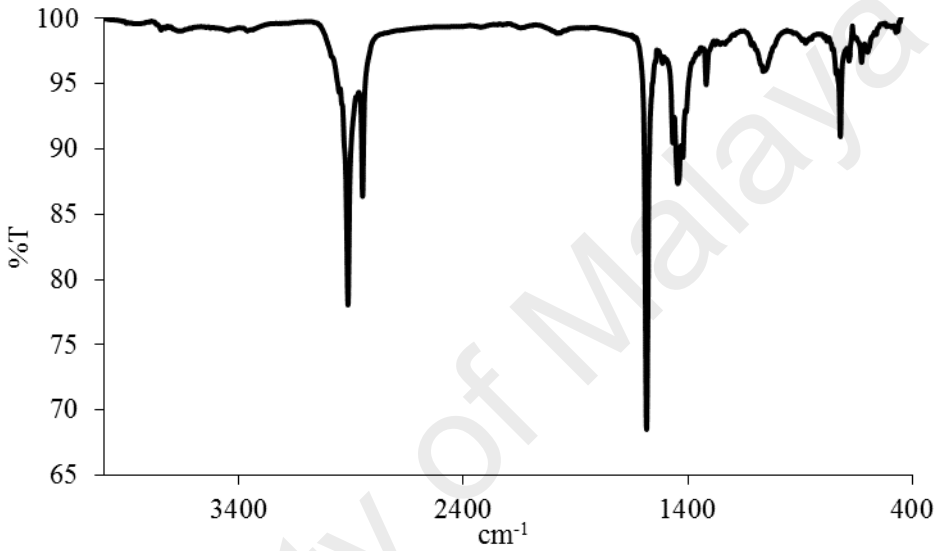

Figure 4.38 FTIR spectrum of $[Cu_2(CH_3(CH_2)_{14}COO)_4]$

Its **UV-vis** spectrum in DMSO (**Figure 4.39**) shows a broad *d-d* band at 669 nm (ε_{max}, 284 M^{-1} cm^{-1}), and a weak shoulder band at 387 nm (ε_{max}, 89.6 M^{-1} cm^{-1}). This suggests a square pyramidal binuclear Cu(II) complex. The electronic transitions, based on the C_{4v} point group at each Cu(II) centre, are assigned to $^2B_1 \rightarrow {}^2B_2$ and $^2B_1 \rightarrow {}^2E$ transitions, respectively [27]. An intense absorption band is also observed at 253 nm (ε_{max}, 1808.5 M^{-1} cm^{-1}), assigned to the LMCT transition. Its E_o**,** calculated from λ_{edge} = 282 nm, was 4.4 eV.

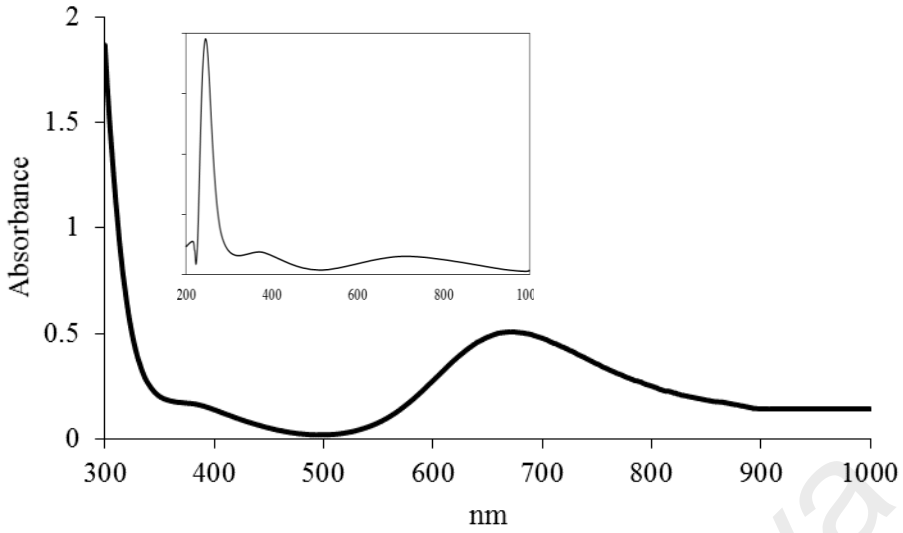

Figure 4.39 UV-vis spectrum of $[Cu_2(CH_3(CH_2)_{14}COO)_4]$

Upon excitation at 253 nm (LMCT transition), its **fluorescence** spectrum shows a peak at λ_{max} 275 nm (**Figure 4.40**). Its E_o, calculated from λ_{edge} = 285 nm, was 4.3 eV, and from its decay curve (**Figure 4.41**), the $\boldsymbol{\tau}$ value was 5.4 ns. Its Stokes shift value was 22 nm.

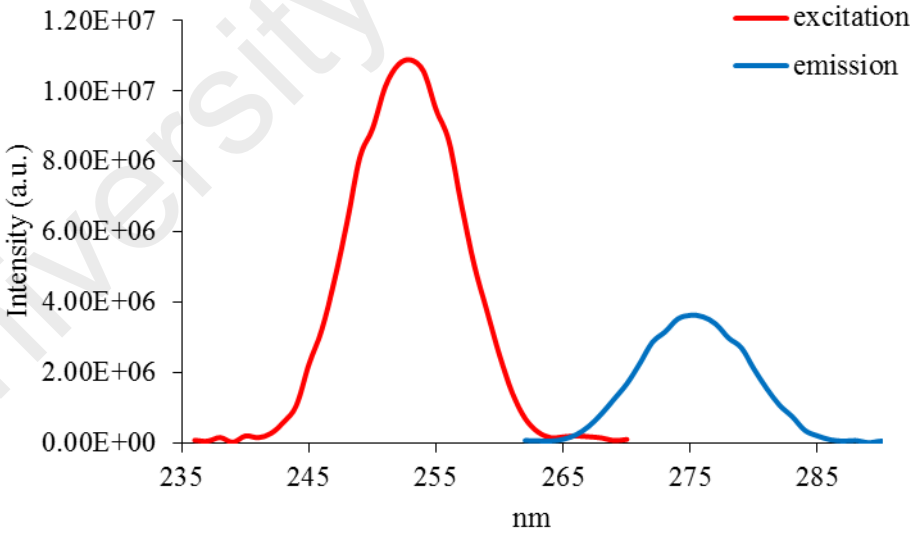

Figure 4.40 Fluorescence spectrum of $[Cu_2(CH_3(CH_2)_{14}COO)_4]$ (λ_{ex} = 253 nm)

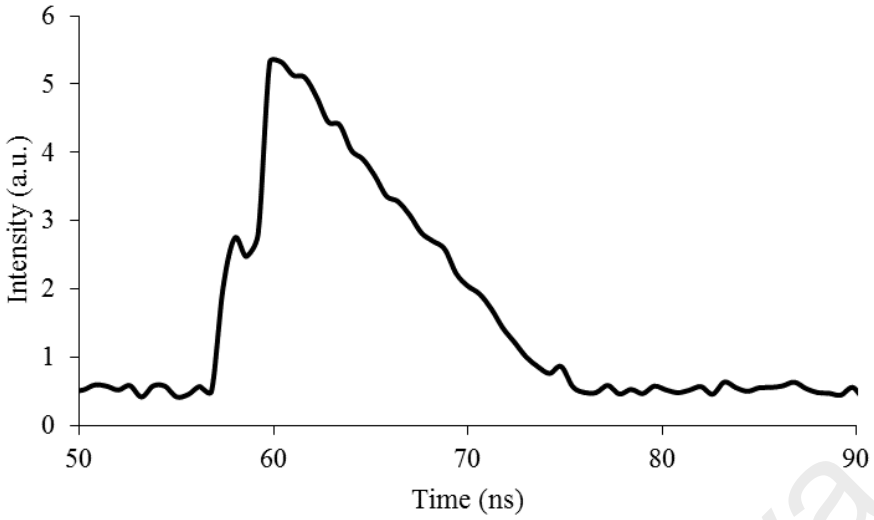

Figure 4.41 Fluorescence decay of $[Cu_2(CH_3(CH_2)_{14}COO)_4]$

However, upon excitation at 387 nm (*d-d* transition), its **fluorescence** spectrum shows a peak at λ_{max} 424 nm (**Figure 4.42**). Hence its E_o, calculated from λ_{edge} = 458 nm, was 2.7 eV, and its $\boldsymbol{\tau}$ value was 3.5 ns. Its Stokes shift value was 37 nm.

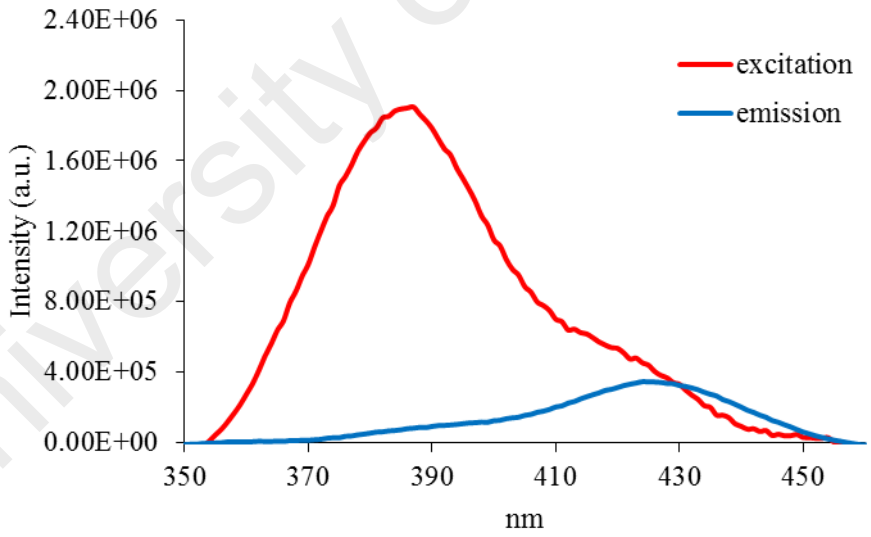

Figure 4.42 Fluorescence spectrum of $[Cu_2(CH_3(CH_2)_{14}COO)_4]$ (λ_{ex} = 387 nm)

Its **CV** scan (**Figure 4.43**), recorded cathodically from 0 V within the potential window -1.5 V to +1.5 V. It showed no distinctive cathodic peak (E_c) when the electrode potential was reduced from 0 V to -1.5 V. However, when the potential was changed from -1.5 V to +1.5 V, there was an anodic peak (E_a) at +1.1 V. This is

assigned to ligand-based oxidation process. It indicates that Cu(II) ion in the complex was redox inactive. Hence, its E_e cannot be calculated.

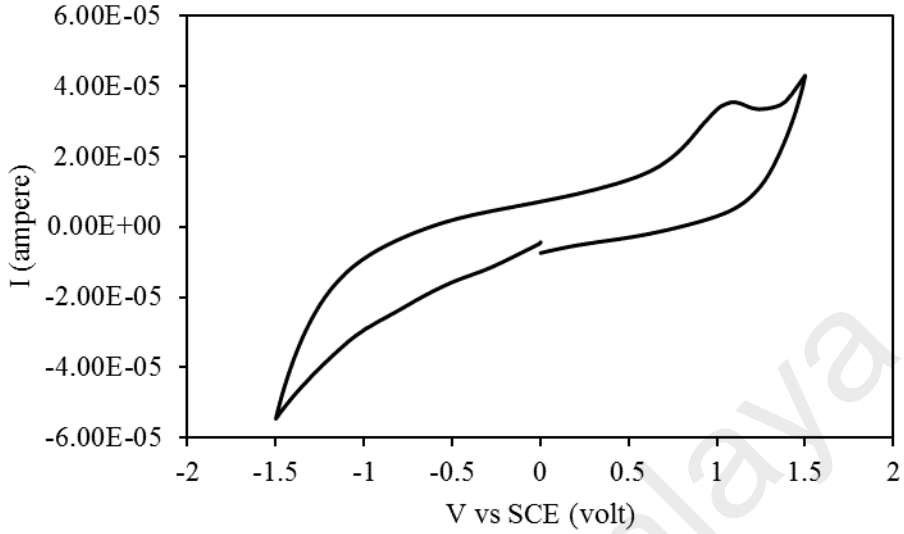

Figure 4.43 CV for $[Cu_2(CH_3(CH_2)_{14}COO)_4]$

Its μ_{eff} value, calculated as before from the values of FM = 1148.76 g mol^{-1}, χ_g = 1.2 x 10^{-6} cm^3 g^{-1}, χ_M = 1.32 x 10^{-3} cm^3 mol^{-1}, and χ_{dia} = -7.59 x 10^{-4} cm^3 mol^{-1}, was 2.27 B.M. at 298 K. This is slightly lower than the expected value for a dimeric copper(II) complex (2.45 B.M.) [12]. Hence, there exists an antiferromagnetic interaction between the two Cu(II) centres, postulated to occur through the bridging $CH_3(CH_2)_{14}COO$ ligand. This finding further supports the above proposed paddle-wheel structure for the complex [26, 28, 29].

Its **TGA** trace (**Figure 4.44**) shows a total weight loss of 82.6% in the temperature range of 273 - 650 °C, assigned to the decomposition of all $CH_3(CH_2)_{14}COO$ ligands (expected, 88.9%). The amount of residue at temperature above 650 °C was 17.4% (expected, 11.1% assuming pure CuO) [16, 30]. The higher value is probably due to incomplete combustion of the organic ligands. It is noted that $[Cu_2(CH_3(CH_2)_{14}COO)_4]$ (T_{dec} = 273 °C) was as thermally stable as $[Cu_2(C_6H_5COO)_4(H_2O)_2]$ (T_{dec} = 280 °C) reported by Siqueira *et al*. [31, 32].

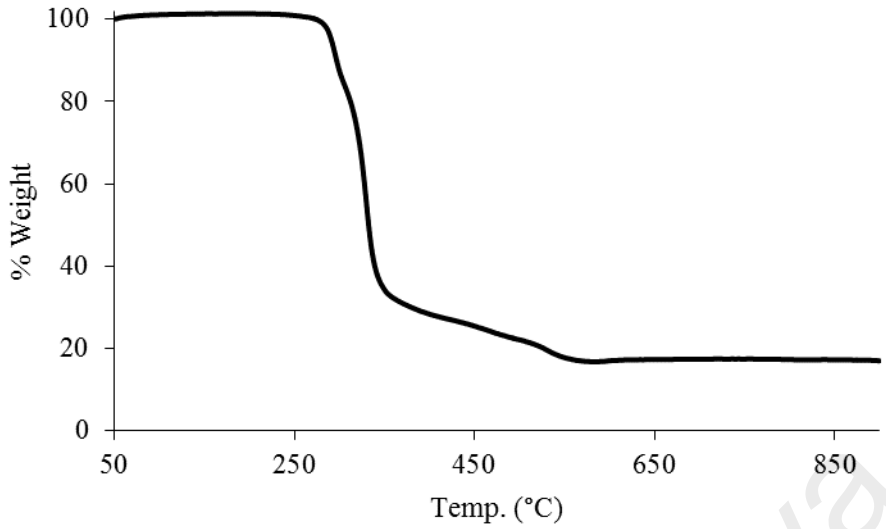

Figure 4.44 TGA of $[Cu_2(CH_3(CH_2)_{14}COO)_4]$

Its **DSC** scan (**Figure 4.45**) was recorded for one heating-and-cooling cycle (from 25 °C to 145 °C to 25 °C). On heating, there was one endothermic peak at 115.8 °C (ΔH = +108.9 kJ mol^{-1}), assigned to its melting temperature (T_m). On cooling, there were a weak exothermic peak at 90 °C and a stronger exothermic peak at 70 °C (ΔH_{comb} = -94.3 kJ mol^{-1}), assigned to I-to-M and M-to-Cr phase transitions, respectively (I = isotropic, M = mesophase, Cr = crystal).

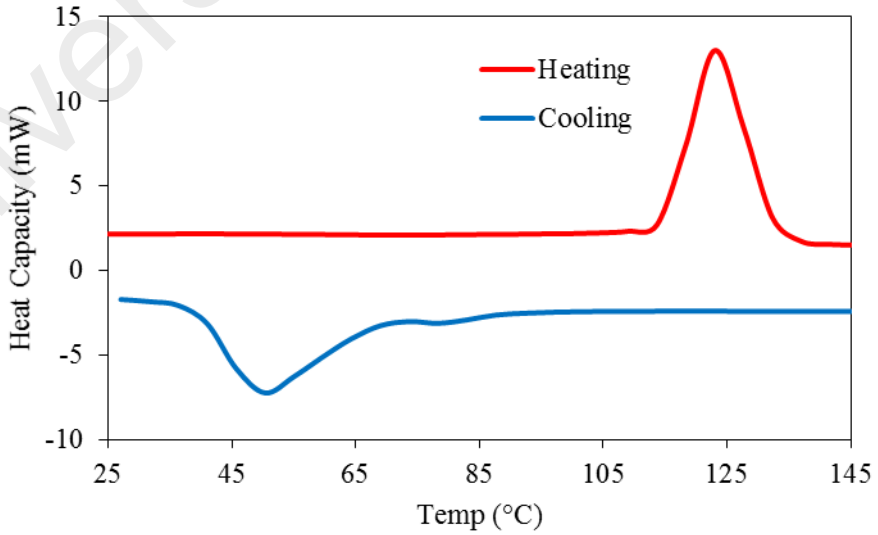

Figure 4.45 DSC for $[Cu_2(CH_3(CH_2)_{14}COO)_4]$

Its **POM** was recorded for two heating-cooling cycles from 25 °C to 150 °C. On cooling from 150 °C, an optical texture was observed at 78 °C (**Figure 4.46**).

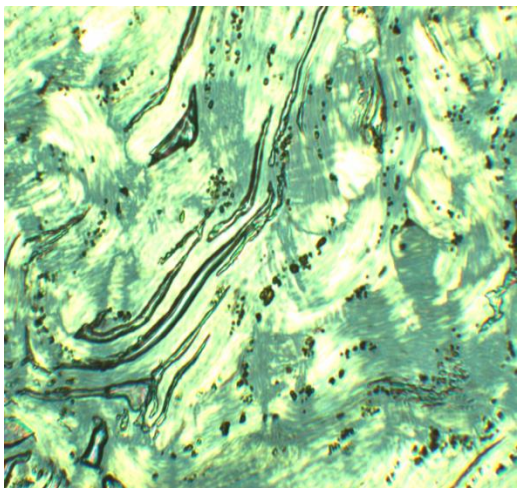

Figure 4.46 Photomicrographs of $[Cu_2(CH_3(CH_2)_{14}COO)_4]$ on cooling from 150 ^oC at 78 ^oC

$[Cu_2(CH_3(CH_2)_{14}COO)_4]$ reacted with *H_2L1* (mole ratio 1:1) to give a green powder (**Complex 5**), and the yield was 75%. Its solubility was similar to the previously discussed complexes.

The results from the **elemental analyses** (61.9% C; 7.5% H; 10.4% N) were in excellent agreement with those calculated for the chemical formula $Cu_2C_{51}H_{75}N_7O_4$ (62.7% C; 7.7% H; 10.0% N; formula weight, 977.28 g mol^{-1}). Combining these with the spectroscopic data discussed below, its proposed structural formula is $[Cu_2(CH_3(CH_2)_{14}COO)_2(L1)]$ (**Figure 4.47**).

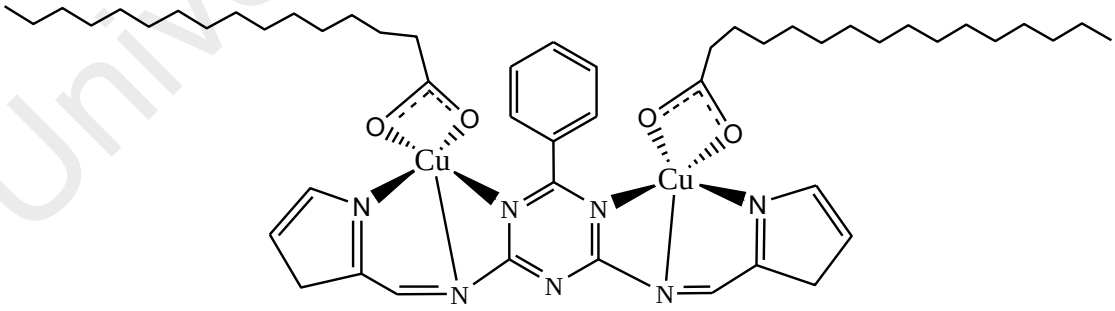

Figure 4.47 Proposed structure of **Complex 5**

Its **FTIR** spectrum (**Table 4.2**; **Figure 4.48**) shows the presence of the expected functional groups. The ΔCOO value (134 cm^{-1}) suggests a chelating binding mode for

$CH_3(CH_2)_{14}COO^-$ ligand [1]. This value is rather similar to $[Cu_2(CH_3(CH_2)_{14}COO)_4]$ (138 cm^{-1}).

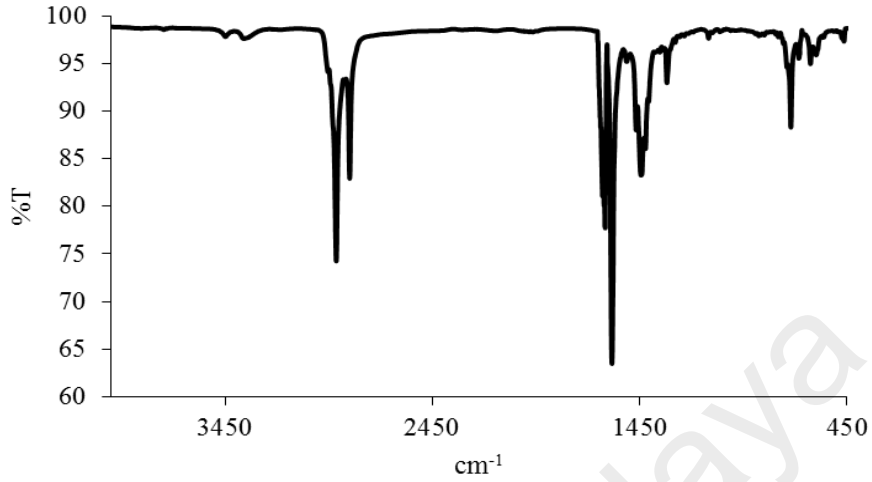

Figure 4.48 FTIR spectrum of **Complex 5**

Its **UV-vis** spectrum in DMSO (**Figure 4.49**) shows a broad *d-d* band at 713 nm (ε_{max}, 292 M^{-1} cm^{-1}), assigned as $^2B_1 \rightarrow {}^2B_2$ transition, a shoulder band at 400 nm (ε_{max}, 876 M^{-1} cm^{-1}) assigned as $^2B_1 \rightarrow {}^2E$ transition, and an intense LMCT band at 275 nm (ε_{max}, 2430 M^{-1} cm^{-1}). The results were similar to $[Cu_2(CH_3(CH_2)_{14}COO)_4]$, and may be similarly explained.

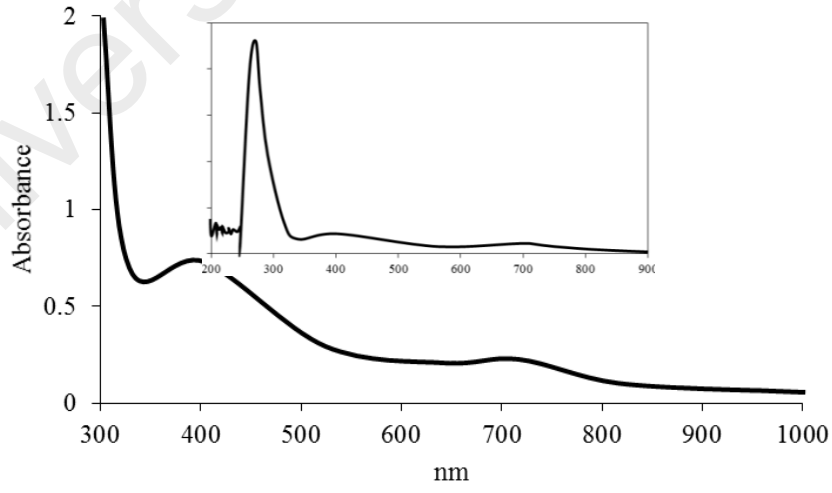

Figure 4.49 UV-vis spectrum of **Complex 5**

Its E_o, calculated from λ_{edge} = 326 nm, was 3.8 eV. This is just slightly higher compared to **Complex 1** ($[Cu_2(CH_3COO)_2(H_2O)_2(L1)]$; 3.4 eV).

Upon excitation at 275 nm (LMCT transition), its **fluorescence** spectrum shows two peaks at 421 nm and 550 nm (**Figure 4.50**). This suggests two different paths for the excited complex to return to the ground state. Its E_o value, calculated from λ_{edge} = 600 nm, was 2.1 eV. This value is slightly wider than **Complex 1** (1.8 eV). Its Stokes shift value was 146 nm.

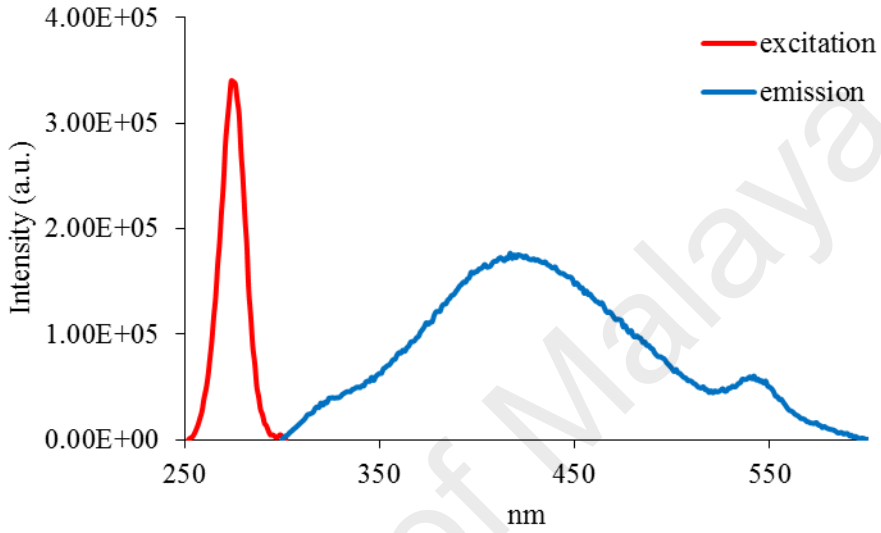

Figure 4.50 Fluorescence spectrum of **Complex 5** (λ_{ex} = 275 nm)

Its $\boldsymbol{\tau}$, calculated as before from its decay curve (**Figure 4.51**), was 3.0 ns. This is similar to **Complex 1** ($\boldsymbol{\tau}$ = 2.8 ns), suggesting an insignificant effect of the long alkyl chain on the lifetime of the excited complex.

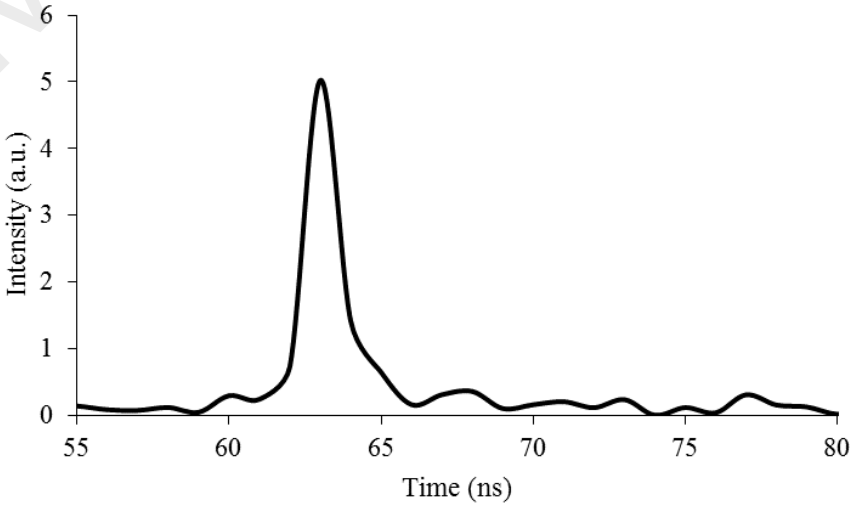

Figure 4.51 Fluorescence decay of **Complex 5**

Also, upon excitation at 400 nm (*d-d* transition), its **fluorescence** spectrum shows two overlapping peaks at λ_{max} 390 nm and 425 nm (**Figure 4.52**). This also suggests two different paths for the excited complex to return to the ground state. Its E_o value, calculated from λ_{edge} = 528 nm, was 2.3 eV, and its $\boldsymbol{\tau}$ value, calculated as before from its decay curve, was 3.2 ns. The Stokes shift value was 25 nm.

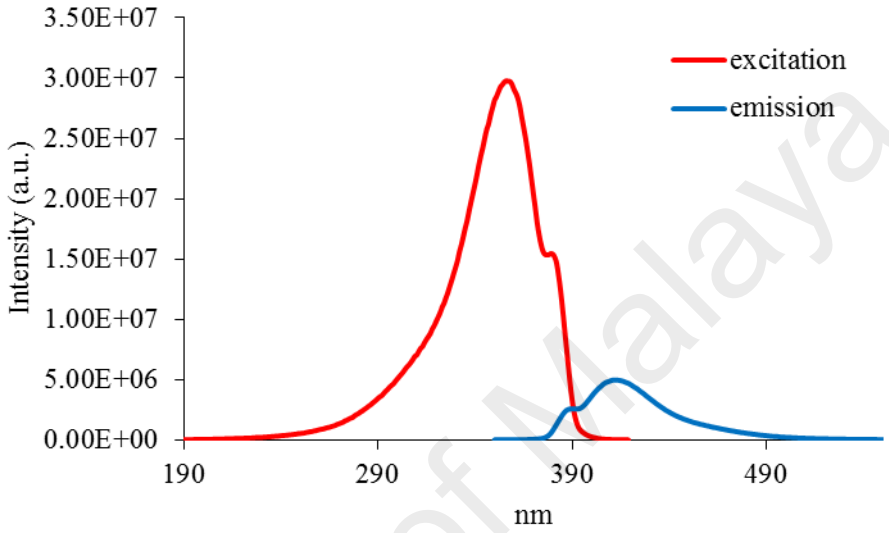

Figure 4.52 Fluorescence spectrum of **Complex 5** (λ_{ex} = 400 nm)

Its **CV** (**Figure 4.53**), recorded cathodically from 0 V within the potential window of -1.5 V to +1.5 V. It showed a cathodic peak when the electrode potential was reduced from 0 V to -1.5 V. This is assigned to ligand-based reduction. Additionally, when the electrode potential was increased from -1.5 V to +1.5 V, there were two anodic peaks at -0.21 V and +1.13 V. These are assigned to ligand-based oxidation processes. However, there was no Cu(II) based redox process. This indicates that Cu(II) is inactive redox. Hence, its E_e value cannot be calculated.

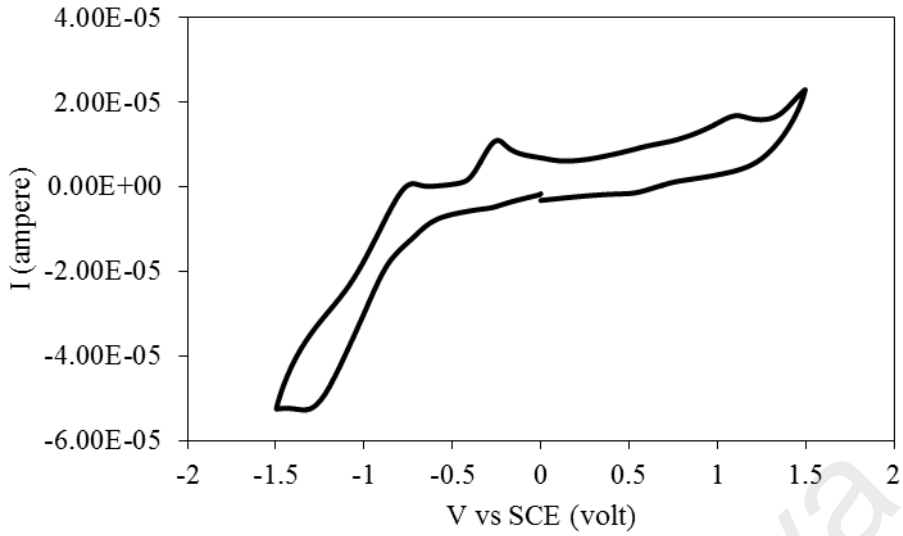

Figure 4.53 CV of **Complex 5**

Its μ_{eff} value, calculated as before from the values of FM = 977.28 g mol^{-1}, χ_g = 0.13 x 10^{-5} cm^3 g^{-1}, χ_M = 1.29 x 10^{-3} cm^3 mol^{-1}, and χ_{dia} = -5.42 x 10^{-4} cm^3 mol^{-1}, was 2.13 B.M. at 298 K. This value is similar to **Complex 1** ($[Cu_2(CH_3COO)_2(H_2O)_2(L1)]$; 2.15 B.M.), indicating an insignificant effect of the long alkyl chain on the magnetic properties of these complexes.

Its **TGA** trace (**Figure 4.54**) shows a total weight loss of 92.9% in the temperature range of 239 - 900 °C, assigned to the decomposition of two $CH_3(CH_2)_{14}COO^-$ and *L1* ligands (expected, 93.2%). The amount of residue at temperatures above 900 °C was 7.1% (expected, 6.8% assuming pure CuO). Hence, **Complex 5** (T_{dec} = 239 °C) is as thermally stable as **Complex 1** (T_{dec} = 231 °C). This indicates that the long alkyl chain has insignificant effect on the thermal stability of these complexes.

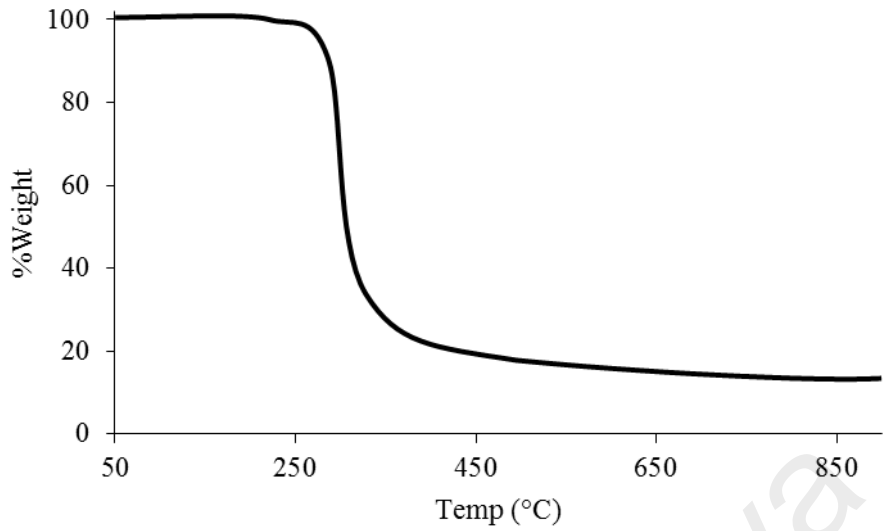

Figure 4.54 TGA of **Complex 5**

Its **DSC** scan (**Figure 4.55**), recorded from 25 °C to 235 °C, showed two overlapping endothermic peaks at 205 °C ($\Delta H_{combined}$ = +128.6 kJ mol^{-1}), assigned to Cr-to-M transition. On cooling, there was an exothermic peak at 193 °C (ΔH = -117.8 kJ mol^{-1}), assigned to M-to-Cr transition.

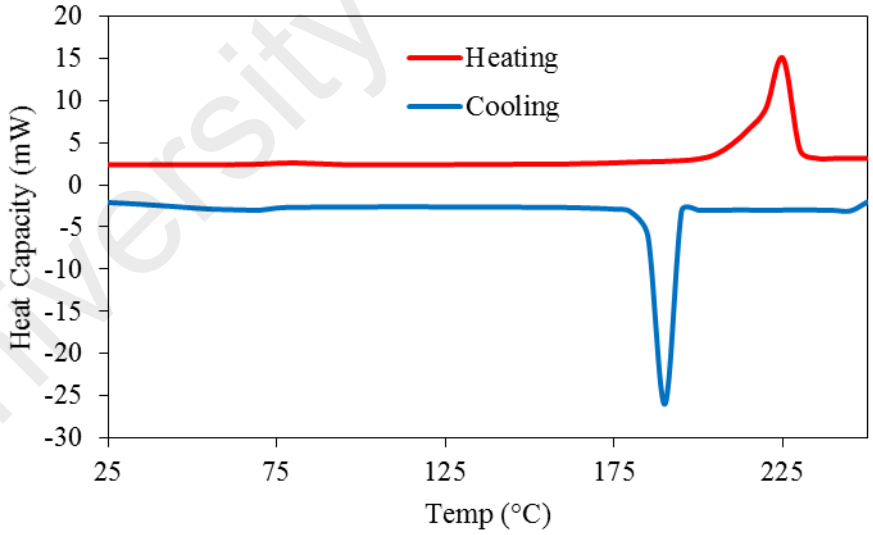

Figure 4.55 DSC of **Complex 5**

Its **POM** photomicrographs were recorded for two heating-cooling cycles from 25 °C to 230 °C. On cooling from 230 °C, an optical texture was observed at about 209 °C, and then the sample solidified at 182 °C (**Figure 4.56**).

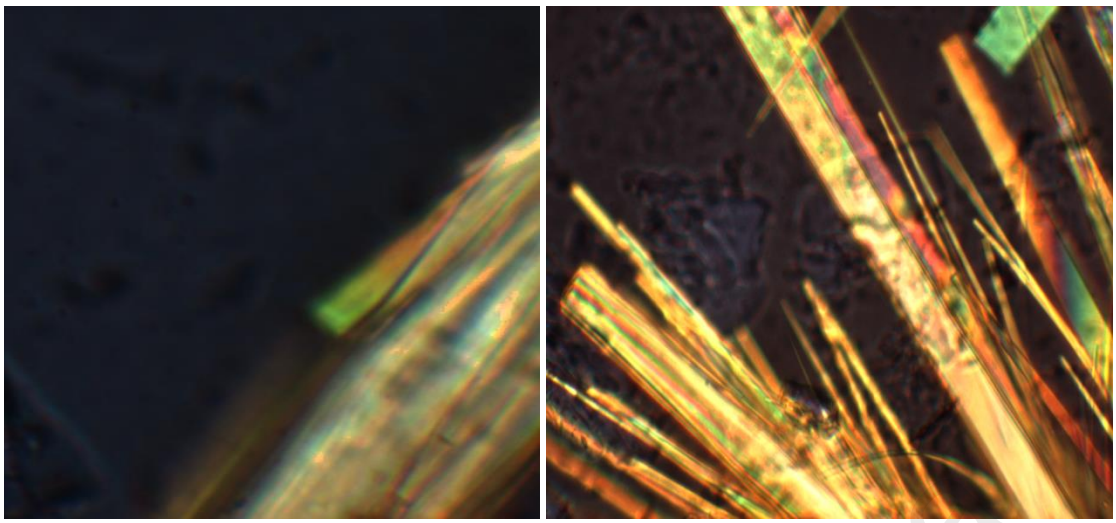

(a) **(b)**

Figure 4.56 Photomicrographs of **Complex 5** on cooling from 230 ^{o}C: (a) at 209 ^{o}C; and (b) at 182 ^{o}C (solid).

4.2.7 Reaction of nickel(II) hexadecanoate with H_2L1

Nickel(II) hexadecanoate was obtained as a pale-green powder from the reaction of sodium hexadecanoate with nickel(II) chloride hexahydrate. Its **elemental analytical** results (58.1% C; 10.9% H) were in excellent agreement with the values calculated for ($[Ni(CH_3(CH_2)_{14}COO)_2(H_2O)_2].3H_2O$ (58.3% C; 11.0% H; formula weight, 659.6 g mol^{-1}). Its proposed structural formula is shown in **Figure 4.57**.

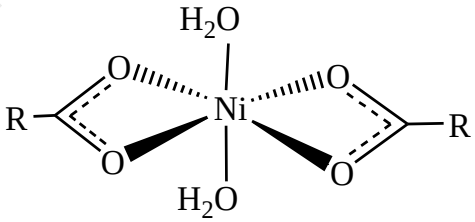

R = $CH_3(CH_2)_{14}$

Figure 4.57 Proposed structural formula for $[Ni(CH_3(CH_2)_{14}COO)_2(H_2O)_2].3H_2O$ (lattice H_2O molecules are not shown)

Its **FTIR** spectrum (**Table 4.3**; **Figure 4.58**) shows the presence of the expected functional groups. The ΔCOO value (121 cm^{-1}) suggests chelating $CH_3(CH_2)_{14}COO^-$ ligand.

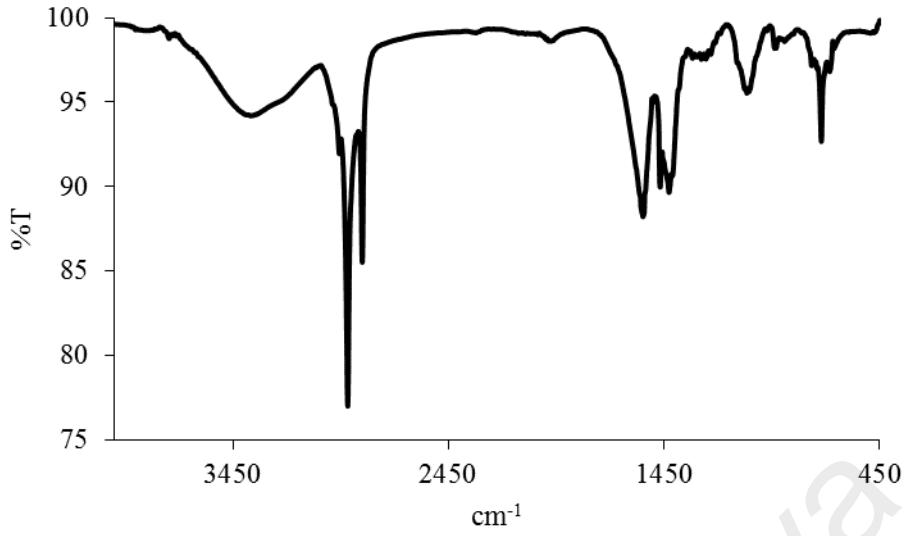

Figure 4.58 FTIR spectrum of $[Ni(CH_3(CH_2)_{14}COO)_2(H_2O)_2].3H_2O$

Its **UV-vis** spectrum in DMSO (**Figure 4.59**) shows a weak *d-d* band at 848 nm (ε_{max}, 8 M^{-1} cm^{-1}) assigned to $^3A_{2g}$ (F) $\rightarrow$ $^3T_{2g}$ (F) transition, 657 nm (ε_{max}, 242 M^{-1} cm^{-1}) assigned to $^3A_{2g}$ (F) $\rightarrow$ $^3T_{1g}$ (F) transition, and a shoulder at 402 nm (ε_{max}, 138 M^{-1} cm^{-1}) assigned to $^3A_{2g}$ (F) $\rightarrow$ $^3T_{1g}$ (P) transition. These electronic transitions suggest an octahedral geometry at Ni(II) centre [33, 34]. Also observed is an intense MLCT band at 252 nm (ε_{max}, 4149 M^{-1} cm^{-1}).

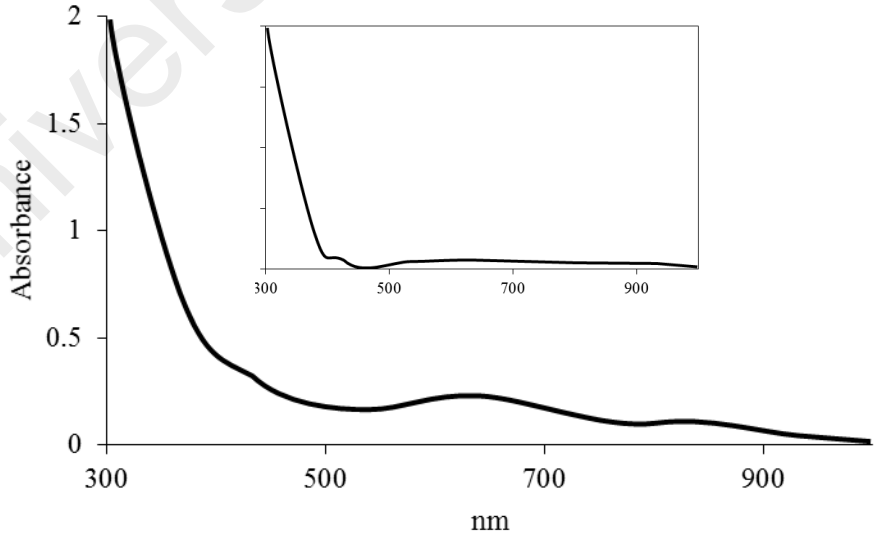

Figure 4.59 UV-vis spectrum of $[Ni(CH_3(CH_2)_{14}COO)_2(H_2O)_2].3H_2O$

Its E_o, calculated from λ_{edge} = 278 nm, was 4.4 eV. The value is similar to $[Cu_2(CH_3(CH_2)_{14}COO)_4]$ (4.4 eV).

Upon excitation at 252 nm (MLCT transition), its **fluorescence** spectrum shows a peak at λ_{max} 264 nm (**Figure 4.60)**. Its E_o, calculated from λ_{edge} = 269 nm, was 4.6 eV. The value is quite similar as that obtained from its absorption spectroscopy. Its τ value, calculated from its **decay curve** (**Figure 4.61**), was 5.4 ns. This is similar to $[Cu_2(CH_3(CH_2)_{14}COO)_4]$ (τ = 5.4 ns). Its Stokes shift was 12 nm.

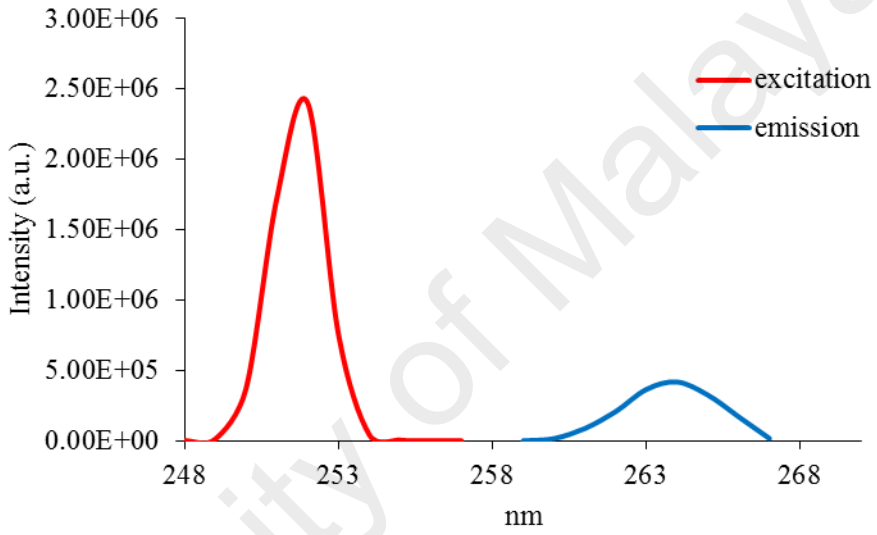

Figure 4.60 Fluorescence spectrum of $[Ni(CH_3(CH_2)_{14}COO)_2(H_2O)_2].3H_2O$ (λ_{ex} = 252 nm)

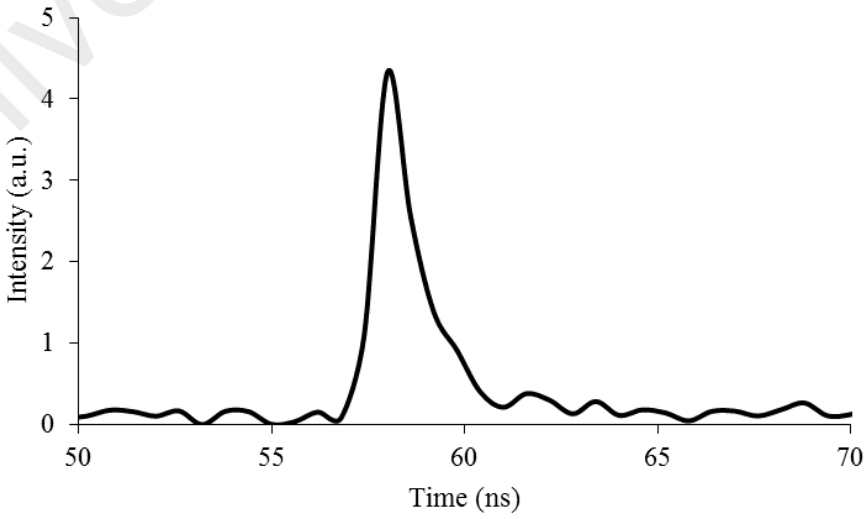

Figure 4.61 Fluorescence decay of $[Ni(CH_3(CH_2)_{14}COO)_2(H_2O)_2].3H_2O$

However, upon excitation at 402 nm (*d-d* transition), its **fluorescence** spectrum shows a peak at 429 nm (**Figure 4.62)**. Its E_o**,** calculated from λ_{edge} = 435 nm, was 2.8 eV and its τ, calculated as before from its **decay curve**, was 3.2 ns. Additionally its Stokes shift was 27 nm.

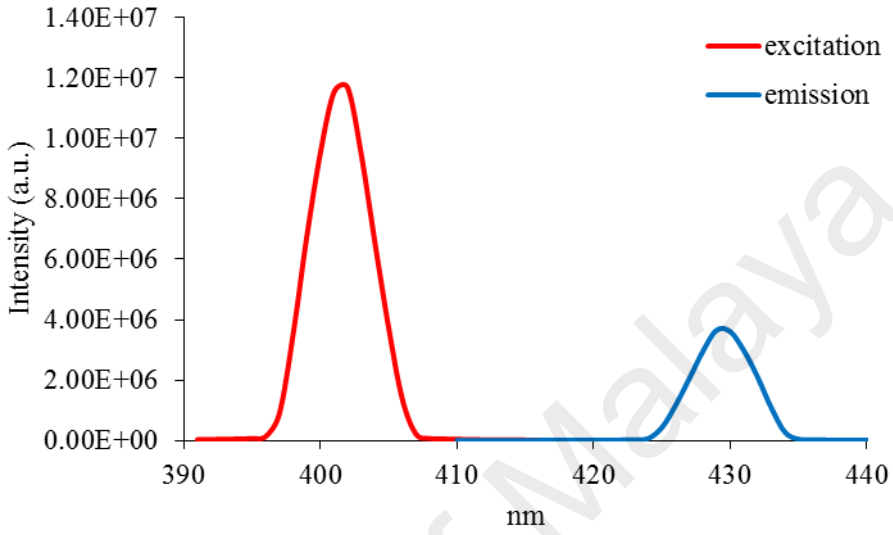

Figure 4.62 Fluorescence spectrum of $[Ni(CH_3(CH_2)_{14}COO)_2(H_2O)_2].3H_2O$ (λ_{ex} = 402 nm)

Its **CV** scan (**Figure 4.63**), recorded anodically from 0 V within the potential window +1.5 V to -1.5 V, showed one anodic peak at +0.99 V. This is assigned to the oxidation of Ni(II) to Ni(III), which was irreversible. Hence, its E_e value cannot be calculated.

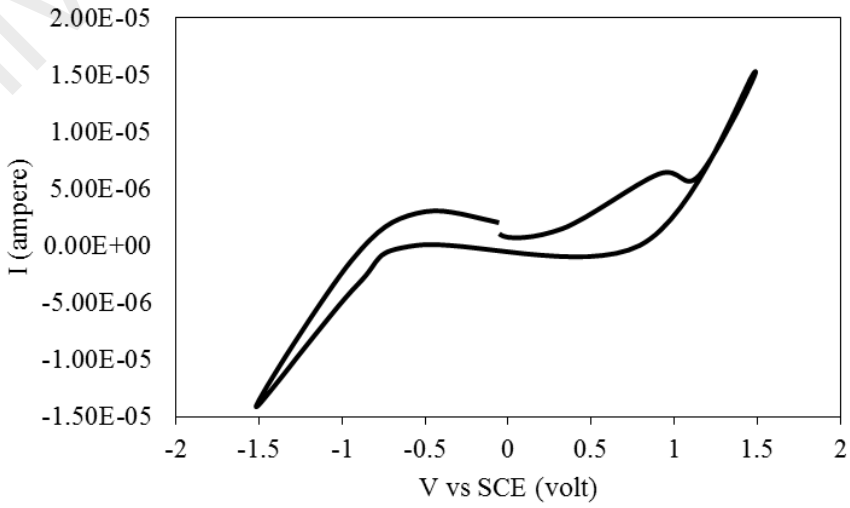

Figure 4.63 CV for $[Ni(CH_3(CH_2)_{14}COO)_2(H_2O)_2].3H_2O$

Its μ_{eff} value, calculated as before from the values of FM = 659.6 g mol^{-1}, χ_g = 0.76 x 10^{-5} cm^3 g^{-1}, χ_M = 5.05 x 10^{-3} cm^3 mol^{-1}, and χ_{dia} = -4.96 x 10^{-4} cm^3 mol^{-1}, was 3.66 B.M. at 298 K. This is significantly higher than the expected μ_{eff} value for a Ni(II) complex ($3d^8$; 2 unpaired electrons; 2.83 B.M.), indicating a significant spin-orbit coupling and/or ferromagnetic interaction [35].

Its **TGA** trace (**Figure 4.64**) shows an initial weight loss of 8.1% in the temperature range of 139 - 361 °C is assigned to the evaporation of three H_2O molecules (expected, 8.1%). The next weight loss of 60.1% in the temperature range of 310 - 900 °C is assigned to the decomposition of two coordinated H_2O molecules and two $CH_3(CH_2)_{14}COO^-$ ligands (expected, 82.9%). The amount of residue at temperatures above 900 °C cannot be ascertained due to incomplete decomposition. Hence, $[Ni(CH_3(CH_2)_{14}COO)_2(H_2O)_2].3H_2O$ (T_{dec} = 310 °C) was significantly more thermally stable than $[Cu_2(CH_3(CH_2)_{14}COO)_4]$ (T_{dec} = 273 °C).

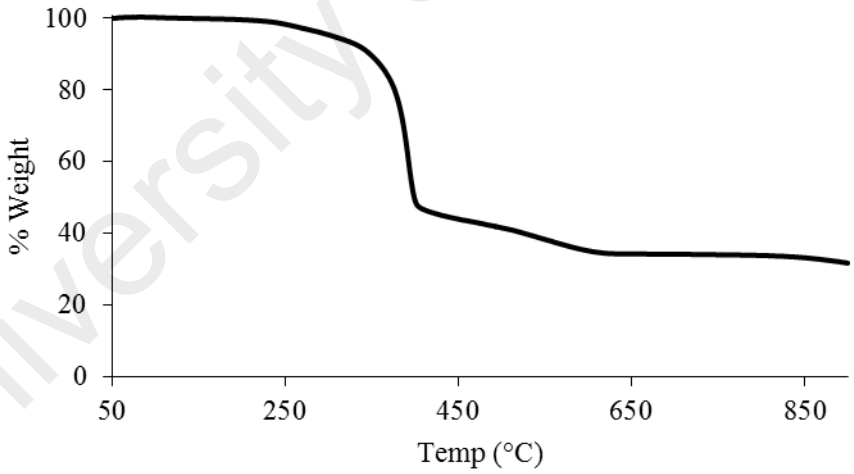

Figure 4.64 TGA of $[Ni(CH_3(CH_2)_{14}COO)_2(H_2O)_2].3H_2O$

Its **DSC** scan (**Figure 4.65**) was recorded as before from 25 °C to 250 °C. On heating, there were an endothermic peak at 93.1 °C (ΔH = +61.6 kJ mol^{-1}), assigned to the breaking of Ni-OH_2 bond, and two overlapping peaks at 132.3 °C ($\Delta H_{combined}$ = +49.4 mol^{-1}), assigned to the breaking of Ni-$OOC(CH_2)_{14}CH_3$ bond. On cooling, there was an exothermic peak at 78.3 °C (ΔH = -27.9 kJ mol^{-1}), assigned to the

formation H-bond of H_2O. The **POM** for $[Ni(CH_3(CH_2)_{14}COO)_2(H_2O)_2].3H_2O$ was recorded for two heating-cooling cycles in the temperature range 25 – 250 ^oC. However, there was no optical texture during observation.

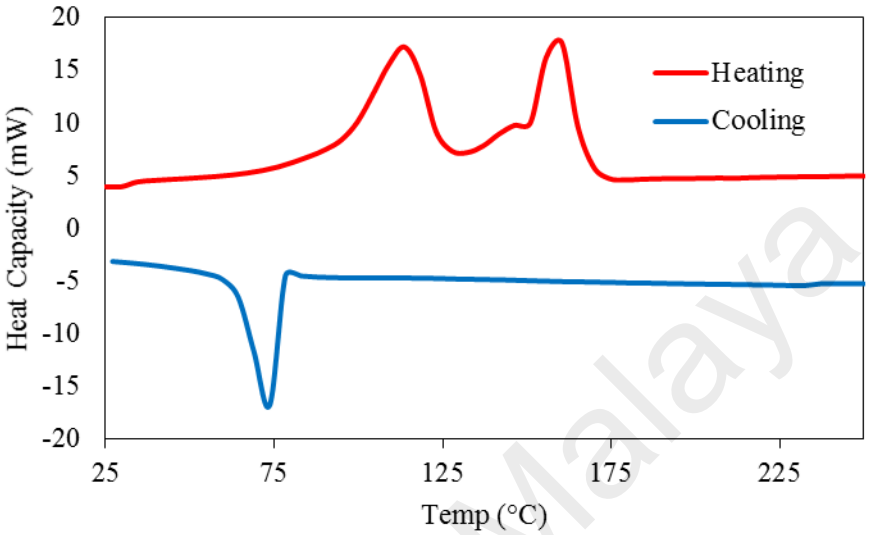

Figure 4.65 DSC for $[Ni(CH_3(CH_2)_{14}COO)_2(H_2O)_2].3H_2O$

$[Ni(CH_3(CH_2)_{14}COO)_2(H_2O)_2].3H_2O$ reacted with *H_2L1* (mole ratio 1:1) to give a greenish powder (**Complex 6**), and the yield was 92.8%. Its solubility was similar to the previously discussed complexes.

The **elemental analytical** data (60.8% C; 7.7% H; 9.8% N) were in excellent agreement with those calculated for chemical formula $Ni_2C_{51}H_{79}N_7O_6$ (61.0% C; 7.9% H; 9.7% N; formula weight, 1003.6 g mol^{-1}). Combining these with the spectroscopic data discussed below, the proposed structural formula for **Complex 6** is ($[Ni_2(CH_3COO)_2(H_2O)_2(L1)]$) (**Figure 4.66**).

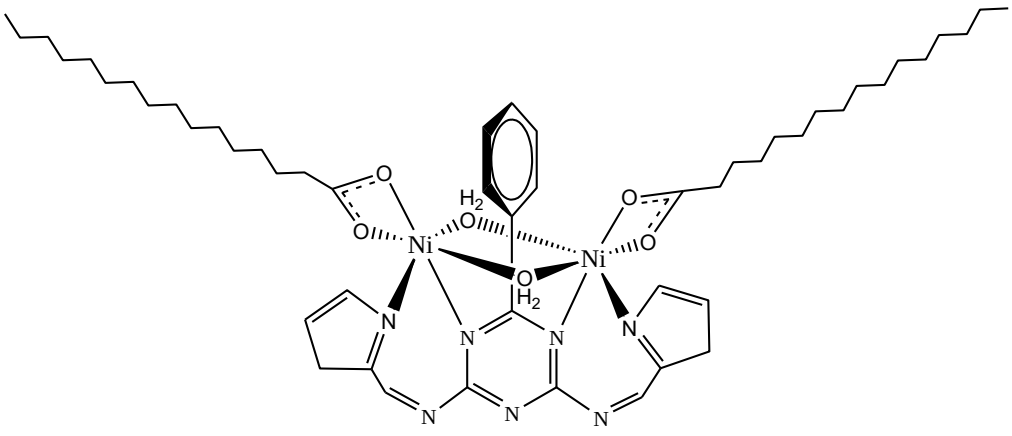

Figure 4.66 Proposed structure of **Complex 6**

Its **FTIR** spectrum (**Table 4.2**; **Figure 4.67**) shows the presence of the expected functional groups. The ΔCOO value (138 cm^{-1}) suggests a chelating $CH_3(CH_2)_{14}COO^-$ ligand.

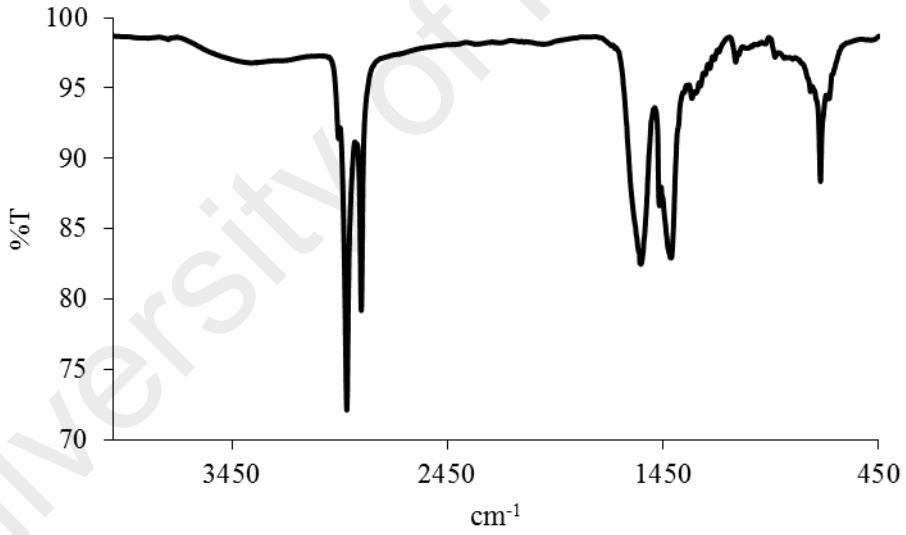

Figure 4.67 FTIR spectrum of **Complex 6**

Its **UV-vis** spectrum in DMSO (**Figure 4.68**) shows a broad band at 802 nm (ε_{max}, 53.3 $M^{-1}\,cm^{-1}$) assigned to $^3A_{2g}$ (F) → $^3T_{2g}$ (F) transition, and a shoulder at 422 nm (ε_{max}, 203.3 $M^{-1}cm^{-1}$) assigned to $^3A_{2g}$ (F) → $^3T_{1g}$ (F) transition. These bands suggest an octahedral geometry at Ni(II) atoms. An intense MLCT band is observed at 268 nm (ε_{max}, 20362 $M^{-1}\,cm^{-1}$).

Its E_o, calculated from λ_{edge} = 318 nm, was 3.8 eV. The value is the same as for **Complex 5** ($[Cu_2(CH_3(CH_2)_{14}COO)_2(L1)]$; 3.8 eV), suggesting that the optical bandgap does not depend on the differences in the metal centre.

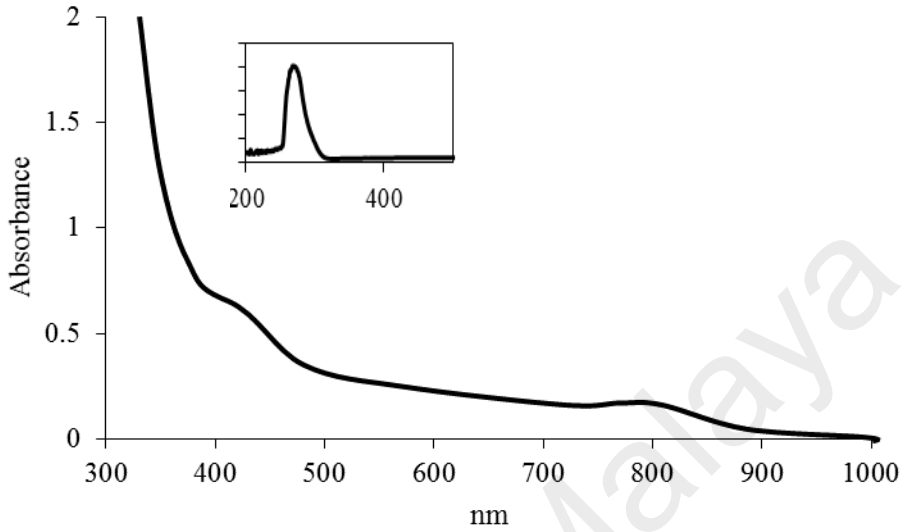

Figure 4.68 UV-vis spectrum of **Complex 6**

Upon excitation at 268 nm (MLCT transition), its **fluorescence** spectrum shows two overlapping peaks at λ_{max} 410 nm and 550 nm (**Figure 4.69**). These suggest two different paths for the excited complex to return to the ground state. Its E_o value, calculated from λ_{edge} = 617 nm, was 2.0 eV. This value is similar to **Complex 5** ($[Cu_2(CH_3COO)_2(L1)]$, 2.1 eV). Additionally, its Stokes shift was 142 nm.

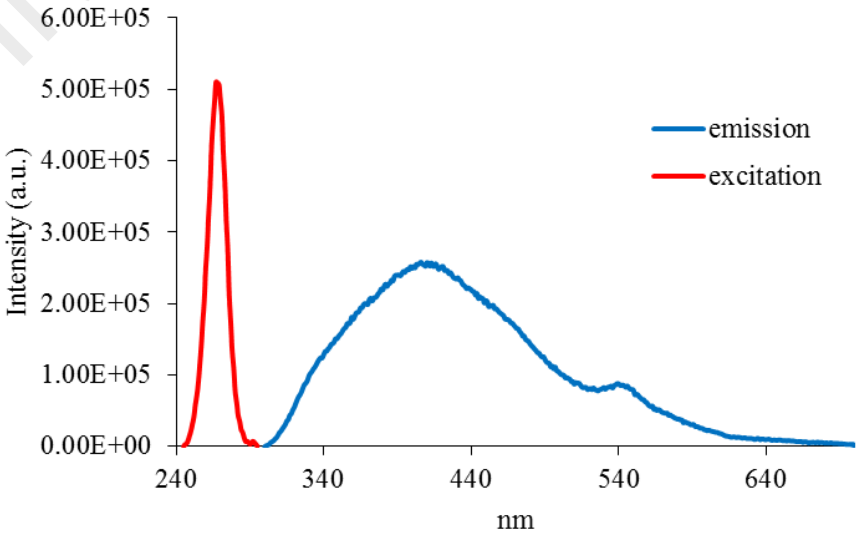

Figure 4.69 Fluorescence spectrum of **Complex 6** (λ_{ex} = 268 nm)

Its τ value, calculated as before from its **decay** curve (**Figure 4.70**), was 3.1 ns. Hence, the excited state lifetime of the complex is similar to that from **Complex 5** (3.0 ns).

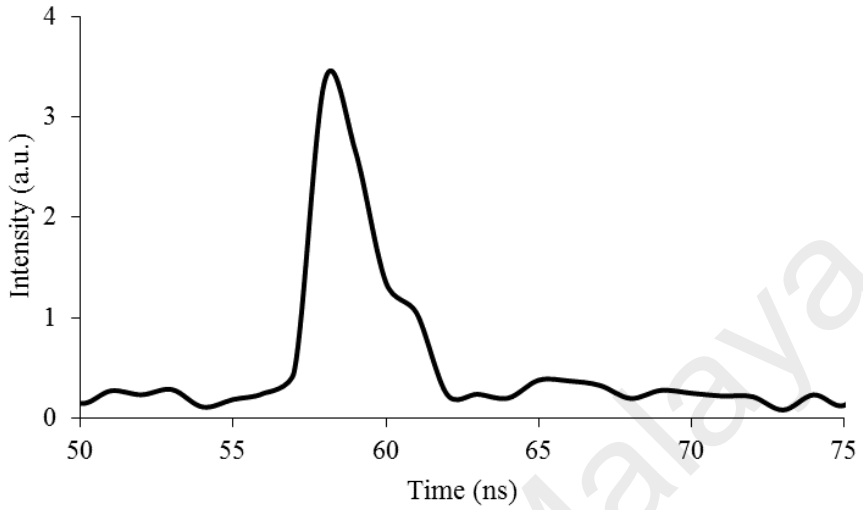

Figure 4.70 Fluorescence decay of **Complex 6**

However, upon excitation at 422 nm (*d-d* transition), its **fluorescence** spectrum shows a peak at λ_{max} 563 nm (**Figure 4.71)**. Its E_o value, calculated from λ_{edge} = 589 nm, was 2.1 eV, and its τ value, calculated from its decay curve, was 3.2 ns. Its Stokes shift was 141 nm.

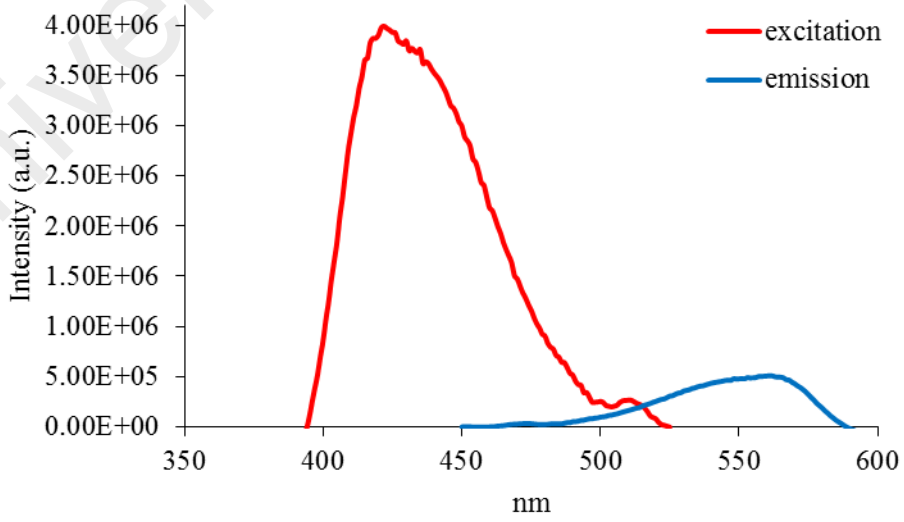

Figure 4.71 Fluorescence spectrum of **Complex 6**

Its **CV** (**Figure 4.72**), recorded anodically from 0 V within the potential window of +1.5 V to -1.5 V, showed two anodic peaks at +0.85 V assigned to the oxidation of [Ni(II)Ni(II)] to [Ni(II)Ni(III)], and at -0.17 V assigned to the oxidation of [Ni(II)Ni(III)] to [Ni(III)Ni(III)]. Since these oxidation processes were irreversible, its E_e cannot be calculated.

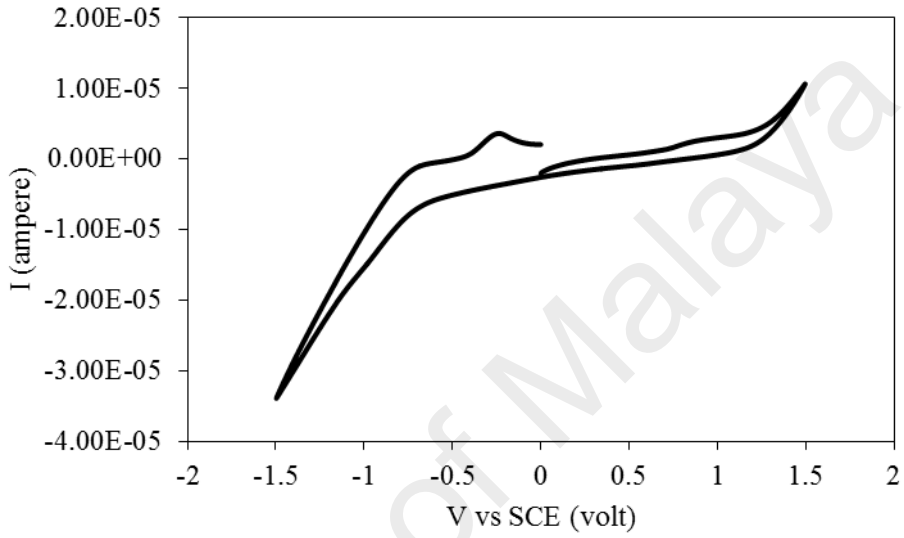

Figure 4.72 CV of **Complex 6**

Its μ_{eff} value, calculated as before from the values of FM = 1003.6 g mol^{-1}, χ_g = 1.01 x 10^{-5} cm^3 g^{-1}, χ_M = 1.02 x 10^{-2} cm^3 mol^{-1}, and χ_{dia} = -5.89 x 10^{-4} cm^3 mol^{-1}, was 5.08 B.M. at 298 K. The value is higher than the expected μ_{eff} value for dinuclear Ni(II) complex (4.0 B.M.). This indicates a strong ferromagnetic interaction in the complex, which is similar to $[Ni(CH_3(CH_2)_{14}COO)_2(H_2O)_2].3H_2O$.

Its **TGA** trace (**Figure 4.73**) shows an initial weight loss of 3.6% in the temperature range of 189 – 245 °C, assigned to the evaporation of two coordinated H_2O molecules (expected, 3.6%). The next weight loss of 51.3% in the temperature range of 245 – 406 °C was assigned to the decomposition of two $CH_3(CH_2)_{14}COO^-$ ligands (expected, 50.9%). The third weight loss of 35.0% from 406 - 900 °C was assigned to the decomposition of *L1* ligand (expected, 33.8%). The amount of residue cannot be

calculated due to incomplete combustion of the organic ligands. Hence, the complex (T_{dec} = 245 °C) is as thermally stable as **Complex 5** (T_{dec} = 239 °C).

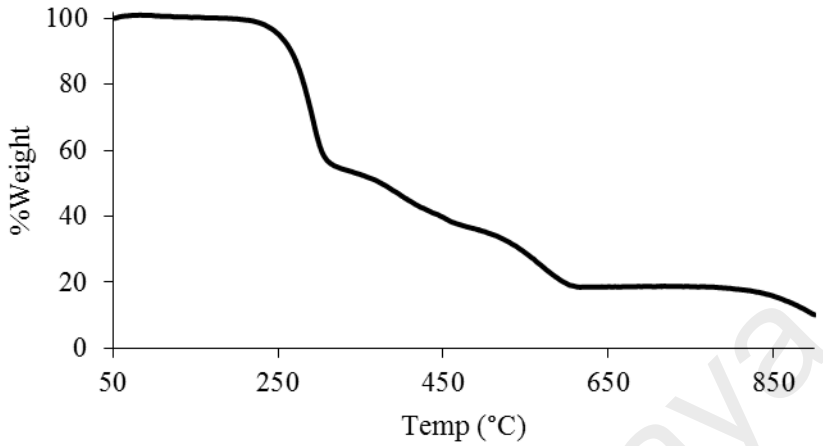

Figure 4.73 TGA of **Complex 6**

Its **DSC** scan (**Figure 4.74**) was done for one cycle of heating-cooling in the temperature range 25 - 235 °C. On heating, there were two overlapping endothermic peaks at 55.4 °C ($\Delta H_{combined}$ = +10.1 kJ mol^{-1}) assigned to Cr_1-to-Cr_2 transition, and at 190 °C ($\Delta H_{combined}$ = +60.2 kJ mol^{-1}) assigned to Cr_2-to-M transition and M-to-I transition. On cooling, there was a weak exothermic peak at 205 °C (ΔH = -3.6 kJ mol^{-1}) assigned to I-to-M transition, a stronger exothermic peak at 190 °C (ΔH = -51.2 kJ mol^{-1}) assigned to M-to-Cr_2 transition, and a weak exothermic peak at 109 °C (ΔH = -8.1 kJ mol^{-1}) assigned to Cr_2-to-Cr_1 transition.

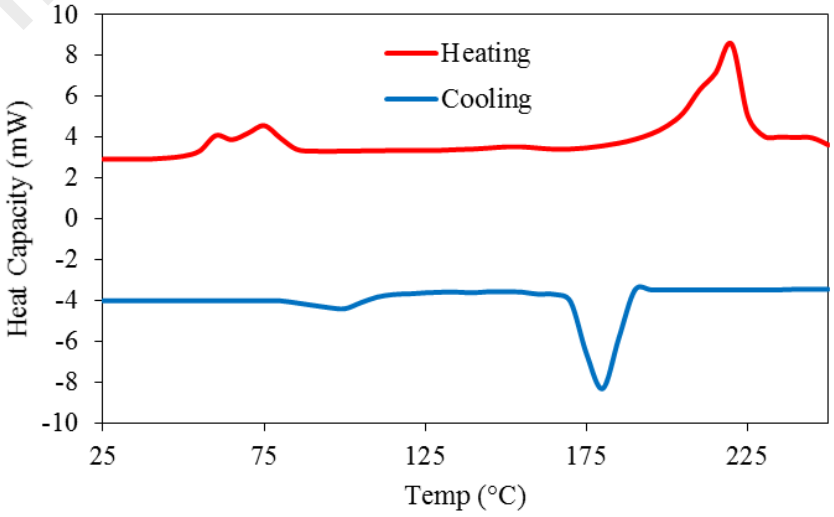

Figure 4.74 DSC of **Complex 6**

Its **POM** photomicrographs were recorded for two heating-cooling cycles in the temperature range 25 – 235 ^{o}C. On cooling from 235 ^{o}C, an optical texture was first observed at about 210 ^{o}C, which solidified at 165 ^{o}C (**Figure 4.75**).

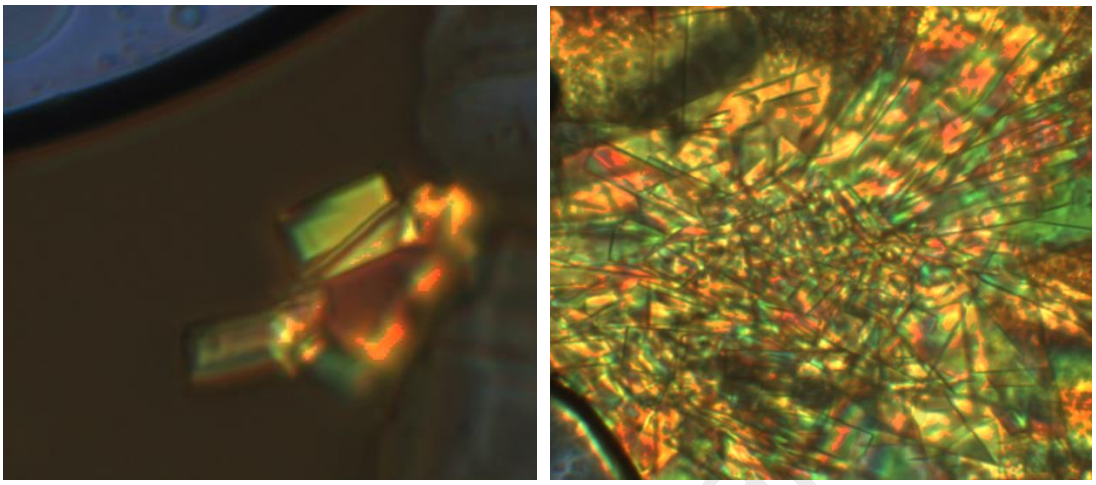

(a) **(b)**

Figure 4.75 Photomicrographs of **Complex 6** on cooling from 235 ^{o}C: (a) at 210 ^{o}C, and (b) at 165 ^{o}C (solid).

4.2.8 Reaction of cobalt(II) hexadecanoate with H_2L1

Cobalt(II) hexadecanoate ($[Co(CH_3(CH_2)_{14}COO)_2(H_2O)_2]$) was obtained as a purple powder from the reaction of sodium hexadecanoate with cobalt(II) chloride hexahydrate. The **elemental analytical** results (63.6% C; 10.7% H) are in excellent agreement with those calculated for $CoC_{32}H_{66}O_6$ (63.4% C; 10.9% H; formula weight, 605.8 g mol^{-1}). Combining these with the spectroscopic data discussed above, its proposed structural formula is similar to $[Ni(CH_3(CH_2)_{14}COO)_2(H_2O)_2].3H_2O$ (**Figure 4.57**).

Its **FTIR** spectrum (**Table 4.3**; **Figure 4.76**) shows the presence of the expected functional groups. The ΔCOO value (111 cm^{-1}) suggests a chelating $CH_3(CH_2)_{14}COO^-$ ligand.

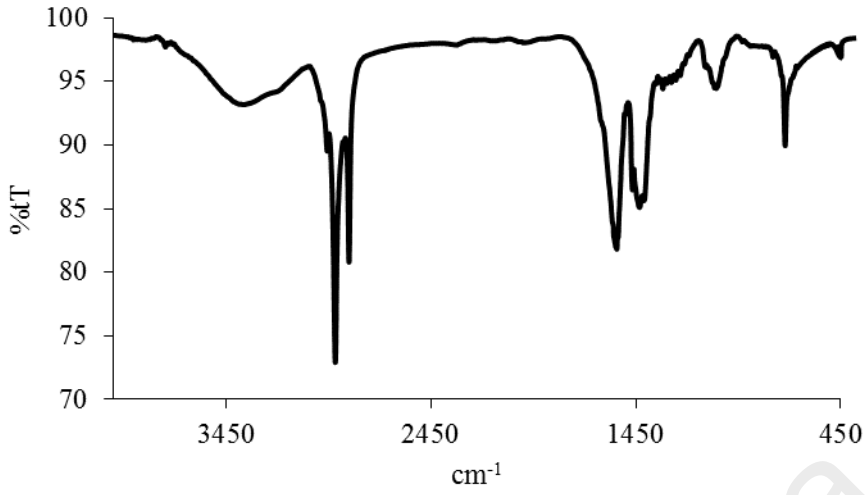

Figure 4.76 FTIR spectrum of $[Co(CH_3(CH_2)_{14}COO)_2(H_2O)_2]$

Its **UV-vis** spectrum in DMSO (**Figure 4.77**) shows three overlapping *d-d* bands at 563 nm (ε_{max}, 184 M^{-1} cm^{-1}) assigned to $^4T_{1g}$ (F) → $^4T_{2g}$ (F), 520 nm (ε_{max}, 156 M^{-1} cm^{-1}) assigned to $^4T_{1g}$ (F) → $^4T_{1g}$ (P), and 470 nm (ε_{max}, 128 M^{-1} cm^{-1}) assigned to $^4T_{1g}$ (F) → $^4A_{2g}$ (F) transitions. These bands suggest an octahedral geometry at the Co(II) centre. Also seen is an intense MLCT band at 252 nm (ε_{max}, 9159 M^{-1} cm^{-1}).

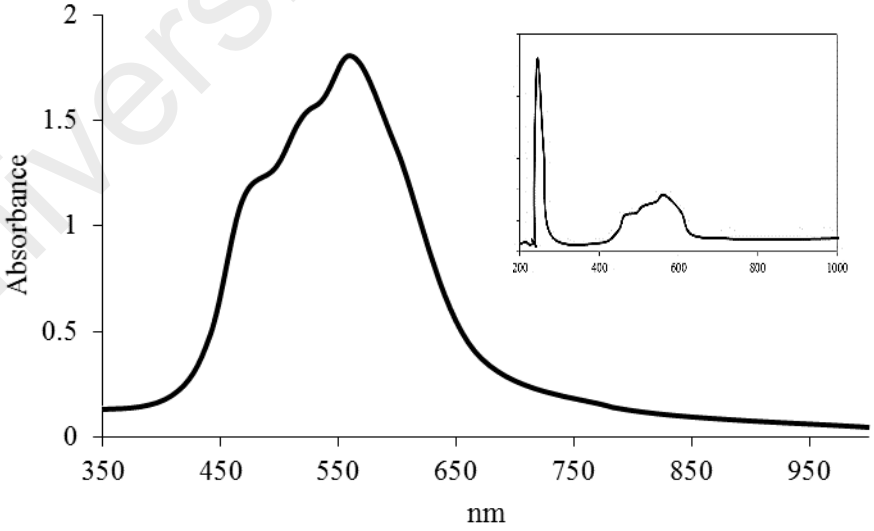

Figure 4.77 UV-vis spectrum of $[Co(CH_3(CH_2)_{14}COO)_2(H_2O)_2]$

Its E_o**,** calculated λ_{edge} = 262 nm was 4.7 eV. The value is just slightly higher than $[Ni(CH_3(CH_2)_{14}COO)_2(H_2O)_2].3H_2O$ (4.4 eV) and $[Cu_2(CH_3(CH_2)_{14}COO)_4]$ (4.4 eV).

Upon excitation at 252 nm (MLCT transition), its **fluorescence** spectrum shows a peak at λ_{max} 274 nm (**Figure 4.78)**. Its E_o**,** calculated from λ_{edge} = 280 nm, was 4.4 eV. Its τ value, calculated from its decay curve (**Figure 4.79**), was 5.2 ns. This is similar to $[Cu_2(CH_3(CH_2)_{14}COO)_4]$ (5.4 ns). Its Stokes shift was 22 nm.

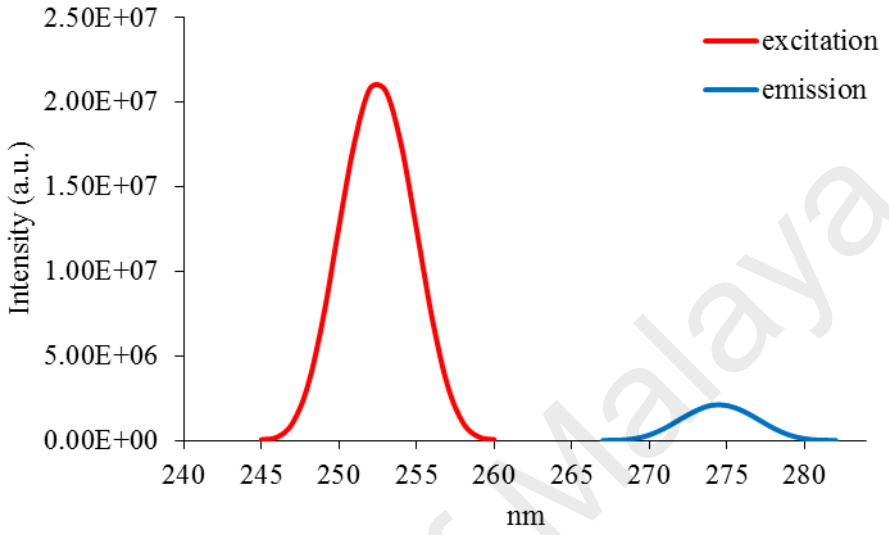

Figure 4.78 Fluorescence spectrum of $[Co(CH_3(CH_2)_{14}COO)_2(H_2O)_2]$ (λ_{ex} = 252 nm)

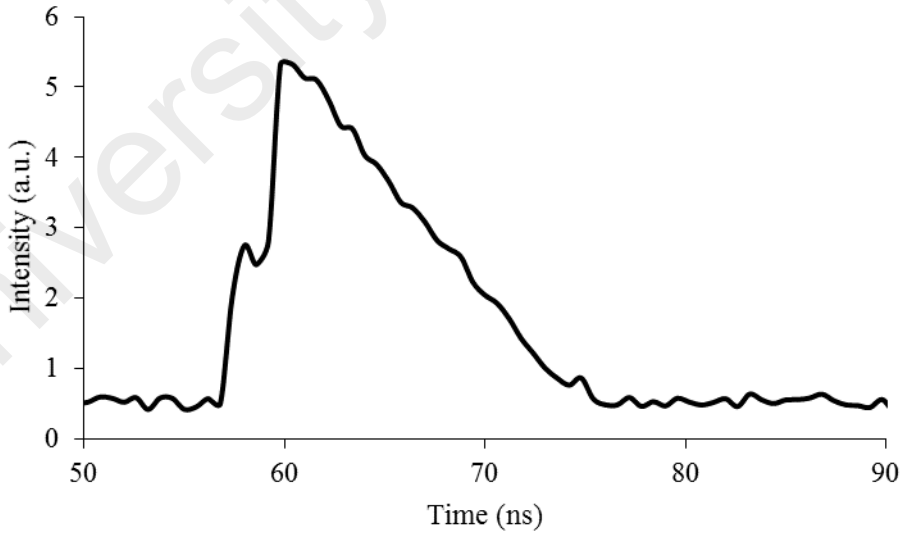

Figure 4.79 Fluorescence decay of $[Co(CH_3(CH_2)_{14}COO)_2(H_2O)_2]$

However, upon excitation at 470 nm (*d-d* transition), its **fluorescence** spectrum shows a peak at λ_{max} 484 nm (**Figure 4.80)**. Its E_o**,** calculated from λ_{edge} = 489 nm, was

2.5 eV. Its τ value, calculated as before from its **decay** curve, was 3.5 ns. Its Stokes shift was 14 nm.

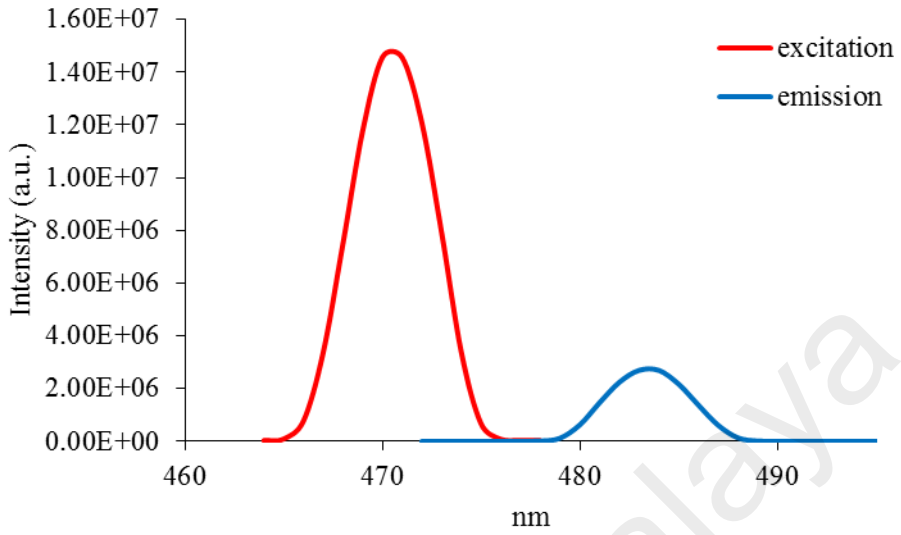

Figure 4.80 Fluorescence spectrum of $[Co(CH_3(CH_2)_{14}COO)_2(H_2O)_2]$ (λ_{ex} = 470 nm)

Its **CV** (**Figure 4.81**), recorded anodically from 0 V within the potential window +1.5 V to +1.5 V, showed an anodic peak at +0.87 V for the irreversible oxidation of Co(II) to Co(III). Hence, its E_e value cannot be calculated.

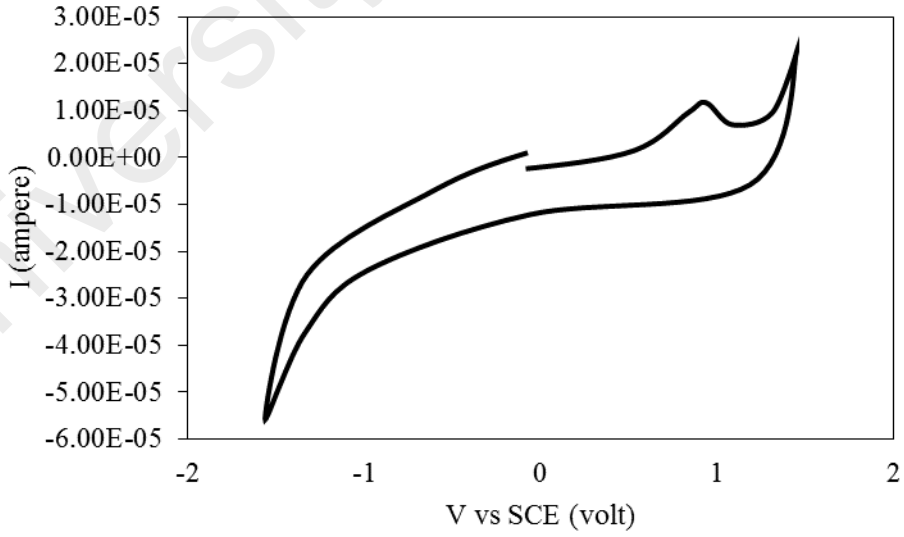

Figure 4.81 CV for $[Co(CH_3(CH_2)_{14}COO)_2(H_2O)_2]$

Its $\boldsymbol{\mu_{eff}}$ value, calculated from the values of FM = 605.8 g mol^{-1}, χ_g = 1.08 x 10^{-6} cm^3 g^{-1}, χ_M = 6.54 x 10^{-3} cm^3 mol^{-1}, and χ_{dia} = -4.26 x 10^{-4} cm^3 mol^{-1}, was 4.09 B.M. at 298 K. This is slightly higher than the spin-only value for high-spin

Co(II) complexes (d^7; three unpaired electrons; 3.87 BM), but in agreement with the values reported in the literatures [36].

Its **TGA** scan (**Figure 4.82**) shows the total weight loss of 82.9% in the temperature range of 272 - 580 °C assigned to the evaporation of two H_2O molecules and the decomposition of two $CH_3(CH_2)_{14}COO^-$ ligands (expected, 80.2%). The amount of residue at temperatures above 580 °C was 17.1% (expected, 19.8% assuming pure CoO). Hence, the complex (T_{dec} = 272 °C) was as thermally stable as $[Cu_2(CH_3(CH_2)_{14}COO)_4]$

(T_{dec} = 273 °C).

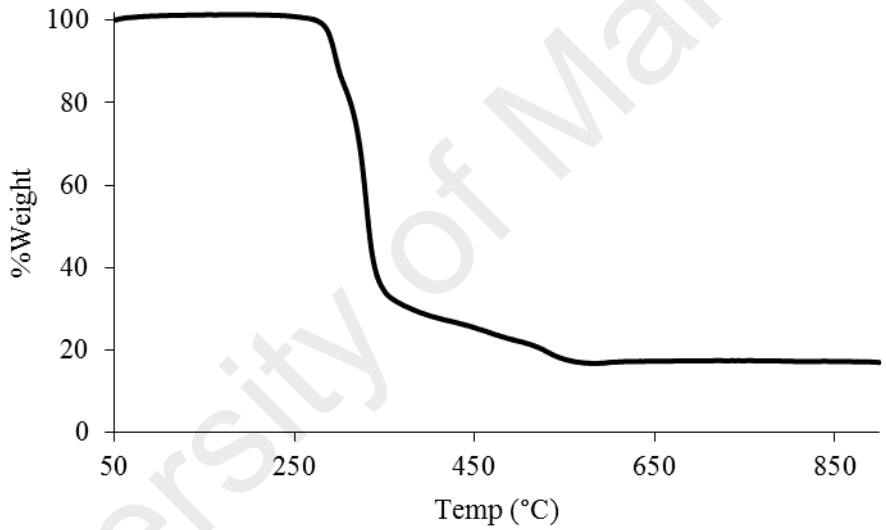

Figure 4.82 TGA of $[Co(CH_3(CH_2)_{14}COO)_2(H_2O)_2]$

Its **DSC** (**Figure 4.83**) was measured for one heating-and-cooling cycle in the temperature range of 25 - 150 °C. On heating, there were two overlapping endothermic peaks at 93.2 °C ($\Delta H_{combined}$ = +93.7 kJ mol^{-1}) assigned to the breaking of Co-OH_2 bond, and Co-$OOC(CH_2)_{14}CH_3$ bond. On cooling, there was a weak exothermic peak at 72.9 °C (ΔH = -9.4 kJ mol^{-1}) assigned to formation of H-bond of H_2O. Similar to $[Ni(CH_3(CH_2)_{14}COO)_2(H_2O)_2].H_2O$, this compound did not show any optical texture under the **POM.**

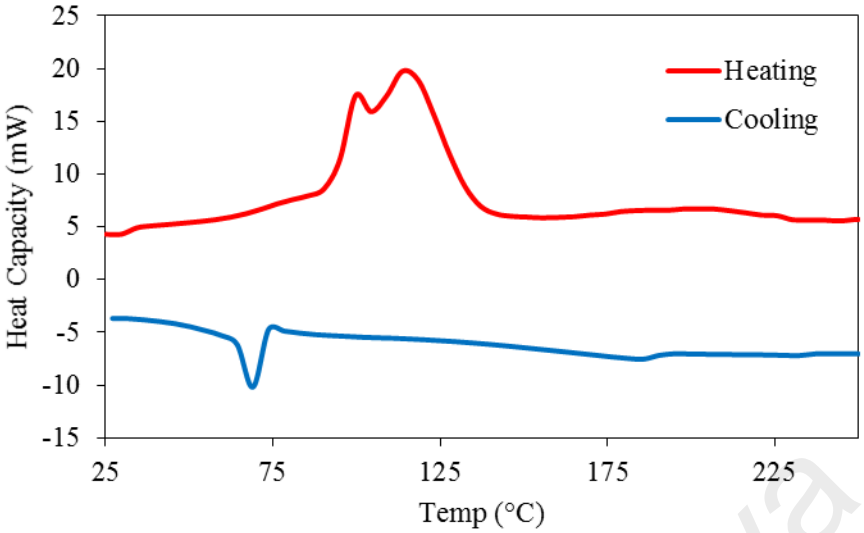

Figure 4.83 DSC for $[Co(CH_3(CH_2)_{14}COO)_2(H_2O)_2]$

Similar to previously discussed complexes, $[Co(CH_3(CH_2)_{14}COO)_2(H_2O)_2]$ reacted with *H_2L1* (mole ratio 1:1) to give a blue powder (**Complex 7**), and the yield was 75%. Its solubility was similar to the previously discussed complexes.

The results of the **elemental** analyses (61.3% C; 7.7% H; 9.8% N) are in excellent agreement with those calculated for $[Co_2(CH_3(CH_2)_{14}COO)_2(H_2O)_2(L1)]$ (chemical formula $Co_2C_{51}H_{79}N_7O_6$, 61.0% C; 7.9% H; 9.8% N; formula weight, 1004.1 g mol^{-1}). Combining these with the spectroscopic data discussed below, its proposed structural formula for **Complex 7** is similar as for the corresponding Ni(II) complexes (**Figure 4.84**).

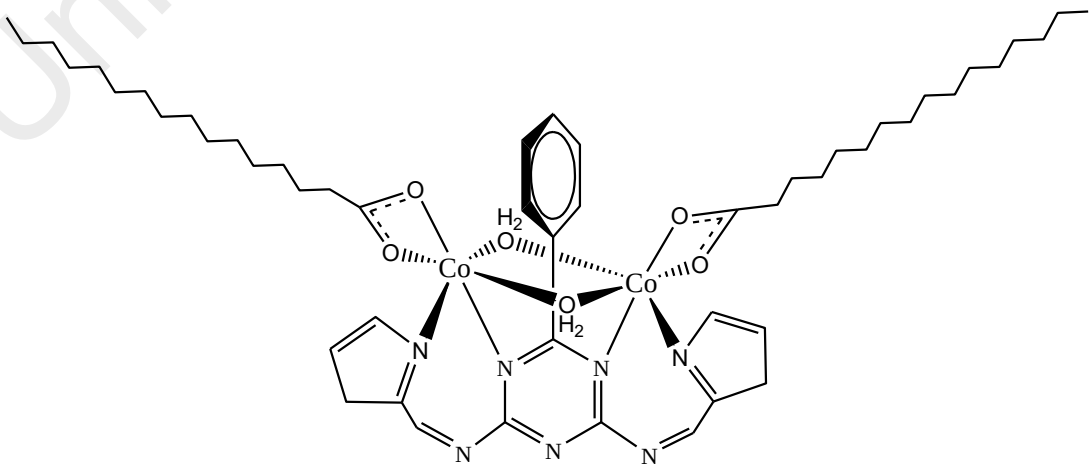

Figure 4.84 Proposed structure of **Complex 7**

Its **FTIR** spectrum (**Table 4.2**; **Figure 4.85**) shows the presence of the expected functional groups. The ΔCOO value (130 cm^{-1}) suggests a chelating $CH_3(CH_2)_{14}COO^-$ ligand.

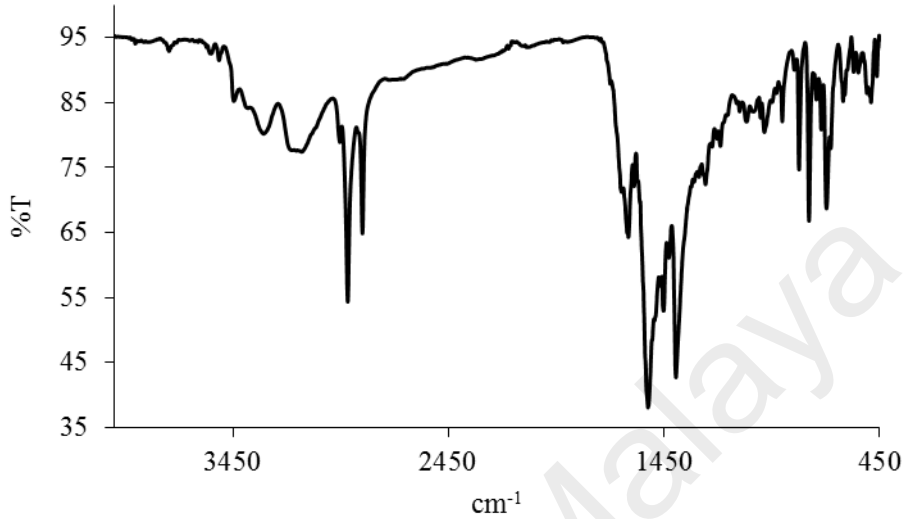

Figure 4.85 FTIR spectrum of **Complex 7**

Its **UV-vis** spectrum in DMSO (**Figure 4.86**) shows three *d-d* bands at 832 nm (ε_{max}, 104 M^{-1} cm^{-1}), assigned to $^4T_{1g}$ (F) → $^4T_{2g}$ (F), 685 nm (ε_{max}, 226 M^{-1} cm^{-1}), assigned to $^4T_{1g}$ (F) → $^4T_{1g}$ (P), and 433 nm (ε_{max}, 373 M^{-1} cm^{-1}), assigned to $^4T_{1g}$ (F) → $^4A_{2g}$ (F) transitions. These suggest an octahedral high-spin Co(II) complex. Also observed is an intense MLCT band at 270 nm (ε_{max}, 2363 M^{-1} cm^{-1}).

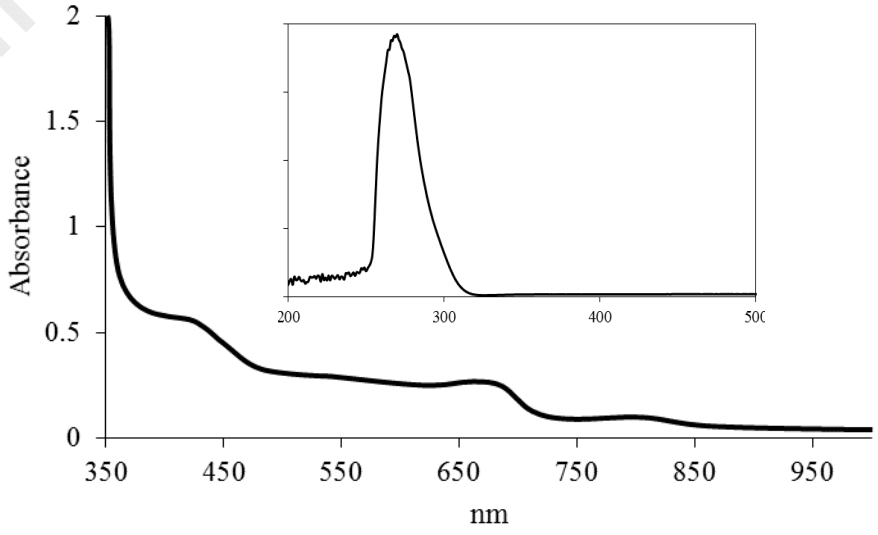

Figure 4.86 UV-vis spectrum of **Complex 7**

Its E_o value, calculated from λ_{edge} = 320 nm, was 3.9 eV. This is similar to **Complexes 5** ($[Cu_2(CH_3(CH_2)_{14}COO)_2(L1)]$, 3.8 eV) and **6** ($[Ni_2(CH_3(CH_2)_{14}COO)_2(H_2O)_2(L1)]$, 3.8 eV).

Upon excitation at 270 nm (MLCT transition), its **fluorescence** spectrum shows two overlapping peaks at λ_{max} 410 nm and 550 nm (**Figure 4.87)**. These are also similar to **Complexes 5** and **6**, and may be similarly explained. Its E_o value, calculated from λ_{edge} = 628 nm, was 1.9 eV, which is quite similar to **Complexes 5** (2.0 eV) and **6** (2.1 eV). Its τ, calculated as before from its **decay** curve (**Figure 4.88**), was 3.0 ns, which is similar to **Complex 6** (3.0 ns). Its Stokes shift was 140 nm.

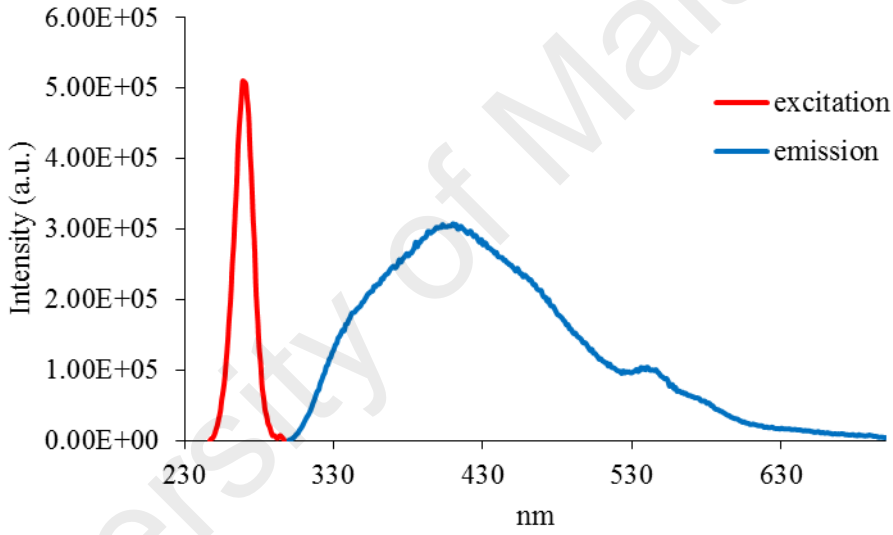

Figure 4.87 Fluorescence spectrum of **Complex 7** (λ_{ex} = 270 nm)

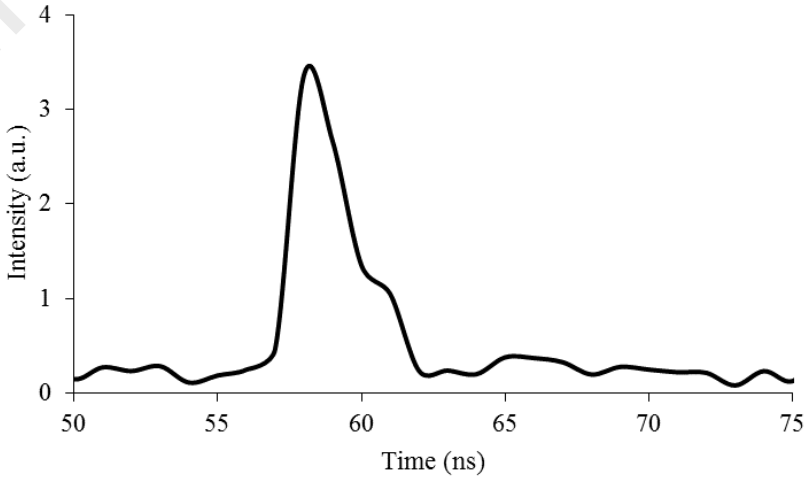

Figure 4.88 Fluorescence decay of **Complex 7**

However, upon excitation at 433 nm (*d-d* transition), its **fluorescence** spectrum shows a peak at λ_{max} 482 nm (**Figure 4.89)**. Its E_o value, calculated from λ_{edge} = 580 nm, was 2.1 eV. Its τ value, calculated from its **decay** curve, was 3.1 ns. Additionally its Stokes shift was 49 nm.

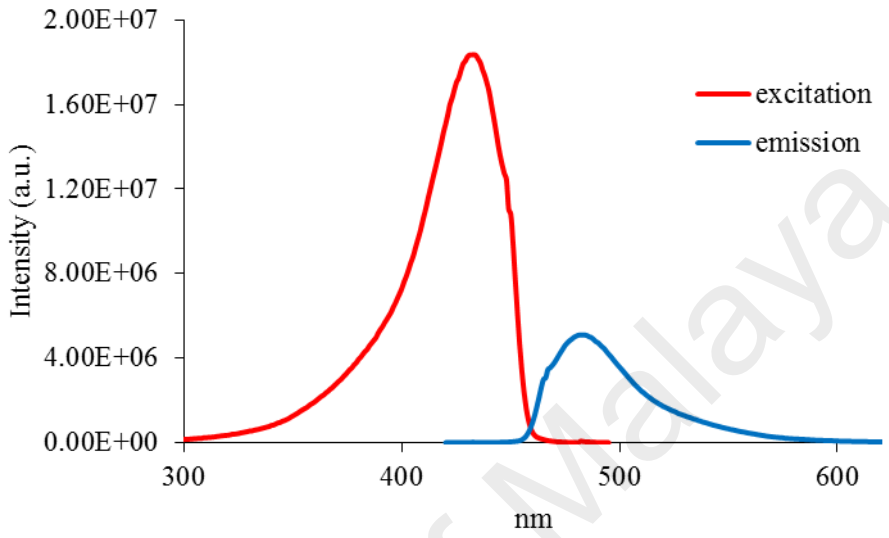

Figure 4.89 Fluorescence spectrum of **Complex 7** (λ_{max} = 433 nm)

Its **CV** (**Figure 4.90**), recorded anodically from 0 V within the potential window of +1.5 V to -1.5 V. It showed no distinctive anodic peak, when the potential was increased from 0 V to +1.5 V. Additionally, there was no distinctive cathodic peak, when the potential was decreased from +1.5 V to -1.5 V, However, an anodic peak observed at -0.29 V is assigned to an irreversible oxidation of Co(II) to Co(III) process. Thus, E_e value cannot be calculated.

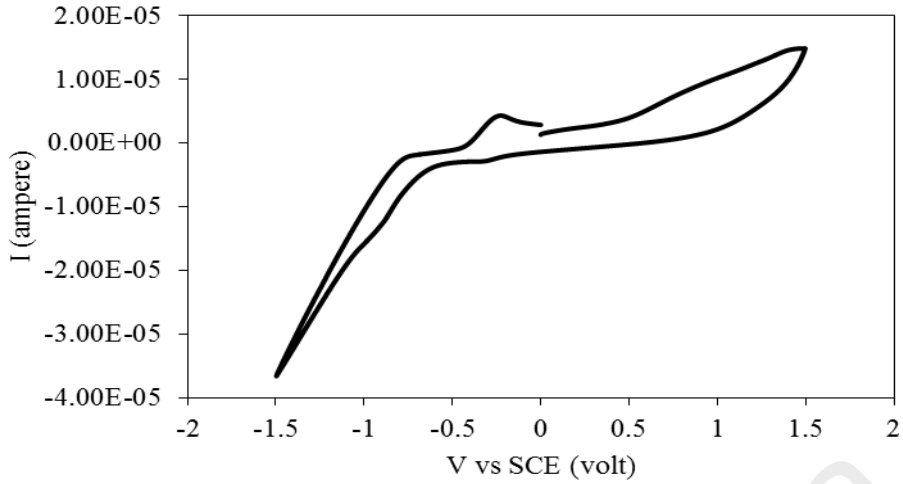

Figure 4.90 CV of **Complex 7**

Its μ_{eff} value, calculated as before from the values of FM = 1004.1 g mol^{-1}, χ_g = 9.9 x 10^{-6} cm^3 g^{-1}, χ_M = 9.9 x 10^{-4} cm^3 mol^{-1}, and χ_{dia} = -5.89 x 10^{-4} cm^3 mol^{-1}, was 5.02 B.M. at 298 K. This is in agreement with the expected value for a high-spin dinuclear Co(II) complex (d^7) (5.48 BM) [37].

Its **TGA** trace (**Figure 4.91**) shows an initial weight loss of 1.8% in the temperature range of 185 - 231 °C assigned to the evaporation of two coordinated H_2O molecules (expected 1.8%). The next weight loss of 79.6% is assigned to the decomposition of two $CH_3(CH_2)_{14}COO^-$ and *L1* ligands (expected, 84.7%). The amount of residue at temperatures above 629 ºC was 18.6% (expected, 13.5% assuming pure CoO). Hence, the complex (T_{dec} = 231 °C) was slightly less thermally stable compared to **Complex 6** ($[Ni_2(CH_3(CH_2)_{14}COO)_2(H_2O)(L1)]$; T_{dec} = 245 °C).

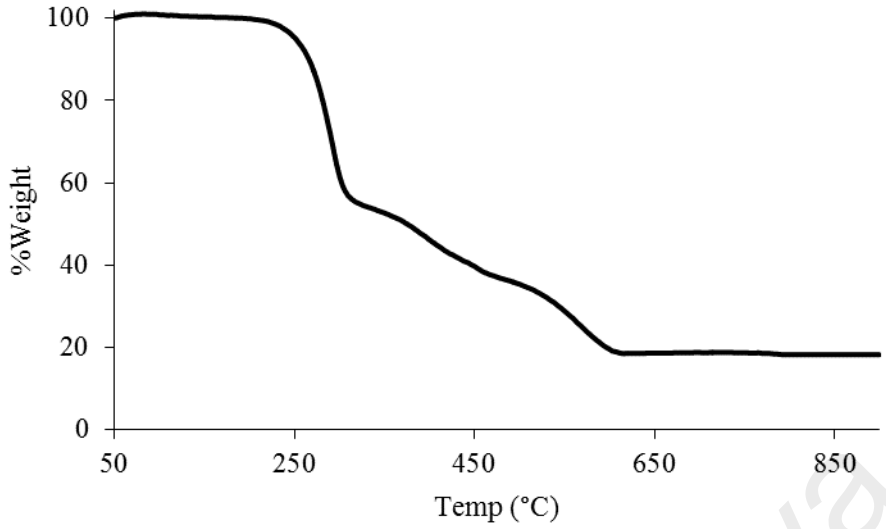

Figure 4.91 TGA of **Complex 7**

Its **DSC** scan (**Figure 4.92**) was done for one heating-cooling cycle in the temperature range 25 - 230 °C. On heating, there were two overlapping endothermic peaks at 55.8 °C ($\Delta H_{combined}$ = +23.4 kJ mol^{-1}) assigned to Cr-to-Cr transition and Cr-to-M transition, and another overlapping endothermic peaks at 200 °C ($\Delta H_{combined}$ = +106.3 kJ mol^{-1}) assigned to the M_1-to-M_2 transition, and M_2-to-I transition. On cooling, there were a small exothermic peak at 195 °C (ΔH = -68.9 kJ mol^{-1}) assigned to I-to-M transition, and a very weak peak at 110 °C (ΔH = -10.4 kJ mol^{-1}) assigned to M-to-Cr transition.

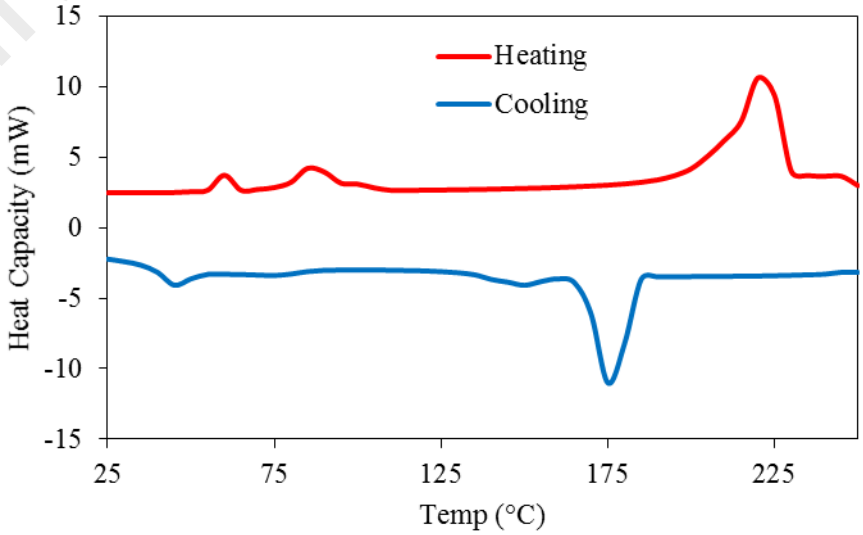

Figure 4.92 DSC of **Complex 7**

Its **POM** photomicrographs were recorded for two heating-cooling cycles in the temperature range 25 – 235 ^{o}C. The complex was observed to melt at about 200 ^{o}C and to clear at 230 ^{o}C. On cooling from 230 ^{o}C, an optical texture was observed at about 197 ^{o}C, which then solidified at 178 ^{o}C (**Figure 4.93**).

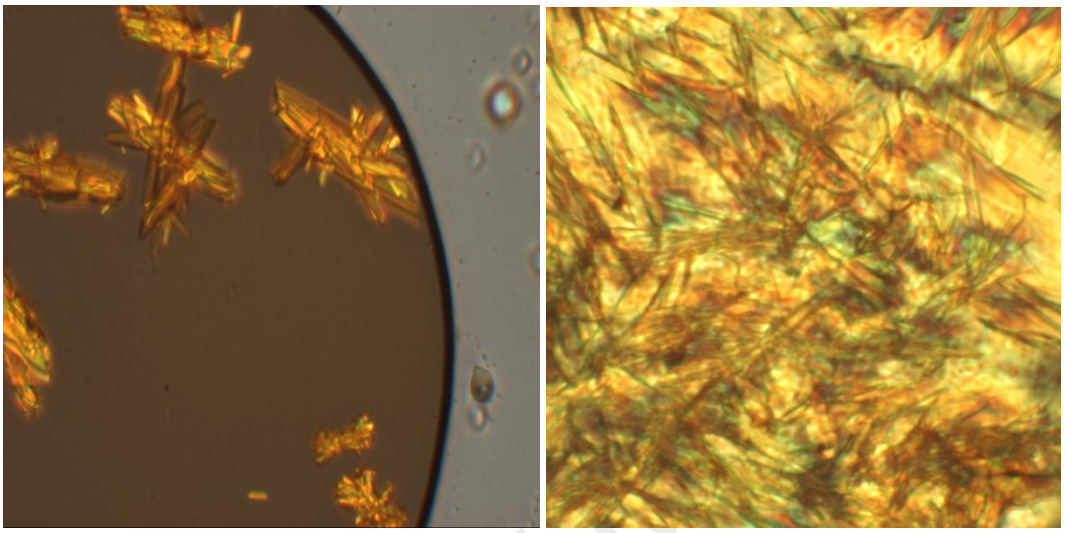

(a) **(b)**

Figure 4.93 Photomicrographs of **Complex 7** on cooling from 230 ^{o}C, at: (a) 197 ^{o}C; and (b) 178 ^{o}C (solid).

4.2.9 Reaction of iron(II) hexadecanoate with H_2L1

Iron(II) hexadecanoate was obtained as a brown powder from the reaction of sodium hexadecanoate with iron(II) chloride tetrahydrate. The **elemental analytical** results (63.1% C; 10.9% H) are in excellent agreement with those calculated for $[Fe(CH_3(CH_2)_{14}COO)_2(H_2O)_2]$ (formula, $FeC_{32}H_{66}O_6$; 63.8% C; 11.0% H; formula weight, 602.71 g mol^{-1}). Combining these with the spectroscopic data discussed below, its proposed structural formula is the same as $[Ni(CH_3(CH_2)_{14}COO)_2(H_2O)_2].3H_2O$ (**Figure 4.57**).

Its **FTIR** spectrum (**Table 4.3**; **Figure 4.94**) shows the presence of the expected functional groups. The ΔCOO value (134 cm^{-1}) suggests a chelating $CH_3(CH_2)_{14}COO^-$ ligand.

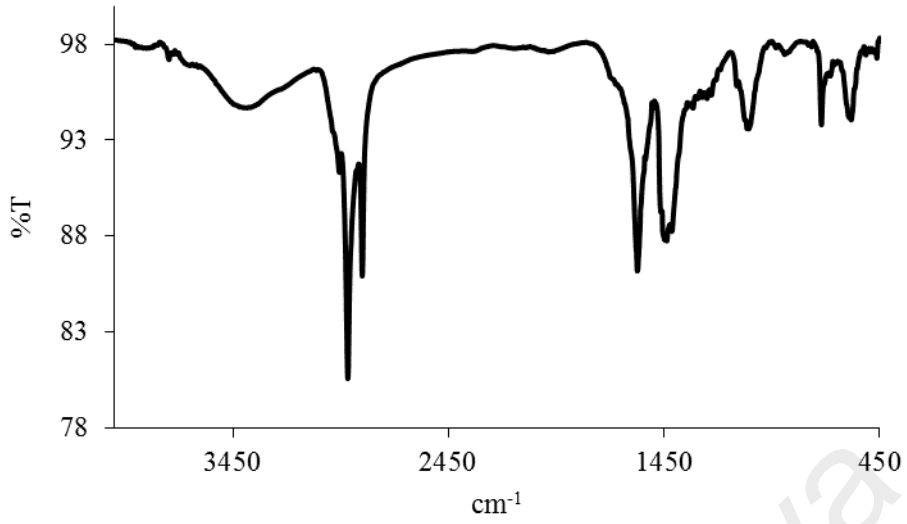

Figure 4.94 FTIR spectrum of $[Fe(CH_3(CH_2)_{14}COO)_2(H_2O)_2]$

Its **UV-vis** spectrum in DMSO (**Figure 4.95**) shows a broad band at 841 nm (ε_{max}, 120 M^{-1} cm^{-1}) assigned to ${}^5T_{2g} \rightarrow {}^5E_g$. This suggests an octahedral high-spin Fe(II) complex [38]. Also seen is an intense MLCT band at 253 nm (ε_{max}, 1824 M^{-1} cm^{-1}).

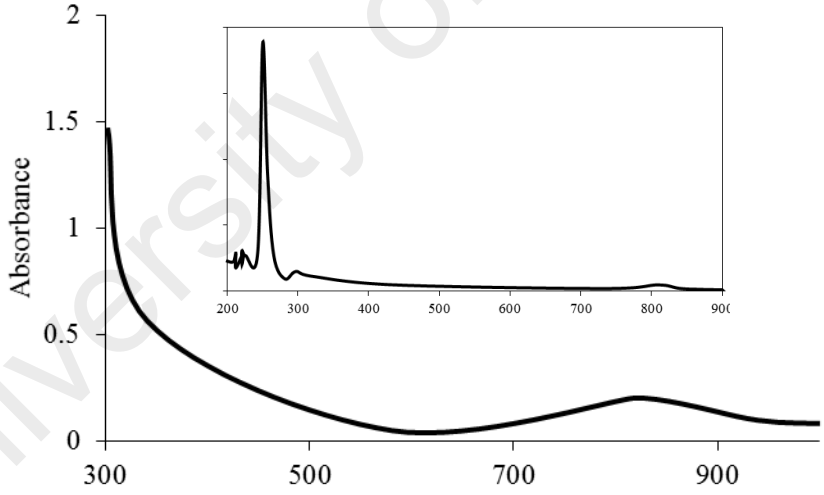

Figure 4.95 UV-vis spectrum of $[Fe(CH_3(CH_2)_{14}COO)_2(H_2O)_2]$

Its E_o value**,** calculated from λ_{edge} = 283 nm, was 4.3 eV. This is similar to $[Cu(CH_3(CH_2)_{14}COO)_4]$ (4.4 eV) and $[Ni(CH_3(CH_2)_{14}COO)_2(H_2O)_2].3H_2O$ (4.4 eV).

Upon excitation at 253 nm (MLCT transition), its **fluorescence** spectrum shows a peak at λ_{max} 263 nm (**Figure 4.96**). Its E_o value, calculated from λ_{edge} = 269 nm, was 4.6 eV. Its τ value, calculated from its decay curve (**Figure 4.97**), was 5.4 ns. The value

is the same as found for $[Cu(CH_3(CH_2)_{14}COO)_4]$, $[Ni(CH_3(CH_2)_{14}COO)_2(H_2O)_2].3H_2O$, and $[Co(CH_3(CH_2)_{14}COO)_2(H_2O)_2]$ (5.4 ns). Its Stokes shift was 10 nm.

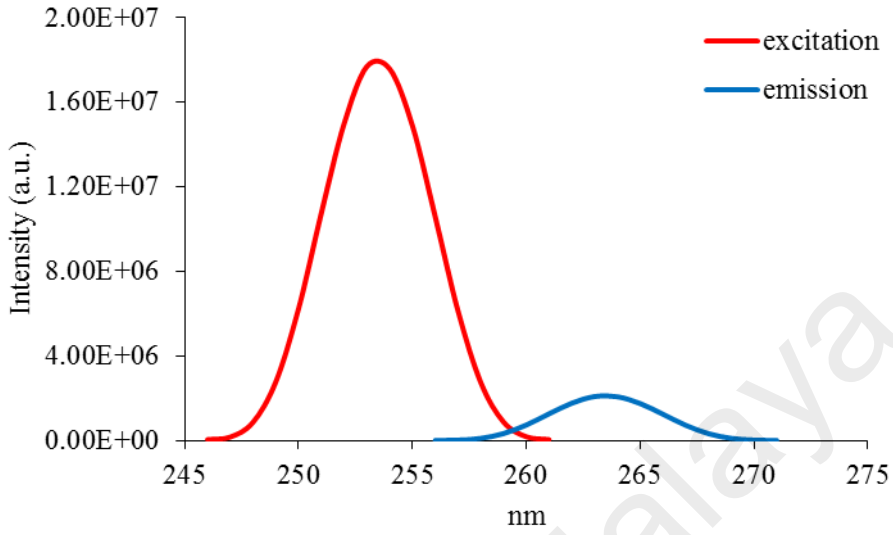

Figure 4.96 Fluorescence spectrum of $[Fe(CH_3(CH_2)_{14}COO)_2(H_2O)_2]$ (λ_{ex} = 253 nm)

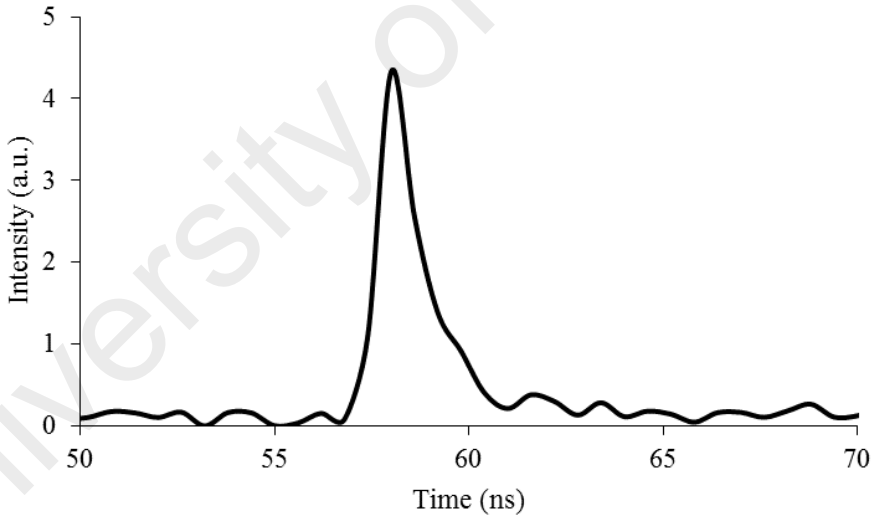

Figure 4.97 Fluorescence decay of $[Fe(CH_3(CH_2)_{14}COO)_2(H_2O)_2]$

However, upon excitation at 841 nm (*d-d* transition), its **fluorescence** spectrum shows a peak at λ_{max} 872 nm (**Figure 4.98)**. Its E_o value, calculated from λ_{edge} = 880 nm, was 1.4 eV, while its τ value, calculated from its **decay** curve, was 0.99 ns. And, its Stokes shift was 31 nm.

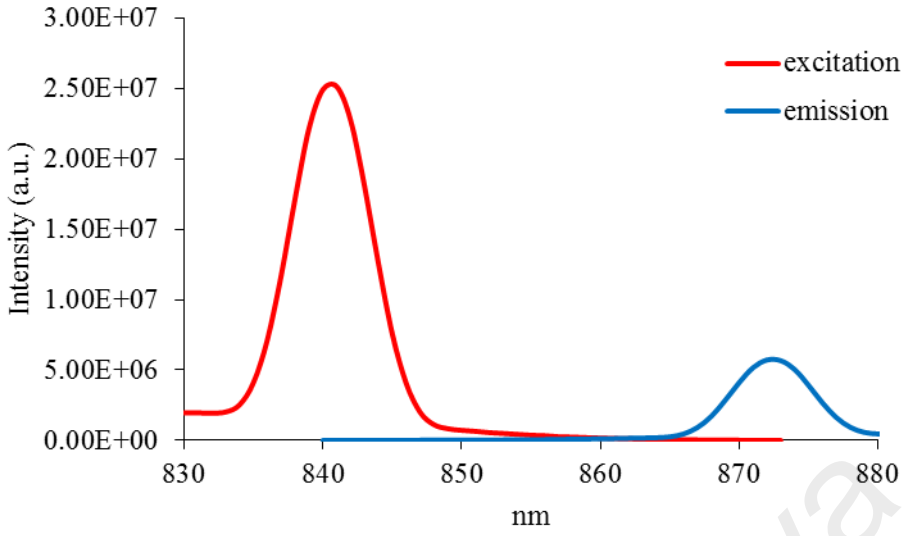

Figure 4.98 Fluorescence spectrum of $[Fe(CH_3(CH_2)_{14}COO)_2(H_2O)_2]$ (λ_{ex} = 841 nm)

Its **CV** (**Figure 4.99**), recorded anodically from 0 V within the potential window -1.5 V to +1.5 V, showed only an anodic peak at +0.77 V. This suggests an irreversible oxidation of Fe(II) to Fe(III). Hence, its E_e value cannot be calculated.

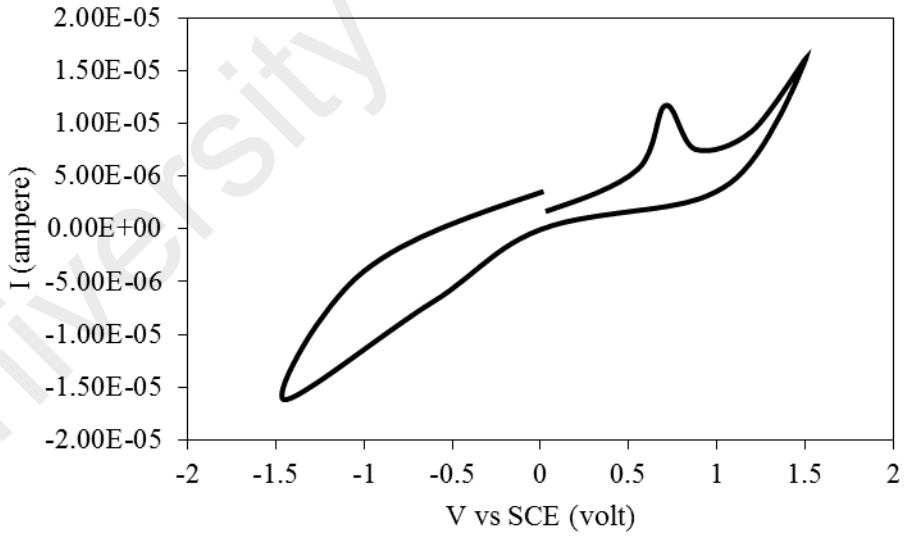

Figure 4.99 CV for $[Fe(CH_3(CH_2)_{14}COO)_2(H_2O)_2]$

Its $\boldsymbol{\mu_{eff}}$ value, calculated as before from the values of FM = 602.71 g mol^{-1}, χ_g = 1.70 x 10^{-5} cm^3 g^{-1}, χ_M = 1.03 x 10^{-2} cm^3 mol^{-1}, and χ_{dia} = -4.26 x 10^{-4} cm^3 mol^{-1}, was 5.06 B.M. at 298 K. This is slightly higher than the expected spin-only value for a

high-spin Fe(II) complex (d^6; four unpaired electrons; 4.89 BM), suggesting a ferromagnetic interaction [39].

Its **TGA** scan (**Figure 4.100**) shows an initial weight loss of 5.9% in the temperature range of 113 - 264 ^oC, assigned to the evaporation of two H_2O molecules (expected 5.9%). The next weight loss of 80.2% in the temperature range of 264 - 550 °C is assigned to the decomposition of two $CH_3(CH_2)_{14}COO^-$ ligands (expected, 84.8%). The amount of residue at temperatures above 550 ^oC was 13.9% (expected 9.3%, assuming pure FeO). Hence, the complex was the least thermally stable (T_{dec} = 264 ^oC) compared to $[Cu(CH_3(CH_2)_{14}COO)_4]$ (T_{dec} = 273 ^oC), $[Ni(CH_3(CH_2)_{14}COO)_2(H_2O)_2].3H_2O$ (T_{dec} = 314 ^oC), and $[Co(CH_3(CH_2)_{14}COO)_2(H_2O)_2]$ (T_{dec} = 274 ^oC).

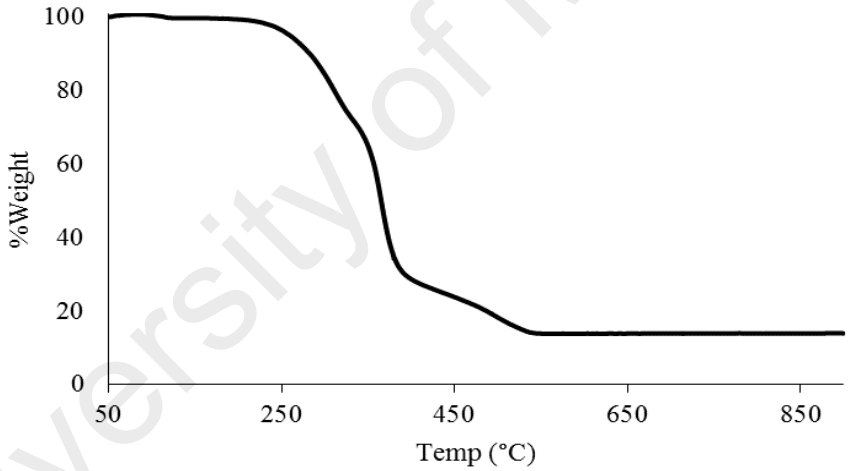

Figure 4.100 TGA of $[Fe(CH_3(CH_2)_{14}COO)_2(H_2O)_2]$

Its **DSC** (**Figure 4.101**) was recorded by heating the sample from 25 ^oC to 180 ^oC, and then cooling it back to 25 ^oC. On heating, there were two endothermic peaks at 81 ^oC (ΔH = +52.1 kJ mol^{-1}) assigned to the breaking of Fe-OH_2 bond, and at 151 ^oC (ΔH = +19.7 kJ mol^{-1}) assigned to the breaking of Fe-$OOC(CH_2)_{14}CH_3$ bond. On cooling, there was an exothermic peak at 64 ^oC (ΔH = -12.5 kJ mol^{-1}) the formation of H-bond of H_2O. This compound has no optical texture under the **POM**, which is similar to $[Ni(CH_3(CH_2)_{14}COO)_2(H_2O)_2].3H_2O$ and $[Co(CH_3(CH_2)_{14}COO)_2(H_2O)_2]$.

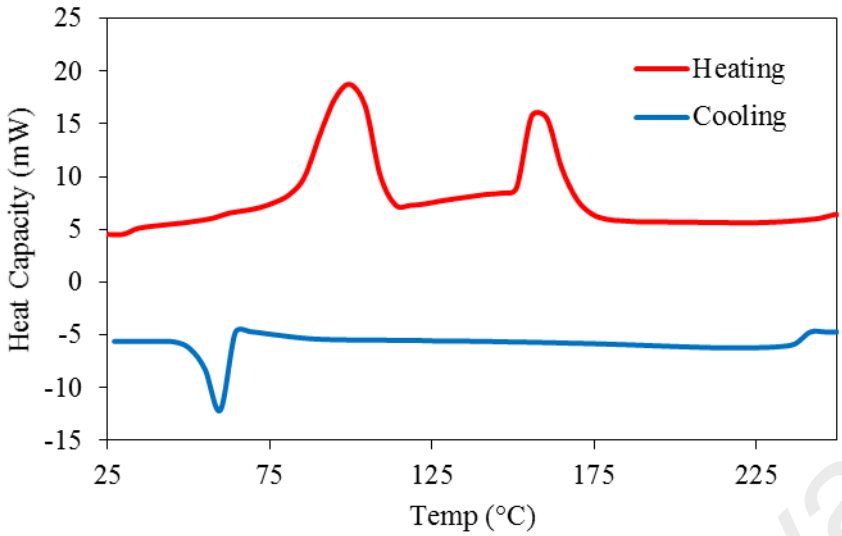

Figure 4.101 DSC for $[Fe(CH_3(CH_2)_{14}COO)_2(H_2O)_2]$

$[Fe(CH_3(CH_2)_{14}COO)_2(H_2O)_2]$ reacted with *H_2L1* (mole ratio 1:1) to give a pale yellow powder (**Complex 8**), and the yield was 87.5%. Its solubility was similar to the previously discussed complexes. The **elemental analytical data** for the complex (61.4% C; 7.9% H; 9.1% N) are in excellent agreement with those calculated for $[Fe_2(CH_3(CH_2)_{14}COO)_2(H_2O)_2(L1)]$ (chemical formula $Fe_2C_{51}H_{79}N_7O_6$; 61.3% C; 7.6% H; 9.81% N; formula weight, 999.92 g mol^{-1}). Combining these with the spectroscopic data discussed below, its proposed structural formula is (**Figure 4.102**).

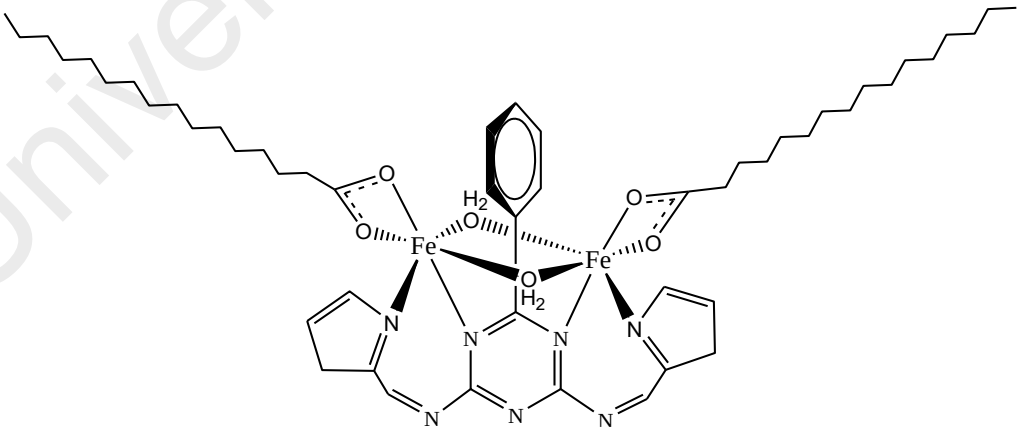

Figure 4.102 Proposed structure of **Complex 8**

Its **FTIR** spectrum (**Table 4.2**; **Figure 4.103**) shows the presence of the expected functional groups. The ΔCOO value (137 cm^{-1}) suggests a chelating $CH_3(CH_2)_{14}COO^-$ ligand.

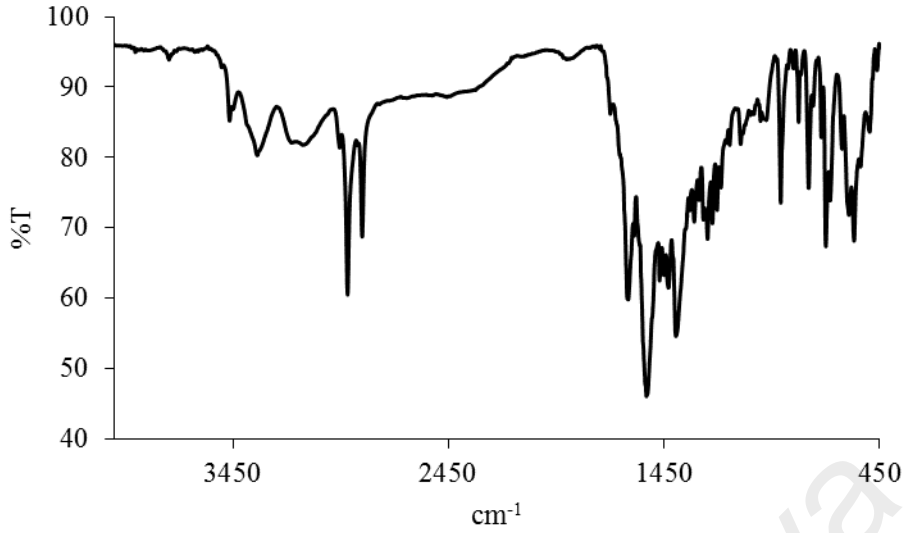

Figure 4.103 FTIR spectrum of **Complex 8**

Its **UV-vis** spectrum in DMSO (**Figure 4.104**) shows a weak *d-d* band at 773 nm (ε_{max}= 489 M^{-1} cm^{-1}) assigned to $^5T_{2g} \rightarrow {}^5E_g$ electronic transition. An intense band observed at 271 (ε_{max}= 3478 M^{-1} cm^{-1}) is assigned to MLCT band.

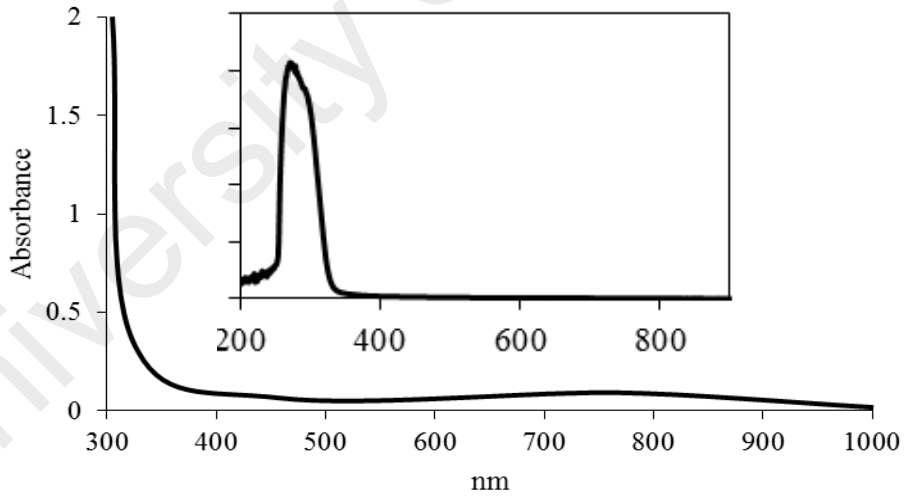

Figure 4.104 UV-vis spectrum of **Complex 8**

Its E_o value, calculated from λ_{edge} = 320 nm, was 3.7 eV. This is quite similar to **Complexes 5** ($[Cu_2(CH_3(CH_2)_{14}COO)_2(L1)]$, 3.8 eV), **6** ($[Ni_2(CH_3(CH_2)_{14}COO)_2(H_2O)(L1)]$, 3.8 eV) and **7** ($[Co_2(CH_3(CH_2)_{14}COO)_2(L1)]$, 3.9 eV).

Upon excitation at 271 nm (MLCT transition), its **fluorescence** spectrum shows four overlapping peaks at λ_{max} 360 nm, 409 nm, 464 nm and 573 nm (**Figure 4.105)**. These suggest four different paths for excited complex to return to ground state. Its E_o value, calculated from λ_{edge} = 656 nm, was 1.8 eV, and its τ, calculated from its **decay** curve (**Figure 4.106**), was 2.9 ns. This is similar to **Complexes 5** (3.0 ns), **6** (3.1 ns) and **7** (3.0 ns). Additionally, the Stokes shift value was 193 nm.

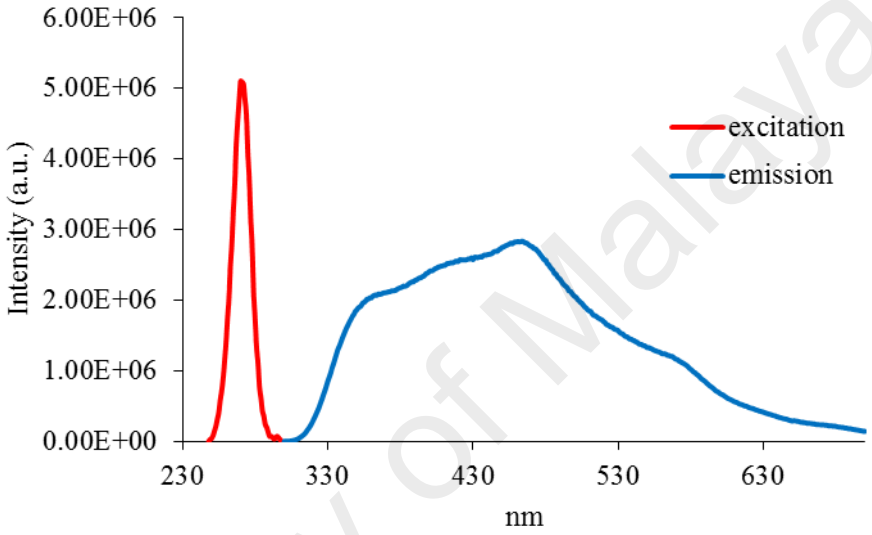

Figure 4.105 Fluorescence spectrum of **Complex 8** (λ_{ex} = 271 nm)

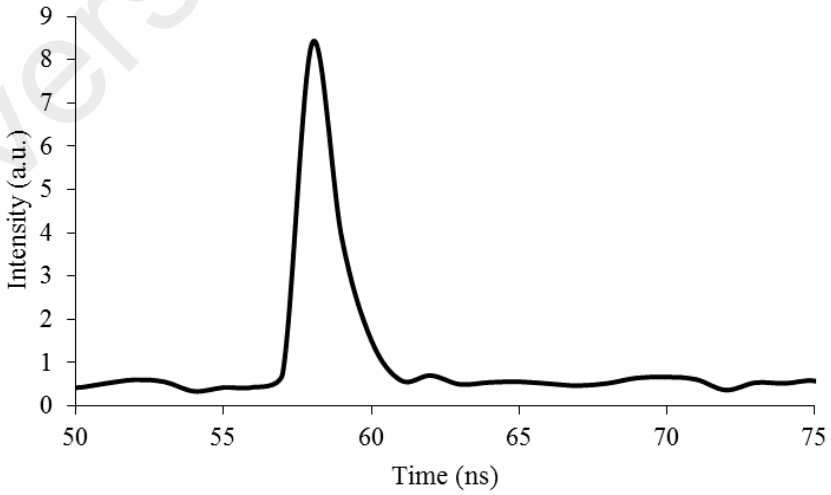

Figure 4.106 Fluorescence decay of **Complex 8**

However, upon excitation at 773 nm (*d-d* transition), its **fluorescence** spectrum shows a peak at λ_{max} 830 nm (**Figure 4.107**). Its E_o, calculated from λ_{edge} = 950 nm, was 1.3 eV. Its τ, calculated from its **decay** curve, was 1.0 ns. Its Stokes shift was 57 nm.

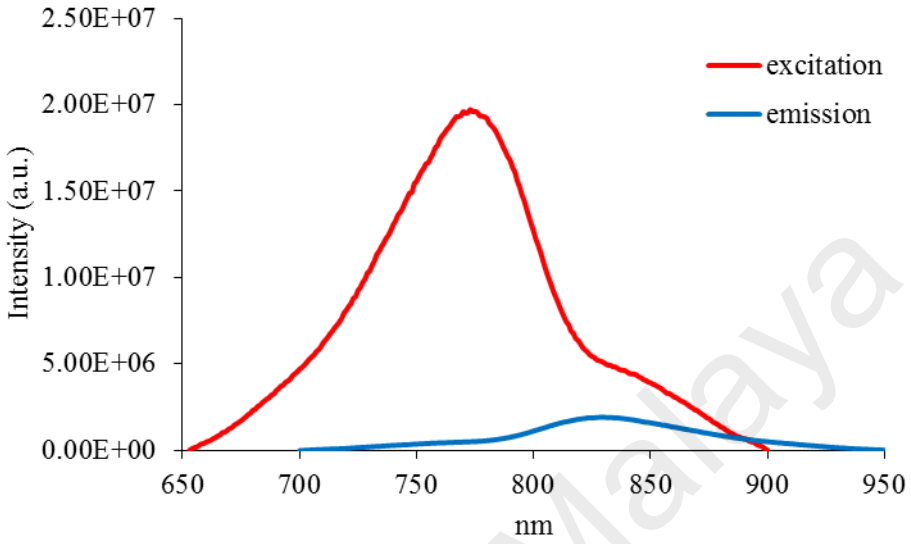

Figure 4.107 Fluorescence spectrum of **Complex 8** (λ_{ex} = 773 nm)

Its **CV** (**Figure 4.108**), recorded anodically from 0 V within the potential window of +1.5 V to -1.5 V, showed one anodic peak at +0.95 V and the corresponding cathodic peak at -0.32 V. These are assigned to oxidation of [Fe(II)Fe(II)] to [Fe(II)Fe(III)] and the reduction of [Fe(II)Fe(III)] to [Fe(II)Fe(II)], respectively. The peak separation (ΔE_p = 1270 mV), which indicates quasireversible process. Also observed is an anodic peak at -0.28 V, assigned to the reoxidation of [Fe(II)Fe(II)] to [Fe(II)Fe(III)], which is irreversible process.

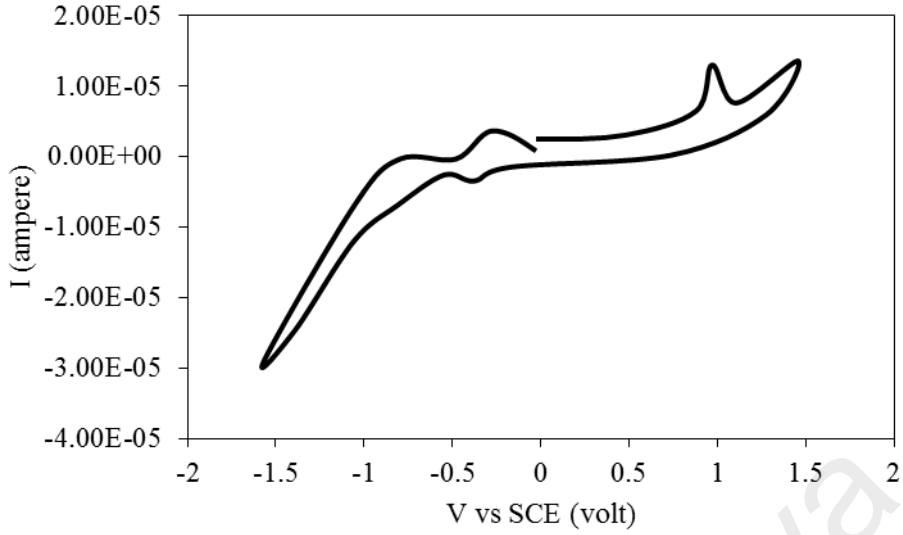

Figure 4.108 CV of **Complex 8**

The HOMO and LUMO values, calculated from the onset oxidation potential (+0.86 V) and onset reduction potential (-0.23 V), were 5.26 eV and 4.17 eV (versus SCE), respectively. Thus, its E_e was 1.09 eV.

Its μ_{eff} value, calculated as before from the values of FM = 999.92 g mol^{-1}, χ_g = 2.01 x 10^{-5} cm^3 g^{-1}, χ_M = 2.01 x 10^{-2} cm^3 mol^{-1}, and χ_{dia} = -5.89 x 10^{-4} cm^3 mol^{-1}, was 7.0 B.M. at 298 K. The value is in good agreement with the expected value for a high-spin dinuclear Fe(II) complex (d^6; 6.9 BM), suggesting a negligible interaction between the two Fe(II) centres [12].

The **TGA** trace (**Figure 4.109**) shows a rapid weight loss of 90.4% on heating from about 205 ^oC to 620 ^oC. This may be due to evaporation of two coordinated H_2O molecules and decomposition of two $CH_3(CH_2)_{14}COO^-$ ligands and *L1* ligand (expected, 88.8%). The amount of residue above this temperature was 9.6% (expected, 11.2% assuming pure Fe). Hence, the complex (T_{dec} = 205 ^oC) was the least thermally stable compared to **Complexes 5** (T_{dec} = 212 ^oC), **6** (T_{dec} = 245 ^oC), and **7** (T_{dec} = 231 ^oC).

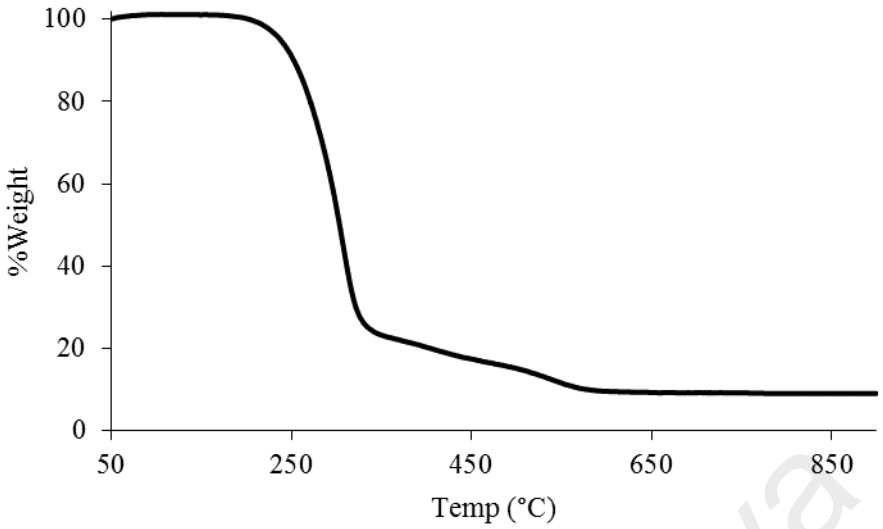

Figure 4.109 TGA of **Complex 8**

Its **DSC** scan was done for heating-cooling cycles, in the temperature range 25 - 225 ºC (**Figure 4.110**). It showed three endothermic peaks on heating at 55.4 °C (ΔH = +11.7 kJ mol^{-1}) assigned to Cr_1-to-Cr_2 transition, at 83.2 °C (ΔH = +64.2 kJ mol^{-1}) assigned to Cr_2-to-M transition, and 176.8 °C (ΔH = +55.6 kJ mol^{-1}) assigned to M-to-I transition. On cooling from 225 ºC, there were three exothermic peaks at 166.4 °C (ΔH = -31.8 kJ mol^{-1}) assigned to I-to-M transition, 57.6 °C (ΔH = -21.9 kJ mol^{-1}) assigned to M-to-Cr_2 transition, and 40.6 °C (ΔH = -28.6 kJ mol^{-1}) assigned to Cr_2-to-Cr_1 transition.

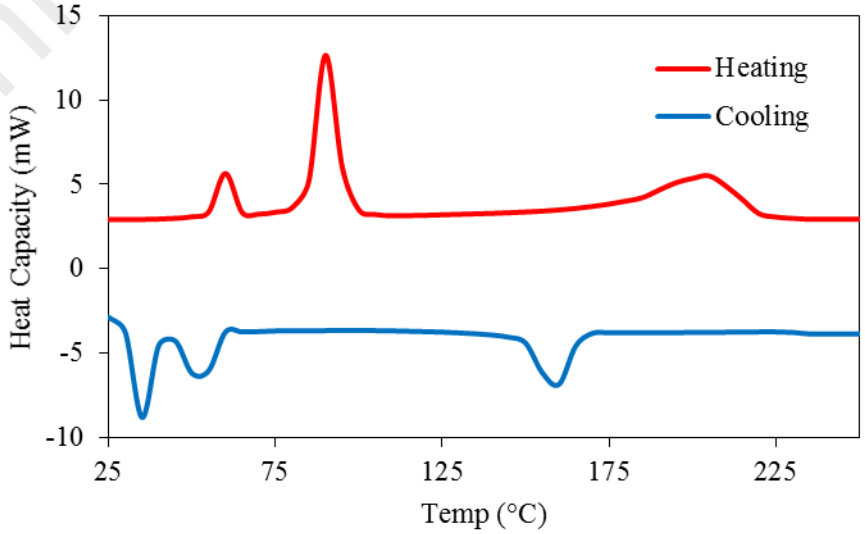

Figure 4.110 DSC of **Complex 8**

Its **POM** photomicrographs were recorded for two heating-cooling cycles in the temperature range 25 – 235 ^{o}C. It was found to darken at about 83 ^{o}C and then melted at about 175 ^{o}C, forming box-like optical textures with strong birefringence. On further heating, the textures changed to an isotropic liquid at 233 ^{o}C, which quickly decomposed. On cooling from 235 ^{o}C, an optical texture was initially observed at about 215 ^{o}C (below its melting temperature), which became solid at 180 ^{o}C (**Figure 4.111**).

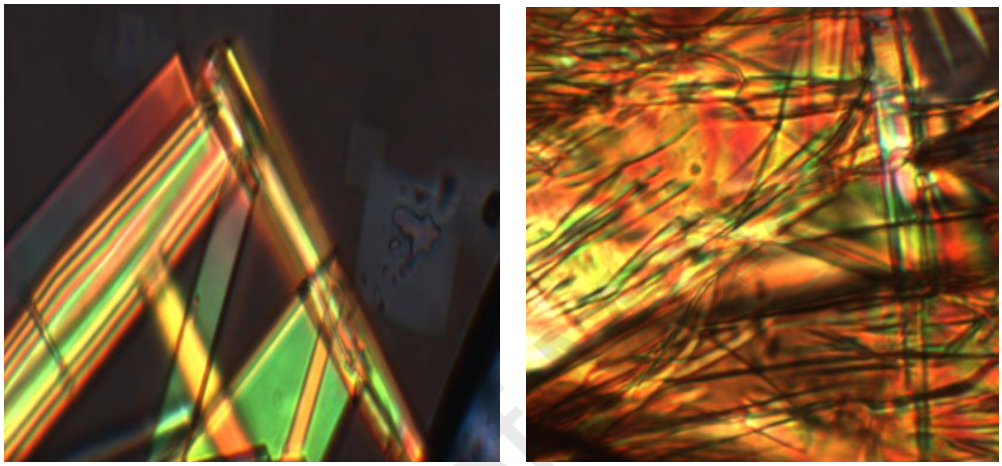

(a) **(b)**

Figure 4.111 The photomicrographs of **Complex 8** on cooling from 235 ^{o}C: (a) at 215 ^{o}C; and (b) at 180 ^{o}C (solid).

4.2.10 Summary

To summarise, the chemical formula, bandgaps, magnetic and thermal data for these complexes are shown in **Table 4.4**.

Table 4.4 Summary of complexes with *H_2L1*

Complex	**Chemical Formula**	**Bandgap (eV)**			**τ (ns)**	**μ_{eff} (B.M.)**	**T_{dec} (^{o}C)**	**LC**
		E_o (abs)	E_o (em)	E_e				
1	$[Cu_2(CH_3COO)_2(H_2O)_2(L1)]$	3.4	2.1	0.2	2.8	2.15	231	-
2	$[Ni_2(CH_3COO)_2(H_2O)_2(L1)]$	3.4	1.8	-	27	4.52	238	-
3	$[Co_2(CH_3COO)_2(H_2O)_2(L1)]$	34	1.8	-	2.7	6.06	241	-
4	$[Fe_3(CH_3COO)_4(H_2O)_3(L1)]$	3.5	2.1	-	2.8	2.23	199	-
5	$[Cu_2(CH_3(CH_2)_{14}COO)_2(L1)]$	3.8	2.1	-	3.0	2.13	239	M

6	$[Ni_2(CH_3(CH_2)_{14}COO)_2(H_2O)_2(L1)]$	3.8	2.0	-	3.1	5.08	245	M
7	$[Co_2(CH_3(CH_2)_{14}COO)_2(H_2O)_2(L1)]$	3.9	1.9	-	3.0	5.02	231	M
8	$[Fe_2(CH_3(CH_2)_{14}COO)_2(H_2O)_2(L1)]$	3.7	1.8	1.09	2.9	7.0	205	M

= CH_3COO; R'= $CH_3(CH_2)_{14}COO$; M = mesomorphic

All complexes, except **Complex 4**, were dinuclear. **Complex 4** was trinuclear. Their optical bandgaps were similar, and the values calculated from the absorption bands (3.4 eV– 3.9 eV) higher than from the emission bands (1.8 eV – 2.1 eV). Fluorescence is expected from the lowest vibrational energy level of excited state to the highest vibrational energy level of the ground state (π orbital of ligand) (**Figure 4.112**).

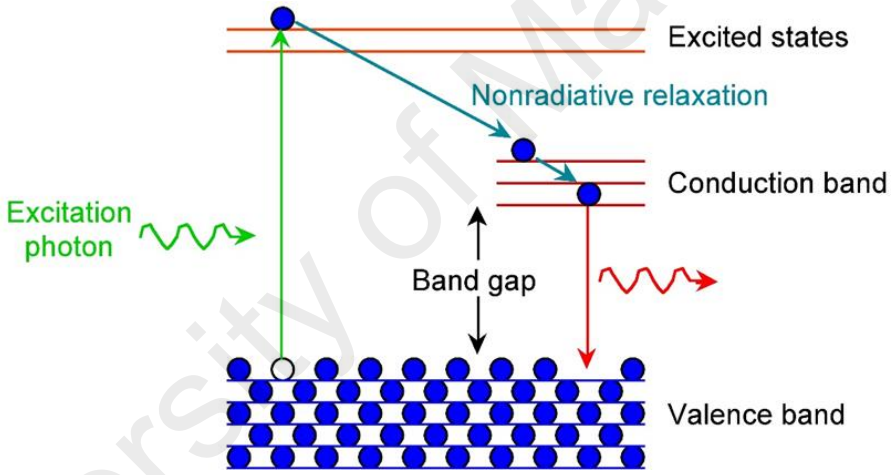

Figure 4.112 Absorption and fluorescence process

The results seem to suggest that the bandgaps were independent of the metal(II) centres, nuclearity of complexes and the chain length in the alkylcarboxylate ions.

In contrast, the electrochemical bandgaps could only be calculated for **Complexes 1** (Cu(II) and **8** (Fe(II) since all the other complexes were either redox inactive or irreversibly oxidised. The value for **Complex 1** was much lower than for **Complex 8**, which was ascribed to a more facile reduction of Cu(II) to Cu(I) compared to oxidation of Fe(II) to Fe(III).

The Stokes shift values of all complexes from CT transition are in the range 140 – 229 nm. Except for **Complex 6** (141 nm), the Stokes shift values from d-d transition are 9 – 74 nm. It might be assumed that the e_g antibonding orbital of Ni(II) is lower than Co(II) and Fe(II). It can be concluded that the larger stokes shift from CT transition is more favourable as photosensitizer application than *d-d* transition.

The lifetimes of all of the excited complexes were also similar (2.7 – 3.1 ns). There were also more than one returning paths for the excited complex to return to the ground state. These intramolecular transitions may occur as follows: an electron in a π orbital of the ligand (ground state) absorbed the photonic energy and was promoted to a π^* orbital of the ligand. It then released the energy through: (a) $\pi^* \rightarrow d_{x^2-y^2}$ (b) $\pi^* \rightarrow n$; and $\pi^* \rightarrow \pi$ **(Figure 4.113)**.

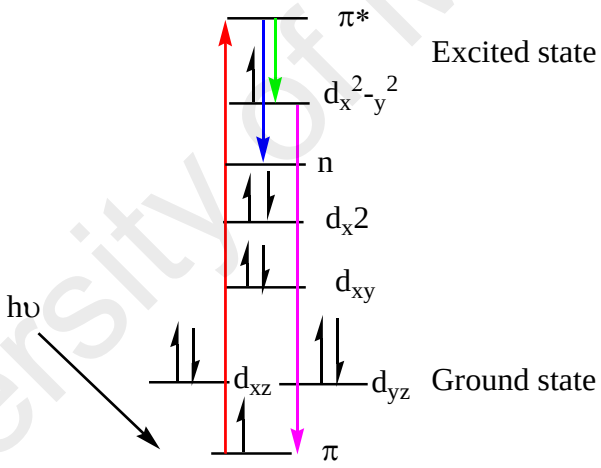

Figure 4.113 Photoluminescence of intraligand transition in **Complex 1** (red: excitation, purple: emission (1), blue: emission (2), green: emission (3))

All complexes were paramagnetic. The Cu(II) complexes showed a weak antiferromagnetic interaction between the metal centres, while the Ni(II) complexes complex showed negligible interactions between the metal centres. Both Co(II) and Fe(II) complexes were high spin. These results suggest that the both the alkylcarboxylate and *L1* were weak field ligands which did not promote electronic communication between the metal(II) ions.

All complexes were thermally stable. Their decomposition temperatures ranged from 199^{o}C to 245^{o}C. The least thermally stable was the trinuclear complex (**Complex 4**), while the thermal stability of the other complexes were almost the same. Since the decomposition of these complexes are ascribed to the decarboxylation of the carboxylate ligands [10], it may be inferred that the increase number of metal(II) ions in a complex resulted in a weaker R-COO bonds.

Finally, all of metal(II) hexadecanoate complexes were mesomorphic, indicating the anisotropy in polarity and molecular shape. The type of mesomorphisms cannot be assigned with certainty based on the DSC and OPM data, but differs from the usual discotic and calamitic liquid crystals.

4.3 Metal(II) Complexes of *L2*

4.3.1 Synthesis of L2

The ligand *L2* was obtained as a yellow powder from the reaction of 2,6-diamino-4-phenyl-1,3,5-triazine with 2,5-thiophene dicarboxaldehyde. The yield was 88.7%. The reaction equation is shown in **Scheme 4.4**.

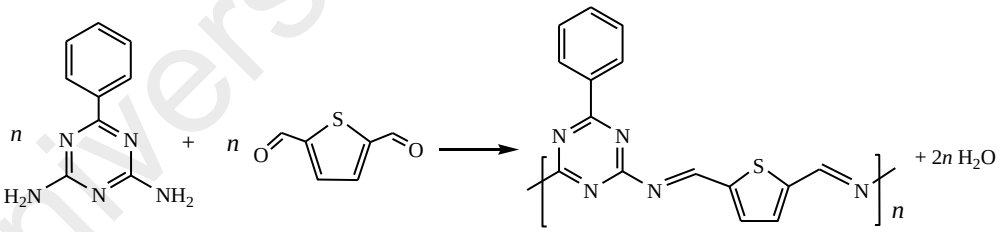

Scheme 4.4 Reaction equation for the preparation of *L2*

The results of the **elemental analyses** (60.1% C, 5.0% H, 18.3% N) are in good agreement with those calculated for the repeat unit *L2*.2C_2H_5OH (formula, $C_{19}H_{21}N_5O_2S$; formula weight, 383.47 g mol^{-1}; 59.5% C, 5.5% H, 18.3% N).

Its **^{1}H-NMR** spectrum (**Figure 4.114**) supported the proposed structural formula. The azomethine protons appear as a singlet at 8.26 ppm and all of the aromatic protons appear as a multiplet in the range 6.75 - 8.23 ppm.

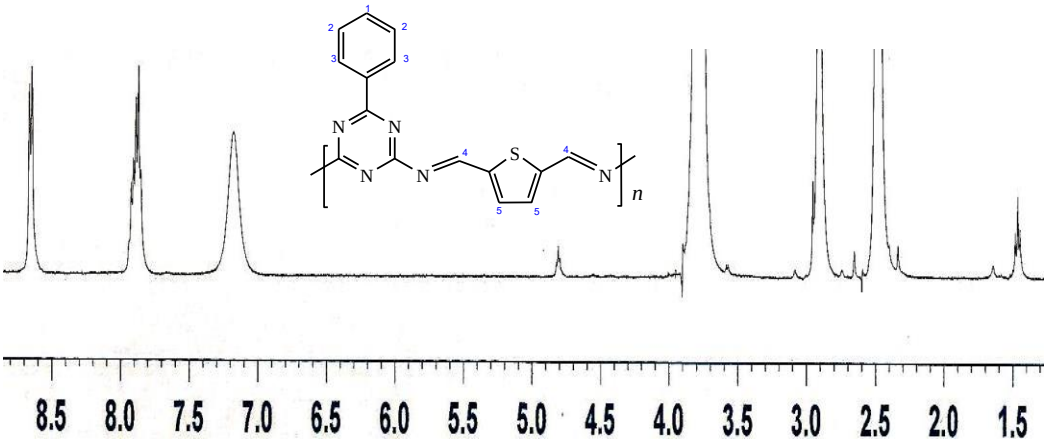

Figure 4.114 ^{1}H-NMR spectrum for *L2.2C$_2$H$_5$OH*

Table 4.5 The ^{1}H-NMR peak assignment for *L2.2C$_2$H$_5$OH*

Chemical Shift (ppm)	**Integral**	**Multiplicity**	**Assignment**
1.45 – 1.48	0.69	triplet	CH_3 from ethanol
3.81	7.34	broad	CH_2 of ethanol overlapped with DMSO
4.78	0.21	doublet	OH of ethanol
6.77	3.96	broad	H-4, H-5, H-6
7.44 - 7.53	3.08	multiplet	H-1, H-2
8.24 - 8.26	2.00	doublet	H-3

Its **FTIR** spectrum is shown in **Figure 4.115**, and the peak assignments are given in **Table 4.6** (which also include the data for the corresponding metal(II) complexes for later discussion). Hence, the spectrum shows the functional groups expected for the ligand.

Table 4.6 FTIR data (in cm^{-1}) and assignments for *L2.2C₂H₅OH* and its complexes

	O-H	CH_2 (asym)	CH_2 (sym)	C=N	COO (asym)	COO (sym)	M-N
L2	-	-	-	1662s	-	-	-
9	3127m	-	-	1623m	1538s	1410s	580w
10	3302br	-	-	1661s	1537s	1393s	538w
11	3299br	-	-	1661m	1534s	1391s	514w
12	3290br	-	-	1590w	1537s	1399s	492m
13	-	2915s	2849m	1665m	1537s	1413s	597m
14	3349w	2916s	2849s	1664m	1542s	1409s	532w
15	3317w	2916s	2848m	1665m	1527s	1454w	587w
16	3373w	2915s	2848s	1662s	1524w	1443w	497s

s = strong; m = medium; w = weak; br = broad

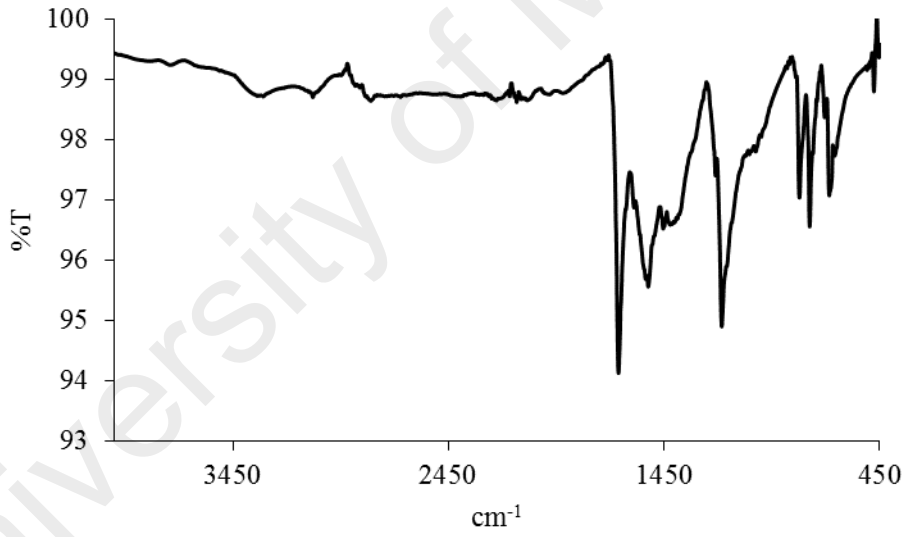

Figure 4.115 FTIR spectrum of *L2.2C₂H₅OH*

4.3.2 Reaction of copper(II) ethanoate with L2

Copper(II) ethanoate ($[Cu_2(CH_3COO)_4]$) reacted with *L2* (mole ratio 1:1) to give a green powder (**Complex 9**) and the yield was 70.2%. It was soluble in DMSO, but insoluble in water and other common organic solvents.

The results from the **elemental analyses** (46.7% C; 3.9% H; 14.7% N) are in excellent agreement with those calculated for the repeat unit $CuC_{19}H_{17}N_5O_5S$

(46.5% C; 3.5% H; 14.3% N; formula weight, 490.98 g mol^{-1}). Combining these with the spectroscopic data discussed below, its proposed structural formula is $\{[Cu(CH_3COO)_2(L2)].H_2O\}_n$.

Its **FTIR** spectrum (**Table 4.6**; **Figure 4.116**) shows the presence of the expected functional groups. The ΔCOO value (128 cm^{-1}) suggests a chelating binding mode for CH_3COO^- ligand [1].

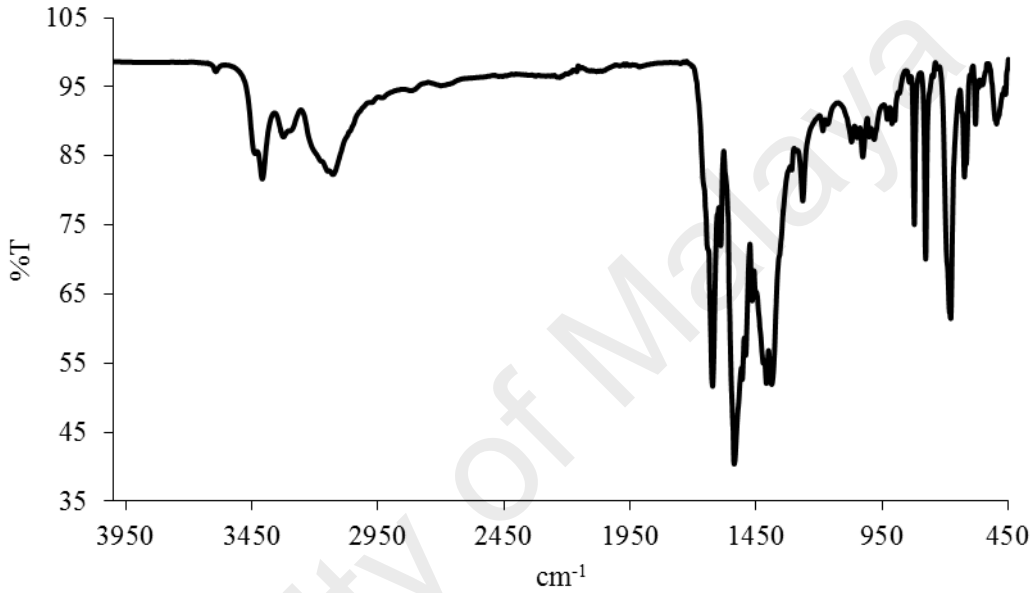

Figure 4.116 FTIR spectrum of **Complex 9**

Its **UV-vis** spectrum in DMSO (**Figure 4.117**) shows a broad *d-d* band at 701 nm (ε_{max}, 194.5 $M^{-1}cm^{-1}$) assigned to $^2B_2 \rightarrow {}^2B_1$ electronic transition, and an intense LMCT band at 247 nm (ε_{max}, 39483 $M^{-1}cm^{-1}$). This suggests that the Cu(II) centre has a square pyramidal geometry.

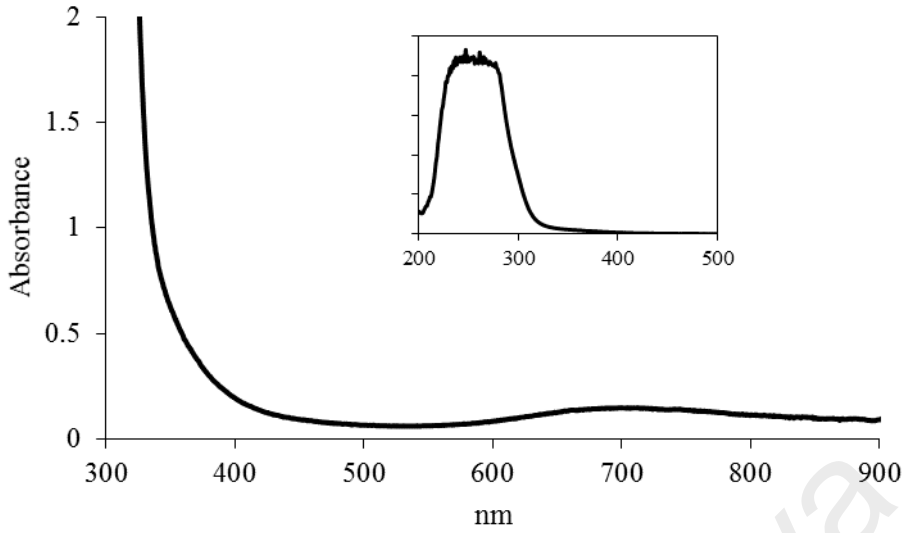

Figure 4.117 UV-vis spectrum of **Complex 9**

Its E_o, calculated as before (λ_{edge} = 322 nm) was 3.8 eV. Upon excitation at 247 nm (LMCT transition), its **fluorescence** spectrum shows three peaks at λ_{max} 299 nm, 400 nm, and 523 nm (**Figure 4.118)**. This suggests two different paths for the excited complex to return to the ground state. Its E_o value (calculated from λ_{edge} = 575 nm) was 2.1 eV. Its τ, calculated as before from its **decay** curve (**Figure 4.119**), was 3.6 ns. Its Stokes shift was 153 nm.

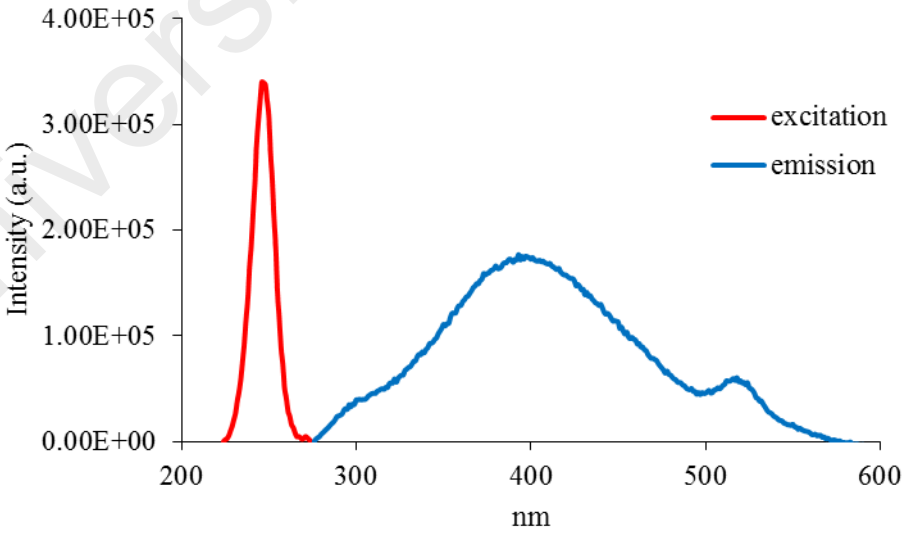

Figure 4.118 Fluorescence spectrum of **Complex 9** (λ_{ex} = 247 nm)

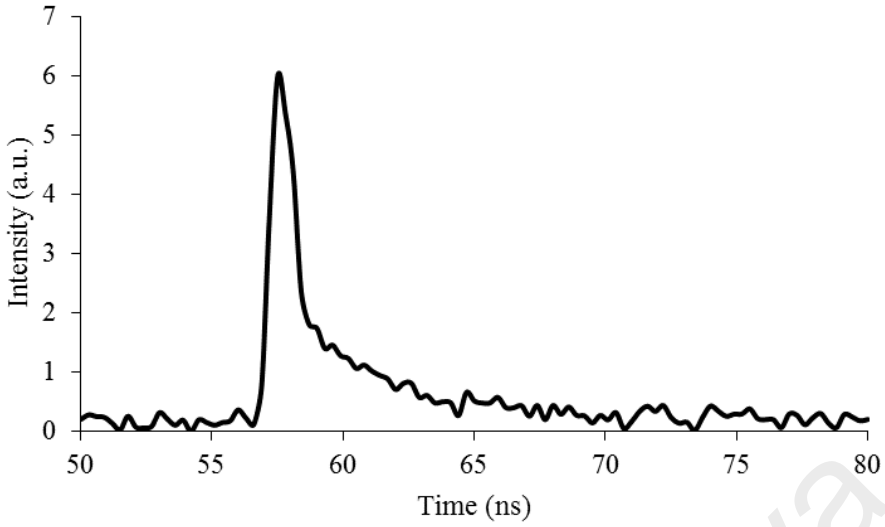

Figure 4.119 Fluorescence decay of **Complex 9**

Also, upon excitation at 701 nm (*d-d* transition), its **fluorescence** spectrum shows a peak at λ_{max} 729 nm (**Figure 4.120**). Its E_o value (calculated from λ_{edge} = 736 nm) was 1.7 eV, and its $\boldsymbol{\tau}$ value, calculated as before from its decay curve, was 2.6 ns. Its Stokes shift was 28 nm.

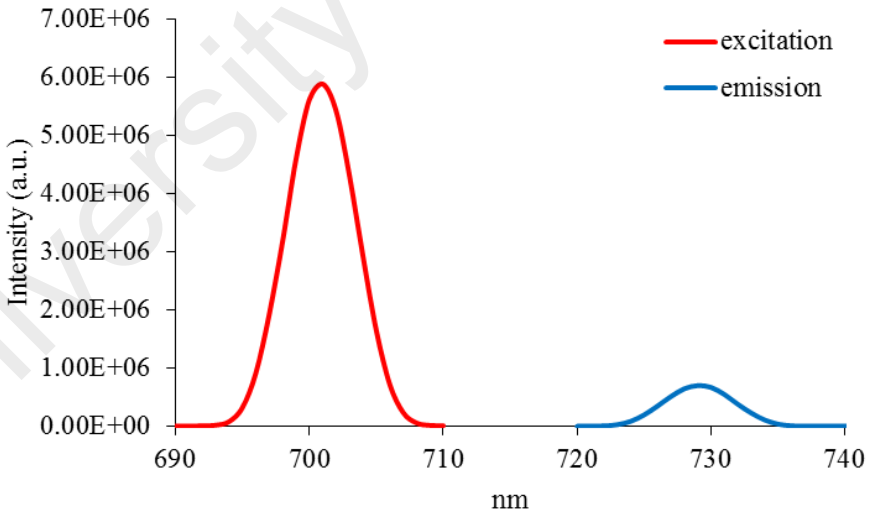

Figure 4.120 Fluorescence spectrum of **Complex 9** (λ_{ex} = 701 nm)

Its **CV** (**Figure 4.121**), recorded cathodically from 0 V within the potential window of -1.5 V to +1.5 V, showed one cathodic peak at -0.65 V and two anodic peaks at +0.47 V and +1.1 V. The Cu(II) based redox is shown in **Scheme 4.5**. Hence,

the peak separation (ΔE_p) was 1120 mV, indicating a quasireversible redox reaction. The anodic peak at +1.1 V is tentatively attributed to ligand-based oxidation process.

$$[Cu(II)] \underset{+0.47}{\overset{-0.65\ V}{\rightleftharpoons}} [Cu(I)]$$

Scheme 4.5. The redox process for **Complex 9**

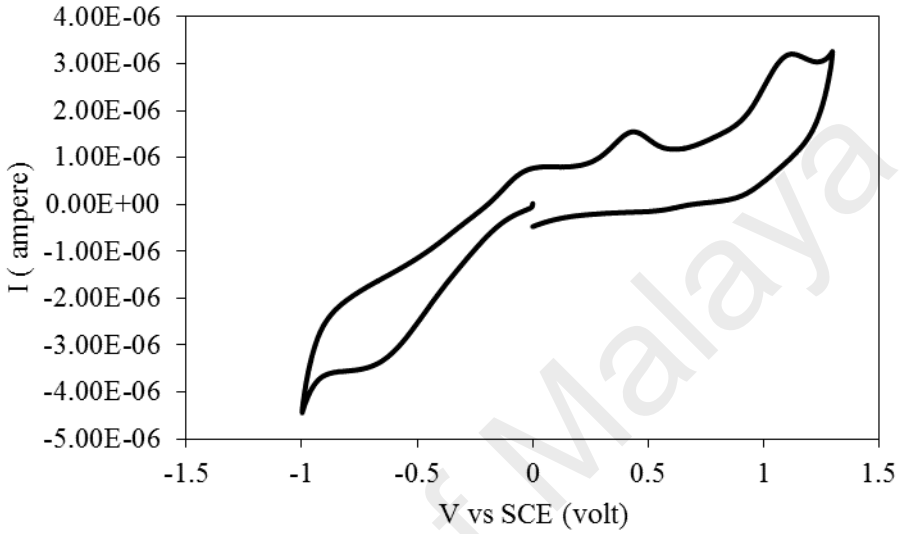

Figure 4.121 CV of **Complex 9**

The HOMO and LUMO values, calculated from the onset oxidation potential (+0.27 V) and onset reduction potential (-0.20 V), were 4.67 eV and 4.20 eV versus SCE, respectively. Thus, its E_e was 0.47 eV.

Its $\boldsymbol{\mu_{eff}}$ value, calculated as before from the values of FM = 490.98 g mol^{-1} (repeat unit), χ_g = 0.12 x 10^{-5} cm^3 g^{-1}, χ_M = 6.04 x 10^{-4} cm^3 mol^{-1}, and χ_{dia} = -2.45 x 10^{-4} cm^3 mol^{-1}, was 1.47 B.M. at 298 K. The value is significantly lower than expected for one Cu(II) atom in the unit (1.73 B.M.). This suggests a strong antiferromagnetic interaction between the Cu(II) atoms in the polymeric complex.

Its **TGA** trace (**Figure 4.122**) shows that it suffered an initial weight loss of 3.9% in the temperature range of 135 – 162 °C, assigned to the evaporation of one coordinated H_2O molecule (expected 3.7%). The next weight losses in the temperature range of 162 – 900 °C was 71.9%, assigned to the decomposition of two CH_3COO^- and *L2* ligands (expected, 83.3%). However, the amount of residue above 900 °C cannot be

calculated due to incomplete combustion of the organic ligands. It is noted that its decomposition temperature T_{dec}) was 162 °C.

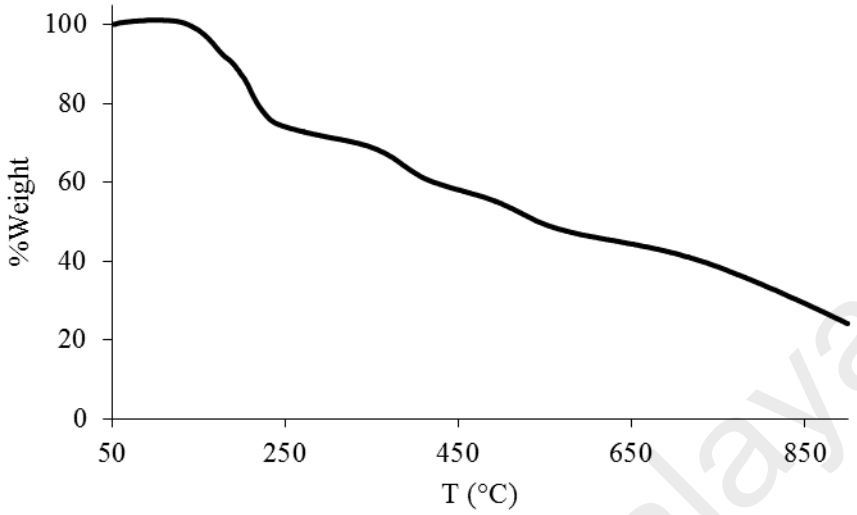

Figure 4.122 TGA of **Complex 9**

4.3.3 Reaction of nickel(II) ethanoate with L2

Nickel(II) ethanoate tetrahydrate ($[Ni(CH_3COO)_2].4H_2O$) reacted with *L2* (mole ratio 1:1) to give a pale green powder (**Complex 10**), and the yield was 78.8%. Its solubility was similar to the previously discussed complexes.

The **elemental analytical** data for the complex (45.7% C; 3.7% H; 13.7% N) are in excellent agreement with those calculated for the repeat unit $NiC_{19}H_{19}N_5O_6S_2$ (45.3% C; 3.8% H; 13.9% N; formula weight, 504.14 g mol^{-1}). Combining these with the spectroscopic data discussed below, its proposed structural formula is $\{[Ni(CH_3COO)_2(L2)].2H_2O\}_n$.

Its **FTIR** spectrum (**Table 4.6**; **Figure 4.123**) shows the presence of the expected functional groups. The ΔCOO value was 144 cm^{-1}, suggesting chelating CH_3COO^- ligands.

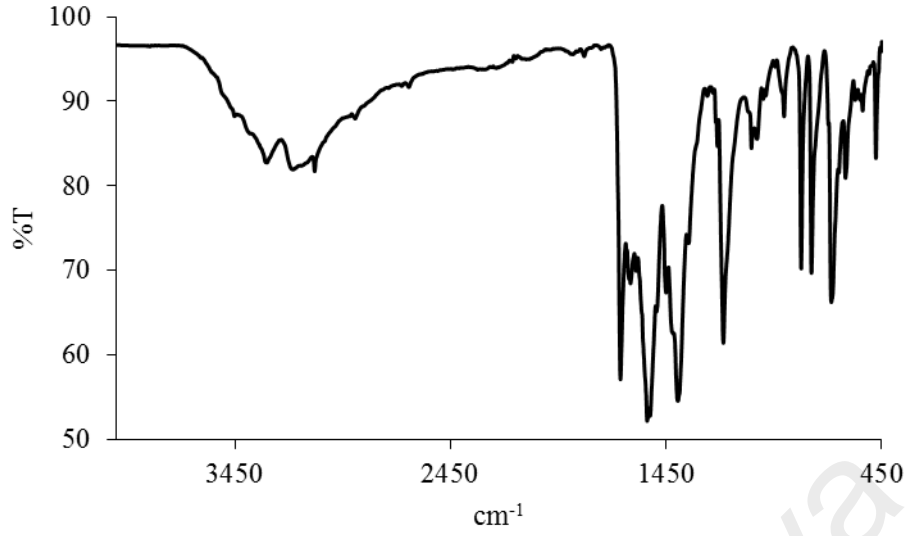

Figure 4.123 FTIR spectrum of **Complex 10**

Its **UV-vis** spectrum in DMSO (**Figure 4.124**) shows a weak broad band at 753 nm (ε_{max}, 34.3 M^{-1} cm^{-1}) assigned to $^3A_{2g}$ (F)→ $^3T_{1g}$ (F), 598 nm (ε_{max}, 157 M^{-1} cm^{-1}) assigned to $^3A_{2g}$ (F) →$^3T_{2g}$ (F), and 451 nm (ε_{max}, 571 M^{-1} cm^{-1}) assigned to $^3A_{2g}$ (F)→ $^3T_{1g}$ (P) electronic transitions. These suggest an octahedral geometry at the Ni(II) centre. Also observed is an intense MLCT band at 306 nm (ε_{max}, 9117 M^{-1} cm^{-1}).

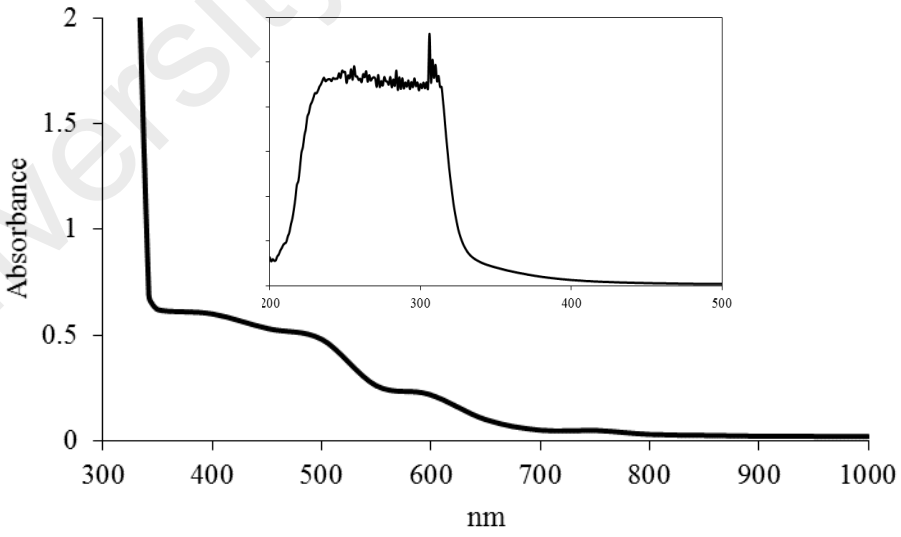

Figure 4.124 UV-vis spectrum of **Complex 10**

Its E_o**,** calculated from λ_{edge} = 342 nm, was 3.6 eV. The value is slightly narrower than for **Complex 9 (**{[Cu(CH_3COO)$_2$(L2)].H_2O}$_n$; 3.8 eV), which might be due to the different geometry at the metal centre between the two complexes.

Upon excitation at 306 nm (MLCT transition), its **fluorescence** spectrum shows three overlapping peaks at λ_{max} 362 nm, 465 nm and 545 nm (**Figure 4.125**). This suggests three different paths for the excited complex to return to the ground state. Its Stokes shift was 159 nm.

Its E_o, calculated from λ_{edge} = 666 nm, was 1.8 eV. This value is significantly lower than **Complex 9** (2.1 eV). Its τ value, calculated as before from its **decay** curve (**Figure 4.126**), was 2.7 ns. Hence, the excited state lifetime of the complex is similar to **Complex 9** (2.6 ns).

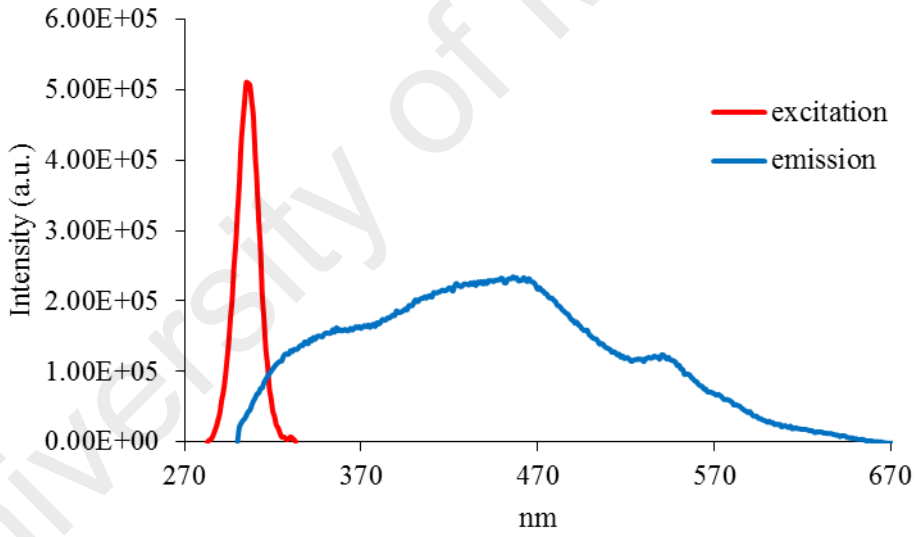

Figure 4.125 Fluorescence spectrum of **Complex 10** (λ_{ex} = 306 nm)

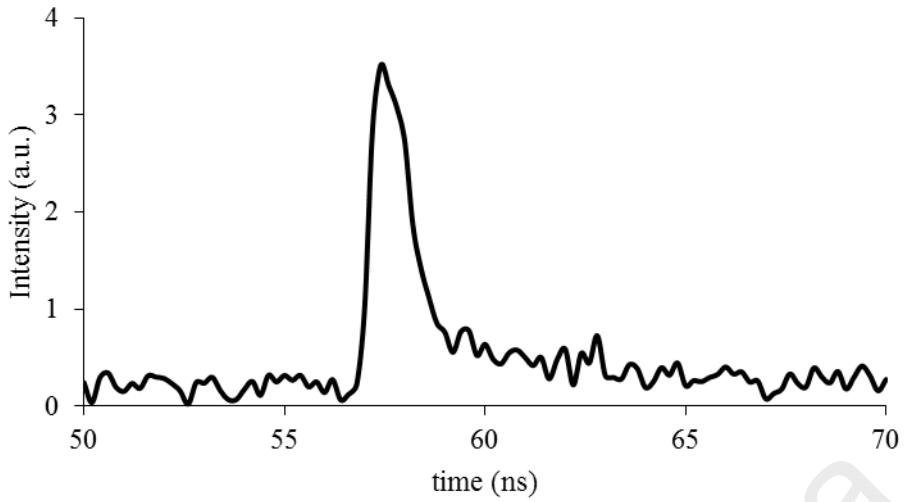

Figure 4.126 Fluorescence decay of **Complex 10**

Also, upon excitation at 451 nm (*d-d* transition), its **fluorescence** spectrum shows a peak at λ_{max} 475 nm (**Figure 4.127**). Its E_o, calculated from λ_{edge} = 507 nm, was 2.4 eV, and its τ value, calculated from its **decay curve**, was 3.2 ns. In addition, its Stokes shift was 24 nm.

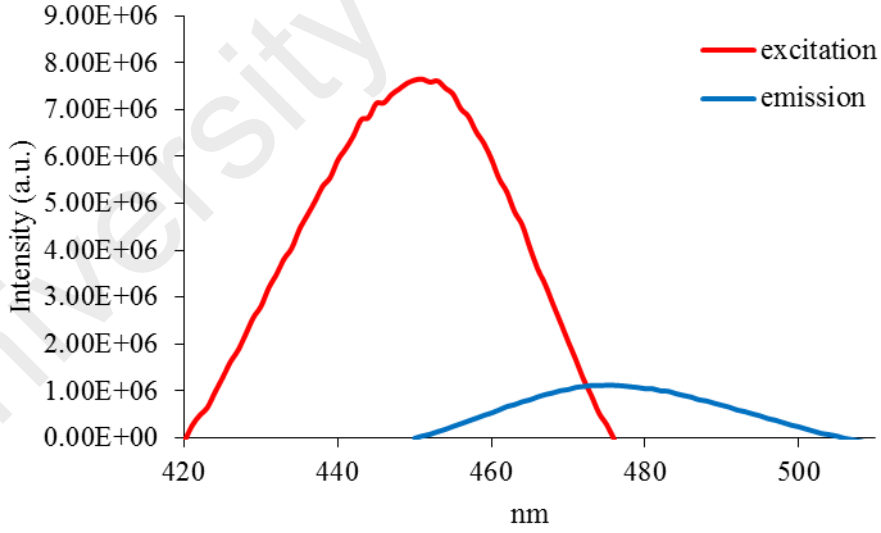

Figure 4.127 Fluorescence spectrum of **Complex 10** (λ_{ex} = 451 nm)

The **CV** (**Figure 4.128**), recorded anodically from 0 V within the potential window of +1.5 V to -1.5 V. It showed an anodic peak at +1.03 V, when the potential was increased from 0 V to +1.5 V. There was a cathodic peak observed at -1.21 V,

when the potential was decreased from +1.5 V to -1.5 V. Both anodic and cathodic peaks above are assigned to the ligand-based redox process. Additionally, when the potential was increased from -1.5 V to 0 V, an anodic peak observed at -0.35 V. It is assigned to oxidation of Ni(II) to Ni(III) [40], which indicates irreversible process. Hence, its E_e cannot be calculated.

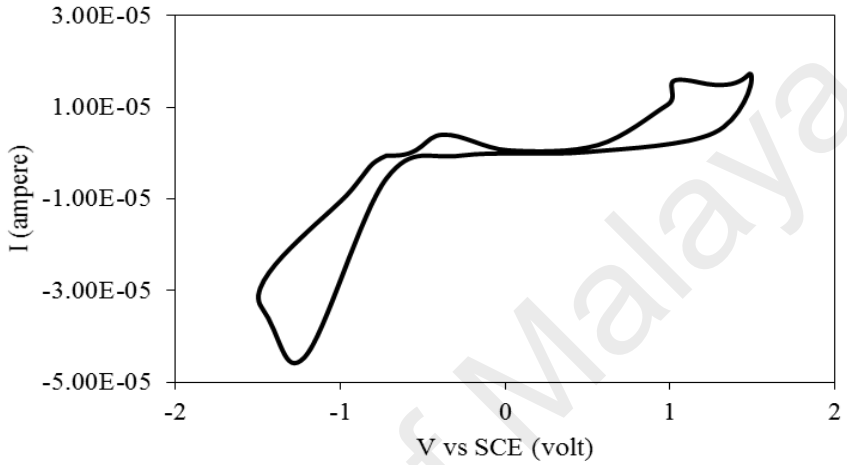

Figure 4.128 CV of **Complex 10**

Its $\boldsymbol{\mu_{eff}}$ value, calculated as before from the values of FM = 504.14 g mol^{-1} (repeat unit), χ_g = 5.18 x 10^{-6} cm^3 g^{-1}, χ_M = 2.61 x 10^{-2} cm^3 mol^{-1}, and χ_{dia} = -2.68 x 10^{-4} cm^3 mol^{-1}, was 2.65 B.M. at 298 K. This is lower than the spin only value expected for one Ni(II) atom (2.83 B.M.). Hence, as similarly observed for the corresponding Cu(II) complex (**Complex 9**), there was also an antiferromagnetic interaction between the Ni(II) atoms in the polymeric complex.

Its **TGA** trace (**Figure 4.129**) shows an initial weight loss of 7.5% in the temperature range of 65 – 164 °C, assigned to the evaporation of two H_2O molecules (expected 7.1%). The next weight loss of 75.8% in the temperature range of 164 – 756 °C is assigned to the decomposition of two CH_3COO^- and *L2* ligands (expected, 81.2%). The amount of residue at temperatures above 756 °C was 16.7% (expected, 16.3% assuming pure NiO). Hence, **Complex 10** (T_{dec} = 164 °C) was as thermally stable as **Complex 9** (T_{dec} = 162 °C).

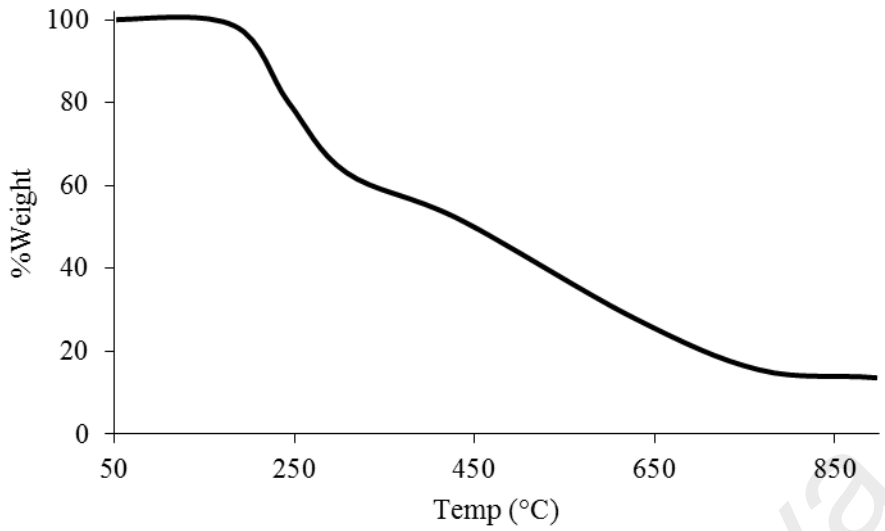

Figure 4.129 TGA of **Complex 10**

4.3.4 Reaction of cobalt(II) ethanoate with L2

Cobalt(II) ethanoate tetrahydrate ($Co(CH_3COO)_2.4H_2O$) reacted with *L2* (mole ratio 1:1) to give a purple powder (**Complex 11**), and the yield was 81.4%. Its solubility was similar to the previously discussed complexes.

The **elemental analytical** data for the complex (44.9% C; 3.9% H; 13.2% N) are in excellent agreement with those calculated for the repeat unit $CoC_{19}H_{19}N_5O_6S$ (45.2% C; 3.8% H; 13.9% N; formula weight, 504.38 g mol^{-1}). Combining these with the spectroscopic data discussed below, its proposed structural formula is $\{[Co(CH_3COO)_2(L2)].2H_2O\}_n$, which is similar to **Complex 10** (**(**$\{[Ni(CH_3COO)_2(L2)].2H_2O\}_n$).

Its **FTIR** spectrum (**Table 4.6**; **Figure 4.130**) shows the presence of the expected functional groups. The ΔCOO value was 143 cm^{-1}, suggesting chelating CH_3COO^- ligands.

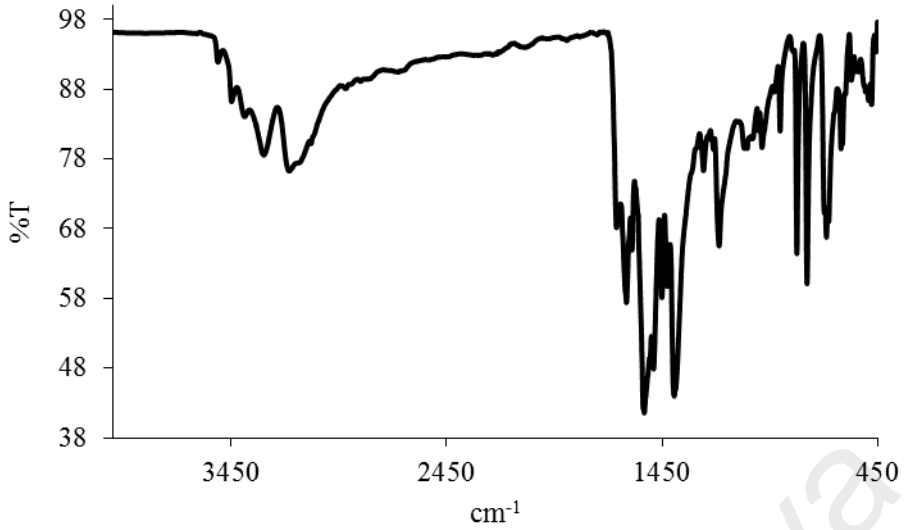

Figure 4.130 FTIR spectrum of **Complex 11**

Its **UV-vis** spectrum in DMSO (**Figure 4.131**) shows three overlapping *d-d* bands at 897 nm (ε_{max}, 41.7 M^{-1} cm^{-1}), 600 nm (ε_{max}, 208.3 M^{-1} cm^{-1}) and 504 nm (ε_{max}, 233 M^{-1} cm^{-1}). These electronic transitions are assigned as $^4T_{1g}$ (F) → $^4T_{2g}$ (F), $^4T_{1g}$ (F) → $^4T_{1g}$ (P), and $^4T_{1g}$ (F) → $^4A_{2g}$ (F), respectively. Hence, the geometry at the high-spin Co(II) centre was octahedral. An intense MLCT band is observed at 271 nm (ε_{max}, 10940 M^{-1} cm^{-1}).

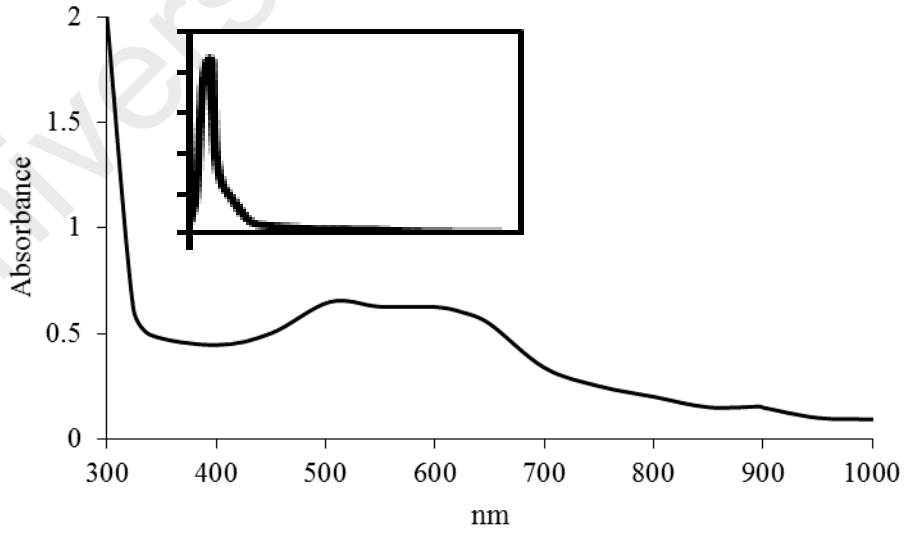

Figure 4.131 UV-vis spectrum of **Complex 11**

Its E_o value, calculated as before from λ_{edge} = 324 nm, was 3.8 eV. The value is similar to **Complex 9** ({[$Cu(CH_3COO)_2(L2)].H_2O$}$_n$; 3.8 eV).

Upon excitation at 271 nm (MLCT transition), its **fluorescence** spectrum shows three peaks at 327 nm, 365 nm and 465 nm (**Figure 4.132**). Its E_o, calculated from λ_{edge} = 550 nm, was 2.2 eV. This value is slightly wider than **Complex 10** (1.8 eV). The value of its $\boldsymbol{\tau}$, calculated as before from its **decay** curve (**Figure 4.133**), was 3.4 ns. Hence, the lifetime of excited **Complex 11** is much longer than from **Complex 10** (2.7 ns). Its Stokes shift was 56 nm.

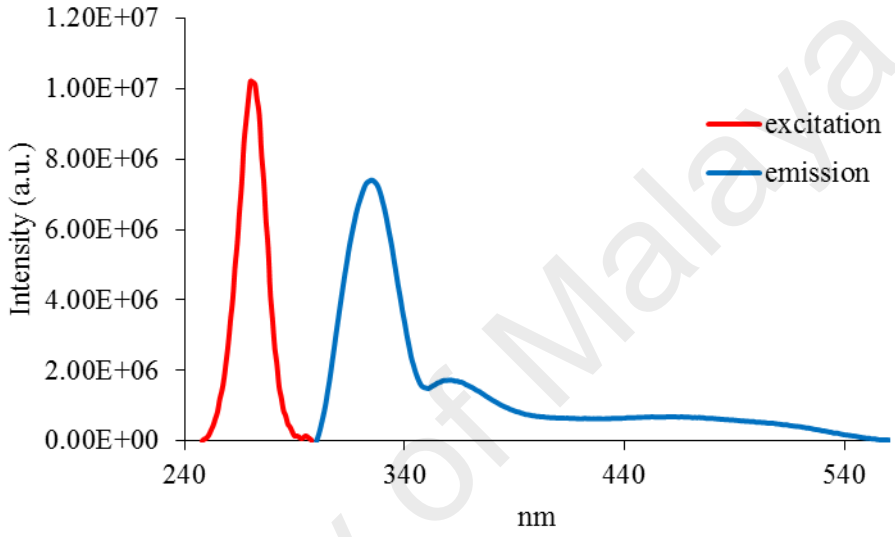

Figure 4.132 Fluorescence spectrum of **Complex 11** (λ_{ex} = 271 nm)

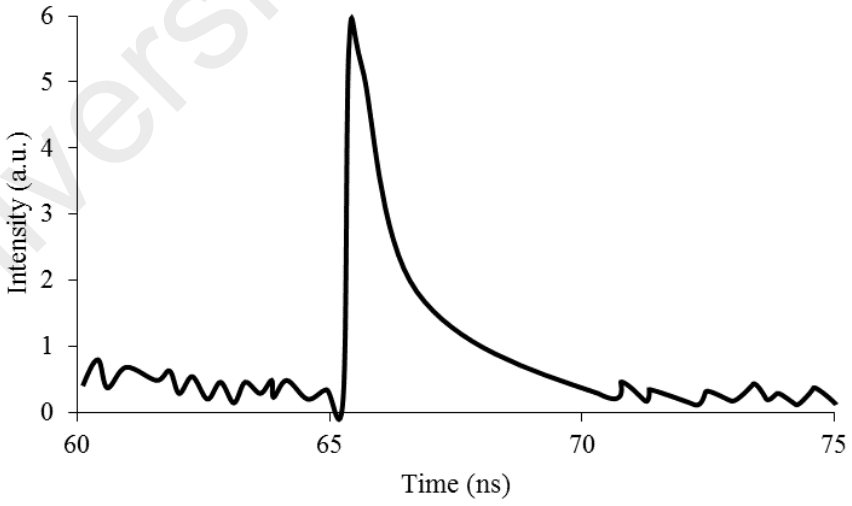

Figure 4.133 Fluorescence decay of **Complex 11**

Upon excitation at 504 nm, (*d-d* transition), its **fluorescence** spectrum shows a peak at λ_{max} 529 nm (**Figure 4.134**). Its E_o, calculated from λ_{edge} = 538 nm, was 2.3 eV.

Its τ value, calculated as before from its **decay** curve, was 3.3 ns. Also, its Stokes shift was 25 nm.

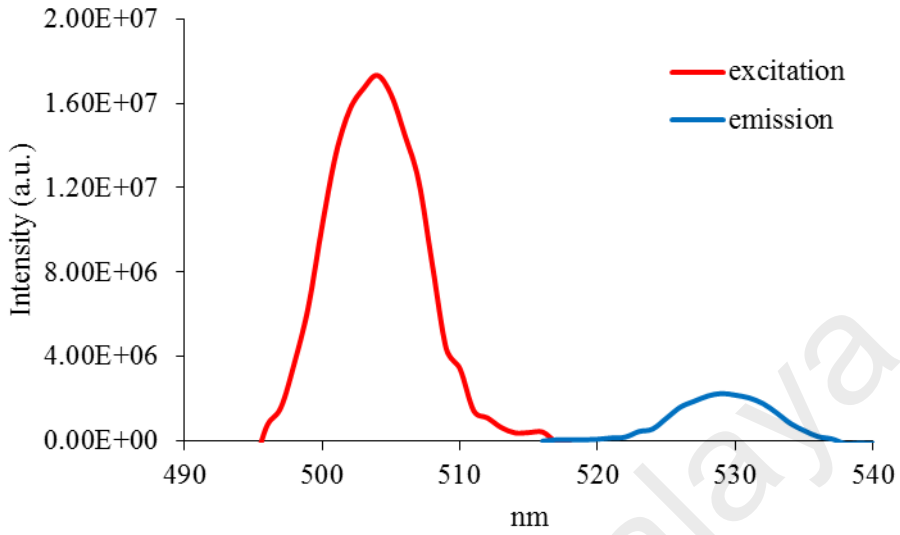

Figure 4.134 Fluorescence spectrum of **Complex 11** (λ_{ex} = 504 nm)

Its **CV** (**Figure 4.135**), recorded anodically from 0 V within the potential window of +1.5 V to -1.5 V, showed only one peak at +1.12 V. This is assigned to ligand-based oxidation process, which is irreversible process. This indicates that Co(II) ion is redox inactive. Thus, its E_e value cannot be calculated.

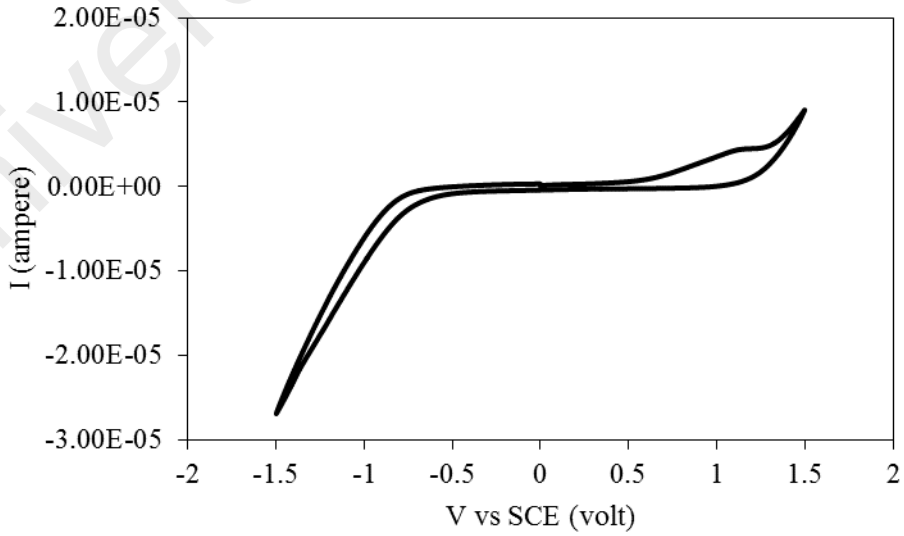

Figure 4.135 CV of **Complex 11**

Its μ_{eff} value, calculated as before from the values of FM = 504.38 g mol^{-1} (repeat unit), χ_g = 1.26 x 10^{-5} cm^3 g^{-1}, χ_M = 6.32 x 10^{-3} cm^3 mol^{-1}, and χ_{dia} = -2.68 x 10^{-4} cm^3 mol^{-1}), was 3.98 B.M. at 298 K. This is in agreement with the spin-only value for a high-spin Co(II) atom (d^7; 3.89 B.M.), suggesting an insignificant magnetic interaction between the Co(II) centres in the polymeric chain.

Its **TGA** trace (**Figure 4.136**) shows an initial weight loss of 7.1% in the temperature range of 123 – 222 °C, assigned to evaporation of two H_2O molecules (expected, 7.1%). The next weight loss of 88.3% in the temperature range of 222 – 717 °C is assigned to the decomposition of two CH_3COO^- and *L2* ligands (expected, 81.2%). The amount of residue above 717 °C was 4.6% (expected 4.3%, assuming pure CoO). Hence, the complex was much more thermally stable (T_{dec} = 222 °C) than **Complex 10** (T_{dec} = 136 °C).

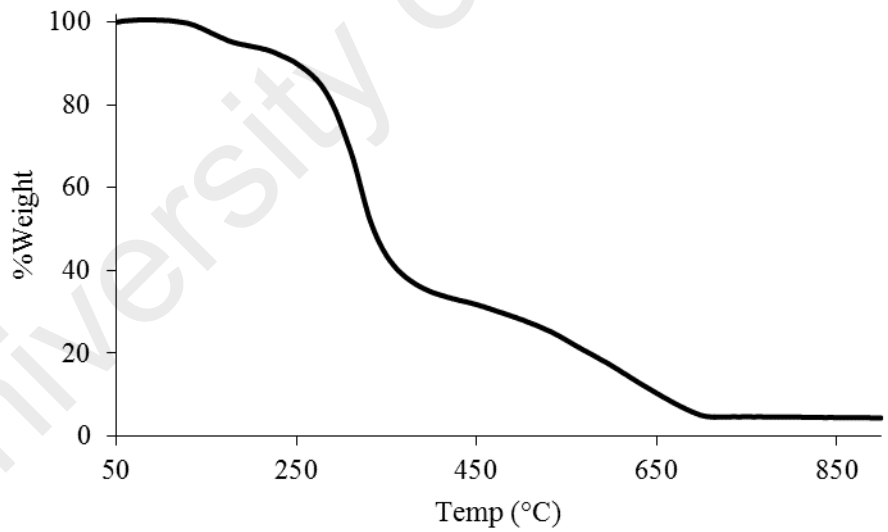

Figure 4.136 TGA of **Complex 11**

4.3.5 Reaction of iron(II) ethanoate with L2

Iron(II) ethanoate ($[Fe(CH_3COO)_2]$) reacted with *L2* (mole ratio 1:1) to give a brown powder (**Complex 12**), and the yield was 82.7%. Its solubility was similar to the previously discussed complexes.

The **elemental analytical** data for the complex (45.7% C; 3. 90% H; 14.0% N) are in excellent agreement with those calculated for the repeat unit $FeC_{19}H_{19}N_5O_6S$ (45.5% C; 3.8% H; 13.9% N; formula weight, 501.29 g mol^{-1}). Combining these with the spectroscopic data discussed below, its proposed structural formula is $\{[Fe(CH_3COO)_2(L2)].2H_2O\}_n$, which is similar to **Complex 10 (**$\{[Ni(CH_3COO)_2(L2)].2H_2O\}_n$**)** and **11** ($\{[Co(CH_3COO)_2(L2)].2H_2O\}_n$).

Its **FTIR** spectrum (**Table 4.6**; **Figure 4.137**) shows the presence of the expected functional groups. The ΔCOO value was 141 cm^{-1}, suggesting chelating CH_3COO^- ligands.

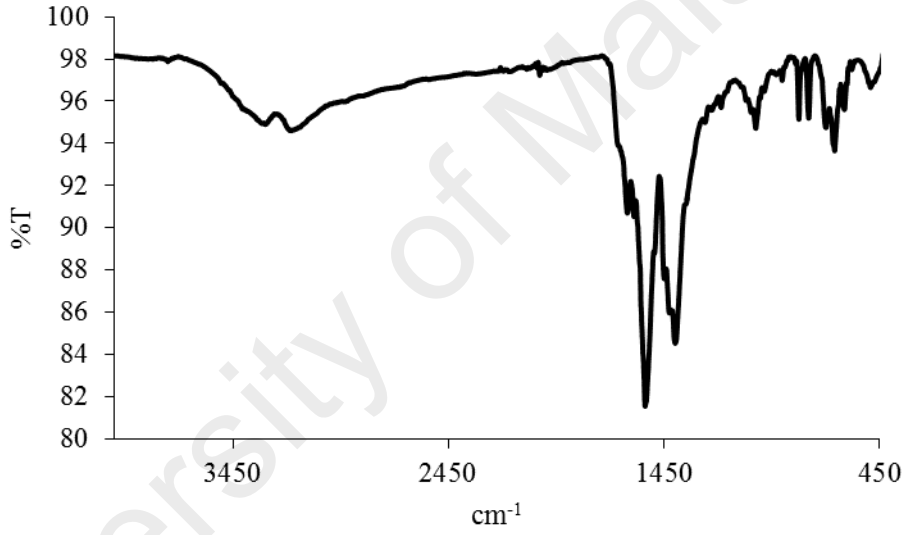

Figure 4.137 FTIR spectrum of **Complex 12**

Its **UV-vis** spectrum in DMSO (**Figure 4.138**) shows a broad band at 841 nm (ε_{max}, 113 M^{-1} cm^{-1}) assigned to ${}^5T_{2g} \rightarrow {}^5E_g$ electronic transition, and an intense MLCT band at 235 nm (ε_{max}, 8692 M^{-1} cm^{-1}). This suggests that the geometry at the high-spin Fe(II) centre was octahedral.

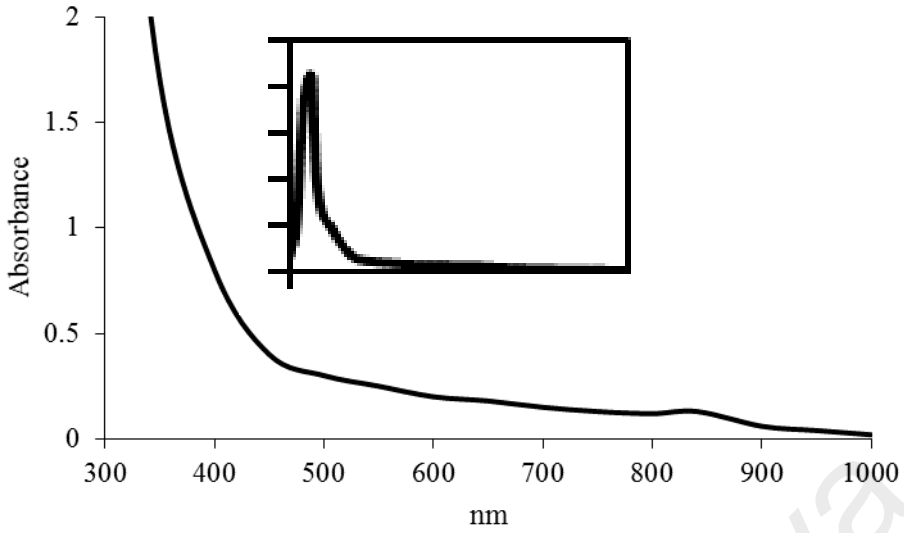

Figure 4.138 UV-vis spectrum of **Complex 12**

Its E_o value, calculated as before from λ_{edge} = 349 nm, was 3.5 eV. The value is slightly lower than **Complex 11** ({[Co(CH$_3$COO)$_2$(L2)].2H$_2$O}$_n$; 3.8 eV).

Upon excitation at 235 nm (MLCT transition), its **fluorescence** spectrum shows two bands at 344 nm, and 426 nm (**Figure 4.139**). Its E_o, calculated from λ_{edge} = 448 nm, was 2.7 eV. This value is higher than **Complex 9** ({[Cu(CH$_3$COO)$_2$(L2)].H$_2$O}$_n$; 2.4 eV). The value of its τ, calculated as before from its **decay curve** (**Figure 4.140**), was 3.8 ns. Its Stokes shift was 193 nm.

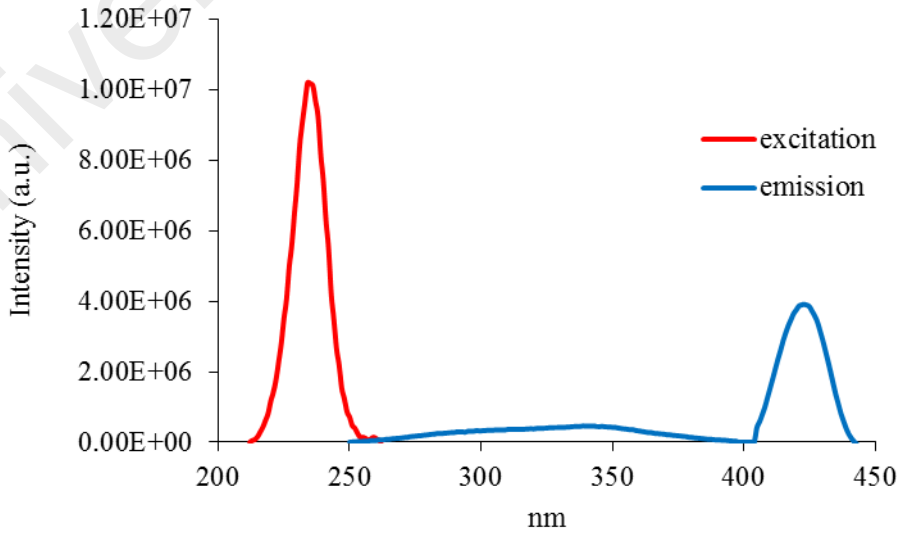

Figure 4.139 Fluorescence spectrum of **Complex 12** (λ_{ex} = 235 nm)

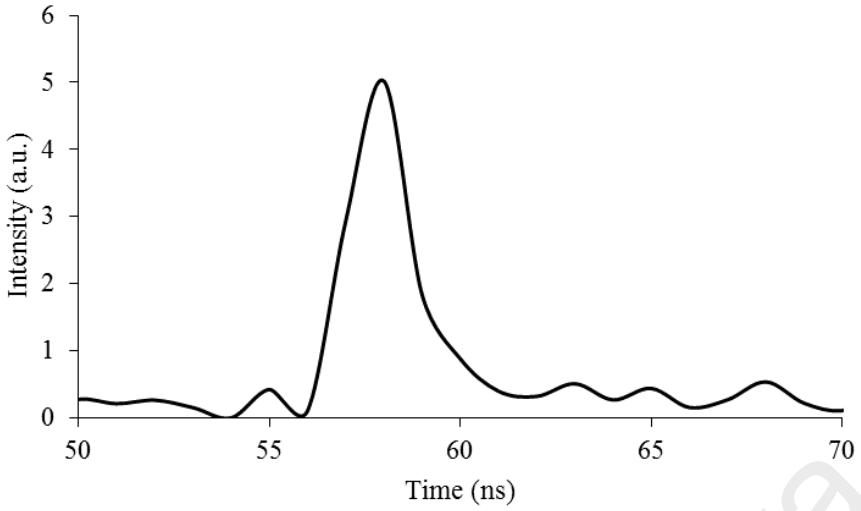

Figure 4.140 Fluorescence decay of **Complex 12**

Also, upon excitation at 841 nm (*d-d* transition), its **fluorescence** spectrum shows a peak at λ_{max} 890 nm (**Figure 4.141**). Its E_o, calculated from λ_{edge} = 999 nm, was 1.2 eV, while its τ value, calculated from its **decay** curve, was 0.99 ns. Additionally, its Stokes shift was 49 nm.

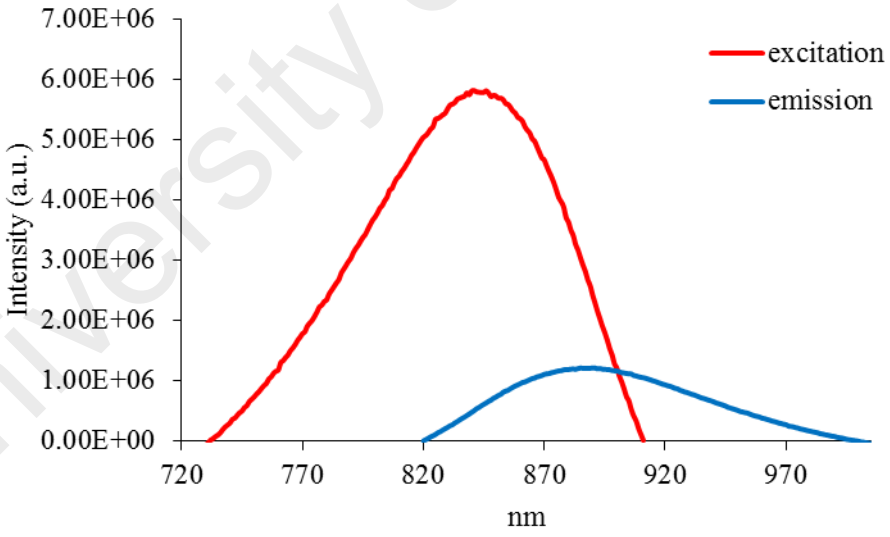

Figure 4.141 Fluorescence spectrum of **Complex 12** (λ_{ex} = 253 nm)

Its **CV** (**Figure 4.142**), recorded anodically from 0 V within the potential window of +1.5 V to -1.5 V, showed one peak at +0.99 V. This suggests an irreversible oxidation of Fe(II) to Fe(III). Hence, its E_e value cannot be calculated.

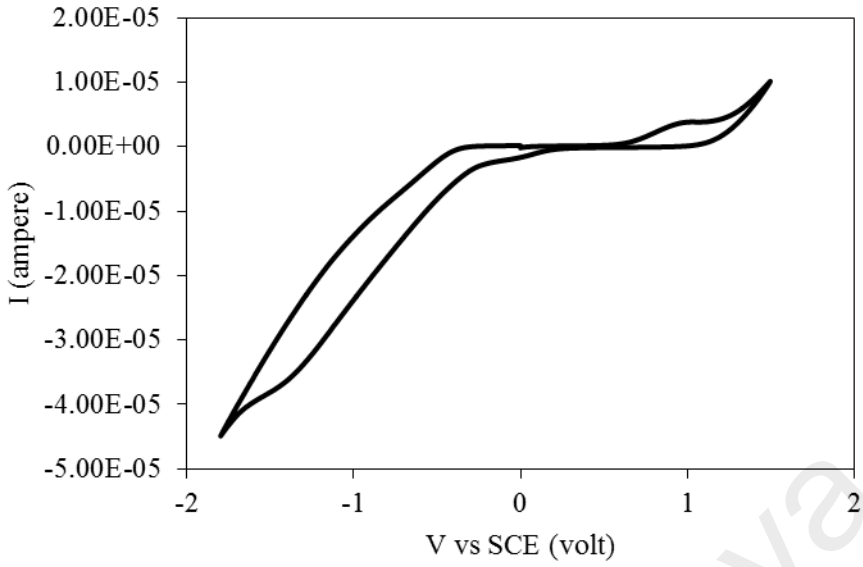

Figure 4.142 CV of **Complex 12**

Its μ_{eff} value, calculated as before from the values of FM = 501.29 g mol^{-1} (repeat unit), χ_g = 2.06 x 10^{-5} cm^3 g^{-1}, χ_M = 1.03 x 10^{-3} cm^3 mol^{-1}, and χ_{dia} = -2.68 x 10^{-4} cm^3 mol^{-1}, was 5.04 B.M. This is slightly higher than the expected spin-only value for a high-spin Fe(II) atom (d^6; four unpaired electrons; 4.89 BM). This suggests a ferromagnetic interaction between the metal centres in the polymeric chain [39].

Its **TGA** scan (**Figure 4.143**) shows that it initially suffered a gradual initial weight loss of 7.2% in the temperature range of 100 – 189 °C, assigned to the evaporation of two H_2O molecules (expected, 7.2%). The next weight loss of 23.5% in the temperature range 189 - 301 °C is assigned to decomposition of two CH_3COO^- ligands (expected, 23.5%). This is followed by another weight loss of 51.9% at 302 °C, assigned to the decomposition of *L2* ligand (expected, 58.1%). The amount of residue above 607 °C is 17.4% (expected, 11.2%, assuming pure FeO). Hence the complex was less thermally stable (T_{dec} = 189 °C) than the corresponding Co(II) complex (**Complex 11;** T_{dec} = 222 °C).

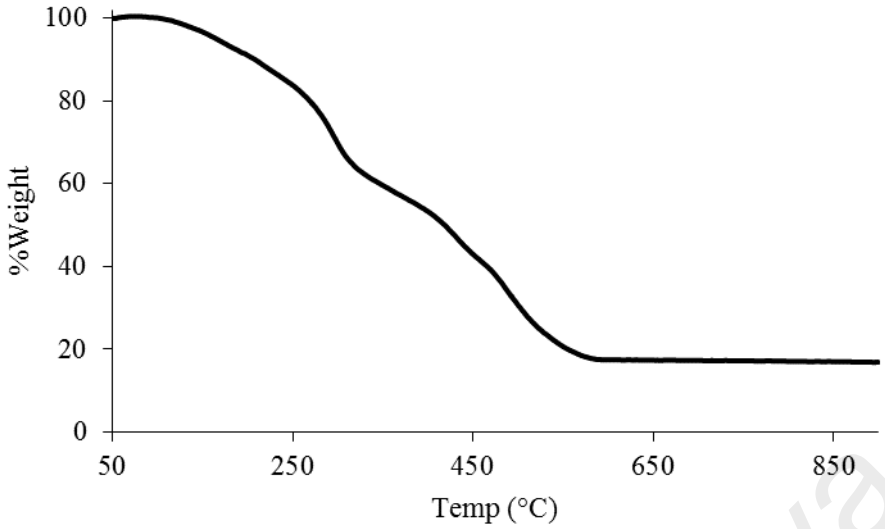

Figure 4.143 TGA of **Complex 12**

4.3.6 Reaction of copper(II) hexadecanoate with L2

Copper(II) hexadecanoate ($[Cu_2(CH_3(CH_2)_{14}COO)_4]$) reacted with *L2* (mole ratio 1:1) to give a green powder (**Complex 13**), and the yield was 85.5%. Its solubility was similar to the previously discussed complexes.

The **elemental analytical** data for the complex (64.1% C; 8.6% H; 7.3% N) are in excellent agreement with those calculated for the repeat unit $CuC_{47}H_{73}N_5O_5S$ (63.8% C; 8.3% H; 7.9% N; formula weight, 883.72 g mol^{-1}). Combining these with the spectroscopic data discussed below, its proposed structural formula is $\{[Cu(CH_3(CH_2)_{14}COO)_2(L2)].H_2O\}_n$, which is similar to **Complex 9** $\{[Cu(CH_3COO)_2(L2)].H_2O\}_n$.

Its **FTIR** spectrum (**Table 4.6**; **Figure 4.144**) shows the presence of the expected functional groups. The ΔCOO value was 124 cm^{-1}, suggesting chelating CH_3COO^- ligands.

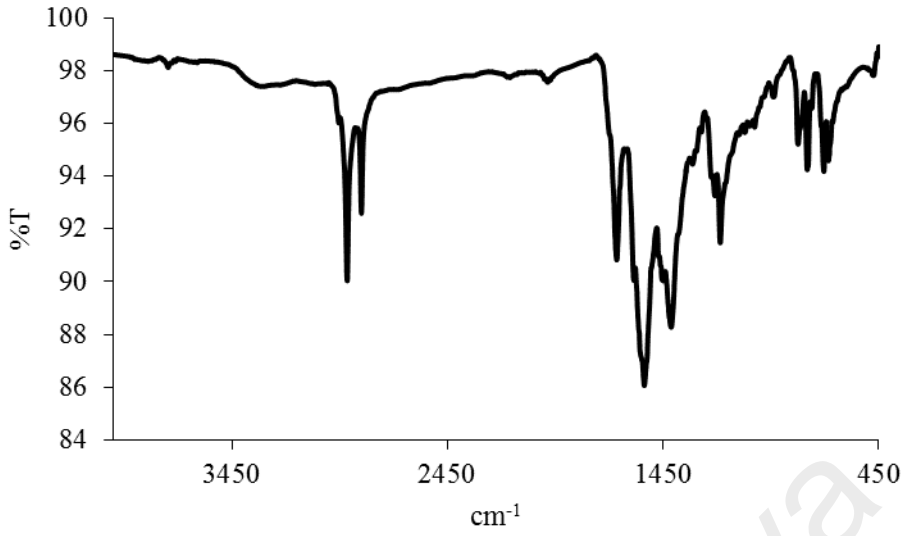

Figure 4.144 FTIR spectrum of **Complex 13**

Its **UV-vis** spectrum in DMSO (**Figure 4.145**) shows a broad *d-d* bands at 657 nm (ε_{max}, 166.7 M^{-1} cm^{-1}) and an intense LMCT band at 265 nm (ε_{max}, 4076 M^{-1} cm^{-1}). The results were similar to **Complex 9**, and may be similarly explained.

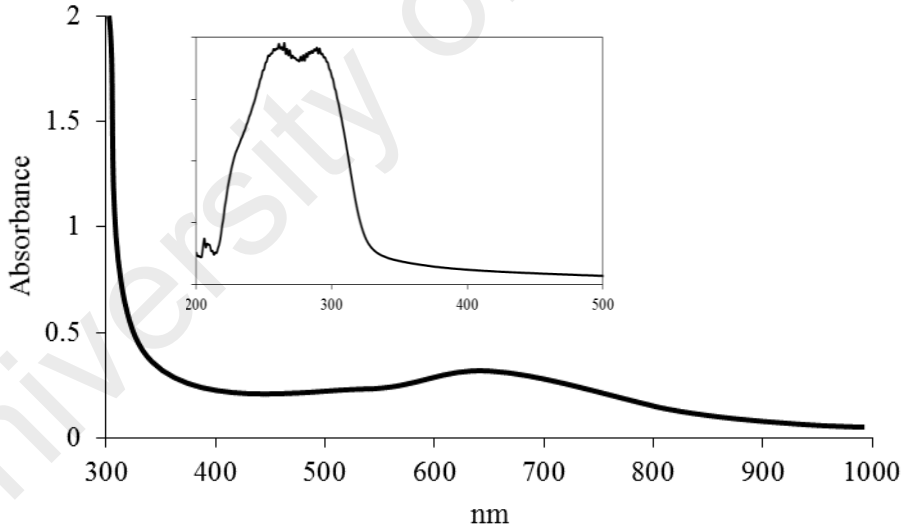

Figure 4.145 UV-vis spectrum of **Complex 13**

Its E_o value, calculated from λ_{edge} = 337 nm, was 3.6 eV. This is slightly narrower than **Complex 9** (3.8 eV), which indicates that the long alkyl chain has insignificant effect on its E_o.

Upon excitation at 265 nm (LMCT transition), its **fluorescence** spectrum shows four overlapping peaks at λ_{max} 359 nm, 416 nm, 464 nm and 569 nm (**Figure 4.146**). These suggest four different paths for the excited complex to return to the ground state. Its E_o, calculated from λ_{edge} = 646 nm, was 1.9 eV. Its Stokes shift was 199 nm.

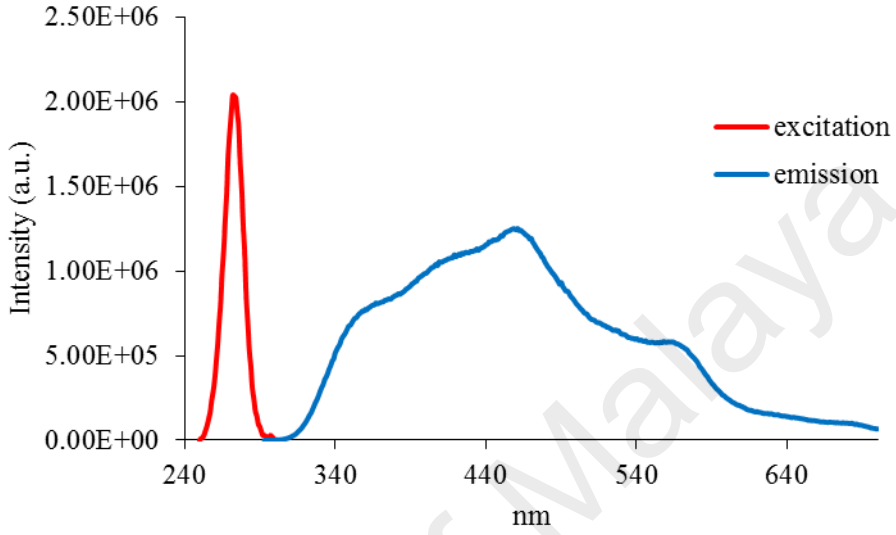

Figure 4.146 Fluorescence spectrum of **Complex 13** (λ_{ex} = 265 nm)

Its $\boldsymbol{\tau}$, calculated as before from its **decay** curve (**Figure 4.147**), was 2.8 ns. This is lower than **Complex 9** ({[Cu(CH$_3$COO)$_2$(L2)].H$_2$O}$_n$; $\boldsymbol{\tau}$ = 3.8 ns), suggesting that the long alkyl chain was less effective on stabilising the excited complex.

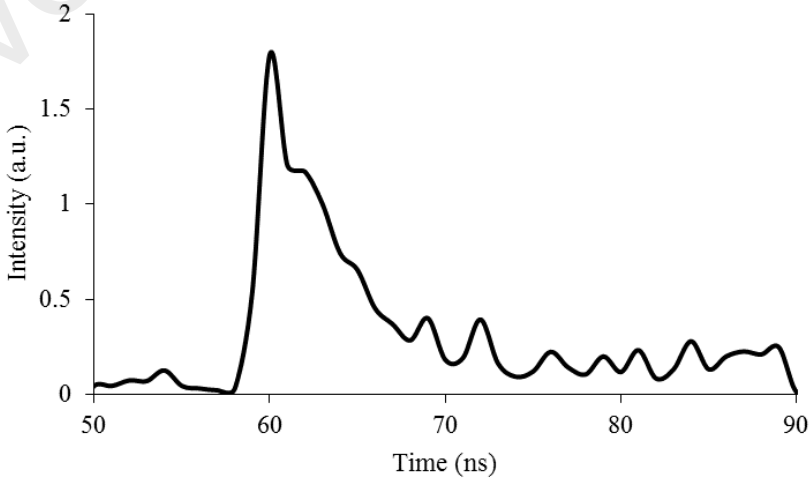

Figure 4.147 Fluorescence decay of **Complex 13**

Upon excitation at 657 nm, (*d-d* transition), its **fluorescence** spectrum shows a peak at λ_{max} 680 nm (**Figure 4.148**). Its E_o, calculated from λ_{edge} = 683 nm, was 1.8 eV and its $\boldsymbol{\tau}$ value, calculated as before from its **decay** curve, was 2.7 ns. Additionally, its Stokes shift was 23 nm.

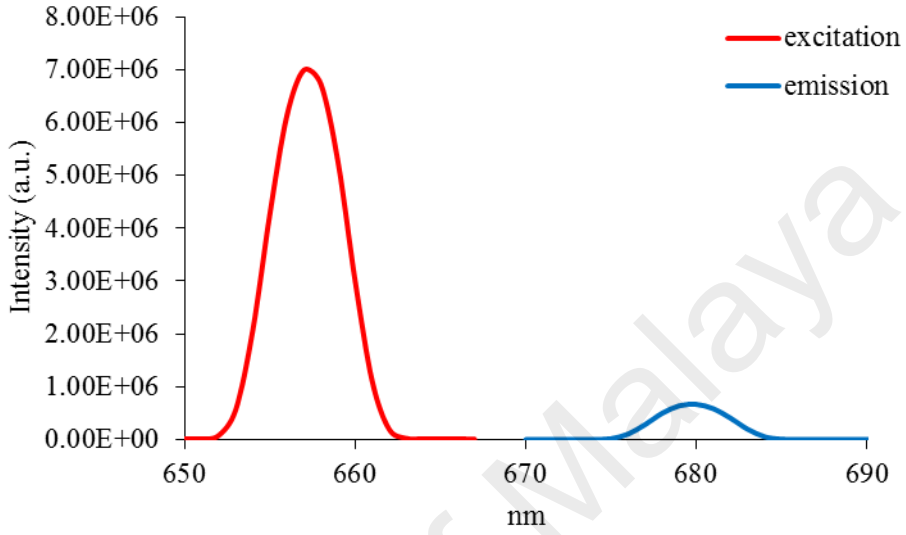

Figure 4.148 Fluorescence spectrum of **Complex 13** (λ_{ex} = 657 nm)

The **CV** (**Figure 4.149**), recorded cathodically from 0 V within the potential window of -1.5 V to +1.5 V, showed no distinctive reduction peak. On reversing the voltage, there was a peak at +1.06 V, assigned to ligand-based oxidation process. The results indicates that Cu(II) ion of **Complex 13** was redox inactive. Thus, its E_e cannot be calculated.

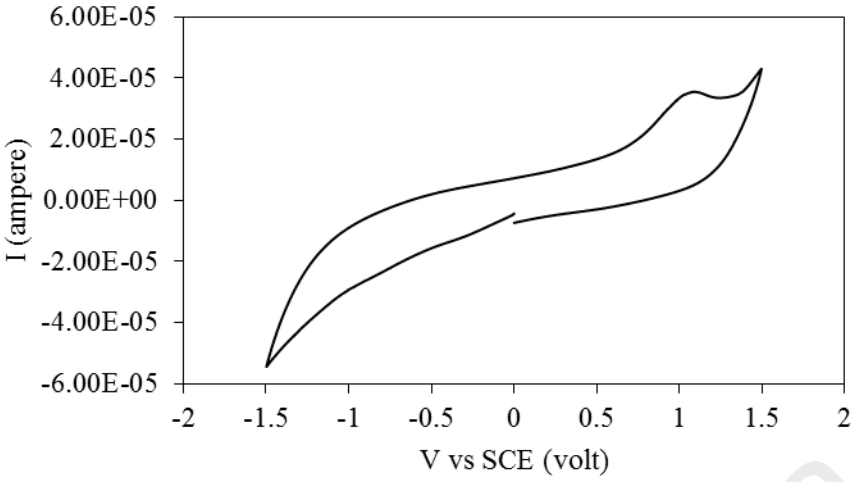

Figure 4.149 CV of **Complex 13**

Its μ_{eff} value, calculated as before from the values of FM = 883.72 g mol^{-1} (repeat unit), χ_g = 0.57 x 10^{-6} cm^3 g^{-1}, χ_M = 5.03 x 10^{-4} cm^3 mol^{-1}, and χ_{dia} = -5.29 x 10^{-4} cm^3 mol^{-1}, was 1.61 B.M. at 298 K. This value is slightly lower than **Complex 9** ({[$Cu(CH_3COO)_2(L2)$].H_2O}$_n$; 1.47 B.M.), indicating a weak antiferromagnetic interaction.

Its **TGA** trace (**Figure 4.150**) shows the total weight loss of 87.1% in the temperature range of 142 – 900 °C, assigned to the evaporation one H_2O molecule and decomposition of two $CH_3(CH_2)_{14}COO$ and *L2* ligands (expected, 92.7%). The amount of residue at temperatures above 900 ^oC cannot be calculated due to incomplete combustion of the organic ligands (expected, 7.3% assuming pure CuO) Hence, **Complex 11** (T_{dec} = 160 ^oC) was as thermally stable as **Complex 9** (T_{dec} = 162 ^oC). From this, it may be suggested that the long alkyl chain has an insignificant effect on the thermal stability of this complex.

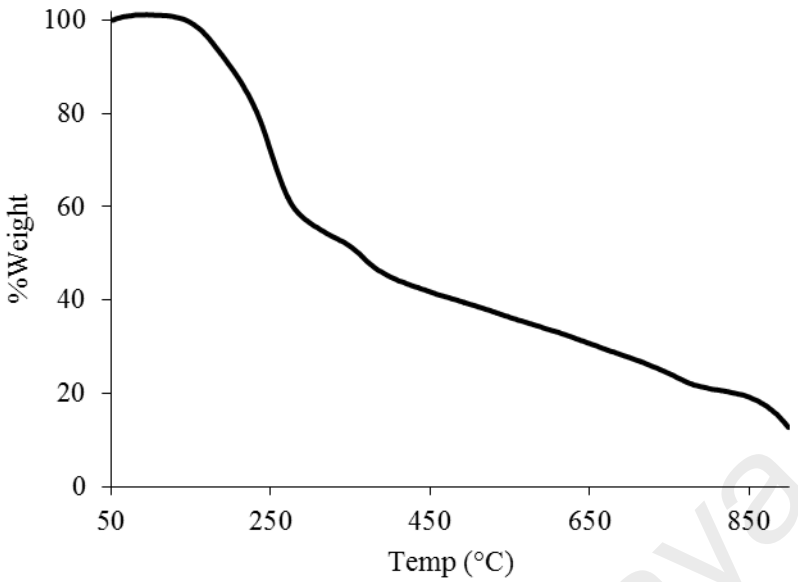

Figure 4.150 TGA of **Complex 13**

Its **DSC** scan (**Figure 4.151**), recorded from 25 ^{o}C to 150 ^{o}C for one heating-cooling cycle, showed two endothermic peak at 54.8 $^{\circ}$C (ΔH = +22.6 kJ mol^{-1}) assigned to the breaking of H-bond of H_2O, and a broad peaks at 73 $^{\circ}$C (ΔH = +25.3 kJ mol^{-1}) assigned to the breaking of Cu-OOC$(CH_2)_{14}CH_3$. On cooling, there was one exothermic peak at 43 $^{\circ}$C (ΔH = -44.9 kJ mol^{-1}), which is tentatively assigned to the formation of H-bond of H_2O. According to **POM** observation, there was no optical texture formed during cooling process.

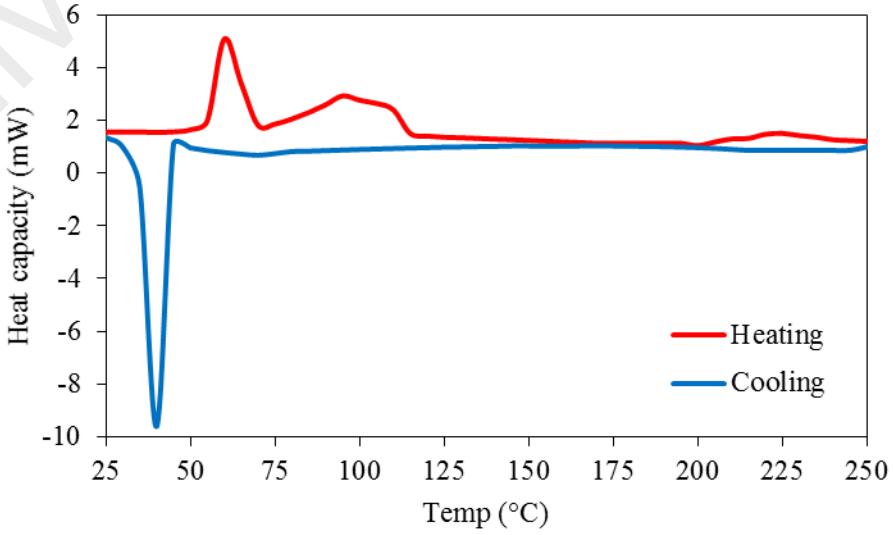

Figure 4.151 DSC of **Complex 13**

4.3.7 Reaction of nickel(II) hexadecanoate with L2

Nickel(II) hexadecanoate ($[Ni(CH_3(CH_2)_{14}COO)_2(H_2O)_2].3H_2O$) reacted with *L2* (mole ratio 1:1) to give a yellow-green powder (**Complex 14**), and the yield was 66.7%. Its solubility was similar to the previously discussed complexes.

The **elemental analytical** data for the complex (63.0% C; 8.2% H; 8.1% N) are in excellent agreement with those calculated for the repeat unit $NiC_{47}H_{75}N_5O_6S$ (62.9% C; 8.4% H; 7.8% N; formula weight, 896.89 g mol^{-1}). Combining these with the spectroscopic data discussed below, its proposed structural formula is $\{[Ni(CH_3(CH_2)_{14}COO)_2(L2)].2H_2O\}_n$, which is similar to **Complex 10** ($\{[Ni(CH_3COO)_2(L2)].2H_2O\}_n$).

Its **FTIR** spectrum (**Table 4.6**; **Figure 4.152**) shows the presence of the expected functional groups. The ΔCOO value was 133 cm^{-1}, suggesting chelating $CH_3(CH_2)_{14}COO^-$ ligand.

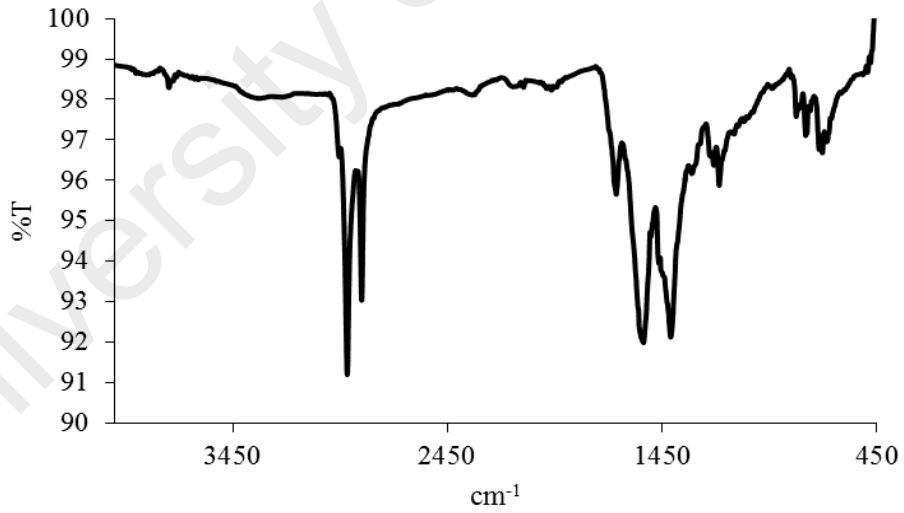

Figure 4.152 FTIR spectrum of **Complex 14**

Its **UV-vis** spectrum in DMSO (**Figure 4.153**) shows a broad band at 800 nm (ε_{max}, 127.7 M^{-1} cm^{-1}) assigned to $^3A_{2g}$ (F) → $^3T_{2g}$, (F) 550 nm (ε_{max}, 229 M^{-1} cm^{-1}) assigned to $^3A_{2g}$ (F) → $^3T_{1g}$ (F), and 398 nm (ε_{max}, 378 $M^{-1}cm^{-1}$) assigned to $^3A_{2g}$ (F)→ $^3T_{1g}$ (P) transitions. These electronic transitions suggest an octahedral

geometry at Ni(II) centre. An intense MLCT band is also observed at 261 nm (ε_{max}, 1016 M^{-1} cm^{-1}).

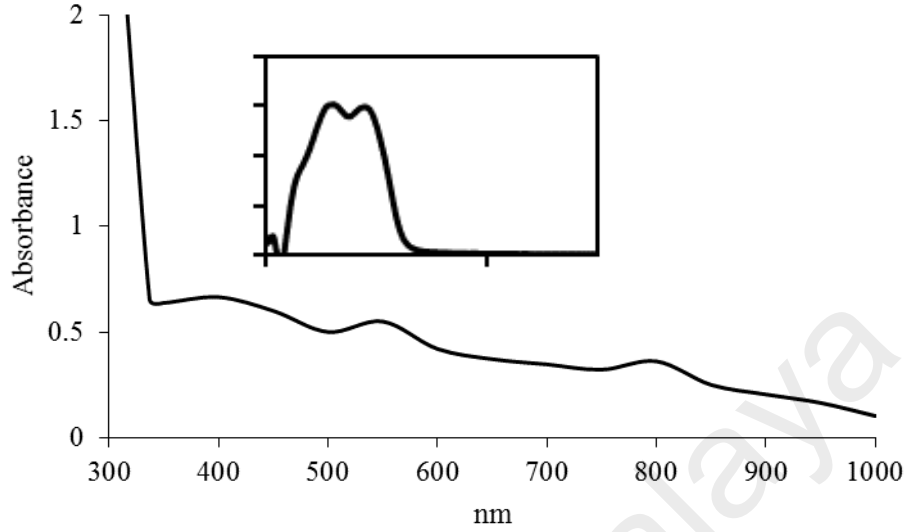

Figure 4.153 UV-vis spectrum of **Complex 14**

Its E_o value, calculated from λ_{edge} = 337 nm, was 3.6 eV. The value is the same as **Complex 10** ({[$Ni(CH_3COO)_2(L2)].2H_2O$}$_n$; 3.6 eV).

Upon excitation at 261 nm (MLCT band), its **fluorescence** spectrum shows broad overlapping peaks λ_{max} 373 nm, 405 nm, 445 nm and 576 nm (**Figure 4.154**). These suggest four different paths for the excited complex to return to the ground state. Its E_o, calculated from λ_{edge} = 627 nm, was 1.9 eV. The value is slightly higher than **Complex 10** (1.8 eV). The value of its $\boldsymbol{\tau}$, calculated as before from its **decay** curve (**Figure 4.155**), was 2.8 ns. Moreover, its Stokes shift was 184 nm.

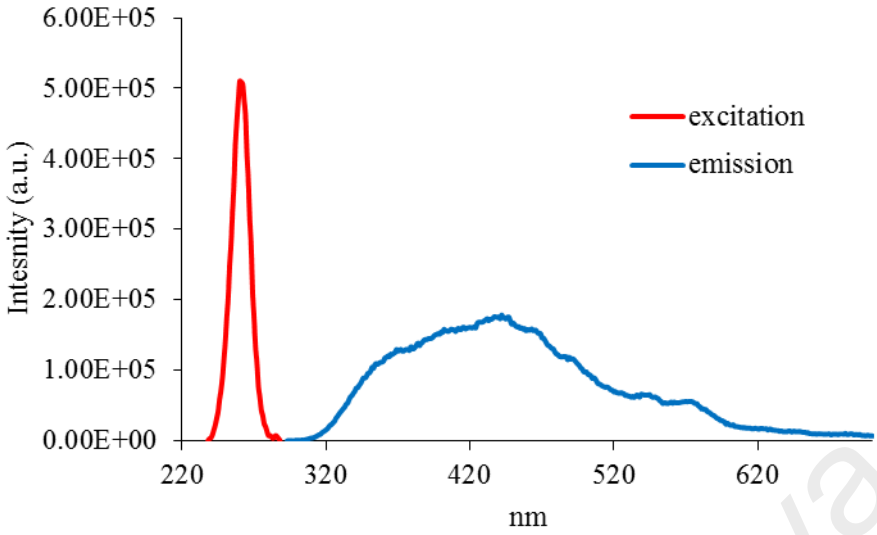

Figure 4.154 Fluorescence spectrum of **Complex 14** (λ_{ex} = 261 nm)

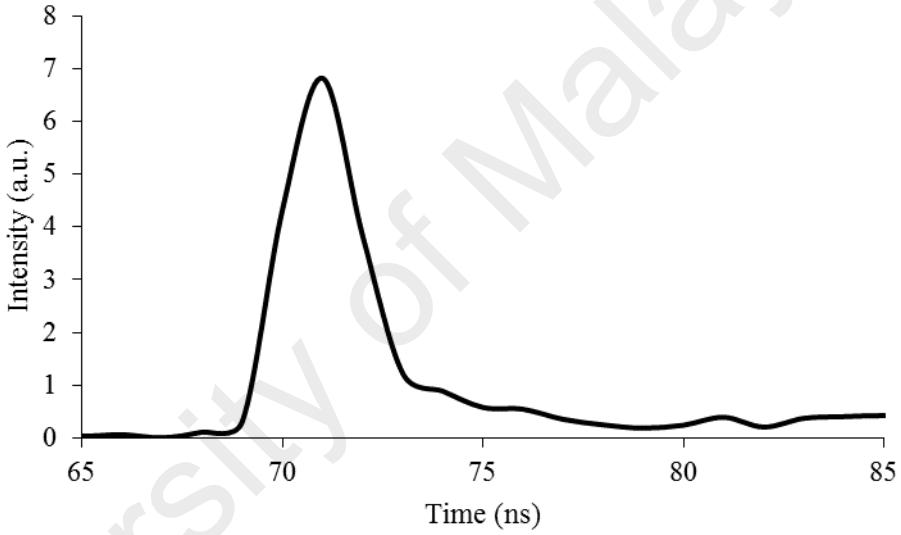

Figure 4.155 Fluorescence decay of **Complex 14**

However, upon excitation at 398 nm, (*d-d* transition), its **fluorescence** spectrum shows a peak at λ_{max} 419 nm (**Figure 4.156)**. Its E_o, calculated from λ_{edge} = 424 nm, was 2.9 eV. Its τ, calculated as before from its **decay** curve, was 3.5 ns. Its Stokes shift was 30 nm.

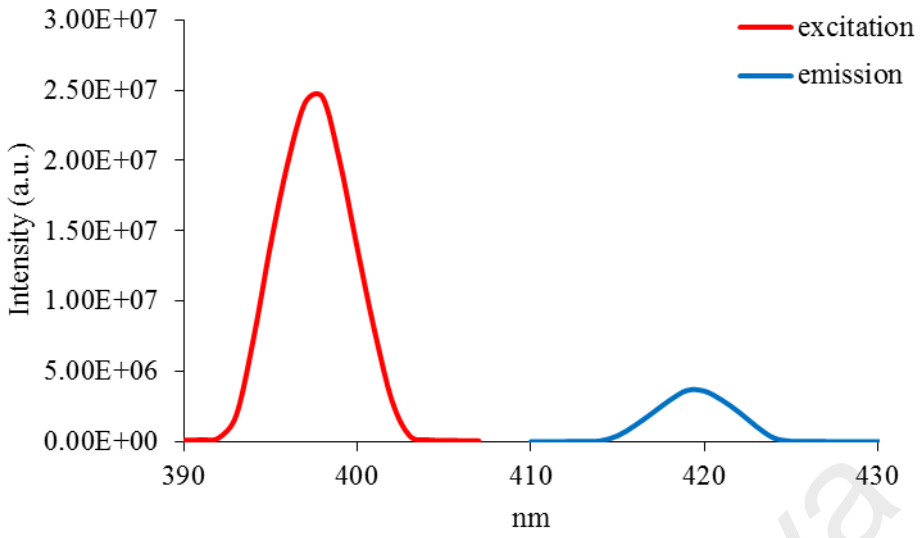

Figure 4.156 Fluorescence spectrum of **Complex 14** (λ_{ex} = 398 nm)

Its **CV** (**Figure 4.157**), recorded anodically from 0 V within the potential window of +1.5 V to -1.5 V, showed one oxidation peak at +1.02 V. This is assigned to ligand-based oxidation. The result suggests that Ni(II) atom in the complex was redox inactive. Hence, its E_e cannot be calculated.

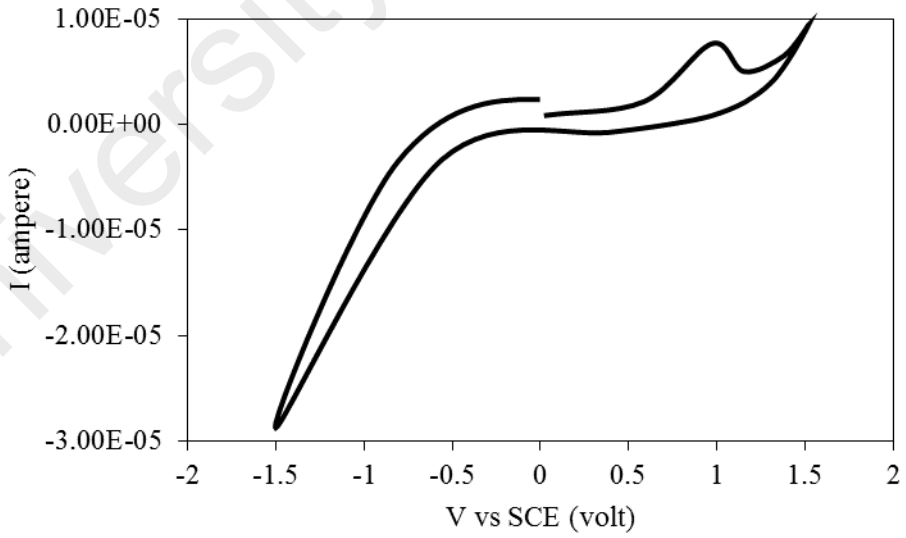

Figure 4.157 CV of **Complex 14**

Its μ_{eff} value, calculated as before from the values of FM = 896.89 g mol^{-1} (repeat unit), χ_g = 4.53 x 10^{-6} cm^3 g^{-1}, χ_M = 4.06 x 10^{-3} cm^3 mol^{-1}, and χ_{dia} = -5.52 x 10^{-4} cm^3 mol^{-1}, was 3.34 B.M. at 298 K. This is significantly higher than

the expected μ_{eff} value for one Ni(II) atom ($3d^8$; 2 unpaired electrons; 2.83 B.M.), indicating a significant ferromagnetic interaction between the metal centres [41].

Its **TGA** trace (**Figure 4.158**) shows a total weight loss of 83.6% in the temperature range of 100 – 900 °C, assigned to the evaporation of two coordinated H_2O molecules and decomposition of two $CH_3(CH_2)_{14}COO^-$ and *L2* ligands (expected, 93.4%). The amount of residue above 900 °C was 16.4% (expected, 6.6% assuming pure NiO). Hence, the complex (T_{dec} = 170 °C) was significantly more thermally stable than **Complex 10** ($\{[Ni(CH_3COO)_2(H_2O)_2(L2)]\}_n$; T_{dec} = 136 °C).

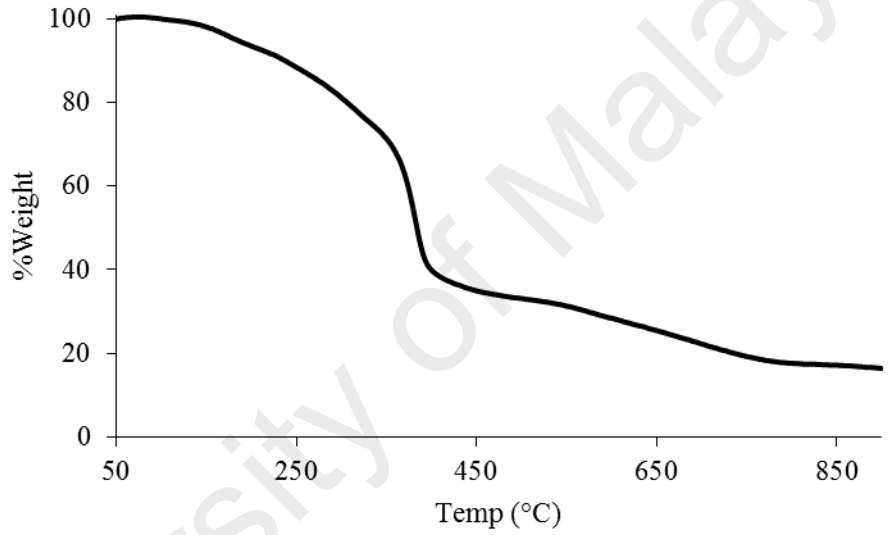

Figure 4.158 TGA of **Complex 14**

Its **DSC** scan was recorded from 25 to 125 °C for one heating-and-cooling cycle (**Figure 4.159**). On heating, there were two overlapping endothermic peaks at 56.3 °C (ΔH = +64.2 kJ mol^{-1}), assigned to Cr_1-to-Cr_2 transition, and Cr_2-to-Cr_3 transition; and a peak at 85 °C (ΔH = +6.9 kJ mol^{-1}), assigned to Cr_3-to-M transition. On cooling, there were an exothermic peak at 80 °C (ΔH = -7.6 kJ mol^{-1}), assigned to M-to-Cr_1 transition.

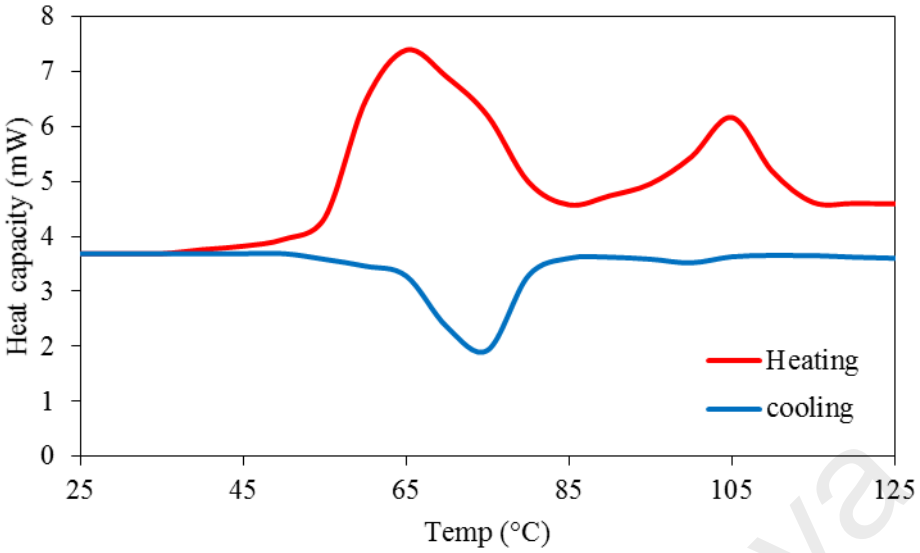

Figure 4.159 DSC of **Complex 14**

The **POM** was recorded for two heating-cooling cycles in the temperature range 25 – 120 °C. On cooling from 120 °C, an optical texture was initially observed at about 80 °C, which then solidified at 63 °C (**Figure 4.160**).

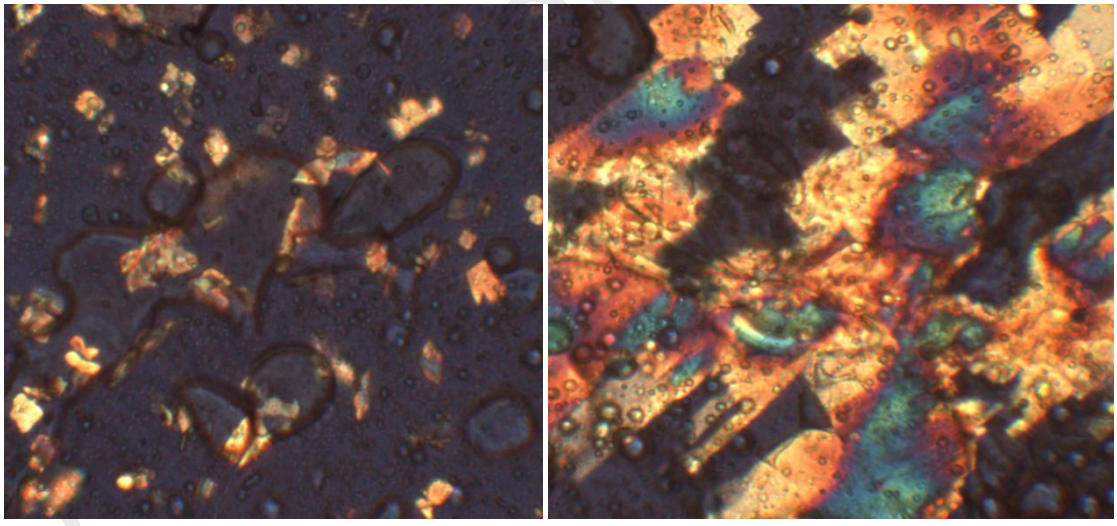

(a) (b)

Figure 4.160 The photomicrographs of **Complex 14** on cooling from 120 °C: (a) at 80 °C; and (b) at 63 °C (solid).

4.3.8 Reaction of cobaltII) hexadecanoate with L2

Cobalt(II) hexadecanoate ($[Co(CH_3(CH_2)_{14}COO)_2(H_2O)_2].4H_2O$) reacted with *L2* (mole ratio 1:1) to give a pale purple powder (**Complex 15**), and the yield was 82.6%. Its solubility was similar to the previously discussed complexes.

The **elemental analytical** data for the complex (63.0% C; 8.7% H; 7.9% N) are in excellent agreement with those calculated for the repeat unit $CoC_{47}H_{75}N_5O_6S$ (62.9% C; 8.4% H; 7.8% N; formula weight, 897.13 g mol^{-1}). Combining these with the spectroscopic data discussed below, its proposed structural formula for **Complex 15** is $\{[Co(CH_3(CH_2)_{14}COO)_2(L2)].2H_2O\}_n$, which is similar to **Complex 11** $\{[Co(CH_3COO)_2(L2)].2H_2O\}_n$.

Its **FTIR** spectrum (**Table 4.6**; **Figure 4.161**) shows the presence of the expected functional groups. The ΔCOO value was 73 cm^{-1}, suggesting chelating $CH_3(CH_2)_{14}COO^-$ ligands.

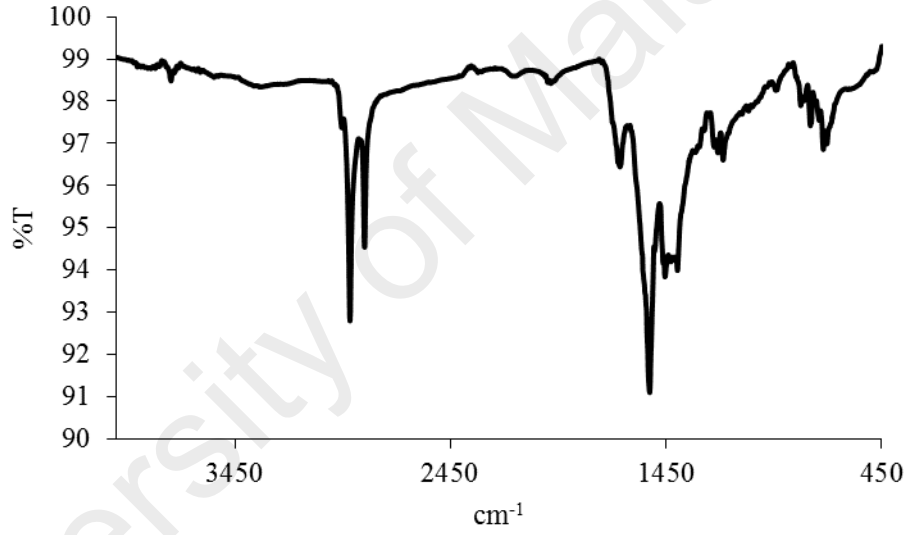

Figure 4.161 FTIR spectrum of **Complex 15**

Its **UV-vis** spectrum in DMSO (**Figure 4.162**) shows broad overlapping peaks at 830 nm (ε_{max}, 91.9 M^{-1} cm^{-1}) assigned to $^4T_{1g}$ (F) → $^4T_{2g}$ (F), 652 nm (ε_{max}, 167.7 M^{-1} cm^{-1}), assigned to $^4T_{1g}$ (F) → $^4T_{1g}$ (P), and 551 nm (ε_{max}, 183.5 M^{-1} cm^{-1}), assigned to $^4T_{1g}$ (F) → $^4A_{2g}$ (F) transitions. These electronic transitions suggest an octahedral geometry at high-spin Co(II) centres [36]. Also observed is an intense MLCT band at 249 nm (ε_{max}, 1712 M^{-1} cm^{-1}).

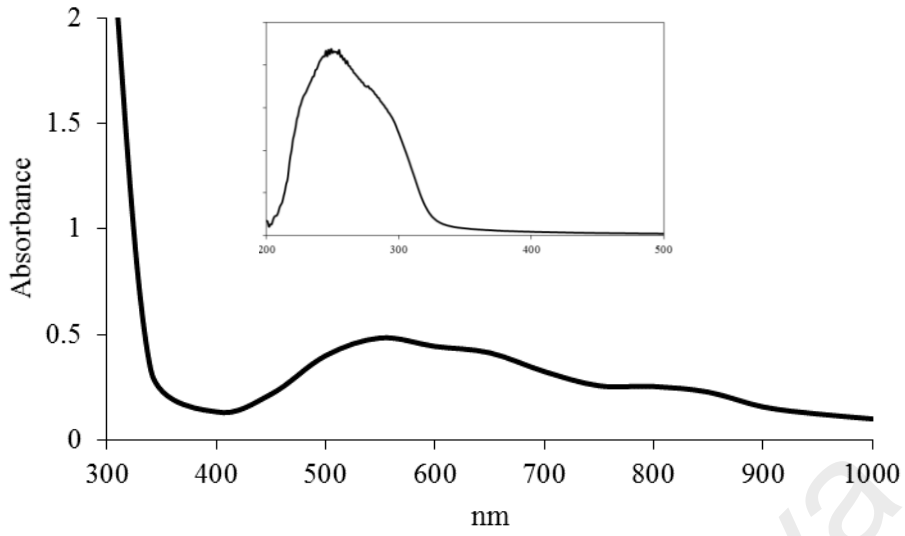

Figure 4.162 UV-vis spectrum of **Complex 15**

Its E_o value, calculated from λ_{edge} = 340 nm, was 3.6 eV. This value is slightly lower than **Complex 11** ($\{[Co(CH_3COO)_2(L2)].2H_2O\}_n$; 3.8 eV).

Upon excitation at 249 nm (MLCT transition), its **fluorescence** spectrum shows three peaks at λ_{max} 352 nm, 465 nm and 576 nm (**Figure 4.163**). These suggest three different paths for the excited complex to return to the ground state. Its E_o, calculated from λ_{edge} = 630 nm, was 1.9 eV. This value is slightly lower than **Complex 11** (2.1 eV). Its Stokes shift was 216 nm.

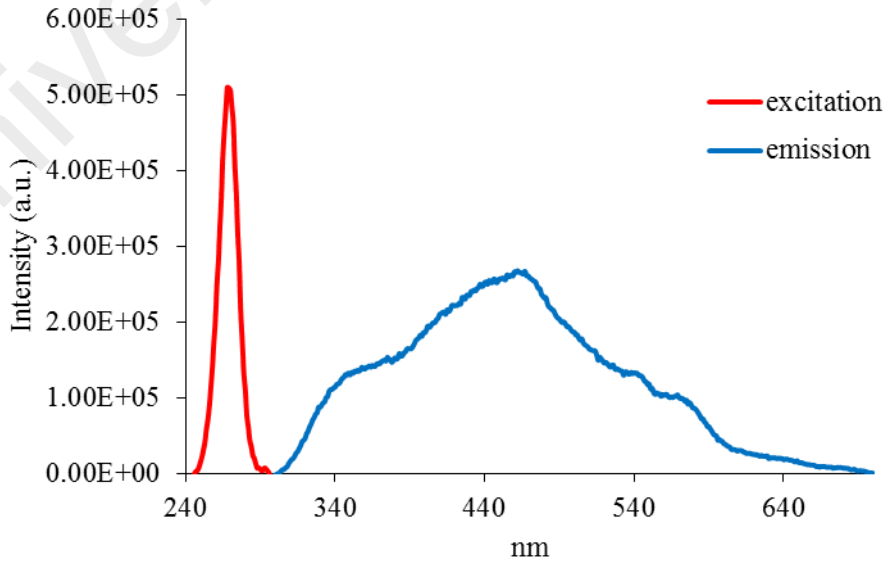

Figure 4.163 Fluorescence spectrum of **Complex 15** (λ_{ex} = 249 nm)

The value of its τ, calculated as before from its **decay** curve (**Figure 4.164**), was 2.9 ns. Hence, the excited state lifetime of the complex was significantly shorter than **Complex 11** (3.4 ns).

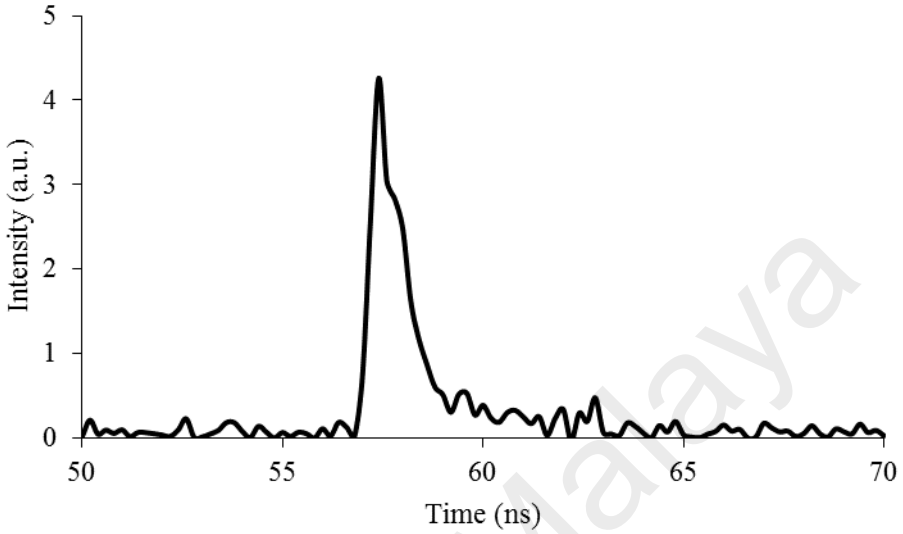

Figure 4.164 Fluorescence decay of **Complex 15**

However, upon excitation at 551 nm (*d-d* transition), its **fluorescence** spectrum shows a peak at λ_{max} 577 nm (**Figure 4.165)**. Its E_o (λ_{edge} = 583 nm) was 2.1 eV, and its τ value, calculated from its **decay** curve, was 3.0 ns. Additionally, its Stokes shift was 26 nm.

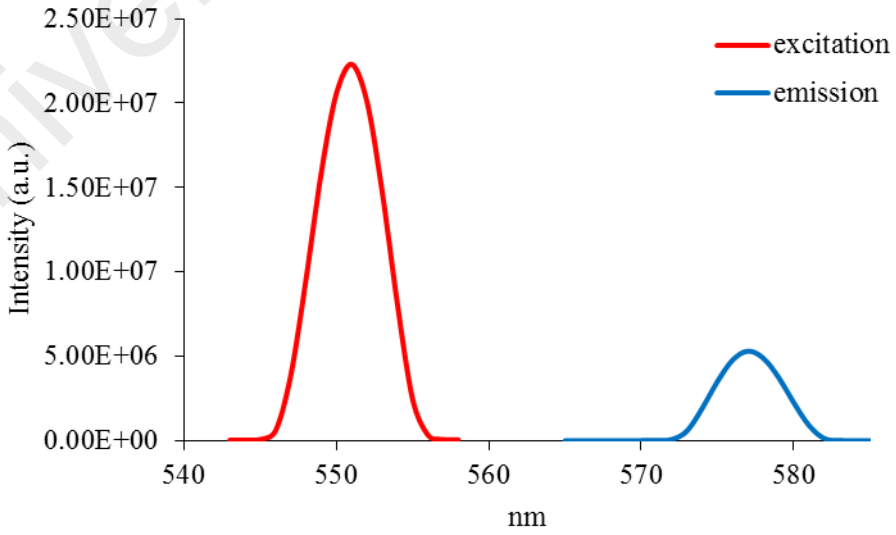

Figure 4.165 Fluorescence spectrum of **Complex 15**

Its **CV** (**Figure 4.166**), recorded anodically from 0 V within the potential window of +1.5 V to -1.5 V, showed one anodic peak at +1.22 V when the potential was increased from 0 V to +1.5 V. This is assigned to the irreversible oxidation of [Co(II)] to [Co(III)] [42]. However, there was no distinctive cathodic peak observed when the potential was decreased from +1.5 V to -1.5 V. Accordingly, its E_e cannot be calculated.

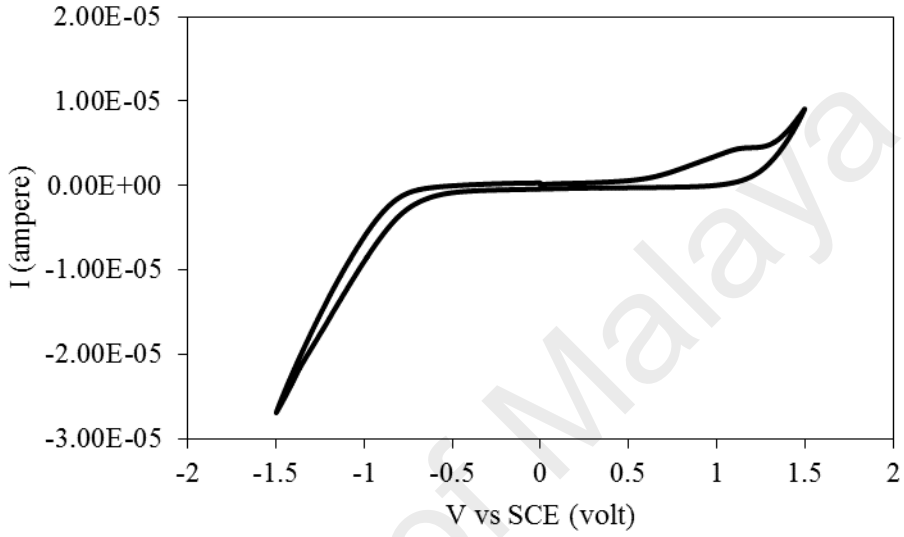

Figure 4.166 CV of **Complex 15**

Its μ_{eff} value, calculated as before from the values of FM = 897.13 g mol^{-1} (repeat unit), χ_g = 5.71 x 10^{-5} cm^3 g^{-1}, χ_M = 5.12 x 10^{-3} cm^3 mol^{-1}, and χ_{dia} = -5.52 x 10^{-4} cm^3 mol^{-1}, was 3.69 B.M. at 298 K. This value is slightly lower than the expected value for a high-spin Co(II) atom (d^7) (3.87 B.M.), suggesting a weak antiferromagnetic interaction between the metal centres [43].

Its **TGA** trace (**Figure 4.167**) shows a total weight loss 75.8% in the temperature range of 120 - 900 °C, assigned to the evaporation of two H_2O molecules and decomposition of two $CH_3(CH_2)_{14}COO^-$ and *L2* ligands (expected, 93.4%). The amount of residue above 900 ^oC cannot be determined due to incomplete combustion of the organic ligands. Hence, **Complex 15** (T_{dec} = 231 °C) was as thermally stable as **Complex 11** ({[Co($CH_3COO)_2$(L2)].2H_2O}$_n$; T_{dec} = 222 °C).

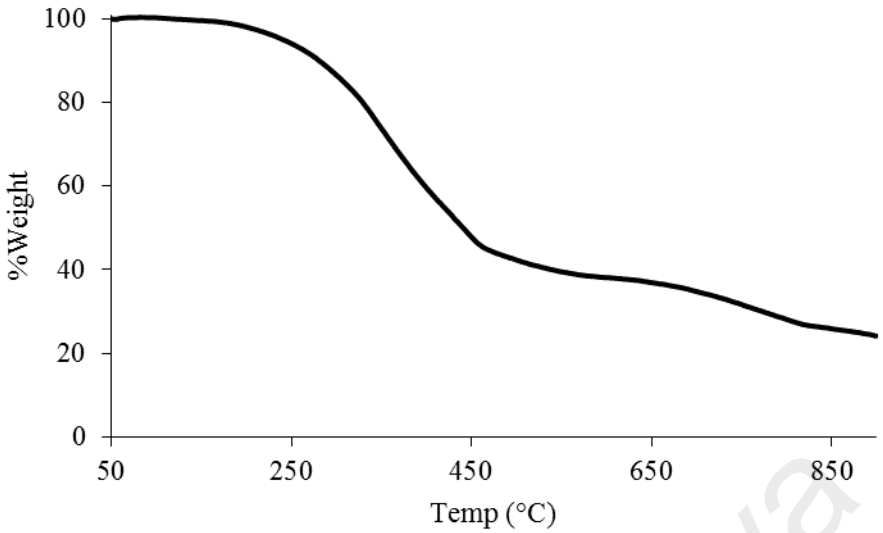

Figure 4.167 TGA of **Complex 15**

Its **DSC** scan (**Figure 4.168**) was done from 25 to 225 ºC for one heating-cooling cycle. On heating, there were two endothermic peaks at 57.3 ºC (ΔH = +23.7 kJ mol^{-1}) assigned to Cr_1-to-Cr_2 transition, and at 75 ºC (ΔH = +131 kJ mol^{-1}) assigned to Cr_2-to-M_1 and M_1-to-M_2 transitions. However, there was no peak on cooling.

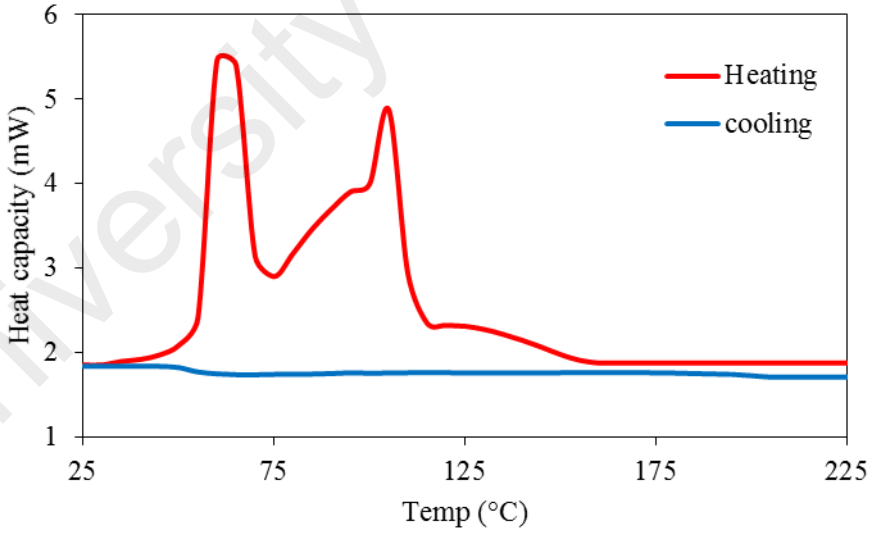

Figure 4.168 DSC of **Complex 15**

The **POM** for **Complex 15** did not show any optical texture. It might be due to the decomposition occurred after clearing process. This is consistent with the DSC scan result.

4.3.9 Reaction of iron(II) hexadecanoate with L2

Iron(II) hexadecanoate ($[Fe(CH_3(CH_2)_{14}COO)_2(H_2O)_2].4H_2O$) reacted with *L2* (mole ratio 1:1) to give an orange-brown powder (**Complex 16**), and the yield was 62.6%. Its solubility was similar to the previously discussed complexes.

The **elemental analytical** data for the complex (62.9% C; 8.0% H; 7.3% N) are in excellent agreement with those calculated for the repeat unit $FeC_{47}H_{75}N_5O_6S$ (63.1% C; 8.5% H; 7.8% N; formula weight, 894.04 g mol^{-1}). Combining these with the spectroscopic data discussed below, its proposed structural formula for **Complex 16** is $\{[Fe(CH_3(CH_2)_{14}COO)_2(L2)].2H_2O\}_n$, which is similar to **Complex 12** $\{[Fe(CH_3COO)_2(L2)].2H_2O\}_n$.

Its **FTIR** spectrum (**Table 4.6**; **Figure 4.169**) shows the presence of the expected functional groups. The ΔCOO value was 81 cm^{-1}, suggesting chelating $CH_3(CH_2)_{14}COO^-$ ligands.

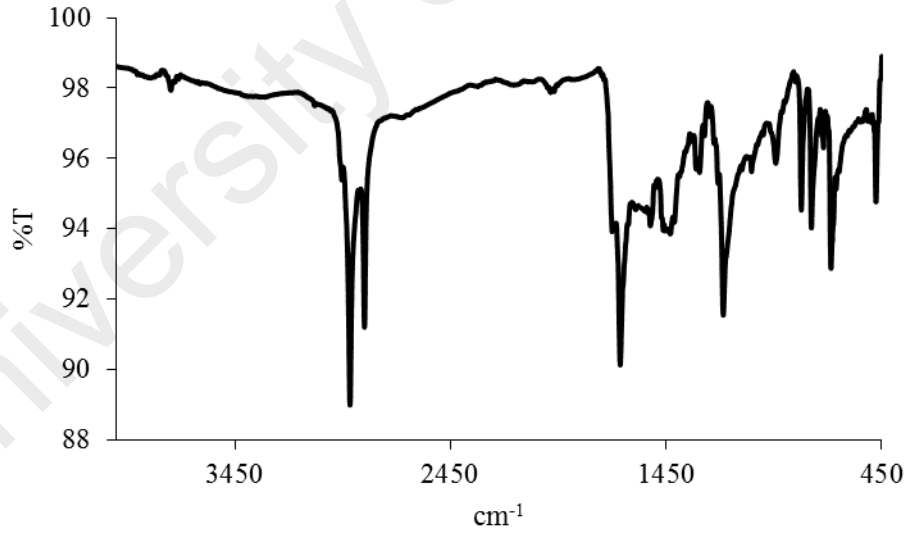

Figure 4.169 FTIR spectrum of **Complex 16**

Its **UV-vis** spectrum in DMSO (**Figure 4.170**) shows a broad band at 863 nm (ε_{max}= 163 M^{-1} cm^{-1}) assigned to ${}^5T_{2g} \rightarrow {}^5E_g$ electronic transition, and an intense band at 313 nm (ε_{max}, 3414 M^{-1} cm^{-1}) assigned to MLCT transition. This suggest the geometry at Fe(II) centre was octahedral.

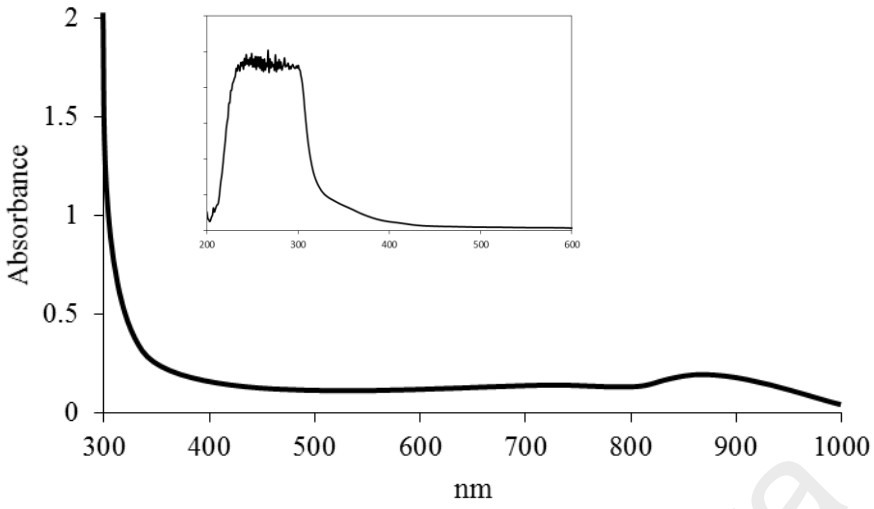

Figure 4.170 UV-vis spectrum of **Complex 16**

Its E_o value, calculated from λ_{edge} = 341 nm, was 3.6 eV. This value is slightly higher than **Complex 12** (3.5 eV).

Upon excitation at 313 nm (MLCT transition), its **fluorescence** spectrum shows four overlapping peaks at λ_{max} 365 nm, 411 nm, 465 nm and 545 nm (**Figure 4.171**). Its E_o, calculated from λ_{edge} = 647 nm, was 1.9 eV. This value is also significantly lower than **Complex 12** (2.7 eV). Its Stokes shift was 152 nm.

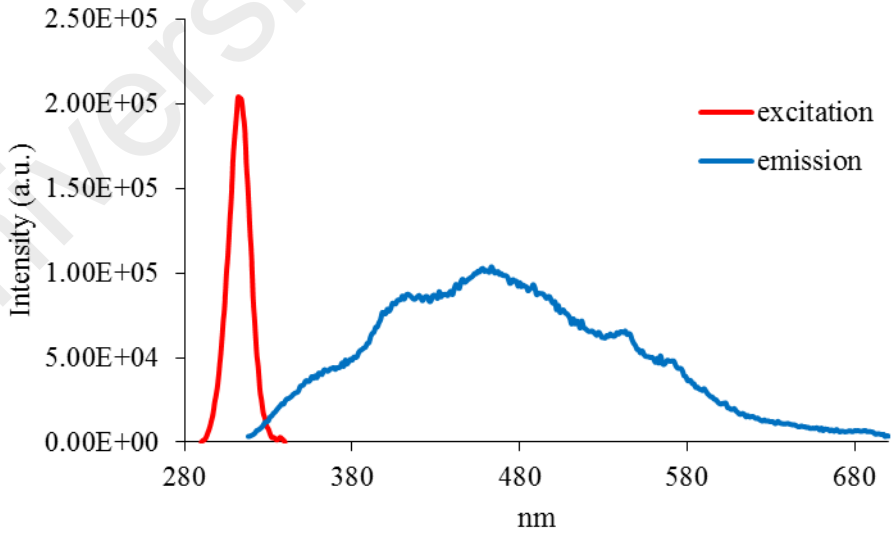

Figure 4.171 Fluorescence spectrum of **Complex 16** (λ_{ex} = 313 nm)

Its τ value, calculated as before from its **decay** curve (**Figure 4.172**), was 2.8 ns. Hence, the lifetime of excited complex was significantly less stable than **Complex 12** ($\{[Fe(CH_3COO)_2(L2)].2H_2O\}_n$; 3.7 ns).

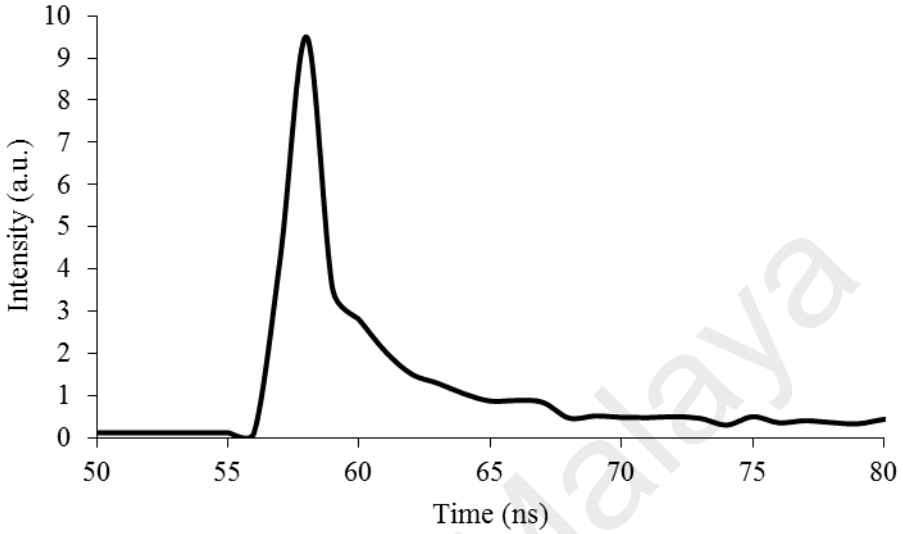

Figure 4.172 Fluorescence decay of **Complex 16**

Also, upon excitation at 863 nm (*d-d* transition), its **fluorescence** spectrum shows a peak at λ_{max} 882 nm (**Figure 4.173**). Its E_o, calculated from λ_{edge} = 888 nm, was 1.4 eV. This value is slightly higher than **Complex 12** (1.2 eV). Its τ value, calculated as before from its **decay** curve, was 1.1 ns. Its Stokes shift was 19 nm.

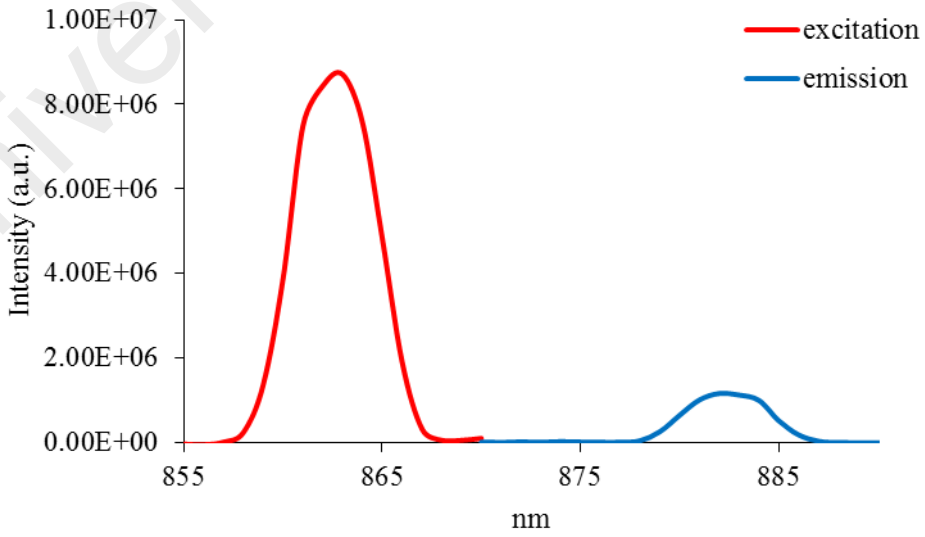

Figure 4.173 Fluorescence spectrum of **Complex 16** (λ_{ex} = 863 nm)

Its **CV** (**Figure 4.174**), recorded anodically from 0 V within the potential window of +1.5 V to -1.5 V, showed no distinctive peaks for oxidation and reduction which may be assigned to Fe(II) atom. This suggests that Fe(II) atom was redox inactive. Accordingly, its E_e cannot be calculated.

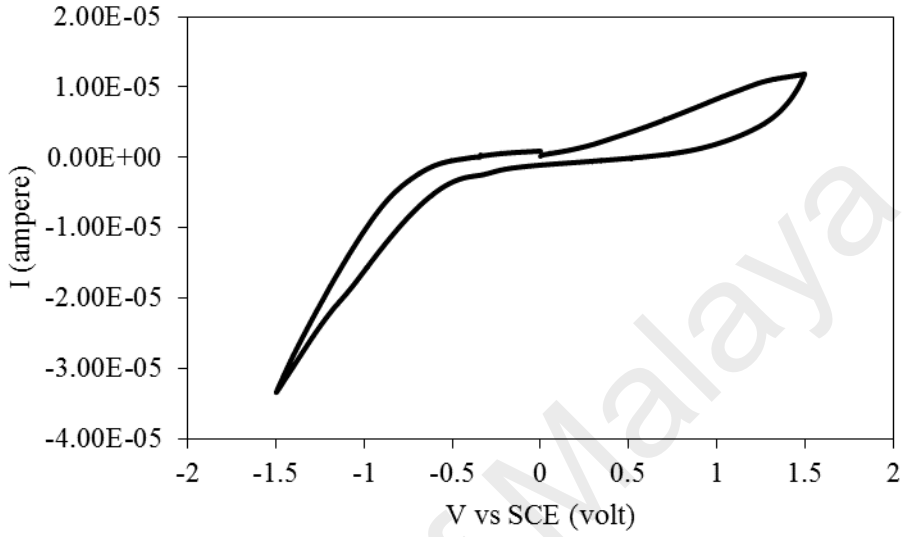

Figure 4.174 CV of **Complex 16**

Its $\boldsymbol{\mu_{eff}}$ value, calculated as before from the values of FM = 894.04 g mol^{-1}, χ_g = 7.5 x 10^{-6} cm^3 g^{-1}, χ_M = 6.72 x 10^{-3} cm^3 mol^{-1}, and χ_{dia} = -5.52 x 10^{-4} cm^3 mol^{-1}, was 4.18 B.M. at 298 K. It is lower than the spin-only value for one high-spin Fe(II) atom (d^6; 4.89 B.M.), suggesting an antiferromagnetic interaction between the metal centres [44].

Its **TGA** trace (**Figure 4.175**) shows a total weight loss of 91.6% on heating from about 158 ^oC to 900 ^oC, assigned to the evaporation of two H_2O molecules and decomposition of two $CH_3(CH_2)_{14}COO^-$ and *L2* ligands (expected, 93.6%). The amount of residue above 900 °C cannot be calculated due to incomplete combustion organic ligand process. Hence, the thermal stability of the complex (T_{dec} = 199 °C) was similar to **Complex 12** ($\{[Fe(CH_3COO)_2(L2)].2H_2O\}_n$; T_{dec} = 189 ^oC).

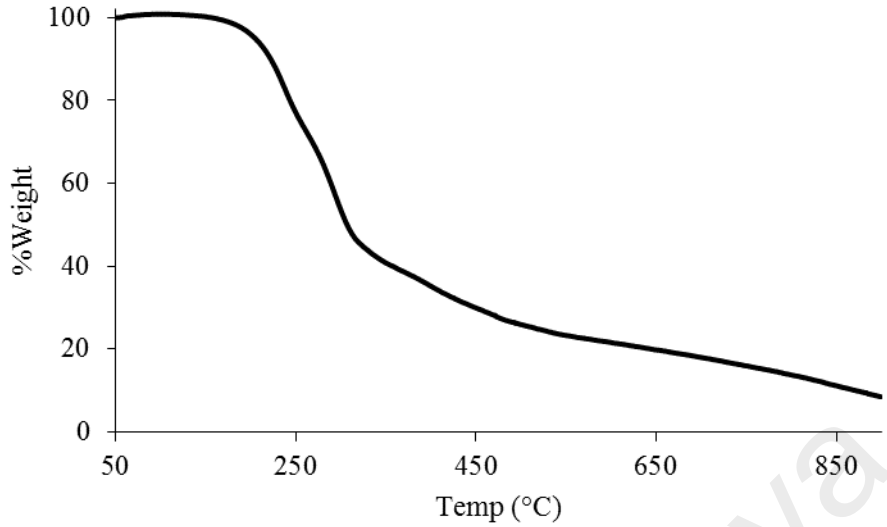

Figure 4.175 TGA of **Complex 16**

Its **DSC** scan (**Figure 4.176**) was recorded from 25 to 125 ºC for one heating-cooling cycle. On heating, there was a broad endothermic peak at 54.3 °C (ΔH = +39.5 kJ mol^{-1}), assigned to Cr_1-to-Cr_2 transition, and two overlapping peaks at about 80 °C (ΔH = +114 kJ mol^{-1}), assigned to Cr_2-M transition and M-to-I transition. On cooling, there was an exothermic peak at 95 °C (ΔH = -35.7 kJ mol^{-1}), assigned to I-to-M transition.

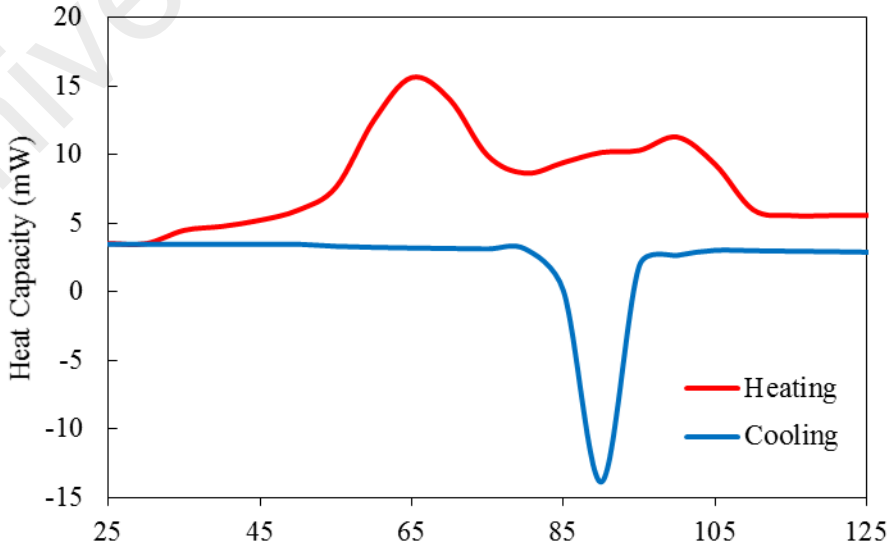

Figure 4.176 DSC of **Complex 16**

The **POM** for **Complex 16** was recorded for two heating-cooling cycles from 25 °C to 110 °C. On cooling from 110 °C, an optical texture was first observed at about 103 °C, then the sample solidified at 67 °C (**Figure 4.177**).

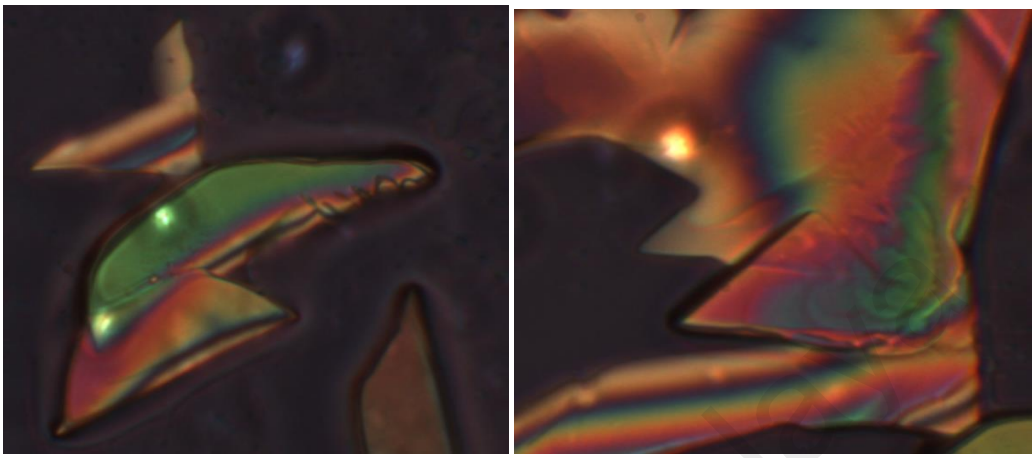

(a) (b)

Figure 4.177 The photomicrographs of **Complex 16** on cooling from 110 °C: (a) at 103 °C; and (b) at 67 °C (solid).

4.3.10 Summary

To summarise, the chemical formula, bandgaps, magnetic and thermal data for these complexes are shown in **Table 4.7**.

Table 4.7 Summary of complexes with *L2*

Complex	Chemical Formula	Bandgap (eV)			τ (ns)	μ_{eff} (BM)	T_{dec} (°C)	LC
		E_o (abs)	E_o (em)	E_e				
9	{[Cu(CH_3COO)$_2$(L2)].H_2O}$_n$	3.8	2.1	0.47	3.8	1.47	162	-
10	{[Ni(CH_3COO)$_2$(L2)].2H_2O}$_n$	3.6	1.8	-	2.7	2.65	164	-
11	{[Co(CH_3COO)$_2$(L2)].2H_2O}$_n$	3.8	1.8	-	3.4	3.98	222	-
12	{[Fe(CH_3COO)$_2$(L2)].2H_2O}$_n$	3.5	2.7	-	3.7	5.04	189	-
13	{[Cu($CH_3(CH_2)_{14}COO$)$_2$(L2)].H_2O}$_n$	3.6	1.9	-	2.8	1.61	160	-
14	{[Ni($CH_3(CH_2)_{14}COO$)$_2$(L2)].2H_2O}$_n$	3.6	1.9	-	2.8	3.34	170	M

15	$\{[Co(CH_3(CH_2)_{14}COO)_2(L2)].2H_2O\}_n$	3.6	1.9	-	2.9	3.69	231	-
16	$\{[Fe(CH_3(CH_2)_{14}COO)_2(L2)].2H_2O\}_n$	3.6	1.9	-	2.8	4.18	199	M

M = mesophase

All complexes were polymeric, made up of mononuclear repeat units. The optical bandgaps were similar (3.5 eV – 3.8 eV from absorption spectroscopy, 1.8 eV – 2.7 eV from emission spectroscopy). The results are similar to complexes of *L1*, and maybe similarly explained. The electrochemical bandgap was only obtained for **Complex 9** (0.47 eV) as the other complexes were either irreversibly oxidised or redox inactive.

The lifetimes of all of the excited complexes were similar (2.8 – 3.8 ns). This is consistent with the similar values of the bandgaps from the emission bands for all of the above complexes. The Stokes shift values are in the range 152 – 216 nm (CT transition), and 24 - 49 nm (*d-d* transition). It indicates that the large stokes shift (CT transition) is potential to be apply for dye material.

All complexes are paramagnetic. The Cu(II) complexes showed antiferromagnetic interactions between the metal centres, while the Ni(II) hexadecanoate complex showed a weak antiferromagnetic interaction between the metal centres. Both Co(II) and Fe(II) complexes were high spin. These complexes were also thermally stable. Their decomposition temperatures range from 160 ^oC to 231 ^oC. Finally, only Ni(II) and Fe(II) hexadecanoate complexes were mesomorphic.

4.4 Metal(II) Complexes of *L3*

4.4.1 Synthesis of L3

The ligand *L3* was obtained as a white powder from the reaction of 2,6-diamino-4-phenyl-1,3,5-triazine with 2,5-thiophenedicarboxylic acid. The yield was 97.9%. The reaction equation is shown in **Scheme 4.6**.

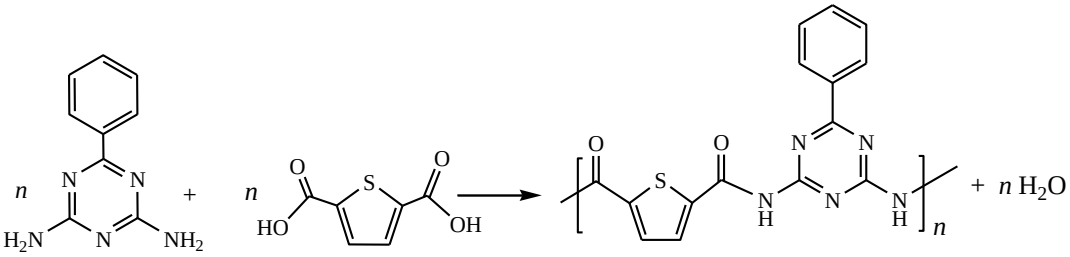

Scheme 4.6 Reaction equation for the preparation of *L3*

The results of the **elemental analyses** (52.6% C, 3.9% H, 20.7% N) were in good agreement with those calculated for the repeat unit *L3*.H_2O (formula, $C_{15}H_{11}N_5O_3S$, formula weight, 341.34 g mol^{-1}; 52.8% C, 3.3% H, 20.5% N).

Its **^{1}H-NMR** spectrum (**Figure 4.178**) supported the proposed structural formula. The amide protons appear as a singlet at 7.71 ppm, and all aromatic protons appear as a multiplet in the range 7.44 - 7.51 ppm.

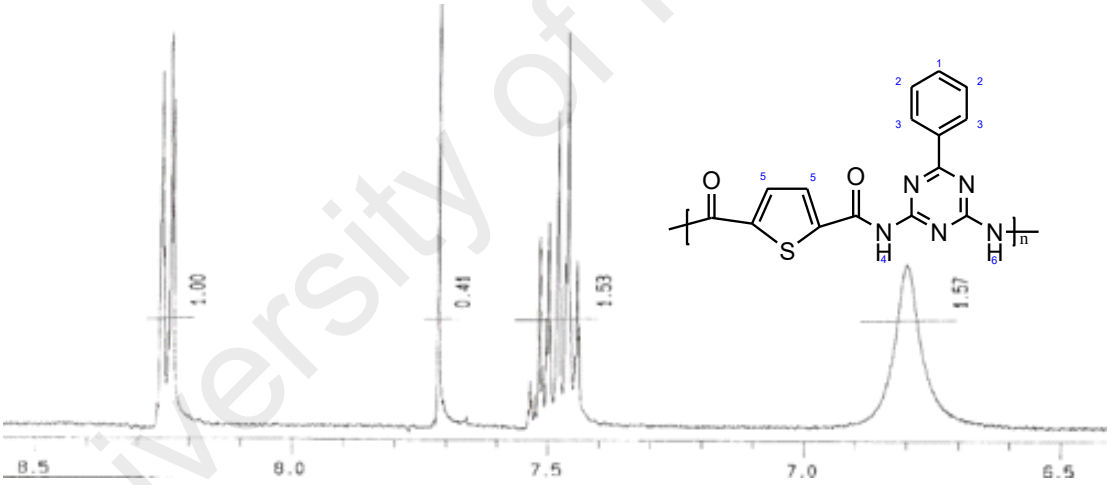

Figure 4.178 ^{1}H-NMR spectrum for *L3*.H_2O. The peak for H_2O overlapped with that of DMSO at 2.5 ppm

Table 4.8 The ^{1}H-NMR peak assignment for *L3*.H_2O

Chemical Shift (ppm)	Integral	Multiplicity	Assignment
6.80	1.57	broad	H-5, H-6
7.44 - 7.51	1.53	multiplet	H-1, H-2
7.71	0.41	singlet	H-4
8.23 - 8.25	1.00	doublet	H-3

Its **FTIR** spectrum is shown in **Figure 4.179**, and the peak assignments are given in **Table 4.9** (which also include the data for the corresponding metal(II) complexes for later discussion). Hence, the spectrum shows the functional groups expected for the ligand.

Table 4.9 FTIR data (in cm^{-1}) and assignments for *L3*.H_2O and its complexes

	NH -OH	CH_2 (asym)	CH_2 (sym)	C=O (amide)	COO (asym)	COO (sym)	M-N
***L3*.H_2O**	3324br	-	-	1672w	-	-	-
17	3381m	-	-	1660m	1524s	1418s	541w
18	3324m	-	-	1621m	1522s	1386s	568w
19	3325m	-	-	1637m	1522s	1386s	563w
20	3316m	-	-	1637m	1522s	1394s	595m
21	3326m	2917s	2850m	1622m	1532s	1395s	569m
22	3326m	2916s	2849s	1617m	1525s	1395s	569w
23	3317w	2916s	2848m	1622m	1527s	1454w	516w
24	3373w	2915s	2848s	1622m	1524w	1443w	569s

s = strong; m = medium; w = weak; br = broad

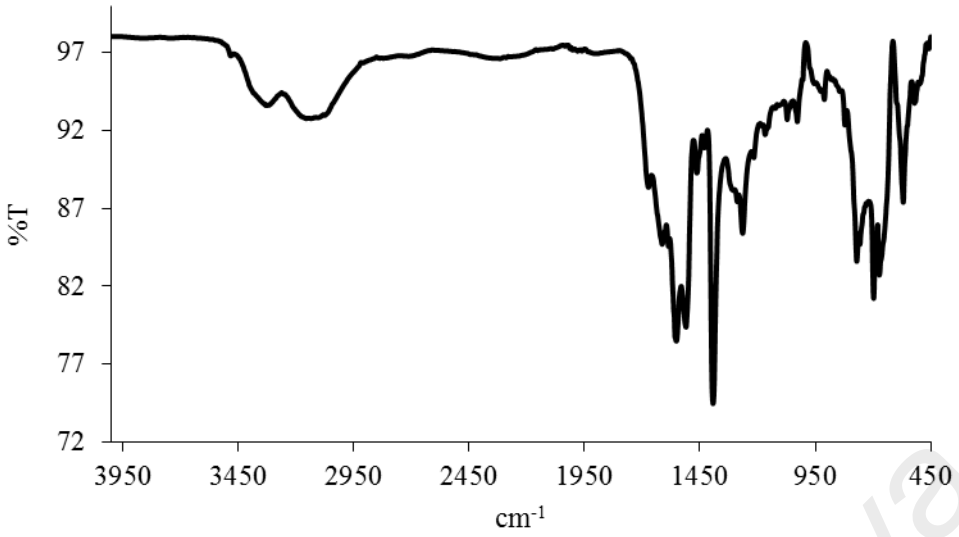

Figure 4.179 FTIR spectrum of *L3*.H_2O

4.4.2 Reaction of copper(II) ethanoate with L3

Copper(II) ethanoate ([$Cu(CH_3COO)_2$]) reacted with *L3* (mole ratio 1:1) to give a green powder (**Complex 17**), and the yield was 67.5%. Its solubility was similar to the previously discussed complexes.

The results from the **elemental analyses** of the complex (45.4% C; 3.2% H; 13.7% N) were in excellent agreement with those calculated for the repeat unit $CuC_{19}H_{15}N_5O_6S$ (45.2% C; 2.9% H; 13.9% N; formula weight, 504.96 g mol^{-1}). Combining these with the spectroscopic data discussed below, the proposed structural formula for **Complex 17** is $\{[Cu(CH_3COO)_2(L3)]\}_n$.

Its **FTIR** spectrum (**Table 4.9**; **Figure 4.180**) shows the presence of the expected functional groups. The ΔCOO value (106 cm^{-1}) suggests a chelating binding mode for CH_3COO^- ligand [1].

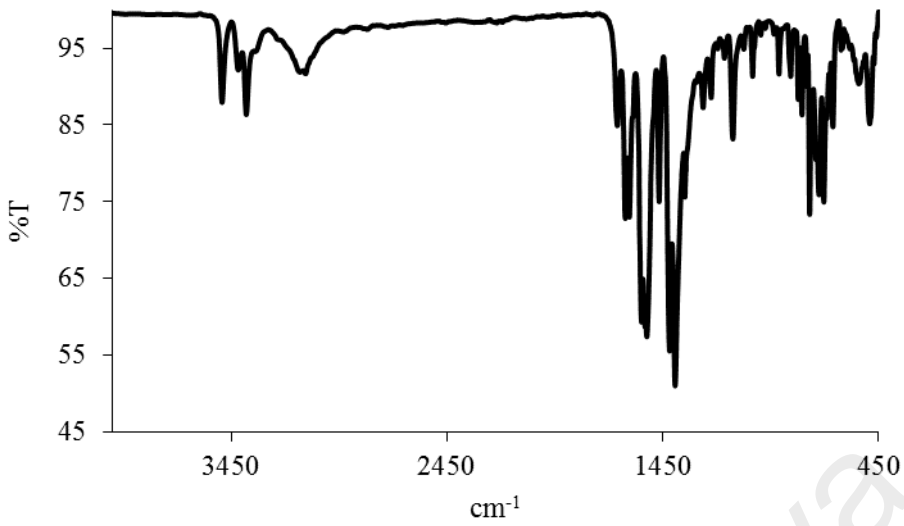

Figure 4.180 FTIR spectrum of **Complex 17**

Its **UV-vis** spectrum in DMSO (**Figure 4.181**) shows a broad *d-d* band at 769 nm (ε_{max}, 113.6 $M^{-1}cm^{-1}$), assigned as $^2B_2 \rightarrow {}^2B_1$ transition, and an intense LMCT band at 253 nm (ε_{max}, 1091 $M^{-1}cm^{-1}$). This suggests that the geometry at the Cu(II) centre was square pyramidal.

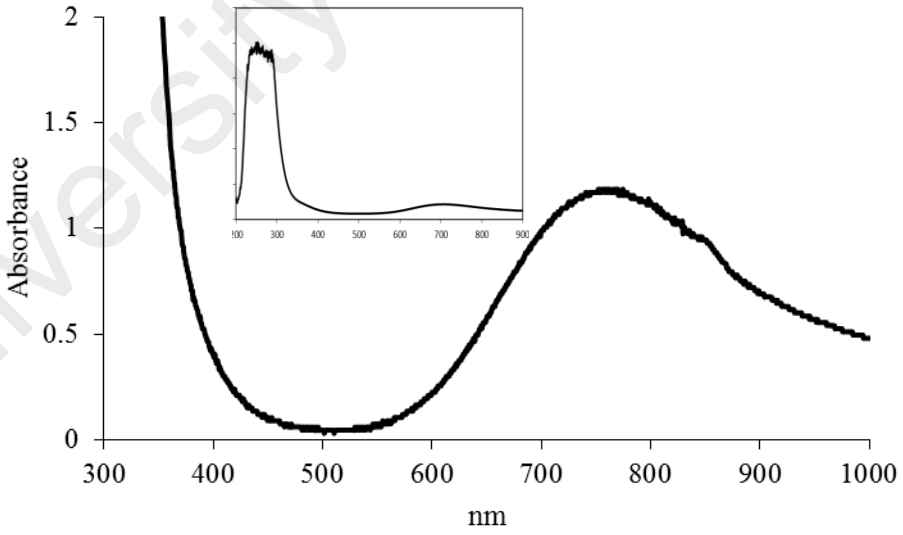

Figure 4.181 UV-vis spectrum of **Complex 17**

Its E_o, calculated as before (λ_{edge} = 372 nm), was 3.3 eV. Upon excitation at 253 nm (LMCT transition), its **fluorescence** spectrum shows four overlapping peaks at λ_{max} 356 nm, 416 nm, 477 nm and 544 nm (**Figure 4.182)**. This suggests four different

paths for the excited complex to return to the ground state. Its E_o value (calculated from λ_{edge} = 608 nm) was 2.0 eV. Its τ, calculated as before from its **decay** curve (**Figure 4.183**), was 2.8 ns. Additionally, the Stokes shift value was 103 nm.

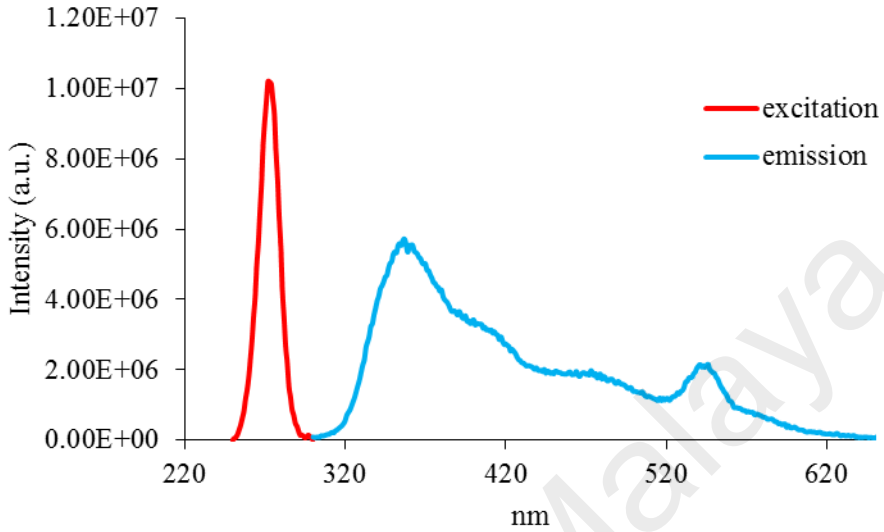

Figure 4.182 Fluorescence spectrum of **Complex 17** (λ_{ex} = 253 nm)

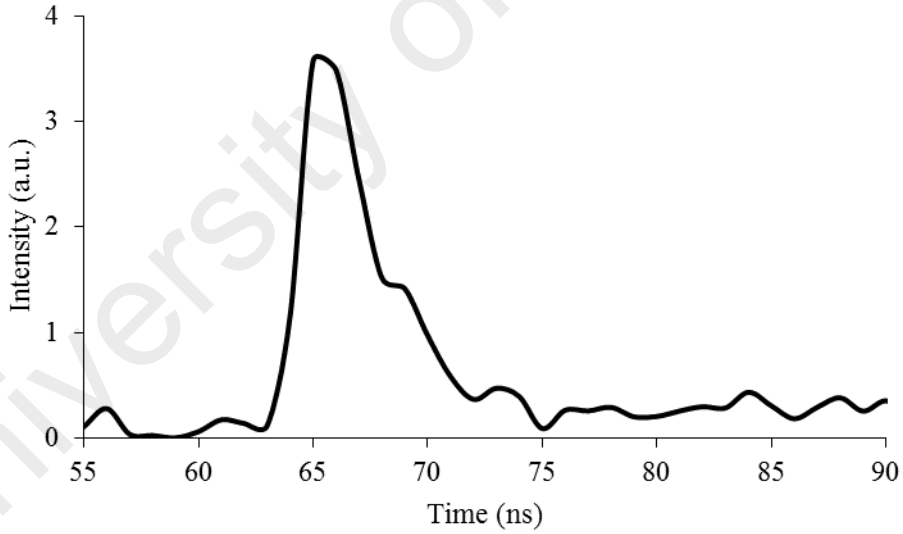

Figure 4.183 Fluorescence decay of **Complex 17**

Additionally, upon excitation at 769 nm (*d-d* transition), its **fluorescence** spectrum shows a peak at λ_{max} 785 nm (**Figure 4.184**). Its E_o value (calculated from λ_{edge} = 790 nm) was 1.6 eV, and its $\boldsymbol{\tau}$ value, calculated as before from its **decay** curve, was 2.5 ns. Its Stokes shift was 16 nm.

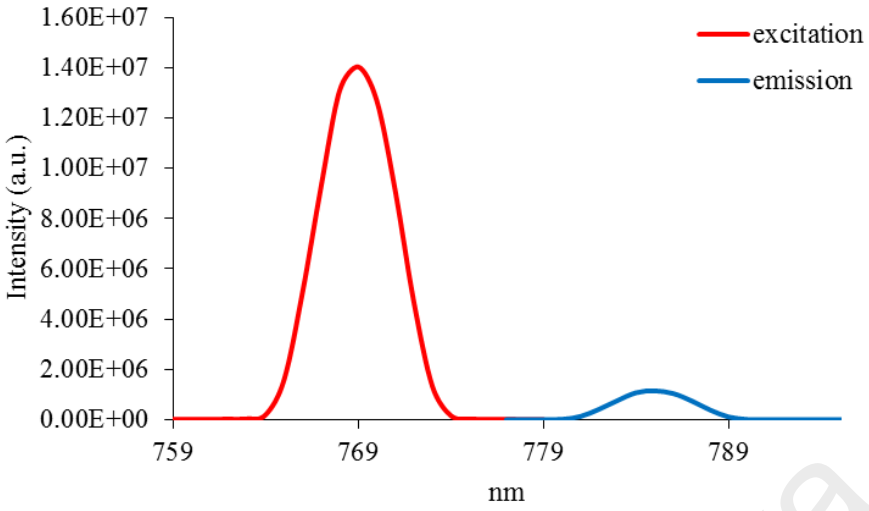

Figure 4.184 Fluorescence spectrum of **Complex17** (λ_{ex} = 769 nm)

Its **CV** (**Figure 4.185**), recorded cathodically from 0 V within the potential window -1.5 V to +1.5 V. It showed two cathodic peaks at −0.39 V and −1.34 V, and two anodic peaks at −0.21 V and +0.3 V. The Cu(II) based redox is shown in **Scheme 4.7**. Hence, the peak separation (ΔE_p) was 180 mV, indicating a quasireversible redox reaction. The cathodic peak at -1.34 V and anodic peak at +0.3 V are tentatively attributed to ligand-based redox process.

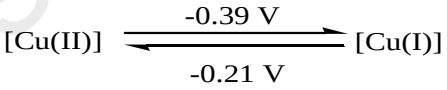

Scheme 4.7 The redox process for **Complex 17**

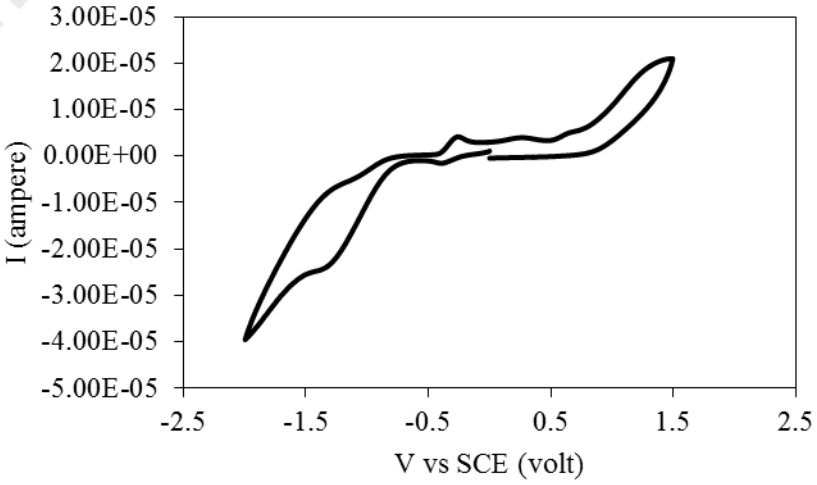

Figure 4.185 CV of **Complex 17**

The HOMO and LUMO values, calculated from the onset oxidation potential (-0.39 V) and onset reduction potential (-0.19 V), were 4.01 eV and 4.21 eV (versus SCE), respectively. Thus, its E_e was 0.20 eV.

Its μ_{eff} value, calculated as before from the values of FM = 504.96 g mol^{-1} (repeat unit), χ_g = 0.15 x 10^{-5} cm^3 g^{-1}, χ_M = 7.47 x 10^{-4} cm^3 mol^{-1}, and χ_{dia} = -2.14 x 10^{-4} cm^3 mol^{-1}, was 1.56 B.M. at 298 K. The value is significantly lower than expected for a mononuclear Cu(II) complex (1.73 B.M.). This suggests a strong antiferromagnetic interaction between the Cu(II) atoms in the polymeric complex.

Its **TGA** trace (**Figure 4.186**) shows the total weight loss of 92.1% in the temperature range of 180 – 900 °C, assigned to the decomposition of two CH_3COO and *L3* ligands (expected, 87.4%). However, the amount of residue at temperatures above 900 °C cannot be ascertained due to incomplete combustion of the organic ligands (expected, 12.6% assuming pure CuO). Hence, the decomposition temperature of **Complex 17** was 180 °C.

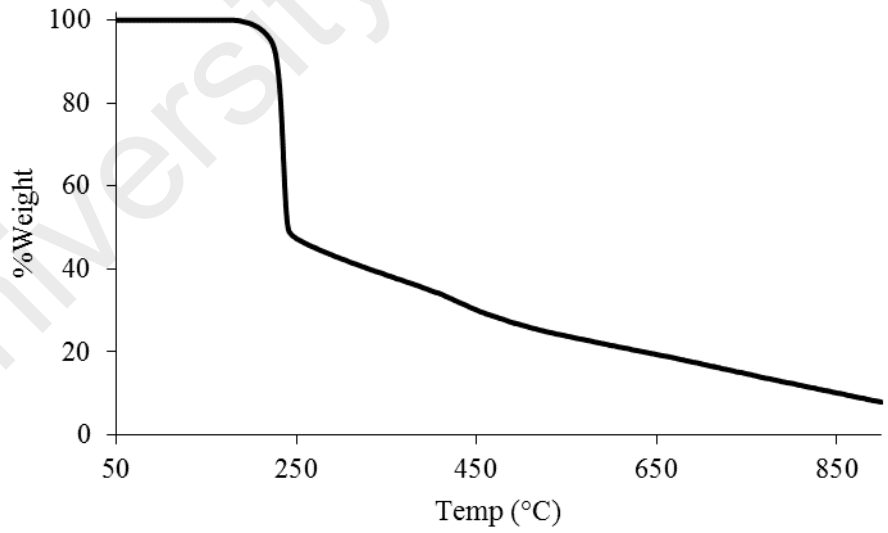

Figure 4.186 TGA of **Complex 17**

4.4.3 Reaction of nickel(II) ethanoate with L3

Nickel(II) ethanoate tetrahydrate ($[Ni(CH_3COO)_2].4H_2O$) reacted with *L3* (mole ratio 1:1) to give a green powder (**Complex 18**), and the yield was 77.7%. Its solubility was similar to previously discussed complexes.

The results from the **elemental analyses** for the complex (35.8% C; 4.0% H; 8.9% N) were in excellent agreement with those calculated for the repeat unit $Ni_2C_{23}H_{31}N_5O_{15}S$ (36.0% C; 4.1% H; 9.1% N; formula weight, 766.97 g mol^{-1}). Combining these with the spectroscopic data discussed below, its proposed structural formula is $\{[Ni_2(CH_3COO)_4(L3)].5H_2O\}_n$.

Its **FTIR** spectrum (**Table 4.9**; **Figure 4.187**) shows the presence of the expected functional groups. The ΔCOO value (136 cm^{-1}) suggests a chelating binding mode for CH_3COO^- ligand.

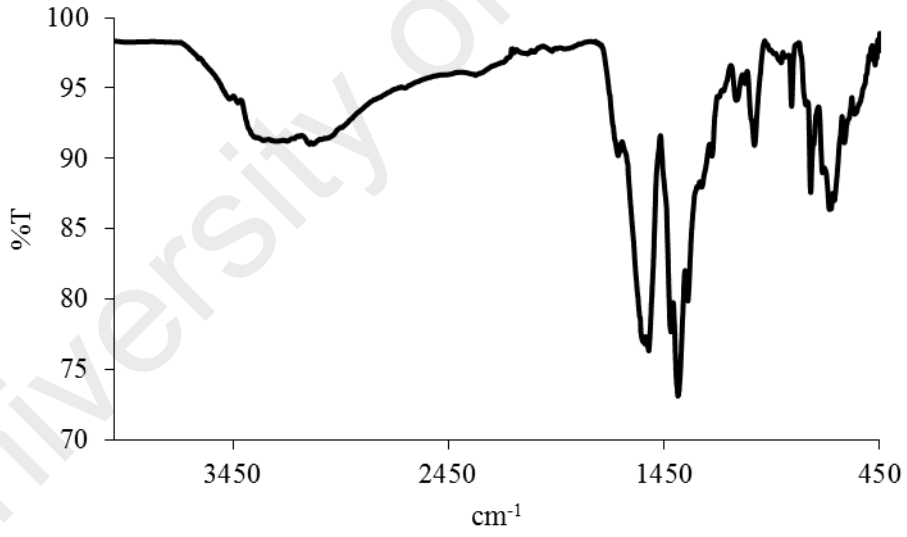

Figure 4.187 FTIR spectrum of **Complex 18**

Its **UV-vis** spectrum in DMSO (**Figure 4.188**) shows two overlapping peaks at 775 nm (ε_{max}, 162.8 M^{-1} cm^{-1}) and 694 nm (ε_{max}, 139.5 M^{-1} cm^{-1}), assigned to $^3A_{2g}$ (F) → $^3T_{2g}$ (F) and $^3A_{2g}$ (F) → $^3T_{1g}$ (F), respectively, and 418 nm (ε_{max}, 441.8 M^{-1} cm^{-1}) assigned to $^3A_{2g}$ (F) → $^3T_{1g}$ (P) electronic transitions. These

suggest that the geometry at the Ni(II) centres was octahedral. Also observed is an intense MLCT band at 258 nm (ε_{max}, 1459 M^{-1} cm^{-1}).

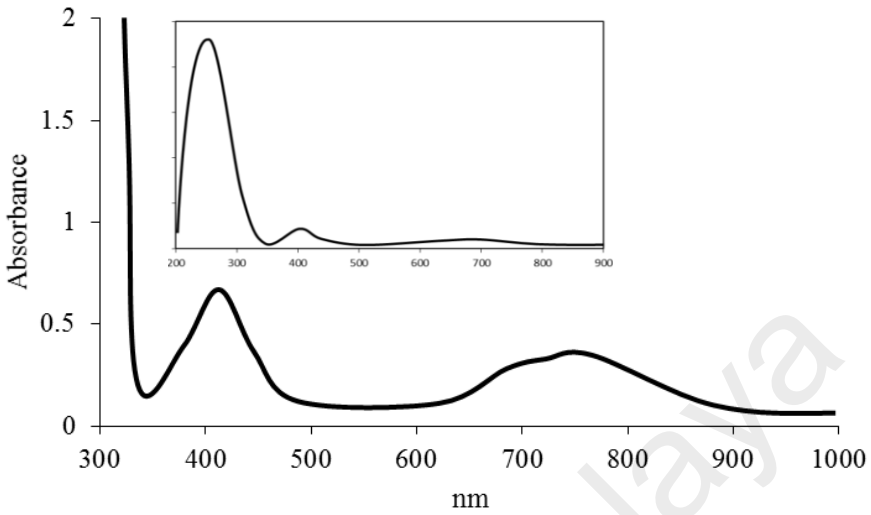

Figure 4.188 UV-vis spectrum of **Complex 18**

Its E_o**,** calculated from λ_{edge} = 355 nm, was 3.5 eV. The value is just slightly higher than for **Complex 17 (**$\{[Cu(CH_3COO)_2(L3)]\}_n$; 3.3 eV), which might be due to the different metal(II) ions in these complexes.

Upon excitation at 258 nm (MLCT transition), its **fluorescence** spectrum shows three overlapping peaks at λ_{max} 357 nm, 467 nm and 547 nm (**Figure 4.189**). This suggests three different paths for the excited complex to return to the ground state. Its E_o value, calculated from λ_{edge} = 605 nm, was 2.0 eV. Its Stokes shift was 99 nm.

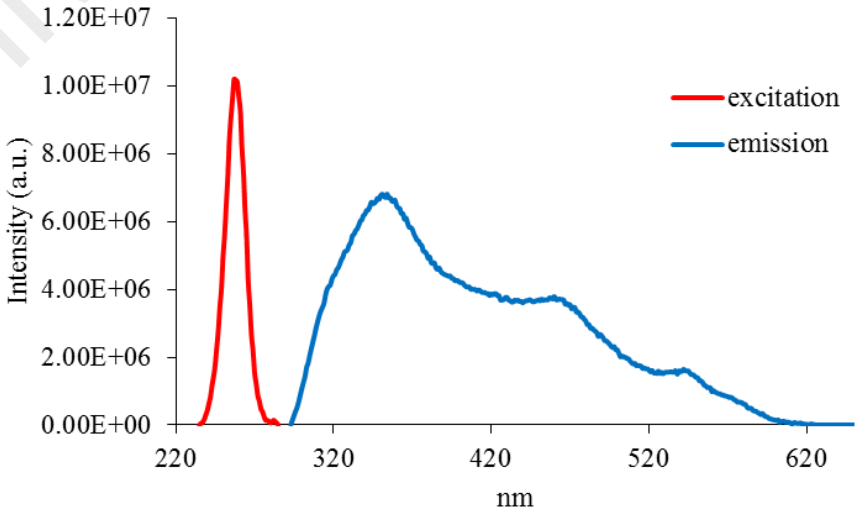

Figure 4.189 Fluorescence spectrum of **Complex 18** (λ_{ex} = 258 nm)

Its τ value, calculated as before from its decay curve (**Figure 4.190**), was 2.8 ns. Hence, the excited state lifetime of the complex is also similar to **Complex 17** (2.8 ns).

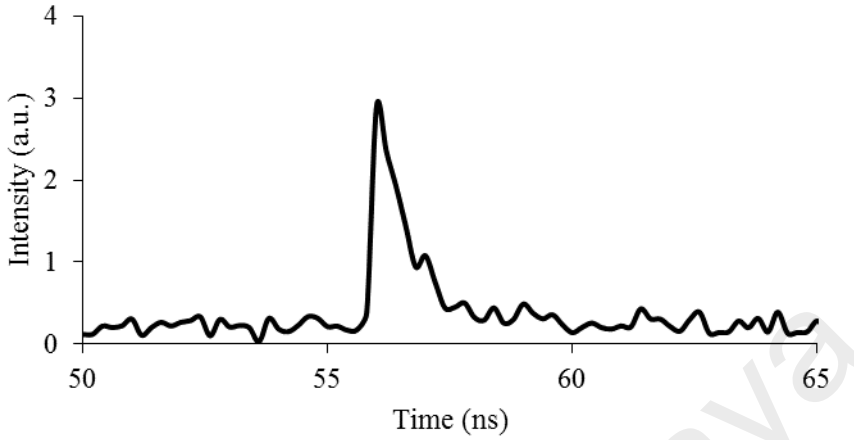

Figure 4.190 Fluorescence decay of **Complex 18**

Also, upon excitation at 418 nm (*d-d* transition), its **fluorescence** spectrum shows a peak at λ_{max} 431 nm (**Figure 4.191**). Its E_o value, calculated from λ_{edge} = 437 nm, was 2.8 eV, and its τ value, calculated from its **decay** curve, was 3.7 ns. Its Stokes shift was 13 nm.

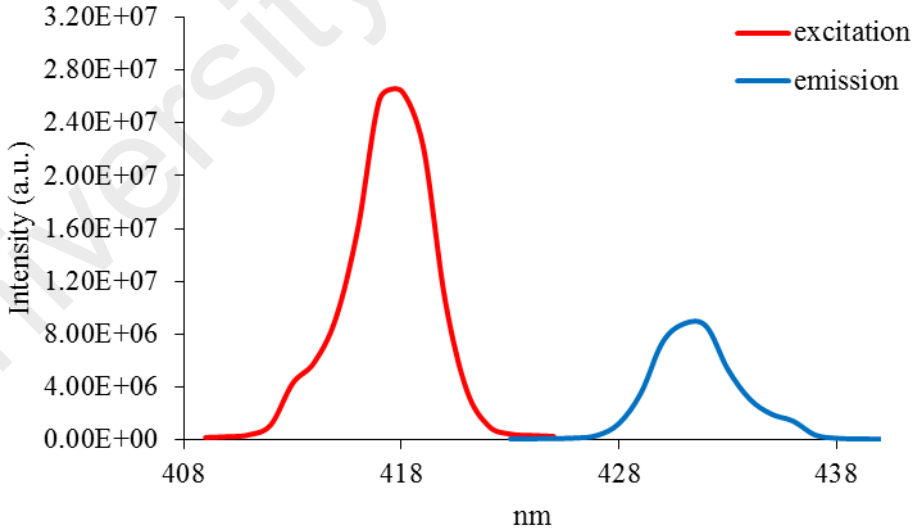

Figure 4.191 Fluorescence spectrum of **Complex 18** (λ_{ex} = 418 nm)

Its **CV** (**Figure 4.192**), recorded anodically from 0 V within the potential window of +1.5 V to -1.5 V. It showed an anodic peak at +1.13 V and a corresponding cathodic

peak at -1.17 V. This is assigned to ligand-based redox process. Hence, its E_e cannot be calculated.

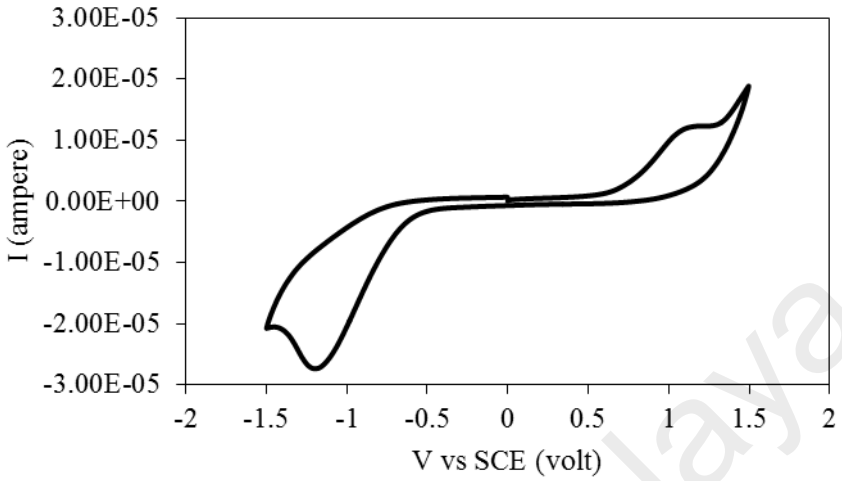

Figure 4.192 CV of **Complex 18**

Its μ_{eff} value, calculated as before from the values of FM = 766.97 g mol^{-1} (repeat unit), χ_g = 1.16 x 10^{-5} cm^3 g^{-1}, χ_M = 8.86 x 10^{-3} cm^3 mol^{-1}, and χ_{dia} = -4.4 x 10^{-4} cm^3 mol^{-1}, was 4.72 B.M. at 298 K. This is higher than the expected value for a dinuclear nickel(II) complex (4.0 B.M.), indicating a weak ferromagnetic interactions between the metal centres.

Its **TGA** trace (**Figure 4.193**) shows an initial weight loss of 11.4% in the temperature range of 82 – 216 °C, assigned to the evaporation of five H_2O molecules (expected, 11.7%). The next weight loss of 67.4% in the temperature range of 216 - 900 °C is assigned to the decomposition of four CH_3COO and *L3* ligands (expected, 72.9%). However, the amount of residue at temperatures above 900 ºC cannot be accurately ascertained due to incomplete combustion of the organic ligands. Hence, the complex (T_{dec} = 216 °C) was more thermally stable than **Complex 17** ($\{[Cu(CH_3COO)_2(L3)]\}_n$; T_{dec} = 180 °C).

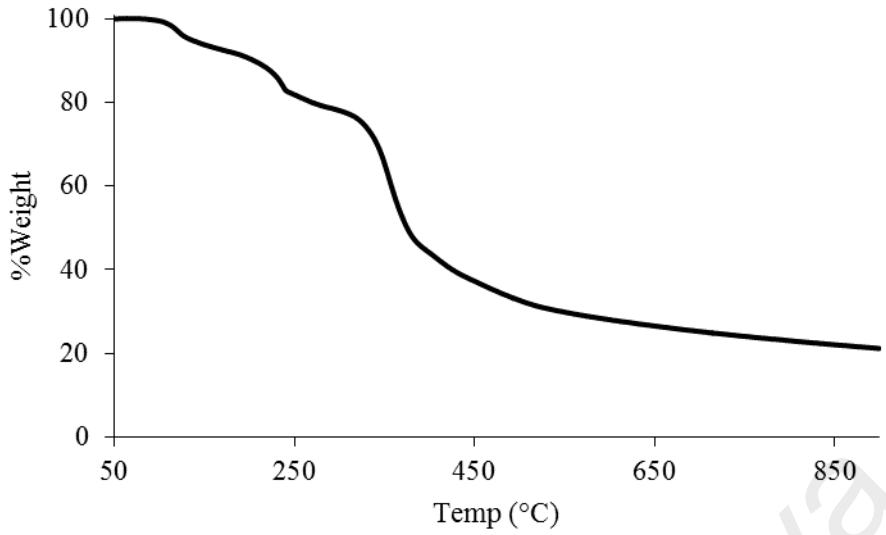

Figure 4.193 TGA of **Complex 18**

4.4.4 Reaction of cobalt(II) ethanoate with L3

Cobalt(II) ethanoate tetrahydrate ($[Co(CH_3COO)_2].4H_2O$) reacted with *L3* (mole ratio 1:1) to give a purple powder (**Complex 19**), and the yield was 78.1%. Its solubility was similar to the previously discussed complexes.

The results from the **elemental analyses** for the complex (42.4% C; 3.6% H; 13.7% N) were in excellent agreement with those calculated for the repeat unit $CoC_{19}H_{18}N_5O_7S$ (42.5% C; 3.6% H; 13.1% N; formula weight, 536.98 g mol^{-1}). Combining these with the spectroscopic data discussed below, its proposed structural formula is $\{[Co(CH_3COO)_2(L3)].2H_2O\}_n$.

Its **FTIR** spectrum (**Table 4.9**; **Figure 4.194**) shows the presence of the expected functional groups. The ΔCOO value (136 cm^{-1}) suggests a chelating binding mode for CH_3COO^- ligand [1].

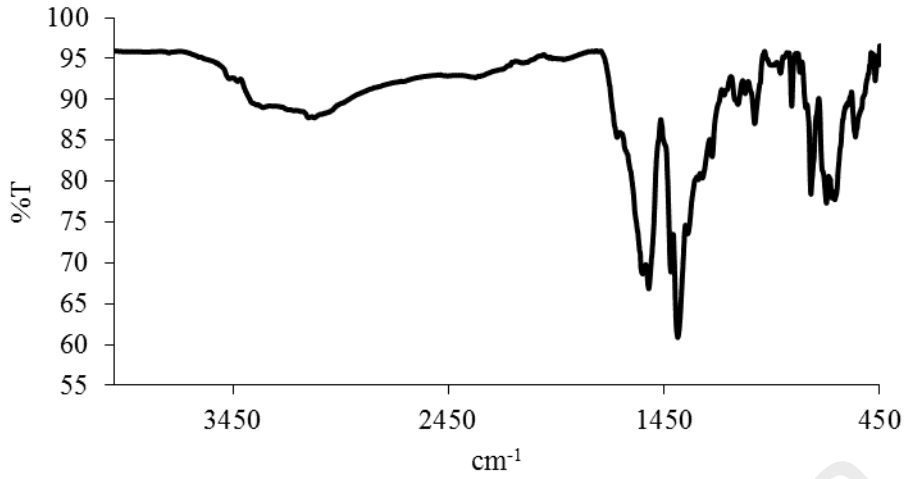

Figure 4.194 FTIR spectrum of **Complex 19**

Its **UV-vis** spectrum in DMSO (**Figure 4.195**) shows overlapping *d-d* bands at 639 nm (ε_{max}, 103.6 M^{-1} cm^{-1}), assigned to $^4T_{1g}$ (F)→ $^4T_{2g}$ (F), $^4T_{1g}$ (F) → $^4T_{1g}$ (P), and 561 nm (ε_{max}, 193.3 M^{-1} cm^{-1}), assigned to $^4T_{1g}$ (F) → $^4A_{2g}$ (F) electronic transitions, respectively. Hence, the geometry at the HS Co(II) centre was octahedral. Also found was an intense MLCT band at 263 nm (ε_{max}, 1325.5 M^{-1} cm^{-1}).

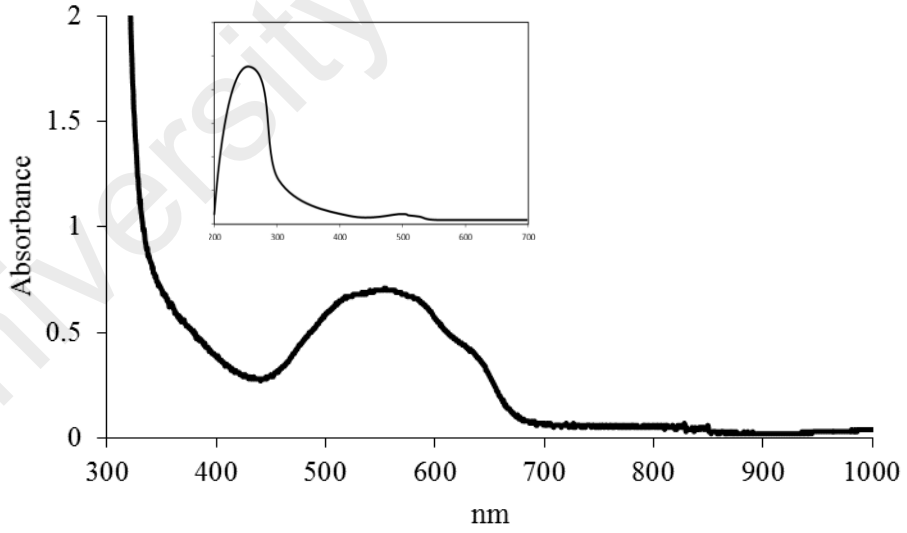

Figure 4.195 UV-vis spectrum of **Complex 19**

Its E_o value, calculated as before from λ_{edge} = 375 nm, was 3.3 eV. The value is the same as **Complex 17** ($\{[Cu(CH_3COO)_2(L3)]\}_n$; 3.3 eV).

Upon excitation at 263 nm (MLCT transition), its **fluorescence** spectrum shows four overlapping peaks at λ_{max} 359 nm, 435 nm, 546 nm and 630 nm (**Figure 4.196)**.

This suggests four different paths for the excited complex to return to the ground state. Its E_o value, calculated from λ_{edge} = 634 nm, was 1.9 eV. In addition, the value of Stokes shift was 96 nm.

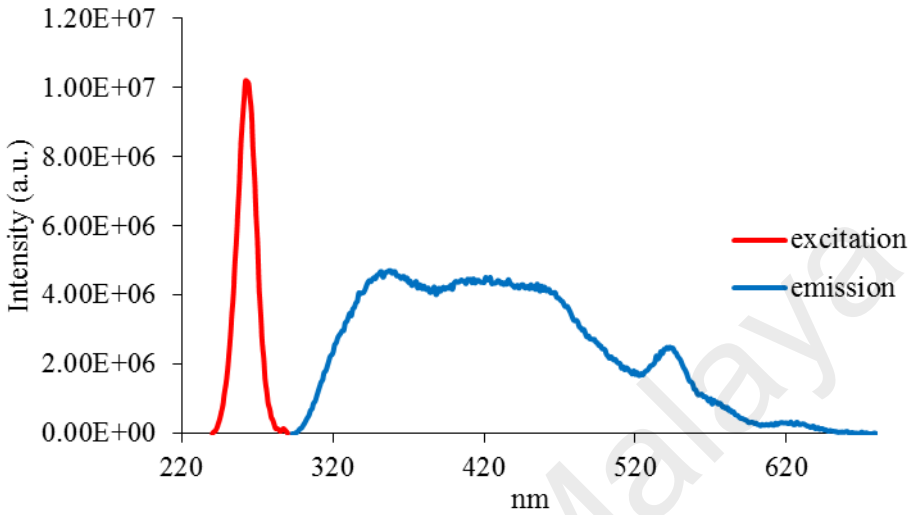

Figure 4.196 Fluorescence spectrum of **Complex 19** (λ_{ex} = 263 nm)

The value of its τ, calculated as before from its **decay** curve (**Figure 4.197**), was 2.8 ns. Hence, the lifetime of excited **Complex 19** was the same as **Complexes 17** ($\{[Cu(CH_3COO)_2(L3)]\}_n$; 2.8 ns) and **18 (**$\{[Ni_2(CH_3COO)_4(L3)].5H_2O\}_n$; 2.8 ns).

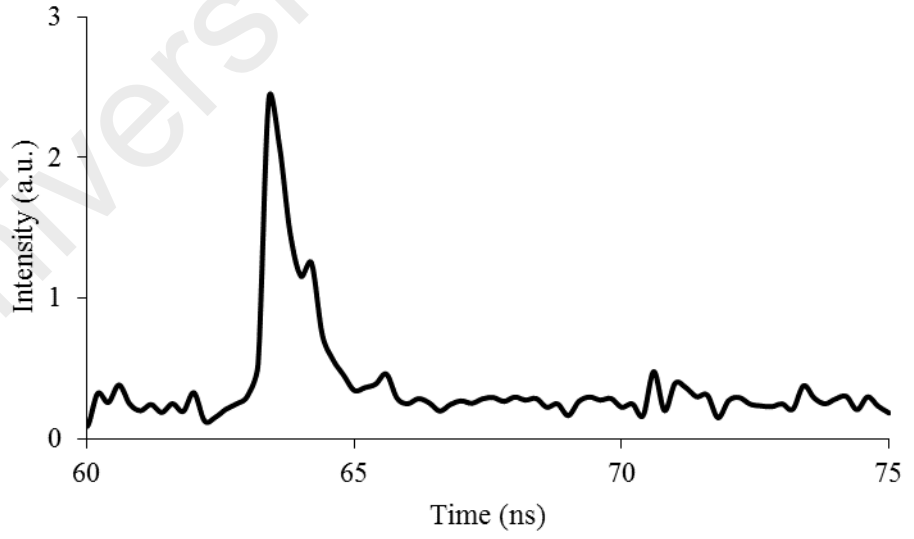

Figure 4.197 Fluorescence decay of **Complex 19**

Upon excitation at 561 nm (*d-d* transition), its **fluorescence** spectrum of the complex shows a peak at λ_{max} 583 nm (**Figure 4.198**). Its E_o, calculated from

λ_{edge} = 601 nm, was 2.0 eV. Its τ value, calculated as before from its **decay** curve, was 2.6 ns. Its Stoke shift was 22 nm.

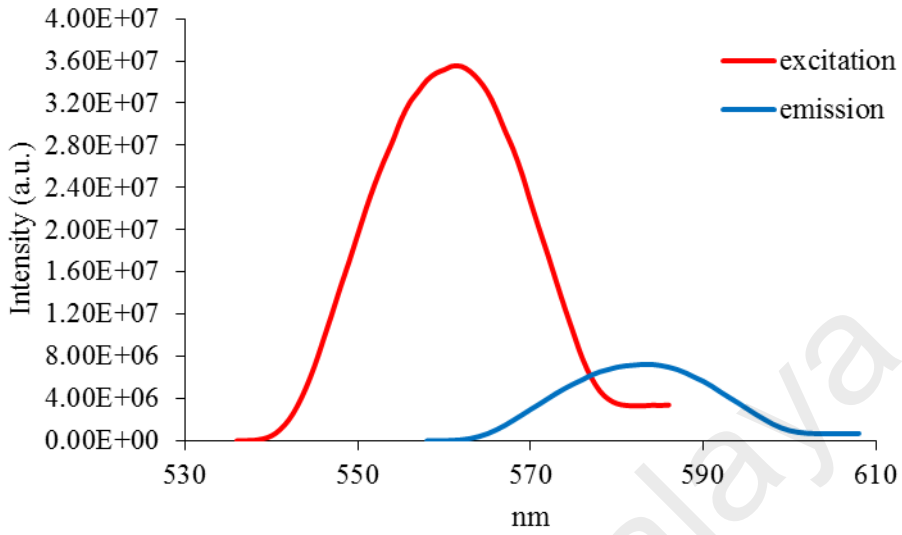

Figure 4.198 Fluorescence spectrum of **Complex 19** (λ_{ex} = 561 nm)

Its **CV** (**Figure 4.199**), recorded anodically from 0 V within the potential window of +1.5 V to -1.5 V, showed only one anodic peak at +0.98 V. This is assigned to oxidation of [Co(II)] to [Co(III)], which was irreversible process. Accordingly, its E_e value cannot be calculated.

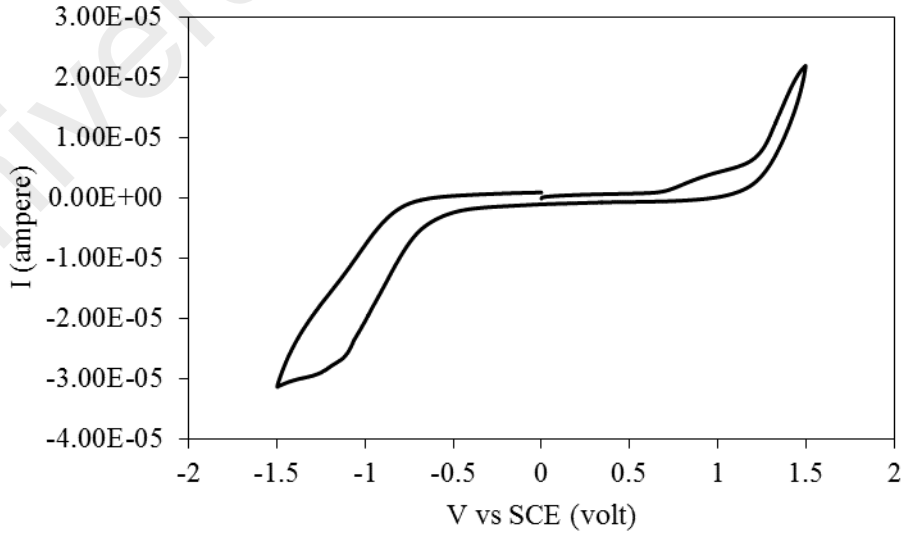

Figure 4.199 CV of **Complex 19**

Its μ_{eff} value, calculated as before from the values of FM = 536.98 g mol^{-1} (repeat unit), χ_g = 1.06 x 10^{-5} cm^3 g^{-1}, χ_M = 5.68 x 10^{-3} cm^3 mol^{-1}, and χ_{dia} = -2.62 x 10^{-4} cm^3 mol^{-1}) is 3.78 B.M. at 298 K. This is similar with the expected μ_{eff} value for a HS Co(II) complex (d^7) (3.89 B.M.), suggesting an insignificant magnetic between the Co(II) centres in the polymeric chain [45].

Its **TGA** trace (**Figure 4.200**) shows an initial weight loss of 6.7% in the temperature range of 82 – 184 °C, assigned to evaporation of two H_2O molecules (expected, 6.7%). The next weight loss of 79.3% in the temperature range of 184 – 800 °C is assigned to the decomposition of two CH_3COO and *L3* ligand (expected, 82.2%). The amount of residue at temperatures above 800 ^oC was 14.0% (expected 14.4%, assuming pure CoO). Hence, the complex was much less thermally stable (T_{dec} = 184 °C) compared to **Complex 18** ({$[Ni_2(CH_3COO)_4(L3)].5H_2O\}_n$; T_{dec} = 216^oC).

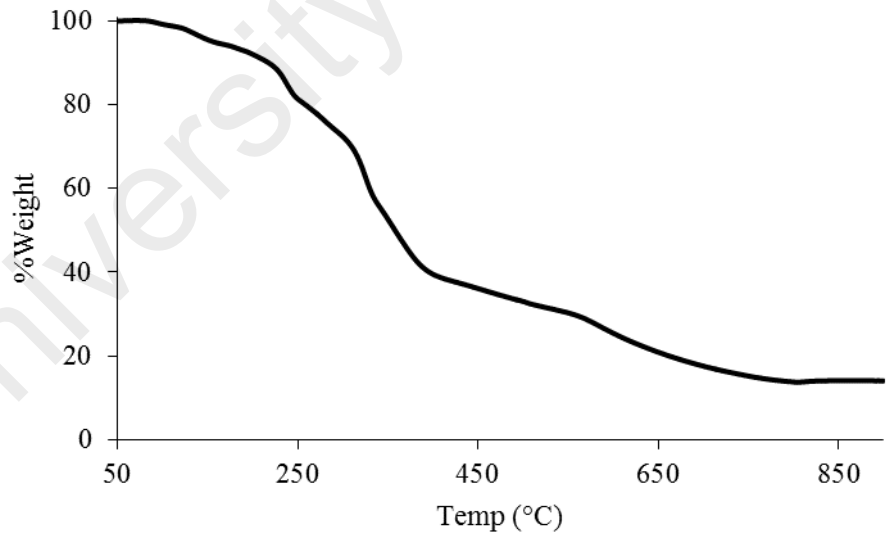

Figure 4.200 TGA of **Complex 19**

4.4.5 Reaction of iron(II) ethanoate with L3

Iron(II) ethanoate ($[Fe(CH_3COO)_2]$) reacted with *L3* (mole ratio 1:1) to give a brown powder (**Complex 20**), and the yield was 87.8%. Its solubility was similar to the previously discussed complexes.

The results from the **elemental analyses** for the complex (39.3% C; 3.3% H; 9.9% N) were in excellent agreement with those calculated for the repeat unit $Fe_2C_{23}H_{25}N_5O_{12}S$ (39.1% C; 3.6% H; 9.9% N; formula weight, 707.23 g mol^{-1}). Combining these with the spectroscopic data discussed below, its proposed structural formula is $\{[Fe_2(CH_3COO)_4(L3)].2H_2O\}_n$.

Its **FTIR** spectrum (**Table 4.9**; **Figure 4.201**) shows the presence of the expected functional groups. The ΔCOO value (128 cm^{-1}) suggests a chelating binding mode for CH_3COO^- ligand.

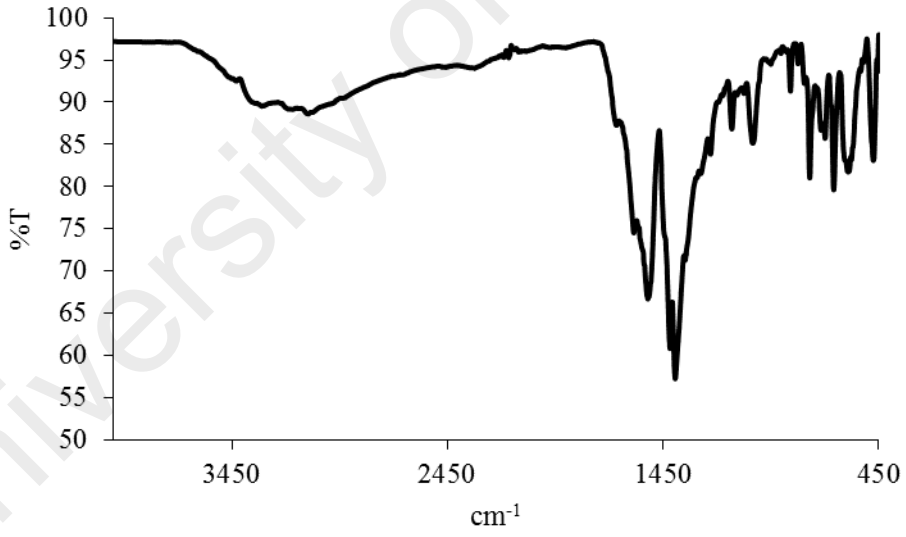

Figure 4.201 FTIR spectrum of **Complex 20**

Its **UV-vis** spectrum in DMSO (**Figure 4.202**) shows a weak and broad peak at 831 nm (ε_{max}, 20.6 M^{-1} cm^{-1}) assigned to ${}^5T_{2g} \rightarrow {}^5E_g$ electronic transition, a shoulder band at 487 nm (ε_{max}, 3.6x10^3 M^{-1} cm^{-1}) assigned to $n \rightarrow \pi^*$ transition, and an intense band at 241 nm (ε_{max}, 1.3x10^4 M^{-1} cm^{-1}) assigned to MLCT. This suggests that the geometry at the HS Fe(II) centre is octahedral.

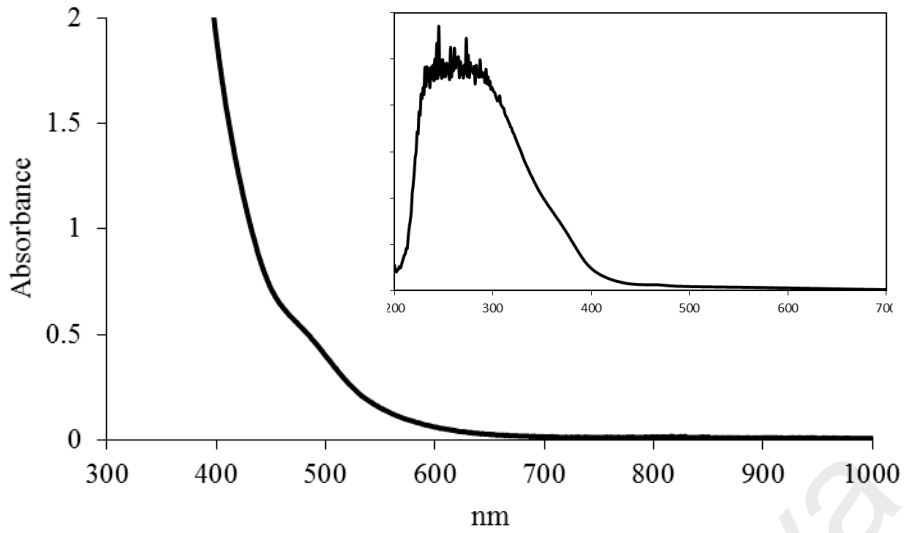

Figure 4.202 UV-vis spectrum of **Complex 20**

Its E_o value, calculated as before from λ_{edge} = 561 nm, was 2.2 eV. The value is significantly narrower than **Complex 19** ({[Co(CH$_3$COO)$_2$(L3)].2H$_2$O}$_n$; 3.3 eV).

Upon excitation at 241 nm (MLCT transition), its **fluorescence** spectrum shows three overlapping peaks at λ_{max} 456 nm, 552 nm and 580 nm (**Figure 4.203**). This suggests three different paths for the excited complex to return to the ground state. Its E_o value, calculated from λ_{edge} = 619 nm, was 2.0 eV. The value of its $\boldsymbol{\tau}$, calculated as before from its **decay** curve (**Figure 4.204**), was 2.7 ns. Its Stokes shift was 215 nm.

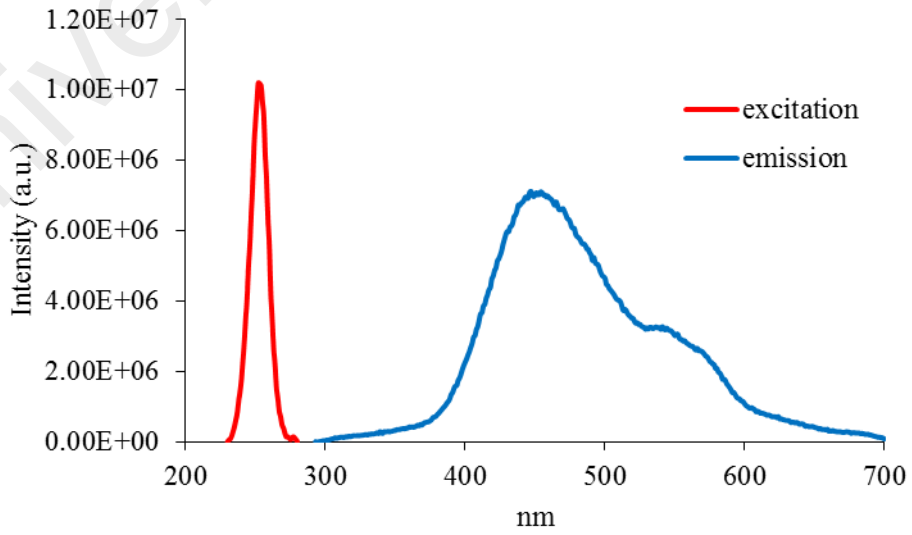

Figure 4.203 Fluorescence spectrum of **Complex 20** (λ_{ex} = 241 nm)

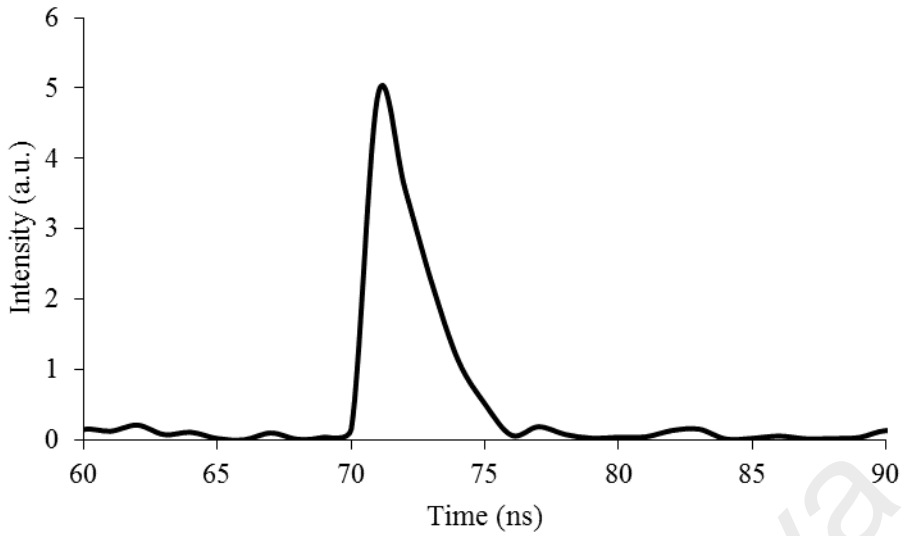

Figure 4.204 Fluorescence decay of **Complex 20**

Additionally, upon excitation at 831 nm, (*d-d* transition), its **fluorescence** spectrum shows a peak at λ_{max} 865 nm (**Figure 4.205**). Its E_o, calculated from λ_{edge} = 885 nm, was 1.4 eV, while its τ value, calculated from its **decay** curve, was 2.2 ns. Its Stokes shift was 34 nm.

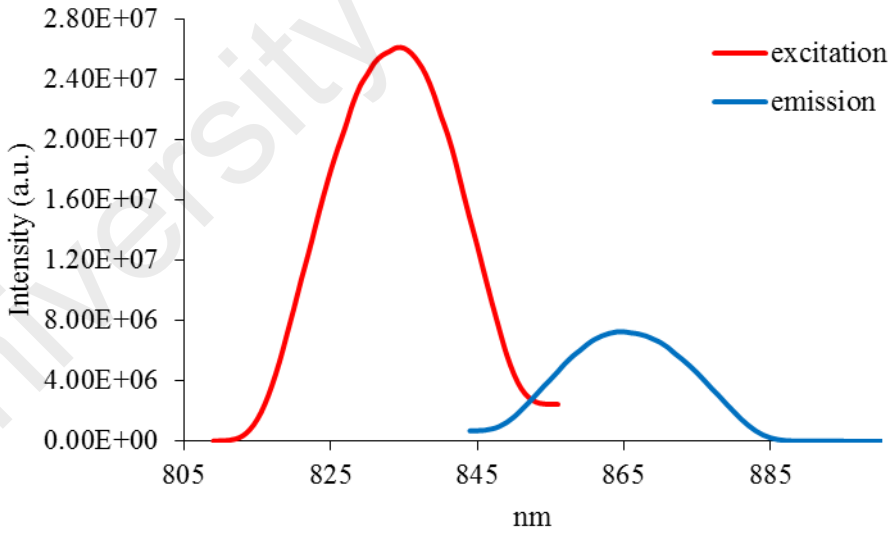

Figure 4.205 Fluorescence spectrum of **Complex 20** (λ_{ex} = 831 nm)

Its **CV** (**Figure 4.206**), recorded anodically from 0 V within the potential window of +1.5 V to -1.5 V. It showed an anodic peak at +0.93 V assigned to oxidation [Fe(II)Fe(II)] to [Fe(II)Fe(III)], and the corresponding cathodic peak at -0.99 V,

assigned to reduction of [Fe(II)Fe(III)] to [Fe(II)Fe(II)]. The large peak separation (ΔE_p = 1920 mV) indicates a quasireversible process.

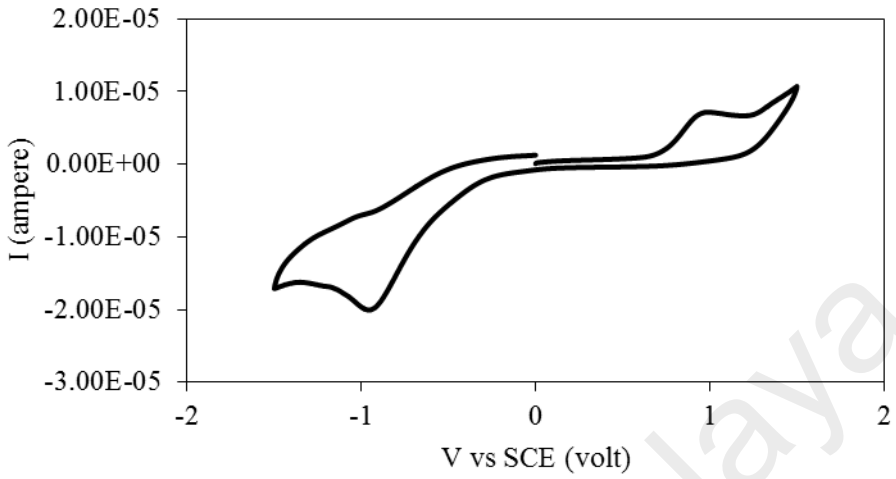

Figure 4.206 CV of **Complex 20**

The HOMO and LUMO values, calculated from the onset oxidation potential (+0.75 V) and onset reduction potential (-0.44 V), were 5.15 eV and 3.96 eV (versus SCE), respectively. Hence, its E_e value was 1.19 eV.

The μ_{eff} value, calculated as before from the values of FM = 707.23 g mol^{-1} (repeat unit), χ_g = 3.14 x 10^{-5} cm^3 g^{-1}, χ_M = 2.21 x 10^{-2} cm^3 mol^{-1}, and χ_{dia} = -3.69 x 10^{-4} cm^3 mol^{-1}), was 7.35 B.M., which is higher than the expected μ_{eff} value for two HS Fe(II) atoms (6.93 B.M.). This indicates a ferromagnetic interaction between the Fe(II) centres in the polymeric chains.

The **TGA** trace (**Figure 4.207**) shows that the complex initially suffered a gradual initial weight loss of 5.1% in the temperature range of 75 - 191 °C, assigned to the evaporation of two H_2O molecules (expected, 5.1%). The next weight loss of 80.4% in the temperature range 191 - 900 °C is assigned to decomposition of four CH_3COO and *L3* ligands (expected, 79.1%). However, the amount of residue at temperatures above 900 °C cannot be ascertained due to incomplete combustion of the organic ligands.

Hence, **Complex 20** (T_{dec} = 191 °C) was as thermally stable as **Complex 19** ({[$Co(CH_3COO)_2(L3)].2H_2O$}$_n$; T_{dec} = 184 °C).

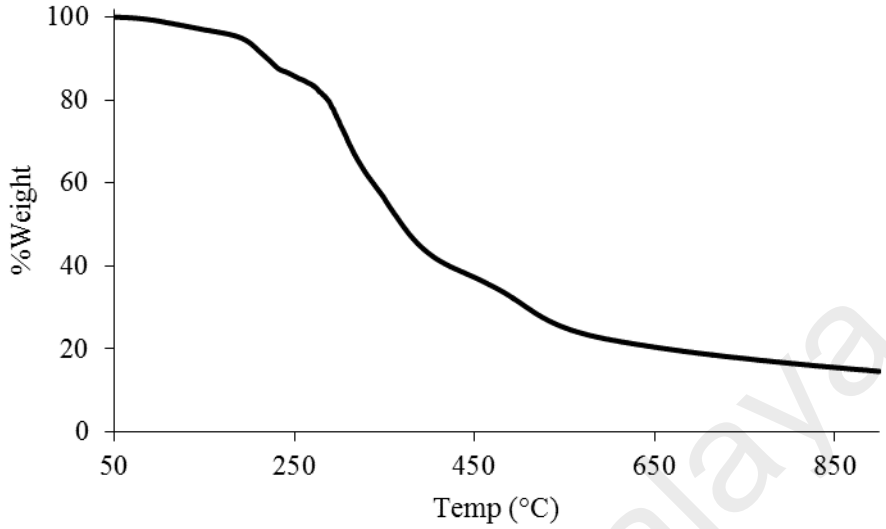

Figure 4.207 TGA of **Complex 20**

4.4.6 Reaction of copper(II) hexadecanoate with L3

Copper(II) hexadecanoate ([$Cu_2(CH_3(CH_2)_{14}COO)_4$] reacted with *L3* (mole ratio 1:1) to give a yellow powder (**Complex 21**), and the yield was 75.7%. Its solubility was similar to the previously discussed complexes.

The **elemental analytical** data for the complex (62.5% C; 9.1% H; 4.7% N) were in excellent agreement with those calculated for the repeat unit $Cu_2C_{79}H_{137}N_5O_{12}S$ (62.9% C; 9.2% H; 4.6% N; formula weight, 1508.12 g mol^{-1}). Combining these with the spectroscopic data discussed below, its proposed structural formula is {[$Cu_2(CH_3(CH_2)_{14}COO)_4(L3)].2H_2O$}$_n$, which is different compared to **Complex 17** {[$Cu(CH_3COO)_2(L3)$]}$_n$.

Its **FTIR** spectrum (**Table 4.9**; **Figure 4.208**) shows the presence of the expected functional groups. The ΔCOO value (137 cm^{-1}) suggests a chelating binding mode for $CH_3(CH_2)_{14}COO^-$ ligand.

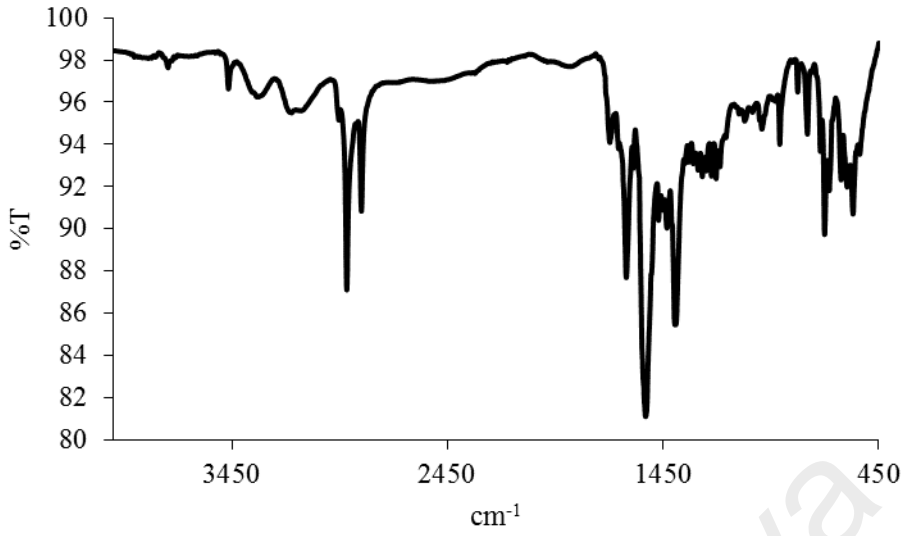

Figure 4.208 FTIR spectrum of **Complex 21**

Its **UV-vis** spectrum in DMSO (**Figure 4.209**) shows a broad *d-d* band at 650 nm (ε_{max}, 224 M^{-1} cm^{-1}) assigned to $^2B_2 \rightarrow {}^2B_1$ electronic transition, and an intense band at 249 nm (ε_{max}, 5152 M^{-1} cm^{-1}) assigned to LMCT transition. This suggests the geometry at each Cu centre was square pyramidal geometry.

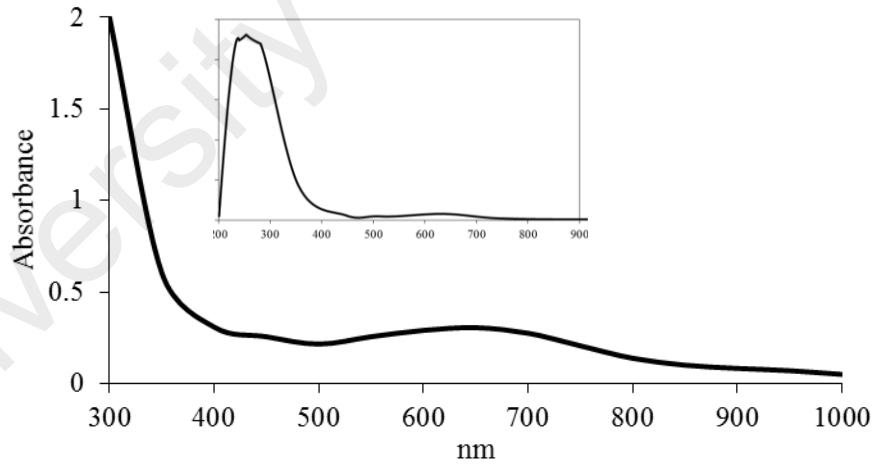

Figure 4.209 UV-vis spectrum of **Complex 21**

Its E_o value, calculated from λ_{edge} = 337 nm, was 3.7 eV. This is just slightly higher than **Complex 17** ($\{[Cu(CH_3COO)_2(L3)]\}_n$; 3.3 eV), which indicates that the long alkyl chain and nuclearity have a small effect on the value of E_o.

Upon excitation at 249 nm (LMCT transition), its **fluorescence** spectrum shows two overlapping peaks at λ_{max} 446 nm and 530 nm (**Figure 4.210**). This suggests two

different paths for the excited complex to return to the ground state. Its E_o value (calculated from λ_{edge} = 644 nm) was 1.9 eV. Additionally, its Stokes shift was 197 nm.

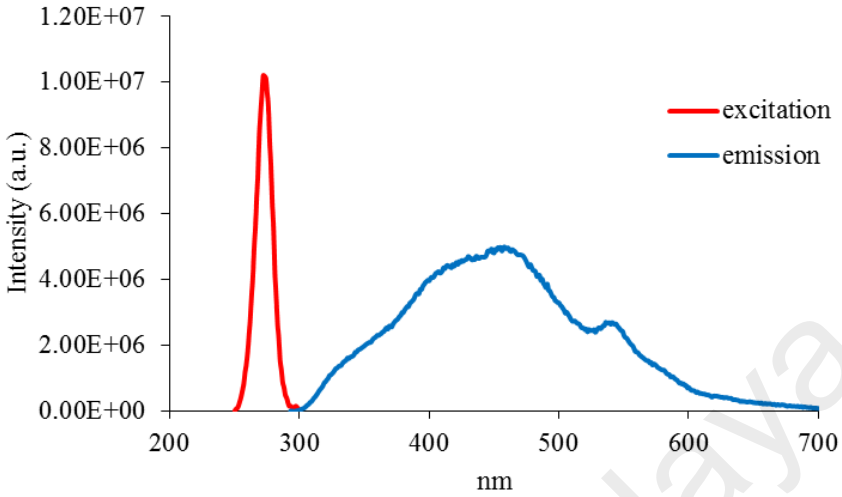

Figure 4.210 Fluorescence spectrum of **Complex 21** (λ_{ex} = 249 nm)

Its $\boldsymbol{\tau}$, calculated as before from its **decay** curve (**Figure 4.211**), was 2.8 ns. This is the same as **Complex 17** ($\boldsymbol{\tau}$ = 2.8 ns), suggesting that the different chain length of the carboxylate ligands has no significant effect on the stability of the excited complex.

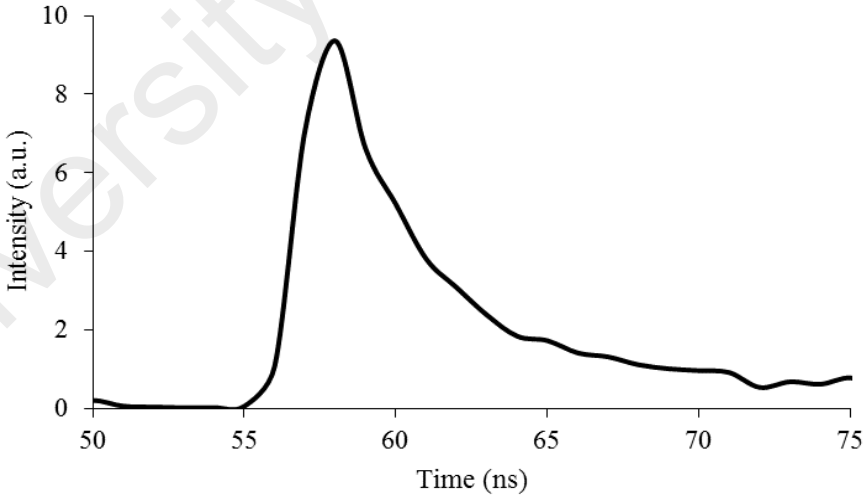

Figure 4.211 Fluorescence decay of **Complex 21**

Upon excitation at 650 nm (*d-d* transition), its **fluorescence** spectrum shows a peak at λ_{max} 680 nm (**Figure 4.212**). Its E_o, calculated from λ_{edge} = 687 nm, was 1.8 eV and its $\boldsymbol{\tau}$ value, calculated as before from its decay curve, was 2.6 ns. Its Stokes shift was 30 nm.

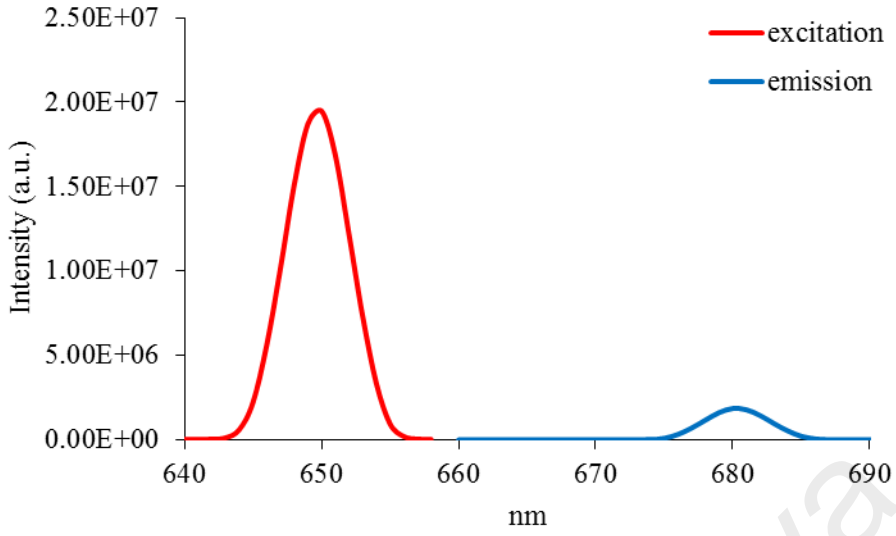

Figure 4.212 Fluorescence spectrum of **Complex 21** (λ_{ex} = 650 nm)

Its **CV** (**Figure 4.213**), recorded cathodically from 0 V within the potential window of -1.5 V to +1.5 V. It showed two cathodic peaks at -0.37 V and -1.1 V, when the potential was decreased from 0 V to -1.5 V; and two corresponding anodic peaks at -0.18 V and +1.3 V, when the potential was decreased from -1.5 V to +1.5 V. The redox processes are shown in **Scheme 4.8**. The large peak separations (ΔE_{p1} = 930 mV and ΔE_{p2} = 1280 mV) indicate quasireversible processes.

$$[\text{Cu(II)Cu(II)}] \underset{+1.30\ \text{V}}{\overset{-0.37\ \text{V}}{\rightleftharpoons}} [\text{Cu(II)Cu(I)}] \underset{-0.18\ \text{V}}{\overset{-1.10\ \text{V}}{\rightleftharpoons}} [\text{Cu(I)Cu(I)}]$$

Scheme 4.8 The redox process of **Complex 21**

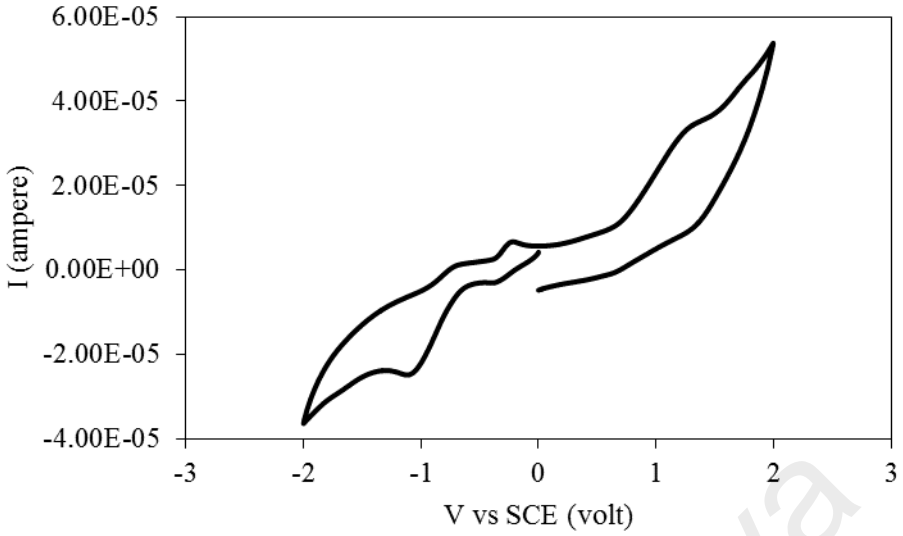

Figure 4.213 CV of **Complex 21**

The HOMO and LUMO values, calculated as before from the onset oxidation potential (-0.37 V) and onset reduction potential (-0.02 V), are 4.03 eV and 4.38 eV (versus SCE), respectively. Thus, its E_e value was 0.35 eV, which is slightly wider than **Complex 17** ($\{[Cu(CH_3COO)_2(L3)]\}_n$; 0.2 eV).

Its μ_{eff} value, calculated as before from the values of FM = 1508.12 g mol^{-1} (repeat unit), χ_g = 1.32 x 10^{-6} cm^3 g^{-1}, χ_M = 1.99 x 10^{-4} cm^3 mol^{-1}, and χ_{dia} = -9.21 x 10^{-4} cm^3 mol^{-1}) was 2.66 B.M. at 298 K. This is slightly higher than expected value for dinuclear Cu(II) complexes (2.45 B.M.), indicating a ferromagnetic interaction between the metal centres along the polymeric chain.

Its **TGA** trace (**Figure 4.214**) shows a sharp drop of about 93.1% in the temperature range of 238 – 672 °C, which is assigned to the evaporation of two H_2O molecules, the decomposition of four $CH_3(CH_2)_{14}COO$ and *L3* ligands (expected, 91.5%). The amount of residue above 672 ^oC was 6.9% (expected, 10.5% assuming pure CuO). Hence, **Complex 21** (T_{dec} = 238 ^oC) was significantly more thermally stable than **Complex 17** (T_{dec} = 180 ^oC).

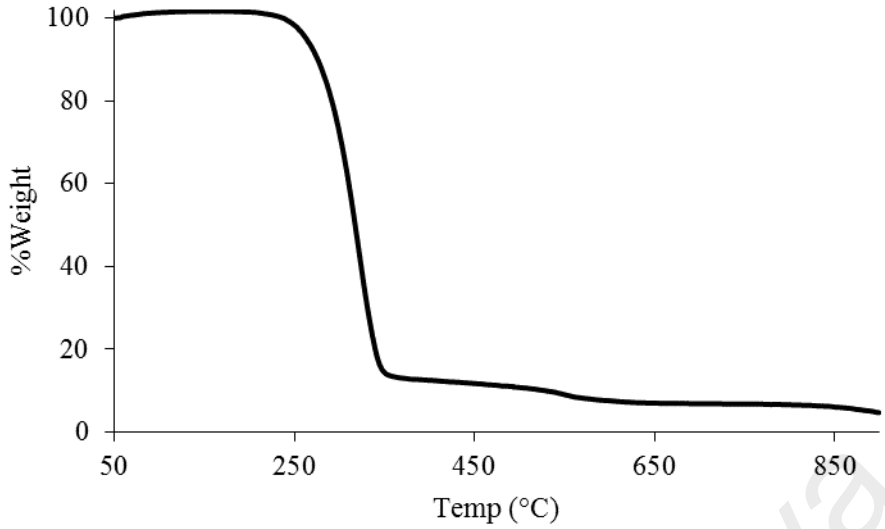

Figure 4.214 TGA of **Complex 21**

Its **DSC** scan (**Figure 4.215**) was done for heating-cooling cycles, in the temperature range 25 - 225 ºC. It shows three endothermic peaks at 55˚C ($\Delta H = +43.5$ kJ mol^{-1}) assigned to Cr_1-to-Cr_2 transition, at 84.5 ˚C ($\Delta H = +95.2$ kJ mol^{-1}) assigned to Cr_2-to-M transition, and at 177 ˚C ($\Delta H = +41.3$ kJ mol^{-1}) assigned to M_1-to-M_2 transitions. On cooling, there were three exothermic peaks at 159 ˚C ($\Delta H = -33.5$ kJ mol^{-1}) assigned to M_2-to-M_1 transition, at 80 ˚C ($\Delta H = -51.3$ kJ mol^{-1}) assigned to M_1-to-Cr_2 transition, and at 50 ˚C ($\Delta H = -67.4$ kJ mol^{-1}) assigned to Cr_2-to-Cr_1 transition.

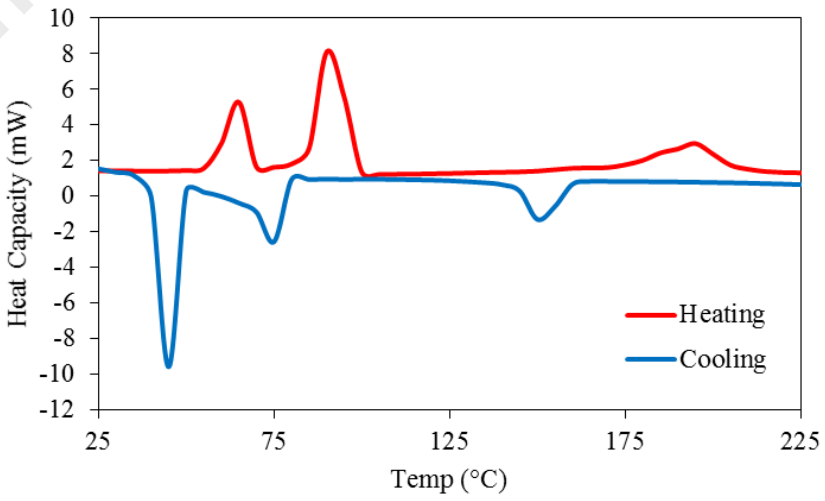

Figure 4.215 DSC of **Complex 21**

Its **POM** was recorded for two heating-cooling cycles in the temperature range 25 – 225 ^{o}C. On cooling, there was an optical texture at 141 ^{o}C. The textures then grew slowly on further cooling to room temperature (**Figure 4.216**).

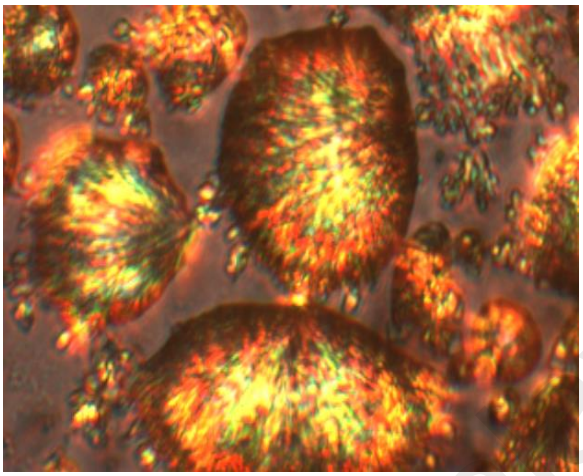

Figure 4.216 The photomicrographs of **Complex 21** on cooling at 141 ^{o}C

4.4.7 Reaction of nickel(II) hexadecanoate with L3

Nickel(II) hexadecanoate ($[Ni(CH_3(CH_2)_{14}COO)_2(H_2O)_2].3H_2O$) reacted with *L3* (mole ratio 1:1) to give a greenish powder (**Complex 22**), and the yield was 65.6%. Its solubility was similar to previously discussed complexes.

The **elemental analytical** data for the complex (64.6% C; 9.4% H; 4.1% N) were in excellent agreement with those calculated for the repeat unit $Ni_2C_{79}H_{133}N_5O_{10}S$ (64.9% C; 9.2% H; 4.8% N; formula weight, 1462.38 g mol^{-1}). Combining these with the spectroscopic data discussed below, its proposed structural formula is $\{[Ni_2(CH_3(CH_2)_{14}COO)_4(L3)]\}_n$. Hence, it is a dinuclear Ni(II) complex similar to **Complex 18** $\{[Ni_2(CH_3COO)_4(L3)].5H_2O\}_n$.

Its **FTIR** spectrum (**Table 4.9**; **Figure 4.217**) shows the presence of the expected functional groups. The ΔCOO value (95 cm^{-1}) suggests a chelating binding mode for $CH_3(CH_2)_{14}COO^-$ ligand.

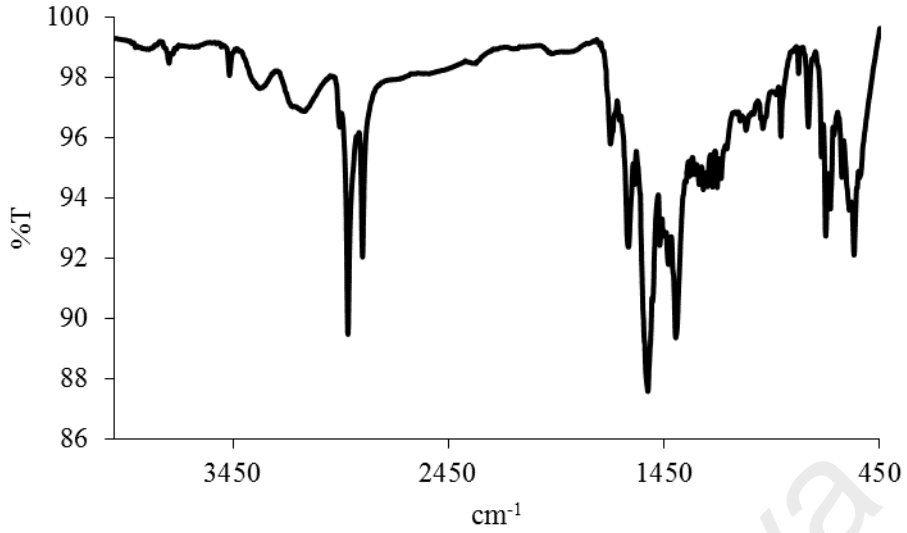

Figure 4.217 FTIR spectrum of **Complex 22**

Its **UV-vis** spectrum in DMSO (**Figure 4.218**) shows a weak broad band at 852 nm (ε_{max}, 158.8 M^{-1} cm^{-1}), assigned to $^3A_{2g}$ (F) → $^3T_{2g}$ (F); 625 nm (ε_{max}, 243.8 $M^{-1}cm^{-1}$), assigned to $^3A_{2g}$ (F) → $^3T_{1g}$ (F); and 400 nm (ε_{max}, 243.8 $M^{-1}cm^{-1}$), assigned to $^3A_{2g}$ (F) → $^3T_{1g}$ (P). These electronic transitions suggest an octahedral geometry at Ni(II) centre. An intense MLCT band is also observed at 248 nm (ε_{max}, 2.7x10^3 M^{-1} cm^{-1}).

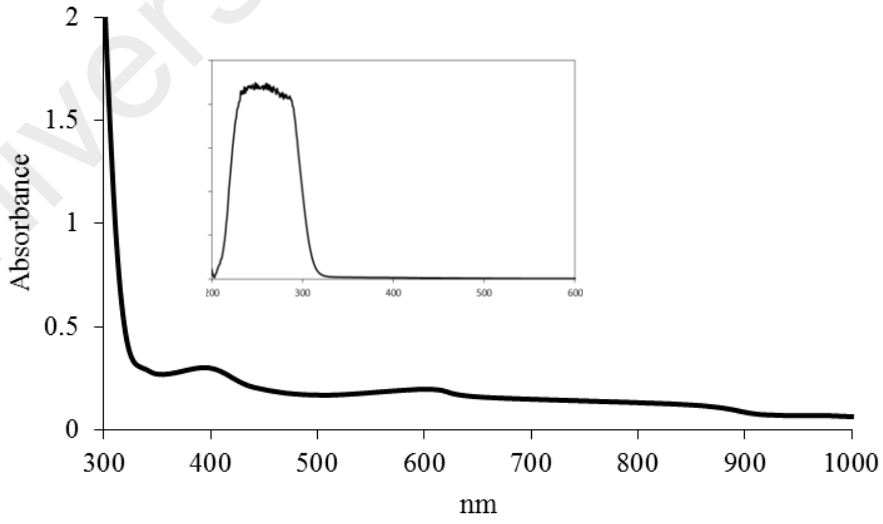

Figure 4.218 UV-vis spectrum of **Complex 22**

Its E_o value, calculated from λ_{edge} = 346 nm, was 3.6 eV. The value is similar to **Complex 18** ($\{[Ni_2(CH_3COO)_4(L3)].5H_2O\}_n$; 3.5 eV).

Upon excitation at 248 nm (MLCT transition), its **fluorescence** spectrum shows three overlapping peaks at λ_{max} 330 nm, 435 nm and 530 nm (**Figure 4.219)**. This suggests three different paths for the excited complex to return to the ground state. Its E_o value (calculated from λ_{edge} = 652 nm) was 1.9 eV. This is similar to **Complex 18** (2.0 eV). The value of its $\boldsymbol{\tau}$, calculated as before from its **decay** curve (**Figure 4.220**), was 2.9 ns. Its Stokes shift was 187 nm.

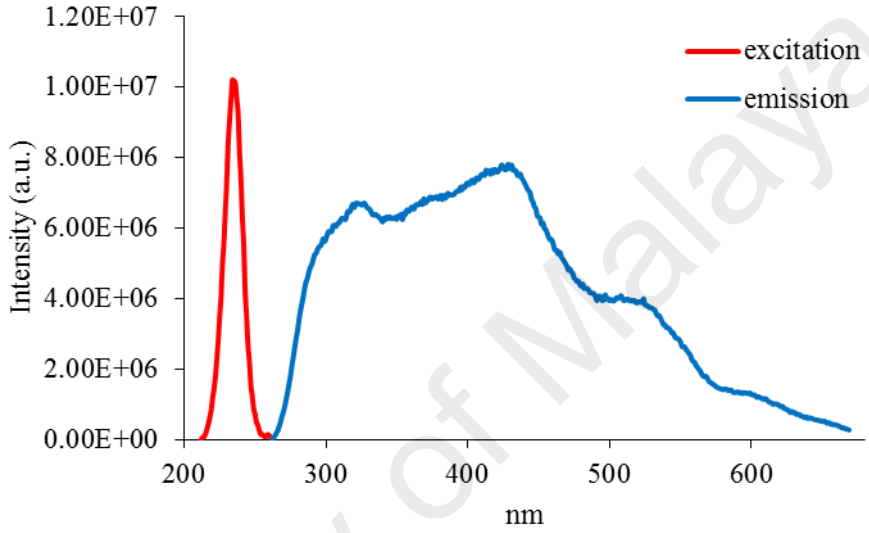

Figure 4.219 Fluorescence spectrum of **Complex 22** (λ_{ex} = 248 nm)

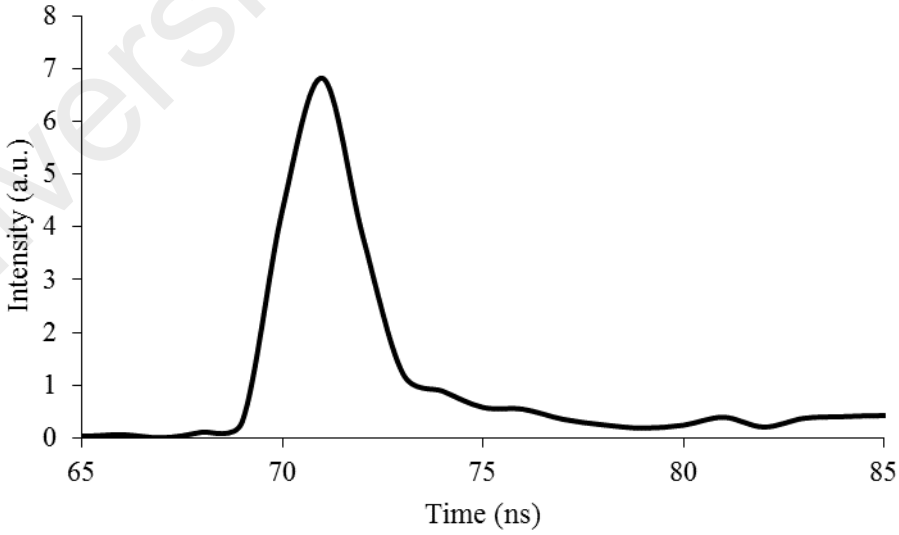

Figure 4.220 Fluorescence decay of **Complex 22**

However, upon excitation at 400 nm, (*d-d* transition), its **fluorescence** spectrum shows a peak at λ_{max} 419 nm (**Figure 4.221**). Its E_o, calculated from λ_{edge} = 426 nm, was

2.9 eV, and its τ, calculated as before from its **decay** curve, was 3.5 ns. In addition, its Stokes shift was 19 nm.

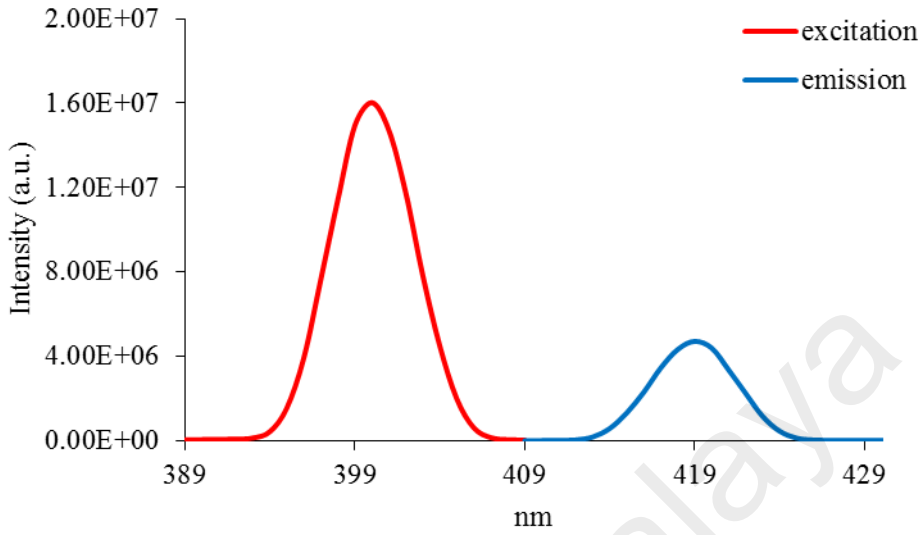

Figure 4.221 Fluorescence spectrum of **Complex 22** (λ_{ex} = 400 nm)

Its **CV** (**Figure 4.222**), recorded anodically from 0 V within the potential window of +1.5 V to -1.5 V. It showed a weak anodic peak at +1.02 V, when the potential was increased from 0 V to +1.5 V. This is assigned to ligand-based oxidation. The result suggests that Ni(II) atom in the complex was redox inactive. Hence, its E_e cannot be calculated.

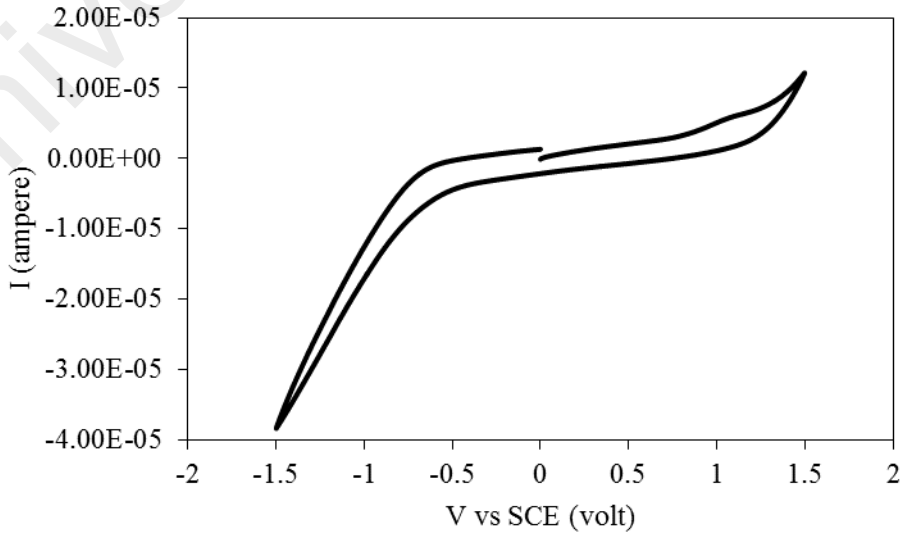

Figure 4.222 CV of **Complex 22**

Its μ_{eff} value, calculated as before from the values of FM = 1462.38 g mol^{-1} (repeat unit), χ_g = 8.41 x 10^{-6} cm^3 g^{-1}, χ_M = 1.23 x 10^{-2} cm^3 mol^{-1}, and χ_{dia} = -0.87 x 10^{-3} cm^3 mol^{-1}, was 5.62 B.M. at 298 K. This is in agreement with the expected value for a dinuclear Ni(II) complex (5.66 B.M). It indicates that **Complex 22** was paramagnetic with no magnetic interaction between the Ni(II) centres in the polymeric chain.

Its **TGA** trace (**Figure 4.223**) shows the total weight loss of 95.6% in the temperature range of 225 – 772 °C, assigned to the decomposition of four $CH_3(CH_2)_{14}COO^-$ and *L3* ligands (expected, 92%). The amount of residue at temperature above 772 °C is 4.4% (expected, 5.1% assuming pure NiO). Hence, it was slightly more thermally stable (T_{dec} = 225 °C) compared to **Complex 18** ($\{[Ni_2(CH_3COO)_4(L3)].5H_2O\}_n$; T_{dec} = 216 °C).

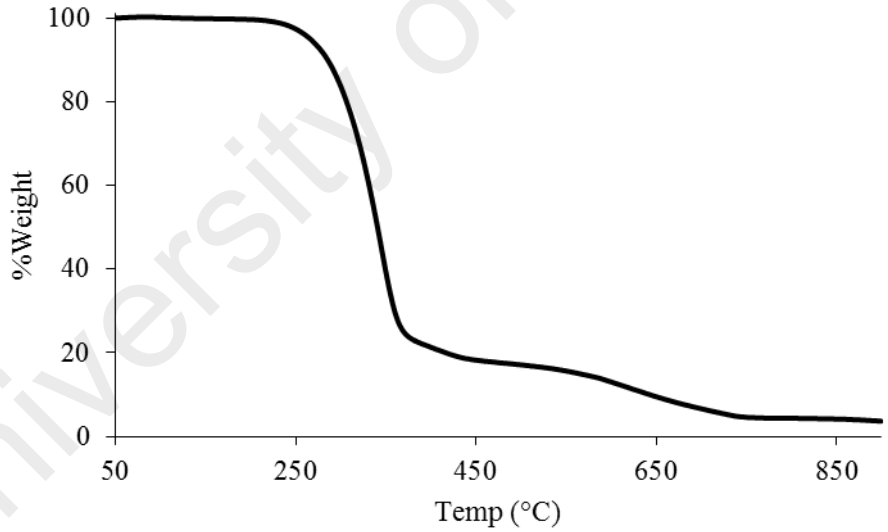

Figure 4.223 TGA of **Complex 22**

Its **DSC** scan (**Figure 4.224**) was recorded from 25 to 200 °C for one heating-and-cooling cycle. On heating, there were three endothermic peaks at 56.3 °C (ΔH = +38.3 kJ mol^{-1}), assigned to Cr_1-to-Cr_2 transition, at 85 °C (ΔH = +50.9 kJ mol^{-1}), assigned to Cr_2-to-M_1 transition, and 141.5 °C (ΔH = +1.7 kJ mol^{-1}), assigned to

M_1-to-M_2 transition. On cooling, there were two exothermic peaks at 156 °C (ΔH = -51.5 kJ mol^{-1}), assigned to M_2-to-Cr_2 transition and at 60 °C (ΔH = -20.3 kJ mol^{-1}), assigned to Cr_2-to-Cr_1 transition.

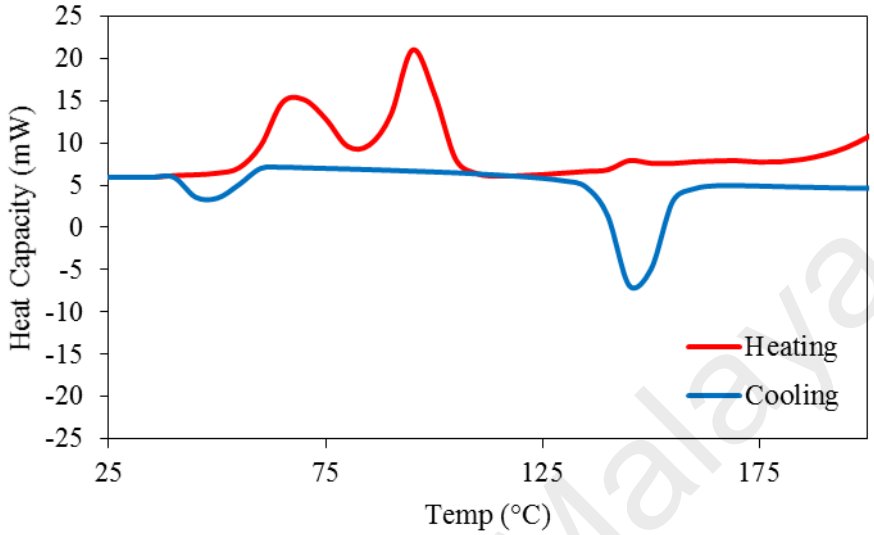

Figure 4.224 DSC of **Complex 22**

The **POM** for the complex was recorded for two heating-cooling cycles from 25 °C to 200 °C. It was observed to melt at about 180 °C. On cooling from 200 °C, an optical texture was first observed at about 158 °C, which solidified at 115 °C (**Figure 4.225**).

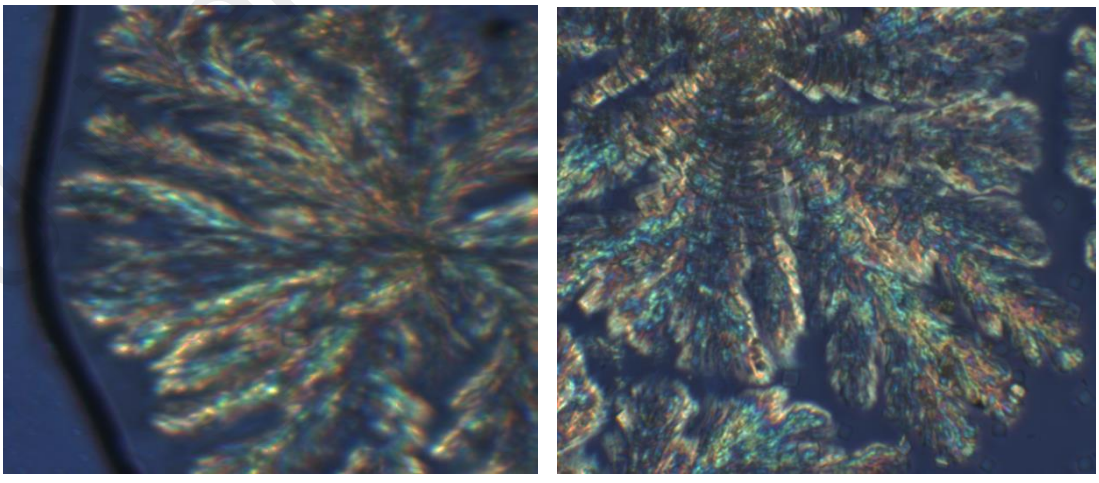

(a) (b)

Figure 4.225 The photomicrographs of **Complex 22** on cooling from 200 °C: (a) at 158 °C; and (b) at 115 °C (solid).

4.4.8 Reaction of cobalt(II) hexadecanoate with L3

Cobalt(II) hexadecanoate ($[Co(CH_3(CH_2)_{14}COO)_2(H_2O)_2].4H_2O$) reacted with *L3* (mole ratio 1:1) to give a purplish powder (**Complex 23**), and the yield was 82.6%. Its solubility was similar to previously discussed complexes.

The **elemental analytical** data for the complex (63.0% C; 7.7% H; 7.9% N) were in excellent agreement with those calculated for the repeat unit $CoC_{47}H_{71}N_5O_6S$ (63.2% C; 8.0% H; 7.8% N; formula weight, 893.09 g mol^{-1}). Combining these with the spectroscopic data discussed below, the proposed structural formula for **Complex 23** is $\{[Co(CH_3(CH_2)_{14}COO)_2(L3)]\}_n$.

Its **FTIR** spectrum (**Table 4.9**; **Figure 4.226**) shows the presence of the expected functional groups. The ΔCOO value (73 cm^{-1}) suggests a chelating binding mode for $CH_3(CH_2)_{14}COO^-$ ligand.

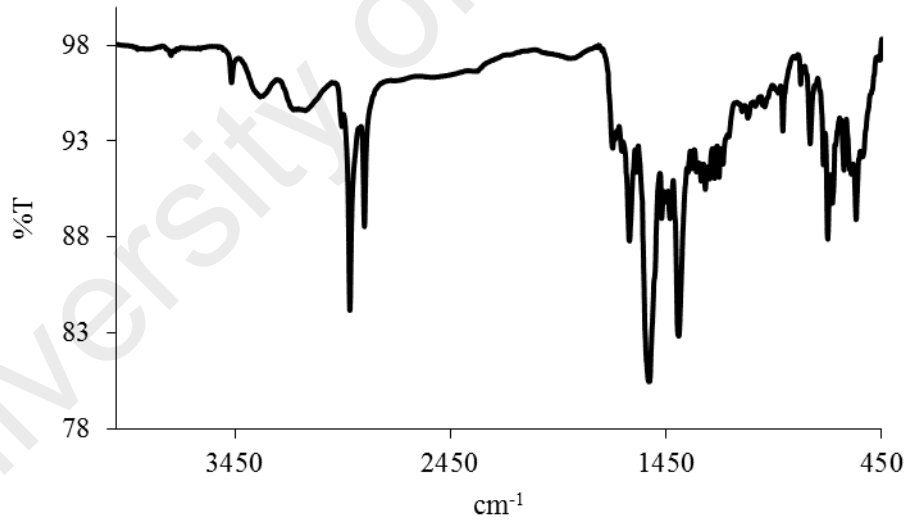

Figure 4.226 FTIR spectrum of **Complex 23**

Its **UV-vis** spectrum in DMSO (**Figure 4.227**) shows broad overlapping *d-d* bands at 664 nm (ε_{max}, 124 M^{-1} cm^{-1}), assigned to $^4T_{1g}$ (F) → $^4T_{2g}$ (F); at 553 nm (ε_{max}, 141 M^{-1} cm^{-1}), assigned to $^4T_{1g}$ (F) → $^4T_{1g}$ (P); and at 399 nm (ε_{max}, 239.7 M^{-1} cm^{-1}) assigned to $^4T_{1g}$ (F) → $^4A_{2g}$ (F). These suggest an octahedral

geometry at HS Co(II) centres. Also observed is an intense MLCT band at 241 nm (ε_{max}, 1758 M^{-1} cm^{-1}).

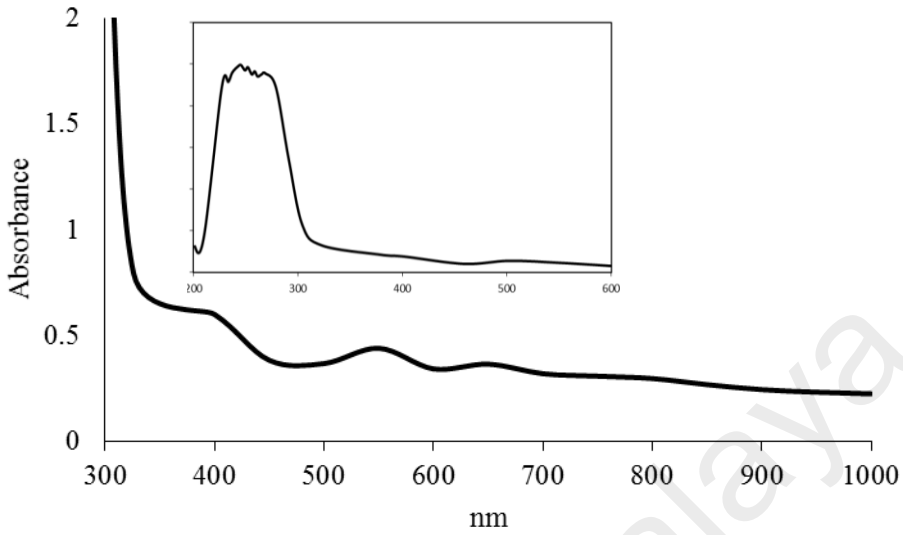

Figure 4.227 UV-vis spectrum of **Complex 23**

Its E_o value, calculated from λ_{edge} = 347 nm, was 3.6 eV. This value is slightly higher than **Complex 19** ({[$Co(CH_3COO)_2(L3)].2H_2O\}_n$; 3.3 eV).

Upon excitation at 241 nm (MLCT transition), its **fluorescence** spectrum shows three overlapping peaks at λ_{max} 294 nm, 397 nm and 517 nm (**Figure 4.228)**. This suggests three different paths for the excited complex to return to the ground state. Its E_o value (calculated from λ_{edge} = 574 nm) was 2.1 eV. The value of its $\boldsymbol{\tau}$, calculated as before from its **decay** curve (**Figure 4.229**), was 3.0 ns. Hence, the excited state lifetime of the complex is slightly longer than **Complex 19** (2.8 ns). In addition, its Stokes shift was 156 nm.

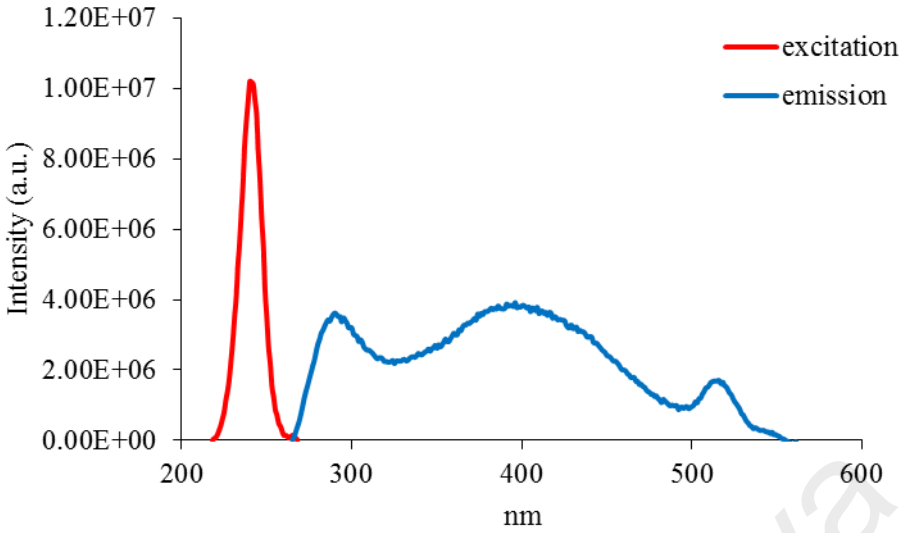

Figure 4.228 Fluorescence spectrum of **Complex 23** (λ_{ex} = 241 nm)

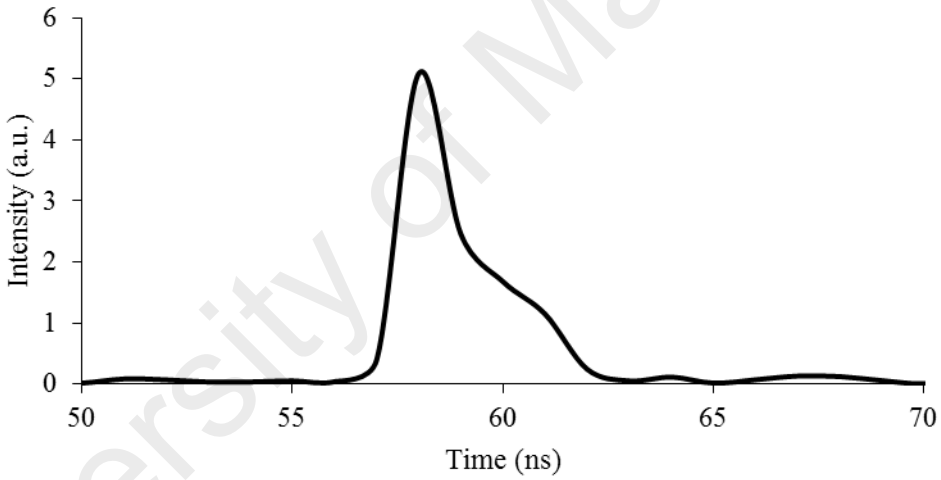

Figure 4.229 Fluorescence decay of **Complex 23**

However, upon excitation at 399 nm (*d-d* transition), its **fluorescence** spectrum shows a peak at λ_{max} 410 nm (**Figure 4.230**). Its E_o, calculated from λ_{edge} = 429 nm, was 2.9 eV, and its τ value, calculated from its **decay** curve, was 3.4 ns. Its Stokes shift was 11 nm.

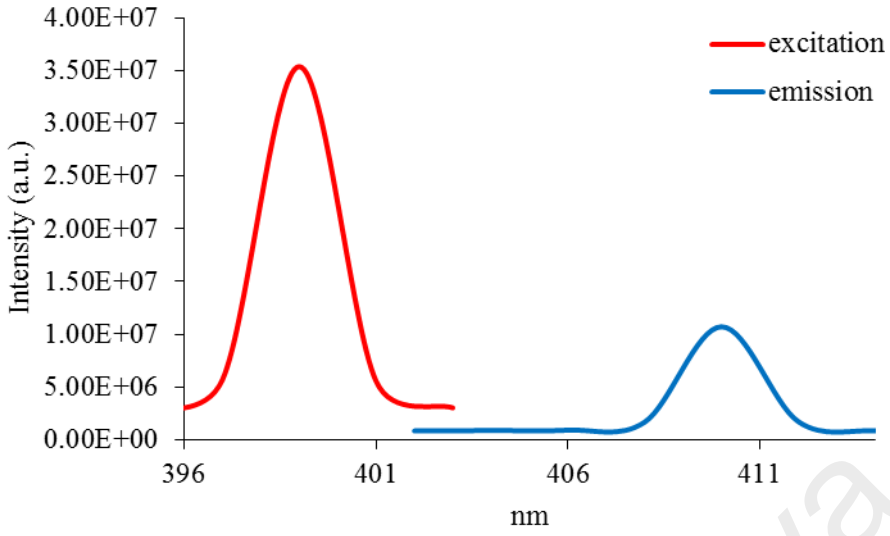

Figure 4.230 Fluorescence spectrum of **Complex 23** (λ_{ex} = 399 nm)

Its **CV** (**Figure 4.231**) was recorded anodically from 0 V within the potential window of +1.5 V to -1.5 V. It does not show any distinct oxidation and reduction peaks. Thus, **Complex 23** is redox inactive. Accordingly, its E_e cannot be calculated.

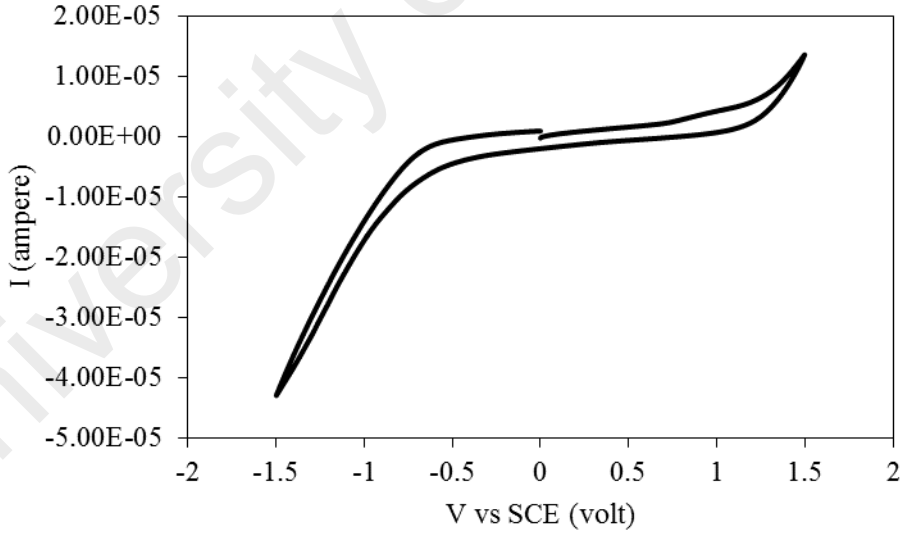

Figure 4.231 CV of **Complex 23**

Its $\boldsymbol{\mu_{eff}}$ value, calculated as before from the values of FM = 893.09 g mol^{-1} (repeat unit), χ_g = 5.9 x 10^{-6} cm^3 g^{-1}, χ_M = 5.27 x 10^{-3} cm^3 mol^{-1}, and χ_{dia} = -4.86 x 10^{-4} cm^3 mol^{-1}), was 3.73 B.M. at 298 K. This is similar to the expected

value for a HS Co(II) complex (d^7) (3.87 B.M.), suggesting a negligible magnetic interaction between the Co(II) centres in the polymeric chain [45].

Its **TGA** trace (**Figure 4.232**) shows the total weight loss of 92.4% in the temperature range of 205 - 720 °C, assigned to the decomposition of two $CH_3(CH_2)_{14}COO$ and *L3* ligands (expected, 93.4%). The amount of residue at temperatures above 720 °C was 7.6% (expected, 8.4% assuming pure CoO). Hence, **Complex 22** (T_{dec} = 205 °C) was thermally more stable than **Complex 19** ($\{[Co(CH_3COO)_2(L3)].2H_2O\}_n$; T_{dec} = 184 °C).

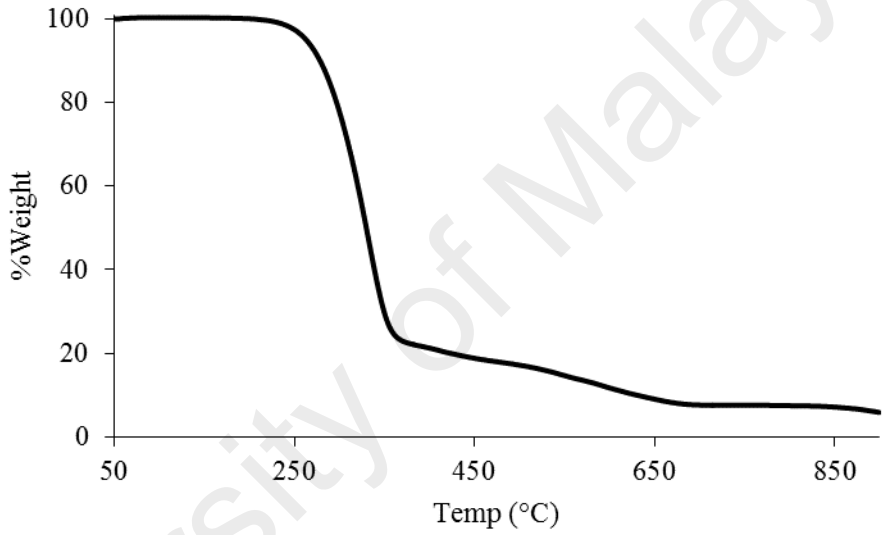

Figure 4.232 TGA of **Complex 23**

Its **DSC** scan (**Figure 4.233**) was done for one heating-cooling cycle, in the temperature range 25 - 130 °C. On heating, there were two endothermic peaks at 57.3 °C (ΔH = +21.2 kJ mol^{-1}), assigned to Cr_1-to-Cr_2 transition, and at 75 °C (ΔH = +53.9 kJ mol^{-1}), assigned to Cr_2-to-M transition. On cooling, there were two exothermic peaks at 80 °C (ΔH = -40.2 kJ mol^{-1}), assigned to M-to-Cr_2 transition, and at 45 °C (ΔH = -5.2 kJ mol^{-1}), assigned to Cr_2-to-Cr_1 transition.

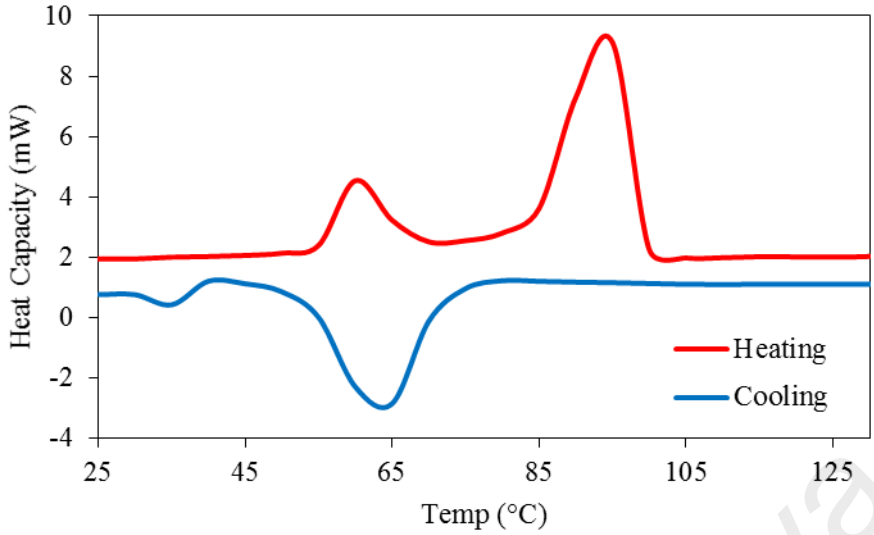

Figure 4.233 DSC of **Complex 23**

The **POM** for **Complex 23** was recorded for two heating-cooling cycles from 25 to 180 ºC. Up to 130 ºC, there was no melting process and clearing. On cooling from 130 ºC, it was observed that the texture becomes darker at about 80 ºC (**Figure 4.234**).

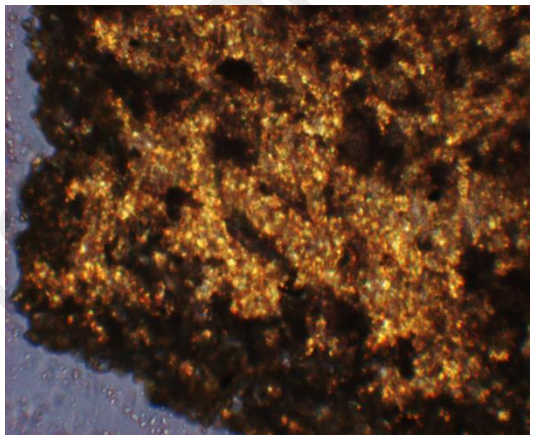

Figure 4.234 The photomicrographs of **Complex 23** at 80 ºC on cooling from 130 ºC

4.4.9 Reaction of iron(II) hexadecanoate with L3

Iron(II) hexadecanoate ($[Fe(CH_3(CH_2)_{14}COO)_2(H_2O)_2].4H_2O$) reacted with *L3* (mole ratio 1:1) to give a pale pink powder (**Complex 24**), and the yield was 73.0%. Its solubility was similar to the previously discussed complexes.

The **elemental analytical** data for the complex (59.9% C; 8.0% H; 7.0% N) were in excellent agreement with those calculated for the repeat unit $FeC_{47}H_{77}N_5O_9S$

(59.8% C; 8.2% H; 7.4% N; formula weight, 944.05 g mol^{-1}). Combining these with the spectroscopic data discussed below, the proposed structural formula for **Complex 24** is $\{[Fe(CH_3(CH_2)_{14}COO)_2(L3)].3H_2O\}_n$.

Its **FTIR** spectrum (**Table 4.9**; **Figure 4.235**) shows the presence of the expected functional groups. The ΔCOO value (81 cm^{-1}) suggests a chelating binding mode for $CH_3(CH_2)_{14}COO^-$ ligand.

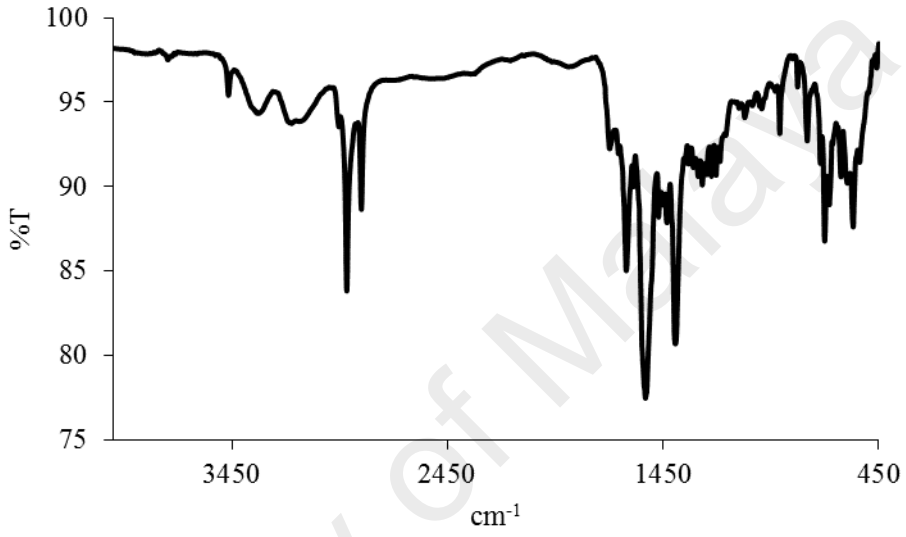

Figure 4.235 FTIR spectrum of **Complex 24**

Its **UV-vis** spectrum in DMSO (**Figure 4.236**) shows a broad band at 894 nm (ε_{max}= 163 M^{-1} cm^{-1}), assigned to $^5T_{2g} \rightarrow {}^5E_g$ electronic transition, and an intense band at 263 nm (ε_{max}= 3.9x10^3 M^{-1} cm^{-1}), assigned to MLCT transition. This suggest the geometry at the HS Fe(II) centre was octahedral.

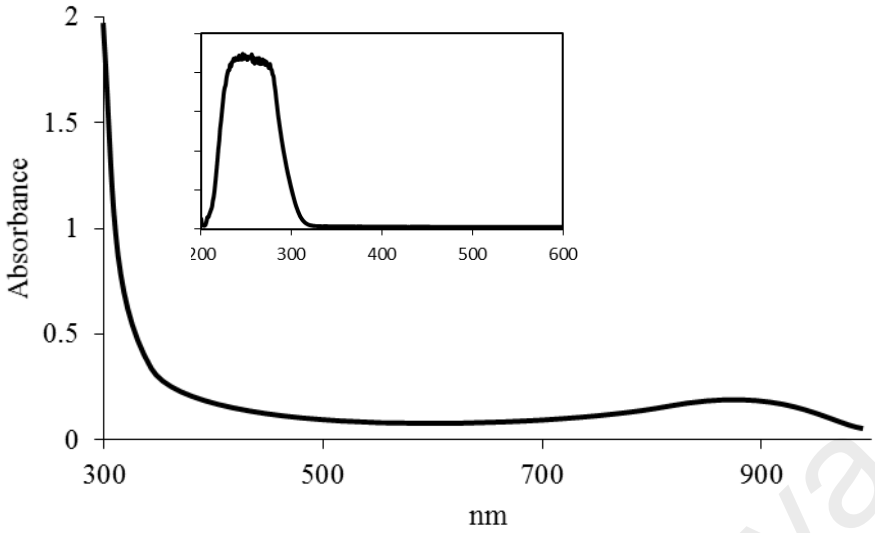

Figure 4.236 UV-vis spectrum of **Complex 24**

Its E_o value, calculated from λ_{edge} = 350 nm, was 3.5 eV. This value is significantly higher than **Complex 20** ($\{[Fe_2(CH_3COO)_4(L3)].2H_2O\}_n$; 2.2 eV).

Upon excitation at 263 nm (MLCT transition), its **fluorescence** spectrum shows three overlapping peaks at λ_{max} 319 nm, 431 nm and 544 nm (**Figure 4.237)**. These suggest three different paths for the excited complex to return to the ground state. Its E_o value (calculated from λ_{edge} = 575 nm) was 2.1 eV. Additionally, its Stokes shift was 168 nm.

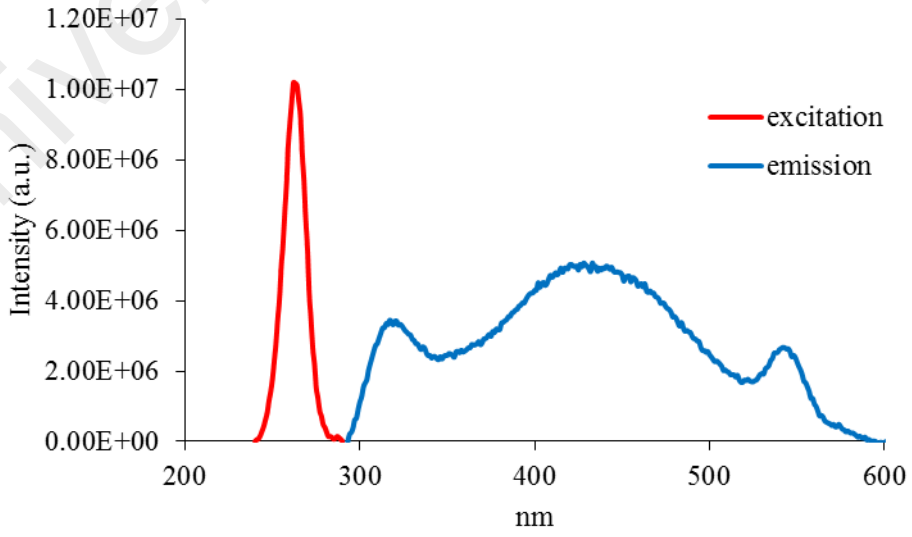

Figure 4.237 Fluorescence spectrum of **Complex 24** (λ_{ex} = 263 nm)

Its $\boldsymbol{\tau}$ value, calculated as before from its **decay** curve (**Figure 4.238**), was 3.0 ns. Hence, the lifetime of the excited complex was slightly longer than **Complex 20** ($\{[Fe_2(CH_3COO)_4(L3)].2H_2O\}_n$; 2.7 ns).

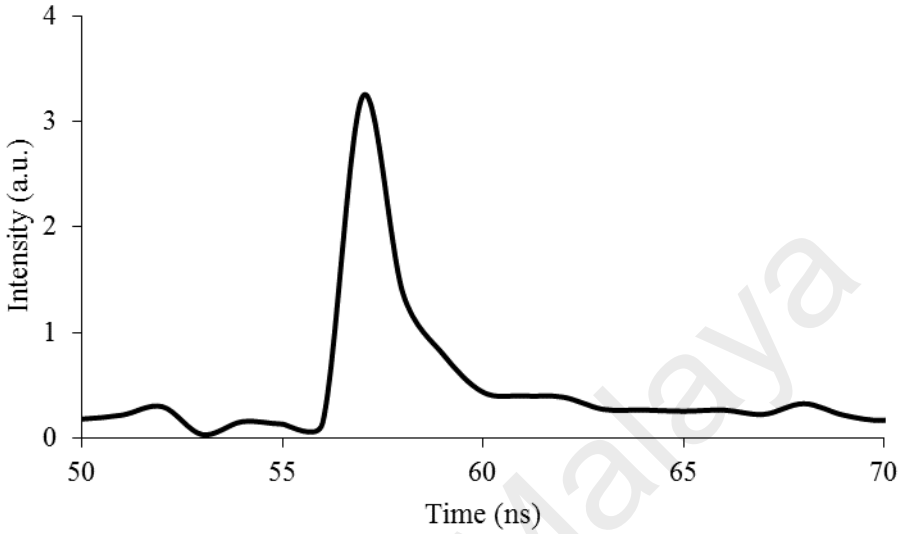

Figure 4.238 Fluorescence decay of **Complex 24**

Also, upon excitation at 894 nm (*d-d* transition), its **fluorescence** spectrum shows a peak at λ_{max} 900 nm (**Figure 4.239**). Its E_o, calculated from λ_{edge} = 904 nm, was 1.4 eV. This value was the same as **Complex 20** (1.4 eV). Its τ value, calculated as before from its **decay** curve, was 2.1 ns. Its Stokes shift was 6 nm.

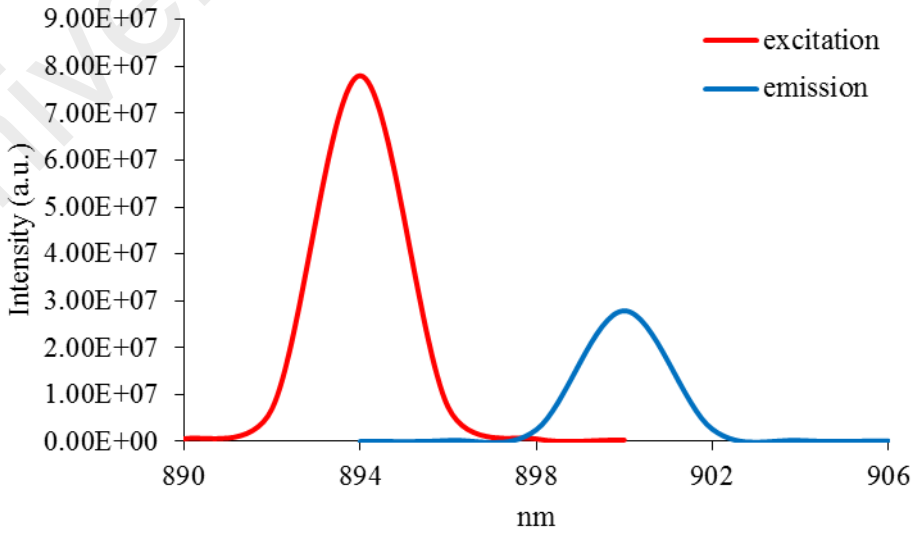

Figure 4.239 Fluorescence spectrum of **Complex 24** (λ_{ex} = 894 nm)

Its **CV** (**Figure 4.240**), recorded anodically from 0 V within the potential window of +1.5 V to -1.5 V, showed only one peak at -0.2 V. This is assigned to the irreversible oxidation of Fe(II) to Fe(III). Accordingly, its E_e cannot be calculated.

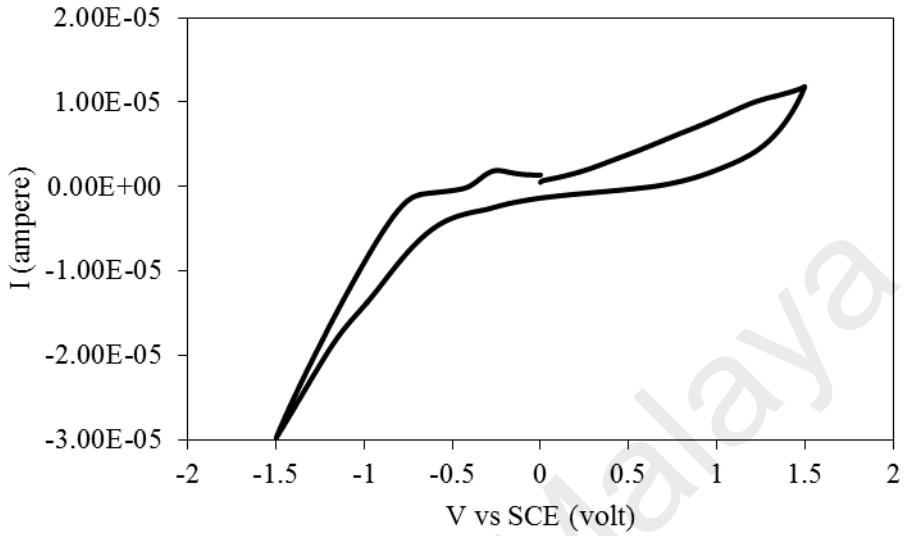

Figure 4.240 CV of **Complex 24**

Its μ_{eff} value, calculated as before from the values of FM = 944.05 g mol^{-1} (repeat unit), χ_g = 1.03 x 10^{-5} cm^3 g^{-1}, χ_M = 9.69 x 10^{-3} cm^3 mol^{-1}, and χ_{dia} = -5.57 x 10^{-4} cm^3 mol^{-1}), was 4.96 B.M. at 298 K. This is similar to the expected value for a HS Fe(II) complex (d^6) (4.89 B.M.), suggesting a negligible magnetic interaction between the Fe(II) centres in the polymeric chain [12].

Its **TGA** trace (**Figure 4.241**) shows a total weight loss of 93.3% from about 220 ^{o}C to 683 ^{o}C, assigned to the evaporation of three H_2O molecules, and the decomposition of two $CH_3(CH_2)_{14}COO$ and *L3* ligands (expected, 94%). The amount of residue above 683 ^{o}C was 6.7% (expected, 7.9% assuming pure FeO). Hence, the complex (T_{dec} = 220 °C) was more thermally stable than **Complex 20** ($\{[Fe_2(CH_3COO)_4(L3)].2H_2O\}_n$; T_{dec} = 191 ^{o}C).

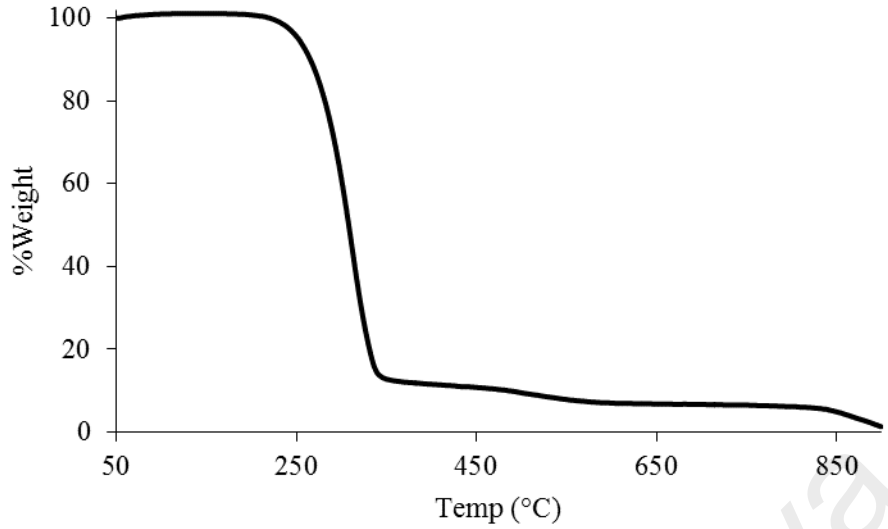

Figure 4.241 TGA of **Complex 24**

Its **DSC** scan (**Figure 4.242**) was recorded from 25 to 200 ºC for one heating-cooling cycle. On heating, there were two endothermic peaks at 54.3 °C (ΔH = +35.2 kJ mol^{-1}), assigned to Cr-to-M_1 transition, and at 80 °C (ΔH = +97.2 kJ mol^{-1}), assigned to M_1-to-M_2 transition. On cooling, there were exothermic peaks at 145 °C (ΔH = -19.7 kJ mol^{-1}), assigned to I-to-M_2 transition, 80 °C (ΔH = -47.4 kJ mol^{-1}), assigned to M_2-to-M_1 transition, and 45 °C (ΔH = -47.1 kJ mol^{-1}), assigned to M_1-Cr transition.

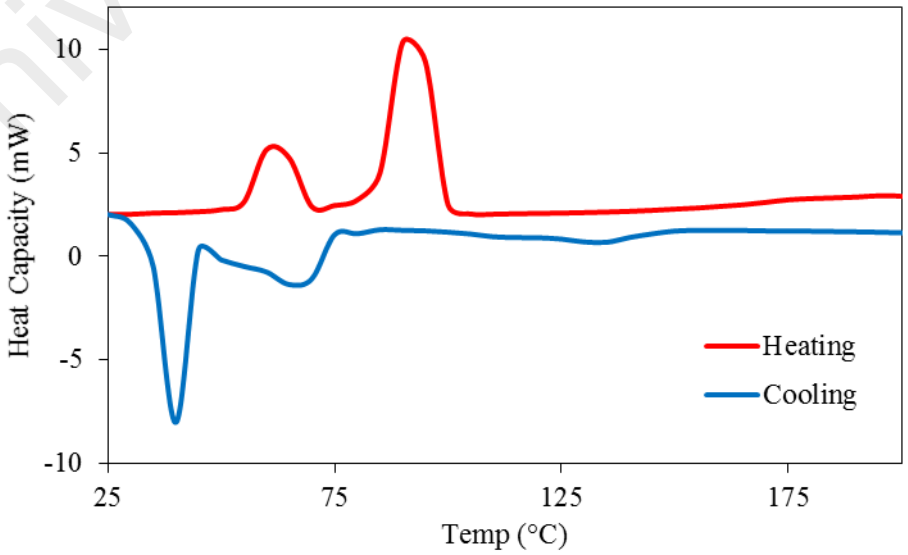

Figure 4.242 DSC of **Complex 24**

The **POM** for **Complex 24** was recorded for two heating-cooling cycles from 25 ^{o}C to 200 ^{o}C. The complex was observed to melt at about 150 ^{o}C, but did not clear completely at 200 ^{o}C. On cooling from 200 ^{o}C, an optical texture was first observed at about 185 ^{o}C, which grew on further cooling at 150 ^{o}C before it solidified at 46 ^{o}C (**Figure 4.243**).

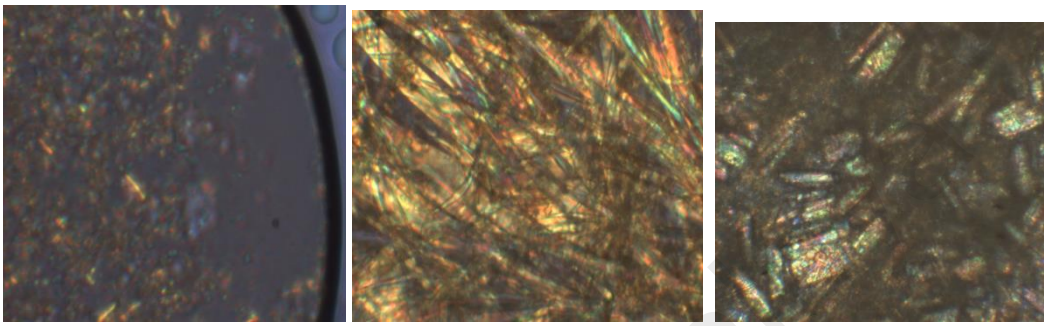

(a) (b) (c)

Figure 4.243 The photomicrographs of **Complex 24** on cooling from 200 ^{o}C: (a) at 185 ^{o}C; (b) at 150 ^{o}C; and (c) at 46 ^{o}C (solid).

4.4.10 Summary

To summarise, the chemical formulas, bandgaps, magnetic and thermal data for these complexes are shown in **Table 4.10**.

All complexes were polymers. Complexes **17**, **19**, **23** and **24** were made up of mononuclear repeat units, while complexes **18**, **20**, **21** and **22** were made up of dinuclear repeat units.

Except for **Complex 20** ($\{[Fe_2(CH_3COO)_4(L3)].2H_2O\}_n$, the optical bandgaps from the CT absorption bands for all complexes were similar (3.3 eV– 3.7 eV). The optical bandgap for **Complex 20** was the lowest (2.2 eV). This may be due to a more antibonding HOMO orbitals in HS Fe(II) atoms in the polymer. However, the optical bandgaps from the emission bands for all complexes were similar (1.9 eV – 2.1 eV). It is noted that the electrochemical bandgap was lowest for the Cu(II) complexes compared to the corresponding Ni(II) and Fe(II) complexes. This suggests a more facile

reduction of Cu(II) to Cu(I) compared to oxidation of Ni(II) to Ni(III) and Fe(II) to Fe(III).

The lifetimes of all of the excited complexes were similar (2.7 – 3.0 ns). This is consistent with the similar values of the bandgaps from the emission bands for all of the above complexes.

The Stokes shift for CT transition are in the range 96 -311 nm. **Complex 20** has the larger Stokes shift (311 nm), making it potential as photoseensitizer. On the other hand, stokes shift for *d-d* transition are similar for all complexes 11 – 34 nm.

All complexes are paramagnetic. The Cu(II) complexes showed antiferromagnetic interactions between the metal centres, while the Ni(II) hexadecanoate complex showed a weak antiferromagnetic interaction between the metal centres. Both Co(II) and Fe(II) complexes were high spin.

All complexes were thermally stable. Their decomposition temperatures range from 180 ^{o}C to 238 ^{o}C. Finally, all hexadecanoate complexes were mesomorphic.

Table 4.10 Complexes of *L3.H₂O*

Complex	Chemical Formula	Bandgap (eV)			τ (ns)	μeff (B.M.)	Tdec (°C)	LC
		Eo (abs)	Eo (em)	Ee				
17	$\{[Cu(CH_3COO)_2(L3)]\}_n$	3.3	2.0	0.20	2.8	1.56	180	-
18	$\{[Ni_2(CH_3COO)_4(L3)].5H_2O\}_n$	3.5	2.0		2.8	4.72	216	-
19	$\{[Co(CH_3COO)_2(L3)].2H_2O\}_n$	3.3	1.9	-	2.8	3.78	184	-
20	$\{[Fe_2(CH_3COO)_4(L3)].2H_2O\}_n$	2.2	2.0	1.19	2.7	7.35	191	-
21	$\{[Cu_2(CH_3(CH_2)_{14}COO)_4(L3)].2H_2O\}_n$	3.7	1.9	0.35	2.8	2.66	238	M
22	$\{[Ni_2(CH_3(CH_2)_{14}COO)_4(L3)]\}_n$	3.6	1.9	-	2.9	3.34	225	M
23	$\{[Co(CH_3(CH_2)_{14}COO)_2(L3)]\}_n$	3.6	2.1	-	3.0	3.73	205	M
24	$\{[Fe(CH_3(CH_2)_{14}COO)_2(L3)].3H_2O\}_n$	3.5	2.1	-	3.0	4.96	220	M

M = mesophase

4.5 Metal(II) Complexes of *L4*

4.5.1 Synthesis of L4

The ligand *L4* was obtained as a yellowish powder from the reaction of 2,6-diamino-4-phenyl-1,3,5-triazine with acetylenedicarboxylic acid. The yield was 78.4%. The reaction equation is shown in **Scheme 4.8**

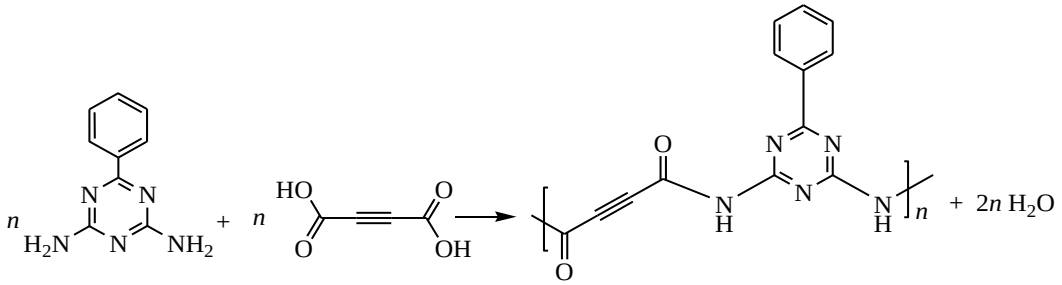

Scheme 4.8 Reaction equation for the preparation of *L4*

The results of the **elemental analyses** (58.3% C, 2.6% H, 26.1% N) were in good agreement with those calculated for the repeat unit for *L4* (formula, $C_{13}H_7N_5O_2$; formula weight, 256.06 g mol^{-1}; 58.9% C, 2.7% H, and 26.4% N).

Its **^{1}H-NMR** spectrum (**Figure 4.244**) supported the chemical formula. The amide proton appears as a broad at 6.87 ppm and all aromatic protons appear as a multiplet and doublet in the range 7.45 – 8.25 ppm.

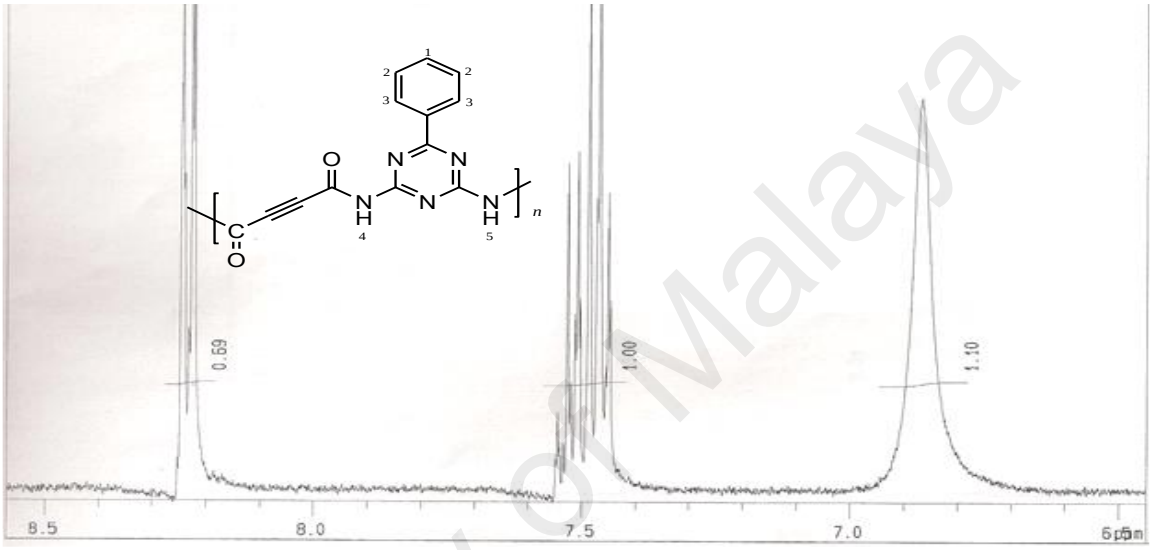

Figure 4.244 ^{1}H-NMR spectrum for *L4*

Table 4.11 The ^{1}H-NMR peak assignment for *L4*

Chemical Shift (ppm)	Integral	Multiplicity	Assignment
6.87	1.10	broad	H-4, H-5
7.45 - 7.54	1.00	multiplet	H-1, H-2
8.22 - 8.25	0.69	doublet	H-3

Its **FTIR** spectrum is shown in **Figure 4.245**, and the peak assignments are given in **Table 4.12** (which also include the data for the corresponding metal(II) complexes for later discussion). Hence, the spectrum shows the presence of the functional groups expected for the ligand.

Table 4.12 FTIR data (in cm^{-1}) and assignments for *L4* and its complexes

	NH -OH	CH_2 (asym)	CH_2 (sym)	C≡C	C=O (amide)	COO (asym)	COO (sym)	M-N
L4	3367w	-	-	2975m	1626m	-	-	-
25	3410m	-	-	2974w	1623m	1535s	1390m	580m
26	3446m	-	-	2964br	1616m	1536s	1396s	501m
27	3295m	-	-	2974w	1616m	1535s	1395s	500m
28	3297m	-	-	2979w	1617m	1534s	1396m	502m
29	3323m	2917s	2850m	2954w	1699m	1532s	1403m	591m
30	3336m	2916s	2849s	2953w	1698m	1532s	1391m	541m
31	3330m	2916s	2848m	2953w	1698m	1530s	1394m	568m
32	3322m	2915s	2848s	2953w	1695m	1530m	1409m	499m

s = strong; m = medium; w = weak; br = broad

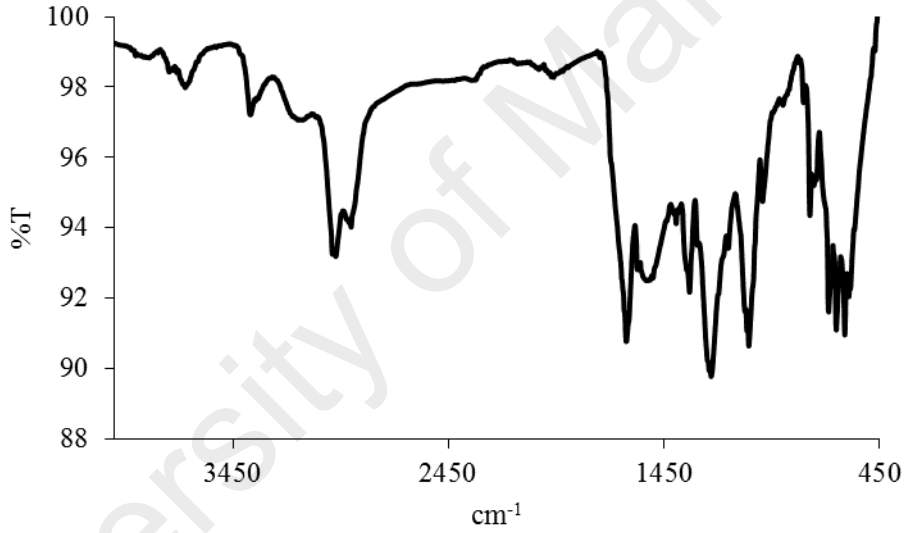

Figure 4.245 FTIR spectrum of *L4*

4.5.2 Reaction of copper(II) ethanoate with L4

Copper(II) ethanoate ($[Cu(CH_3COO)_2]$) reacted with *L4* (mole ratio 1:1) to give a green powder (**Complex 25**), and the yield was 98.4%. Its solubility was similar to the previously-discussed complexes.

The **elemental analytical** data for the complex (45.2% C; 2.9% H; 15.1% N) were in excellent agreement with those calculated for the repeat unit $CuC_{17}H_{13}N_5O_6$ (45.7% C; 2.9% H; 15.7% N; formula weight, 446.86 g mol^{-1}). Combining these with

the spectroscopic data discussed below, the proposed structural formula of **Complex 25** is $\{[Cu(CH_3COO)_2(L4)]\}_n$.

Its **FTIR** spectrum (**Figure 4.246**) shows the presence of the expected functional groups (**Table 4.12**). The ΔCOO value is 145 cm^{-1}, suggesting chelating CH_3COO^- ligands [1].

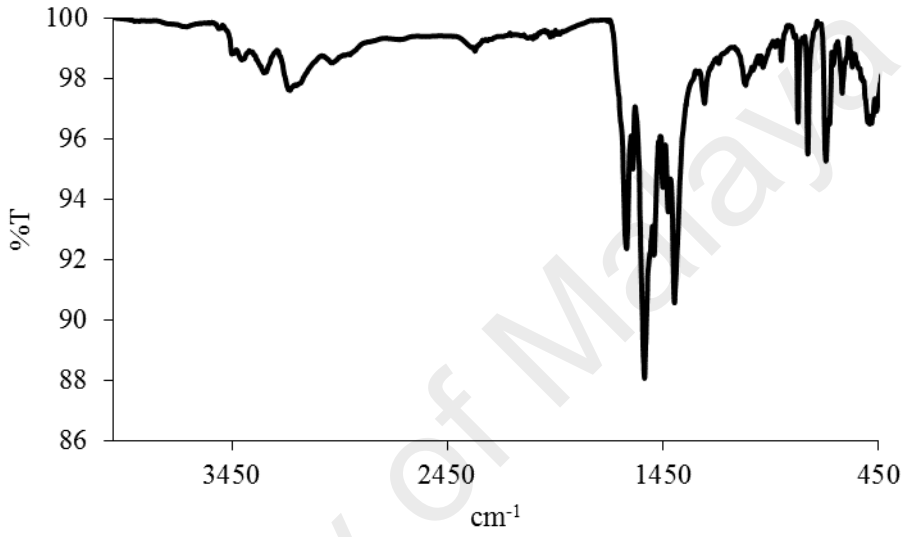

Figure 4.246 FTIR spectrum of **Complex 25**

Its **UV-vis** spectrum in DMSO (**Figure 4.247**) shows a *d-d* band at 677 nm (ε_{max}, 294.7 M^{-1} cm^{-1}), assigned as $^2B_2 \rightarrow {}^2B_1$, and an intense LMCT band at 252 nm transition (ε_{max}, 40748 M^{-1} cm^{-1}). This suggests a square pyramidal geometry at Cu(II) centre.

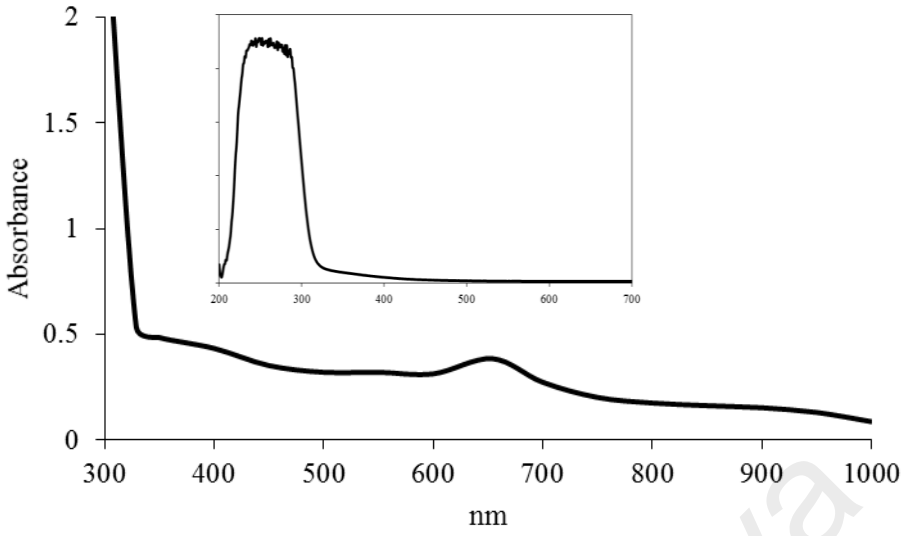

Figure 4.247 UV-vis spectrum of **Complex 25**

Its E_o, calculated as before (λ_{edge} = 329 nm) was 3.8 eV. Upon excitation at 252 nm (LMCT transition), its **fluorescence** spectrum shows two overlapping peaks at λ_{max} 469 nm and 547 nm (**Figure 4.248)**. This suggests two different paths for the excited complex to return to the ground state. Its E_o value (calculated from λ_{edge} = 639 nm) was 1.9 eV. Its E_o value (calculated from λ_{edge} = 608 nm) was 2.0 eV. Its τ, calculated as before from its **decay** curve (**Figure 4.249**), was 2.6 ns. Additionally, its Stokes shift was 217 nm.

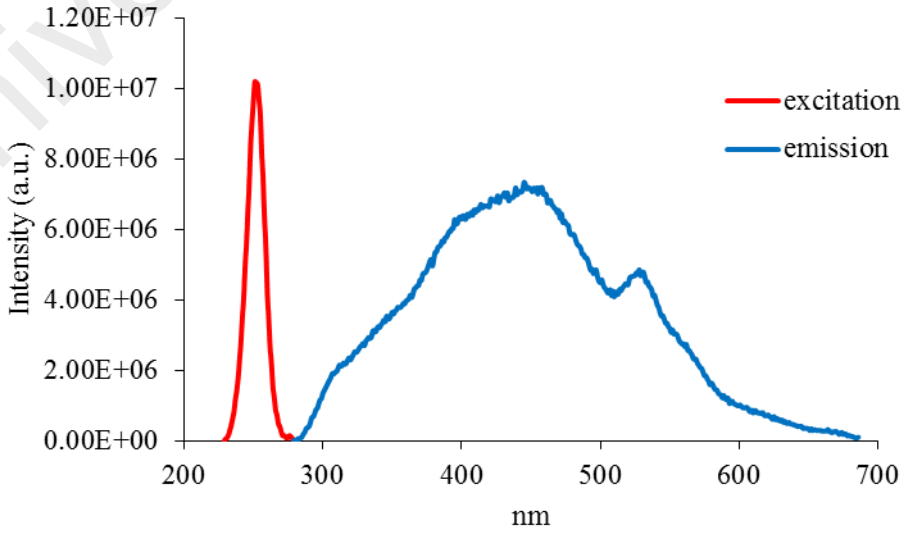

Figure 4.248 Fluorescence spectrum of **Complex 25** (λ_{ex} = 252 nm)

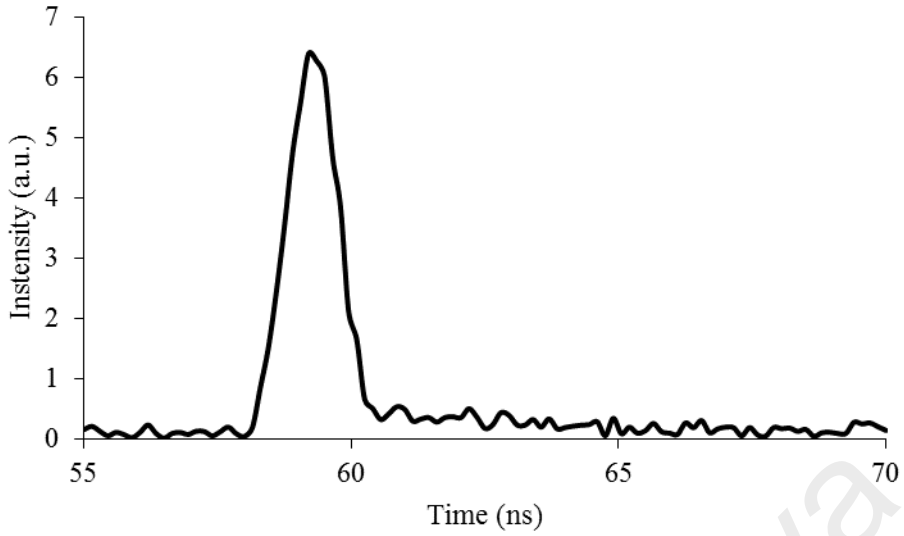

Figure 4.249 Fluorescence decay of **Complex 25**

Additionally, upon excitation at 677 nm (*d-d* transition), its **fluorescence** spectrum shows a peak at λ_{max} 681 nm (**Figure 4.250)**. Its E_o value, calculated from λ_{edge} = 685 nm, was 1.8 eV, and its $\boldsymbol{\tau}$ value, calculated as before from its **decay** curve, was 2.5 ns. Its Stokes shift was 4 nm.

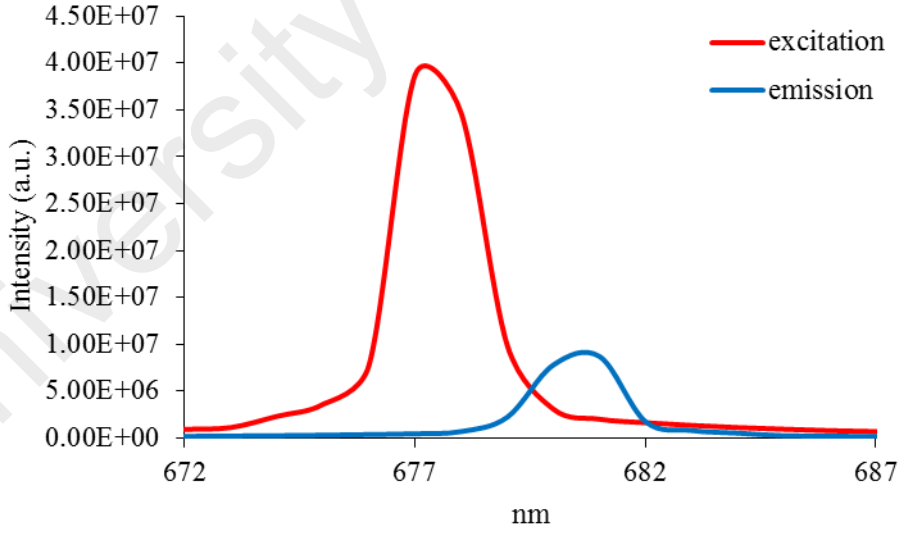

Figure 4.250 Fluorescence spectrum of **Complex 25** (λ_{ex} = 677 nm)

Its **CV** scan (**Figure 4.251**), recorded cathodically from 0 V within the potential window -1.5 V to +1.5 V, showed a weak cathodic peak at −0.33 V, and the corresponding anodic peak at −0.27 V. These are assigned to the reduction of Cu(II) to

Cu(I), and the oxidation of Cu(I) to Cu(II), respectively. Hence, the peak separation (ΔE_p) was 60 mV, indicating a quasireversible redox reaction. There also two overlapping anodic peaks at +0.68 V and +1.16 V, assigned to the oxidation of *L4*.

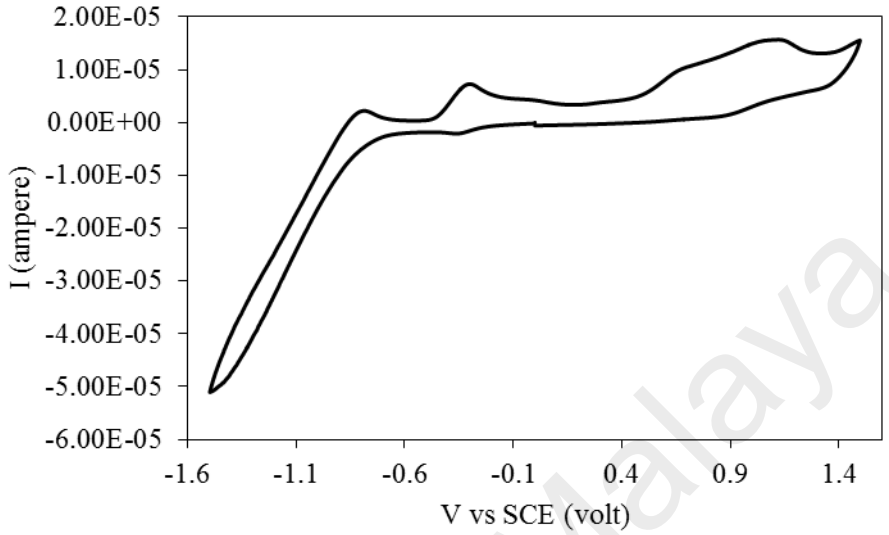

Figure 4.251 CV of **Complex 25**

The HOMO and LUMO values, calculated from the onset oxidation potential (-0.48 V) and onset reduction potential (-0.21 V), were 3.92 eV and 4.19 eV (versus SCE), respectively. Thus, its E_e was 0.27 eV.

Its $\boldsymbol{\mu_{eff}}$ value, calculated as before from the values of FM = 446.86 g mol^{-1} (repeat unit), χ_g = 2.4 x 10^{-6} cm^3 g^{-1}, χ_M = 1.08 x 10^{-3} cm^3 mol^{-1}, and χ_{dia} = -1.84 x 10^{-4} cm^3 mol^{-1}, was 1.78 B.M. at 298 K. The value is in good agreement with the expected value of mononuclear Cu(II) complexes (1.73 B.M.) [12], indicating a negligible interaction between the Cu(II) atoms in the polymeric chain.

Its **TGA** trace (**Figure 4.252**) shows the total weight loss of 68% in the temperature range of 168 – 900 °C, assigned to the decomposition of two CH_3COO and a half of *L4* ligands (expected 69%). However, the amount of residue at temperatures above 900 ^oC cannot be ascertained due to incomplete combustion of the organic ligands. Hence, the decomposition temperature of **Complex 25** was 168 °C.

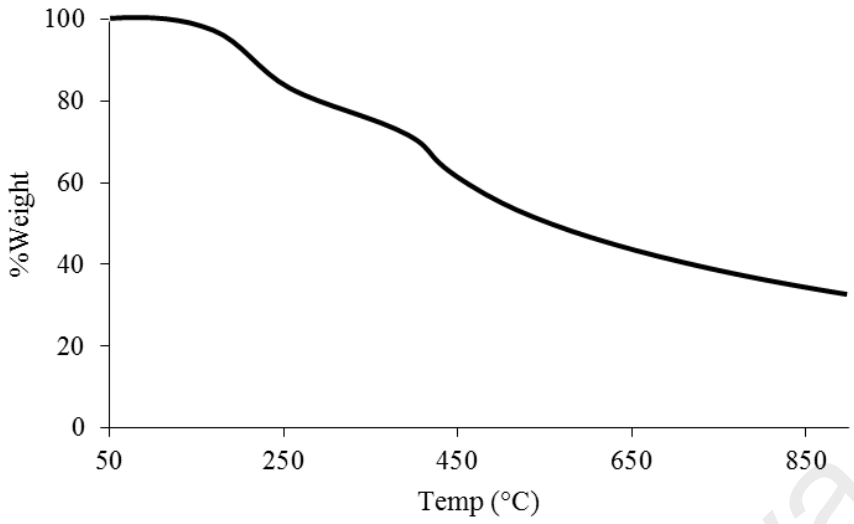

Figure 4.252 TGA of **Complex 25**

4.5.3 Reaction of nickel(II) ethanoate with L4

Nickel(II) ethanoate tetrahydrate ($[Ni(CH_3COO)_2].4H_2O$) reacted with *L4* (mole ratio 1:1) to give a greenish powder (**Complex 26**), and the yield was 91.1%. Its solubility was similar to the previously-discussed complexes.

The results from the **elemental analyses** (40.7% C; 2.9% H; 11.8% N) are in excellent agreement with those calculated for the repeat unit $Ni_2C_{21}H_{19}N_5O_{10}$ (40.7% C; 3.1% H; 11.3% N; formula weight, 618.79 g mol^{-1}). Combining these with the spectroscopic data discussed below, its proposed structural formula is $\{[Ni_2(CH_3COO)_4(L4)]\}_n$.

Its **FTIR** spectrum (**Table 4.12**; **Figure 4.253**) shows the presence of the expected functional groups. The ΔCOO value (140 cm^{-1}) suggests a chelating binding mode for CH_3COO^- ligand.

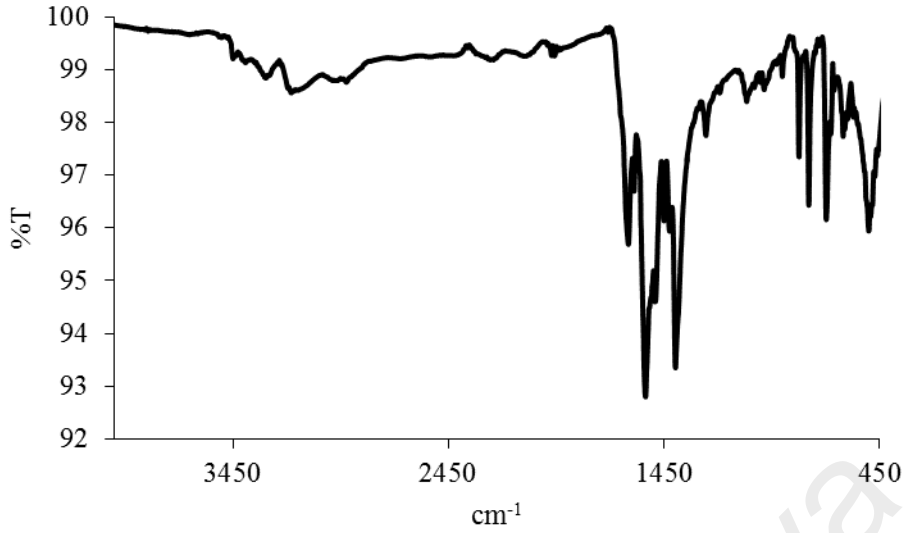

Figure 4.253 FTIR spectrum of **Complex 26**

Its **UV-vis** spectrum in DMSO (**Figure 4.254**) shows a broad peak at 837 nm (ε_{max}, 257.2 M^{-1} cm^{-1}), assigned to $^3A_{2g}$ (F) → $^3T_{2g}$ (F) transition; 602 nm (ε_{max}, 183.7 M^{-1} cm^{-1}), assigned to $^3A_{2g}$ (F) → $^3T_{1g}$ (F) transition; and 382 nm (ε_{max}, 367.4 M^{-1} cm^{-1}) assigned to $^3A_{2g}$ (F) → $^3T_{1g}$(P) transition. These suggest that the geometry at Ni(II) centres was octahedral. Also observed is an intense MLCT band at 246 nm (ε_{max}, 4.2x10^3 M^{-1} cm^{-1}).

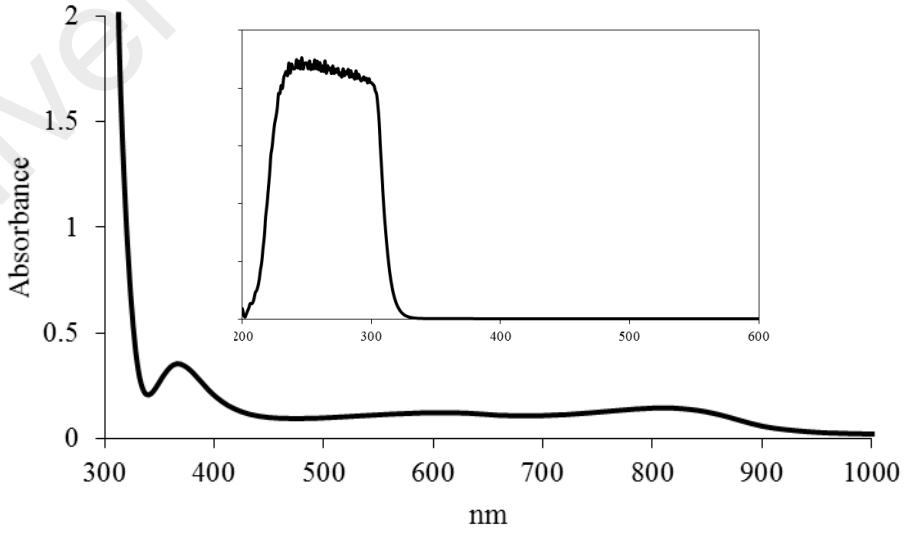

Figure 4.254 UV-vis spectrum of **Complex 26**

Its E_o**,** calculated as before from λ_{edge} = 330 nm, was 3.8 eV. The value is the same as **Complex 25** ({[Cu(CH_3COO)$_2$(L4)]}$_n$; 3.8 eV), which indicates that the nuclearity and geometry at the metal centre has insignificant effect on their E_o values.

Upon excitation at 246 nm (MLCT transition), its **fluorescence** spectrum shows two overlapping peaks at λ_{max} 407 nm and 527 nm (**Figure 4.255**). This suggests two different paths for the excited complex to return to the ground state. Its E_o value, calculated from λ_{edge} = 632 nm, was 1.9 eV. Additionally, its Stokes shift was 161 nm.

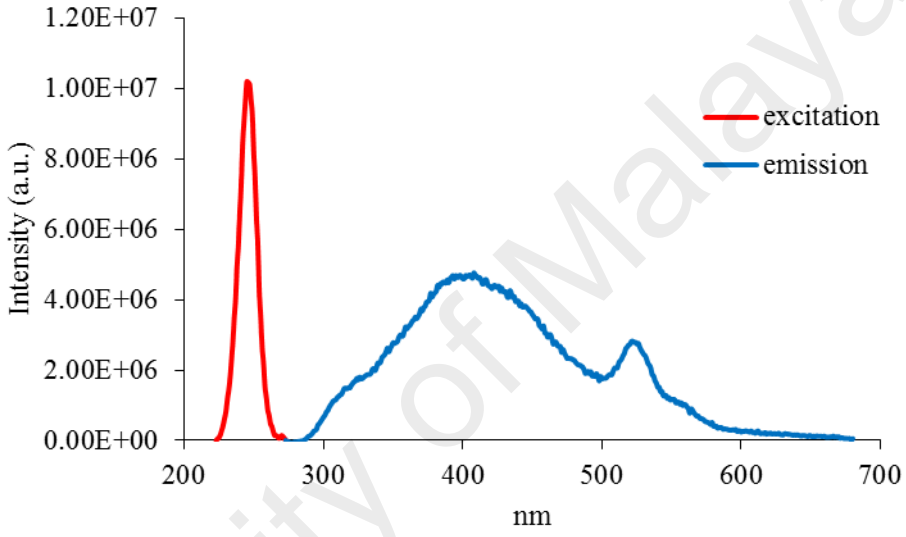

Figure 4.255 Fluorescence spectrum of **Complex 26** (λ_{ex} = 246 nm)

Its $\boldsymbol{\tau}$ value, calculated as before from its decay curve (**Figure 4.256**), was 2.6 ns. Hence, the lifetime of the excited complex is also the same as **Complex 25** (2.6 ns).

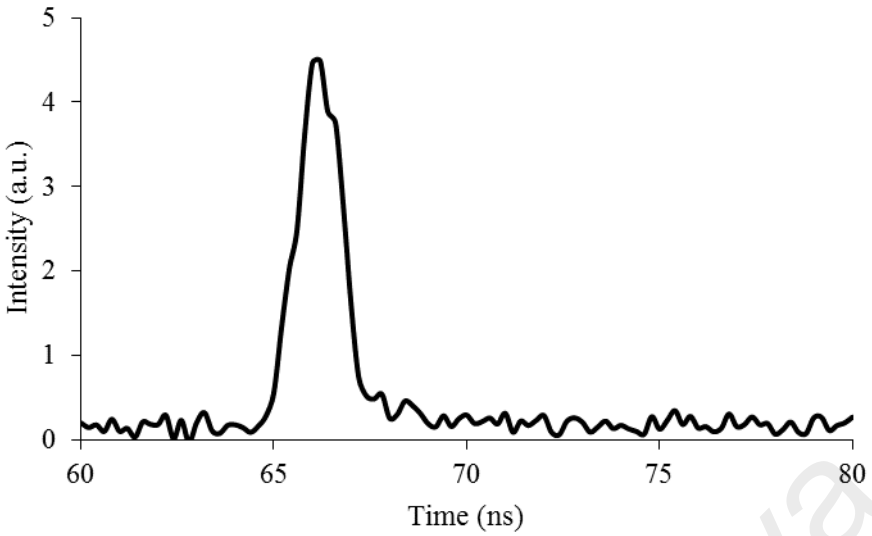

Figure 4.256 Fluorescence decay of **Complex 26**

Also, upon excitation at 382 nm (*d-d* transition), its **fluorescence** spectrum shows a peak at λ_{max} 387 nm (**Figure 4.257**). Its E_o value, calculated from λ_{edge} = 389 nm, was 3.1 eV, and its τ value, calculated from its decay curve, was 3.7 ns. Its Stokes shift was 5 nm.

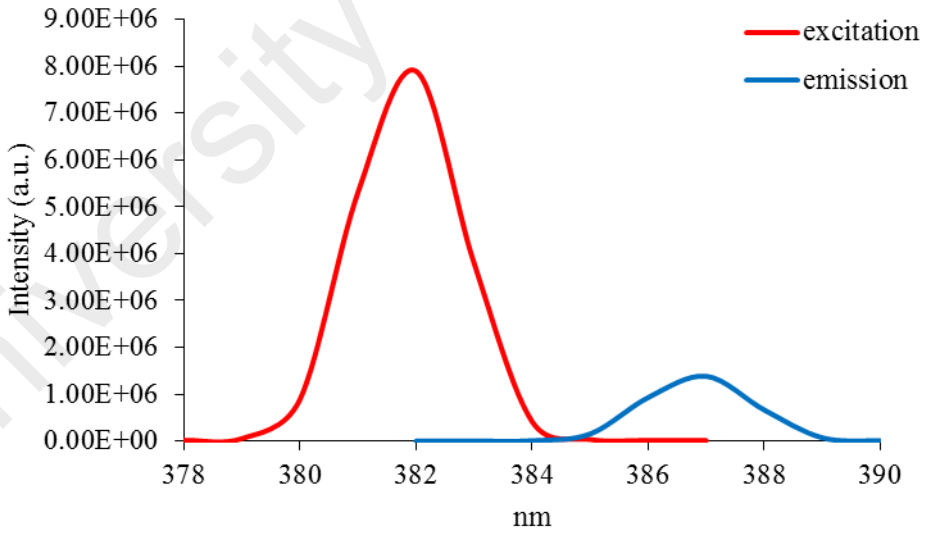

Figure 4.257 Fluorescence spectrum of **Complex 26** (λ_{ex} = 382 nm)

Its **CV** (**Figure 4.258**), recorded anodically from 0 V within the potential window of +1.5 V to -1.5 V. It showed a broad anodic peak at about +1.22 V, but no corresponding reduction peak. This is assigned to ligand-based oxidation. However,

when the potential was increased from -1.5 V to 0 V, an anodic peak appeared at -0.25 V, which is assigned to the oxidation of [Ni(II)Ni(II)] to [Ni(II)Ni(III)]. Both redox processes were irreversible. Hence, its E_e value cannot be calculated.

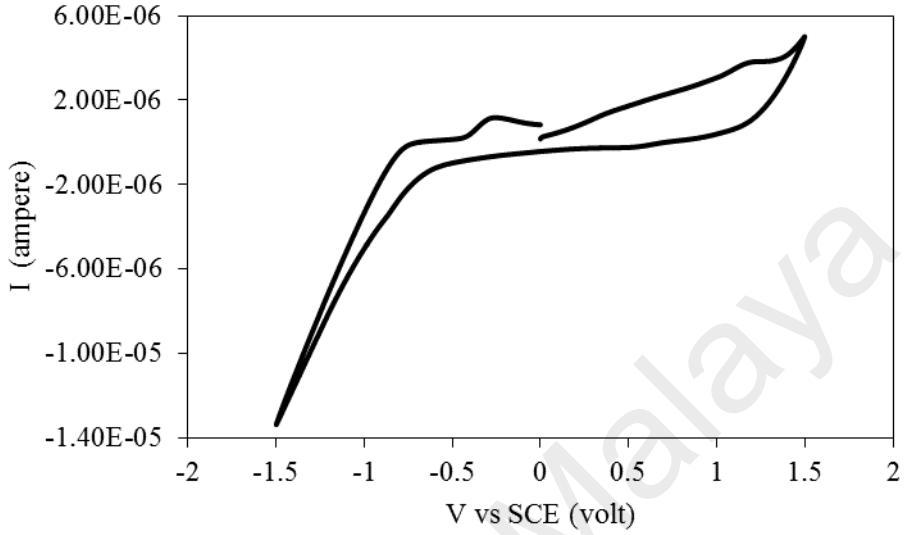

Figure 4.258 CV of **Complex 26**

Its μ_{eff} value, calculated as before from the values of FM = 618.79 g mol^{-1}, χ_g = 8.2 x 10^{-6} cm^3 g^{-1}, χ_M = 5.09 x 10^{-3} cm^3 mol^{-1}, and χ_{dia} = -2.92 x 10^{-4} cm^3 mol^{-1}, was 3.60 B.M. at 298 K. This is lower than the expected value for a dinuclear Ni(II) complex (4.00 B.M.), indicating an antiferromagnetic interactions between the Ni(II) centres in the polymer chain.

Its **TGA** trace (**Figure 4.259**) shows the total weight loss of 69.1% in the temperature range of 180 – 900 °C, assigned to the decomposition of four CH_3COO and a half of *L4* ligands (expected 69.1%). However, the amount of residue at temperatures above 900 ^oC cannot be accurately ascertained due to incomplete combustion of the organic ligands (expected, 19% assuming pure NiO). Hence, the complex (T_{dec} = 180 °C) was more thermally stable than **Complex 25** ($\{[Cu(CH_3COO)_2(L4)]\}_n$; T_{dec} = 168°C).

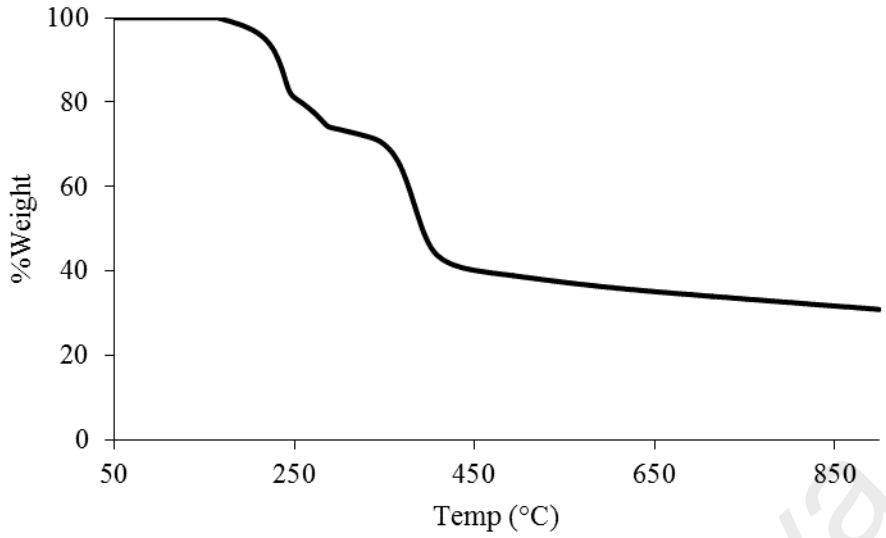

Figure 4.259 TGA of **Complex 26**

4.5.4 Reaction of cobalt(II) ethanoate with L4

Cobalt(II) ethanoate tetrahydrate ($[Co(CH_3COO)_2].4H_2O$) reacted with *L4* (mole ratio 1:1) to give a purple powder (**Complex 27**), and the yield was 85.4%. Its solubility was similar to the previously-discussed complexes.

The **elemental analytical** data for the complex (42.4% C; 3.5% H; 14.2% N) are in excellent agreement with those calculated for the repeat unit $CoC_{17}H_{17}N_5O_8$ (42.7% C; 3.6% H; 14.6% N; formula weight, 478.28 g mol^{-1}). Combining these with the spectroscopic data discussed below, the proposed structural formula of the complex is $\{[Co(CH_3COO)_2(L4)].2H_2O\}_n$.

Its **FTIR** spectrum (**Table 4.12**; **Figure 4.260**) shows the presence of the expected functional groups. The ΔCOO value (139 cm^{-1}) suggests a chelating binding mode for CH_3COO^- ligand [1].

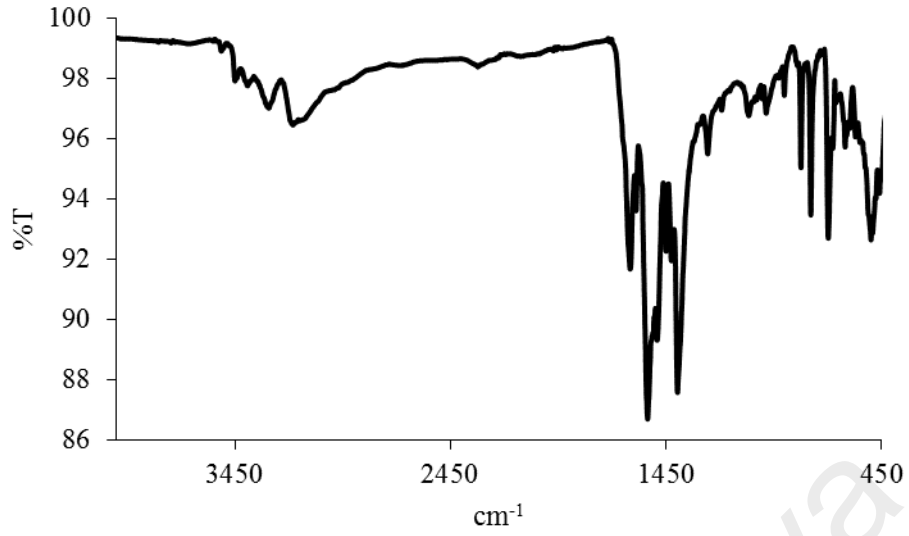

Figure 4.260 FTIR spectrum of **Complex 27**

Its **UV-vis** spectrum in DMSO (**Figure 4.261**) shows a broad overlapping band at about 602 nm (ε_{max}, 103.6 M^{-1} cm^{-1}), assigned to $^4T_{1g}$ (F) → $^4T_{2g}$ (F) and $^4T_{1g}$ (F) → $^4T_{1g}$ (P) transitions, and at 432 nm (ε_{max}, 193.3 M^{-1} cm^{-1}), assigned to $^4T_{1g}$ (F) → $^4A_{2g}$ (F) transition. Hence, the complex was made up of high-spin Co(II) centre. An intense band at 247 nm (ε_{max}, 1.9x10^3 M^{-1} cm^{-1}) is assigned to the MLCT transition.

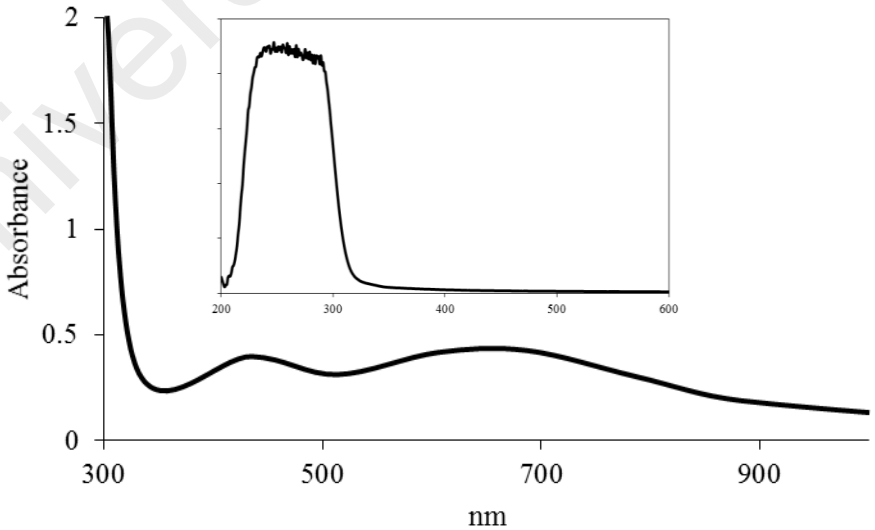

Figure 4.261 UV-vis spectrum of **Complex 27**

Its E_o value, calculated as before from λ_{edge} = 333 nm, was 3.7 eV. The value is similar to **Complex 26** ($\{[Ni_2(CH_3COO)_4(L4)]\}_n$; 3.8 eV).

Upon excitation at 247 nm (MLCT transition), its **fluorescence** spectrum shows four overlapping peaks at λ_{max} 356 nm, 425 nm, 467 nm and 550 nm (**Figure 4.262**). This suggests four different paths for the excited complex to return to the ground state. Its E_o value (calculated from λ_{edge} = 648 nm) was 1.9 eV. In addition, its Stokes shift was 220 nm.

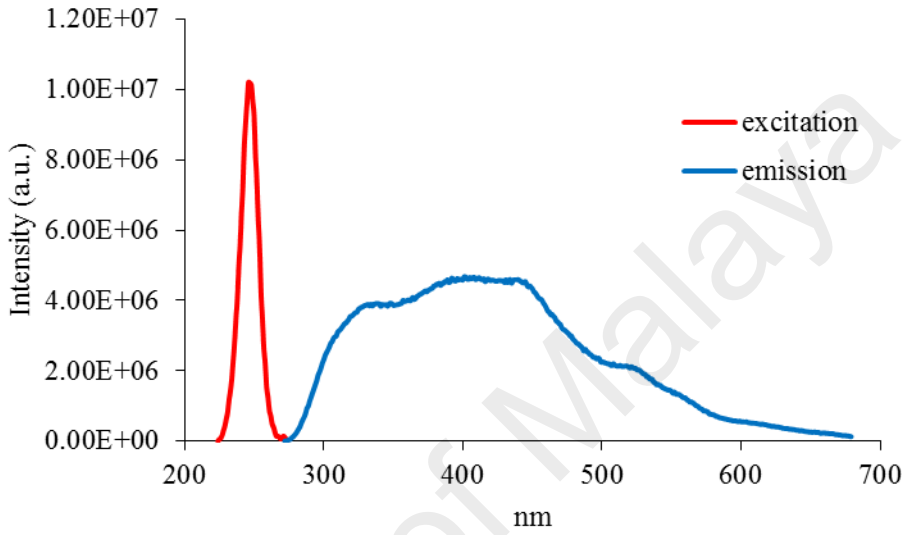

Figure 4.262 Fluorescence spectrum of **Complex 27** (λ_{ex} = 247 nm)

The value of its $\boldsymbol{\tau}$, calculated as before from its **decay** curve (**Figure 4.263**), was 2.7 ns. Hence, the lifetime of the excited **Complex 27** was similar to **Complexes 25** ($\{[Cu(CH_3COO)_2(L4)]\}_n$; 2.6 ns) and **26** $\{[Ni_2(CH_3COO)_4(L4)]\}_n$; 2.6 ns).

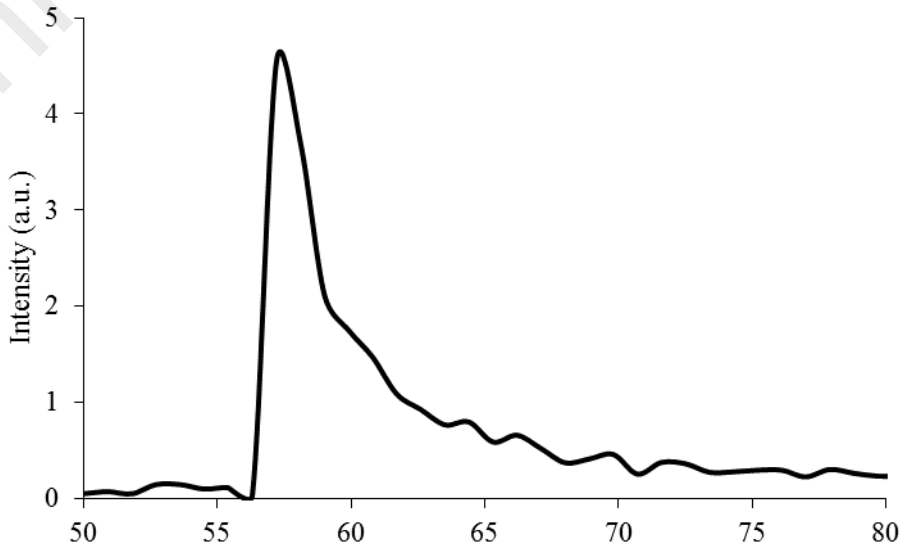

Figure 4.263 Fluorescence decay of **Complex 27**

Upon excitation at 432 nm (*d-d* transition), its **fluorescence** spectrum shows a peak at λ_{max} 439 nm (**Figure 4.264)**. Its E_o, calculated from λ_{edge} = 445 nm, was 2.7 eV. Its τ value, calculated as before from its **decay** curve, was 3.3 ns. Its Stokes shift was 7 nm.

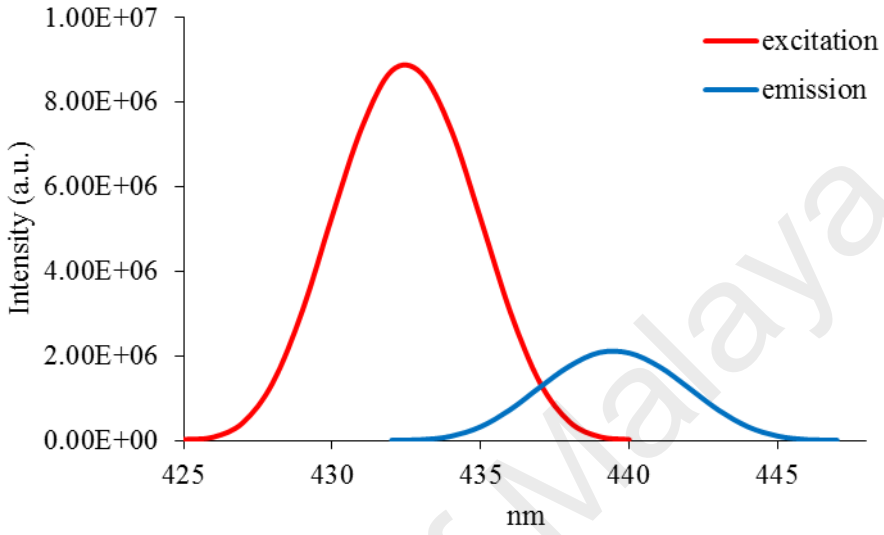

Figure 4.264 Fluorescence spectrum of **Complex 27** (λ_{ex} = 432 nm)

Its **CV** (**Figure 4.265**), recorded anodically from 0 V within the potential window of +1.5 V to -1.5 V. It showed an anodic peak at +0.87 V, assigned to the oxidation of Co(II) to Co(III), but no cathodic peak observed when the potential was reversed. Hence, the redox process was irreversible. Accordingly, its E_e value cannot be calculated. Another anodic peak observed at -0.23 V, when the potential was increased from -1.5 V to 0 V. This is assigned to the oxidation of the ligand [42].

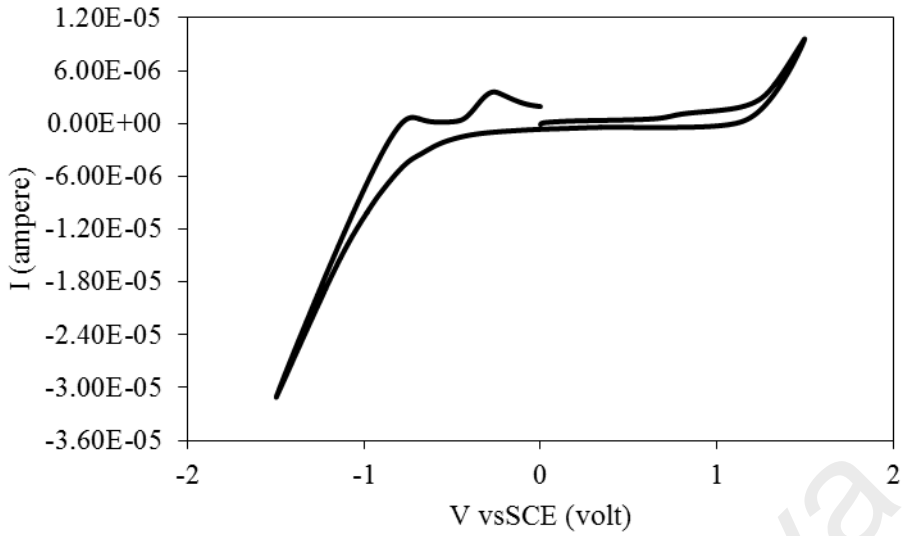

Figure 4.265 CV of **Complex 27**

Its $\boldsymbol{\mu_{eff}}$ value, calculated as before from the values of FM = 478.28 g mol^{-1} (repeat unit), χ_g = 1.57 x 10^{-5} cm^3 g^{-1}, χ_M = 7.52 x 10^{-3} cm^3 mol^{-1}, and χ_{dia} = -2.18 x 10^{-4} cm^3 mol^{-1}, was 4.31 B.M. at 298 K. This is higher than the expected μ_{eff} value for a HS Co(II) complex (d^7) (3.87 B.M.), suggesting a ferromagnetic interaction between the Co(II) centres in the polymeric chain [43].

Its **TGA** trace (**Figure 4.266**) shows an initial weight loss of 7.5% in the temperature range of 75 – 191 °C, assigned to the evaporation of two H_2O molecules (expected, 7.5%). The next weight loss of about 75.5% in the temperature range of 191 - 900 °C is assigned to the decomposition of two CH_3COO and *L4* ligands (expected, 80%). However, the amount of residue at temperatures above 900 ^oC cannot be accurately ascertained due to incomplete combustion of the organic ligands. Hence, the complex (T_{dec} = 191 °C) was slightly more thermally stable than **Complex 26** ($\{[Ni_2(CH_3COO)_4(L4)]\}_n$; T_{dec} = 180 °C).

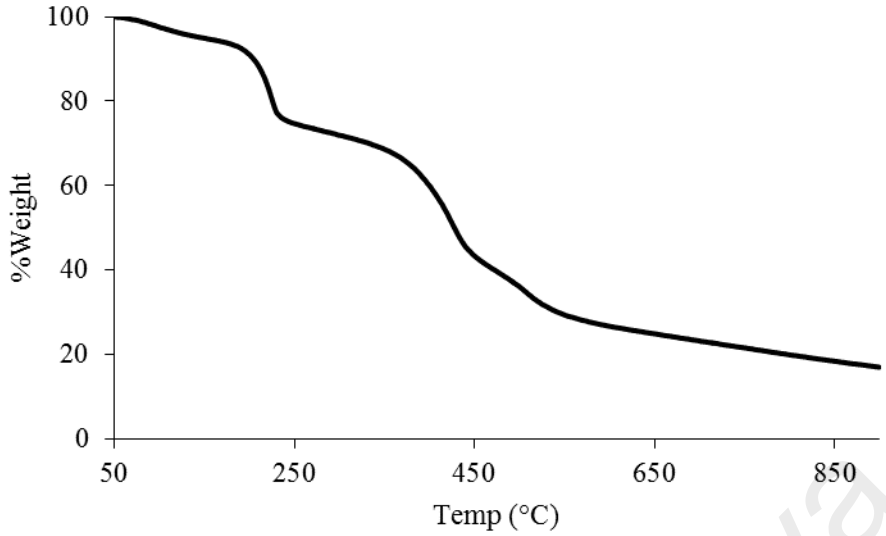

Figure 4.266 TGA of **Complex 27**

4.5.5 Reaction of iron(II) ethanoate with L4

Iron(II) ethanoate ($[Fe(CH_3COO)_2]$) reacted with *L4* (mole ratio 1:1) to give a brown powder (**Complex 28**), and the yield was 79.4%. Its solubility was similar to the previously-discussed complexes.

The results from the **elemental analyses** (38.6% C; 3.6% H; 10.3% N) are in excellent agreement with those calculated for the repeat unit $Fe_2C_{21}H_{23}N_5O_{12}$ (38.9% C; 3.6% H; 10.8% N; formula weight, 649.12 g mol^{-1}). Combining these with the spectroscopic data discussed below, the proposed structural formula of **Complex 28** is $\{[Fe_2(CH_3COO)_4(L4)].2H_2O\}_n$.

Its **FTIR** spectrum (**Table 4.12**; **Figure 4.267**) shows the presence of the expected functional groups. The ΔCOO value (138 cm^{-1}) suggests a chelating binding mode for CH_3COO^- ligand.

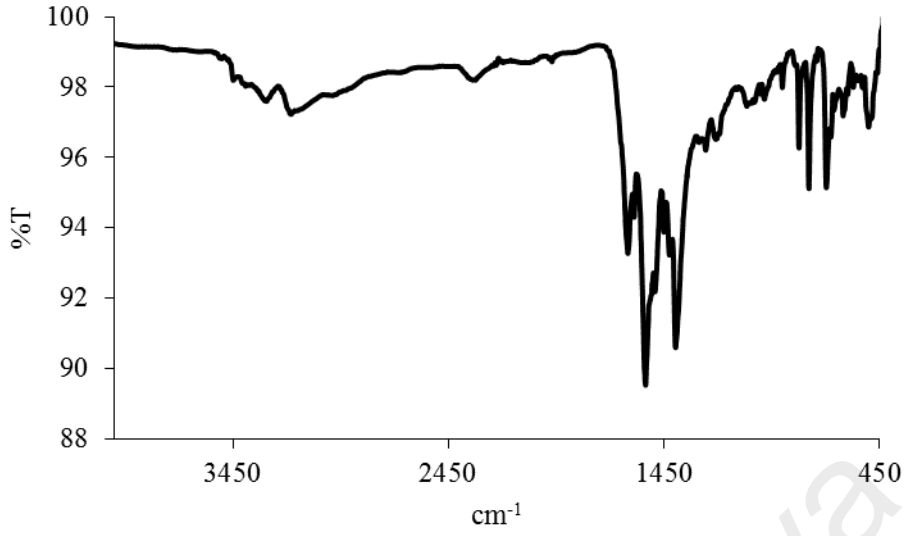

Figure 4.267 FTIR spectrum of **Complex 28**

Its **UV-vis** spectrum in DMSO (**Figure 4.268**) shows a broad band at 818 nm (ε_{max}, 284 M^{-1} cm^{-1}) assigned to $^5T_{2g} \rightarrow {}^5E_g$ electronic transition, and an intense MLCT band at 247 nm (ε_{max}, 7.6x10^3 M^{-1} cm^{-1}). This suggests that the geometry at the HS Fe(II) centre is octahedral.

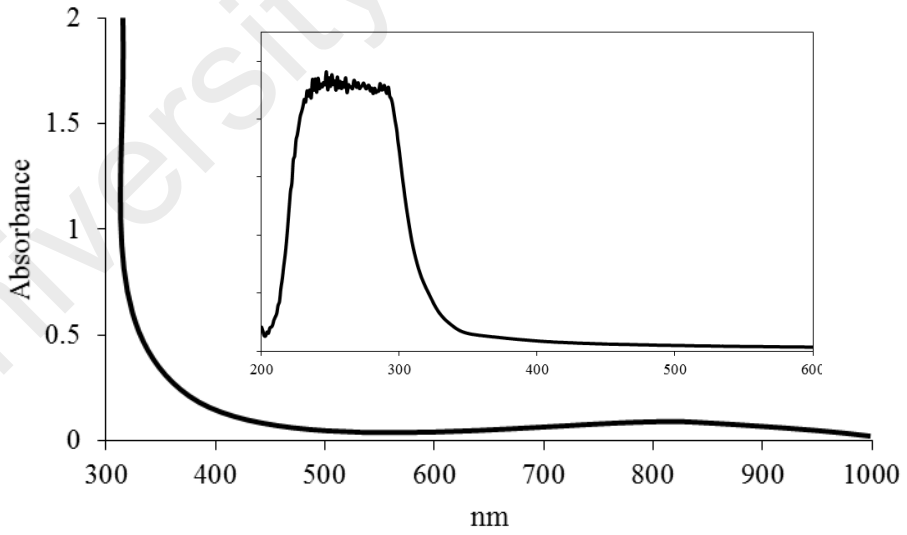

Figure 4.268 UV-vis spectrum of **Complex 28**

Its E_o value, calculated as before from λ_{edge} = 349 nm, was 3.6 eV. The value is slightly narrower than **Complex 27** ({[$Co(CH_3COO)_2(L4)$)].$2H_2O$}$_n$; 3.7 eV).

Upon excitation at 247 nm (MLCT transition), its **fluorescence** spectrum shows two overlapping peaks at λ_{max} 446 nm and 552 nm (**Figure 4.269**). This suggests two different paths for the excited complex to return to the ground state. Its E_o value (calculated from λ_{edge} = 638 nm) was 1.9 eV. The value of its $\boldsymbol{\tau}$, calculated as before from its decay curve (**Figure 4.270**), was 2.6 ns. Additionally, its Stokes shift was 199 nm.

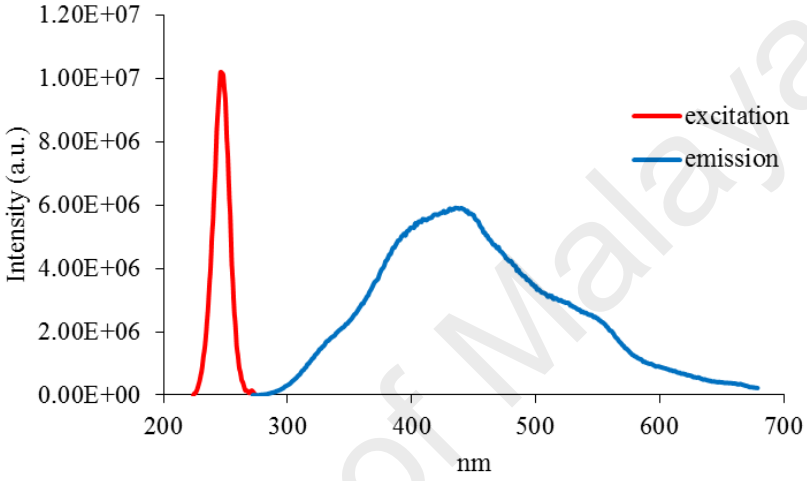

Figure 4.269 Fluorescence spectrum of **Complex 28** (λ_{ex} = 247 nm)

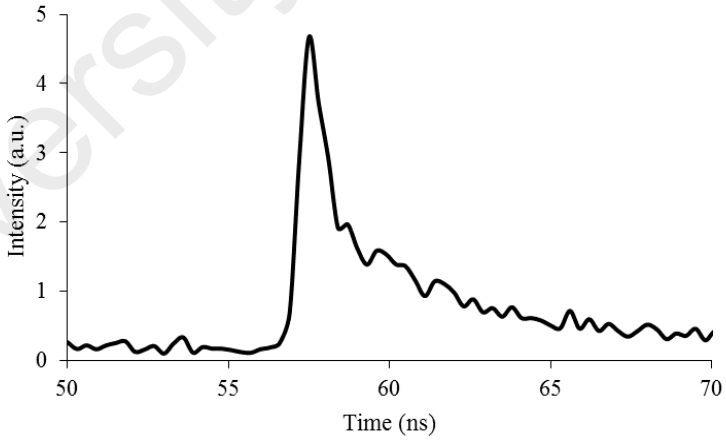

Figure 4.270 Fluorescence decay of **Complex 28**

Additionally, upon excitation at 818 nm, (*d-d* transition), its **fluorescence** spectrum shows a peak at λ_{max} 826 nm (**Figure 4.271)**. Its E_o, calculated from

λ_{edge} = 830 nm, was 1.4 eV, while its τ value, calculated from its **decay** curve, was 2.2 ns. Its Stokes shift was 8 nm.

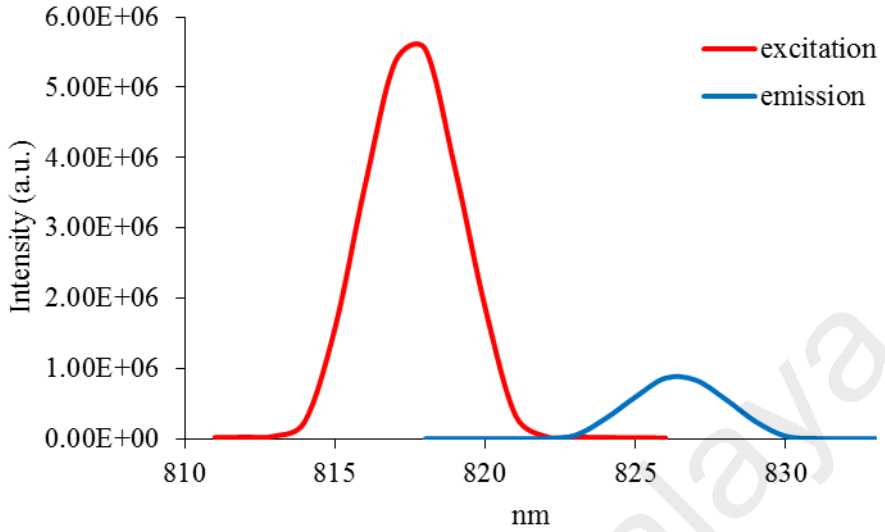

Figure 4.271 Fluorescence spectrum of **Complex 28** (λ_{ex} = 818 nm)

Its **CV** (**Figure 4.272**), recorded anodically from 0 V within the potential window of +1.5 V to -1.5 V. It showed a broad anodic peak at about +0.8 V, when the potential was increased from 0 V to +1.5 V. This is assigned to the oxidation of [Fe(II)Fe(II)] to [Fe(II)Fe(III)]. However, when the potential was reduced from +1.5 V to -1.5 V, there was no cathodic peak. Hence, the redox process was irreversible, and the E_e value cannot be calculated for the complex. Additionally, there was also an anodic peak at -0.23 V, when the potential was increased from -1.5 V to 0 V. This is assigned to ligand-based oxidation process as similarly observed for **Complex 27** ($\{[Co(CH_3COO)_2(L4)].2H_2O\}_n$; E_a = -0.23 V).

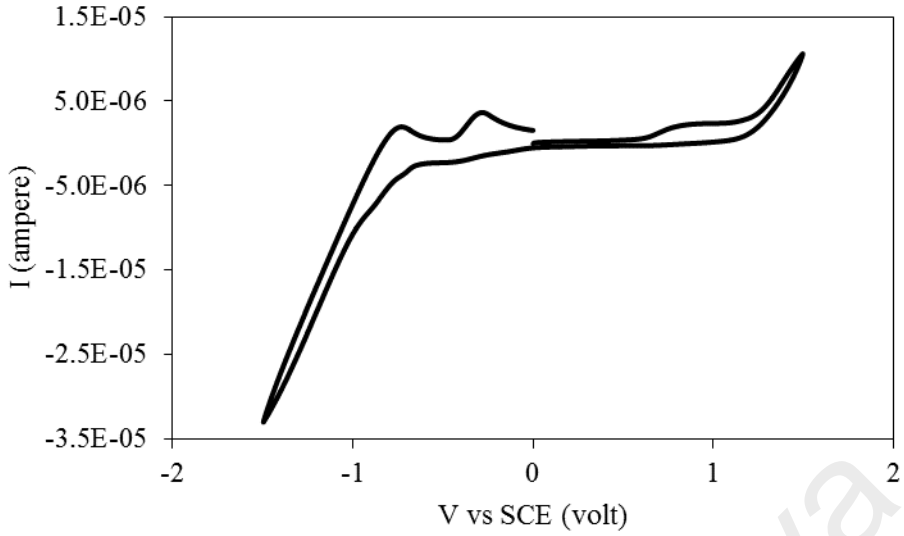

Figure 4.272 CV of **Complex 28**

Its μ_{eff} value, calculated as before from the values of FM = 649.12 g mol^{-1} (repeat unit), χ_g = 3.14 x 10^{-5} cm^3 g^{-1}, χ_M = 2.03 x 10^{-2} cm^3 mol^{-1}, and χ_{dia} = -3.39 x 10^{-4} cm^3 mol^{-1}, was 7.04 B.M. at 298 K. This is in agreement with the expected μ_{eff} value for a dinuclear HS Fe(II) complex (6.93 B.M.), indicating a negligible interaction between the Fe(II) centres in the polymeric chains.

Its **TGA** trace (**Figure 4.273**) shows an initial weight loss of 5.5% in the temperature range of 141 – 183 °C, assigned to the evaporation of two H_2O (expected, 5.5%). The next weight loss of about 85.6% in the temperature range of 183 - 900 °C is assigned to the decomposition of four CH_3COO and *L4* ligands (expected, 77.2%). However, the amount of residue at temperatures above 900 ^oC cannot be ascertained due to incomplete combustion of the organic ligands. Hence, **Complex 28** (T_{dec} = 183 ^oC) was slightly less thermally stable than **Complex 27** ({[Co($CH_3COO)_2$(L4))].2H_2O}$_n$; T_{dec} = 191 ^oC).

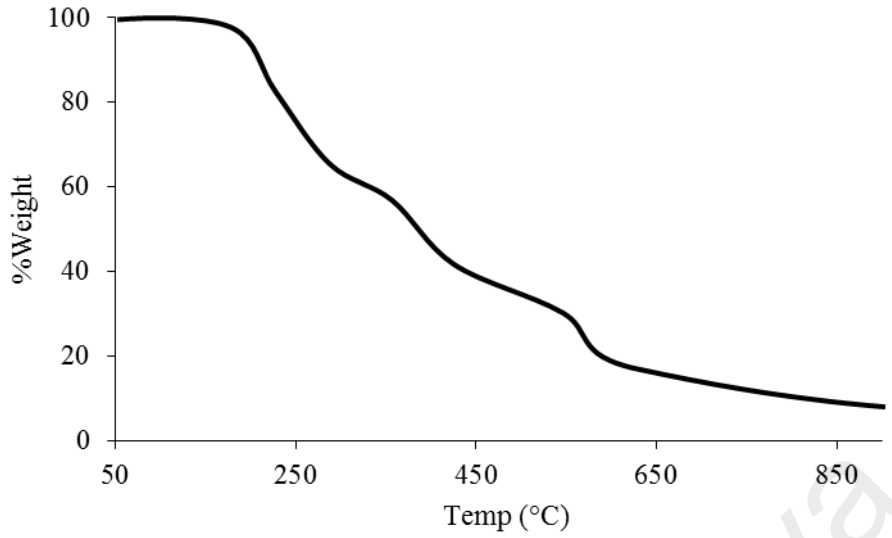

Figure 4.273 TGA of **Complex 28**

4.5.6 Reaction of copper(II) hexadecanoate with L4

Copper(II) hexadecanoate ($[Cu_2(CH_3(CH_2)_{14}COO)_4]$) reacted with *L4* (mole ratio 1:1) to give a bluish-green powder (**Complex 29**), and the yield was 89.2%. Its solubility was similar to the previously-discussed complexes.

The **elemental analytical** data for the complex (64.9% C; 8.7% H; 8.2% N) are in excellent agreement with those calculated for the repeat unit $CuC_{45}H_{69}N_5O_6$ (64.4% C; 8.3% H; 8.3% N; formula weight, 839.61 g mol^{-1}). Combining these with the spectroscopic data discussed below, the proposed structural formula of the complex is $\{[Cu(CH_3(CH_2)_{14}COO)_2(L4)]\}_n$.

Its **FTIR** spectrum (**Table 4.13**; **Figure 4.274**) shows the presence of the expected functional groups. The ΔCOO value (129 cm^{-1}) suggests a chelating binding mode for $CH_3(CH_2)_{14}COO^-$ ligand.

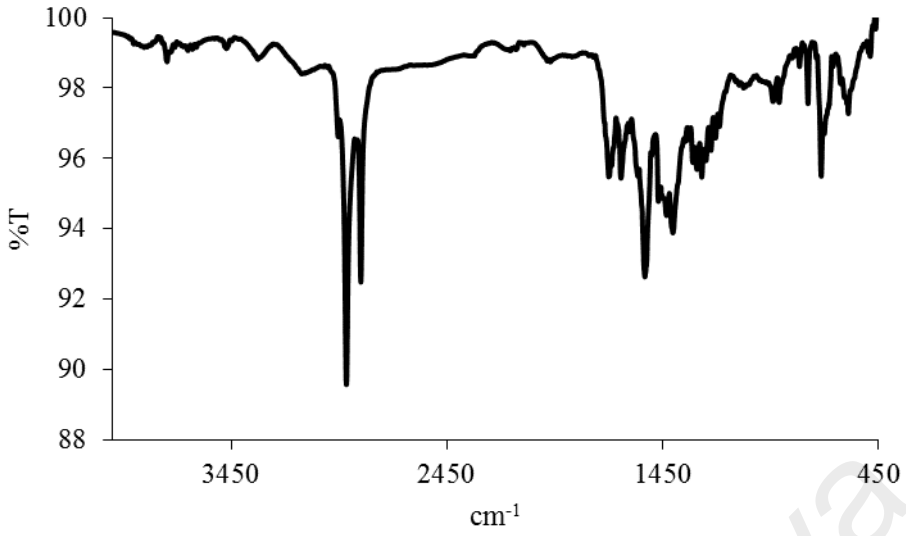

Figure 4.274 FTIR spectrum of **Complex 29**

Its **UV-vis** spectrum in DMSO (**Figure 4.275**) shows a *d-d* band at 700 nm (ε_{max}, 186.4 M^{-1} cm^{-1}), assigned as $^2B_2 \rightarrow {}^2B_1$ electronic transition, and an intense band at 250 nm (ε_{max}, 2948 M^{-1} cm^{-1}), assigned to LMCT transition. This suggests the geometry at Cu(II) centre was square pyramidal.

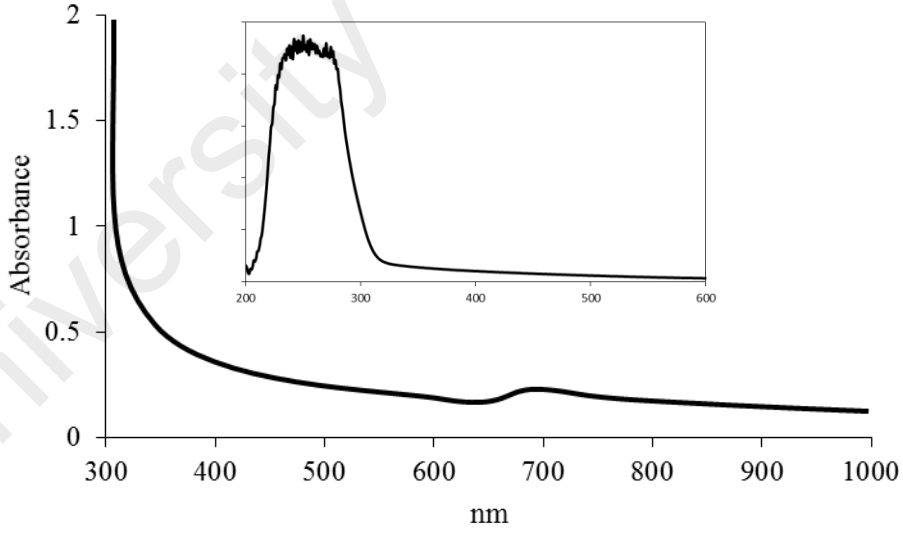

Figure 4.275 UV-vis spectrum of **Complex 29**

Its E_o value, calculated from λ_{edge} = 322 nm, was 3.8 eV. This is similar to **Complex 25** ($\{[Cu_2(CH_3COO)_4(L4)]\}_n$; 3.8 eV), indicating that the alkyl chain length and nuclearity have insignificant effect on the value of E_o.

Upon excitation at 250 nm (LMCT transition), its **fluorescence** spectrum shows three overlapping peaks at λ_{max} 300 nm, 436 nm and 523 nm (**Figure 4.276**). This suggests three different paths for the excited complex to return to the ground state. Its E_o value (calculated from λ_{edge} = 650 nm) was 1.9 eV. In addition, its Stokes shift was 186 nm.

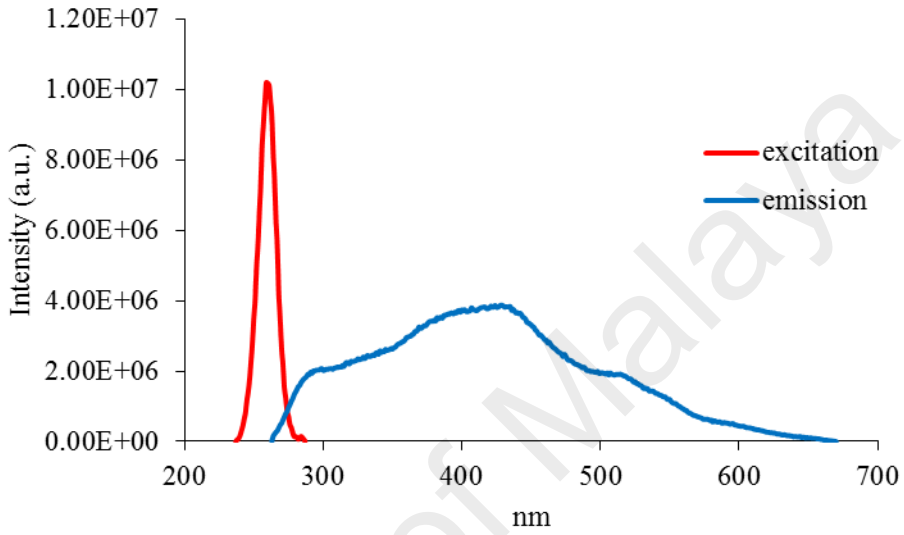

Figure 4.276 Fluorescence spectrum of **Complex 29** (λ_{ex} = 250 nm)

Its $\boldsymbol{\tau}$, calculated as before from its **decay** curve (**Figure 4.277**), was 2.6 ns. This is the same as **Complex 25** ($\boldsymbol{\tau}$ = 2.6 ns), suggesting that the different chain length of the carboxylate ligands has no significant effect on the stability of the excited complex.

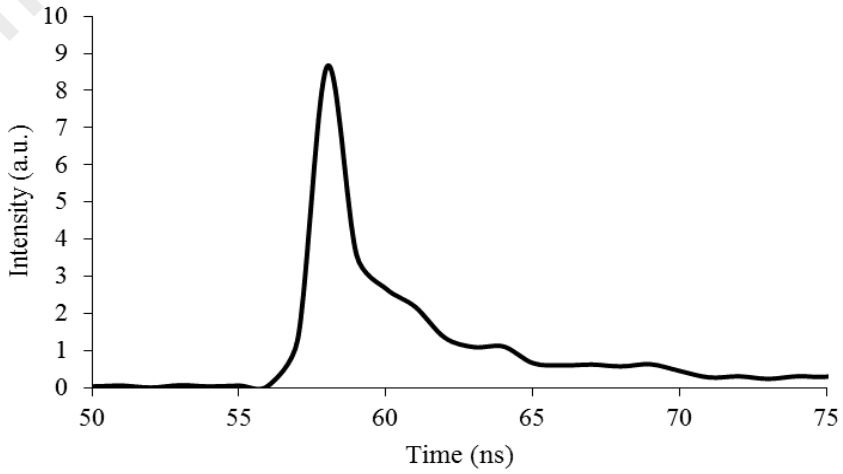

Figure 4.277 Fluorescence decay of **Complex 29**

Upon excitation at 700 nm (*d-d* transition), its **fluorescence** spectrum shows a peak at λ_{max} 720 nm (**Figure 4.278)**. Its E_o, calculated from λ_{edge} = 729 nm, was 1.7 eV, and its $\boldsymbol{\tau}$ value, calculated as before from its decay curve, was 2.5 ns. Its Stokes shift was 20 nm.

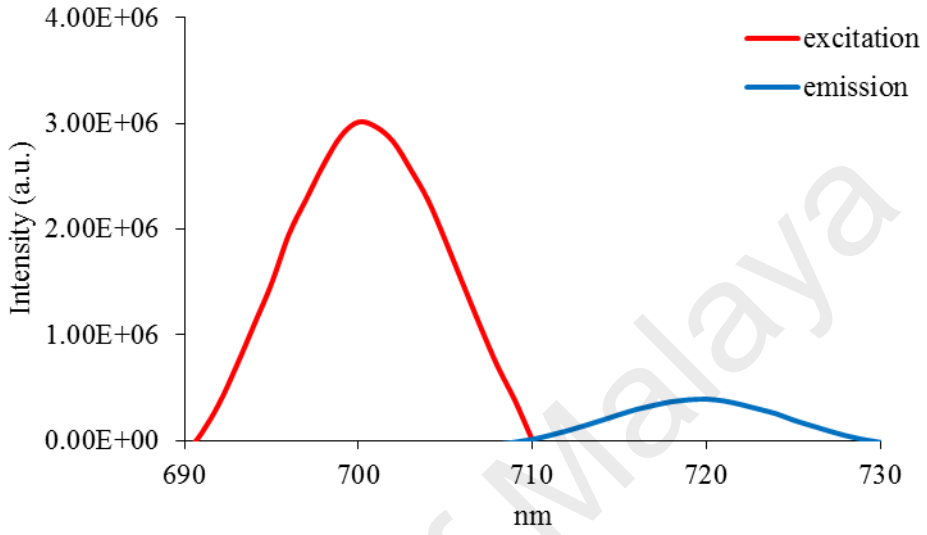

Figure 4.278 Fluorescence spectrum of **Complex 29** (λ_{ex} = 700 nm)

Its **CV** scan (**Figure 4.279**) was recorded cathodically from 0 V within the potential window -1.5 V to +1.5 V. It shows two cathodic peaks at -0.46 V and -1.3 V, and one anodic peak at -0.16 V. The Cu-based redox process is summarized in **Scheme 4.9**. The peak separation (ΔE_p = 300 mV) indicates a quasireversible process. The cathodic peak at -1.3 V is assigned to the ligand-based redox process.

$$[\text{Cu(II)}] \underset{-0.16\ \text{V}}{\overset{-0.46\ \text{V}}{\rightleftharpoons}} [\text{Cu(I)}]$$

Scheme 4.9 The redox process for **Complex 29**

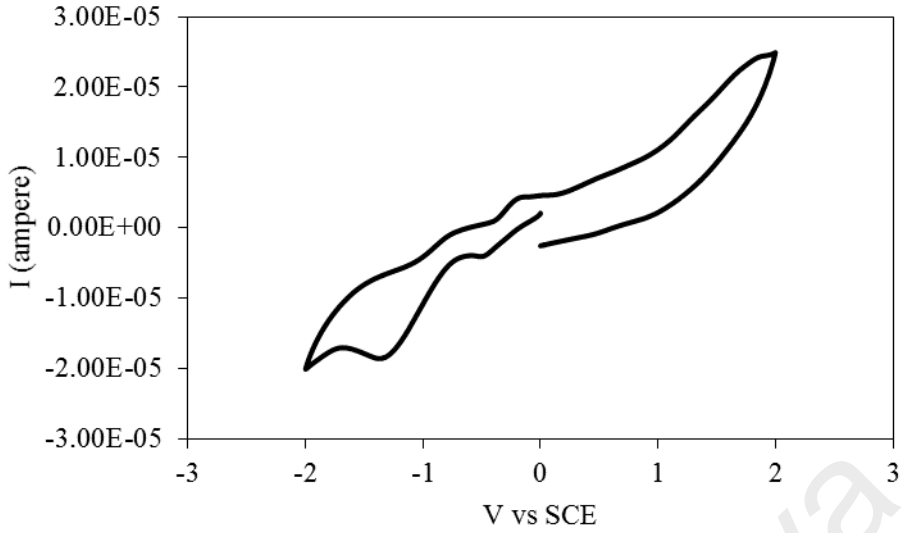

Figure 4.279 CV of **Complex 29**

The HOMO and LUMO values, calculated from the onset oxidation potential (-0.37 V) and onset reduction potential (0 V), are 4.03 eV and 4.4 eV (versus SCE), respectively. Thus, its E_e value was 0.37 eV, which is wider than **Complex 17** ($\{[Cu_2(CH_3COO)_4(L4)]\}_n$; 0.27 eV).

Its $\boldsymbol{\mu_{eff}}$ value, calculated as before from the values of FM = 839.61 g mol^{-1} (repeat unit), χ_g = 9.0 x 10^{-7} cm^3 g^{-1}, χ_M = 8.31 x 10^{-4} cm^3 mol^{-1}, and χ_{dia} = -4.68 x 10^{-4} cm^3 mol^{-1}, was 1.80 B.M. at 298 K. The value is in agreement with the spin-only value for mononuclear copper(II) complexes (1.73 B.M.) [12], indicating a negligible magnetic interaction between the Cu(II) centres in the polymeric chain.

Its **TGA** trace (**Figure 4.280**) shows the total weight loss of 92.4% in the temperature range of 200 – 843 °C, assigned to the decomposition of two $CH_3(CH_2)_{14}COO$ and *L4* ligands (expected, 92.4%). The amount of residue at temperature above 843 °C was 7.6% (expected, 7.6% assuming pure CuO). Hence, **Complex 29** (T_{dec} = 200 ^oC) was more thermally stable than **Complex 25** (T_{dec} = 168 ^oC).

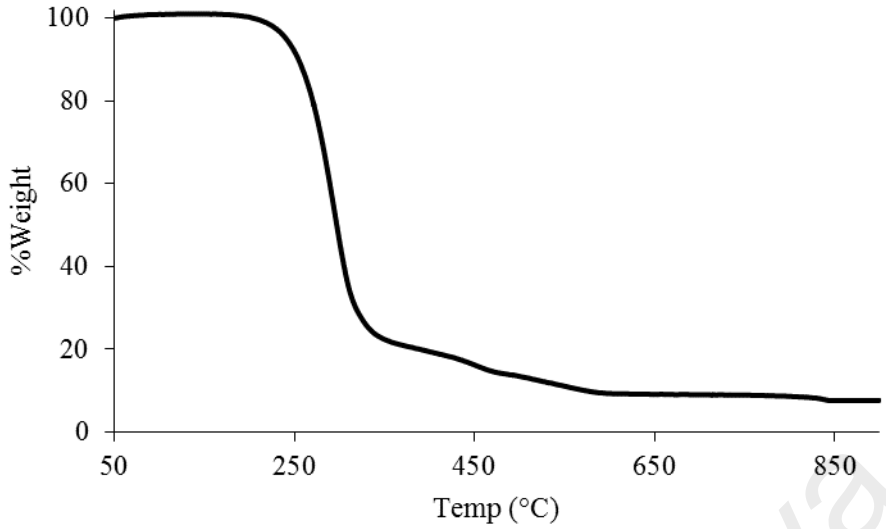

Figure 4.280 TGA of **Complex 29**

The **DSC** scan (**Figure 4.281**) was done for one heating-cooling cycle, in the temperature range 25 - 180 ^{o}C. It shows three overlapping endothermic peaks at 25 ^{o}C (ΔH = +271.2 kJ mol^{-1}) assigned to a combination of intermolecular van der Waals forces between the long alkyl chains, Cr-to-Cr, and Cr-to-M_1 transitions; and a weak peak at 75 ^{o}C (ΔH = +19.4 kJ mol^{-1}) assigned to M_1-M_2 transition. On cooling, there were two overlapping exothermic peaks at 70 $^{\circ}$C (ΔH = -100.4 kJ mol^{-1}), assigned to M_2-to-M_1 and M_1-to-Cr_1 transitions.

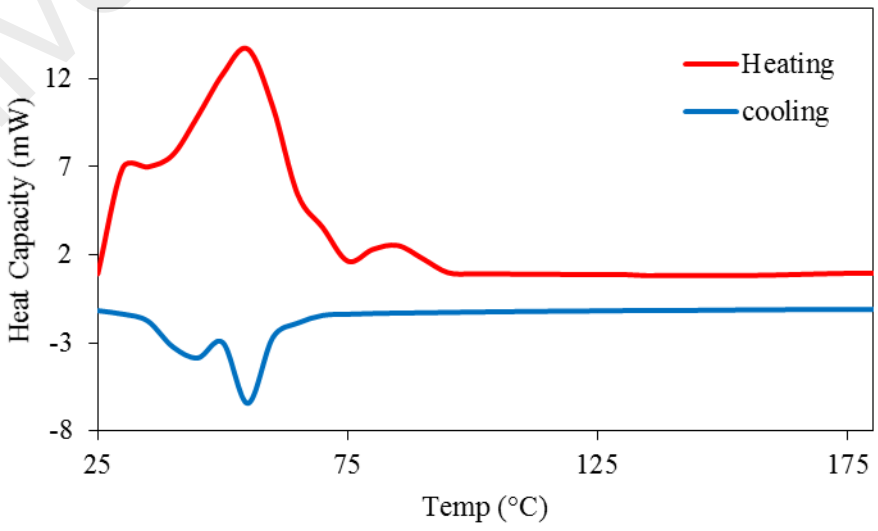

Figure 4.281 DSC of **Complex 29**

The **POM** for **Complex 29** was recorded for two heating-cooling cycles in the temperature range 25 – 180 ^{o}C. On cooling from 180 ^{o}C, an optical texture was initially observed at 74 ^{o}C, which then grew slowly until 50 ^{o}C (**Figure 4.282**). Hence, the complex exhibited liquid crystal properties.

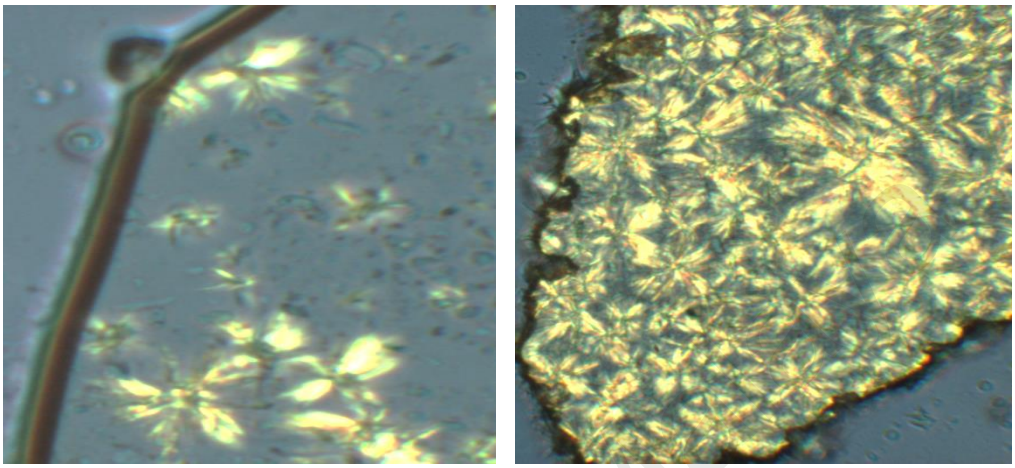

(a) (b)

Figure 4.282 The photomicrographs of **Complex 29** on cooling from 180 ^{o}C: (a) at 74 ^{o}C; and (b) at 50 ^{o}C.

4.5.7 Reaction of nickel(II) hexadecanoate with L4

Nickel(II) hexadecanoate ($[Ni(CH_3(CH_2)_{14}COO)_2(H_2O)_2].3H_2O$) reacted with *L4* (mole ratio 1:1) to give a greenish powder (**Complex 30**), and the yield was 60.6%. Its solubility was similar to the previously-discussed complexes.

The results from the **elemental analyses** (65.8% C; 9.5% H; 5.1% N) are in excellent agreement with those calculated for the repeat unit $Ni_2C_{77}H_{131}N_5O_{10}$ (65.9% C; 9.4% H; 4.9% N; formula weight, 1404.28 g mol^{-1}). Combining these with the spectroscopic data discussed below, its proposed formula is $\{[Ni_2(CH_3(CH_2)_{14}COO)_4(L4)]\}_n$.

Its **FTIR** spectrum (**Table 4.12**; **Figure 4.283**) shows the presence of the expected functional groups. The ΔCOO value (141 cm^{-1}) suggests a chelating or pseudo-bridging binding mode for $CH_3(CH_2)_{14}COO^-$ ligand.

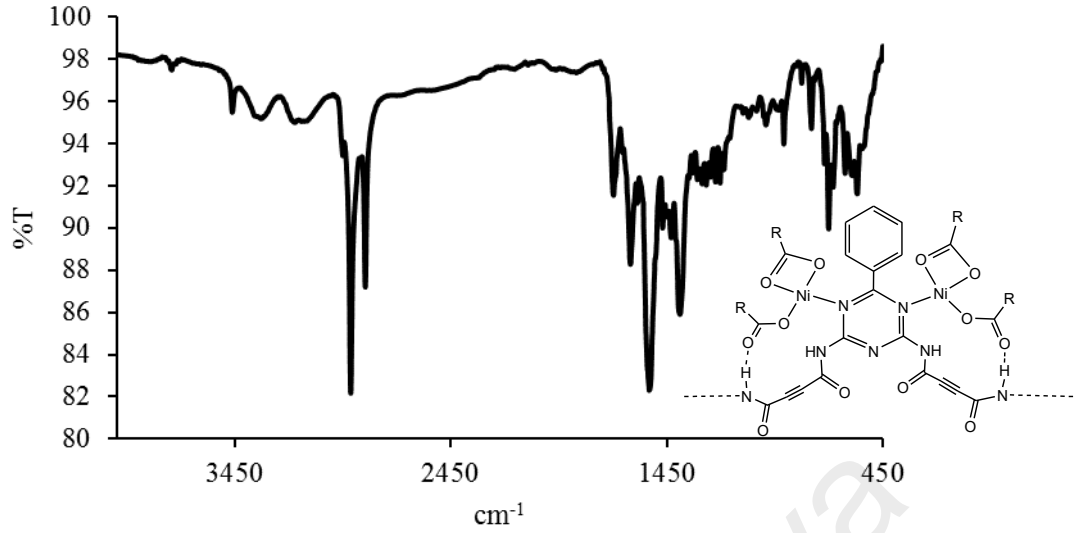

Figure 4.283 FTIR spectrum of **Complex 30**

Its **UV-vis** spectrum in DMSO (**Figure 4.284**) shows a small peak at 904 nm (ε_{max}, 247 M^{-1} cm^{-1}), assigned to $d_{xy} \rightarrow d_{x^2-y^2}$ transition; a broad peak at 624 nm (ε_{max}, 597 M^{-1} cm^{-1}), assigned to $d_{z^2} \rightarrow d_{x^2-y^2}$ transition; and a shoulder at 530 nm (ε_{max}, 523 M^{-1} cm^{-1}), assigned to $(d_{xz}, d_{yz}) \rightarrow d_{x^2-y^2}$ transition. These electronic transitions suggest a square planar geometry at Ni(II). An intense MLCT band is also observed at 250 nm (ε_{max}, 5579 M^{-1} cm^{-1}).

Its E_o value, calculated from λ_{edge} = 334 nm, was 3.7 eV. The value is similar to **Complex 26** ($\{[Ni_2(CH_3COO)_4(L4)]\}_n$; 3.8 eV).

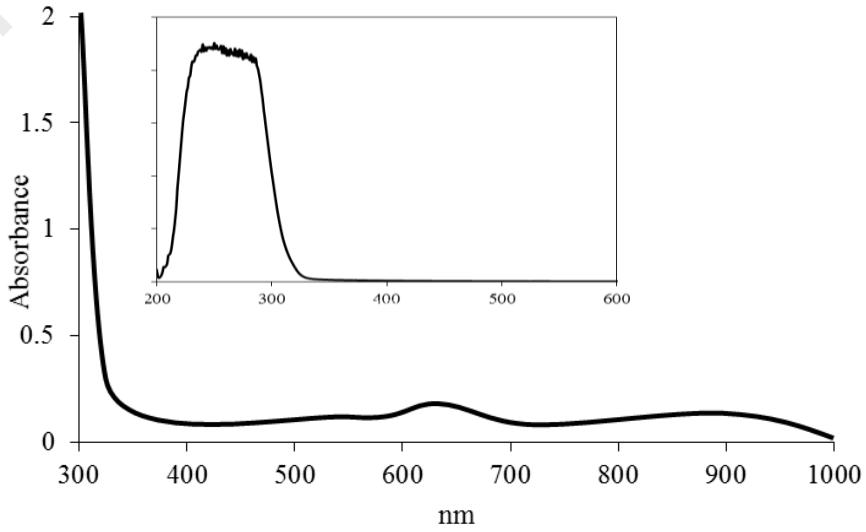

Figure 4.284 UV-vis spectrum of **Complex 30**

Upon excitation at 250 nm (MLCT transition), its **fluorescence** spectrum shows two overlapping peaks at λ_{max} 419 nm and 527 nm (**Figure 4.285)**. This suggests two different paths for the excited complex to return to the ground state. Its E_o value (calculated from λ_{edge} = 640 nm) was 1.9 eV. This is similar to **Complex 26** (1.9 eV). The value of its $\boldsymbol{\tau}$, calculated as before from its **decay** curve (**Figure 4.286**), was 2.6 ns. Additionally, its Stokes shift was 169 nm.

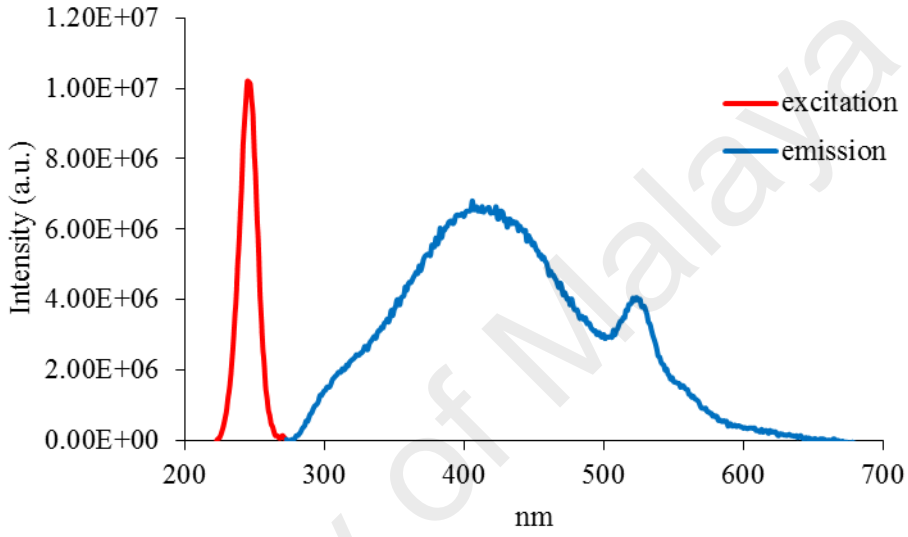

Figure 4.285 Fluorescence spectrum of **Complex 30** (λ_{ex} = 250 nm)

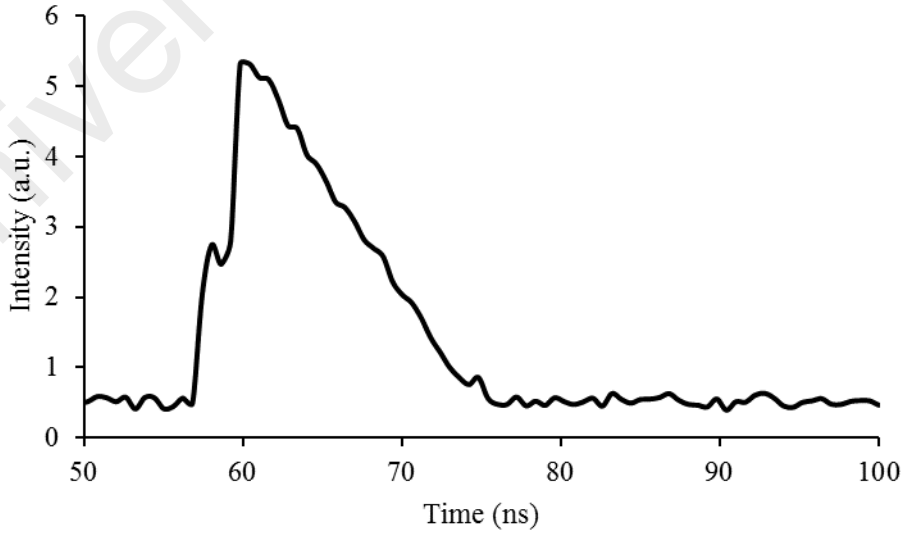

Figure 4.286 Fluorescence decay of **Complex 30**

However, upon excitation at 530 nm (*d-d* transition), its **fluorescence** spectrum shows three peaks at λ_{max} 555 nm, 557 nm, and 559 nm (**Figure 4.287)**. This suggests three different paths for the excited complex to return to the ground state. Its E_o, calculated from λ_{edge} = 560 nm, was 2.2 eV, and its τ, calculated as before from its **decay** curve, was 3.0 ns. Its Stokes shift was 25 nm.

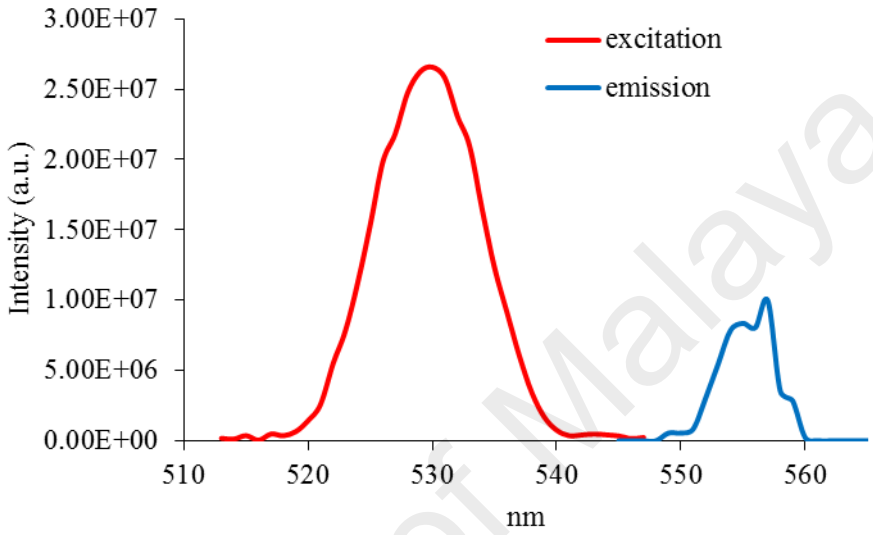

Figure 4.287 Fluorescence spectrum of **Complex 30**

Its **CV** (**Figure 4.288**) was recorded anodically from 0 V within the potential window of +1.5 V to -1.5 V. It showed two anodic peaks at +0.96 V and -0.23 V, but no cathodic peaks. The positive anodic peaks is assigned to the irreversible oxidation of [Ni(II)Ni(II)] to [Ni(II)Ni(III)]. Hence, its E_e cannot be calculated. Additionally, the negative anodic peak is assigned to the ligand-based oxidation process, which similarly observed for **Complexes 27** and **28**.

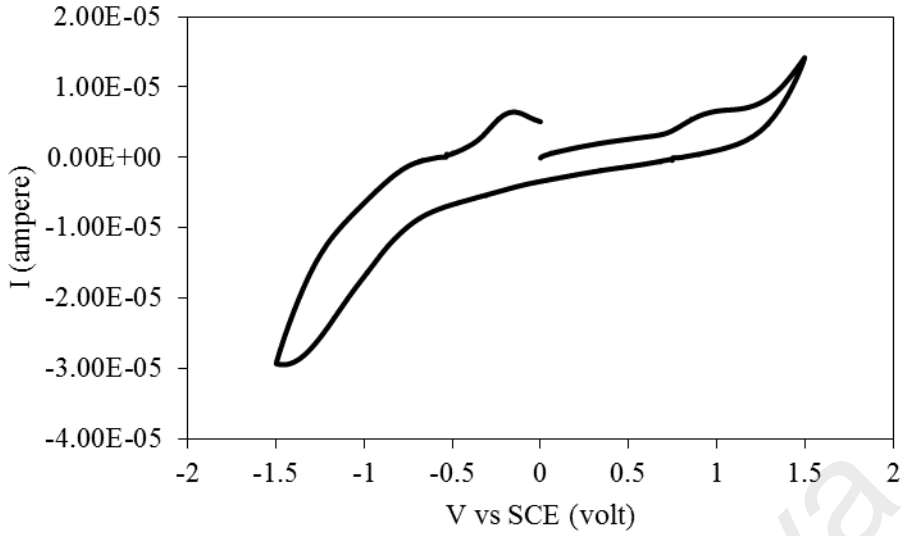

Figure 4.288 CV of **Complex 30**

Its $\boldsymbol{\mu_{eff}}$ value was 0, as χ_g value was negative (-0.8 x 10^{-7} cm^3 g^{-1}) at 298 K. Hence, the complex was diamagnetic. This indicates the geometry of the Ni(II) atoms in the polymeric chain was square planar [12].

Its **TGA** trace (**Figure 4.289**) shows the total weight loss of 92.1% in the temperature range of 196 – 654 °C, assigned to the decomposition of four $CH_3(CH_2)_{14}COO^-$ and *L4* ligands (expected, 91.7%). The amount of residue above 654 °C was 7.9% (expected, 8.3% assuming pure NiO). Hence, **Complex 30** (T_{dec} = 196 ^oC) was slightly more thermally stable than **Complex 26** ($\{[Ni_2(CH_3COO)_4(L4)]\}_n$; T_{dec} = 180 ^oC).

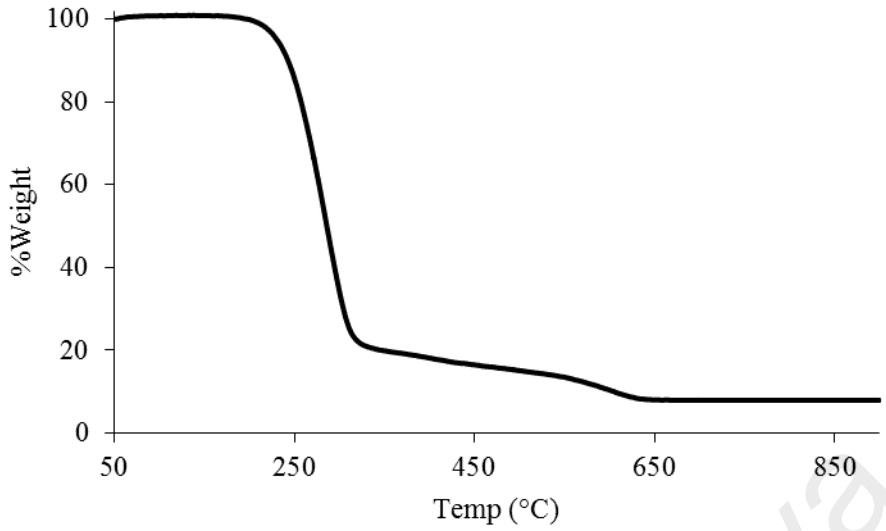

Figure 4.289 TGA of **Complex 30**

The **DSC** scan (**Figure 4.290**) was done for one heating-cooling cycle, in the temperature range 25 - 150 °C. On heating, there were two endothermic peaks at 57 °C (ΔH = +57.7 kJ mol^{-1}), assigned to Cr_1-to-Cr_2 transition, and at 86 °C (ΔH = +89.6 kJ mol^{-1}), assigned to Cr_2-to-M transition. On cooling, there were two overlapping exothermic peaks at 75 °C (ΔH_{comb} = -96.8 kJ mol^{-1}), assigned to M_2-to-M_1 transition and M_1-to-Cr_2 transition, and at 40 °C (ΔH = -20.3 kJ mol^{-1}), assigned to Cr_2-to-Cr_1 transition.

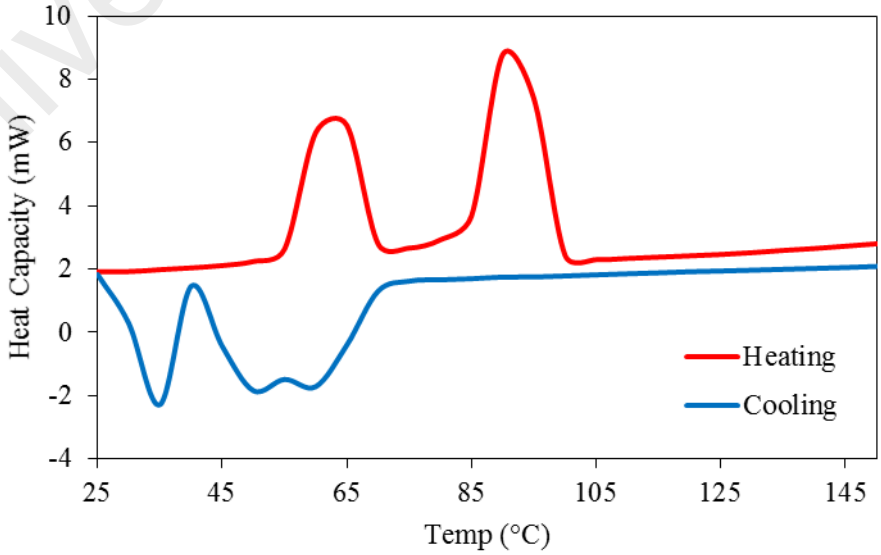

Figure 4.290 DSC of **Complex 30**

The **POM** for **Complex 30** was recorded for one heating-cooling cycle in the temperature range 25 – 150 ^{o}C. On cooling from 150 ^{o}C, an optical texture was observed at 105 ^{o}C, which grew slowly on further cooling to 84 ^{o}C (**Figure 4.291**). Hence, the complex has mesomorphic properties.

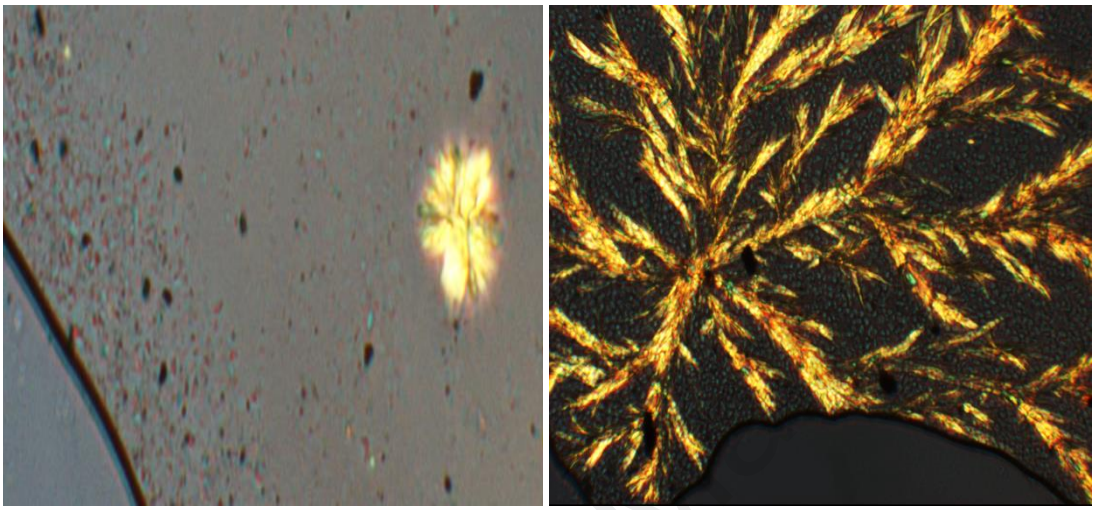

(a) (b)

Figure 4.291 The photomicrograph of **Complex 30** on cooling from 150 ^{o}C at: (a) 105 ^{o}C; and (b) 84 ^{o}C.

4.5.8 Reaction of cobalt(II) hexadecanoate with L4

Cobalt(II) hexadecanoate ($[Co(CH_3(CH_2)_{14}COO)_2(H_2O)_2].4H_2O$) reacted with *L4* (mole ratio 1:1) to give a purple powder (**Complex 31**), and the yield was 60.7%. Its solubility was similar to the previously discussed complexes.

The **elemental analytical** data for the complex (62.8% C; 8.7% H; 8.7% N) are in excellent agreement with those calculated for the repeat unit $CoC_{45}H_{73}N_5O_8$ (62.1% C; 8.5% H; 8.0% N; formula weight, 871.02 g mol^{-1}). Combining these with the spectroscopic data discussed below, the proposed structural formula of the complex is $\{[Co(CH_3(CH_2)_{14}COO)_2(L4)].2H_2O\}_n$, which is similar to **Complex 27** ($\{[Co(CH_3COO)_2(L4)].2H_2O\}_n$).

Its **FTIR** spectrum (**Table 4.12**; **Figure 4.292**) shows the presence of the expected functional groups. The ΔCOO value (136 cm^{-1}) suggests a chelating binding mode for $CH_3(CH_2)_{14}COO^-$ ligand.

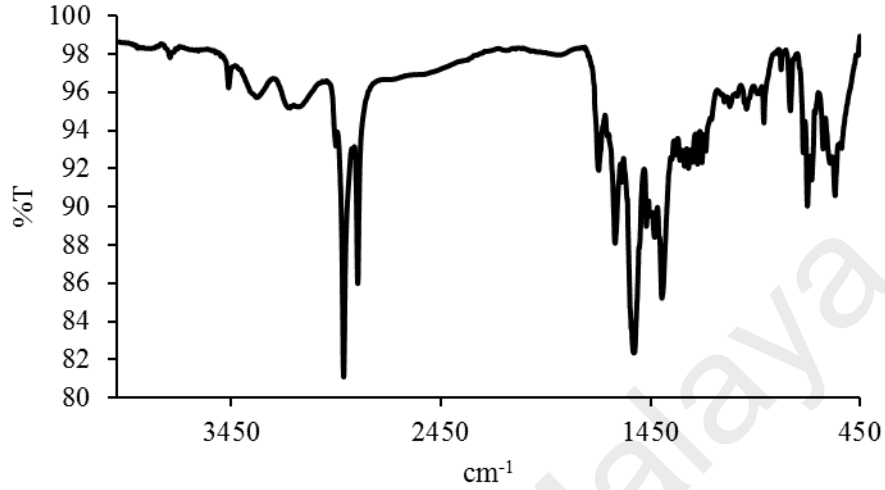

Figure 4.292 FTIR spectrum of **Complex 31**

Its **UV-vis** spectrum in DMSO (**Figure 4.293**) shows a *d-d* band at 655 nm (ε_{max}, 197.6 M^{-1} cm^{-1}) assigned to $^4T_{1g}$ (F) → $^4T_{2g}$ (F) transition, a broad overlapping band centred at 540 nm (ε_{max}, 196.1 M^{-1} cm^{-1}) assigned to $^4T_{1g}$ (F) → $^4T_{1g}$ (P) transition and $^4T_{1g}$ (F) → $^4A_{2g}$ (F) transitions. These suggest an octahedral geometry at HS Co(II) centres. Hence, the complex was made up of high-spin Co(II) centres. Additionally, an intense band is observed at 254 nm (ε_{max}, 3478 M^{-1} cm^{-1}), assigned to MLCT transition.

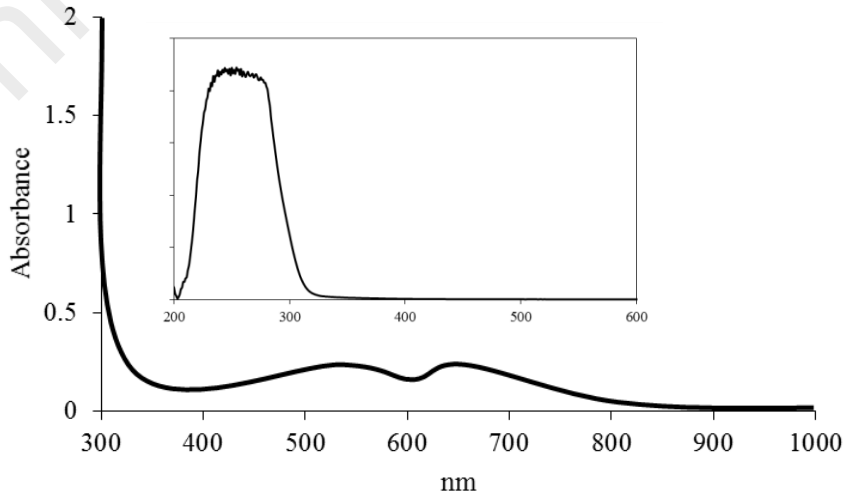

Figure 4.293 UV-vis spectrum of **Complex 31**

Its E_o value, calculated from λ_{edge} = 325 nm, was 3.8 eV. This value is similar to **Complex 27** ({[Co(CH_3COO)$_2$(L4))].2H_2O}$_n$; 3.7 eV).

Upon excitation at 254 nm (MLCT transition), its **fluorescence** spectrum shows two peaks at λ_{max} 330 nm, and 526 nm (**Figure 4.294)**. This suggests two different paths for the excited complex to return to the ground state. Its E_o value (calculated from λ_{edge} = 600 nm) was 2.0 eV. Additionally, its Stokes shift was 76 nm.

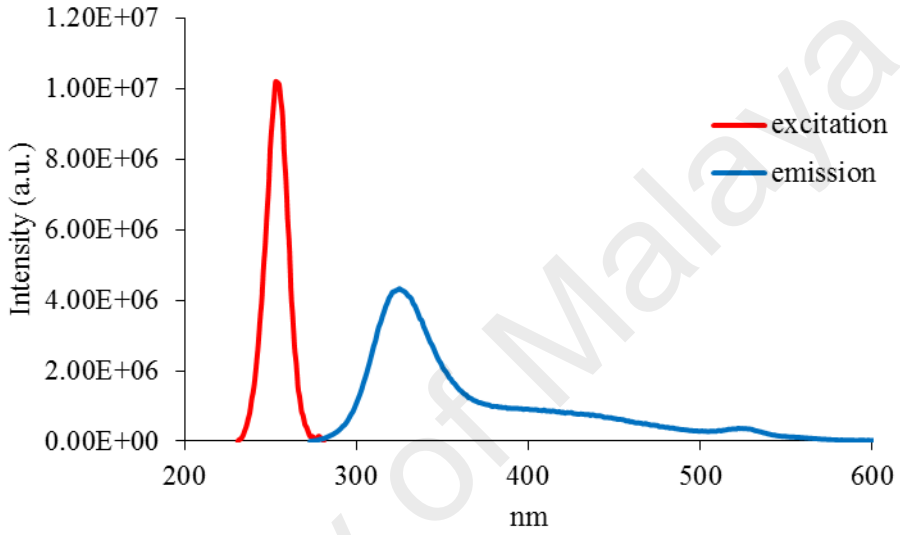

Figure 4.294 Fluorescence spectrum of **Complex 31** (λ_{ex} = 254 nm)

The value of its $\boldsymbol{\tau}$, calculated as before from its **decay** curve (**Figure 4.295**), was 2.8 ns. Hence, the excited state lifetime of the complex is slightly longer than **Complex 27** (2.6 ns).

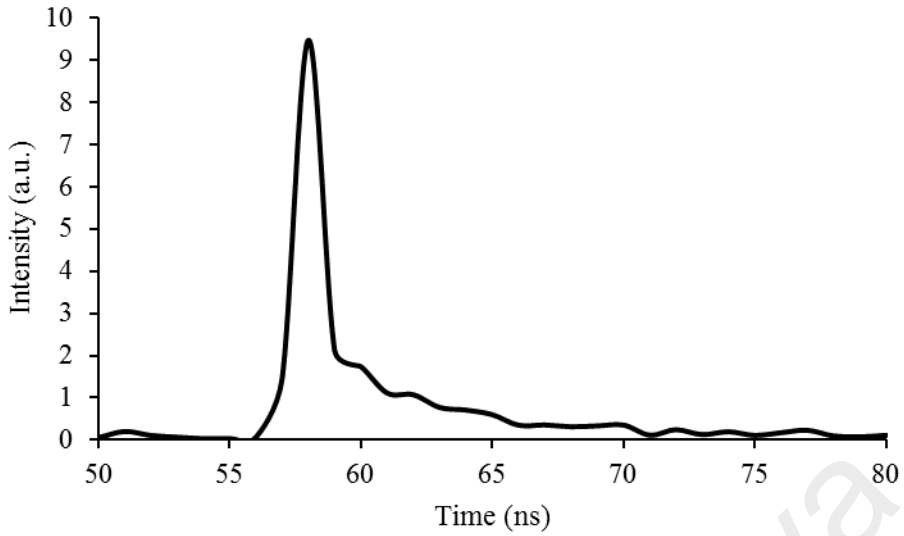

Figure 4.295 Fluorescence decay of **Complex 31**

Upon excitation at 540 nm (*d-d* transition), its **fluorescence** spectrum shows a peak at λ_{max} 552 nm **(Figure 4.306)**. Its E_o, calculated from λ_{edge} = 560 nm, was 2.2 eV, and its τ value, calculated from its **decay** curve, was 2.8 ns. Its Stokes shift was 12 nm.

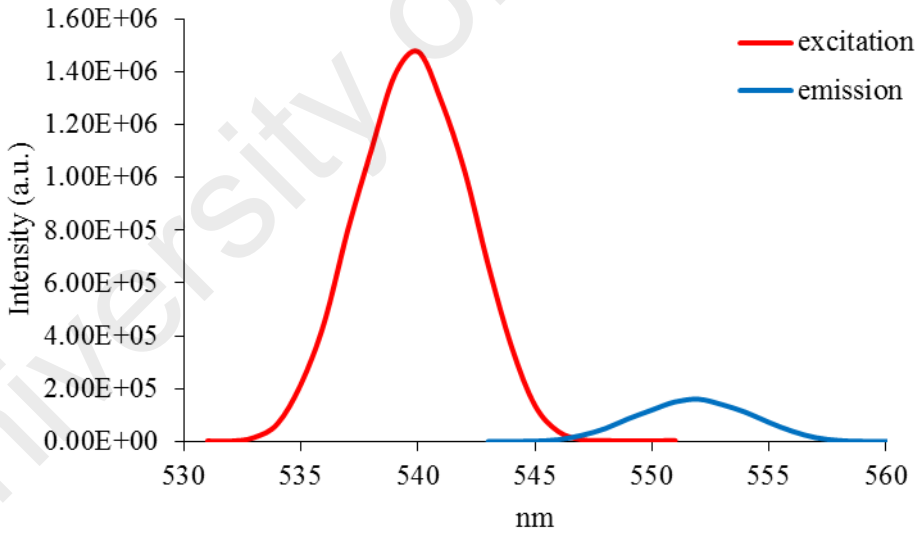

Figure 4.296 Fluorescence spectrum of **Complex 31** (λ_{ex} = 540 nm)

Its **CV** (**Figure 4.297**), recorded anodically from 0 V within the potential window of +1.5 V to -1.5 V, showed a broad anodic peak at about +0.93 V, but no cathodic peaks. The anodic peak is assigned to the oxidation of Co(II) to Co(III), which was irreversible. Accordingly, its E_e cannot be calculated.

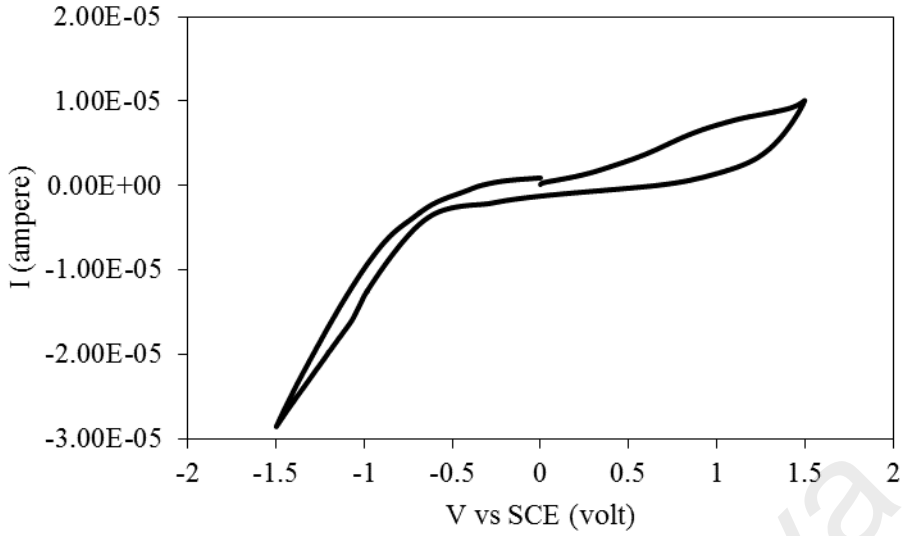

Figure 4.297 CV of **Complex 31**

Its μ_{eff} value, calculated as before from the values of FM = 871.02 g mol^{-1} (repeat unit) χ_g = 7.2 x 10^{-6} cm^3 g^{-1}, χ_M = 6.29 x 10^{-3} cm^3 mol^{-1}, and χ_{dia} = -5.15 x 10^{-4} cm^3 mol^{-1}, was 4.05 B.M. at 298 K. This is slightly higher than the expected value for a HS Co(II) complex (d^7) (3.87 B.M.), suggesting a ferromagnetic interaction between the Co(II) centres in the polymeric chain.

Its **TGA** trace (**Figure 4.298**) shows the total weight loss of 92.7% in the temperature range of 200 – 805 °C, assigned to the evaporation of two H_2O molecules, the decomposition of two $CH_3(CH_2)_{14}COO$ and *L4* ligands (expected, 93.2%). The amount of residue at temperatures above 805 ^oC was 7.3% (expected, 6.8% assuming pure CoO). Hence, **Complex 31** (T_{dec} = 200 ^oC) was slightly thermally more stable than **Complex 27** ({[Co($CH_3COO)_2$(L4))].2H_2O}$_n$; T_{dec} = 191 ^oC).

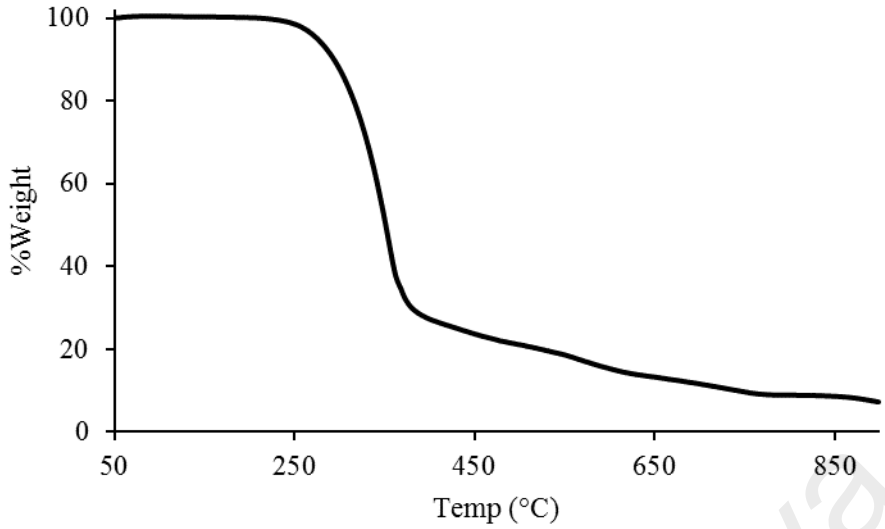

Figure 4.298 TGA of **Complex 31**

Its **DSC** scan (**Figure 4.299**) was done for one heating-cooling cycle, in the temperature range 25 - 150 ^{o}C. On heating, there were two overlapping endothermic peaks at 56 ^{o}C ($\Delta H_{combined}$ = +74.2 kJ mol^{-1}), assigned to the breaking of intermolecular van der Waals forces, Cr_1-to-Cr_2 and Cr_2-to-Cr_3 transitions. On cooling, there was an exothermic peak at 47.5 ^{o}C (ΔH = -54.7 kJ mol^{-1}), assigned to the Cr_3-to-Cr_1 transition.

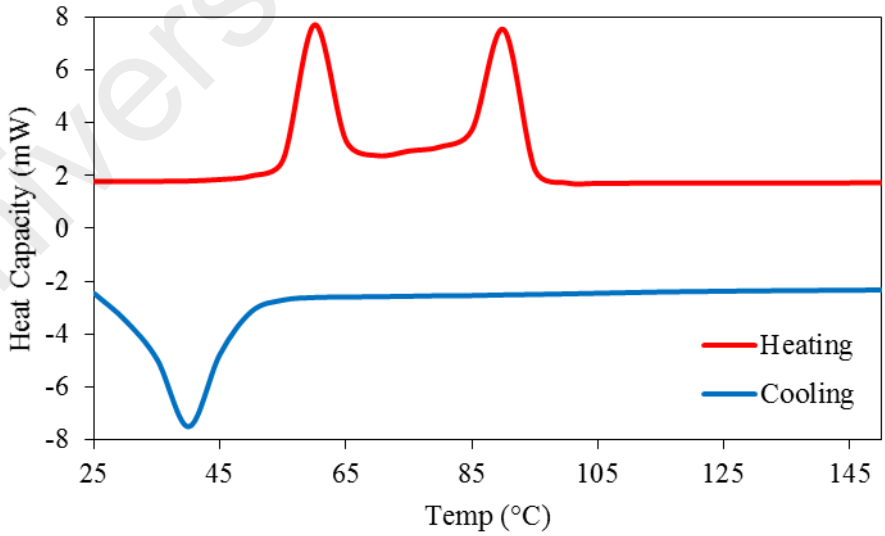

Figure 4.299 DSC of **Complex 31**

The P**OM** for **Complex 31** was recorded for two heating-cooling cycles in the temperature range 25 – 150 ^{o}C. However, the optical texture was not observed upon cooling process. It indicates that Complex 31 does not have liquid crystal properties.

4.5.9 Reaction of iron(II) hexadecanoate with L4

Iron(II) hexadecanoate ($[Fe(CH_3(CH_2)_{14}COO)_2(H_2O)_2].4H_2O$) reacted with *L4* (mole ratio 1:1) to give a brown powder (**Complex 32**), and the yield was 61.0%. Its solubility was similar to the previously-discussed complexes.

The results from the **elemental analyses** (64.9% C; 9.4% H; 5.3% N) are in excellent agreement with those calculated for the repeat unit $Fe_2C_{77}H_{135}N_5O_{12}$ (64.5% C; 9.5% H; 4.9% N; formula weight, 1434.61 g mol^{-1}). Combining these with the spectroscopic data discussed below, its proposed structural formula is $\{[Fe_2(CH_3(CH_2)_{14}COO)_4(L4)].2H_2O\}_n$, which is similar to **Complex 28** $\{[Fe_2(CH_3COO)_4(L4)].2H_2O\}_n$.

Its **FTIR** spectrum (**Table 4.12**; **Figure 4.300**) shows the presence of the expected functional groups. The ΔCOO value (121 cm^{-1}) suggests a chelating binding mode for $CH_3(CH_2)_{14}COO^-$ ligand.

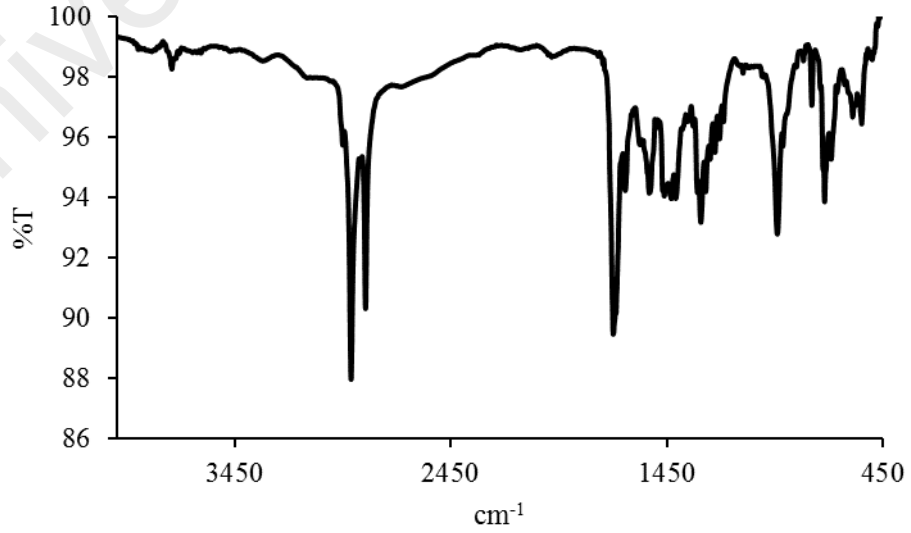

Figure 4.300 FTIR spectrum of **Complex 32**

Its **UV-vis** spectrum in DMSO (**Figure 4.301**) shows a broad band at 855 nm (ε_{max}= 283 M^{-1} cm^{-1}), assigned to $^5T_{2g} \rightarrow {}^5E_g$ electronic transition, a shoulder band at 371 nm (ε_{max}, 849 M^{-1} cm^{-1}), assigned to $n \rightarrow \pi^*$, and an intense MLCT band at 267 nm (ε_{max}, 1.4x10^4 M^{-1} cm^{-1}). This suggests an octahedral geometry at the HS Fe(II) centres.

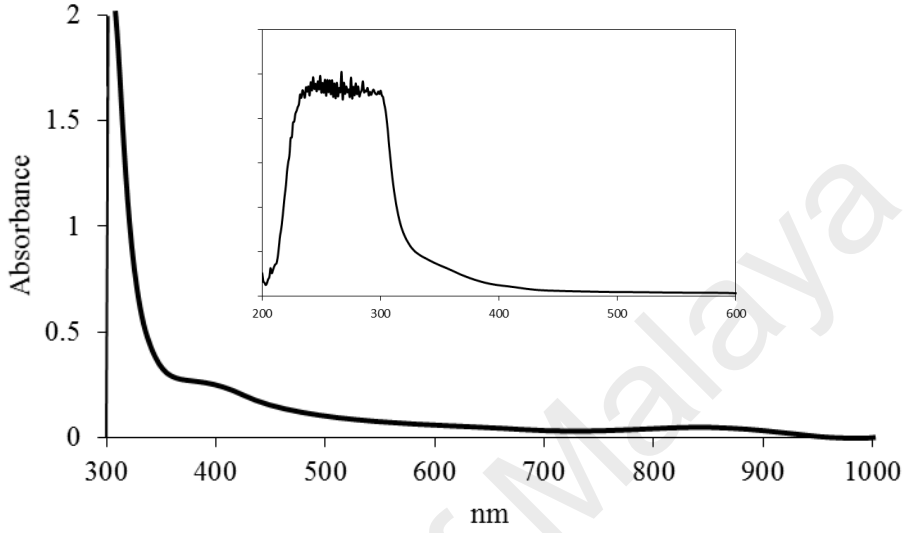

Figure 4.301 UV-vis spectrum of **Complex 32**

Its E_o value, calculated from λ_{edge} = 334 nm, was 3.7 eV. This value is similar to **Complex 28** ({$[Fe_2(CH_3COO)_4(L4)].2H_2O\}_n$; 3.6 eV).

Upon excitation at 267 nm (MLCT transition), its **fluorescence** spectrum shows three overlapping peaks at λ_{max} 454 nm, 549 nm and 630 nm (**Figure 4.302**). This suggests three different paths for the excited complex to return to the ground state. Its E_o value (calculated from λ_{edge} = 671 nm) was 1.8 eV. The Stokes shift value was 187 nm.

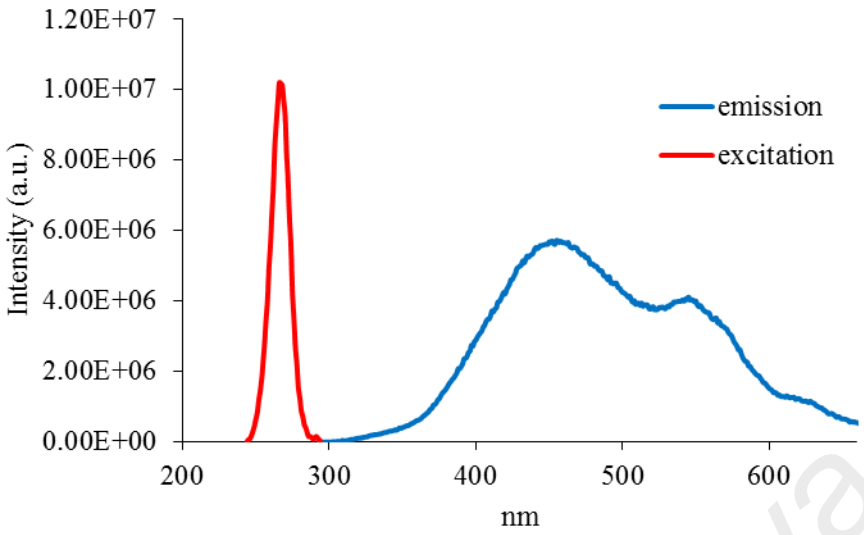

Figure 4.302 Fluorescence spectrum of **Complex 32** (λ_{ex} = 267 nm)

Its ***τ*** value, calculated as before from its **decay** curve (**Figure 4.303**), was 2.5 ns. Hence, the lifetime of excited complex was similar to **Complex 28** ($\{[Fe_2(CH_3COO)_4(L4)].2H_2O\}_n$; 2.6 ns).

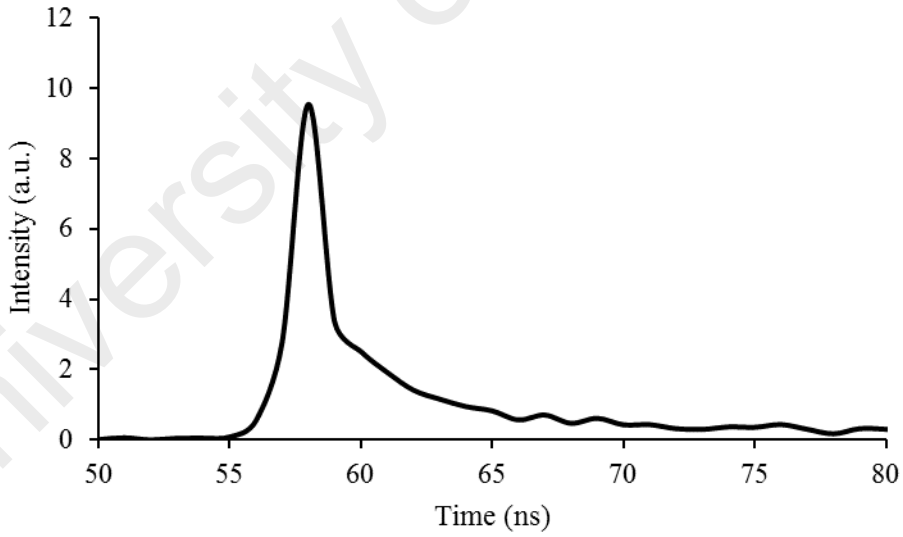

Figure 4.303 Fluorescence decay of **Complex 32**

Also, upon excitation at 855 nm (*d-d* transition), its **fluorescence** spectrum shows a peak at λ_{max} 888 nm (**Figure 4.304**). Its E_o, calculated from λ_{edge} = 895 nm, was 1.4 eV. This value was the same as **Complex 28** (1.4 eV). Its τ value, calculated as before from its **decay** curve, was 2.2 ns. It Stokes shift was 33 nm.

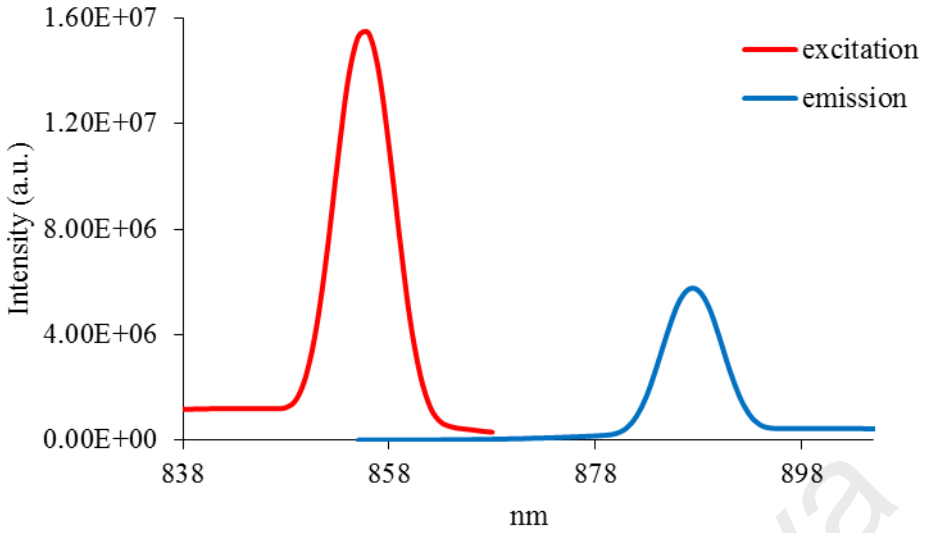

Figure 4.304 Fluorescence spectrum of **Complex 32** (λ_{ex} = 855 nm)

Its **CV** (**Figure 4.305**), recorded anodically from 0 V within the potential window of +1.5 V to -1.5 V, showed an anodic peak at +0.84 V and the corresponding cathodic peak at -0.16 V. These are assigned to the oxidation of [Fe(II)Fe(II)] to [Fe(II)Fe(III)], and the reduction of [Fe(III)Fe(II)] to [Fe(II)Fe(II)], respectively. Hence, the peak separation was ΔE_p = 1000 mV, indicating a quasireversible redox process.

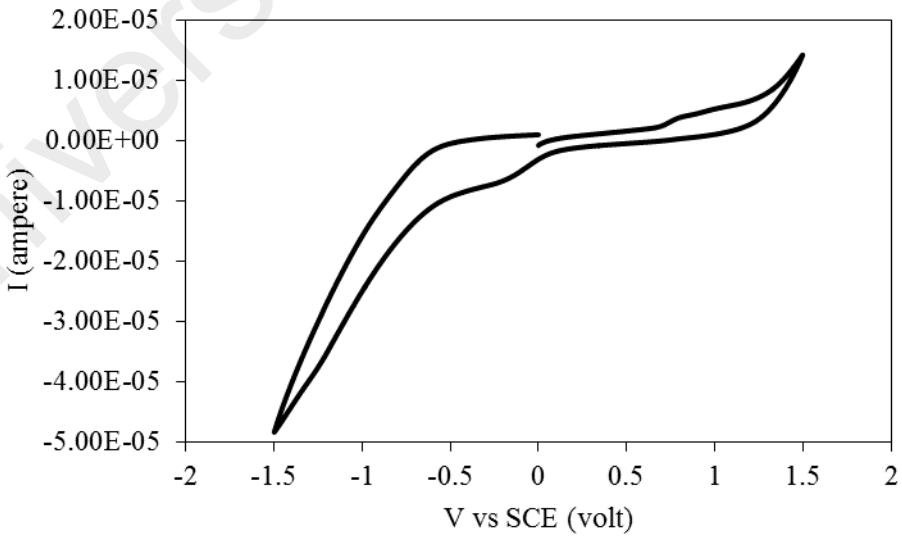

Figure 4.305 CV of **Complex 32**

The HOMO and LUMO values, calculated from the onset oxidation potential (+0.68 V) and onset reduction potential (-0.08 V), are 5.08 eV and 4.32 eV (versus SCE), respectively. Thus, its E_e was 0.76 eV.

Its μ_{eff} value, calculated as before from the values of FM = 1434.61 g mol^{-1} (repeat unit), χ_g = 1.25 x 10^{-5} cm^3 g^{-1}, χ_M = 1.79 x 10^{-2} cm^3 mol^{-1}, and χ_{dia} = -9.07 x 10^{-4} cm^3 mol^{-1}, was 6.71 B.M. at 298 K. The value is similar to the expected μ_{eff} value for a dinuclar HS Fe(II) complex (6.93 B.M). This indicates a negligible magnetic interaction between the Fe(II) centres in the polymeric chain.

Its **TGA** trace (**Figure 4.306**) shows the weight loss of 93.6% in the temperature range of 254 – 679 °C, assigned to the decomposition of four $CH_3(CH_2)_{14}COO$ and *L4* ligand (expected, 91.9%). The amount of residue above 679 °C is 6.4% (expected, 8.1% assuming pure FeO). Hence, **Complex 32** (T_{dec} = 254 °C) was much more thermally stable than **Complex 28** (T_{dec} = 183 °C).

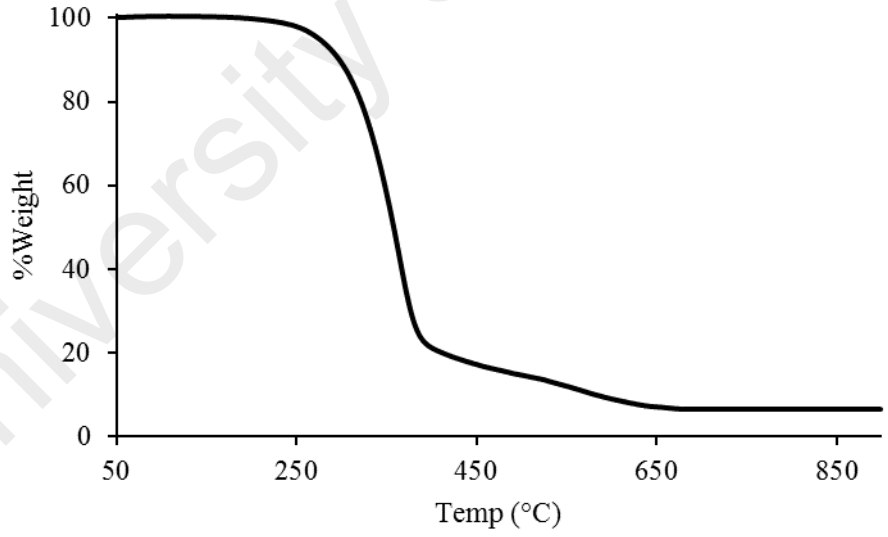

Figure 4.306 TGA of **Complex 32**

Its **DSC** scan (**Figure 4.307**) was recorded from 25 to 135 °C for one heating-cooling cycle. On heating, there were three endothermic peaks at 57.8 °C (ΔH = +169 kJ mol^{-1}), assigned to the breaking of intermolecular van der Waals forces

and Cr-to-M transition. On cooling, there was an exothermic peak at 41.1 °C (ΔH = -165 kJ mol^{-1}), assigned to M-to-Cr transition.

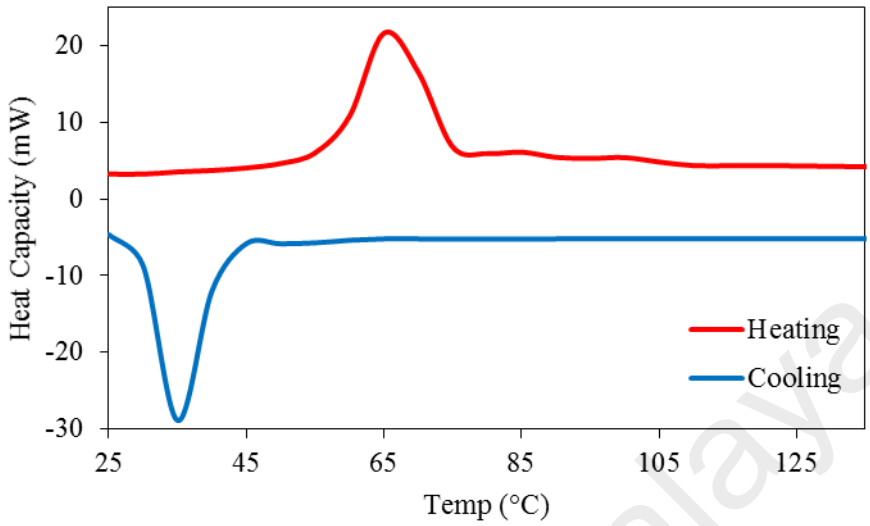

Figure 4.307 DSC of **Complex 32**

The **POM** for **Complex 32** was recorded for two heating-cooling cycles from 25 °C to 110 °C. On cooling from this temperature, it was observed the mesophase (optical texture) at 52 °C and continuously grow until 42 °C (**Figure 4.308**).

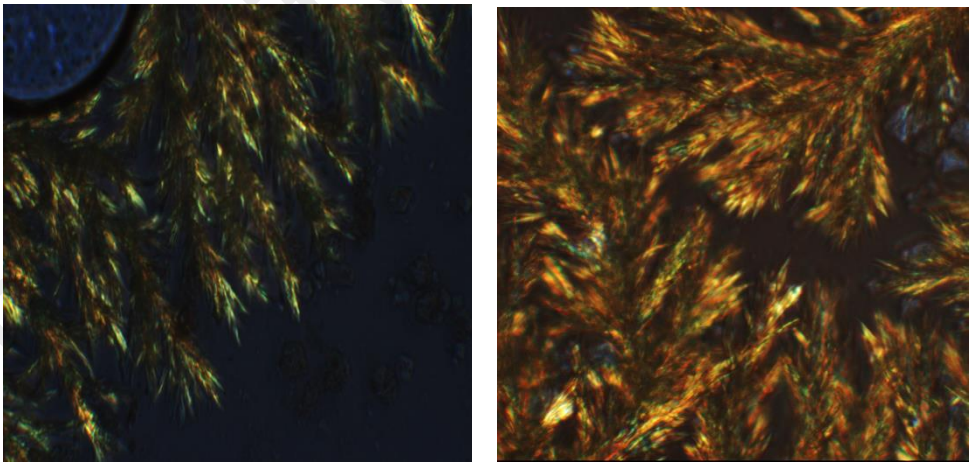

(a) (b)

Figure 4.308 The photomicrograph of **Complex 32** on cooling from 110 °C at (a) 52 °C, (b) 42 °C

4.5.10 Summary

To summarise, the chemical formula, bandgaps, magnetic and thermal data for these complexes are shown in **Table 4.13**.

Table 4.13 Summary of complexes with *L4*

Complex	Chemical Formula	Bandgap (eV)			τ (ns)	μ_{eff} (B.M.)	T_{dec} (^oC)	LC
		E_o (abs)	E_o (em)	E_e				
25	$\{[Cu(CH_3COO)_2(L4)]\}_n$	3.8	1.9	0.27	2.6	1.78	168	-
26	$\{[Ni_2(CH_3COO)_4(L4)]\}_n$	3.8	1.9	-	2.6	3.60	180	-
27	$\{[Co(CH_3COO)_2(L4))].2H_2O\}_n$	3.7	1.9	-	2.7	4.31	191	-
28	$\{[Fe_2(CH_3COO)_4(L4)].2H_2O\}_n$	3.6	1.9	-	2.6	7.04	183	-
29	$\{[Cu(CH_3(CH_2)_{14}COO)_2(L4)]\}_n$	3.8	1.9	0.37	2.6	1.80	200	M
30	$\{[Ni_2(CH_3(CH_2)_{14}COO)_4(L4)]\}_n$	3.7	1.9	-	2.6	-	196	M
31	$\{[Co(CH_3(CH_2)_{14}COO)_2(L4)].2H_2O\}_n$	3.8	1.9	-	2.8	4.05	200	-
32	$\{[Fe_2(CH_3(CH_2)_{14}COO)_4(L4)].2H_2O\}_n$	3.7	1.8	0.76	2.5	6.71	254	M

M = mesomorphic

All complexes were polymers. The repeat units for the ethanoato and hexadecanoato complexes of Cu(II) and Co(II) were mononuclear, while those of Ni(II) and Fe(II) were dinuclear.

The optical bandgaps for all complexes were similar (3.6 eV– 3.8 eV from absorption spectroscopy and 1.8 eV – 2.0 eV from emission spectroscopy). The electrochemical bandgaps could only be calculated for Cu(II) complexes and hexadecanoate complex of Fe(II) as other complexes were either redox inactive or irreversibly oxidised. The electrochemical bandgaps for Cu(II) complexes were lower than for Fe(II) complex, as previously observed and maybe similarly explained.

The lifetimes of all of the excited complexes were similar (2.5 – 2.8 ns). This is consistent with the similar values of the bandgaps from the emission bands for all of the above complexes

The Stokes shift for all complexes are in the range 76 – 220 nm (CT transition), and 4 – 33 nm (*d-d* transition). These values are also consistent with bandgaps from absorption and emission.

Except **Complex 30**, which was diamagnetic, all of the above complexes are paramagnetic. The Cu(II) complexes showed a negligible interactions between the metal centres, while the Ni(II) ethanoato complex showed a weak antiferromagnetic interaction between the metal centres. Both Co(II) and Fe(II) complexes were high-spin.

All complexes were thermally stable. Their decomposition temperatures ranged from 168 ^{o}C to 254 ^{o}C. Finally, Cu(II), Ni(II), and Fe(II) hexadecanoate complexes were mesomorphic, while Co(II) hexadecanoate complex was not liquid crystal.

Reference

[1] Deacon, G. B., Phillips, R. J., *Coordination Chemistry Reviews*, 33 (**1980**) 227-250.

[2] Gurumoorthy, P., Ravichandran, J., Rahiman, A. K., *Journal of Chemical Science* (Bangalore, India), 126 (**2014**) 783-792.

[3] Leovac, V. M., Češljević, V. I., Vojinović-Ješić, L. S., Divjaković, V., Jovanović, L. S., Szécsényi, K. M., Rodić, M. V., *Polyhedron*, 28 (**2009**) 3570-3576.

[4] Rychlewska, U., Radanović, D. D., Dimitrijević, M. D., Ristanović, D. M., Vasojević, M. M., Radanović, D. J., *Polyhedron*, 20 (**2001**) 2523-2530.

[5] Banciu, A. C., *Review Roumania Chimica*, 43 (**1998**) 935-940.

[6] Wang, Y., Ramos, I., Santiago-Avilés, J. J., *Journal of Applied Physics*, 102 (**2007**).

[7] Oliveira, E. C., Deflon, E., Machado, K. D., Silva, T. G., Mangrich, A. S., *Journal of Physics: Condensed Matter*, 24 (**2012**) 115802.

[8] Rasid, A. A., Wagiran, H., Hashim, S., Hussin, R., Ibrahim, Z., *Advanced Materials Research* (Durnten-Zurich, Switz.), 895 (**2014**) 194-199, 197 pp.

[9] Karthikeyan, S., Rajendiran, T. M., Kannappan, R., Mahalakshmy, R., Venkatesan, R., Rao, P. S., *Journal of Chemical Science*, 113 (**2001**) 245-256.

[10] Mohamadin, M., Abdullah, N., *Centre European Journal of Chemistry*, 8 (**2010**) 1090-1096.

[11] Abdullah, N., Al-Hakem, Y., Abdullah, N., Samsudin, H., Tajidi, N. S. A., *Asian Journal of Chemistry*, 26 (**2014**) 897-990.

[12] Kahn, O., *Molecular Magnetism*, VCH Publisher, Inc., USA, 1993.

[13] Szlyk, E., Surdykowski, A., Barwiolek, M., Larsen, E., *Polyhedron*, 21 (**2002**) 2711-2717.

[14] Garg, B. S., Sharma, R. K., Kundra, E., *Transition Metal Chemistry*, 30 (**2005**) 552-559.

[15] Badea, M., Emandi, A., Marinescu, D., Cristurean, E., Olar, R., Braileanu, A., Budrugeac, P., Segal, E., *Journal of Thermal Analysis and Calorimetry*, 72 (**2003**) 525-531.

[16] Joseyphus, R. S., Nair, M. S., *Arabian Journal of Chemistry*, 3 (**2010**) 195-204.

[17] Kulkarni, A. D., Patil, S. A., Badami, P. S., *International Journal of Electrochemical Science*, 4 (**2009**) 717-729.

[18] Melson, G. A., Crawford, N. P., Geddes, B. J., *Inorganic Chemistry*, 9 (**1970**) 1123-1126.

[19] Ferenc, W., Walków-Dziewulska, A., Sarzynski, J., Paszkowska, B., *Eclética Química*, 31 (**2006**) 53-59.

[20] Narayanan, J., Solano-Peralta, A., Ugalde-Saldivar, V. M., Escudero, R., Höpfl, H., Sosa-Torres, M. E., *Inorganica Chimica Acta*, 361 (**2008**) 2747-2758.

[21] Weber, B., Betz, R., Bauer, W., Schlamp, S., *Zeitschrift für anorganische und allgemeine Chemie*, 637 (**2011**) 102-107.

[22] Cheng, C., Reiff, W. M., *Inorganic Chemistry*, 16 (**1977**) 2097-2103.

[23] Delley, B., *The Journal of Chemical Physics*, 113 (**2000**) 7756-7764.

[24] Decurtins, S., Gutlich, P., Hasselbach, K. M., Hauser, A., Spiering, H., *Inorganic Chemistry*, 24 (**1985**) 2174-2178.

[25] Weber, B., Bauer, W., Pfaffeneder, T., Dîrtu, M. M., Naik, A. D., Rotaru, A., Garcia, Y., *European Journal of Inorganic Chemistry*, 2011 (**2011**) 3193-3206.

[26] van Niekerk, J. N., Schoening, F. R. L., *Acta Crystallographica*, 6 (**1953**) 227-232.

[27] Sathyanarayana, D. N., *Electronic Absorption Sepctroscopy and Related Techniques*, Universities Press (india) limited, Hyderabad, India, 2001.

[28] Jenniefer, S., Muthiah, P., *Chemistry Central Journal*, 7 (**2013**) 1-15.

[29] Paredes-García, V., Santana, R. C., Madrid, R., Vega, A., Spodine, E., Venegas-Yazigi, D., *Inorganic Chemistry*, 52 (**2013**) 8369-8377.

[30] Li, H., Yao, H., Zhang, E., Jia, Y., Hou, H., Fan, Y., *Dalton Transactions*, 40 (**2011**) 9388-9393.

[31] Carvalho, C. T., Siqueira, A. B., Rodrigues, E. C., Ionashiro, M., *Eclética Química*, 30 (**2005**) 19-26.

[32] Siqueira, A. B., Ionashiro, E. Y., Carvalho, C. T. D., Bannach, G., Rodrigues, E. C., Ionashiro, M., *Química Nova*, 30 (**2007**) 318-322.

[33] Shanmuga kala, R., Tharmaraj, P., Sheela, C. D., *Synthesis and Reactivity in Inorganic, Metal-Organic, and Nano-Metal Chemistry*, 44 (**2014**) 1487-1496.

[34] Gudasi, K. B., Patil, S. A., Vadavi, R. S., Shenoy, R. V., Patil, M. S., *Journal of Serbian Chemical Society*, 71 (**2006**) 529–542.

[35] Romero-Tela, E., Mendoza, M. E., Escudero, R., *Journal of Physics: Condensed Matter*, 24 (**2012**) 196003.

[36] Lloret, F., Julve, M., Cano, J., Ruiz-García, R., Pardo, E., *Inorganica Chimica Acta*, 361 (**2008**) 3432-3445.

[37] Sakiyama, H., *Inorganica Chimica Acta*, 359 (**2006**) 2097-2100.

[38] Long, G. J., Baker, W. A., *Journal of the Chemical Society A: Inorganic, Physical, Theoretical*, (**1971**) 2956-2959.

[39] Miller, J. S., Calabrese, J. C., Rommelmann, H., Chittipeddi, S. R., Zhang, J., Reiff, W. M., Epstein, A. J., *Journal of the American Chemical Society*, 109 (**1987**) 769-781.

[40] Smith, S. E., Yang, J. Y., DuBois, D. L., Bullock, R. M., *Angewandte Chemie International Edition*, 51 (**2012**) 3152-3155.

[41] Rosenberg, R. C., Root, C. A., Gray, H. B., *Journal of the American Chemical Society*, 97 (**1975**) 21-26.

[42] Nasr-Esfahani, M., Zendehdel, M., Yaghoobi Nia, N., Jafari, B., Babadi, M. K., *RSC Advances*, 4 (**2014**) 15961-15967.

[43] Caneschi, A., Dei, A., Gatteschi, D., Tangoulis, V., *Inorganic Chemistry*, 41 (**2002**) 3508-3512.

[44] Sanselme, M., Greneche, J. M., Riou-Cavellec, M., Ferey, G., *Chemical Communications*, (**2002**) 2172-2173.

[45] Kumagai, H., Oka, Y., Inoue, K., Kurmoo, M., *Journal of the Chemical Society*, (**2002**) 3442-3446.

CHAPTER 5 CONCLUSIONS AND SUGGESTIONS FOR FUTURE WORKS

5.1 Conclusions

Thirty-two (32) complexes of Cu(II), Ni(II), Co(II), and Fe(II) were successfully obtained by step-wise syntheses, and their structures, bandgap, lifetime, thermal, and mesomorphic properties determined. All complexes were obtained in good yields (60 – 98%). The chemical formulae of these complexes are shown in **Table 5.1**, **5.2**, **5.3** and **5.4**.

Table 5.1 Chemical formulae of *L1* complexes

Complex	Chemical Formula
1	$[Cu_2(CH_3COO)_2(H_2O)_2(L1)]$
2	$[Ni_2(CH_3COO)_2(H_2O)_2(L1)]$
3	$[Co_2(CH_3COO)_2(H_2O)_2(L1)]$
4	$[Fe_3(CH_3COO)_4(H_2O)_3(L1)].H_2O$
5	$[Cu_2(CH_3(CH_2)_{14}COO)_2(L1)]$
6	$[Ni_2(CH_3(CH_2)_{14}COO)_2(H_2O)_2(L1)]$
7	$[Co_2(CH_3(CH_2)_{14}COO)_2(H_2O)_2(L1)]$
8	$[Fe_2(CH_3(CH_2)_{14}COO)_2(H_2O)_2(L1)]$

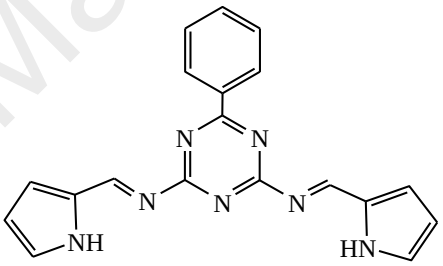

H_2L1

Except **Complex 4**, which was a trinuclear Fe(II) complex, all other complexes with *L1* were dinuclear. The optical bandgaps from the CT absorption bands and lifetimes for all complexes were similar (3.4 eV– 3.9 eV; 2.7 – 3.1 ns). This is consistent with the similar values of the bandgaps from the emission bands for all complexes (1.8 eV – 2.1 eV). The electrochemical bandgap can only be calculated for Cu(II) (0.2 eV) and Fe(II) (1.09 eV) complexes since the Ni(II) and Co(II) complexes were redox inactive. All complexes were paramagnetic and thermally stable (T_{dec} ~ 199 – 245 ^oC), and all hexadecanoate complexes (R' = $CH_3(CH_2)_{14}COO$) were mesomorphic.

Table 5.2 Chemical formulae of *L2* complexes

Complex	Chemical Formula
9	$\{[Cu(CH_3COO)_2(L2)].H_2O\}_n$
10	$\{[Ni(CH_3COO)_2(L2)].2H_2O\}_n$
11	$\{[Co(CH_3COO)_2(L2)].2H_2O\}_n$
12	$\{[Fe(CH_3COO)_2(L2)].2H_2O\}_n$
13	$\{[Cu(CH_3(CH_2)_{14}COO)_2(L2)].H_2O\}_n$
14	$\{[Ni(CH_3(CH_2)_{14}COO)_2(L2)].2H_2O\}_n$
15	$\{[Co(CH_3(CH_2)_{14}COO)_2(L2)].2H_2O\}_n$
16	$\{[Fe(CH_3(CH_2)_{14}COO)_2(L2)].2H_2O\}_n$

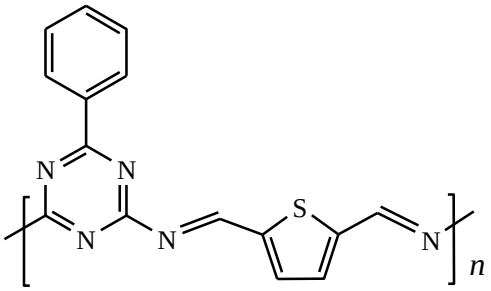

L2

All complexes with *L2* were made of mononuclear repeat units, and paramagnetic. The optical bandgaps from the CT absorption bands for all complexes were similar (3.5 eV– 3.8 eV). The lifetimes of the excited complexes were in the range of 2.8 – 3.8 ns. The electrochemical bandgap can be obtained for **Complex 9** (Cu(II) complex; 0.47 eV) only since Ni(II), Co(II) and Fe(II) complexes were redox inactive. All complexes were thermally stable (T_{dec} ~ 160 - 231 ^oC), and only Ni(II) and Fe(II) hexadecanoate complexes ($CH_3(CH_2)_{14}COO$) are mesomorphic.

Table 5.3 Chemical formulae of *L3* complexes

Complex	Chemical Formula
17	$\{[Cu(CH_3COO)_2(L3)]\}_n$
18	$\{[Ni_2(CH_3COO)_4(L3)].5H_2O\}_n$
19	$\{[Co(CH_3COO)_2(L3)].2H_2O\}_n$
20	$\{[Fe_2(CH_3COO)_4(L3)].2H_2O\}_n$
21	$\{[Cu_2(CH_3(CH_2)_{14}COO)_4(L3)].2H_2O\}_n$
22	$\{[Ni_2(CH_3(CH_2)_{14}COO)_4(L3)]\}_n$
23	$\{[Co(CH_3(CH_2)_{14}COO)_2(L3)]\}_n$
24	$\{[Fe(CH_3(CH_2)_{14}COO)_2(L3)].3H_2O\}_n$

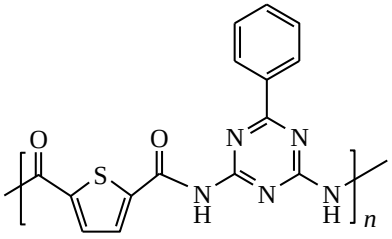

L3

Complexes of Cu(II), Ni(II), Co(II), and Fe(II) with *L3* were made up of either mononuclear or dinuclear repeat units. All complexes were paramagnetic. The optical

bandgaps from the CT absorption bands for all complexes (except **Complex 20**) were similar (3.3 eV– 3.7 eV). **Complex 20** $\{[Fe_2(CH_3COO)_4(L3)].2H_2O\}_n$, has a lower optical bandgap (2.2 eV). The bandgaps from the emission bands for all complexes and lifetimes of all excited complexes were similar (1.9 eV – 2.1 eV; 2.7 – 3.0 ns). All complexes were thermally stable (T_{dec} ~ 180 - 238 ^oC), and Cu(II), Ni(II), and Fe(II) hexadecanoate complexes were mesomorphic.

Table 5.4 Chemical formulae of *L4* complexes

Complex	Chemical Formula
25	$\{[Cu(CH_3COO)_2(L4)]\}_n$
26	$\{[Ni_2(CH_3COO)_4(L4)]\}_n$
27	$\{[Co(CH_3COO)_2(L4))].2H_2O\}_n$
28	$\{[Fe_2(CH_3COO)_4(L4)].2H_2O\}_n$
29	$\{[Cu(CH_3(CH_2)_{14}COO)_2(L4)]\}_n$
30	$\{[Ni_2(CH_3(CH_2)_{14}COO)_4(L4)]\}_n$
31	$\{[Co(CH_3(CH_2)_{14}COO)_2(L4)].2H_2O\}_n$
32	$\{[Fe_2(CH_3(CH_2)_{14}COO)_4(L4)].2H_2O\}_n$

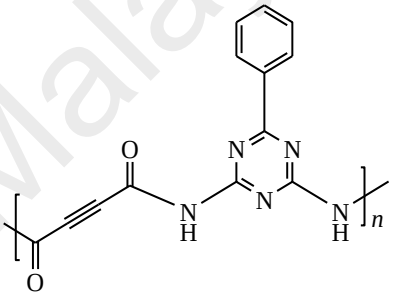

L4

Lastly, complexes of Cu(II) and Co(II) with *L4* were made up of mononuclear repeat units, while complexes of Ni(II) and Fe(II) were made up of dinuclear repeat units. The optical bandgaps from the CT absorption bands, lifetimes and bandgaps from the emission bands for all complexes were similar (3.6 eV– 3.8 eV; 2.5 – 2.8 ns; 1.8 eV – 2.0 eV). Except for **Complex 30** which was diamagnetic, all other complexes were paramagnetic. All complexes were thermally stable (T_{dec} ~ 168 - 254 ^oC), and all hexadecanoate complexes (R' = $CH_3(CH_2)_{14}COO$) were mesomorphic.

5.2 Suggestion for Future Work

The complexes in this research were prepared by using metal(II) acetates and hexadecanoates. It would be interesting to compare their properties with ionic metal(II)

complexes of the same ligands, using non-coordinating counteranions such as BF_4^- ion. This would also increase their solubility in polar solvents.

It would also be interesting to use branched alkylcarboxylate ions as ligands, such as 2-hexyldecanoate ion, to form complexes with low melting temperatures in order to save thermal energy and reduce decomposition, and to use ligands with more extensive conjugations, such as shown in **Figure 5.1**, to form complexes with lower bandgap values.

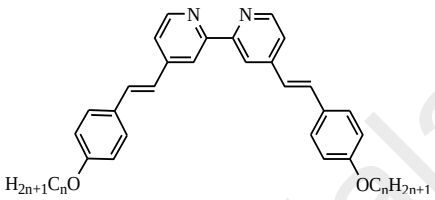

Figure 5.1 A conjugated ligand

The mesomorphisms of complexes prepared in this research may be further ascertained by low angle variable-temperature PXRD [1].

In addition, other potential applications of these complexes may be studied. Examples are as spin crossover (SCO) materials in sensor and memory devices, and in thermoelectricity (a phenomena in which a temperature difference create an electric potential or an electric potential creates a temperature difference) [2]. This may lead to numerous electric and electrical applications, such as thermoelectric cooling of microelectronic products [3], thermoelectric converter for energy conservation, wireless sensor, photon sensing devices and in waste-heat recovery [4].

References

[1] Hayami, S., Kojima, Y., Urakami, D., Ohta, K., Inoue, K., *Polyhedron*, 28 (**2009**) 2053-2057.

[2] Gural'skiy, I. A., Quintero, C. M., Costa, J. S., Demont, P., Molnar, G., Salmon, L., Shepherd, H. J., Bousseksou, A., *Journal of Materials Chemistry C*, 2 (**2014**) 2949-2955.

[3] Kalyanasundaram, K., Grätzel, M., *Coordination Chemistry Reviews*, 177 (**1998**) 347-414.

[4] Tritt, T. M., *Annual Review of Materials Research*, 41 (**2011**) 433-448.